

# *thin Solid films*

*International Journal  
on the Science and  
Technology of  
Condensed Matter  
Films*

Papers presented at the 2nd International Atomic Layer Epitaxy Symposium, Raleigh, NC, USA, June 2-5, 1992

*Guest Editor: Professor Salah M. Bedair*

This document has been approved  
for public release and sale; its  
distribution is unlimited.



*Elsevier Sequoia*

*Editor-in-chief:  
J. E. Greene*

# THIN SOLID FILMS

## Editor-In-Chief

J. E. Greene, University of Illinois at Urbana, Coordinated Science Laboratory, 1101 West Springfield Avenue, Urbana, IL 61801, USA.

## EDITORIAL BOARD

C. J. Adkins (*Cambridge, UK*)  
L. N. Aleksandrov (*Novosibirsk, Minsk*)  
D. E. Aspnes (*Red Bank, NJ, USA*)  
P. B. Barna (*Budapest, Hungary*)  
J.-O. Carlsson (*Uppsala, Sweden*)  
P. J. Dobson (*Oxford, UK*)  
H. Fuchs (*Ludwigshafen, Germany*)  
F. M. d'Heurle (*Yorktown Heights, NY, USA*)  
S. Hofmann (*Stuttgart, Germany*)  
A. Hugot-Le Goff (*Paris, France*)  
A. Kinbara (*Tokyo, Japan*)

M. Kitabatake (*Osaka, Japan*)  
A. E. T. Kuiper (*Eindhoven, The Netherlands*)  
A. Lopez-Otero (*Stanford, CA, USA*)  
P. J. Martin (*Lindfield, Australia*)  
J. W. Mayer (*Ithaca, NY, USA*)  
J. H. van der Merwe (*Pretoria, South Africa*)  
S. Nakahara (*Murray Hill, NJ, USA*)  
B. E. Nieuwenhuys (*Leiden, The Netherlands*)  
A. K. Pal (*Calcutta, India*)  
J. R. Sambles (*Exeter, UK*)  
W. Scharff (*Chemnitz, Germany*)  
I. Schuller (*La Jolla, CA, USA*)  
M. Sugi (*Tsukuba, Japan*)  
R. H. Tredgold (*Lancaster, UK*)  
R. W. Vook (*Syracuse, NY, USA*)  
W. D. Westwood (*Ottawa, Ont., Canada*)  
J. N. Zemel (*Philadelphia, PA, USA*)

## Types Of Contributions

- original papers not previously published
- review articles
- letters, 1800-2500 words
- announcements, reports on conferences, news

## Sections

The journal is divided into the following sections.

- Synthesis and Characterization:** nucleation and growth from the gas, liquid and solid phases; microstructural and microchemical film characterization; new concepts and techniques for film synthesis, modification, processing and characterization.
- Surfaces, Interfaces and Colloidal Behaviour:** surface and interface phenomena: physics, chemistry and applications.
- Metallurgical, Protective and Hard Layers:** fundamental aspects of layers and coatings used in diffusion barrier, corrosion, high-temperature, wear, erosion, and other extreme environments.
- Mechanics and Nanomechanics of Thin Layers:** mechanical properties of thin layers and nanoscale structures; surface forces; micro- and nanoengineering.
- Electronics, Optics and Opto-electronics:** synthesis, properties and processing of layers used in electronic, optical and opto-electronic applications; device engineering.
- Magnetics and Magneto-optics:** fundamental aspects of layers used in magnetic and magneto-optic applications; magnetic, optical and magneto-optical recording devices.
- Superconductivity:** synthesis and properties of layers used in superconducting applications.
- Langmuir-Blodgett, Biological and Related Films:** synthesis and properties of Langmuir-Blodgett, biological and related layers; device applications.
- Thin Film Devices, Sensors and Actuators:** fabrication, processing and properties of devices including sensors and actuators based upon thin layers.

- Condensed Matter Film Behaviour:** interdisciplinary and multidisciplinary topics.

## Submission of Papers

Manuscripts (original and two clear copies) should be sent to: Editorial Office (U.K.) of Elsevier Sequoia, Mayfield House, 256 Banbury Road, Oxford OX2 7DH, UK

All the authors of a paper should sign the covering letter. Contributions are accepted on the understanding that the authors have obtained the necessary authority for publication. Submission of a manuscript implies that it is not under consideration for publication elsewhere.

## Frequency

16 volumes in 1993, two issues per volume.

## Subscription Information

Subscription price for 1993 (Vols 221-236): Sfr. 5520. - (approx. US\$3920. - ) incl. postage.

Issues are sent by surface mail after air delivery to Argentina, Australia, Brazil, Canada, China, Hong Kong, India, Israel, Japan, Malaysia, Mexico, New Zealand, Pakistan, Singapore, South Africa, South Korea, Taiwan, Thailand and the USA. Airmail rates for other countries are available on request.

Subscription orders should be addressed to:

## ELSEVIER SEQUOIA, S.A.

P.O. Box 564, 1001 Lausanne 1, Switzerland.  
Tel. (21) 20 73 81, Telex 450620 ELSA CH, Telefax (21) 235 444.

U.S. and Canadian customers may obtain information from:

ELSEVIER SCIENCE PUBLISHING CO. INC.,  
Attn: Journal Information Center,  
655 Avenue of the Americas, New York, NY 10010, USA.  
Tel. +1 (212) 633 3750, Telex 420 643 AEP UI,  
Telefax +1 (212) 633 3764.

A pamphlet containing more detailed instructions on the preparation of manuscripts for THIN SOLID FILMS may be obtained from the publishers.

*thin*  
*SOLID*  
*films*  
Volume 225 (1993)

Accession For	
NTIS CRA&I	<input checked="" type="checkbox"/>
DTIC TAB	<input type="checkbox"/>
Unannounced	<input type="checkbox"/>
Justification .....	
By .....	
Distribution /	
Availability Codes	
Dist	Avail and/or Special
A-1	

Papers submitted September 17th, 1992

# *thin Solid films*

*An International Journal on the Science  
and Technology of Condensed Matter Films*

Volume 225 containing papers presented at the 2nd International Atomic Layer Epitaxy Symposium, Raleigh, NC, USA, June 2-5, 1992

---

## EDITOR-IN-CHIEF

J. E. Greene (*Urbana, IL*)

## GUEST EDITOR

S. M. Bedair (*Raleigh, NC*)

## EDITORIAL BOARD

C. J. Adkins (*Cambridge, UK*)  
L. N. Aleksandrov (*Novosibirsk, Minsk*)  
D. E. Aspnes (*Red Bank, NJ, USA*)  
P. B. Barna (*Budapest, Hungary*)  
J.-O. Carlsson (*Uppsala, Sweden*)  
P. J. Dobson (*Oxford, UK*)  
H. Fuchs (*Ludwigshafen, Germany*)  
F. M. d'Heurle (*Yorktown Heights, NY, USA*)  
S. Hofmann (*Stuttgart, Germany*)  
A. Hugot-Le Goff (*Paris, France*)  
A. Kinbara (*Tokyo, Japan*)  
M. Kitabatake (*Osaka, Japan*)  
A. E. T. Kuiper (*Eindhoven, The Netherlands*)

A. Lopez-Otero (*Stanford, CA, USA*)  
P. J. Martin (*Lindfield, Australia*)  
J. W. Mayer (*Ithaca, NY, USA*)  
J. H. van der Merwe (*Pretoria, South Africa*)  
S. Nakahara (*Murray Hill, NJ, USA*)  
B. E. Nieuwenhuys (*Leiden, The Netherlands*)  
A. K. Pal (*Calcutta, India*)  
J. R. Sambles (*Exeter, UK*)  
W. Scharff (*Chemnitz, Germany*)  
I. Schuller (*La Jolla, CA, USA*)  
M. Sugi (*Tsukuba, Japan*)  
R. H. Tredgold (*Lancaster, UK*)  
R. W. Vook (*Syracuse, NY, USA*)  
W. D. Westwood (*Ottawa, Ont., Canada*)  
J. N. Zemel (*Philadelphia, PA, USA*)

---

DTIC QUALITY INSPECTED 3



ELSEVIER  
SEQUOIA

19950626 097



***Abstracting-Indexing Services***

This journal is cited by the following Abstracting and/or Indexing Services. Metal Abstracts, Chemical Abstracts, Physics Abstracts, Current Contents – Physical and Chemical Sciences, Current Contents – Engineering, Technology and Applied Sciences, Engineering Index, Cambridge Scientific Abstracts, Physikalische Berichte, Science Citation Index, Research Alert™, PASCAL (Centre National de la Recherche Scientifique), Fiz Karlsruhe.

International Standard Serial Number 0040-6090

© 1993–Elsevier Sequoia. All rights reserved

0925-4005/93/\$6.00

No part of this publication may be reproduced, stored in a retrieval system or transmitted in any form or by any means, electronic, mechanical, photocopying, recording or otherwise, without the prior written permission of the publisher, Elsevier Sequoia, S.A., P.O. Box 564, 1001 Lausanne 1, Switzerland.

Submission of an article for publication implies the transfer of the copyright from the author(s) to the publisher and entails the author(s) irrevocable and exclusive authorization of the publisher to collect any sums or considerations for copying or reproduction payable by third parties.

Upon acceptance of an article by the journal, the author(s) will be asked to transfer copyright of the article to the publisher. This transfer will ensure the widest possible dissemination of information.

**For Material Subject to US Copyright Law**

*Special regulations for readers in the USA*

This journal has been registered with the Copyright Clearance Center, Inc., 21 Congress Street, Salem, MA 01970, U.S.A. Consent is given for copying of articles for personal use, or for the personal use of specific clients. This consent is given on the condition that the copier pays through the Center the per-copy fee stated in the code on the first page of each article for copying beyond that permitted by Sections 107 or 108 of the US Copyright Law. If no code appears in an article, the author has not given broad consent to copy and permission to copy must be obtained directly from the author. All articles published prior to 1982 may be copied for a per-copy fee of US\$2.50, also payable through the Center. This consent does not extend to other kinds of copying, such as for general distribution, resale, advertising and promotion purposes or for creating new collective works. Special written permission must be obtained from the publisher for such copying.

No responsibility is assumed by the Publisher for any injury and/or damage to persons or property as a matter of products liability, negligence or otherwise, or from any use or operation of any methods, products, instructions or ideas contained in the material herein.

## Contents

<b>Preface</b> .....	ix
<b>Committee Members</b> .....	x
<b>Mechanistic Studies, III-V Compounds</b>	
Molecular layer epitaxy of GaAs .....	1
J.-I. Nishizawa, H. Sakuraba and Y. Oyama (Sendai, Japan)	
A model for the atomic layer epitaxy of GaAs .....	7
M. L. Yu (Yorktown Heights, NY, USA)	
Study of surface reactions in atomic layer epitaxy of GaAs using trimethylgallium by reflectance difference spectroscopy and mass spectroscopy .....	12
B. Y. Maa and P. D. Dapkus (Los Angeles, CA, USA)	
The surface chemistry and kinetics of GaAs atomic layer epitaxy .....	17
J. R. Creighton and B. A. Bansenauer (Albuquerque, NM, USA)	
Real-time optical diagnostics for measuring and controlling epitaxial growth .....	26
D. E. Aspnes (Red Bank, NJ, USA), I. Kamiya (Urbana, IL, USA), H. Tanaka (Atsugi, Japan), R. Bhat, L. T. Florez, J. P. Harbison (Red Bank, NJ, USA), W. E. Quinn (Broomfield, CO, USA), M. Tamargo, S. Gregory (Red Bank, NJ, USA), M. A. A. Pudensi (Campinas, Brazil), S. A. Schwarz (Red Bank, NJ, USA), M. J. S. P. Brasil (Campinas, Brazil) and R. E. Nahony (Red Bank, NJ, USA)	
<i>In situ</i> monitoring and control of atomic layer epitaxy by surface photo-absorption .....	32
N. Kobayashi and Y. Kobayashi (Tokyo, Japan)	
Surface photo-absorption study of the laser-assisted atomic layer epitaxial growth process of GaAs .....	40
J. P. Simko, T. Meguro, S. Iwai, K. Ozasa, Y. Aoyagi and T. Sugano (Saitama, Japan)	
<i>In situ</i> optical characterization of GaAs and InP surfaces during chloride atomic layer epitaxy .....	47
K. Nishi, A. Usui and H. Sakaki (Ibaraki, Japan)	
<b>III-V Compounds and Materials</b>	
Study of self-limiting growth mechanism in chloride ALE .....	53
A. Usui (Ibaraki, Japan)	
The impact of short exposure times on the ALE self-limiting process: potential mechanisms .....	59
K. G. Reid, A. F. Myers, N. A. El-Masry and S. M. Bedair (Raleigh, NC, USA)	
Atomic layer epitaxy of InP using trimethylindium and tertiarybutylphosphine .....	64
N. Pan, J. Carter, S. Hein, D. Howe, L. Goldman, L. Kupferberg, S. Brierley (Lexington, MA, USA) and K. C. Hsieh (Urbana, IL, USA)	
Laser-assisted atomic layer epitaxy of GaP in chemical beam epitaxy .....	70
M. Yoshimoto, A. Kajimoto and H. Matsunami (Kyoto, Japan)	
Atomic layer epitaxy of AlAs and (AlAs) <sub>n</sub> (GaAs) <sub>n</sub> .....	74
M. Ishizaki, N. Kano, J. Yoshino and H. Kukimoto (Yokohama, Japan)	
Study of photocatalytic growth-rate enhancement in MOMBE of GaAs on ZnSe by surface photoabsorption .....	78
A. Yoshikawa, A. Iguchi and S. Yamaga (Chiba-shi, Japan)	
Determining lattice mismatch or the composition of a single ultra thin GaInAs layer grown on InP .....	82
F. Ohsawa, H. Fujita, T. Obitsu, H. Ikeda and H. Kawanishi (Tokyo, Japan)	
Conditions for light-induced short-time growth of GaAs and InP by chloride epitaxy .....	86
K. Tempelhoff (Berlin, Germany)	
Wavelength dependence of photoenhanced organometallic chemical vapor deposition .....	91
J. Salzman, O. Kreinin and E. Maayan (Haifa, Israel)	

### III-V Technology and Devices

Cost-effective processing by atomic layer epitaxy .....	96
T. Suntola (Espoo, Finland)	
Atomic layer epitaxy for resonant tunneling devices .....	99
A. C. Seabaugh, J. H. Luscombe, J. N. Randall (Dallas, TX, USA), P. C. Colter, A. Dip, G. M. Eldallal and S. M. Bedair (Raleigh, NC, USA)	
GaAs/AlGaAs atomic layer epitaxy in a commercial MOCVD reactor .....	105
H. Liu, P. A. Zawadzki and P. E. Norris (Somerset, NJ, USA)	
Atomic layer epitaxy of AlAs and $\text{Al}_x\text{Ga}_{1-x}\text{As}$ for device application .....	109
A. Dip, G. M. Eldallal, P. C. Colter and S. M. Bedair (Raleigh, NC, USA)	
Growth and characterization of device quality GaAs produced by laser-assisted atomic layer epitaxy using triethylgallium .....	115
Q. Chen and P. D. Dapkus (Los Angeles, CA, USA)	

### Technology and Atomic Layer Epitaxy

Atomic layer manipulation of III-V compounds .....	120
Y. Aoyagi, K. Shinmura, K. Kawasaki (Osaka, Japan), I. Nakamoto (Tokyo, Japan), K. Gamo and S. Namba (Osaka, Japan)	
Digital etching study and fabrication of fine Si lines and dots .....	124
J. Yamamoto, T. Kawasaki, H. Sakaue, S. Shingubara and Y. Horiike (Hiroshima, Japan)	
Atomic layer epitaxy: chemical opportunities and challenges .....	130
L. Niinistö and M. Leskelä (Espoo, Finland)	
Surface processes in digital etching of GaAs .....	136
T. Meguro (Saitama, Japan), M. Ishii (Osaka, Japan), K. Kodama, Y. Yamamoto (Tokyo, Japan), K. Gamo (Osaka, Japan) and Y. Aoyagi (Saitama, Japan)	
Comparison of $\text{Cl}_2$ and HCl adsorption on $\text{Si}(100)-(2 \times 1)$ .....	140
Q. Gao, C. C. Cheng, P. J. Chen, W. J. Choyke and J. T. Yates, Jr (Pittsburgh, PA, USA)	

### Group IV

Group IV atomic layer epitaxy .....	145
M. N. Yoder (Arlington, VA, USA)	
Atomic H: a reagent for the extraction of chemical species from Si surfaces .....	150
J. T. Yates, Jr., C. C. Cheng, Q. Gao, M. L. Colaianni and W. J. Choyke (Pittsburgh, PA, USA)	
Hydrogen-halogen chemistry on semiconductor surfaces .....	155
S. M. Cohen, T. I. Hukka, Y. L. Yang and M. P. D'Evelyn (Houston, TX, USA)	
Dopants on $\text{Si}(100)$ surfaces: useful probes of silicon atomic layer epitaxy? .....	160
S. M. Gates and D. D. Koleske (Yorktown Heights, NY, USA)	
Atomic layer doping for Si .....	163
D. A. Grützmacher, K. Eberl, A. R. Powell, B. A. Ek, T. O. Sedgwick and S. S. Iyer (Yorktown Heights, NY, USA)	
Atomic layer epitaxy of Si using atomic H .....	168
S. Imai, T. Iizuka, O. Sugiura and M. Matsumura (Tokyo, Japan)	
Potential Si atomic layer epitaxy processes using halogenated Si precursors .....	173
D. D. Koleske, S. M. Gates and D. B. Beach (Yorktown Heights, NY, USA)	
Si atomic layer epitaxy based on $\text{Si}_2\text{H}_6$ and remote He plasma bombardment .....	177
A. Mahajan, J. Irby, D. Kinoshy, R. Qian, S. Thomas, S. Banerjee, A. Tasch (Austin, TX, USA) and T. Picraux (Albuquerque, NM, USA)	
Silicon monolayer growth using dichlorosilane and hydrogen in a near atmospheric pressure chemical vapor deposition reactor .....	183
F. G. McIntosh, P. C. Colter and S. M. Bedair (Raleigh, NC, USA)	
The chemisorption and reaction of $\text{GeCl}_4$ with $\text{Si}(100)$ .....	187
D. A. Lapino-Smith and F. R. McFeely (Yorktown Heights, NY, USA)	

Si <sub>2</sub> H <sub>6</sub> adsorption and dissociation pathways on Ge(001)2 × 1: mechanisms for heterogeneous atomic layer epitaxy . . . .	191
R. Tsu, D. Lubben, T. R. Bramblett and J. E. Greene (Urbana, IL, USA)	
Hydrocarbon surface chemistry on Si(100) . . . . .	196
C. C. Cheng, P. A. Taylor, R. M. Wallace, H. Gutleben, L. Clemen, M. L. Colaianne, P. J. Chen, W. H. Weinberg, W. J. Choyke and J. T. Yates, Jr (Pittsburgh, PA, USA)	
Chemistry of hydrogen on diamond (100). . . . .	203
Y. L. Yang, L. M. Struck, L. F. Sutcu and M. P. D'Evelyn (Houston, TX, USA)	
Novel method for chemical vapor deposition and atomic layer epitaxy using radical chemistry. . . . .	212
T. I. Hukka, R. E. Rawles and M. P. D'Evelyn (Houston, TX, USA)	
<b>High Bandgap (SiC and Nitrides)</b>	
Layer-by-layer growth of SiC at low temperatures . . . . .	219
J. J. Sumakeris, L. B. Rowland, R. S. Kern, S. Tanaka and R. F. Davis (Raleigh, NC, USA)	
Atomic layer epitaxy controlled by surface superstructures in SiC . . . . .	225
T. Fuyuki, T. Yoshinobi and H. Matsunami (Kyoto, Japan)	
Atomic layer epitaxy of 3C-SiC by low pressure vapour deposition with alternating gas supply . . . . .	230
H. Nagasawa and Y. Yamaguchi (Tokyo, Japan)	
Si heterojunction diodes with a thin $\beta$ -SiC layer prepared with gas layer source molecular beam epitaxy . . . . .	235
K. Kim, S.-D. Choi and K. L. Wang (Los Angeles, CA, USA)	
Microscopic mechanisms of accurate layer-by-layer growth of $\beta$ -SiC. . . . .	240
S. Hara, T. Meguro, Y. Aoyagi, M. Kawai (Saitama, Japan), S. Misawa, E. Sakuma and S. Yoshida (Ibaraki, Japan)	
Layer-by-layer epitaxial growth of GaN at low temperatures . . . . .	244
J. Sumakeris, Z. Sitar, K. S. Ailey-Trent (Raleigh, NC, USA), K. L. More (Oak Ridge, TN, USA) and R. F. Davis (Raleigh, NC, USA)	
<b>II-VI Compounds</b>	
Ultra high vacuum atomic layer epitaxy of CdTe . . . . .	250
H. Sitter and W. Faschinger (Linz, Austria)	
Self-limiting growth on zinc chalcogenides and their superlattices . . . . .	256
M. Konagai, Y. Takemura, K. Yamasaki and K. Takahashi (Tokyo, Japan)	
Growth and characterization of CdTe, HgTe and HgCdTe by atomic layer epitaxy . . . . .	261
N. H. Karam, R. G. Wolfson (Bedford, MA, USA), I. B. Bhat, H. Ehsani and S. K. Ghandhi (Troy, NY, USA)	
Growth and characterization of CdTe-ZnTe short-period superlattices . . . . .	265
F. Hauzenberger, W. Faschinger, P. Juza, A. Pesek, K. Lischka and H. Sitter (Linz, Austria)	
Self-limiting monolayer epitaxy of wide gap II-VI superlattices. . . . .	270
W. Faschinger, P. Juza, S. Ferreira, H. Zajicek, A. Pesek, H. Sitter and K. Lischka (Linz, Austria)	
<b>Oxides</b>	
Atomic layer control of the growth of oxide superconductors using laser molecular beam epitaxy . . . . .	275
H. Tabata and T. Kawai (Osaka, Japan)	
Analytical and chemical techniques in the study of surface species in atomic layer epitaxy . . . . .	280
S. Haukka (Helsinki, Finland), E.-L. Lakomaa and T. Suntola (Espoo, Finland)	
Self-limiting adsorption and <i>in situ</i> optical monitoring for atomic layer epitaxy of oxide superconductors . . . . .	284
S. Oda, H. Zama, K. Fujii, K. Sakai and Y. C. Chen (Tokyo, Japan)	
Growth of titanium dioxide thin films by atomic layer epitaxy. . . . .	288
M. Ritala, M. Leskelä (Helsinki, Finland), E. Nykänen, P. Soininen and L. Niinistö (Espoo, Finland)	
Layered tantalum-aluminum oxide films deposited by atomic layer epitaxy . . . . .	296
H. Kattelus, M. Ylilammi, J. Saarilahti, J. Antson and S. Lindfors (Espoo, Finland)	
<b>Author Index</b> . . . . .	299
<b>Subject Index</b> . . . . .	301

## Preface

This special issue of *Thin Solid Films* contains papers presented at the 2nd International Atomic Layer Epitaxy Symposium held in Raleigh, NC, from June 2–5, 1992. This symposium is a follow-up to the first symposium held in Helsinki in 1990. The size, breadth and the technical emphasis of the symposium indicates the continuing growth and interest in the atomic layer epitaxy (ALE) area. The symposium was attended by 130 participants representing eight countries. The meeting lasted for three days whereupon 63 papers were orally presented. Also, a late news/poster session held on the evening of the second day had 11 presentations, which brought the total number of papers to 74.

The symposium provided the forum for specialists in the ALE area to identify and discuss important scientific and technical issues and to chart promising directions. The technical emphasis of this meeting in many ways represented the natural development of the themes established at the first symposium. There was a great deal of emphasis on the self-limiting mechanisms in the ALE growth of GaAs using TMGa. Several models were presented based on *in situ* monitoring techniques. They include the use of surface photoabsorption, reflectance difference spectroscopy and temperature-programmed desorption to identify surface reconstructions and the nature of the adsorbed species, leading to the monolayer growth of GaAs. ALE reactor designs were also addressed for maintaining the self-limiting process, achieving high throughput and high growth rate. ALE of GaAs with growth rates approaching  $1 \mu\text{m h}^{-1}$  was also reported. Problems of high carbon background in ALE-grown III–V compounds were addressed and several ALE devices in GaAs, AlGaAs and GaN systems were reported. The performance of several of these ALE-grown devices are comparable or even better than their MBE or MOCVD counterparts, thus establishing ALE as a future growth technique.

The concept and initial results for digital etching in GaAs and Si structures were presented leading to several quantum structures and 3D investigations. ALE of group IV (Si, SiGe, SiC and diamond) has been addressed and several papers reported the achievement of monolayer growth in these systems. The nature of the adsorbed species when  $\text{SiCl}_2\text{H}_2$  was used, have been investigated by several groups. Industrial interest in the ALE of Si was very apparent at the meeting. ALE in II–VI and oxides for display devices and high  $T_c$  superconductors, respectively, were reported. The symposium demonstrated the interest and potential applications of the ALE in the semiconductor and the superconductor fields.

A rump and a panel discussion, led by M. Yoder, was held on Thursday evening to address "ALE as a Future Technology". The general feeling of those at the rump session was to devote more efforts in addressing the major challenges facing the ALE technique thus leading the way to industrial applications. Dr. Henry Kressel was the keynote speaker for the symposium banquet and gave a talk entitled "Reflections on the Golden Age of Material Science". The talk traced the major scientific and technological milestones in the electronic age and how these spectacular developments have largely been made possible by developments in materials science.

It is a pleasure to express thanks and appreciation to the session chairpersons and to my students in playing key roles in conducting a successful meeting. The editor would also like to acknowledge the help of many referees, and Molly Hodges and Joan Livingood for secretarial support.

S. M. Bedair  
Guest Editor  
Raleigh, NC, USA

## Committee Members

---

### Program Committee

S. Bedair	Symposium Chair, North Carolina State University
D. Aspnes	Bellcore
R. Davis	North Carolina State University
M. Yoder	Office of Naval Research
J. Greene	University of Illinois
D. Dapkus	University of South California
T. Kuech	University of Wisconsin
M. Tischler	IBM
Y. Aoyagi	Riken
N. El-Masry	North Carolina State University
P. Norris	Emcore

### International Committee

Lauri Niinistö	Helsinki University of Technology, Finland
Salah M. Bedair	North Carolina State University, USA
Jun-ichi Nishizawa	Tohoku University, Sendai, Japan
Tuomo Suntola	Microchemistry Ltd., Finland

### Supporting Organizations

The organizing committee would like to thank the following agencies for their generous contributions in support of this symposium:

Office of Naval Research  
Strategic Defense Initiative  
National Science Foundation  
National Renewable Energy Laboratory  
Army Office of Research

### Cooperative Sponsorship

American Vacuum Society  
IEEE  
Electron Devices Society

# Molecular layer epitaxy of GaAs

Jun-ichi Nishizawa

Tohoku University, 2-1-1 Katahira Aoba-ku, Sendai 980 (Japan) and Semiconductor Research Institute, Kawauchi Aoba-ku, Sendai 980 (Japan)

Hiroshi Sakuraba

Faculty of Engineering, Tohoku University, Aramaki Aoba-ku, Sendai 980 (Japan)

Yutaka Oyama

Semiconductor Research Institute, Kawauchi Aoba-ku, Sendai 980 (Japan)

## Abstract

The surface reaction mechanism of trimethylgallium (TMG) on GaAs is investigated using quadrupole mass spectroscopy (QMS). The present QMS measurements, which concern only the surface reaction itself, distinguish the surface reaction of TMG on {100}-oriented GaAs as being of two types. By taking into account the QMS results for the {111} Ga and {111} As surfaces, the surface reaction mechanism on GaAs is discussed. These results are applicable to the molecular layer epitaxy (MLE) of GaAs of high purity.

## 1. Introduction

Recently, precise control of the epitaxial layer thickness and crystal quality has been increasingly required to atomic accuracy for various kinds of device fabrication.

Nishizawa *et al.* first applied the idea of the ALE method [1], which had been used for the preparation of polycrystalline II–VI compounds, to grow monocrystalline GaAs [2]. By applying alternate injections of the gas sources used in the field of metallorganic chemical vapour deposition (MOCVD) in vacuum, monomolecular GaAs crystal was epitaxially grown on substrates on a molecular basis. In view of the reaction and growth mechanisms, this method can be termed molecular layer epitaxy (MLE). In the MLE method the component atomic species are supplied as compounds and the monomolecular layer is formed by the chemical reaction on the crystal surface. Therefore it is essential to understand the surface reaction mechanisms of the source compounds. Whereas the chemical reaction in the vapour phase has been intensively investigated by means of IR absorption spectroscopy analysis [3], etc., various methods of analysis have been widely applied to determine the adsorbed chemical species on the GaAs surface [4–9]. However, our understanding of the surface reaction mechanisms and the adsorbed species on the surface is still far from complete.

In this paper we apply quadrupole mass spectroscopy (QMS) to analyse the trimethylgallium (TMG) reaction on GaAs crystals with three integral crystal orientations

of {100}, {111}A and {111}B [10]. The present QMS measurements were concentrated on the detection of only the surface reaction itself. The transient behaviour of the QMS signal was separated from that in the steady state. This results in the surface reaction mechanism of TMG on the first adsorbed layer being shown to be different from that on the second adsorbed layer. In the light of the present QMS results the possibility of growing high purity GaAs in the TMG/AsH<sub>3</sub> system is shown.

## 2. Experimental details

Figure 1 shows a schematic drawing of the QMS apparatus. The main aim of this construction is to detect the net surface reaction caused only on the GaAs crystals. The GaAs crystals used were horizontal-Bridgman- (HB-) grown substrate material doped with

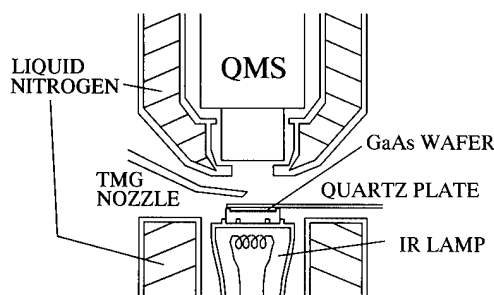


Fig. 1. Schematic drawing of main parts of QMS apparatus.

Si( $n \approx 2 \times 10^{18} \text{ cm}^{-3}$ ). The GaAs crystals are placed on the quartz susceptor containing the IR lamp heater. The QMS analyser is placed just above the GaAs substrate. The movable thin quartz plate [11] is placed just above the GaAs substrate at a distance of 300  $\mu\text{m}$ . This enables us to detect the significant surface reaction of TMG caused only on the GaAs surface. A detailed description of this QMS apparatus is given elsewhere [10].

A GaAs crystal etched with  $\text{H}_2\text{SO}_4 + \text{H}_2\text{O}_2$  solution is placed on the quartz susceptor in vacuum and heated to about 650 °C in  $\text{AsH}_3$  at a pressure of  $2.7 \times 10^{-2} \text{ Pa}$  for a few minutes. Then the GaAs crystal is cooled to the experimental temperature and the  $\text{AsH}_3$  supply is stopped. TMG is introduced into the analysing chamber with the quartz plate covering the GaAs crystal. The TMG pressure in the analysing chamber is  $3 \times 10^{-5} \text{ Pa}$ . This gives the background QMS signal caused on the QMS analyser, chamber wall, etc., but not on the GaAs crystal. After the background QMS signal has stabilized, the quartz plate is removed from the GaAs surface. This procedure gives the net QMS signal of the surface reaction induced only on the GaAs surface.

### 3. Results and discussion

#### 3.1. Surface reaction of TMG in steady state on {100}-oriented GaAs

Figure 2 shows the substrate temperature dependences of the net QMS signals in the steady state. The main QMS signals due to TMG introduction were  $^{99}\text{Ga}(\text{CH}_3)_2^+$ ,  $^{15}\text{CH}_3^+$ ,  $^{69}\text{Ga}^+$  and  $^{84}\text{GaCH}_3^+$ .  $^{114}\text{Ga}(\text{CH}_3)_3^+$  was also detected. When the GaAs surface is covered by the masking quartz plate, the  $^{99}\text{Ga}(\text{CH}_3)_2^+$  signal increases and stabilizes within a few minutes. When the GaAs surface is exposed by

removing the quartz plate, the  $^{99}\text{Ga}(\text{CH}_3)_2^+$  signal shows a rapid decrease and then recovers. This decrease is due to the net adsorption on the surface. In Fig. 2 the net ion current is calibrated by additional experimental results which show the intensity modification by the different scattering positions of TMG between the masking quartz plate and the GaAs crystal. The decrease in  $^{99}\text{Ga}(\text{CH}_3)_2^+$  indicates a different activation energy at around 600 °C. The limiting process of the surface reaction is thought to be adsorption below 600 °C and desorption above 600 °C.

The  $^{15}\text{CH}_3^+$  signal also increases even when the GaAs is covered by the plate. Therefore this signal is not due to the surface reaction. When the GaAs crystal is exposed, the  $^{15}\text{CH}_3^+$  signal shows a maximum value and then saturates. In Fig. 2 the net  $^{15}\text{CH}_3^+$  ion current caused by the surface reaction was also obtained by taking into consideration the change in baseline within the exposure time. From additional experimental results on the appearance voltage of the QMS measurements, it is considered that the present  $^{15}\text{CH}_3^+$  signal is due to the  $\text{CH}_3$  radical ( $\text{CH}_3^*$ ). As seen in Fig. 2, the increase in  $^{15}\text{CH}_3^+$  ion current shows at least three different activation energies at around 400–460, 510–610 and 610–660 °C. The  $^{69}\text{Ga}^+$  and  $^{84}\text{GaCH}_3^+$  signals show almost the same temperature dependences as that of  $^{15}\text{CH}_3^+$ . This means that the surface reaction mechanism in the steady state is classified into at least three different main limiting processes. In view of the QMS consideration of the net ion current in the steady state, the dominant reaction paths of TMG on GaAs surface are deduced as follows:

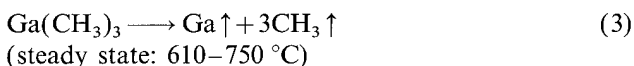
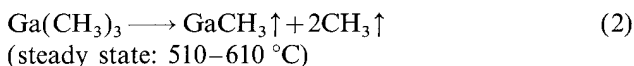
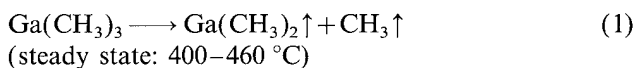


Figure 3 shows the ratio of  $^{15}\text{CH}_3^+$  to  $^{99}\text{Ga}(\text{CH}_3)_2^+$  and the ion current. The ratio in the steady state

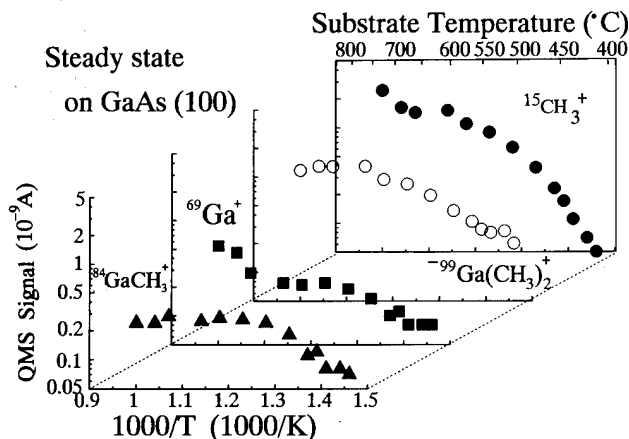


Fig. 2. Substrate temperature dependences of net QMS signals in steady state.

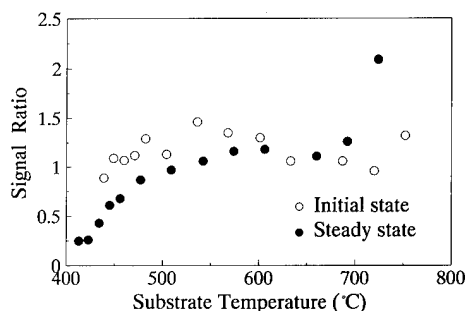


Fig. 3. Temperature dependences of ratio of  $^{15}\text{CH}_3^+$  to  $^{99}\text{Ga}(\text{CH}_3)_2^+$  and ion current in steady state.



remains at about 1.2 at around 570–670 °C. In view of the temperature dependence of the limiting process as shown in Fig. 2,  $^{84}\text{GaCH}_3^+$  will be formed in this temperature range. Therefore it can be deduced that  $^{84}\text{GaCH}_3^+$  and Ga will be formed when the ratio of  $^{15}\text{CH}_3^+$  to  $^{99}\text{Ga}(\text{CH}_3)_2^+$  exceeds 0.6 and 1.2 respectively.

### 3.2. Surface reaction just after TMG exposure on {100} GaAs

Figure 4 shows the temperature dependences of the decrease in  $^{99}\text{Ga}(\text{CH}_3)_2^+$  and the increase in  $^{15}\text{CH}_3^+$  ion current. During the initial state of exposure the ion current ratio of  $^{15}\text{CH}_3^+$  to  $^{99}\text{Ga}(\text{CH}_3)_2^+$  is almost 1.2 even at 400 °C. Although the  $^{84}\text{GaCH}_3^+$  and  $^{69}\text{Ga}^+$  signals do not increase, it is considered that TMG decomposes into GaCH<sub>3</sub> followed by 2CH<sub>3</sub> release from the surface. However, in contrast to the steady state surface reaction,  $^{84}\text{GaCH}_3^+$  is considered to adsorb on the surface just after the exposure of TMG. In the temperature range 500–610 °C the ratio of  $^{15}\text{CH}_3^+$  to  $^{99}\text{Ga}(\text{CH}_3)_2^+$  exceeds 1.2. Therefore it is considered that the exposed TMG decomposes into Ga. At 610–720 °C the ratio also becomes 1.2.  $^{84}\text{GaCH}_3^+$  is considered to be formed and then desorb from the surface because of its short residence time due to the high substrate temperature. At temperatures above 720 °C the ratio also exceeds 1.2. This means that  $^{69}\text{Ga}^+$  will be formed and then desorb from the surface. Above 650 °C decomposition of Ga and As can be observed from the GaAs crystal itself. Therefore it is considered that desorption of  $^{84}\text{GaCH}_3^+$  and  $^{69}\text{Ga}^+$  will occur. Surface inspection by optical microscopy revealed the formation of Ga droplets only just under the TMG injection nozzle at 710 °C. This also suggests the validity of the idea of Ga desorption at higher temperature.

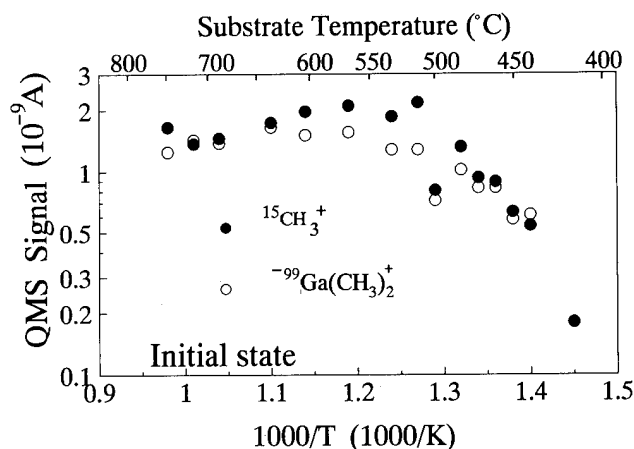
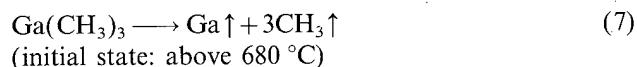
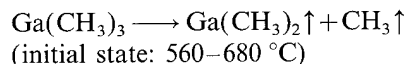
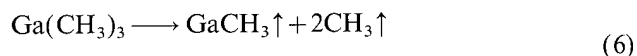
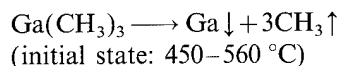
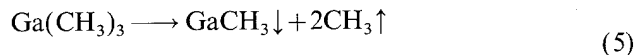
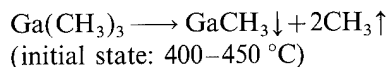
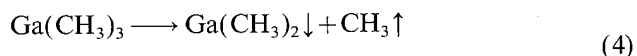


Fig. 4. Temperature dependences of decrease in  $^{99}\text{Ga}(\text{CH}_3)_2^+$  and increase in  $^{15}\text{CH}_3^+$  ion currents at initial state of exposure.

In summary, in the initial surface reaction on {100} GaAs the reaction process will be described as follows:



Next we distinguish two types of net ion current, namely those of the initial and steady states after TMG exposure.

Whereas the  $^{15}\text{CH}_3^+$  and  $^{99}\text{Ga}(\text{CH}_3)_2^+$  signals show a drastic change during the initial state of TMG exposure, the change in the  $^{84}\text{GaCH}_3^+$  and  $^{69}\text{Ga}^+$  signals is small. In the steady state after a few minutes of exposure the  $^{84}\text{GaCH}_3^+$  and  $^{69}\text{Ga}^+$  signals dominate the surface reaction on GaAs. Therefore the observed  $^{15}\text{CH}_3^+$  and  $^{99}\text{Ga}(\text{CH}_3)_2^+$  signals after exposure seem to include both the steady and initial state reactions. In order to distinguish the initial surface reaction from the steady state reaction, two hypotheses are assumed: (1) the  $^{84}\text{GaCH}_3^+$  signal is caused only by the steady state reaction; (2) the steady state ion currents of  $^{15}\text{CH}_3^+$  and  $^{99}\text{Ga}(\text{CH}_3)_2^+$  are proportional to that of  $^{84}\text{GaCH}_3^+$ . Figure 5 shows the substrate temperature dependences of the (a) initial and (b) steady state reactions of TMG on {100} GaAs.

The ion currents of  $^{15}\text{CH}_3^+$  ( $I_{15}$ ) and  $^{99}\text{Ga}(\text{CH}_3)_2^+$  ( $I_{99}$ ) in the initial state reaction are well represented with respect to the exposure time as

$$I_{15} = A \exp(-\tau t) \quad (8)$$

$$I_{99} = B[1 - C \exp(-\delta t)] \quad (9)$$

These kinds of equations which show a simple surface reaction process also verify the validity of the self-limiting growth mechanism in the TMG/AsH<sub>3</sub> system (see Appendix). Here  $\tau$  and  $\delta$  are theoretically deduced from the surface reaction velocity constant  $k$  multiplied by the number of TMG molecules just above the surface. Therefore the activation energy of the surface reaction process at the first layer is obtained from the temperature dependence of  $k$ . The activation energy for  $^{15}\text{CH}_3^+$  is determined to be 17.2 kcal mol<sup>-1</sup> at 420–650 °C. However, the activation energy for  $^{99}\text{Ga}(\text{CH}_3)_2^+$  is quite different from that of  $^{15}\text{CH}_3^+$  and

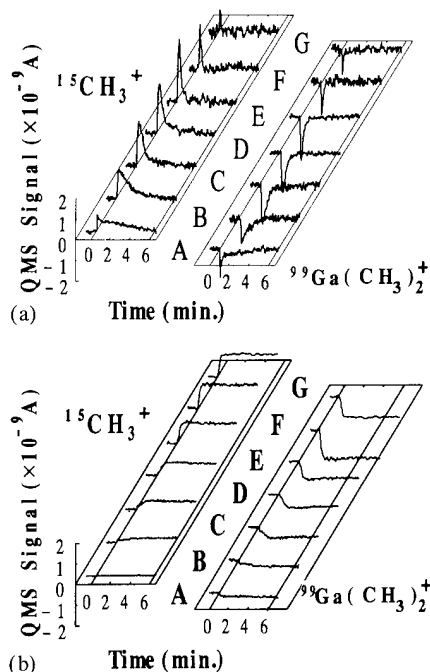


Fig. 5. Substrate temperature dependences of (a) initial and (b) steady state surface reactions of  $^{15}\text{CH}_3^+$  and  $^{99}\text{Ga}(\text{CH}_3)_2^+$ .

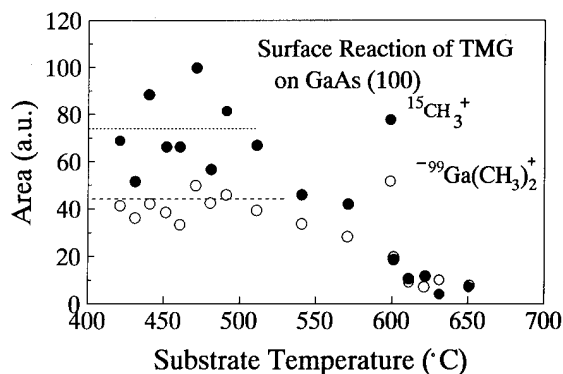


Fig. 6. Substrate temperature dependences of total charge obtained from integration of ion current with exposure time for initial reaction only. This value is proportional to the net amount of adsorbent on the surface.

is determined to be  $12.9 \text{ kcal mol}^{-1}$ . This suggests that the rate-limiting processes for adsorption and desorption with  $^{15}\text{CH}_3^+$  release are different.

Figure 6 shows the substrate temperature dependences of the total charge obtained from the integration of ion current with exposure time for the initial reaction only. This is thought to be proportional to the net amount of adsorbed species. Whereas the peak ion currents of  $^{15}\text{CH}_3^+$  and  $^{99}\text{Ga}(\text{CH}_3)_2^+$  increase with respect to temperature, the net amount of integrated charge is almost the same in the specific temperature range 420–510 °C. This means that the amount of adsorbed species is constant and that the adsorption

process is completed more rapidly at higher temperature.

In order to identify the adsorbed species on the GaAs crystal, the ratio of  $^{15}\text{CH}_3^+$  to  $^{99}\text{Ga}(\text{CH}_3)_2^+$  is considered. The ratio shows a monotonic decrease from 2.0 to 0.4 as the substrate temperature rises in the temperature range 410–650 °C. This leads to the crucial conclusion that the adsorbed species is Ga at the first surface reaction layer at 420–510 °C and that another adsorbent with more  $\text{CH}_3$  will absorb at higher substrate temperature.

### 3.3. Surface reaction of TMG on {100} GaAs

From the QMS results mentioned above, the surface reaction process of TMG can be deduced as follows. At 420–510 °C a single monolayer of Ga will be formed on the GaAs surface as a result of TMG introduction. However, the formation of this adsorbed layer takes a little bit longer when the substrate temperature is lower. In addition, the temporal adsorption phenomenon of  $^{99}\text{Ga}(\text{CH}_3)_2$  and  $^{84}\text{GaCH}_3$  should also occur on the GaAs surface at lower temperature. Above 510 °C the adsorbed layer thickness becomes less than one monolayer, with an additional  $\text{CH}_3$  adsorbed layer. Once the Ga adsorbed layer has been formed on the surface, this accelerates the decomposition of arriving TMG molecules. From the steady state considerations  $^{99}\text{Ga}(\text{CH}_3)_2$  will be formed below 510 °C. At 510–610 °C  $^{84}\text{GaCH}_3$  will be formed on TMG introduction. Finally, Ga will be formed at higher temperature and will accumulate as Ga droplets. Figure 7 shows a schematic drawing of the surface reaction on {100}-oriented GaAs.

### 3.4. Surface reaction process of TMG on {111}B GaAs surface

Similar QMS measurements were also applied on the {111}B surface. In contrast to the {100} surface, it takes longer to saturate the decrease in  $^{99}\text{Ga}(\text{CH}_3)_2^+$  and increase in  $^{15}\text{CH}_3^+$  ion currents. The net ion currents of

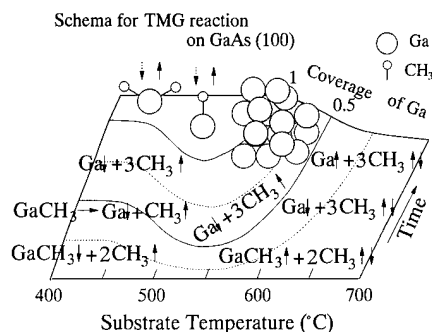


Fig. 7. Schematic drawing of surface reaction of TMG on {100} GaAs surface.

$^{84}\text{GaCH}_3^+$  and  $^{15}\text{CH}_3^+$  show similar dependences as a function of temperature. On the  $\{111\}B$  surface optical inspection reveals the formation of Ga droplets above  $460^\circ\text{C}$ . X-ray photoelectron spectroscopy (XPS) measurements detected an increase in Ga on the surface even without Ga droplet formation when the TMG introduction was stopped at the initial stage of exposure just before the ion current increased at  $480^\circ\text{C}$ . Therefore it is considered that Ga or Ga compounds on the surface seem to accelerate the decomposition of TMG.

An Arrhenius plot of the steady state QMS signal shows the existence of three types of reaction process at around  $450^\circ\text{C}$ , between  $450$  and  $500^\circ\text{C}$  and above  $500^\circ\text{C}$ . An Arrhenius plot of the initial state QMS signal shows at least two sorts of reaction process below and above  $500^\circ\text{C}$ . The ratio of  $^{15}\text{CH}_3^+$  to  $^{99}\text{Ga}(\text{CH}_3)_2^+$  indicates that Ga formation will occur above  $490^\circ\text{C}$  in the steady state. At the initial state of exposure the ratio, which indicates  $^{84}\text{GaCH}_3^+$  formation above  $0.6$  and Ga formation above  $1.2$  respectively, shows that  $^{84}\text{GaCH}_3^+$  formation will occur around  $460^\circ\text{C}$  and that Ga will be formed above  $490^\circ\text{C}$ . In addition, the ratio at the initial state of exposure becomes lower than that at the steady state. This indicates that the adsorbed  $^{99}\text{Ga}(\text{CH}_3)_2$  and  $^{84}\text{GaCH}_3$  will decompose gradually into Ga on the surface. The detection of the  $^{84}\text{GaCH}_3^+$  signal also indicates a surface reaction process by collisions among adsorbed  $^{99}\text{Ga}(\text{CH}_3)_2$  and  $^{84}\text{GaCH}_3$  or arriving TMG molecules.

### 3.5. Surface reaction process on $\{111\}A$ GaAs

On the  $\{111\}A$  surface the net substrate temperature dependence of the QMS signal shows only one type of activation process. This means, in contrast to the  $\{100\}$  and  $\{111\}B$  surfaces, that only one kind of surface reaction will proceed at both the initial and steady states after TMG exposure. Indeed, no epitaxial layer could be obtained on the  $\{111\}A$  surface in the TMG/ $\text{AsH}_3$  system. This means that decomposition of TMG will occur on the  $\{111\}A$  surface simultaneously, but that the decomposed chemical species from TMG cannot adsorb on the  $\{111\}A$  surface. Below  $450^\circ\text{C}$ , whereas a decrease in the  $^{99}\text{Ga}(\text{CH}_3)_2^+$  ion current could be observed, no increase in the  $^{84}\text{GaCH}_3^+$  and  $^{15}\text{CH}_3^+$  ion currents could be detected. This means that the arriving TMG will not decompose at this low temperature and adsorb on the  $\{111\}A$  surface as it is. This kind of adsorption of TMG without any decomposition could be also observed on the  $\{100\}$  and  $\{111\}B$  surfaces below  $250^\circ\text{C}$ .

## 4. Summary

QMS analysis was applied to investigate the surface reaction of TMG on  $\{100\}$ -,  $\{111\}A$ - and  $\{111\}B$ -oriented GaAs crystals. The present QMS measurements

clarify the change in the  $\text{CH}_3^*$  and  $\text{GaCH}_3$  signals caused only on the crystal as a function of the exposure time and surface orientation. On the  $\{100\}$  surface significant decomposition is observed, especially just after the exposure, and a single monolayer of adsorbed Ga is formed. Then  $\text{Ga}(\text{CH}_3)_2$  and  $\text{GaCH}_3$  formation proceeds on the Ga adsorbed layer. Finally, Ga accumulation and formation of Ga droplets can be expected. On the  $\{111\}B$  surface a time delay of decomposition is observed after substrate exposure. This means that collisions between adsorbed species and reactions between adsorbed species and the introduced TMG must be taken into account in considering the surface reaction. On the  $\{111\}A$  surface TMG shows no significant decomposition below  $450^\circ\text{C}$  and adsorbs simultaneously on the surface. Further quantitative consideration will complement the present QMS results.

From the QMS results mentioned above, it is expected in the TMG/ $\text{AsH}_3$  system that the temporal adsorption of Ga compounds with  $x\text{CH}_3$  will occur at lower temperature and that a Ga desorbed layer will be formed with additional  $\text{CH}_3$  adsorption at higher temperature. This results in the serious incorporation of carbon into the epitaxial layer. Therefore it is expected that a high purity GaAs layer will be obtained in the TMG/ $\text{AsH}_3$  system at the appropriate substrate temperature and remaining time of adsorbence. Figure 8 shows the spatial distribution of carrier concentration obtained by capacitance voltage (CV) measurements. Epitaxial growth was carried out at  $490^\circ\text{C}$  on  $\{100\}$ -oriented  $n^+$  ( $n = 2 \times 10^{18} \text{ cm}^{-3}$ ) GaAs doped with Si. TMG and  $\text{AsH}_3$  were introduced alternately at pressures of  $3.3 \times 10^{-5}$  and  $3.3 \times 10^{-2} \text{ Pa}$  in the growth chamber respectively. The background pressure of the growth system was  $1.3 \times 10^{-7} \text{ Pa}$ . The carrier concentration obtained was in the range  $(4-8) \times 10^{17} \text{ cm}^{-3}$  at  $297 \text{ K}$ . In our previous studies on the TMG and  $\text{AsH}_3$  pressure dependences of carrier concentration the lowest carrier concentration obtained was above  $1 \times 10^{18} \text{ cm}^{-3}$ . More precise determination of the surface

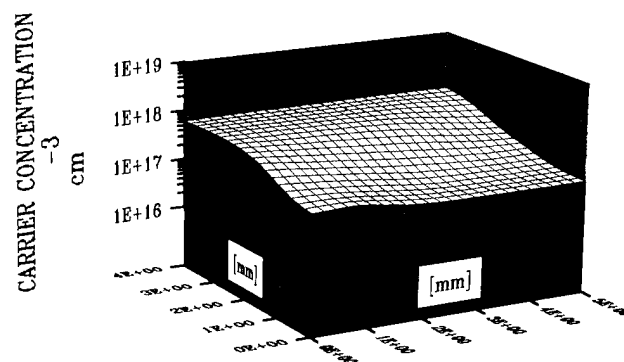


Fig. 8. Spatial distribution of carrier concentration obtained from CV measurements. The carrier concentration obtained was in the range  $(4-8) \times 10^{17} \text{ cm}^{-3}$  at  $297 \text{ K}$ .

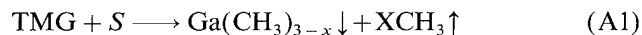
reaction mechanism will enable us to grow high purity GaAs in the TMG/AsH<sub>3</sub> system with the self-limiting process.

## References

- 1 M. Ahonen, M. Pessa and T. Suntola, *Thin Solid Films*, **65** (1980) 301.
- 2 J. Nishizawa, H. Abe and T. Kurabayashi, *J. Electrochem. Soc.*, **132** (1983) 1197.
- 3 J. Nishizawa and T. Kurabayashi, *J. Electrochem. Soc.*, **130** (1983) 413.
- 4 Y. Aoyagi and S. Namba, *Appl. Phys. Lett.*, **48** (1986) 1787.
- 5 K. Kodama, M. Ozeki, K. Mochizuki and N. Ohotuka, *Appl. Phys. Lett.*, **54** (1989) 666.
- 6 H. Ishii, H. Ohono, K. Matsuzaki and H. Hasegawa, *J. Cryst. Growth*, **95** (1989) 132.
- 7 M. L. Yu, U. Memmert and T. F. Kuech, *Appl. Phys. Lett.*, **55** (1989) 1011.
- 8 U. Memmert and M. L. Yu, *Appl. Phys. Lett.*, **58** (1990) 1883.
- 9 J. R. Creighton, *Surf. Sci.*, **234** (1990) 287.
- 10 J. Nishizawa and H. Sakuraba, *Surf. Sci. Rep.*, **15**(4-5) (1992) 137.
- 11 P. A. Taylor, R. M. Wallace, W. J. Choyke, M. J. Dresser and J. T. Yates Jr., *Surf. Sci. Lett.*, **L286** (1989) 215.

## Appendix

The surface reaction of TMG on GaAs is represented as



Therefore the reaction velocity  $r$  can be obtained as

$$r = k[\text{TMG}]S \quad (\text{A2})$$

where  $S$  is the number of adsorption sites and  $k$  is the reaction velocity constant. Equation (A2) is valid under

the assumption that the reverse reaction is negligible. It is considered that one adsorbent adsorbs on one adsorption site, because the self-limiting growth of one monolayer can be achieved in the TMG/AsH<sub>3</sub> system. The reaction velocity equation can be written as

$$\frac{dq}{dt} = kQS(t) \quad (\text{A3})$$

where  $q$  is the number of adsorbents and  $Q$  is the constant number of TMG molecules arriving on the GaAs surface. The summation of the number of remaining adsorption sites and the number of adsorbents equals the initial number of adsorption sites. Therefore

$$S_0 = S(t) + q(t) \quad (\text{A4})$$

From eqns. (A3) and (A4) the following equation is obtained:

$$S_0 = \frac{1}{kQ} \frac{dq}{dt} + q(t) \quad (\text{A5})$$

The general solution for the above equation is

$$q = S_0[1 - \exp(-kQt)] \quad (\text{A6})$$

The reaction velocity is obtained as

$$\frac{dq}{dt} = kQS_0 \exp(-kQt) \quad (\text{A7})$$

The ion currents obtained from <sup>15</sup>CH<sub>3</sub><sup>+</sup> ( $I_{15}$ ) and <sup>99</sup>Ga(CH<sub>3</sub>)<sub>2</sub><sup>+</sup> ( $I_{99}$ ) are represented as

$$I_{15} = \alpha x k QS_0 \exp(-kQt) \quad (\text{A8})$$

$$I_{99} = \beta(3-x)[Q - kQS_0 \exp(-kQt)] \quad (\text{A9})$$

where  $\alpha$  and  $\beta$  are the sensitivities of QMS for <sup>15</sup>CH<sub>3</sub><sup>+</sup> and <sup>99</sup>Ga(CH<sub>3</sub>)<sub>2</sub><sup>+</sup> respectively.

# A model for the atomic layer epitaxy of GaAs

Ming L. Yu

IBM Research Division, T. J. Watson Research Center, Yorktown Heights, NY 10598 (USA)

## Abstract

A simple model for the self-limiting Ga deposition by trimethylgallium in the atomic layer epitaxy of GaAs is proposed. The model features both the site blocking of adsorbed  $\text{CH}_3$  groups on the surface and the surface-stoichiometry-dependent desorption of  $\text{CH}_3\text{Ga}$ . It successfully reproduces both the self-limiting Ga deposition at temperatures below a critical temperature and its failure at higher temperatures.

## 1. Introduction

One of the best-studied atomic layer epitaxy (ALE) processes is the growth of GaAs(100) by reacting the GaAs(100) substrate with trimethylgallium,  $(\text{CH}_3)_3\text{Ga}$  (TMGa), and arsine,  $\text{AsH}_3$ , in an alternating sequence. Nishizawa *et al.* [1] have demonstrated that at a TMGa pressure of  $5 \times 10^{-5}$  Torr and with 4 s exposure per cycle, close to a monolayer (ML) of GaAs could be deposited per growth cycle when the reaction temperature was in the vicinity of 500 °C. That ALE worked at such a low gas pressure indicated that the process was driven by surface reactions. It is now well accepted that the success of this ALE process hinges on the self-limiting deposition of Ga to approximately a monolayer on the As-terminated GaAs(100) surface during the TMGa cycle. Two major factors have been proposed to be important for the self-limiting Ga deposition. The first is the passivation of the GaAs surface by the  $\text{CH}_3$  groups from the adsorbed TMGa molecules [1, 2]. The second factor is the change in surface chemistry with the stoichiometric ratio of As to Ga on the surface as the GaAs(100) surface evolves from As rich to Ga rich during the Ga deposition [3, 4]. The purpose of this paper is to elucidate these two factors and offer a model which utilizes both concepts to explain some phenomena observed in growth experiments.

This ALE process has a few important properties. The self-limiting deposition of Ga was evidenced by the fact that the growth per cycle was independent of the TMGa dosage (pressure  $\times$  time) once the latter exceeded a minimum value to produce a monolayer [1]. Temperature was a very important parameter. The GaAs deposition rate was not necessarily 1 ML per TMGa cycle. It increased steadily from about 0.1 ML per cycle at 350 °C to close to 1 ML per cycle at 500 °C. Then there was a critical temperature of about 520 °C above which the Ga deposition was no longer self-limit-

ing and ALE failed. Deposition of Ga droplets was observed at these high temperatures [1]. These results were obtained under very low pressure growth conditions. The reactor pressure apparently has an effect on the value of this critical temperature. Ozeki *et al.* [5, 6] have reported successful ALE growth up to 550 °C in their 20 Torr reactor with the growth rate independent of TMGa pulse duration and flow rate (partial pressure). Recently Aoyagi and his coworkers [7] found that this critical temperature could be shifted upward by using higher flow rates of  $\text{H}_2$  carrier gas. In addition, Reid *et al.* [8] have demonstrated that ALE at atmospheric pressure could be achieved at 600 °C and above. They have proposed that TMGa decomposition in the gas phase could play an important role. On the other hand, DenBaars *et al.* [9] have observed deviations from ideal ALE at 500 °C in their atmospheric pressure reactor. We do not have a good explanation of the effects of the reactor pressure at this moment. Hence we shall focus our discussion on the low pressure results of Nishizawa *et al.* where both gas phase reactions and gas dynamics did not play an important role. Our goal is to establish a model of ALE which gives the correct behavior with respect to temperature and TMGa exposure.

## 2. Surface chemistry

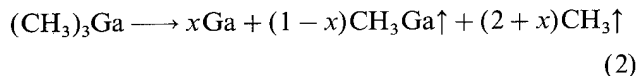
The surface reaction of TMGa on GaAs(100) surfaces has been studied by many groups [4, 10–14]. Here we shall summarize the experimental observations that are relevant for the development of the ALE model. For the following discussion all the coverages will be in units of monolayer, which is the number density of Ga atoms in one molecular plane of GaAs(100) ( $6.26 \times 10^{14} \text{ cm}^{-2}$ ). The initial sticking coefficient  $s_0$  of TMGa on GaAs(100) was found to decrease from about 0.6 at 375 °C to about 0.4 at 500 °C and was not sensitive to

the Ga:As stoichiometric ratio of the surface [4]. The  $\text{CH}_3$  group is large and the saturation coverage on GaAs(100) at room temperature has been reported to be between about 0.2 [10] and 0.25 ML [14]. Hence the steric hindrance factor  $\alpha \approx 4$ , meaning that each adsorbed  $\text{CH}_3$  group passivates four sites on average. The sticking coefficient  $s$  is hence given in the first approximation by

$$s = s_0(1 - \alpha[\text{CH}_3]) \quad (1)$$

where  $[\text{CH}_3]$  is the  $\text{CH}_3$  coverage.

We found that the reaction pathway was [4]



where  $x$  is stoichiometry dependent.  $\text{CH}_3$  was found to adsorb on two kinds of sites with different desorption rates, but the slower pathway dominated at the temperatures of interest [11]. Hence we shall use the following measured desorption rate for  $\text{CH}_3$  in our model:

$$k = 10^{14.48} \exp\left(-\frac{45.0 \text{ kcal mol}^{-1}}{k_B T}\right) \text{ s}^{-1} \quad (3)$$

where  $k_B$  is the Boltzmann constant and  $T$  is the absolute temperature. The desorption of  $\text{CH}_3\text{Ga}$  is first order in  $[\text{CH}_3]$ . Its desorption rate depends on the As:Ga stoichiometric ratio on the surface and increases rapidly with Ga coverage once the latter exceeds a critical value. This is depicted in Fig. 1, where the desorbed  $\text{CH}_3\text{Ga}$  signal is plotted against the increase in Ga coverage. The relative increase in Ga coverage was determined by the simultaneous determination of the sticking coefficient during the experiment. The detailed analysis will be reported in future publications. The uppermost curve is for 375 °C, where the starting surface was the As-stabilized  $c(2 \times 8)$  surface. The  $\text{CH}_3\text{Ga}$  desorption was small and Ga coverage independent initially [4]. Then the yield increased rapidly with the Ga coverage  $[\text{Ga}]$  when the latter reached a critical value  $[\text{Ga}]_0$ . We found that this rapid increase could be approximated by the expression

$$f(\text{Ga}) = ([\text{Ga}] - [\text{Ga}]_0)^3 \quad (4)$$

The fit to the experimental data is shown by the solid curve. The Ga coverage reached a self-limiting value as expected. It is difficult to determine  $[\text{Ga}]_0$ . However, if we assume an estimate of 0.6 ML for the limiting Ga coverage, as guided by the published experimental values, and since the starting  $c(2 \times 8)$  surface has 0.25 ML Ga [15],  $[\text{Ga}]_0$  will be about 0.37 ML Ga. We shall use the round-off value 0.4 ML for  $[\text{Ga}]_0$  in this paper. We increased the sample temperature so that the starting surface had higher initial Ga coverage (by the desorption of As). As the curves in Fig. 1 show, at 425 °C the initial coverage-independent segment disappeared and the data fit eqn. (4) well. At 475 °C the starting surface

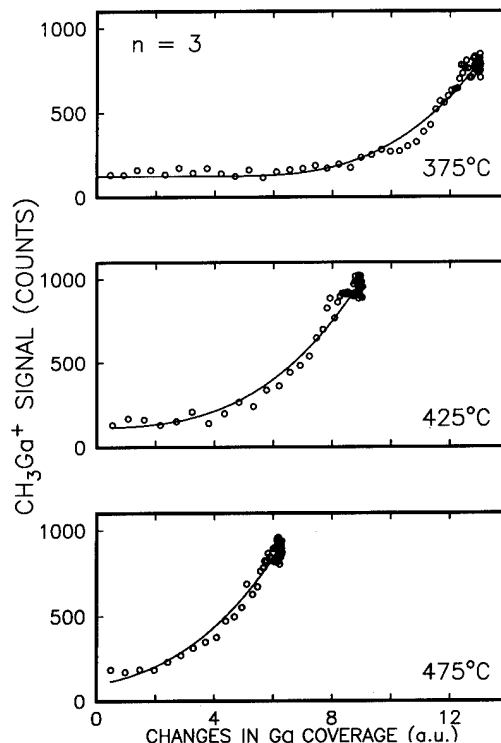


Fig. 1.  $\text{CH}_3\text{Ga}^+$  mass spectrometric signal as a function of changes in Ga coverage in arbitrary units during TMGa exposure at 375, 425 and 475 °C.

had even higher Ga coverage and the  $\text{CH}_3\text{Ga}$  desorption increased immediately with Ga coverage. It is important to note that the maximum value of  $f(\text{Ga})$  is  $f(1) = 0.216$ , which is attained at 1 ML Ga coverage. When  $[\text{Ga}]$  exceeds 1 ML, only 1 ML Ga will contribute to the surface reaction and  $f(\text{Ga})$  stays at 0.216. The increase in surface area due to Ga droplets will not be discussed in this paper since we have little knowledge about the droplet formation process. We shall also neglect the small stoichiometry-independent component of the  $\text{CH}_3\text{Ga}$  desorption since its effect is equivalent to lowering the effective sticking coefficient slightly in the first order. The rate of  $\text{CH}_3\text{Ga}$  desorption is hence given by

$$\tilde{k}[\text{CH}_3]f(\text{Ga}) \quad (5)$$

The rate constant  $\tilde{k}$  was not determined in our experiment, since experimental limitations did not permit us to do the necessary measurements of the Ga and  $\text{CH}_3$  coverages in real time. Instead,  $\tilde{k}$  is determined from the growth data as discussed below.

### 3. The reaction model

The surface chemistry can be summarized qualitatively by the following equations for the surface coverages of Ga and  $\text{CH}_3$  respectively:

$$\begin{aligned}\frac{d[\text{Ga}]}{dt} &= I_B s_0 (1 - \alpha[\text{CH}_3]) - \tilde{k}[\text{CH}_3]f(\text{Ga}) \\ \frac{d[\text{CH}_3]}{dt} &= 3I_B s_0 (1 - \alpha[\text{CH}_3]) - k[\text{CH}_3] - \tilde{k}[\text{CH}_3]f(\text{Ga})\end{aligned}\quad (6)$$

We shall base our model on these equations with experimentally determined parameters. Nishizawa *et al.* [1] used a TMGa exposure of  $5 \times 10^{-5}$  Torr, which is equivalent to a dosage rate of about  $15 \text{ ML s}^{-1}$ . The total exposure time was 4 s. These parameters will be used in all the calculations reported in this paper unless stated otherwise. The initial sticking coefficient  $s_0$  is linearly extrapolated from the values quoted above. The steric factor  $\alpha = 4$ . The desorption constant  $\tilde{k}$  for  $\text{CH}_3$  is given by eqn. (3). The rate constant  $k$  is to be determined by fitting the model to the experimental growth data of Nishizawa *et al.* [1]. We shall make the simplifying assumptions that the starting surface is As terminated, so the initial Ga coverage is zero, and the self-limiting Ga coverage at  $520^\circ\text{C}$  is exactly one monolayer. The calculation presented here is an attempt to attain useful insight to the ALE process by a qualitative examination of the different factors in the model.

## 4. Discussion

### 4.1. Effect of $\text{CH}_3$ desorption

We first examine the case without  $\text{CH}_3\text{Ga}$  desorption ( $\tilde{k} = 0$ ). Figure 2, curve (a) shows the Ga coverage as a function of TMGa exposure time for  $k = 7.5 \text{ s}^{-1}$  and  $s_0 = 0.48$ , which were the measured values at about

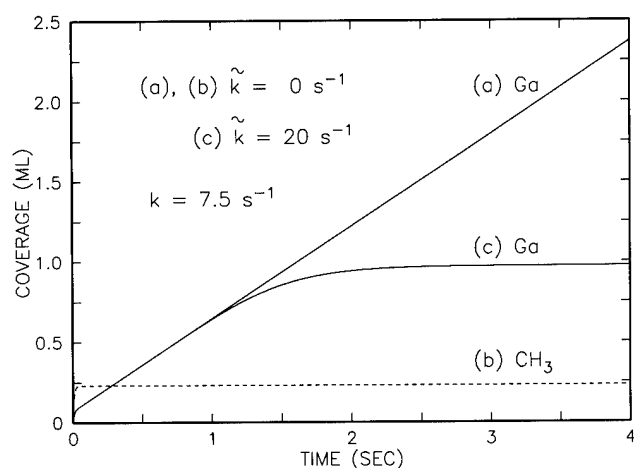


Fig. 2. Model calculation results for (a, c) Ga and (b)  $\text{CH}_3$  coverages as a function of time. The TMGa dosage rate is  $15 \text{ ML s}^{-1}$ ;  $k$  and  $s_0$  are  $7.5 \text{ s}^{-1}$  and  $0.48$  respectively; (a) and (b) are for the case without  $\text{CH}_3\text{Ga}$  desorption ( $\tilde{k} = 0$ ), while (c) is with  $\text{CH}_3\text{Ga}$  desorption ( $\tilde{k} = 20 \text{ s}^{-1}$ ).

$450^\circ\text{C}$ . It can be readily seen that even though the  $\text{CH}_3$  coverage ( $0.23 \text{ ML}$ , curve (b)) is quite close to the value of  $0.25$  which is needed to completely passivate the GaAs surface, the desorption  $\text{CH}_3$  always opens up new sites for the adsorption of TMGa. This can be seen from eqn. (6). The steady state  $\text{CH}_3$  coverage  $[\text{CH}_3]_s$  is equal to  $3I_B s_0 (3I_B s_0 \alpha + k)^{-1}$  and is always smaller than  $\alpha^{-1}$ , which is the required amount to passivate the surface completely. This dynamic state allows the Ga coverage to steadily increase with time and the Ga deposition is not self-limiting. Hence the site blocking by  $\text{CH}_3$  alone is not sufficient to self-limit deposition under the dynamic situation at elevated temperatures.

### 4.2. Effect of $\text{CH}_3\text{Ga}$ desorption

Self-limiting Ga deposition can be achieved by introducing the  $\text{CH}_3\text{Ga}$  desorption channel. Curve (c) in Fig. 2 was calculated for the same experimental conditions but with  $\tilde{k} = 20 \text{ s}^{-1}$ . Indeed, the Ga coverage is self-limiting to about  $0.97 \text{ ML}$ . The mechanism for the self-limiting Ga deposition is the following. There is a continual deposition of Ga on the surface by the pyrolysis of TMGa as discussed above. The rapid non-linear increase in the  $\text{CH}_3\text{Ga}$  desorption with Ga coverage provides a negative feedback by which the Ga coverage is stabilized to a self-limiting value. At this coverage the depositing Ga flux is exactly balanced by the outgoing Ga flux through the desorption of  $\text{CH}_3\text{Ga}$ . Hence this "flux balance" model is able to provide a Ga self-limiting coverage under this dynamic state condition.

Equation (6) allows us to relate the steady state Ga coverage to the values of  $k$  and  $\tilde{k}$ . At steady state  $d[\text{Ga}]/dt = d[\text{CH}_3]/dt = 0$ . This leads to the following relation for steady state Ga coverage  $[\text{Ga}]_s$ :

$$\begin{aligned}\frac{k}{2\tilde{k}} &= f(\text{Ga})_s = ([\text{Ga}]_s - [\text{Ga}]_0)^3 \\ \text{or} \\ [\text{Ga}]_s &= [\text{Ga}]_0 + \left(\frac{k}{2\tilde{k}}\right)^{1/3}\end{aligned}\quad (7)$$

The dependence on the ratio between the two rate constants reflects the competition between the desorption of  $\text{CH}_3$  and the desorption of  $\text{CH}_3\text{Ga}$ . The desorption of  $\text{CH}_3$  of the adsorbed TMGa on the surface results in the deposition of Ga, while the desorption of  $\text{CH}_3\text{Ga}$  causes the removal of Ga. It is important to note that the steady state coverage, eqn. (7), is independent of the TMGa flux  $I_B$ , the initial sticking coefficient  $s_0$ , the steric factor  $\alpha$  and the total time of exposure. This is expected for the ideal ALE process. However, these parameters do control the initial time dependence of the Ga coverage and the steady state  $\text{CH}_3$  coverage.

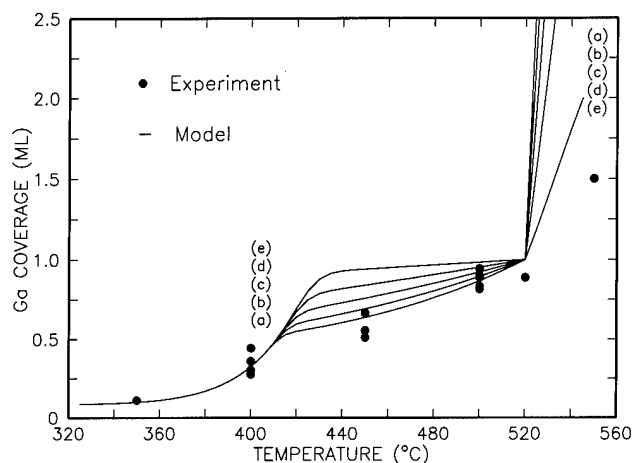


Fig. 3. Comparison between experimental Ga coverage data (●) from ref. 1 and model calculations for  $\tilde{k} =$  (a) 0, (b) 10, (c) 20, (d) 30 and (e) 40 kcal mol<sup>-1</sup>. The TMGa exposure was 15 ML s<sup>-1</sup> for 4 s.

#### 4.3. Temperature dependence

According to eqn. (7), the temperature dependence is determined by the ratio of the two rate constants. The temperature dependence of  $k$  is given by eqn. (2). We estimate  $\tilde{k}$  by fitting the model to the experimental temperature dependence observations of Nishizawa *et al.* [1]. It is convenient to write  $\tilde{k}$  in the Arrhenius form with a temperature-independent pre-exponential factor  $A$  and an activation energy  $E_A$ . The fact that ALE is 1 ML per cycle at 520 °C means that  $k/2\tilde{k}$  equals  $f(1)$  ( $=0.216$ ) at this temperature. This gives a relation between  $A$  and  $E_A$  and hence  $E_A$  is the only unknown parameter.

Figure 3 is a comparison between the experimental Ga coverage (filled circles) as a function of temperature as reported by Nishizawa *et al.* [1] and the prediction of the model (solid curves) for  $\tilde{k}$  with various values of  $E_A$ : (a) 0, (b) 10, (c) 20, (d) 30 and (e) 40 kcal mol<sup>-1</sup>. The model calculation gives a reasonable qualitative agreement with the experiment with  $E_A$  lying between 0 and 10 kcal mol<sup>-1</sup>. We shall let  $E_A$  be 10 kcal mol<sup>-1</sup> in this paper for our qualitative discussion. Since  $E_A$  is smaller than the activation energy of  $k$  (45 kcal mol<sup>-1</sup> in eqn. (3)),  $k/2\tilde{k}$  increases with temperature and exceeds  $f(1)$  at temperatures above 520 °C.  $[Ga]_s$  in eqn. (7) will exceed 1 ML and self-limiting deposition is no longer possible. The physical reason is that the desorption rate of CH<sub>3</sub>Ga cannot match the desorption rate of CH<sub>3</sub> (hence the Ga deposition rate). The Ga flux balance condition cannot be maintained. Gallium will be deposited continuously to beyond a monolayer and Ga droplets can be formed. The Ga deposition rate increases with temperature, since the higher desorption rate of CH<sub>3</sub> opens up more sites on the surface for reaction with TMGa. Hence the model successfully

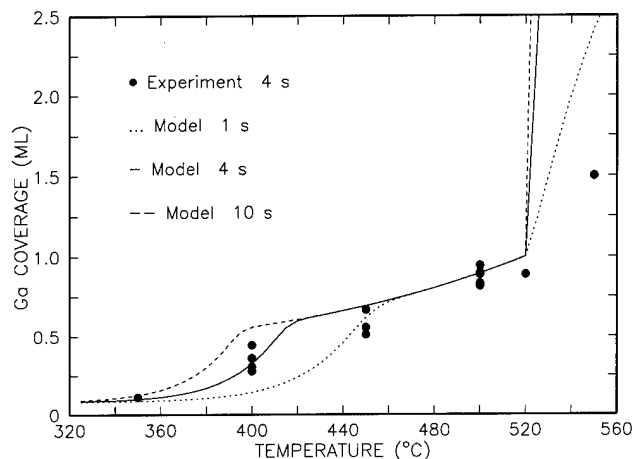


Fig. 4. Comparison between Ga coverages from model calculations for TMGa dosage times of 1 s (dotted curve), 4 s (solid curve) and 10 s (dashed curve) with experiment data (●) from ref. 1 for 4 s.

reproduces the non-self-limiting growth at temperatures above 520 °C. The model gives a higher deposition rate than was shown by the experiment. This may be related to the assumption of the same sticking coefficient  $s_0$  and desorption rates  $k$  and  $\tilde{k}$  for both the Ga and GaAs surfaces. The formation of Ga droplets may also change the effective surface area for the reaction. The important result is that the model predicts an ALE process with temperature-dependent self-limiting Ga coverages and the failure of the ALE process at temperatures above a critical temperature, all in good qualitative agreement with experimental observations.

It is interesting to observe that there is an obvious drop in Ga coverage at temperatures below 420 °C in Fig. 3. More careful examination of the model shows that below this temperature the reaction is so slow that the Ga deposition is limited by the TMGa dosage time and fails to reach the self-limiting coverage. This is hence no longer a true ALE process. The "ALE" region is from 420 to 520 °C only. The effect of the TMGa dosage time on the width of the "ALE" region is illustrated in Fig. 4. The model calculations are shown for dosage times of 1 s (dotted curve), 4 s (solid curve) and 10 s (dashed curve) and are compared with the experimental data for 4 s dosage time. The low temperature limit of the "ALE" region is extended from 450 °C for 1 s to 420 °C for 4 s and 390 °C for 10 s.

#### 5. Conclusions

A simple model for the ALE of GaAs which is based on the observations of TMGa surface chemistry is



developed to explain the self-limiting Ga deposition. The model includes two important factors: the blocking of adsorption sites by the adsorbed  $\text{CH}_3$  and the sensitivity of the surface chemistry to the Ga:As stoichiometric ratio of the GaAs surface during growth. The model successfully reproduces several important features. It shows that the self-limiting Ga deposition is temperature dependent and is not necessarily at 1 ML. Its value is independent of TMGa exposure time provided that the TMGa exposure is enough to reach the self-limiting state. It also shows that the self-limiting Ga deposition will fail at temperatures above a critical value. This simple model can form the basis of a more complete model where gas phase phenomena can be incorporated.

### Acknowledgments

The author would like to thank his coworkers N. I. Buchan, T. F. Kuech, U. Memmert, A. Naermann and R. Souda for their collaborations in the experimental work.

### References

- 1 J. Nishizawa, T. Kurabayashi, H. Abe and A. Nozoe, *Surf. Sci.*, **185** (1987) 249.
- 2 J. R. Creighton, K. R. Lykke, V. A. Shamamian and B. D. Kay, *Appl. Phys. Lett.*, **57** (1990) 279.
- 3 Y. Sakuma, M. Ozeki, N. Ohtsuka and K. Kodama, *J. Appl. Phys.*, **68** (1990) 5660.
- 4 M. L. Yu, N. I. Buchan, R. Souda and T. F. Kuech, *MRS Symp. Proc.*, **222** (1991) 3.
- 5 M. Ozeki, K. Mochizuki, N. Ohtsuka and K. Kodama, *Appl. Phys. Lett.*, **53** (1988) 1509.
- 6 M. Ozeki, N. Ohtsuka, Y. Sakuma, and K. Kodama, *J. Cryst. Growth*, **107** (1991) 102.
- 7 Y. Aoyagi, personal communication, 1992.
- 8 K. G. Reid, H. M. Urdianyk, N. A. El-Masry and S. M. Bedair, *MRS Symp. Proc.*, **222** (1991) 133.
- 9 P. DenBaars, P. D. Dapkus, C. A. Beyler, A. Hariz and K. M. Dzurko, *J. Cryst. Growth*, **93** (1988) 195.
- 10 M. L. Yu, U. Memmert and T. F. Kuech, *Appl. Phys. Lett.*, **55** (1989) 1011.
- 11 U. Memmert and M. L. Yu, *Appl. Phys. Lett.*, **56** (1990) 1884.
- 12 J. R. Creighton, *Surf. Sci.*, **234** (1990) 287.
- 13 J. A. McCaulley, R. J. Shul and V. M. Donnelly, *J. Vac. Sci. Technol. A*, **9** (1991) 2872.
- 14 J. R. Creighton and B. A. Banse, *MRS Symp. Proc.*, **222** (1991) 15.
- 15 C. Deparis and J. Massies, *J. Cryst. Growth*, **108** (1991) 157.

# Study of surface reactions in atomic layer epitaxy of GaAs using trimethylgallium by reflectance difference spectroscopy and mass spectroscopy

B. Y. Maa and P. D. Dapkus

Department of Electrical Engineering and the Center for Photonic Technology, University of Southern California, Los Angeles, CA 90089-0483 (USA)

## Abstract

An *in situ* real-time study of surface reactions in atomic layer epitaxy (ALE) of GaAs using trimethylgallium (TMGa) by reflectance difference spectroscopy (RDS) and sampled beam mass spectroscopy is reported. These studies reveal several phases in atomic layer epitaxy of GaAs and the self-limiting atomic layer deposition of epilayers using TMGa. The results also lend further support to a proposed reaction kinetics model from a recent RD investigation. The self-limiting mechanism which occurs during TMGa exposure cycles is believed to result from both selective adsorption and reaction of TMGa at As atoms and Ga-vacancy-induced Ga-rich surface reconstructions. It is also shown that strategies for optimal ALE growth of GaAs can be obtained through RD monitoring.

## 1. Introduction

Atomic layer epitaxy (ALE) of III–V compound semiconductors using organometallic precursors holds great promise for crystal growth of layers with uniform thickness and control at the atomic level [1, 2]. ALE is a process which proceeds by separately exposing the semiconductor surface to group III and V reactants. Conditions are chosen which result in the formation of a single monolayer of adsorbate containing each element during the alternate exposures. By careful choice of the reactants, reaction pathways can be found that result in the formation of the desired compound via surface reactions. In this way saturated surface reactions are utilized to deposit exactly one monolayer of the compound over the entire surface on each cycle of exposures. This results in a conformal monolayer-by-monolayer epitaxial growth habit.

In this paper we present results of studies of surface reactions in atomic layer epitaxy of GaAs using trimethylgallium (TMGa) as gallium source. To meet this goal, *in situ* real-time analyses by reflectance difference spectroscopy (RDS) and sampled beam mass spectroscopy are carried out such that complementary surface structural and chemical information is obtained. A kinetics model is established to address the surface reactions during TMGa exposure on GaAs(001) surfaces and the resultant self-limiting mechanism. It is also shown that the optimal growth conditions in ALE of GaAs can be achieved through *in situ* real-time RDS monitoring.

## 2. Experiments

All experiments were performed in an ultrahigh vacuum (UHV) system consisting of an analysis chamber and a reaction chamber as shown in Fig. 1. The analysis chamber is a modified PHI 5100 system equipped with X-ray photoelectron spectroscopy (XPS). The reaction chamber provides for exposure to TMGa and tertiarybutylarsine (TBAs) through UHV leak valves. The RDS set-up is similar to that described by Aspnes *et al.* [3] but is simplified through the use of a single-wavelength He–Ne laser (632.8 nm or 1.96 eV) as light source [4, 5]. Aspnes *et al.* have shown that at this energy (1.96 eV) the major contribution to the RD signal from a GaAs(001) surface is due to the presence of Ga–Ga dimers [6]. The RD signal at 1.96 eV thus acts as an indicator of the surface Ga–Ga dimer popu-

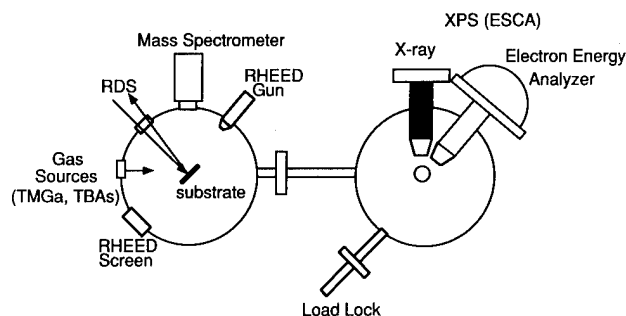


Fig. 1. Schematic diagram of UHV system used to study surface reactions of organometallics on III–V semiconductors.

lation and allows us to follow the formation and annihilation of surface Ga-Ga dimers. The differently pumped quadrupole mass spectrometer (QMS) is surrounded by a shroud cooled by liquid nitrogen and is in line-of-sight of the GaAs substrate to monitor the reflected reactant and desorbed byproducts. Throughout the experiment we use 22 eV, 0.84 mA electron emission for the ionizer of the QMS to minimize cracking of the molecules. Reflection high energy electron diffraction (RHEED) is used to characterize the surface structures.

### 3. Results

Clean  $2 \times 4$  As-rich (001) GaAs substrates are initially prepared for TMGa exposures. Figure 2 shows the transient behavior of  $\Delta R/R$  ( $\Delta R = R_{110} - R_{\bar{1}\bar{1}0}$ ) and of chemical species with a.m.u. 99, 15 and 84 for a 4 s TMGa exposure at a substrate temperature of 500 °C and a TMGa exposure level of  $2.6 \times 10^{-6}$  Torr. The broken line on the left marks the turn-on of TMGa flow on the substrate and the dotted line on the right marks the turn-off of TMGa injection. The RD signal starts to rise after the TMGa flow is initiated. The RD signal continues to increase even though the TMGa

flow is terminated at the end of 4 s, until a final saturation level is reached. A RHEED  $4 \times 6$  pattern characteristic of a Ga-rich surface is obtained. The gas species with a.m.u. 99 represents the molecular TMGa reflecting from the surface. The sharp rise and fall-off characteristics show rapid on-off switching of our gas manifold. Methyl radicals ( $\text{CH}_3$ ) and monomethylgallium ( $\text{GaCH}_3$ ) are detected at a.m.u. 15 and 84 respectively. In a separate experiment we have found that the contributions of  $\text{CH}_3$  and  $\text{GaCH}_3$  from molecular TMGa cracked by the ionizer are insignificant compared with what we observe here. They are in fact the surface reaction byproducts desorbing from the substrate. The signal of methyl radicals shows an initial rise and then a gradual decrease. After the TMGa supply is turned off, methyl radicals decay to the background level with an exponential tail.  $\text{GaCH}_3$  behaves differently from  $\text{CH}_3$ , with a small initial rise but then a gradual increase.

To inspect in more detail the evolution of the desorbing  $\text{CH}_3$  and  $\text{GaCH}_3$  with respect to the surface stoichiometry, we perform the following experiment. Five consecutive 1 s TMGa exposures are applied to the initial As-rich surface with a 10 s break between each exposure. The transient signals of  $\Delta R/R$ ,  $\text{CH}_3$  and  $\text{GaCH}_3$  are shown in Fig. 3. The broken lines mark the

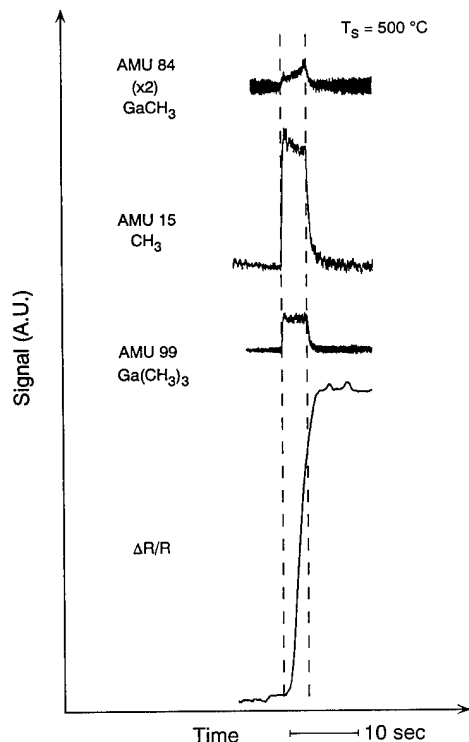


Fig. 2. Transient QMS response of a.m.u. 99, 15 and 84 and RD transient on initiation of TMGa exposure at a substrate temperature of 500 °C and a TMGa flux of  $2.6 \times 10^{-6}$  Torr.

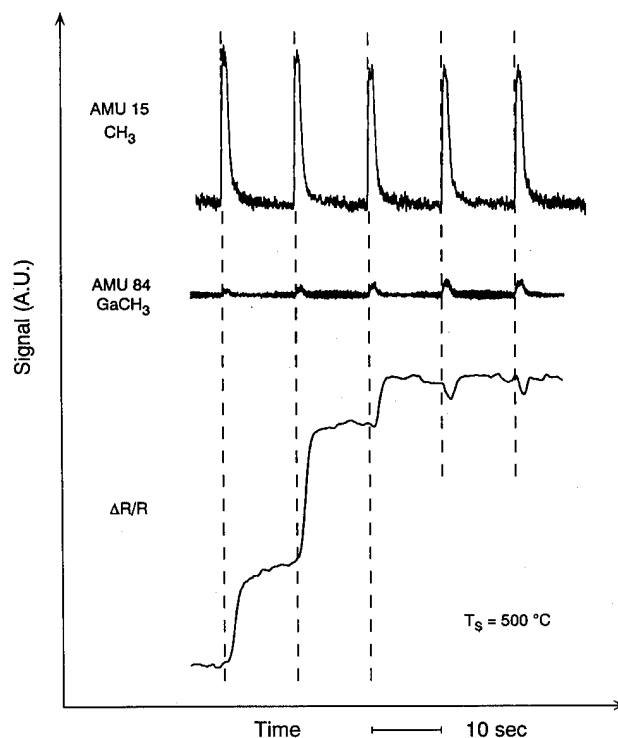


Fig. 3. QMS response of a.m.u. 15 and 84 and RD transient at 500 °C and a TMGa exposure level of  $2.6 \times 10^{-6}$  Torr. Five consecutive 1 s TMGa exposures are applied to the initial As-rich surface with a 10 s break between each exposure. The broken lines mark each turn-on of TMGa exposure.

turn-on of each TMGa exposure. The RD signal increases with each TMGa exposure until the end of the third exposure. At the fourth and fifth TMGa exposures the RD signal falls off on turn-on of the TMGa flow and then rises back to the previous level after the TMGa flow is terminated. This resembles the behavior of Ga-rich surfaces exposed to TMGa [4, 5]. In the meantime we notice both decreased  $\text{CH}_3$  and increased  $\text{GaCH}_3$  desorption with each TMGa exposure until the end of the third exposure, after which they saturate.

#### 4. Discussion

A huge peak of  $\text{CH}_3$  and a small peak of  $\text{GaCH}_3$  on TMGa injection on the GaAs(001) surface are observed as shown in Fig. 2. A recent study by Memmert and Yu [7] shows that TMGa reacts with surface arsenic atoms and dissociates into  $\text{GaCH}_3$ , releasing two  $\text{CH}_3$  radicals on the surface. These methyl radicals desorb in two channels: one for the desorption of  $\text{CH}_3$  from  $\text{GaCH}_3$ , the other for the desorption of  $\text{CH}_3$  from the GaAs(001) surface. Desorption of  $\text{CH}_3$  from the adsorbed  $\text{GaCH}_3$ , as described previously [4, 5], results in the formation of gallium atoms, which tend to form Ga–Ga dimer bonds as judged by the increasing RD signal. On the other hand, the two released  $\text{CH}_3$  radicals associated with TMGa dissociation could be attached to either surface As or Ga atoms [7, 8]. Attachment of  $\text{CH}_3$  radicals to nearby arsenic atoms hinders further reactions between these arsenic atoms and impinging TMGa molecules temporarily. Not until the desorption of  $\text{CH}_3$  radicals from arsenic atoms will these arsenic atoms become active again toward TMGa dissociation. There exists the possibility for  $\text{CH}_3$  radicals to be attached to the newly formed gallium dimers to form a pair of  $\text{GaCH}_3$ , which requires that gallium dimer bonds be broken. Recovery of Ga–Ga dimers is anticipated once  $\text{CH}_3$  radicals desorb from gallium atoms. Nevertheless, reactions involving broken gallium dimer bonds would introduce a decrease in the signal level of RD, which is only sensitive to the existence of Ga–Ga dimer bonds.

When  $2 \times 4$  As-rich surfaces are exposed to TMGa molecules, these reactions proceed simultaneously. In the initial stage the formation of gallium dimers results in a steady increase in the RD signal. However, the RD signal level only reflects the number of gallium atoms possessing dimer-bonding configurations. Those deposited gallium atoms which are attacked by  $\text{CH}_3$  cannot be detected by RD. When the TMGa flow is terminated, those  $\text{CH}_3$  radicals which are bonded to gallium atoms desorb and Ga–Ga dimers appear on the surface. The RD signal therefore continues to increase with the desorption of residual  $\text{CH}_3$  until all Ga–Ga

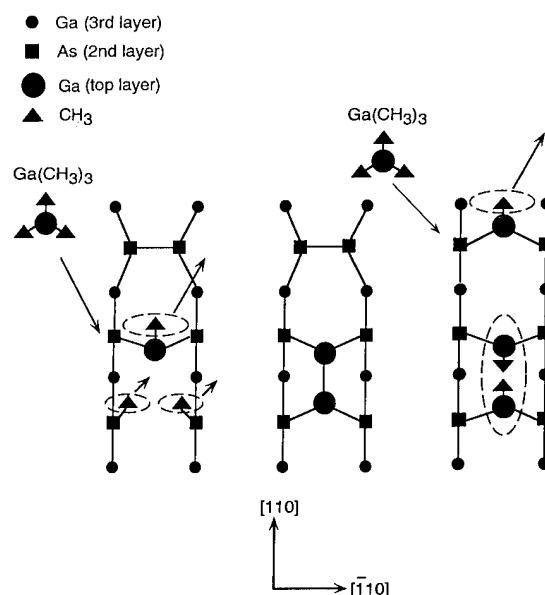


Fig. 4. Schematic diagram illustrating reaction pathways during initial TMGa exposure on (001)GaAs As-rich surfaces.

dimers are recovered. This is evidenced by the good correspondence between the  $\text{CH}_3$  decay tail and Ga–Ga dimer recovery as shown in Fig. 2. A schematic diagram illustrating the reaction pathways mentioned above is shown in Fig. 4.

In the meantime, as depicted in Fig. 2, we observe decreasing  $\text{CH}_3$  and increasing  $\text{GaCH}_3$  desorption as the RD signal increases. It is our contention that as the surface is increasingly filled with gallium atoms, other reaction pathways start to have dominant roles. It is well known that a Ga-rich GaAs(001) surface is not terminated with a complete atomic layer of gallium dimers but instead contains a number of gallium vacancies that expose underlying arsenic atoms to vacuum [9, 10]. Such exposed arsenic atoms are active toward TMGa decomposition to form  $\text{GaCH}_3$  with the release of two  $\text{CH}_3$  radicals. Instead of leaving Ga atoms behind on the surface with desorption of  $\text{CH}_3$  as in the early adsorption stage,  $\text{GaCH}_3$  tends to desorb from the energetically unfavorable Ga vacancy site in order to maintain a stable electronic state with a minimum free energy [11]. This would result in both increasing  $\text{GaCH}_3$  and decreasing  $\text{CH}_3$  desorption. Our observation is consistent with that by Yu *et al.*, who noticed an additional channel of desorption for  $\text{GaCH}_3$  when the TMGa flux and/or exposure are increased [12]. The experiment shown in Fig. 3 provides more support for this argument. Following each TMGa exposure, when the initial As-rich surface is gradually filled with Ga atoms as indicated by the increased RD signal, both increased  $\text{GaCH}_3$  and decreased  $\text{CH}_3$  desorption are observed until the end of the third TMGa exposure. A Ga-rich surface is obtained at this stage. Such Ga-rich

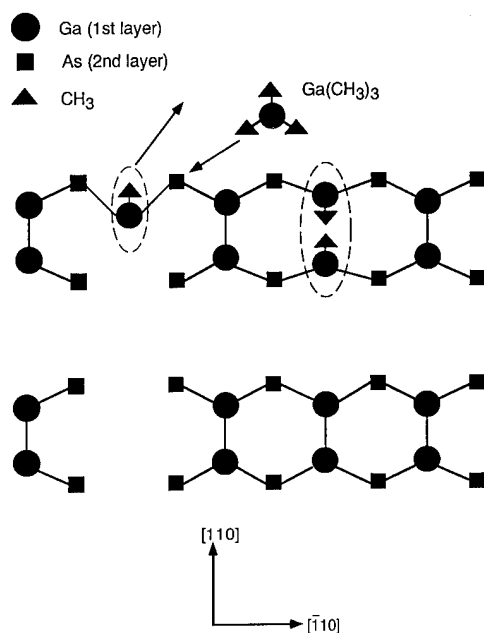


Fig. 5. Schematic diagram illustrating reaction pathways during TMGa exposure on (001)GaAs Ga-rich surfaces.

surfaces are reactive toward TMGa dissociation with a fixed number of exposed arsenic atoms. Desorption of GaCH<sub>3</sub> and CH<sub>3</sub>, therefore saturates on further TMGa exposure on Ga-rich surfaces. It is this Ga-vacancy-induced surface reconstruction and selective TMGa reaction on exposed arsenic atoms that cause the self-limiting mechanism in TMGa-based ALE of GaAs. A schematic diagram illustrating the reaction pathways on Ga-rich surfaces is shown in Fig. 5.

Since we understand the RD transient behavior, we can apply RD as an *in situ* real-time technique to optimize growth conditions in ALE. Shown in Fig. 6 is one example of an RD transient at a substrate temperature of 500 °C and a TMGa flux of  $1.2 \times 10^{-5}$  Torr. On TMGa injection the RD signal increases steadily, then starts to slow down around 1.5 s and eventually a kink shows up. We have observed similar behavior before and interpreted it as resulting from an overdose of TMGa, *i.e.* the supplied TMGa is more than what is needed to deposit one atomic layer of gallium [4, 5]. We notice that the time for the RD signal to slow down coincides with the occurrence of saturated CH<sub>3</sub> and GaCH<sub>3</sub> desorption, an indication that a Ga-rich surface is obtained already. Additional TMGa impingement beyond this point brings about more undesired CH<sub>3</sub> radicals on the surface. Using RD, we can therefore determine the optimal exposure time for a certain TMGa exposure level and the purge time before introducing the arsenic source. Currently we are employing RD in a high vacuum reactor to optimize ALE growth.

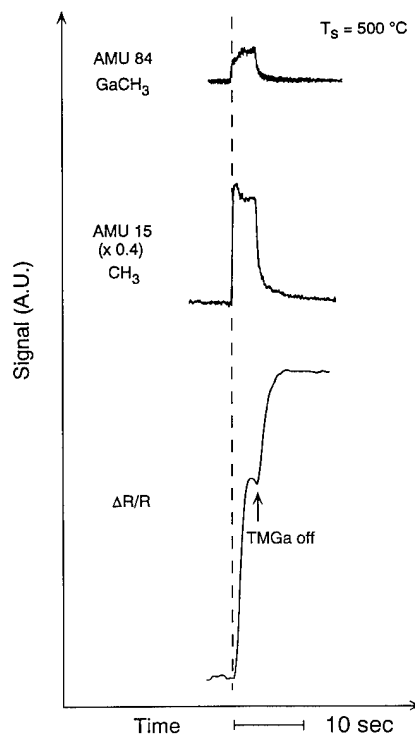


Fig. 6. Transient QMS response of a.m.u. 15 and 84 and RD transient on initiation of TMGa exposure at a substrate temperature of 500 °C and a TMGa flux of  $1.2 \times 10^{-5}$  Torr. The broken line marks the turn-on of TMGa exposure.

## 5. Conclusions

*In situ* real-time RD and mass spectroscopy are applied to study surface reactions of TMGa on GaAs(001). Different reaction pathways occur depending on the surface stoichiometry. A kinetics model based on our study is established to account for various phases during TMGa exposure. The self-limiting atomic layer deposition of gallium atoms occurs because of both selective adsorption and reaction of TMGa at As atoms and Ga-vacancy-induced Ga-rich surface reconstructions. The application of RDs to *in situ* real-time control growth in ALE is also discussed.

## Acknowledgments

The authors would like to acknowledge the support of the Office of Naval Research and the National Renewable Energy Laboratory for portions of this work.

## References

- 1 S. P. DenBaars, C. A. Beyler, A. Hariz and P. D. Dapkus, *Appl. Phys. Lett.*, 51 (1987) 1530.

- 2 K. Mori, M. Yoshida, A. Usui and H. Terao, *Appl. Phys. Lett.*, **52** (1988) 27.
- 3 D. E. Aspnes, J. P. Harbison, A. A. Studna and L. T. Florez, *J. Vac. Sci. Technol. A*, **6** (1988) 1327.
- 4 B. Y. Maa and P. D. Dapkus, *Appl. Phys. Lett.*, **58** (1991) 2261.
- 5 B. Y. Maa and P. D. Dapkus, *MRS Symp. Proc.*, **222** (1991) 25.
- 6 D. E. Aspnes, Y. C. Chang, A. A. Studna, L. T. Florez, H. H. Farrell and J. P. Harbison, *Phys. Rev. Lett.*, **64** (1990) 192.
- 7 U. Memmert and M. Yu, *Appl. Phys. Lett.*, **56** (1990) 1883.
- 8 J. R. Creighton, K. R. Lykke, V. A. Shamamian and B. D. Kay, *Appl. Phys. Lett.*, **57** (1990) 279.
- 9 G. X. Qian, R. M. Martin and D. J. Chadi, *J. Vac. Sci. Technol. B*, **5** (1987) 1482.
- 10 D. K. Biegelsen, R. D. Bringans, J. E. Northup and L. E. Swartz, *Phys. Rev. Lett.*, **41** (1990) 5701.
- 11 H. H. Farrell, J. P. Harbison and L. D. Peterson, *J. Vac. Sci. Technol. B*, **5** (1987) 1482.
- 12 M. Yu, N. I. Buchan, R. Souda and T. F. Kuech, *MRS Symp. Proc.*, **222** (1991) 3.

# The surface chemistry and kinetics of GaAs atomic layer epitaxy

J. Randall Creighton and Barbara A. Bansenauer

Sandia National Laboratories, Division 1126, Albuquerque, NM 87185-5800 (USA)

## Abstract

We discuss the chemical and kinetic aspects of GaAs atomic layer epitaxy (ALE). Explanations of the stoichiometry problems of GaAs ALE are proposed. We review the proposed ALE mechanisms that deal with trimethylgallium exposure. Results conclusively invalidate the selective adsorption ALE mechanism. Kinetic results indicate that the GaAs surface is covered with  $\text{CH}_3$  groups during typical ALE conditions, as proposed by the adsorbate inhibition mechanism. Measurements of excess gallium deposition at typical ALE partial pressures are in good agreement with predictions of a unimolecular reaction mechanism using kinetic parameters determined by surface science techniques. Two simple ALE kinetic models based on unimolecular surface reaction mechanisms are constructed and the predictions are in good agreement with atmospheric pressure ALE results. The possible role of the flux balance mechanism is discussed.

## 1. Introduction

Atomic layer epitaxy (ALE) [1–11] has generated considerable interest for depositing compound semiconductors with precise thickness control and superb thickness uniformity. Ideally, ALE achieves monolayer scale growth control through alternation of the group V and group III precursors, with each step exhibiting self-limiting deposition, *i.e.* deposition ceases at 1 ML (1 ML =  $6.26 \times 10^{14}$  atoms  $\text{cm}^{-2}$ ), so the overall growth per cycle ( $G_c$ ) is 1 ML. However, the utility of GaAs ALE has been limited owing to its relatively narrow operating window and also to the high unintentional carbon doping levels that are typically produced. The reported size of the operating window and the conditions for producing ALE behavior vary considerably between laboratories [2–9]. The three independent variables to which ideal ALE exhibits insensitivity are precursor pressure (or flux), exposure time and temperature. Most results demonstrate good ALE behavior ( $G_c \approx 1$  ML) with respect to precursor pressure, but with a few exceptions the time and temperature dependences of  $G_c$  are less than ideal. The narrow operating window is generally believed to be due to loss of self-limiting deposition during the gallium cycle. At high temperatures and/or large trimethylgallium (TMGa) exposures excess gallium is deposited, which leads to non-ideal ALE ( $G_c > 1$  ML). Gas phase TMGa pyrolysis is often thought to be the main source of excess gallium deposition [5, 8, 9, 12]. However, the low pressure ALE results of Nishizawa *et al.* [2, 3] clearly show that a heterogeneous (surface) pathway for excess gallium deposition exists. The relative importance of the heterogeneous chemistry *vs.* the homogeneous

chemistry for excess gallium deposition is still the subject of debate.

In this paper we review the proposed mechanisms for GaAs ALE [1–5, 8, 9, 11–24] that deal with the gallium cycle. We demonstrate via kinetic arguments that the GaAs surface is covered with  $\text{CH}_3$  groups during typical ALE conditions and that measurements of excess gallium deposition are in good agreement with the heterogeneous TMGa reaction rate. We discuss the TMGa surface reaction kinetics in some detail. Two simple ALE kinetic models based on unimolecular surface reaction mechanisms are also introduced. We first briefly discuss the stoichiometric issues of ALE for both the arsenic and gallium cycles.

## 2. Experimental details

Most of the relevant experimental details have been published previously [16]. All the results discussed are for GaAs(100) surfaces. Briefly, experiments were performed in a three-level ultrahigh vacuum (UHV) chamber equipped with a number of surface diagnostics. The upper level can be isolated by a gate valve and used for “high” pressure exposures. This feature was valuable for creating the As-rich surfaces. The lower two levels are equipped with Auger spectroscopy, low energy electron diffraction (LEED) and a differentially pumped quadrupole mass spectrometer (QMS) for temperature-programmed desorption (TPD) and molecular beam experiments. The heating rate used for TPD was typically  $5 \text{ K s}^{-1}$ . An effusive molecular beam is designed to impinge on the GaAs surface while desorbed reactant and products are monitored line-of-sight by the QMS.

This arrangement was used to study the temperature and flux dependence of the TMGa reaction rate on GaAs.

A vacuum microbalance was used to measure gallium deposition on GaAs(100) from TMGa exposures in the millitorr pressure range. The GaAs sample was heated radiatively and the temperature was measured with an optical pyrometer. A more detailed description is to be published [25].

### 3. Surface stoichiometry of GaAs ALE

Most discussions of ALE mechanisms deal with kinetic issues, while the questions regarding surface stoichiometry have often been overlooked. None of the known adsorbate-free GaAs(100) surface reconstructions are terminated with 1 ML coverage of Ga or As [26–32] (most have less than 1 ML coverage). It is then very puzzling how ideal ALE ( $G_c = 1$  ML) is achieved. We have shown that methyl groups stabilize a higher gallium coverage [16] than the “(4 × 6)” gallium-rich GaAs(100) contains (the (4 × 6) surface is terminated with about 0.75 ML Ga). We speculate that the Ga coverage on a CH<sub>3</sub>-terminated surface is actually 1 ML, which would resolve the stoichiometry issue for the gallium cycle. However, the As-rich  $c(2 \times 8)/(2 \times 4)$  surface is still terminated with only 0.75 ML As [27, 31, 32]. Hydrogen desorption occurs at too low a temperature to stabilize a surface with about 1 ML As [24, 33]. Recent work has shown that arsine exposures typically used during ALE (with the exception of Nishizawa *et al.*'s work) [24, 34, 35] will actually create a  $c(4 \times 4)$  “super” As-rich surface with an As coverage as high as 1.75 ML [32]. Temperature-programmed desorption results [34] indicate that the surface residence time for much of this extra As is short (less than 2 s) at typical ALE temperatures (450–500 °C), so a large fraction will desorb during the purge after the arsine cycle. However, about 1 ML of the As is in higher binding energy sites and would survive a typical purge cycle (see ref. 34 for a more detailed discussion). This provides a likely explanation of the stoichiometry issue of the arsenic cycle. The low pressure ALE results of Nishizawa *et al.* [2, 3], where  $G_c$  tended to saturate at 0.8–0.9 ML, can also be reconciled by these results. Their arsine exposures were too low to generate arsenic coverages of 1 ML or more.

### 4. The selective adsorption mechanism of ALE

The selective adsorption mechanism of GaAs ALE assumes that TMGa adsorbs and reacts on the arsenic-terminated but not on the gallium-terminated surface. The selective adsorption mechanism is appealing, since

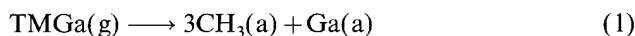
one would expect TMGa to selectively chemisorb on arsenic sites via a Lewis acid–base (donor–acceptor) interaction and there would be no arsenic sites on an ideally terminated (1 ML) gallium-rich surface. This mechanism is often used to explain ALE results [8, 9, 12–14, 17]. However, there is no evidence that an adsorbate-free, ideally terminated gallium-rich surface exists. All theoretical [26, 27] and experimental [28–32] evidence indicates that gallium-rich surfaces have a significant number of gallium vacancies. The vacancies expose arsenic atoms in the second layer which could serve as sites for TMGa chemisorption. In fact, there are many experimental results demonstrating that TMGa chemisorbs and irreversibly decomposes on gallium-rich surfaces [15, 16, 20, 22] at a surprisingly high rate. Molecular-beam-scattering results [21, 24] demonstrate that TMGa reacts with the adsorbate-free Ga-rich GaAs(100) surface with a reactive sticking probability of about 0.5 at typical ALE temperatures. This result shows that ALE cannot arise from differences in the TMGa adsorption rates on adsorbate-free As-rich and Ga-rich surfaces.

There are a number of results used to support the selective adsorption mechanism that we believe are either inconclusive or misinterpreted. The pitfalls of these experiments and their interpretation were outlined in a previous paper [24].

### 5. The adsorbate inhibition mechanism of ALE

The key assumption of the adsorbate inhibition mechanism (also known as the site-blocking mechanism) of ALE is that TMGa converts the arsenic-terminated surface to a gallium-terminated surface covered with adsorbates, *e.g.* methyl groups. At this stage the reaction rate is inhibited by the presence of the adsorbates, which block access to the active surface sites. Most of the previous measurements of the methyl group desorption rate from the Ga-rich surface indicate that it is on the order of  $1 \text{ s}^{-1}$  at 450 °C (see Fig. 1). For a more complete discussion of the CH<sub>3</sub> desorption rate constant measurements, see ref. 24. The effect of this desorption rate on the surface CH<sub>3</sub> coverage can be seen by simply comparing the magnitude of the adsorption and desorption rates. Since the TMGa flux to the surface is many orders of magnitude (typically  $10^2$ – $10^5$  times) higher than the desorption rate constant and the initial sticking coefficient of TMGa is large (about 0.5), the surface will be saturated with methyl groups. This can be described analytically by examining the simple unimolecular surface reaction mechanism below.

TMGa adsorption:





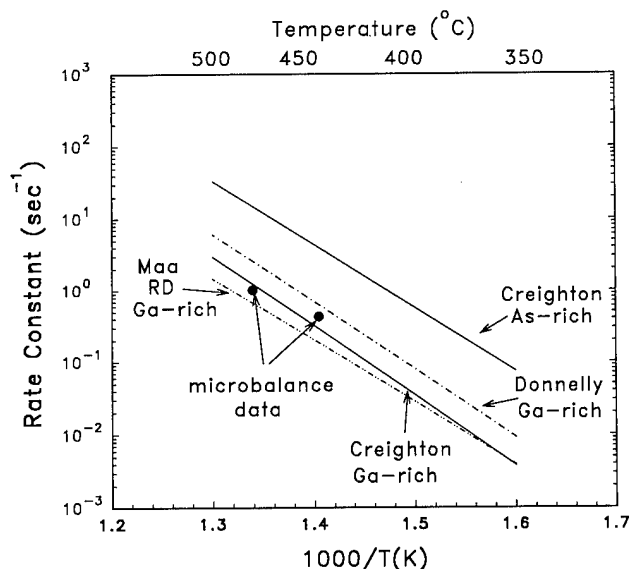


Fig. 1.  $\text{CH}_3$  desorption rate constants measured on the Ga-rich and  $(2 \times 4)$  As-rich GaAs(100) surfaces. Solid points are from direct measurements of Ga deposition rate (see text).

Methyl radical desorption:



Rate equation for  $\text{CH}_3(\text{a})$ :

$$\frac{d\theta_m}{dt} = 3s^\circ \frac{F_T}{N_m} (1 - \theta_m) - k_d \theta_m \quad (3)$$

where  $s^\circ$  is the TMGa initial sticking coefficient,  $F_T$  is the TMGa flux,  $N_m$  is the  $\text{CH}_3$  saturation coverage (molecules  $\text{cm}^{-2}$ ),  $\theta_m$  is the  $\text{CH}_3$  fractional coverage and  $k_d$  is the  $\text{CH}_3$  desorption rate constant.

Steady state solution of  $\theta_m$ :

$$\theta_m = \frac{3s^\circ F_T / N_m}{3s^\circ F_T / N_m + k_d} \quad (4)$$

Rate of TMGa consumption (molecules  $\text{cm}^{-2} \text{s}^{-1}$ ):

$$R_T = \frac{1}{3} k_d \theta_m N_m = \frac{s^\circ F_T k_d}{3s^\circ F_T / N_m + k_d} \quad (5)$$

This mechanism assumes that at ALE temperatures TMGa rapidly dissociates into three equivalent  $\text{CH}_3(\text{a})$  groups and that desorption of TMGa can be neglected. Both these assumptions are supported by surface science experiments described in previous publications [15, 16, 36]. First-order Langmuir adsorption whereby  $\text{CH}_3$  groups block sites is also assumed, *i.e.* the TMGa adsorption rate is proportional to the empty site fraction  $1 - \theta_m$ . Note that the solution for  $\theta_m$  (eqn. (4)) approaches unity asymptotically when  $3s^\circ F_T / N_m \gg k_d$ . Thus the surface  $\text{CH}_3$  coverage is saturated whenever the TMGa flux is large compared with the  $\text{CH}_3$  desorption rate constant.

Despite its simplicity, this unimolecular surface reaction mechanism does a good job at describing the TMGa reaction on the Ga-rich surface between 300 and 525 °C at low fluxes ( $10^{-8}$ – $10^{-7}$  Torr) [24]. The  $\text{CH}_3$  desorption rate constant ( $E_a = 44.1 \text{ kcal mol}^{-1}$ ,  $\nu = 10^{13} \text{ s}^{-1}$ ) was independently determined by TPD [15, 16] and  $s^\circ$  was measured directly to be 0.51 [24]. The saturation coverage of  $\text{CH}_3$  groups was also independently measured by a calibrated molecular beam technique and found to be about 0.3 ML [37]. (We have found that previous  $\text{CH}_3$  coverage determinations [16] were too large by a factor of about 2–3.) There are a number of details in eqns. (4) and (5) which are not precisely correct (*i.e.*  $\text{CH}_3$  does not exactly obey ideal first-order desorption kinetics [16]), but the simple model described above is reasonably accurate over the temperature range of interest for ALE [24].

The temperature and TMGa flux dependence of the reaction rate predicted by this model (eqn. (5)) using the parameters mentioned is displayed in Fig. 2 (for simplicity we have assumed the gas temperature is fixed at 300 K). At low TMGa pressures and/or high temperatures the reaction rate is limited by the TMGa flux (actually  $F_T s^\circ$ ) and exhibits no temperature dependence. Note that as the TMGa flux (or pressure) increases, the reaction rate approaches the limit set by the desorption rate constant (actually  $\frac{1}{3} k_d N_m$ ). Any further increase in flux does not significantly increase the reaction rate; in effect the reaction becomes zero order in TMGa pressure. We refer to this as the “high flux limit” of the reaction kinetics. For these conditions the surface is also saturated with  $\text{CH}_3$  groups and the reaction can be described as “adsorbate inhibited” from the standpoint that the TMGa adsorption rate is much lower than it would be on the clean surface. Note also that this condition is met at very low pressures ( $P \geq 10^{-5}$  Torr) at typical ALE temperatures (450–500 °C) and that  $\text{CH}_3$  saturation exists at temperatures as high as 600 °C for TMGa pressures in the millitorr range. This result clearly shows that the condition proposed for adsorbate inhibition is met for typical ALE pressures and temperatures. However, the reaction of TMGa on the Ga-rich surface still proceeds at a finite rate  $R_T = \frac{1}{3} k_d N_m$ , so the adsorbate inhibition mechanism alone cannot explain the ALE behavior.

Another independent verification of this kinetic model was made by comparing the model predictions with gallium droplet growth rate measurements on the Ga-rich surface. Preliminary experiments were performed in a vacuum microbalance system using a radiatively heated GaAs(100) wafer [25]. TMGa partial pressures used were 2–4 mTorr with total pressures of 2–15 mTorr, the balance being  $\text{H}_2$  which was added in some experiments. The low pressures and temperatures (less than 500 °C) and short reactor residence time (less

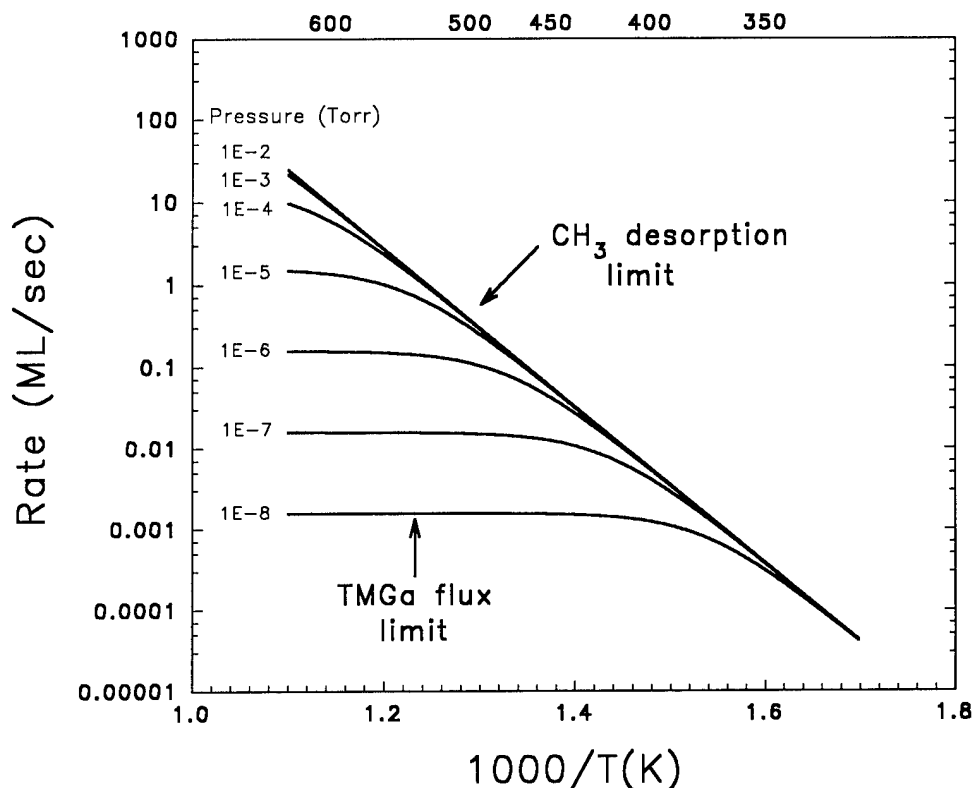


Fig. 2. Predicted Ga deposition rate as a function of temperature and pressure on the Ga-rich surface using a unimolecular surface reaction mechanism. Note that the high pressure limit is reached at very low pressures (about  $10^{-5}$  Torr) for temperatures less than 500 °C.

than 100 ms) should severely limit the potential contribution of TMGa gas phase pyrolysis to Ga deposition. Deposition rate measurements were limited to total effective Ga coverages of less than 50 ML owing to the effect of the Ga droplets on the pyrometric temperature measurement. Instead of presenting the data as growth rate, we have used them to calculate the effective  $\text{CH}_3$  desorption rate constant ( $k_d = 3R_T/N_m$ ) and then compared these results with the rate constant determined by TPD as in Fig. 1. The important result here is that the  $\text{CH}_3$  desorption rate constant determined by Ga deposition rate measurements agrees quantitatively (within a factor of 2) with the rate constant determined by TPD for the Ga-rich surface. Conversely, the deposition rates predicted by the model agree quantitatively with experimental measurements. Therefore the rate of excess Ga desorption in this temperature range can be entirely explained by the heterogeneous reaction of TMGa with the GaAs surface. Work is in progress to expand the range of experimental growth rate measurements for comparison with model predictions.

## 6. ALE kinetics

ALE behavior will occur if the reaction rate of TMGa on the As-rich surface is significantly faster than

the reaction rate on the Ga-rich surface. In fact, TPD results from the  $c(2 \times 8)/(2 \times 4)$  As-rich surface indicate that the approximate rate constant for  $\text{CH}_3$  desorption ( $k_d^{\text{As}}$ ) is roughly 10 times larger than the rate constant ( $k_d^{\text{Ga}}$ ) for  $\text{CH}_3$  desorption from the Ga-rich surface [24]. The approximate rate constant  $k_d^{\text{As}}$  ( $E_d = 40.4 \text{ kcal mol}^{-1}$ ,  $\nu = 10^{13} \text{ s}^{-1}$ ) is plotted in Fig. 1 for comparison with the Ga-rich data. The unimolecular surface reaction mechanism (eqns. (1)–(5)) can be extended to account for the difference in reactivity between the As-rich and Ga-rich surfaces. While the kinetics of TMGa reactivity on the As-rich surface are not completely understood, we can make a few reasonable assumptions and also glean some results from published ALE results. To reach the “high flux limit” on the As-rich surface may require the use of higher pressures than is needed for the Ga-rich surface, but most results indicate that the limit is reached in the TMGa pressure range from  $10^{-5}$  to  $10^{-2}$  Torr [2, 3, 9, 38]. In any case, ALE, by definition, is always operated under conditions where  $G_c$  is independent (or very nearly independent) of TMGa pressure. This allows us to use the simplified form of eqn. (5), i.e.  $R_T = \frac{1}{3}k_d^{\text{As}}N_m^{\text{As}}$ , to describe the reaction rate of TMGa on the As-rich surface. For convenience we will assume that the coverage of  $\text{CH}_3$  on the As-rich surface is the same as the coverage on the Ga-rich surface (TPD results indicate

that this assumption is valid to within a factor of 2). Given these criteria, the disparity in the TMGa reaction rate on the As-rich *vs.* the Ga-rich surface is due to the difference in the  $\text{CH}_3$  desorption rate constants, *i.e.*  $k_d^{\text{As}}$  *vs.*  $k_d^{\text{Ga}}$ .

In order to develop a complete ALE mechanism, we need some method of treating the conversion of the As-rich surface to the Ga-rich surface. In this paper we consider two simple but reasonable examples of the As-rich–Ga-rich conversion kinetics. In the first example we propose that the overall reaction rate proceeds at the As-rich surface reaction rate until 1 ML Ga has been deposited and then proceeds at the Ga-rich surface reaction rate thereafter:

$$R_T = \begin{cases} \frac{1}{3}k_d^{\text{As}}N_m^{\text{As}} & \text{for } \theta_{\text{Ga}} \leq 1 \text{ ML} \\ \frac{1}{3}k_d^{\text{Ga}}N_m^{\text{Ga}} & \text{for } \theta_{\text{Ga}} > 1 \text{ ML} \end{cases} \quad (6)$$

This mechanism can easily be solved to express the growth per cycle ( $G_c$ ) as a function of TMGa exposure time or pulse width ( $t_p$ ):

$$G_c = \begin{cases} \frac{1}{3}k_d^{\text{As}}N_m^{\text{As}}t_p/N_s & \text{for } t_p \leq t_m \\ 1 + \frac{1}{3}k_d^{\text{Ga}}N_m^{\text{Ga}}t_p/N_s & \text{for } t_p > t_m \end{cases} \quad (7)$$

where  $t_m = (\frac{1}{3}k_d^{\text{As}}N_m^{\text{As}}/N_s)^{-1}$  is the time required to deposit the first ML of Ga and  $N_s$  is the surface atom density, *i.e.*  $6.26 \times 10^{14} \text{ cm}^{-2}$ . We refer to eqn. (7) as the linear–linear ALE mechanism, since the growth is described by two linear time dependences (as depicted in Fig. 3). In partial support of this mechanism we note that our molecular beam results indicate that the reaction rate of TMGa with the As-rich  $c(2 \times 8)/(2 \times 4)$  surface is nearly constant for at least the first approximately 0.5 ML of Ga deposition [37]. The reflectance

difference spectroscopy (RDS) results of Aspnes *et al.* [39] also demonstrate that the reaction rate is virtually constant until the latter stage of reaction.

For the second example of ALE growth we propose that reaction occurs on expanding regions of Ga-rich surface and on shrinking regions of As-rich surface. We define the fractional area of As-rich surface as  $F_{\text{As}}$  and of Ga-rich surface as  $F_{\text{Ga}}$ , such that  $F_{\text{As}} + F_{\text{Ga}} = 1$ . The overall reaction rate can then be described by

$$R_T = \frac{1}{3}k_d^{\text{As}}N_m^{\text{As}}F_{\text{As}} + \frac{1}{3}k_d^{\text{Ga}}N_m^{\text{Ga}}F_{\text{Ga}} \quad (8)$$

Since the solution to this expression is more complicated, we define the following terms for convenience:

$$R_T^{\text{As}} = \frac{1}{3}k_d^{\text{As}}N_m^{\text{As}}$$

$$R_T^{\text{Ga}} = \frac{1}{3}k_d^{\text{Ga}}N_m^{\text{Ga}}$$

Now eqn. (8) can be solved to determine the time dependence for  $G_c$  assuming  $R_T^{\text{As}} > R_T^{\text{Ga}}$  (the rate on the As-rich surface is faster than the rate on the Ga-rich surface):

$$G_c = \begin{cases} R_T^{\text{As}}[1 - \exp(-\Delta R t_p)]/\Delta R & \text{for } t_p \leq t_m \\ 1 + R_T^{\text{Ga}}(t_p - t_m)/N_s & \text{for } t_p > t_m \end{cases} \quad (9)$$

where  $\Delta R = (R_T^{\text{As}} - R_T^{\text{Ga}})/N_s$  and  $t_m = (1/\Delta R) \ln(R_T^{\text{As}}/R_T^{\text{Ga}})$  is the time required to deposit the first ML of Ga. We refer to this mechanism (eqn. (9)) as the exponential–linear ALE mechanism since it follows exponential then linear growth with exposure time (see Fig. 3).

The temperature dependences of the linear–linear and exponential–linear ALE mechanisms for a 1 s TMGa exposure ( $t_p = 1 \text{ s}$ ) are plotted in Fig. 4 along with the experimental results of DenBaars *et al.* [4], which were also obtained with  $t_p = 1 \text{ s}$ . The first thing to note is the

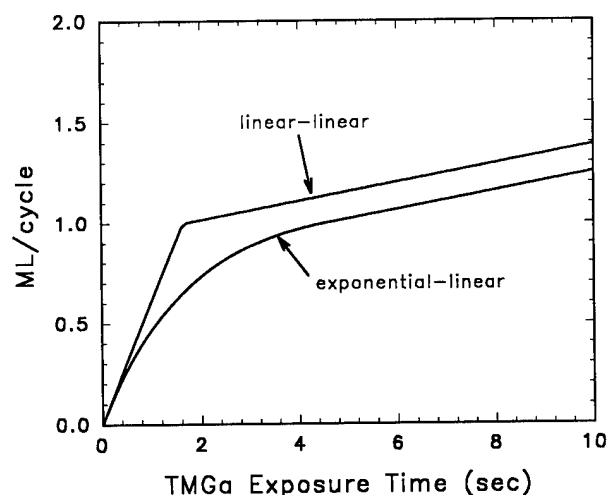


Fig. 3. Time dependence of two simple ALE mechanisms at 450 °C using kinetic parameters determined from surface science experiments.

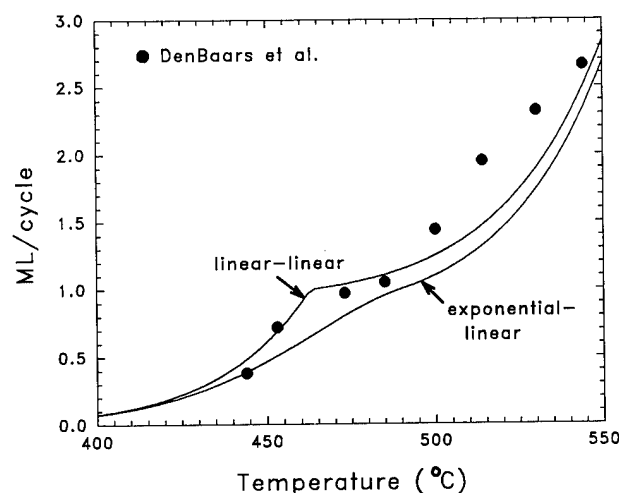


Fig. 4. Temperature dependence of two simple ALE mechanisms using kinetic parameters determined from surface science experiments. The data points are ALE measurements of DenBaars *et al.* [4]. TMGa exposure time was 1 s.

reasonable agreement between the *absolute* growth rate measurements and model predictions. The quantitative agreement between the models and the experimental data is in most cases much better than  $\pm 50\%$  and is particularly good below 500 °C. It should be remembered that all the kinetic parameters and saturation coverages in the two ALE models were determined from independent experimental measurements ( $k_d^{\text{Ga}}$ ,  $N_m^{\text{Ga}}$ ,  $k_d^{\text{As}}$ ) or reasonable estimates ( $N_m^{\text{As}}$ ) and were not varied to achieve a better fit to the ALE data. Both models exhibit a tendency for the  $G_c$  temperature dependence to weaken between 460 and 500 °C and this result is also reproduced experimentally. As expected, the temperature “plateau” for the linear-linear mechanism is more pronounced, but neither mechanism (or experiment) exhibits ideal ALE behavior with respect to temperature. The quantitative agreement between the two models and the experimental data worsens somewhat above 500 °C, but the difference in curvature between 500 and 550 °C is perhaps more bothersome. One possible explanation is that mass transport effects are beginning to moderate the experimental growth rate [4] at high temperature. Another possible explanation is that as the Ga droplets become larger (with increasing temperature) they do not act as ideal reservoirs of Ga during the arsine cycle, so an increasing fraction of the metallic Ga does not become incorporated into the GaAs lattice.

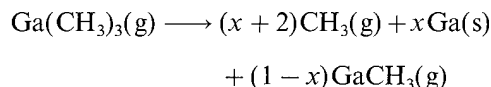
In the temperature range of interest the disparity in reaction rates between the As-rich and Ga-rich surfaces is only a factor of about 10. If the disparity were much larger, then the size of the temperature “plateau” would increase and the GaAs ALE behavior would be much closer to ideal. Doi *et al.* [40, 41] came to a very similar conclusion when explaining their results for laser-assisted ALE. They found that they could explain their results using a model very similar to eqn. (8) and by assuming that the laser-assisted TMGa reaction rate on the As-rich surface was about 100 times faster than the rate on the Ga-rich surface [40].

## 7. The flux balance mechanism of ALE

The key feature of the flux balance mechanism (as proposed by Yu *et al.* [20, 21]) is that TMGa decomposes on the gallium-rich surface, but a gallium-containing product, specifically monomethylgallium (MMGa), leaves the surface quantitatively, so no net gallium deposition occurs. This mechanism, or something similar to it, may be needed to explain the GaAs ALE results of Ozeki *et al.* [8, 9], who observed a very wide temperature window (about 100 °C) and a near-ideal time dependence. Yu *et al.* have made direct observations of MMGa desorbing from GaAs using a pulsed molecular beam technique [20, 21]. While this proposed mechanism

has merit, we believe that the conditions which may lead to quantitative MMGa production have not been adequately explained.

It is instructive to write the TMGa reaction equation allowing for MMGa formation:



where  $x(0 \leq x \leq 1)$  defines the degree of gallium droplet formation *vs.* MMGa formation. For the flux balance mechanism to be significant,  $x$  has to be near zero, *i.e.* most Ga leaves the surface as MMGa. While the molecular beam technique can measure desorbing products such as methyl radicals and gallium alkyl radicals, it cannot directly monitor the formation of gallium droplets. If the rate of  $\text{CH}_3$  and MMGa evolution could be quantitatively measured, then it would be possible to infer the gallium deposition rate from mass balance. Yu *et al.* [20, 21] noted a drop in the  $\text{CH}_3$  yield when the surface converts from the As-rich to the Ga-rich condition and have used this observation to support a change in the branching ratio from  $x = 1$  to 0 (no net Ga deposition). However, the TMGa reactive sticking coefficient falls in synchrony with the  $\text{CH}_3$  signal [21, 37, 42], so the drop in  $\text{CH}_3$  signal may simply reflect a lower rate of TMGa decomposition. We therefore believe that this result does not conclusively demonstrate a significant change in the branching ratio ( $x$ ). We also normally detect an excess  $\text{MMGa}^+$  signal (in agreement with Yu *et al.* [20, 21]) in the 400–500 °C range when TMGa impinges on the Ga-rich surface [37]. Our initial attempts to calibrate the  $\text{MMGa}^+$  signal indicate that for many conditions  $x$  may be near unity (MMGa desorption insignificant, Ga droplets grow), while for other conditions  $x$  is smaller and may be near zero (MMGa desorption significant, Ga droplets do not grow). It is also sometimes difficult to reproduce the magnitude of  $x$  for nominally identical conditions (*i.e.* temperature and flux). We have not yet determined the source of this variation, but we speculate that it is related to the presence of Ga droplets that may exist on the surface before each experiment or that nucleate during TMGa exposure. This is one reason why we believe that the flux balance condition is metastable. During TMGa TPD experiments some MMGa desorption is also detected, but for these conditions it is definitely not formed quantitatively and most of the liberated gallium ends up in Ga droplets [16, 24].

## 8. The source of excess gallium deposition

As we mentioned earlier, the source of excess (*i.e.* greater than 1 ML) gallium deposition is still the

subject of much debate. The controversy centers mainly on the relative roles of heterogeneous and homogeneous chemistry. In this section we review some important issues and offer some speculations that may explain some of the apparently disparate findings, but we do not realistically expect this to end the controversy.

The evidence for a heterogeneous pathway that leads to excess Ga deposition is very strong. The low pressure conditions of Nishizawa *et al.* [2, 3] did not exhibit ideal ALE behavior with respect to temperature, and excess Ga deposition readily occurred. Since gas phase TMGa pyrolysis cannot be responsible for the excess Ga deposition seen by Nishizawa *et al.* (owing to the low pressures), a heterogeneous process must be responsible. We have also observed Ga droplet formation on the GaAs(100) surface in our UHV chamber at TMGa pressures of about  $10^{-7}$  Torr and surface temperatures around 500 °C.

It is reasonable to ask if a heterogeneous pathway is responsible for excess Ga deposition at higher pressures. We have shown (in Section 5) that the gallium deposition rate measurements in the millitorr TMGa pressure range agree quantitatively with the unimolecular surface reaction kinetics obtained by surface science techniques. Complete ALE mechanisms that incorporate the surface reaction kinetics (see Section 6) but no gas-phase pyrolysis are also in good agreement with the atmospheric pressure results of DenBaars *et al.* [4]. Therefore Ga deposition rate measurements at realistic ALE pressures and at least some of the ALE results can be explained solely with a heterogeneous mechanism of excess Ga deposition.

There is another common but overlooked experimental result that strongly suggests that excess Ga deposition arises primarily by a heterogeneous pathway. Virtually all ALE results [2–9, 38] demonstrate a zero-order TMGa pressure dependence on  $G_c$ , even when excess gallium deposition occurs (*i.e.*  $G_c > 1$  ML). Therefore the mechanism of excess gallium deposition exhibits a zero-order TMGa pressure dependence. A zero-order pressure dependence is a common feature of a unimolecular surface reaction mechanism and the model discussed in Section 5 shows this dependence for typical ALE conditions. It would be highly unusual for a gas-phase TMGa pyrolysis mechanism to exhibit a zero-order TMGa pressure dependence. It is worth noting that a zero-order TMGa pressure dependence is a necessary but not sufficient condition for ALE. In other words, it is possible to have a wide region of zero-order TMGa pressure dependence but have absolutely no ALE behavior with respect to temperature or pulse time [38].

Even though there is strong evidence supporting the heterogeneous mechanism of excess gallium deposition, the exceptional ALE results of Ozeki *et al.* [8, 9] are

difficult to reconcile. The lack of gas phase TMGa pyrolysis (owing to reactor design and operating conditions) is often given as the reason why their results show better ALE behavior than results from most other laboratories [8, 9]. However, simply avoiding gas phase TMGa pyrolysis does not ensure ideal ALE behavior, as the low pressure results of Nishizawa *et al.* [2, 3] demonstrated. The flux balance condition (see Section 7) may be responsible for the extended ALE conditions of Ozeki *et al.* [8, 9]. We offer the following speculative explanation to reconcile some of the differences in the ALE results. As we mentioned earlier, we believe the flux balance condition is metastable, because otherwise similar operating conditions lead to excess gallium deposition (even in the absence of gas phase TMGa pyrolysis). For excess gallium deposition to occur, gallium droplets must first nucleate on the GaAs surface. In the absence of gallium droplets any excess gallium liberated by TMGa decomposition may simply desorb as MMGa, thus creating the flux balance condition. However, once gallium droplets nucleate on the GaAs surface, they continue to grow at a rate determined primarily by the TMGa heterogeneous reaction rate. Notice that we are making a distinction between *nucleation* and subsequent *growth*. If the reactor design and operating conditions of Ozeki *et al.* [8, 9] do play a role in the improved ALE performance, we believe it is because they prevent or delay the onset of Ga droplet *nucleation* and not because they would lead to slower Ga droplet *growth*. Droplet nucleation on the Ga-rich surface may not necessarily occur instantaneously and may require an induction period. Kobayashi and Kobayashi [43] reported GaAs ALE results demonstrating metastable behavior, which is consistent with a delay in Ga droplet formation. They showed that once the surface was converted to the Ga-rich condition by TMGa exposure at 470 °C, the surface photoabsorption (SPA) signal remained constant, indicating self-limiting growth. However, this condition was not stable indefinitely and after about 10 s the (SPA) signal began to increase rapidly, evidently signaling the nucleation and growth of Ga droplets.

The narrow ALE operating conditions often seen [2–5] may be due to prompt droplet nucleation once the Ga-rich surface is formed. The two simple heterogeneous ALE mechanisms we described in Section 6 assume that Ga droplet growth is not impeded by nucleation and these models give a reasonable description of the results of DenBaars *et al.* [4]. We do not understand the conditions that determine whether droplet nucleation will be prompt or delayed, but we note that the nucleation phenomenon can be extremely sensitive to a variety of intrinsic and extrinsic parameters.

## 9. TMGa chemisorption on the $c(4 \times 4)$ "super" As-rich surface

Some ALE conditions will generate the  $c(4 \times 4)$  "super" As-rich surface ( $\theta_{\text{As}} = 1.75$  ML) during the arsine cycle (see Section 3), so it is of interest to study the chemisorption properties of TMGa on this surface. Our molecular beam and TPD results indicate that surfaces with more than 1 ML As coverage are less reactive towards TMGa than the  $c(2 \times 8)/(2 \times 4)$  As-rich surface ( $\theta_{\text{As}} = 0.75$  ML). TPD results following low temperature TMGa chemisorption indicate that  $\text{CH}_3$  desorbs at a higher temperature from the "super" As-rich surface than from the  $c(2 \times 8)/(2 \times 4)$  As-rich surface. In fact, the peak temperature is nearly identical to that of  $\text{CH}_3$  desorption from the Ga-rich surface, with some desorption occurring at even higher temperature (see Fig. 5). This indicates that TMGa reacts with the "super" As-rich surface at about the same rate (or perhaps even at a lower rate) as it reacts with the Ga-rich surface. This behavior is not desirable since it destroys the disparity in TMGa reaction rate that is at least partly responsible for GaAs ALE. Fortunately, the fast desorption rate of the excess (greater than 1 ML) As at temperatures above about  $450^\circ\text{C}$  means that most of it will desorb during the purge cycle following arsine exposure [34]. However, the presence of this excess As may limit the ability to perform ALE at lower temperatures. These results are also consistent with chemical beam epitaxy (CBE) data showing a decrease in growth rate at high arsenic flux [44].

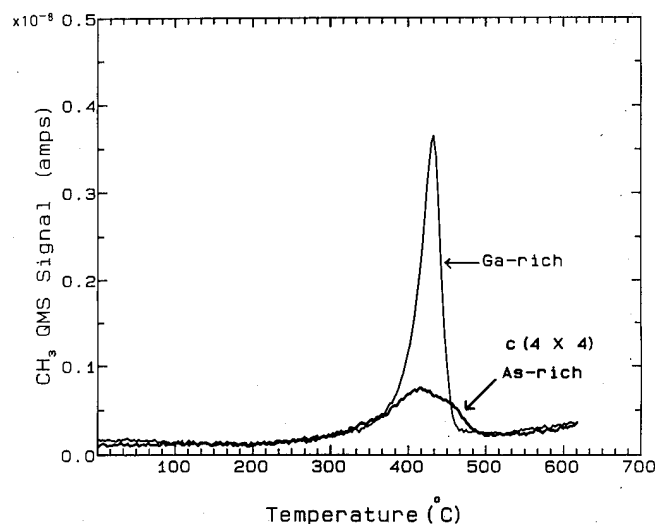


Fig. 5. Comparison of TPD spectra for  $\text{CH}_3$  desorption from the Ga-rich and "super" As-rich GaAs(100) surfaces. Note that the  $\text{CH}_3$  desorption rate from the "super" As-rich surface is about the same as the rate from the Ga rich surface.

## 10. Summary

We briefly discussed likely explanations of the stoichiometry "problem" of GaAs ALE (Section 3). Methyl groups may stabilize a Ga-rich surface with  $\theta_{\text{Ga}} = 1$  ML, while large arsine exposures lead to As coverages of 1 ML or more. Most of the excess (above 1 ML) As desorbs during the purge, but the remaining As is sufficiently stable at typical ALE temperatures.

We also reviewed three proposed mechanisms for GaAs ALE and reviewed or presented data in support of or in contradiction to these mechanisms. A wide range of data indicating that TMGa reacts with the Ga-rich surface disprove the selective adsorption mechanism (Section 4). The kinetics of the TMGa reaction with the Ga-rich surface indicate that the surface is covered with  $\text{CH}_3$  during typical ALE pressures and temperatures, in agreement with the premise of the adsorbate inhibition mechanism (Section 5). However, the adsorbate inhibition mechanism is too simplistic to explain GaAs ALE, since excess Ga deposition still occurs at a finite rate. Preliminary results for the rate of excess Ga deposition in the TMGa millitorr pressure range are in good quantitative agreement with a simple unimolecular surface reaction model using kinetic parameters measured by conventional surface science techniques at much lower pressures. Two simple ALE kinetic models were constructed (Section 6) using the unimolecular surface reaction kinetics determined on the As-rich and Ga-rich surfaces. Predictions of these ALE models are in good agreement with the ALE results of DenBaars *et al.* [4].

The flux balance mechanism (Section 7) may be needed to explain the results of Ozeki *et al.* [8, 9], but the flux balance condition may be metastable. We speculate that the flux balance condition may be due to a delay in or absence of Ga droplet nucleation (Section 8). The differences in the reported ALE results may be due to differences in the onset of Ga droplet nucleation. In some cases the differences in droplet nucleation might result from differences in the reactor fluid mechanics and/or the degree of homogeneous reactions. However, once Ga droplets nucleate, they grow at a rate determined primarily by the TMGa heterogeneous reaction rate on the Ga-rich surface. Without the delay of nucleation, ALE behavior is still observed but over a much narrower range of operating conditions. This baseline ALE behavior is due to the disparity in the TMGa heterogeneous reaction rate towards the As-rich and Ga-rich surfaces, which is caused by the disparity in the  $\text{CH}_3$  desorption rates. Unfortunately, the  $\text{CH}_3$  desorption rate constant for the As-rich surface is only about a factor of 10 larger than the rate constant for the Ga-rich surface, which leads to the "weak" ALE behavior often observed [2–5]. We also note (Section 9) that

if the surface becomes too As rich, *i.e.* "super" As rich, then the disparity in rate constants becomes smaller and the ALE behavior may diminish completely.

### Acknowledgments

The authors thank Kevin Killeen and Mike Coltrin for stimulating scientific discussions and Gary Karpen for technical support. This work was performed at Sandia National Laboratories and supported by the US Department of Energy under contract DE-AC04-76DP000789 for the Office of Basic Energy Sciences.

### References

- 1 C. H. L. Goodman and M. V. Pessa, *J. Appl. Phys.*, **60** (1986) R65.
- 2 J. Nishizawa, T. Kurabayashi, H. Abe and A. Nozoe, *Surf. Sci.*, **185** (1987) 249.
- 3 J. Nishizawa, T. Kurabayashi, H. Abe and N. Sakurai, *J. Electrochem. Soc.*, **134** (1987) 945.
- 4 S. P. DenBaars, P. D. Dapkus, C. A. Beyler, A. Hariz and K. M. Dzurko, *J. Cryst. Growth*, **93** (1988) 195.
- 5 P. D. Dapkus, S. P. DenBaars, Q. Chen, W. G. Jeong and B. Y. Maa, *Prog. Cryst. Growth Charact.*, **19** (1989) 137.
- 6 M. A. Tischler and S. M. Bedair, *Appl. Phys. Lett.*, **48** (1986) 1681.
- 7 K. G. Reid, H. M. Urdianyk and S. M. Bedair, *Appl. Phys. Lett.*, **59** (1991) 2397.
- 8 M. Ozeki, K. Mochizuki, N. Ohtsuka and K. Kodama, *Appl. Phys. Lett.*, **53** (1988) 1509.
- 9 M. Ozeki, N. Ohtsuka, Y. Sakuma and K. Kodama, *J. Cryst. Growth*, **107** (1991) 102.
- 10 G. B. Stringfellow, *Organometallic Vapor-phase Epitaxy*, Academic, San Diego, CA, 1989, pp. 363–367.
- 11 A. Usui and H. Watanabe, *Ann. Rev. Mater. Sci.*, **21** (1991) 185.
- 12 P. D. Dapkus, B. Y. Maa, Q. Chen, W. G. Jeong and S. P. DenBaars, *J. Cryst. Growth*, **107** (1991) 73.
- 13 K. Kodama, M. Ozeki, K. Mochizuki and N. Ohtsuka, *Appl. Phys. Lett.*, **54** (1989) 656.
- 14 M. L. Yu, U. Memmert and T. F. Kuech, *Appl. Phys. Lett.*, **55** (1989) 1011.
- 15 J. R. Creighton, K. R. Lykke, V. A. Shamamian and B. D. Kay, *Appl. Phys. Lett.*, **57** (1990) 279.
- 16 J. R. Creighton, *Surf. Sci.*, **234** (1990) 287.
- 17 H. Ishii, H. Ohno, K. Matsuzaki and H. Hasegawa, *J. Cryst. Growth*, **95** (1989) 132.
- 18 A. Watanabe, T. Isu, M. Hata, T. Kamijoh and Y. Katayama, *Jpn. J. Appl. Phys.*, **28** (1989) L1080.
- 19 B. Y. Maa and P. D. Dapkus, *Appl. Phys. Lett.*, **58** (1991) 2261.
- 20 M. L. Yu, U. Memmert, N. I. Buchan and T. F. Kuech, *MRS Symp. Proc.*, **204** (1991) 37–46.
- 21 M. L. Yu, N. I. Buchan, R. Souda and T. F. Kuech, *MRS Symp. Proc.*, **222** (1991) 3–13.
- 22 V. M. Donnelly, J. A. McCaulley and R. J. Shul, *MRS Symp. Proc.*, **204** (1991) 15–23.
- 23 N. Kobayashi and Y. Horikoshi, *Jpn. J. Appl. Phys.*, **30** (1991) L319.
- 24 J. R. Creighton and B. A. Banse, *MRS Symp. Proc.*, **222** (1991) 15–24.
- 25 J. R. Creighton and B. A. Banse, in preparation.
- 26 D. J. Chadi, *J. Vac. Sci. Technol. A*, **5** (1987) 834.
- 27 P. K. Larsen and D. J. Chadi, *Phys. Rev. B*, **37** (1988) 8282.
- 28 P. Drathen, W. Ranke and K. Jacobi, *Surf. Sci.*, **77** (1978) L162.
- 29 J. Massies, P. Etienne, F. Dezaly and N. T. Linh, *Surf. Sci.*, **99** (1980) 121.
- 30 D. J. Frankel, C. Yu, J. P. Harbison and H. H. Farrell, *J. Vac. Sci. Technol. B*, **5** (1987) 1113.
- 31 M. D. Pashley, K. W. Haberern, W. Friday, J. M. Woodall and P. D. Kirchner, *Phys. Rev. Lett.*, **60** (1988) 2176.
- 32 D. K. Beigelsen, R. D. Bringans, J. E. Northrup and L.-E. Swartz, *Phys. Rev. B*, **41** (1990) 5701.
- 33 B. A. Bansenauer and J. R. Creighton, *Surf. Sci.*, **278** (1992) 317.
- 34 B. A. Bansenauer and J. R. Creighton, *Appl. Phys. Lett.*, **60** (1992) 856.
- 35 I. Kamiya, H. Tanaka, D. E. Aspnes, L. T. Florez, E. Colas, J. P. Harbison and R. Bhat, *Appl. Phys. Lett.*, **60** (1992) 1238.
- 36 J. R. Creighton, *J. Vac. Sci. Technol. A*, **9** (1991) 2895.
- 37 B. A. Banse and J. R. Creighton, in preparation.
- 38 J. Wückerath, P. Czuprin, D. Grundmann, P. Balk, M. Waschbüsch, R. Lückerrath and W. Richter, *J. Cryst. Growth*, **107** (1991) 111.
- 39 D. E. Aspnes, E. Colas, A. A. Studna, R. Bhat, M. A. Koza and V. G. Keramidas, *Phys. Rev. Lett.*, **61** (1988) 2782.
- 40 A. Doi, Y. Aoyagi and S. Namba, *MRS Symp. Proc.*, **75** (1991) 217–222.
- 41 A. Doi, S. Iwai, T. Meguro and S. Namba, *Jpn. J. Appl. Phys.*, **27** (1988) 795.
- 42 M. Yu, personal communication, 1992.
- 43 N. Kobayashi and Y. Kobayashi, *2nd Int. Conf. on Atomic Layer Epitaxy*, June 1992, in *Thin Solid Films*, **225** (1993) 32.
- 44 T. H. Chiu, J. E. Cunningham and A. Robertson, Jr., *J. Cryst. Growth*, **95** (1989) 136.

# Real-time optical diagnostics for measuring and controlling epitaxial growth

D. E. Aspnes<sup>a</sup>, I. Kamiya<sup>b</sup>, H. Tanaka<sup>c</sup>, R. Bhat<sup>a</sup>, L. T. Florez<sup>a</sup>, J. P. Harbison<sup>a</sup>,  
W. E. Quinn<sup>d</sup>, M. Tamargo<sup>a</sup>, S. Gregory<sup>a</sup>, M. A. A. Pudensi<sup>e</sup>, S. A. Schwarz<sup>a</sup>,  
M. J. S. P. Brasil<sup>e</sup> and R. E. Nahory<sup>a</sup>

<sup>a</sup>*Bellcore, Red Bank, NJ 07701-7040 (USA)*

<sup>b</sup>*Department of Physics, University of Illinois, Urbana, IL 61801 (USA)*

<sup>c</sup>*Fujitsu Laboratories Ltd., 10-1 Morinosato-Wakamiya, Atsugi 243-01 (Japan)*

<sup>d</sup>*Bandgap Engineering, Broomfield, CO 80021 (USA)*

<sup>e</sup>*IFGW-UNICAMP, 13081 Campinas, SP (Brazil)*

## Abstract

We summarize recent applications of two real-time optical diagnostic techniques, reflectance difference spectroscopy (RDS) and spectroellipsometry (SE), to epitaxial growth on GaAs and atomic layer epitaxy (ALE) in particular. Using RDS, we obtain the first real-time spectroscopic data of the evolution of the (001) GaAs surface to cyclic and non-cycle exposures of atmospheric pressure  $H_2$ ,  $H_2$  and trimethylgallium, and  $H_2$  and arsine, which simulate growth by ALE. None of our observations is consistent with any previously proposed simple model, emphasizing the necessity of real-time measurements for the analysis of complex surface reactions. Using SE we have constructed a closed-loop system for controlling the compositions of  $Al_xGa_{1-x}As$  layers grown by chemical beam epitaxy. We have produced various graded-compositional structures, including parabolic quantum wells 200 Å wide where the composition was controlled by analysis of the running outermost 3 Å (about 1 monolayer) of depositing material.

## 1. Introduction

Among the various approaches to epitaxial growth, atomic layer epitaxy (ALE) has been singled out for special attention because of its “digital” nature, the uniformity of the resulting layers and its applicability to various III–V materials [1, 2]. However, in the absence of direct information about the state of surfaces during ALE growth, detailed mechanisms remain a source of speculation. In the trimethylgallium ( $Ga(CH_3)_3$ , TMG)–arsine ( $AsH_3$ ) system three common models invoke selective adsorption (SA) [3], adsorption inhibition (AI) [4] and flux balance (FB) [5] as the relevant mechanisms. In the SA model it is assumed that TMG does not adhere to Ga, which is supposedly the outer-layer species that results when (001) GaAs is exposed to TMG. In the AI model the same result is achieved by assuming that each surface Ga atom is capped with a methyl radical ( $CH_3$ ). In the FB model ALE is a result of a dynamic equilibrium between Ga deposited from TMG and Ga desorbed as monomethylgallium ( $GaCH_3$ , MMG). A summary has recently been given by Creighton and Banse [6].

The development of optical diagnostic techniques that can provide real-time information about growth surfaces and deposited material is relevant to ALE for

several reasons. On the one hand, the use of surface-oriented techniques such as reflectance difference spectroscopy (RDS) [7, 8] and surface photoabsorption (SPA) [9, 10] can yield information about growth surfaces in real time and thereby provide new insight to growth mechanisms. On the other hand, the use of spectroellipsometry (SE) to control layer compositions and thicknesses directly [11, 12] eliminates one of the primary reasons for performing ALE.

We have approached the problem of epitaxial growth from both directions, developing RDS to obtain new information about growth chemistry and SE to control growth directly in real time. We have recently developed a multitransient version of RDS and applied it to a simulated ALE cycle involving TMG and  $AsH_3$  in an atmospheric pressure (AP) organometallic chemical vapor deposition (OMCVD) reactor [13]. This system has provided the first real-time spectral view of the evolution of a semiconductor surface to cyclic exposures of reactants. By comparing the results with our previously obtained reflectance difference (RD) spectral database of the various reconstructions on (001) GaAs [14, 15], we show that *none* of the previously proposed simple models of ALE growth applies. In our growth control work we have used a spectroellipsometer as a feedback element on a chemical beam epitaxy (CBE) chamber to



determine the composition of the running outermost few angstroms of depositing material and to adjust deposition parameters to follow preset profiles [12]. The present paper is a report of our progress in both areas.

## 2. (001) GaAs surfaces under cyclic exposures

Because details of our multitransient spectroscopy (MTS) work have been discussed elsewhere [13], we provide only a brief overview and summarize the main results. Experiments were performed with a double-wall horizontal flow OMCVD reactor. GaAs wafers oriented to within  $0.5^\circ$  of (001) were mounted after standard chemical treatments on an SiC-coated graphite susceptor. We also investigated samples oriented  $6^\circ$  off (001) toward [110], but the results showed no difference to within experimental uncertainty. RD spectra are obtained as  $\Delta\tilde{r}/\tilde{r} = \Delta r/r + i\Delta\theta = 2(\tilde{r}_{\Gamma 10} - \tilde{r}_{\Gamma 110})/(\tilde{r}_{\Gamma 10} + \tilde{r}_{\Gamma 110})$ , where  $\tilde{r}_{\Gamma 10}$  and  $\tilde{r}_{\Gamma 110}$  are the complex near-normal-incidence reflectances of light polarized along the  $[\bar{1}10]$  and  $[110]$  axes respectively.

The interpretation of the multitransient results depends on the database of RD spectra that we obtained for (001) GaAs surfaces prepared in ultrahigh vacuum (UHV) by molecular beam epitaxy (MBE) and simultaneously characterized by reflection high energy electron diffraction (RHEED) [14, 15]. Part of this database is shown in Fig. 1. RD spectra are given for the primary reconstructions  $(4 \times 2)$ ,  $(2 \times 4)$ ,  $c(4 \times 4)$  and  $d(4 \times 4)$  on (001) GaAs. These reconstructions involve terminations by zero, one, two, and two or more outer layers of As respectively. Figure 1 shows that the same RD spectra are obtained in both UHV and AP  $H_2$ , which means that the surface reconstructions are similar, possibly even identical, in the two environments. Since RD is sensitive to local atomic structure rather than long-range order, these data demonstrate explicitly that dimer formation is not restricted to UHV and that  $H_2$  does not play a major role in modifying the electronic and atomic structure of (001) GaAs. This observation already eliminates certain classes of models of OMCVD growth and provides indirect support for models of spontaneous ordering in the InGaP system [16–18], which rely on the presence of surface dimers. The result also justifies the application of results obtained for (001) GaAs by UHV surface analysis techniques to OMCVD growth [4–6, 19–21], although, as will be shown, most of the surface reconstructions that have been studied are not those that are relevant to ALE.

We now apply the above results to the evolution of the (001) GaAs surface to cyclic exposures of  $H_2$ ,  $H_2 + TMG$ ,  $H_2 + AsH_3$  and  $H_2$ . The specific cycle investigated here consists of a 4 s  $H_2$  purge, 7 s exposure

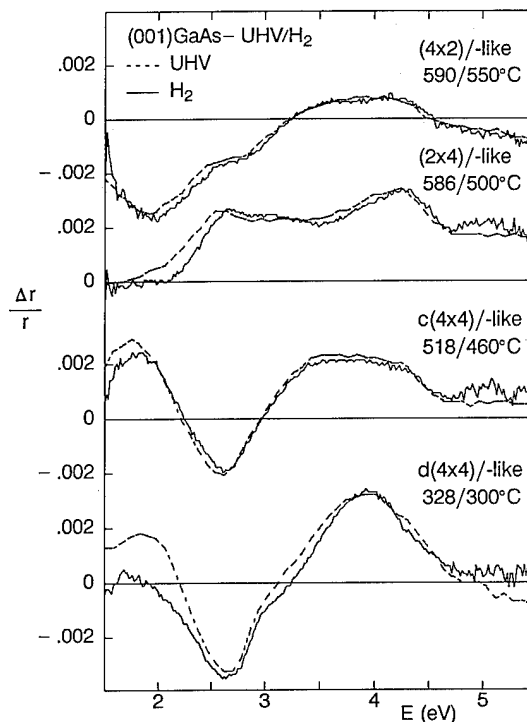


Fig. 1. RD spectral database for the primary reconstructions on (001) GaAs (after ref. 14).

to TMG, a 19 s  $H_2$  purge and 10 s exposure to  $AsH_3$  for a period of 40 s. The partial pressures of  $AsH_3$  and TMG were 2.3 and 0.011 Torr respectively. The sample temperature was  $450^\circ C$ . These conditions and this sequence are those that are typically used for ALE, but exposure and purge periods have been lengthened to better establish surface evolutions. RD spectra of the surface at 250 points during the cycle were obtained by a sampling technique. We first recorded 81 250-point, 37.5 s transients from 5.5 to 1.5 eV at intervals of 0.05 eV, with each transient beginning 4.00 s before the  $AsH_3$  exposure was terminated. We then reorganized the resulting data into 250 81-point spectra separated by time intervals of 150 ms.

To relate the spectra to various events that occur over the cycle, we show two transients in Fig. 2. One is taken at 2.6 eV, where the contribution of As dimers is a maximum. The other is taken at 1.95 eV, near the maximum contribution of Ga dimers and also near the 1.959 eV energy of HeNe lasers commonly used to study kinetic processes. Instants when TMG and  $AsH_3$  flows were changed are indicated. These are also apparent from specific features. For example, the termination of  $AsH_3$  exposure is easily seen at 2.6 eV, while the onset of TMG exposure is most apparent at 1.95 eV. The relatively drastic change on resumption of  $AsH_3$  exposure is obvious in both.

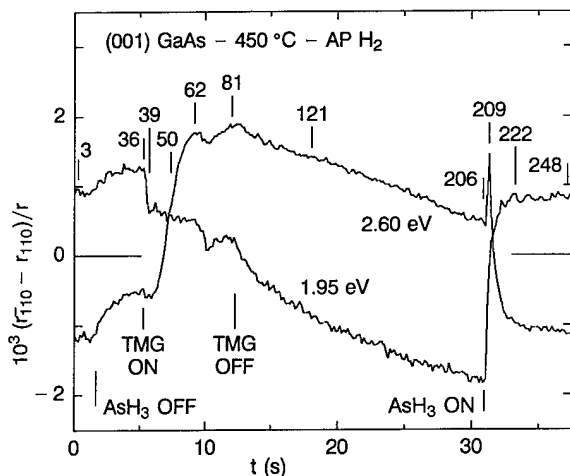


Fig. 2. Two of a set of 81 250-point transients illustrating the evolution of (001) GaAs over an ALE-like cycle of 4 s  $H_2$ , 7 s  $H_2$  + TMG, 19 s  $H_2$  and 10 s  $H_2$  +  $AsH_3$  (after ref. 13).

Selected spectra indicated by the numbers in Fig. 2 are shown in Fig. 3. Spectra 50 and 209 are individual spectra because the surface is changing rapidly with time. Spectra 3 and 248 are averages over the nearest five. The rest are averages over the nearest three, except for 36 and 39 which are averages over 34–36 and 39–41 respectively. Two difference spectra are shown at the bottom:  $\Delta_1$  between 36 and 39 and  $\Delta_2$  between 3

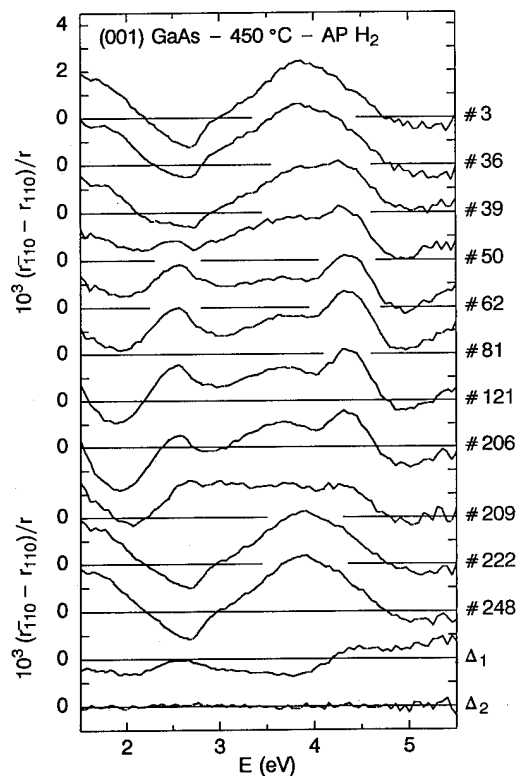


Fig. 3. RD spectra corresponding to the points indicated in Fig. 2 (after ref. 13).

and 248.  $\Delta_1$  describes the initial reaction of the surface when exposed to TMG, while  $\Delta_2$  illustrates the consistency over the set.

We now examine these results in detail, beginning with the surface stabilized with  $AsH_3$ . From spectra 3 and 248 of Fig. 3 the corresponding reconstruction is  $d(4 \times 4)$ -like with more than 1 monolayer (ML) coverage of As, in agreement with previous work [14, 15]. This result alone eliminates all previous simple models of ALE, which have supposed that termination alternates between single-layer coverages of As and Ga. We divide the rest of the cycle into five parts: the evolution of the  $AsH_3$ -stabilized surface during the  $H_2$  purge; that of the purged surface during exposure to TMG; that of the TMG-saturated surface during excess exposure to TMG; that of the TMG-saturated surface during the  $H_2$  purge; and that of the purged surface during exposure to  $AsH_3$ . Spectrum 36 shows that the 4 s  $H_2$  purge removes only a small fraction of As and that the surface immediately prior to TMG exposure is still covered with at least two layers of As.

The TMG-surface reaction is much more complex. A comparison of 36 and 39 (see  $\Delta_1$ ) shows that most of the  $c/d(4 \times 4)$ -like dimers are unaffected by initial exposure to TMG. In view of previous work by Yu and coworkers [5, 21] on the  $(2 \times 4)$  reconstruction, this result is surprising. The Yu *et al.* data showed that the  $(2 \times 4)$  surface cracks TMG into MMG and two  $CH_3$  radicals that attach themselves to the nearest As. However, a global reaction of this type would destroy all  $c/d(4 \times 4)$ -like dimers, leading to large RD changes that are not observed. Instead, after a 1 s incubation period these dimers begin to vanish at a steady rate that depends on the partial pressure of TMG in the ambient (occupancy effects) via a chemisorption enthalpy and decomposition barrier of  $-26$  and  $39$  kcal mol $^{-1}$  respectively, as established by an earlier investigation of the kinetics of the interaction of TMG with this surface [22]. We originally interpreted the reaction bottleneck as excluded-volume chemisorption [22], but the data are also consistent with the TMG-surface reaction occurring only at special sites, *e.g.* the missing dimers of the Farrell *et al.* model [23]. However, constraints on densities and energetics make a special-site model less attractive than steric hindrance for explaining the observed kinetic behavior. Spectra 50 and 62 indicate that these dimers are being replaced by As dimers oriented along  $[110]$ , *i.e.* that the original two or more outer layers of As are becoming one. This is a logical consequence of deposited Ga atoms finding their thermodynamically preferred lattice sites through local bonding rearrangements.

If the TMG-surface reaction were to begin with the  $c(4 \times 4)$  and stop with the  $(2 \times 4)$  reconstruction, a yield of exactly 1 ML per cycle would be naturally

explained. However, the surface terminations that result from saturation exposure of the  $c/d(4 \times 4)$ -like reconstruction to TMG (62 and 81 of Fig. 3) and those that are observed during the  $H_2$  purge (121 and 206) are not themselves primary reconstructions. Nevertheless, an examination of these data reveals several well-defined characteristics. First, neither further TMG exposure after saturation nor termination of TMG exposure has much effect (compare 81 with 62 and 121 with 81 respectively). Secondly, in all previous cases that we have studied, including the  $(3 \times 1)$  and  $(1 \times 6)$  reconstructions as well as those of Fig. 1, the 2.6 and 4.2 eV structures that appear from 50 through 209 have always signaled the presence of surface As [15]. Thus the TMG-saturated surface cannot be entirely terminated by Ga. Thirdly, on exposure to  $AsH_3$  the  $H_2$ -purged surface returns smoothly and directly to the  $AsH_3$ -saturated state through the accumulation of first and second layers of As (spectra 209, 222 and 248). Further work has also shown that, given enough time in the absence of As, this surface evolves to the  $(1 \times 6)$ – $(4 \times 6)$ -like state [13]. A steady increase in Ga dimers during the  $H_2$  purge can also be deduced from the negative trend of the response at 1.9 eV.

Chemical intuition would have the TMG-saturated surface terminated by Ga, possibly capped by  $CH_3$ . If this were the case, we could examine the above data for consistency with previous atomic level studies of the interaction of TMG with Ga-terminated (001) GaAs. The longest directly observed residence times reported for  $CH_3$  on the  $(4 \times 6)$  and  $(4 \times 2)$  reconstructions at 450 °C are about 2 s [19]\*, which is consistent with the fact that the amount of C remaining on TMG-exposed surfaces after several seconds is invariably less than the sensitivity limit of X-ray photoelectron spectroscopy or Auger spectroscopy, of the order of 0.001 ML [6, 19, 24]. In fact, a transient roughly 2 s long is seen on termination of TMG exposure in the 1.95 eV data of Fig. 2, but it is small. Consequently, if  $CH_3$  is initially present in significant quantities, we must conclude that either a substantial fraction remains on this surface after TMG exposure is terminated, in apparent contradiction with the atomic level results, or  $CH_3$  is not a significant factor in establishing the electronic (optical) properties of this surface.

This surface may be related to the  $(4 \times 8)$  reconstruction observed by Chiu [19] in organometallic molecular beam epitaxy following saturation TMG exposure at

550 °C although the connection is indirect. If one assumes that the Arrhenius parameters determined between 430 and 480 °C by Kobayashi and Horikoshi [10] in OMCVD for the slow phase of the recovery (roughly points 95–206) can be extrapolated to 550 °C, calculation shows that the recovery should last about 13 s at 550 °C. This is in reasonable agreement with the 8 s duration reported by Chiu [19].

Pending a direct identification of the RD spectrum of the TMG-saturated  $c/d(4 \times 4)$  surface, we appear to be dealing with a metastable phase that is related to the  $(2 \times 4)$ -like reconstruction but which must be reached by either kinetics or pinning by appropriate reactants, e.g. the double-bonded C in 0.001 ML quantities observed by Annapragada *et al.* [24]. Other examples of kinetically accessed reconstructions on (001) GaAs include the  $(3 \times 1)$  and  $(4 \times 6)$ – $(1 \times 6)$  reconstructions, which can only be obtained under certain conditions by following specific procedures [15]. Although issues of reactivity and connection to other reconstructions need to be resolved with further work, these results already provide additional constraints that must be satisfied by models of ALE appropriate to AP  $H_2$ . For example, except for the  $c/d(4 \times 4)$ -like reconstruction, those observed here have not been seen previously under steady state conditions. The results also indicate that kinetics and thermodynamics cannot be separated but must be treated together, providing additional challenges for performing detailed studies of ALE with atomic level probes.

### 3. Growth control with spectroellipsometry

The achievement of direct control of layer composition and thickness would also have a substantial impact on growth technology. We have also been investigating ways of accomplishing this goal. SE is attractive for this purpose because it is highly accurate and, if the growth rate is known, dynamic ellipsometric measurements can be analyzed for the dielectric response of the outermost region of a depositing layer independent of any knowledge concerning previously deposited layers [11, 12]. This eliminates the possibility of systematic errors that occur in conventional optical analysis if any of the parameters describing previous layers have been determined incorrectly. Given the dielectric response of the outermost region, the composition can be determined. Given the composition of the outermost region, it is possible to construct a closed-loop system that can automatically adjust deposition conditions to follow predetermined composition profiles, including graded profiles [12].

Our experiments illustrating these principles were performed with a VG model V80H diffusion-pumped

\*Recently, M. Sato and M. Weyers (Technical Digest, International Workshop on Science and Technology for Surface Reaction Processes) reported  $CH_3$  evolution nominally from TMG-saturated (001) GaAs over time scales of the order of 1 min. However, the small temperature dependence observed is inconsistent with typical chemisorption enthalpies.

CBE system using triethylgallium ( $\text{Ga}(\text{C}_2\text{H}_5)_3$ , TEG), triisobutylaluminum ( $\text{Al}(\text{CH}_2\text{CH}(\text{CH}_3)_2)_3$ , TIBAL) and cracked  $\text{AsH}_3$  as sources of Ga, Al and As respectively. Growth temperatures ranged between 590 and 600 °C. Nearly-strain-free quartz windows [25] provided optical access to the sample. A rotating polarizer variant of our rotating analyzer spectroellipsometer [26] was used to obtain data at 2.6 eV, where the optical parameters of  $\text{Al}_x\text{Ga}_{1-x}\text{As}$  at 600 °C change most rapidly with composition  $x$ . Data were analyzed for compositions of the outermost depositing layers by a small-term expansion similar to that described previously [11] but with an improved accuracy of better than 0.1%. Possible contributions from surface terminations were implicitly taken into account by referencing all data to the dielectric response measured for the GaAs buffer layer. Calculations were done on-line and the results used to generate corrections to the TIBAL flux reaching the growth surface.

Using this system, we have grown structures with various composition profiles, including half-wave-rectified sine waves [27] and parabolic wells [12], and have analyzed them by secondary ion mass spectrometry, photoreflectance (PR) and photoluminescence (PL). The narrowest structure that we have grown to date is a parabolic  $\text{Al}_x\text{Ga}_{1-x}\text{As}$  quantum well 200 Å wide. The real-time control data for this structure are given in Fig. 4. The top part shows the experimentally determined control parameter  $\epsilon_2(x)$  expressed as composition  $x$  and superimposed on the target composition

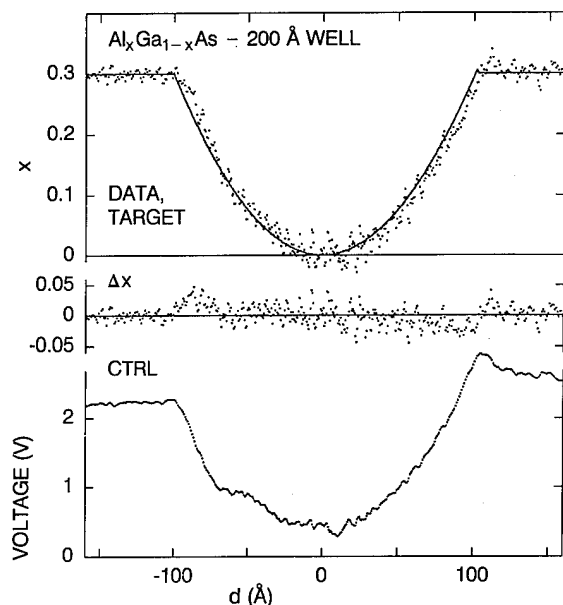


Fig. 4. Control data for the 200 Å  $\text{Al}_x\text{Ga}_{1-x}\text{As}$  parabolic quantum well: top, values of  $\epsilon_2$  for the running outer 3.1 Å of material expressed as  $x$  and compared with target values; center, difference between determined and target values; bottom, control voltage (after ref. 12).

with thickness as the running variable. The difference between determined and target values is shown at the center. The regulation voltage controlling the TIBAL flux is shown at the bottom. Here the GaAs deposition rate was  $0.95 \text{ Å s}^{-1}$  and the cycle time for ellipsometric measurement, data reduction and flow adjustment was 0.65 s. In each cycle approximately 0.08 s was used for stabilization, 0.06 s for baseline determination, 0.43 s for data acquisition and 0.08 s for data reduction and analysis. Five data points were averaged to determine  $x$ , which at minimum  $x$  corresponds to 3.1 Å (1.1 ML) of material. For thick films of constant composition these conditions lead to a short-term precision of about  $\pm 0.015$  in  $x$ .

The difference between ellipsometrically determined and target values of  $x$  provides a check on the performance of the system and control algorithms. During growth of the well the average values of  $x$  track target values to within 0.01 in  $x$ , except for overshoots of about 0.02 at the edges. These overshoots result from the finite response time of the system. Response time effects also lead to a slightly underdamped behavior that can be seen most clearly in the control voltage. These effects can be modeled approximately by the equation  $dx(t)/dt \approx x(t - \tau)/T$ , where  $\tau$  is the delay time of the loop and  $T$  is related to the fraction of the calculated correction actually issued to the controller.

This structure is sufficiently narrow to exhibit quantum confinement in the near-band-gap spectral region. The PR spectrum of this sample shows five primary features at 1.43, 1.507, 1.601, 1.692 and 1.81 eV. The 1.43 and 1.81 eV features arise from the fundamental absorption edges of the GaAs substrate and  $\text{Al}_x\text{Ga}_{1-x}\text{As}$  barrier layers respectively. The remaining structures arise from intersubband transitions  $E_{11}$ ,  $E_{22}$  and  $E_{33}$  within the parabolic well itself, where the subscripts indicate the principal quantum numbers of the confined hole and electron. Overlap considerations lead to the conclusion that only those transitions with the same subband index need be considered. The identity and threshold energy of the  $E_{11}$  structure was confirmed by PL. A quantitative comparison between the observed energies and those calculated for square, parabolic and triangular wells was performed. For an assumed square well profile all transition energies are too low and the calculation predicts a fourth level not seen experimentally. For an assumed triangular well profile all transition energies are too high. In contrast, for an assumed parabolic well profile the energies of all primary transitions are reproduced to within 6 meV, showing that this compositional profile was achieved.

The present results indicate that real-time feedback control of composition can be used to grow quantum structures to a high degree of accuracy. Simple improvements such as providing anticipatory information

when  $x$  is changing rapidly with thickness and optimizing loop parameters should allow closed-loop control to compositional accuracies better than 0.01 in  $x$ . The realization of these capabilities for semiconductor alloys in general, not just  $\text{Al}_x\text{Ga}_{1-x}\text{As}$  in particular, would greatly simplify growth procedures by focusing control issues on the product instead of the process, thereby reducing the need to bring the process itself under direct control.

#### 4. Conclusions

We have shown that real-time optical characterization techniques are now capable of providing structural information about surfaces in real time under actual growth conditions and are also capable of controlling composition directly by an appropriate analysis for the dielectric response of near-surface regions of depositing layers. These capabilities will become increasingly important as growth approaches become more sophisticated and tolerances more stringent.

#### Acknowledgment

One of us (I.K.) would like to acknowledge support by the Office of Naval Research under Contract N-00014-90-J-1267.

#### References

- 1 C. H. L. Goodman and M. V. Pessa, *J. Appl. Phys.*, **60** (1986) R65, and references cited therein.
- 2 M. Ozeki, N. Ohtsuka, Y. Sakuma and K. Kodama, *J. Cryst. Growth*, **107** (1991) 102.
- 3 M. Ozeki, K. Mochizuki, N. Ohtsuka and K. Kodama, *Appl. Phys. Lett.*, **53** (1988) 1509.
- 4 J. Nishizawa, T. Kurabayashi, H. Abe and N. Sakurai, *J. Vac. Sci. Technol. A*, **5** (1987) 1572.
- 5 M. L. Yu, N. I. Buchan, R. Souda and T. F. Kuech, *MRS Symp. Proc.*, **222** (1991) 3.
- 6 J. R. Creighton and B. A. Banse, *MRS Symp. Proc.*, **222** (1991) 15.
- 7 D. E. Aspnes, J. P. Harbison, A. A. Studna and L. T. Florez, *Phys. Rev. Lett.*, **59** (1987) 1687.
- 8 D. E. Aspnes, J. P. Harbison, A. A. Studna and L. T. Florez, *J. Vac. Sci. Technol. A*, **6** (1988) 1327.
- 9 N. Kobayashi and Y. Horikoshi, *Jpn. J. Appl. Phys.*, **28** (1989) L1880.
- 10 N. Kobayashi and Y. Horikoshi, *Jpn. J. Appl. Phys.*, **30** (1991) L319.
- 11 D. E. Aspnes, W. E. Quinn and S. Gregory, *Appl. Phys. Lett.*, **57** (1990) 2707.
- 12 D. E. Aspnes, W. E. Quinn, M. C. Tamargo, M. A. A. Pudensi, S. A. Schwarz, M. J. S. P. Brasil, R. E. Nahory and S. Gregory, *Appl. Phys. Lett.*, **60** (1992) 1244.
- 13 D. E. Aspnes, I. Kamiya, H. Tanaka and R. Bhat, *J. Vac. Sci. Technol.*, **B**, **10** (1992) 1725.
- 14 I. Kamiya, D. E. Aspnes, H. Tanaka, L. T. Florez, J. P. Harbison and R. Bhat, *Phys. Rev. Lett.*, **68** (1992) 627.
- 15 I. Kamiya, D. E. Aspnes, L. T. Florez and J. P. Harbison, *Phys. Rev. B*, **46** (1992) 15894.
- 16 A. Gomyo, T. Suzuki and S. Iijima, *Phys. Rev. Lett.*, **60** (1988) 2645.
- 17 S. Froyen and A. Zunger, *Phys. Rev. Lett.*, **59** (1991) 324.
- 18 G. S. Chen and G. B. Stringfellow, *Appl. Phys. Lett.*, **59** (1991) 324.
- 19 T. H. Chiu, *Appl. Phys. Lett.*, **55** (1989) 1244.
- 20 J. R. Creighton, *Surf. Sci.*, **234** (1990) 287.
- 21 U. Memmert and M. L. Yu, *Appl. Phys. Lett.*, **56** (1990) 1883.
- 22 D. E. Aspnes, E. Colas, A. A. Studna, R. Bhat, M. A. Koza and V. G. Keramidas, *Phys. Rev. Lett.*, **61** (1988) 2782; *J. Vac. Sci. Technol. A*, **7** (1989) 711.
- 23 H. H. Farrell, J. P. Harbison and L. D. Peterson, *J. Vac. Sci. Technol. B*, **5** (1987) 1482.
- 24 A. V. Annapragada, S. Salim and K. F. Jensen, *MRS Symp. Proc.*, **222** (1991) 81.
- 25 A. A. Studna, D. E. Aspnes, L. T. Florez, B. J. Wilkens and R. E. Ryan, *J. Vac. Sci. Technol. A*, **7** (1989) 3291.
- 26 D. E. Aspnes and A. A. Studna, *Appl. Opt.*, **14** (1975) 220; *Rev. Sci. Instrum.*, **49** (1978) 291.
- 27 D. E. Aspnes, R. Bhat, E. Colas, L. T. Florez, S. Gregory, J. P. Harbison, I. Kamiya, W. E. Quinn, S. A. Schwarz, H. Tanaka and M. Wasserman, *MRS Symp. Proc.*, **222** (1991) 63.

# *In situ* monitoring and control of atomic layer epitaxy by surface photo-absorption

Naoki Kobayashi and Yasuyuki Kobayashi

NTT Basic Research Laboratories, 3-9-11, Musashino-shi, Tokyo 180 (Japan)

## Abstract

Surface photo-absorption (SPA) is a real-time optical probe for examining growth and gives us a microscopic insight into atomic processes occurring on a growth surface. SPA observations during GaAs and InP atomic layer epitaxy (ALE) using trimethyl Group III sources and Group V hydrides demonstrate that the adsorption of trimethyl source saturates during the trimethyl source supply period and that the saturated surface corresponds to a metastably methyl-terminated surface with a lifetime of several tens of seconds. In contrast, when the trimethyl source is supplied onto the Group III metal surface, an increase in the SPA reflectivity from the metal surface level is observed, indicating that the trimethyl source molecule decomposes on the Group III metal surface via adsorption. These observations give rise to the conclusion that the growth rate self-limitation in ALE is caused by the inhibited adsorption of excessively supplied Group III source molecules on the methyl-terminated surface, and not by a selective adsorption mechanism. SPA observation also makes it possible to determine readily and precisely the growth parameters for ALE which strongly depend on the reactor design and the gas flow condition.

## 1. Introduction

Atomic layer epitaxy (ALE) is an attractive growth method, because the epitaxial layer thickness is highly uniform over the whole area of the substrate. For the ALE mechanism of GaAs using trimethylgallium (TMG) and arsine, Nishizawa and Kurabayashi [1] proposed an inhibited adsorption model that a methyl-terminated GaAs surface inhibits further heterogeneous decomposition of the TMG and self-limits the growth rate to one monolayer (ML) per cycle. On the basis of the experimental result that a C peak was not observed by X-ray photoelectron spectroscopy (XPS) analysis of the GaAs surface after TMG exposure [2, 3], a selective adsorption mechanism was proposed [3]. In this model, TMG molecule decomposes via a selective adsorption on the As surface, immediately forming a Ga metal surface. Once the Ga metal surface is formed, excessively supplied TMG molecules desorb quickly from the Ga surface prior to decomposition, because the adsorption of the TMG molecules on the Ga surface is weak. Arsine molecules also are selectively adsorbed on the metal Ga surface to form an As surface. Memmert and Yu [4] measured methyl desorption by a combination of pulsed molecular beams and time-resolved mass spectrometry. They reported that the methyl desorption is too fast (a lifetime of 3 ms at 550 °C) to attribute the self-limitation to the methyl-terminated surface. They proposed a flux balance model that TMG decomposes

on the Ga surface but no net Ga deposition occurs owing to a quick desorption of the decomposition fragments containing Ga species, such as monomethyl-gallium.

Surface photo-absorption (SPA) [5] has been developed as a real-time optical probe to examine epitaxial growth and is based on measuring the reflectivity of p-polarized light incident at the Brewster angle. This optical geometry minimizes the bulk reflection, resulting in a highly sensitive detection of reflectivity change caused by surface reactions, such as adsorption and decomposition of source molecules and surface atom desorption. Submonolayer sensitivity has been demonstrated for the Ga deposition on the As surface during GaAs metal-organic chemical vapor deposition (MOCVD) [6] and molecular beam epitaxy (MBE) [5]. The real-time measurement also makes it possible to determine the dynamics of the surface reactions. For example, the decomposition rate of arsine on the Ga metal surface is obtained from the reflectivity decay which corresponds to an increase in As coverage owing to arsine heterogeneous decomposition [7].

In this paper, we apply SPA to clarify the ALE mechanism and to control the ALE process precisely through investigating TMG decomposition on GaAs and trimethylindium (TMI) decomposition on an InP surface. The microscopic information obtained by SPA determines explicitly the ALE mechanism. The SPA monitoring also enables us to obtain readily and pre-

cisely the ALE growth parameters which strongly depend on the reactor design and the gas flow conditions.

## 2. Experimental procedure

We used vertical and horizontal MOCVD reactors with an SPA monitoring system as previously reported [6, 8]. The total gas flow rate was  $9\text{--}10\text{ l min}^{-1}$  and the reactor pressure was  $4\text{--}6\text{ kPa}$ . Under these conditions, the gas flow velocity passing near the substrate is estimated to be about  $1\text{ m s}^{-1}$ , which corresponds to a source gas exchange time of less than  $0.1\text{ s}$ . Also, p-polarized monochromatic light or laser light irradiates the (001)-oriented substrate surface through a chopper at an incidence angle of  $70^\circ$ . The power density at the substrate surface was about  $0.1\text{ mW cm}^{-2}$  for the monochromatic light and about  $0.1\text{ W cm}^{-2}$  for the laser light. Under these optical conditions, the effect of the monitoring light on the growth rate was ignored.

## 3. Results and discussion

### 3.1. SPA study of the Group III source decomposition process and ALE mechanism

The substrate temperature range which shows a growth rate self-limitation depends strongly on the kind of Group III source. Minimizing the gas-phase decomposition of the Group III source by using a high gas flow velocity expands this range to high temperatures, as reported for pulsed jet epitaxy [9]. For GaAs growth using TMG and arsine, ALE is usually achieved in the temperature range between  $400$  and  $500^\circ\text{C}$ . When triethylgallium (TEG) was used, it has been reported that the ALE region becomes very narrow but exists at about  $350^\circ\text{C}$  [10]. ALE of InAs and a submonolayer growth-rate self-limitation for InP were observed at about  $350^\circ\text{C}$  by using TMI as the In source [11, 12]. To clarify the ALE mechanism, it is important to know the decomposition characteristics of the Group III source in the temperature range of ALE. First, we studied the substrate temperature  $T_s$  dependence of the SPA signal when the Group III source was supplied onto the Group V surface.

Figure 1 shows the  $T_s$  dependence of the SPA reflectivity change  $(R_{\text{III}} - R_V)/R_V$ , where  $R_{\text{III}}$  denotes the reflectivity of the surface after a constant amount of Group III source supply and  $R_V$  denotes the reflectivity of the Group V surface. In this figure, the decomposition onset temperature of the Group III source is regarded as the temperature at which  $(R_{\text{III}} - R_V)/R_V$  starts to increase, because the SPA onset agreed well with the growth-initiating temperature. As might be expected from the bond strength between the alkyl

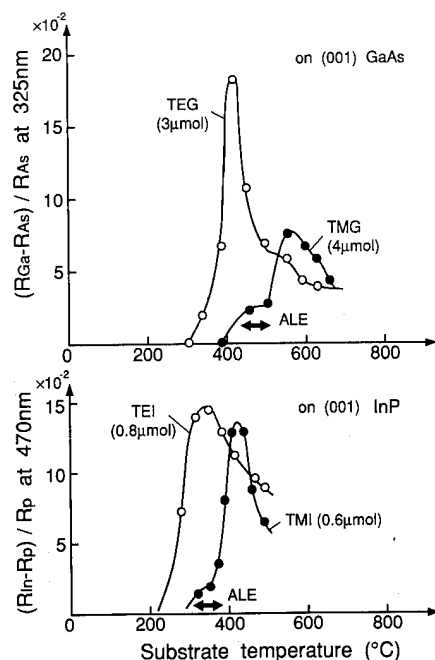


Fig. 1. Substrate temperature dependence of the SPA reflectivity change when a constant amount of Group III source was supplied onto a Group V surface.

group and Group III atom, TEG and triethylindium (TEI) sources have lower onset temperatures ( $300^\circ\text{C}$  for TEG [13] and  $230^\circ\text{C}$  for TEI) than the corresponding trimethyl sources ( $380^\circ\text{C}$  for TMG [13] and  $270^\circ\text{C}$  for TMI). It has been reported that, using mass spectroscopic analysis of the decomposition products, the decomposition onset temperatures in hydrogen are  $375^\circ\text{C}$  for TMG [14],  $230^\circ\text{C}$  [15] and  $250^\circ\text{C}$  [16] for TEG, and  $250\text{--}275^\circ\text{C}$  for TMI [17]. Even if taking into consideration an experimental error in the temperature measurement, a relatively good agreement was obtained between the SPA and mass spectroscopic results. The temperature range which shows a steep increase in the  $(R_{\text{III}} - R_V)/R_V$  ratio after the onset of decomposition is controlled kinetically. In this region, an increase in the growth rate with the substrate temperature was observed also. The  $(R_{\text{III}} - R_V)/R_V$  ratio decreases after showing peaks. For TEG, when  $T_s$  was raised up to  $650^\circ\text{C}$ ,  $(R_{\text{Ga}} - R_{\text{As}})/R_{\text{As}}$  settles down to the level of the Ga metal surface above  $550^\circ\text{C}$ . The temperature region above  $450^\circ\text{C}$  for TEG is mass-transport-controlled, because the growth rate was almost independent of  $T_s$ . Furthermore, in this region, from the scattering light measurement [18], when the supplied amount of Ga exceeds 1 ML, scattered light from the surface was observed. At the low temperatures in the mass-transport-controlled region, when the Group III source is supplied to over 1 ML deposition, the formation of small metal droplets is assumed to be dominant, be-

cause the agglomeration rate of the droplets is considered to be very slow at low temperatures. If the droplet size is smaller than the wavelength of the monitoring light, the surface covered with the high density of such small droplets is optically considered to be a pseudo-Group III multilayer on a Group V plane. This surface raises the SPA reflectivity above the level of 1 ML metal coverage because of an increase in the optical dielectric constant of the surface. In fact, it was observed that the SPA reflectivity increased above 1 ML deposition on the (001) As surface using TEG [13]. When  $T_s$  is increased, it is expected that small metal droplets agglomerate into a larger droplet and the droplet density decreases. The result that the SPA reflectivity decreased, as observed in Fig. 1, when  $T_s$  was increased, is thought to be caused by the agglomeration of the small droplets and the decrease in the droplet density. Furthermore, it was observed that the SPA reflectivity saturates and the scattered light starts to be detected in the vicinity of 1 ML Ga deposition [18]. Excess Ga atoms supplied over 1 ML coverage agglomerate to form a localized droplet. In the Ga deposition with a small excess amount over 1 ML, the surface is approximately considered to be covered with 1 ML Ga atoms, because the droplet density is very small owing to rapid agglomeration. As a result, the SPA reflectivity saturates with an increase in the TEG supply in the vicinity of 1 ML Ga deposition. However, the size of the Ga droplets becomes large enough to scatter the monitoring light. Therefore, the scattered light was observed when the supply amount exceeded 1 ML coverage.

In Fig. 1, the temperature range for ALE is clearly recognized as a shoulder and a plateau (330 to 350 °C for InP, and 440 to 500 °C for GaAs) near the de-

composition onset in the plot for the trimethyl source. In contrast, the triethyl source shows no clear ALE region in the  $T_s$  dependence, presumably because of the narrow ALE region. The ALE regions for the trimethyl sources and TEG (350 °C) belong to the kinetically controlled region, in which Group III source molecules are transported onto the surface without complete decomposition in the gas-phase. Therefore, it is most probable that alkyl groups reside on the surface with a long lifetime after the Group III source supply in the ALE region.

The kinetically controlled temperature region for TMG including GaAs ALE overlaps with the mass-transport-controlled region for TEG. To show clearly the difference in decomposition behavior between TMG and TEG, the SPA reflectivity changes are compared in Fig. 2 [19] in which a 1 s pulse supply of the Ga source onto the As surface of the (001) GaAs is followed by a hydrogen purging at 470 °C. The As surface was stabilized by an  $\text{AsH}_3$  flow of  $1.5 \mu\text{mol s}^{-1}$ . At this temperature, ALE was achieved with TMG and the decomposition belongs to the kinetically controlled region. The TEG decomposition at 470 °C belongs to the mass-transport-controlled region. The amount of TEG supplied was  $0.2 \mu\text{mol}$ , which corresponded to 1 ML Ga deposition. The reflectivity increased with the moment of TEG supplied and, during hydrogen purging, the reflectivity was almost constant. This behavior shows that the TEG molecules decompose immediately to Ga atoms on the As surface within the time constant of SPA signal detection (0.1 s). When the TEG supply increased to more than 1 ML deposition, the reflectivity also increased without showing saturation at a coverage of 1 ML, because of the formation of small Ga droplets, as described before.

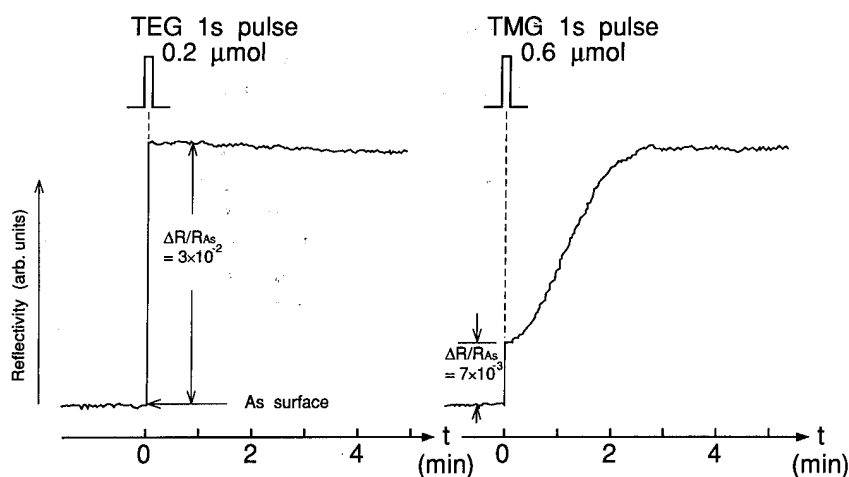


Fig. 2. Comparison of SPA reflectivity change between TEG and TMG when a supply pulse of 1 s onto the As surface is followed by hydrogen purging at 470 °C.  $T_s = 470$  °C;  $\lambda = 470$  nm; [110] azimuth.



In contrast, once 0.6  $\mu\text{mol}$  of TMG has been supplied on the As surface, a small reflectivity change of  $\Delta R/R_{\text{As}} = 7 \times 10^{-3}$  was initially observed. The reflectivity then increased slowly to the saturation level of  $\Delta R/R_{\text{As}} = 3 \times 10^{-2}$ , which is the same as the 1 ML metal Ga deposition obtained using TEG. The TMG supply of 0.6  $\mu\text{mol}$  is enough to achieve an ALE growth of 1 ML cycle $^{-1}$ . The initial reflectivity change in Fig. 2 shows the self-limitation, *i.e.* the reflectivity change saturates as the TMG supply increases. Figure 3 shows the initial reflectivity change as a function of the amount of TMG in a supply pulse of 1 s at  $T_s = 440, 455, 470, 485$  and  $520^\circ\text{C}$  [19]. Below  $485^\circ\text{C}$ , the reflectivity change shows a self-limitation with a saturation value of  $\Delta R/R_{\text{As}} = 7 \times 10^{-3}$ . The growth-rate self-limitation to 1 ML cycle $^{-1}$  was confirmed experimentally at  $T_s = 470$  and  $485^\circ\text{C}$  using an alternating supply of TMG and arsine. At  $T_s = 520^\circ\text{C}$ , no self-limitation was observed in either the reflectivity change or growth-rate.

A large difference observed in the decomposition between TEG and TMG is caused by the bond strength difference between the alkyl group and Ga atom. At  $470^\circ\text{C}$ , the TEG molecules release all the ethyl groups at the moment of TEG adsorption on the As surface to form a Ga metal surface. In contrast, from the experimental result that TMG shows a smaller reflectivity change compared with that for a Ga metal surface formation by TEG, a TMG molecule releases at least one methyl group to combine with surface As atoms at the moment of adsorption. However, it is most probable that methyl groups are left on the surface after the TMG supply to form a

metastably methyl-terminated surface which shows a smaller reflectivity at 470 nm than that for a Ga metal surface. This hypothesis is strongly supported by the SPA reflectivity behavior during hydrogen purging and by the purging period dependence of C acceptor incorporation, as is described later.

The surface which showed a reflectivity saturation during hydrogen purging was identified as a 1 ML Ga metal surface by the spectral dependence measurement [19], *i.e.* the SPA spectrum of this surface agreed with that of the 1 ML Ga metal surface obtained using TEG. Therefore, the reflectivity increase during hydrogen purging is consistent with the formation of a Ga surface by methyl group desorption from the methyl-terminated surface.

By the successive formation of an As surface, a large portion of the methyl groups desorb as methane via the reaction with arsine, but residual methyl groups are incorporated as a C acceptor into As sites of the GaAs. Therefore, a decrease in C incorporation with an increase in the purging period is expected. Figure 4 shows the average sheet hole density which corresponds to the density of a C acceptor incorporated as a function of the hydrogen purging period at  $T_s = 470^\circ\text{C}$  [19]. The layer structure was fabricated by repeating 50 insertions of 1 ML of ALE-grown GaAs layers after every undoped GaAs layer 50 nm thick grown by TEG. The purging period after TMG supply was kept constant in one sample. The average sheet hole density was obtained from the structure with a total of 50 ML of ALE-grown GaAs isolated by an undoped GaAs layer. The undoped GaAs layer was n-type with a carrier concentration of less than  $10^{15}\text{ cm}^{-3}$ , so the effect of the undoped layer on the estimation of the average sheet hole density was negligible. As expected, the average sheet hole density decreased from  $6.4 \times 10^{11}$  to  $5.8 \times 10^{10}\text{ cm}^{-2}$  when the purging period increased from 1 s to 3 min. Furthermore, the rate of decreasing sheet hole density (about  $1 \times 10^{-2}\text{ s}^{-1}$ ) agrees with the increased rate of reflectivity during hydrogen purging. These findings are consistent with the TMG molecule decomposing with the remaining methyl groups to form a metastably methyl-terminated surface in the TMG supply period at ALE growth temperatures.

From the dynamics of methyl group desorption, the stability of the methyl-terminated surface is estimated. The reflectivity change caused by the methyl group desorption was described by the first-order kinetics except the initial stage of desorption. Figure 5 shows an Arrhenius plot of the rate constants for methyl group desorption [19]. The rate equation obtained was

$$k = 10^{7.4} \exp[-1.39 (\text{eV})/RT] \quad (\text{s}^{-1})$$

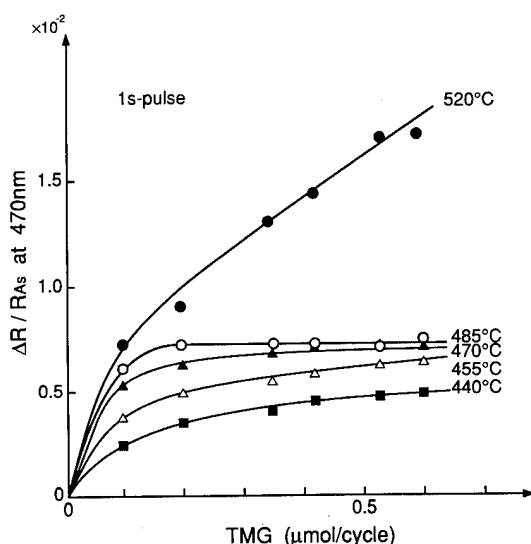


Fig. 3. Initial reflectivity change as a function of the amount of TMG at  $T_s = 440, 455, 470, 485$  and  $520^\circ\text{C}$ .

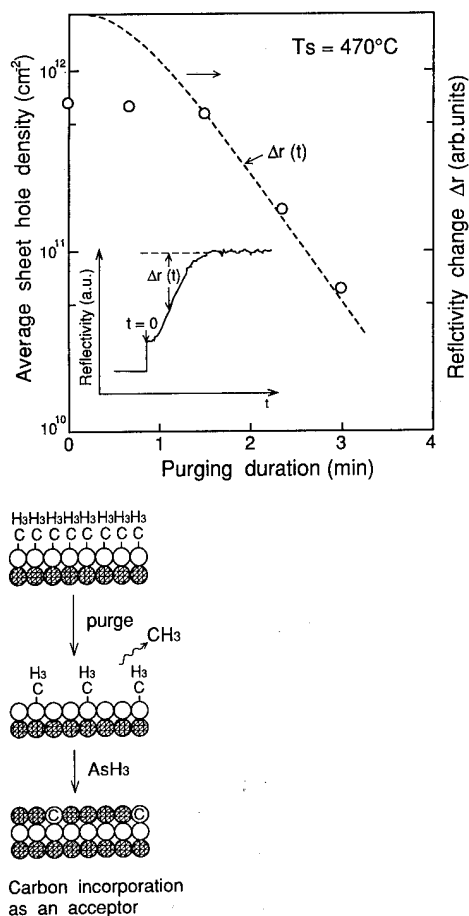


Fig. 4. Average sheet hole density and reflectivity increase as a function of hydrogen purging duration at 470 °C.

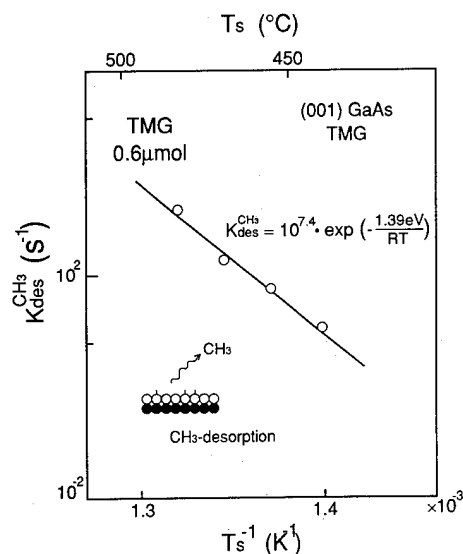


Fig. 5. Arrhenius plot of rate constants for methyl group desorption.

where  $R$  is the gas constant. The desorption lifetime, which corresponds to the stability of the methyl-terminated surface, increases from 50 to 172 s when  $T_s$

decreases from 485 to 440 °C. Therefore, these values are large enough to support the inhibited adsorption mechanism that a metastably methyl-terminated surface inhibits further heterogeneous decomposition of the TMG and self-limits the growth-rate to 1 ML cycle<sup>-1</sup>.

The selective adsorption mechanism is based on the assumption that the adsorption of the TMG molecules on the Ga metal surface is so weak, such that the TMG molecules desorb quickly prior to decomposition. The possibility of this mechanism was studied by SPA observation of TMG supply onto the Ga metal surface. Figure 6 shows the SPA reflectivity trace of ALE growth followed by hydrogen purging for 5 min, a 1 s pulse supply of TMG and another hydrogen purge. A Ga metal surface was formed by the first hydrogen purge. Therefore, the last 1 s supply of TMG corresponds to the TMG supply onto the Ga metal surface. If the TMG molecules desorb quickly from the Ga metal surface prior to decomposition, no reflectivity change is expected. However, a reflectivity increase was observed for TMG supply onto the Ga surface, indicating that the TMG decomposes on the Ga surface via adsorption and that net Ga decomposition occurs on the Ga metal surface. Therefore, this result refutes not only the selective adsorption model but also the flux balance model, in which TMG decomposes on the Ga metal surface but no net Ga deposition occurs.

The SPA observation for TMI decomposition on the P surface of (001) InP [20] demonstrated a similar characteristic to that obtained for TMG decomposition. Figure 7 shows the SPA reflectivity change  $\Delta R/R_P = (R_{TMI} - R_P)/R_P$  as a function of the amount of TMI supplied in a pulse of 1 s at  $T_s = 350, 365, 380$  and 400 °C, where  $R_P$  is the reflectivity of the P-stabilized InP surface and  $R_{TMI}$  is the reflectivity just after the TMI supply. The P surface was stabilized by a  $PH_3$  flow rate of 6  $\mu\text{mol s}^{-1}$ . The reflectivity change shows a self-limitation at  $T_s = 350$  °C, i.e.  $\Delta R/R_P$  saturated at  $2.7 \times 10^{-2}$  as the TMI supply amount increased. The temperature, showing self-limitation, was found as a shoulder in the  $T_s$  dependence shown in Fig. 1 and belongs to the kinetically controlled region. Therefore, in the same manner as the TMG decomposition, the adsorption of TMI molecules saturates and the saturated surface corresponds to the metastably methyl-terminated surface at 350 °C.

Methyl group desorption was also observed for TMI. Figure 8 shows the reflectivity change during hydrogen purging after a 1 s pulse supply of TMI. The amount of TMI varied from 0.1 to 0.6  $\mu\text{mol}$ . For a supply of 0.6  $\mu\text{mol}$ , the TMI adsorption is saturated. The reflectivity change caused by methyl group desorption from the methyl-terminated surface can be described by first-order kinetics. The methyl desorption rate was  $3.0 \times 10^{-2} \text{ s}^{-1}$ , or a lifetime of 34 s at  $T_s = 350$  °C. This

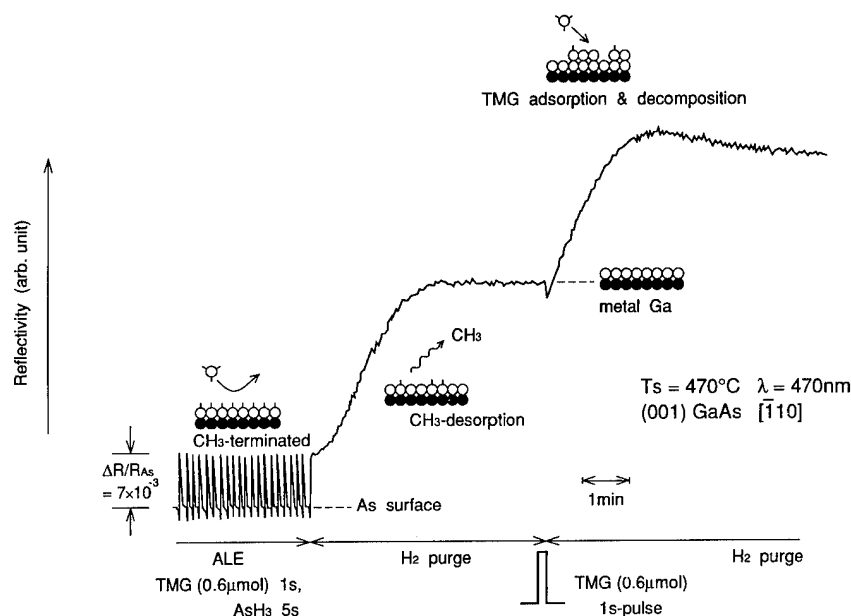


Fig. 6. SPA reflectivity change with ALE growth followed by hydrogen purging for 5 min, a 1 s pulse supply of TMG and further hydrogen purging.

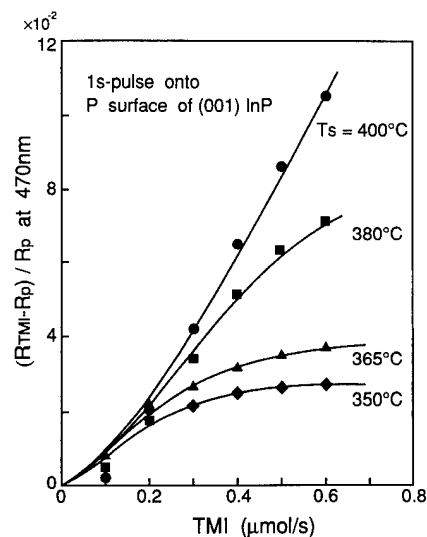


Fig. 7. Initial reflectivity change as a function of the amount of TMI supplied onto the P surface of InP at  $T_s = 350, 365, 380$  and  $400^\circ\text{C}$ .

value is large enough to support the inhibited adsorption mechanism. From an Arrhenius plot of the desorption rates, the rate equation obtained was

$$k = 10^{13.2} \exp[(-1.8 \text{ (eV)}/RT)]$$

The large difference in pre-exponential factor between TMG ( $10^{7.4}$ ) and TMI ( $10^{13.2}$ ) is consistent with the bond strength difference between methyl-Ga and methyl-In. For a supply of  $0.1 \mu\text{mol}$ , the coverage of TMI is estimated to be less than 25%. During hydrogen purging, P desorption occurs simultaneously. The ob-

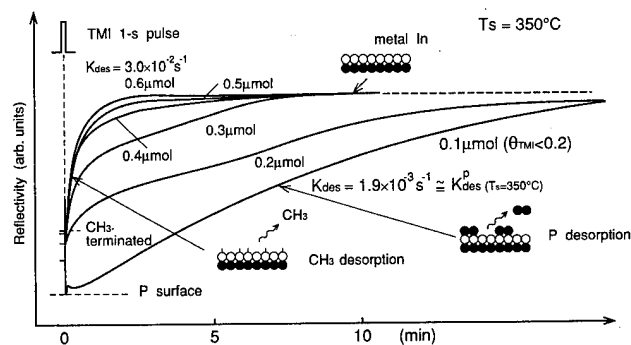


Fig. 8. Reflectivity change during hydrogen purging after a 1 s pulse supply of TMI onto the P surface of InP at  $T_s = 350^\circ\text{C}$ .

served desorption rate of  $1.9 \times 10^{-3} \text{ s}^{-1}$  is slower than the methyl group desorption and is close to the P desorption at  $350^\circ\text{C}$  [21]. This result confirms the methyl group desorption by distinguishing it from P desorption.

### 3.2. In situ monitoring and controlling of ALE

So far, the ALE growth parameters, such as the substrate temperature and source supply period, have been determined through macroscopic thickness measurements after growth. By observing *in situ* a methyl-terminated surface and the formation of the Group V surface, we can determine readily and precisely the growth parameters which are affected greatly by the reactor design and gas flow condition.

Figure 9 shows the TMG flow duration dependence of the SPA reflectivity at  $T_s = 470^\circ\text{C}$  with a constant

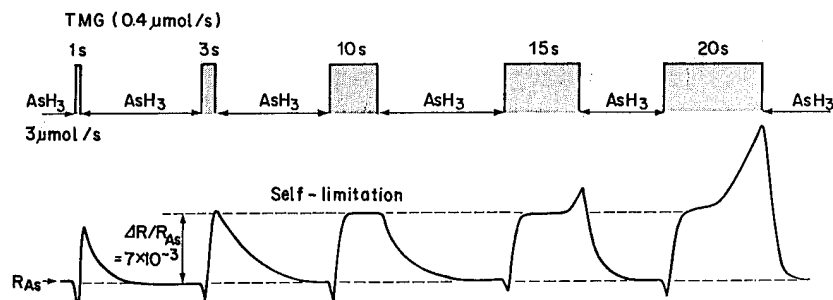


Fig. 9. TMG flow duration dependence of SPA reflectivity at  $T_s = 470^\circ\text{C}$  with  $\lambda = 470\text{ nm}$  and  $[\bar{1}10]$  azimuth.

TMG flow rate of  $0.4\ \mu\text{mol s}^{-1}$ . For durations longer than 3 s, a plateau of  $\Delta R/R_{\text{As}} = 7 \times 10^{-3}$  was observed, indicating that the surface is metastably methyl terminated. However, at durations of 15 and 20 s, a further increase in the reflectivity was observed after about 10 s. This indicates that the inhibited adsorption is not maintained owing to the methyl group desorption followed by the adsorption and decomposition of TMG molecules on the partially formed Ga metal surface. As shown in Fig. 6, TMG molecules can adsorb and decompose on a Ga metal surface.

Figure 10 shows the SPA reflectivity change when the TMG flow duration is increased at  $T_s = 450, 470$  and  $490^\circ\text{C}$ . The duration needed to maintain a methyl-terminated surface increases from 10 s at  $470^\circ\text{C}$  to 18 s at  $450^\circ\text{C}$ . This is consistent with the experimental result that the lifetime of methyl group desorption increases from 77 s ( $470^\circ\text{C}$ ) to 142 s ( $450^\circ\text{C}$ ). At  $490^\circ\text{C}$ , the reflectivity increased almost linearly, indicating that a methyl-terminated surface cannot be maintained with a sufficient lifetime for inhibited adsorption. These results show that the growth parameters for ALE can be precisely determined by SPA.

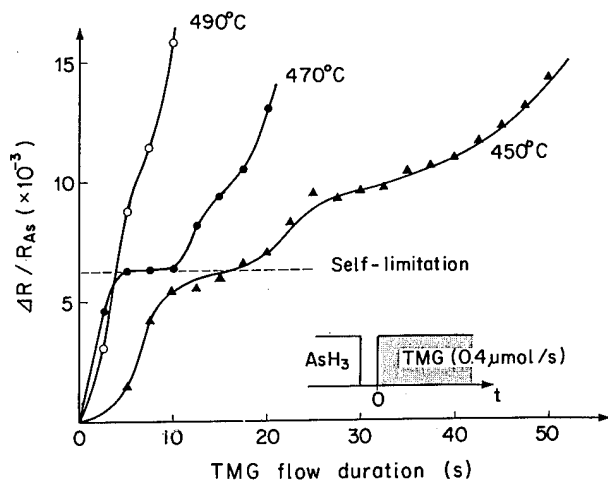


Fig. 10. SPA reflectivity change when TMG flow duration increased at  $T_s = 450, 470$  and  $490^\circ\text{C}$ .

For InAs ALE, a growth rate self-limitation to 1 ML cycle $^{-1}$  has been reported [11, 12]. However, for InP, a self-limitation to less than 1 ML cycle $^{-1}$  also has been reported [11, 12]. Figure 11 shows the comparison of Group V hydride reactivity between a Group III metal surface and a methyl-terminated surface. For GaAs, first, arsine was supplied for 12 s onto the Ga metal surface. After hydrogen purging for 1 s, TMG was supplied for 3 s, followed by a hydrogen purging for 1 s and arsine supply. The second arsine supply corresponds to the supply onto the methyl-terminated surface. It is seen clearly that the arsine decomposition rate is slower on the methyl-terminated surface

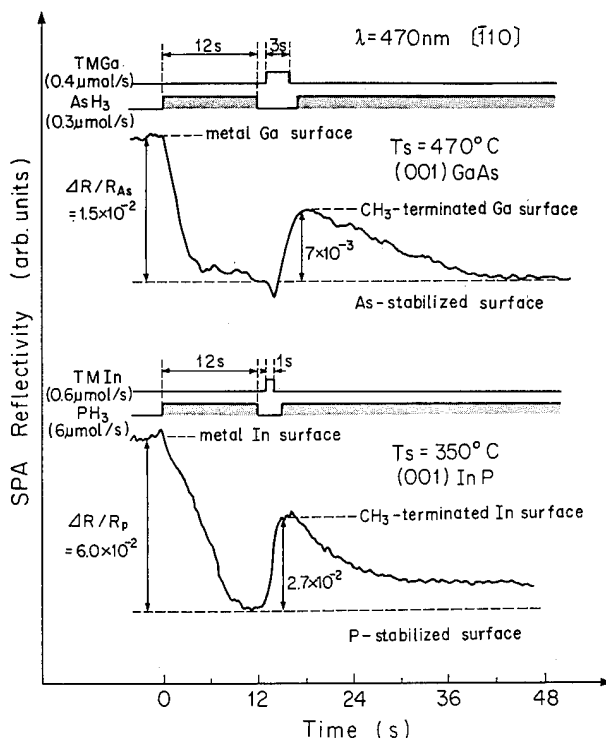


Fig. 11. Comparison of Group V hydride reactivity between Group III metal surface and methyl-terminated surface for arsine/GaAs and phosphine/InP.

( $0.075 \text{ s}^{-1}$ ) than on the Ga metal surface ( $0.37 \text{ s}^{-1}$ ). In the practical ALE condition, about 10 times the amount of arsine ( $3 \mu\text{mol}$ ) is used, so the formation of the As surface is completed within 5 s. For InP, the slow decomposition of phosphine on the methyl-terminated surface also was observed. Regardless of the large amount of phosphine ( $6 \mu\text{mol}$ ), it takes about 3 min to obtain a P surface. Therefore, it is concluded that the InP growth rate self-limitation to a submonolayer is caused by a slow decomposition of the phosphine on the methyl-terminated surface. Photo-assisted or thermally assisted methyl group desorption improves the growth rate per cycle in InP ALE. In fact, methyl group desorption using hydrogen purging for 1 min raised the growth rate per cycle from 0.37 ML to 0.89 ML [20].

#### 4. Conclusions

We applied SPA to the study of Group III source decomposition characteristics on a substrate surface. The microscopic information obtained by SPA determined explicitly the ALE mechanism. The SPA monitoring also enabled us to obtain readily and precisely the ALE growth parameters.

#### Acknowledgments

We would like to thank Dr. Yoshiji Horikoshi for his helpful discussion and encouragement. We also thank Dr. Tatsuya Kimura for his encouragement throughout this work.

#### References

- 1 J. Nishizawa and T. Kurabayashi, *J. Cryst. Growth*, **95** (1988) 132.
- 2 H. Ishii, H. Ohno, K. Matsuzaki and H. Hasegawa, *J. Cryst. Growth*, **95** (1989) 132.
- 3 K. Kodama, M. Ozeki, K. Mochizuki and N. Ohtsuka, *Appl. Phys. Lett.*, **54** (1989) 656.
- 4 U. Memmert and M. L. Yu, *Appl. Phys. Lett.*, **56** (1990) 1883.
- 5 N. Kobayashi and Y. Horikoshi, *Jpn. J. Appl. Phys.*, **28** (1989) L1880.
- 6 T. Makimoto, Y. Yamauchi, N. Kobayashi and Y. Horikoshi, *Jpn. J. Appl. Phys.*, **29** (1990) L207.
- 7 Y. Yamauchi, T. Makimoto, N. Kobayashi and Y. Horikoshi, *Jpn. J. Appl. Phys.*, **29** (1990) L1353.
- 8 N. Kobayashi and Y. Horikoshi, *Jpn. J. Appl. Phys.*, **29** (1990) L702.
- 9 M. Ozeki, K. Mochizuki, N. Ohtsuka and K. Kodama, *Appl. Phys. Lett.*, **53** (1988) 1509.
- 10 H. Ohno, S. Ohtsuka, H. Ishii, Y. Matsubara and H. Hasegawa, *Appl. Phys. Lett.*, **54** (1989) 2000.
- 11 W. G. Jeong, E. P. Menu and P. D. Dapkus, *SPIE*, **1144** (1989) 86.
- 12 M. Ozeki, N. Ohtsuka, Y. Sakuma and K. Kodama, *J. Cryst. Growth*, **107** (1991) 102.
- 13 T. Makimoto, Y. Yamauchi, N. Kobayashi and Y. Horikoshi, *Jpn. J. Appl. Phys.*, **29** (1990) L645.
- 14 C. A. Larsen, N. I. Buchan, S. H. Li and G. B. Stringfellow, *J. Cryst. Growth*, **93** (1988) 15.
- 15 M. Yoshida, H. Watanabe and F. Uesugi, *J. Electrochem. Soc.* **132** (1985) 677.
- 16 P. W. Lee, T. R. Omstead, D. R. McKenna and K. F. Jensen, *J. Cryst. Growth*, **85** (1987) 165.
- 17 N. I. Buchan, C. A. Larsen and G. B. Stringfellow, *J. Cryst. Growth*, **92** (1988) 591.
- 18 Y. Yamauchi, N. Kobayashi and Y. Horikoshi, *Jpn. J. Appl. Phys.*, **30** (1991) L918.
- 19 N. Kobayashi and Y. Horikoshi, *Jpn. J. Appl. Phys.*, **30** (1991) L319.
- 20 Y. Kobayashi and N. Kobayashi, *Jpn. J. Appl. Phys.*, **31** (1992) L71.
- 21 N. Kobayashi and Y. Kobayashi, *Jpn. J. Appl. Phys.*, **30** (1991) L1699.

# Surface photo-absorption study of the laser-assisted atomic layer epitaxial growth process of GaAs

J. P. Simko

*Frontier Research Program, RIKEN, Wako-shi, Saitama 351-01 (Japan)*

T. Meguro, S. Iwai and K. Ozasa

*RIKEN, 2-1 Hirosawa, Wako-shi, Saitama 351-01 (Japan)*

Y. Aoyagi\* and T. Sugano

*Frontier Research Program, RIKEN, Wako-shi, Saitama 351-01 (Japan)*

## Abstract

Thermal and laser-assisted decomposition of trimethylgallium (TMG) and triethylgallium (TEG) on GaAs surfaces under atomic layer epitaxy (ALE) processing conditions were monitored in real time using the (SPA) surface photo-absorption reflectivity technique to elucidate the mechanism of self-limiting deposition. When As-terminated (001) GaAs surfaces held between 340 and 390 °C were exposed to TMG, the SPA reflectivity decreased to a steady state, indicative of alkylgallium on the surface. Upon laser irradiation, this surface changed to an 'intermediate' steady state surface that was found to be in equilibrium with gas-phase alkylgallium species. Alkyl species then desorb from this surface when the TMG flow is stopped, leaving a self-limited deposit of Ga on the surface. No self-limiting deposition of Ga could be detected using TEG in laser-assisted ALE or thermal ALE. In this case, the observation of self-limiting alkylgallium deposition could explain successful ALE growth using TEG.

## 1. Introduction

The layer-by-layer growth of GaAs that is possible using atomic layer epitaxy (ALE) recently has been extended to a laser-assisted technique, whereby, taking advantage of a photo-enhanced reaction, selected-area ALE growth at reduced substrate temperatures is possible [1, 2]. This laser-assisted ALE (LALE) is extremely interesting because of its potential use in patterned growth and novel structure formation with growth control in both lateral and vertical dimensions.

In both ALE and LALE, the control of growth to one monolayer is achieved by directing group III (usually a trialkylgallium) and group V (usually arsine) source gases in an alternating sequence to a heated substrate, where they undergo self-limiting decomposition. Thermal ALE growth has been successfully reported on substrates from 470 to 510 °C [3–5], with one report as low as 450 °C [6]. By exposing the growing surface to light of the proper wavelength during trialkylgallium dosing, LALE growth is possible at substrate temperatures from 330 to 420 °C [7]. LALE growth also is possible using either trimethylgallium (TMG) or triethylgallium (TEG), though only one

instance of thermal ALE using TEG has ever been reported [8].

Currently, use of these techniques for high quality crystal growth is limited by a poor definition of the proper process conditions and uncontrollable C incorporation from the group III source gas (*i.e.* TMG). These problems have prompted numerous studies and the proposal of many mechanisms to describe the self-limiting growth [9–16]. Even with this wealth of information, confusion still exists as to how growth stops at one layer per gas sequence. Because of the C contamination, most attention has focused on the TMG sequence and Ga surface. In fact, a recent study has shown directly the presence of three or more As-containing layers on the GaAs surface after the arsine sequence, further stressing the importance of TMG decomposition [17]. With growth studies and using mass spectrometry (TPD), it has been shown that alkyl groups stay on the substrate surface before desorbing at 500 °C, and that excess Ga deposits on the surface at higher temperatures during TMG exposure [12]. This has led to the proposal that the adsorbed alkyl species prevent further decomposition of TMG on the surface, thereby limiting the growth. This mechanism has been supported by other mass spectrometric measurements (TPD, TP secondary ion mass spectroscopy), low energy electron diffraction (LEED) [9, 10, 13, 14] and

\*Also at RIKEN, 2-1 Hirosawa, Wako-shi, Saitama 351-01, Japan.

direct observation using *in situ* optical techniques (reflectance difference spectroscopy [18], surface photo-absorption (SPA) [19]). Another proposed mechanism (called 'flux-balance') supported by such data involves an equilibrium between adsorbed alkylgallium species and those in the gas phase, thereby keeping the amount of Ga on the surface constant [11]. Other mechanisms have been proposed [5, 15, 16].

Although closely related to thermal ALE, few mechanistic studies of the LALE process have been performed [7, 20]. Since similarities between the two processes are numerous and the self-limiting growth mechanism is not completely understood for either case, a comparative study between LALE and thermal ALE was performed using both TMG and TEG as the group III sources. The results show the first real-time observation of the growing surface during LALE. The SPA reflectivity measurement technique was used to monitor the GaAs surface *in situ* during LALE processing [21]. This technique involves measuring the intensity of p-polarized light reflected from a surface at the Brewster's angle, where the substrate reflectivity is at a minimum. At such a condition, reflectivity changes of the order of 1% are detectable when a monolayer of adsorbate is present on the surface.

Using this technique, three different surface conditions were detected on GaAs during TMG exposure and were attributed to various steps in the decomposition of TMG to Ga. Self-limiting Ga deposition was also observed using TMG and was attributed to an equilibrium between alkylgallium species on the substrate surface and the gas phase, similar to the proposed 'flux-balance' mechanism [11]. No self-limiting Ga deposition was detected when using TEG for either LALE or thermal ALE. Successful LALE when using TEG could be explained by the self-limiting deposition of alkylgallium under the proper process conditions.

## 2. Experimental details

Experiments reported here involved monitoring GaAs surfaces by SPA during exposure to process conditions similar to those for typical LALE and thermal ALE in order to determine what changes the surfaces undergo at each step of the ALE sequence. Unlike conventional ALE, the gas pulse and purge durations used here were determined by allowing the surface to reach a steady state, as monitored by SPA, which operated continuously during all the process phases. Arsine was used as the As source gas, while either TMG or TEG was used as the Ga source. Substrate temperatures from 300 to 450 °C were investigated.

Samples used for the experiments were 1 cm<sup>2</sup> (001) p-type GaAs that were degreased and acid etched to

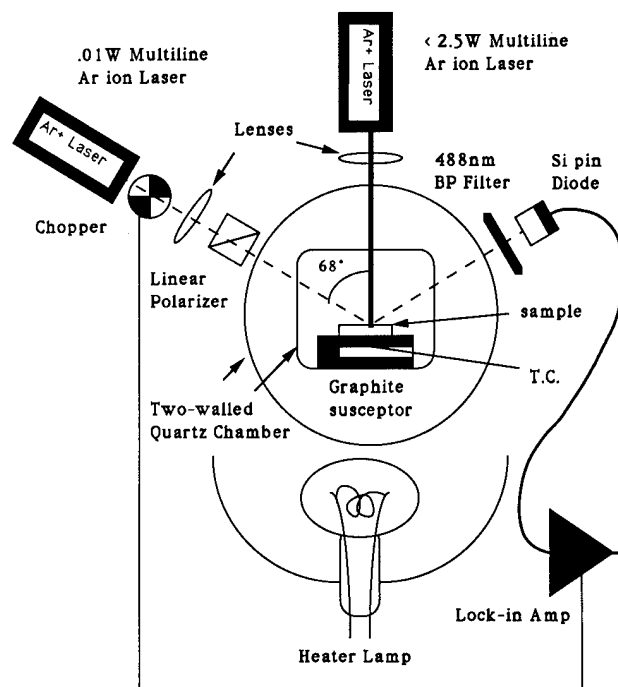


Fig. 1. Schematic diagram of the SPA instrument mounted on the quartz-walled reactor chamber used here.

remove impurities and surface oxide before being individually placed on a graphite susceptor in a two-walled quartz reactor chamber. After evacuating the chamber, each sample was then heated to 700 °C in 10 Torr of 5% AsH<sub>3</sub> in H<sub>2</sub> for 15 min to remove any remaining oxide.

The chamber base pressure was  $1 \times 10^{-7}$  Torr and is schematically shown in Fig. 1 along with the SPA apparatus. During processing, the sample was kept under a constant H<sub>2</sub> flow of 2400 sccm, making the operating pressure 10 Torr. During each respective gas pulse step, either  $1 \times 10^{-7}$  mol s<sup>-1</sup> TMG flux (0.0017 Torr partial pressure) or  $6 \times 10^{-7}$  mol s<sup>-1</sup> TEG flux (0.0009 Torr), and  $5 \times 10^{-5}$  mol s<sup>-1</sup> arsine flux (0.35 Torr) were fed to the sample. The laser power from an Ar<sup>+</sup> laser directed normal to the surface was kept constant at 120 W cm<sup>-2</sup>. This radiation produced a temperature rise that has been calculated to be less than 40 °C [7].

The SPA apparatus was a 10 mW, 488 nm line from another Ar<sup>+</sup> laser, and is shown in Fig. 1. The light source was polarized parallel to the plane of incidence of the sample and incident in the [110] direction of the sample at 68° from the normal. It was also focused to a point within the irradiation area of the process laser, so the effects of the laser process could be monitored. The light source was modulated at 330 Hz using a chopper and the output from the Si pin diode 1 cm in diameter was fed through a lock-in amplifier to increase the signal-to-noise ratio. The amplified signal was recorded on a chart recorder. Because the same type of

laser was used for both the process beam and the SPA monitoring beam, scattered light during process laser irradiation had to be subtracted from the SPA signals manually.

### 3. Results and discussion

#### 3.1. Trimethylgallium

Figure 2 shows a schematic comparison of typical SPA signals taken from GaAs at  $T_s = 360^\circ\text{C}$  during exposure to an ALE-type growth sequence with and without laser irradiation (real data are shown in Fig. 3 for comparison). The possible identities of the surface species present are also shown and are discussed below. For the purely thermal case (upper curve), a decrease in the signal to a steady state is detected when TMG is directed to the As-terminated surface. This surface is stable, even when the TMG flow is halted, and only recovers after exposure to arsine for over 200 s. The growth rate studies at this temperature showed growth to be of the order of 0.1 monolayers per cycle, indicating that much less than one monolayer of Ga is present in this state [3]. While unambiguous identification of this surface is impossible with a single wavelength technique, a theoretical calculation for a GaAs surface

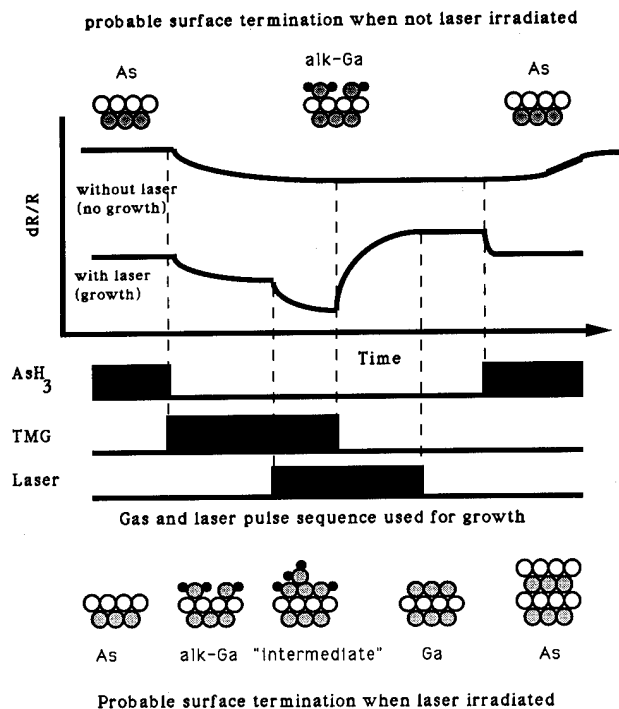


Fig. 2. Schematic diagram of typical SPA signals detected from GaAs through the gas sequencing steps of ALE with (lower) and without (upper) laser exposure. Substrate temperature is  $360^\circ\text{C}$ . Probable surface species are shown for each stable state reached during the sequence.

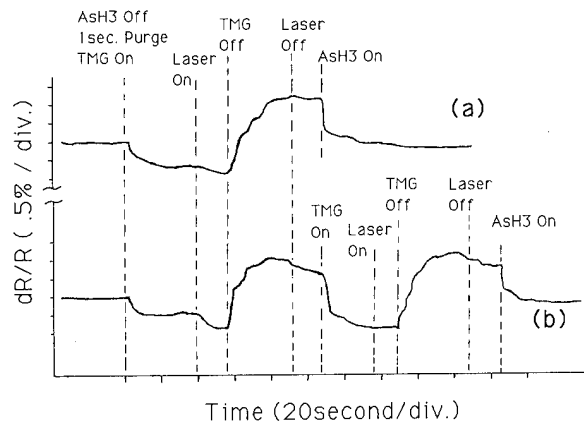


Fig. 3. Comparison of typical SPA signals detected during single and two-consecutive TMG gas pulse sequences to GaAs at  $360^\circ\text{C}$ : (a) surface exposed to only one pulse of TMG; (b) GaAs exposed to two consecutive TMG pulses.

covered with alkyl species showed that the SPA signal should decrease and that the surface is most likely covered with alkylgallium [22]. Mass spectrometric studies have also shown that the surface at this temperature is either monomethylgallium [14] or diethylgallium [12, 13], supporting this conclusion.

If the substrate is exposed to the laser during TMG exposure (lower curve in Fig. 2), the SPA signal decreases further to a different steady state than the alkylgallium state seen in the purely thermal case. This 'intermediate' step is only stable under continued TMG flux, as can be seen in its transformation to a high reflectivity state when the TMG flow is turned off. This high reflectivity state has been examined using reflection high energy electron diffraction during migration-enhanced epitaxy and shown to be indicative of a Ga layer on the surface [21]. When the arsine is introduced, the SPA signal quickly returns to the original signal detected under As-terminated conditions, indicating that the Ga surface has reacted with the arsine. A growth rate study of LALE for these conditions also yielded monolayer per cycle growth, indicating that these conditions provide self-limiting Ga deposition [1, 7].

Because the 'intermediate' step is only stable under both TMG and laser exposure, its exact identification is difficult. Therefore, to gain more understanding of what this 'intermediate' might be, and to investigate self-limiting Ga deposition, an experiment with two consecutive TMG pulses was performed and is compared with a one-pulse experiment in Fig. 3. These typical examples of real data traces show that reflectivity changes of 0.5%–2% are detected as the surface reaches different steady states during exposure to TMG and the laser. The steady states take about 10–30 s to be reached, depending on the process step.



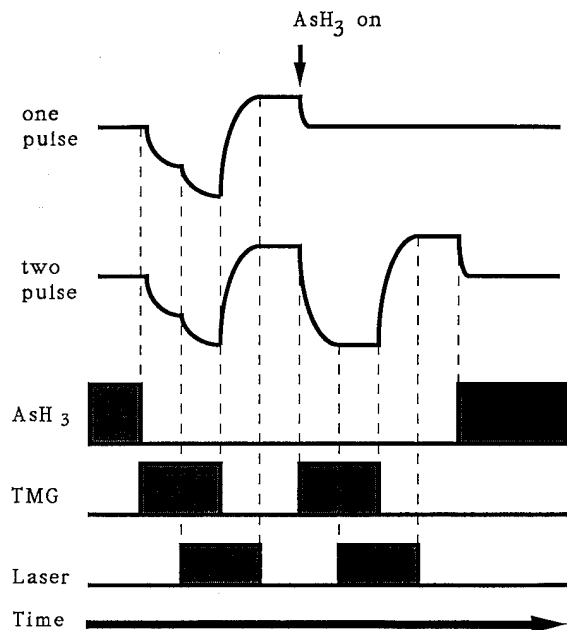


Fig. 4. Schematic diagram of the data presented in Fig. 3. Comparison of typical SPA signals detected during single and two-consecutive TMG gas pulse sequences to As-terminated GaAs at 360 °C.

A simplified view of these data is shown exaggeratedly in the schematic diagram of Fig. 4. The SPA curve plotted for the one-pulse experiment directly corresponds to the lower curve shown in Fig. 2 and has been explained previously. The lower curve shows the signal obtained during TMG exposure of the Ga surface and shows three interesting results. First, the 'intermediate' step is re-established, even though laser exposure is not present, indicating that further TMG exposure destroys the Ga surface. Then, turning the laser on causes no change in the 'intermediate' level. This indicates that the extra energy provided by the laser is needed to break alkylgallium bonds when no Ga metal is present. Once Ga metal is produced, the interaction between the surface and gas phases is able to re-establish the 'intermediate' level without extra energy. The third result is that the same Ga level is recovered once the TMG flow is stopped, showing that Ga deposition is indeed self-limiting. Further switching on and off of the TMG and laser pulses in the sequence shown always led to alternation between the 'intermediate' step and the Ga surface, showing that it is a reversible process. Therefore, self-limiting Ga deposition is obtained through an equilibrium between the alkylgallium species on the substrate surface and those in the gas phase, analogous to the 'flux balance' mechanism [11]. When TMG is present, alkylation of the Ga surface occurs reversibly and, when all the alkylgallium species are removed from the gas phase, those remaining on the surface desorb. This same behavior was detected on samples ranging in temperature from 340 to 390 °C, with the

only difference being the rate at which the steady states were established. At temperatures lower than 340 °C, evolution of the Ga surface did not occur, while continuous deposition of Ga was observed for temperatures above 410 °C.

Although self-limiting Ga deposition has been observed, identification of the 'intermediate' surface still could not be made. Two simple models of the 'intermediate' can be easily constructed to explain the observed results but are not discernible using SPA. One model involves exchange reactions directly between the existing Ga metal surface and the gas phase species. This could involve both alkylation of the Ga surface and then the possibility of alkylgallium exchange between the surface and gas phase species. When the TMG supply is stopped, desorption of the remaining methyl groups on the surface would restore the Ga surface. The other explanation involves the adsorption of an alkylgallium layer on top of the existing Ga layer. The same reactions as stated above could still occur but with no effect on the Ga metal layer underneath. Once the TMG flow is stopped, the remaining alkylgallium on the surface would then desorb to restore the Ga surface.

### 3.2. Triethylgallium

While self-limiting Ga deposition was observed using TMG, no self-limiting deposition was detected using TEG. This is shown in the SPA traces of Fig. 5, where As-terminated surfaces at temperatures from 300 to 420 °C were exposed to TEG with and without simultaneous laser irradiation. For surfaces hotter than 400 °C, and for surfaces hotter than 300 °C and exposed to

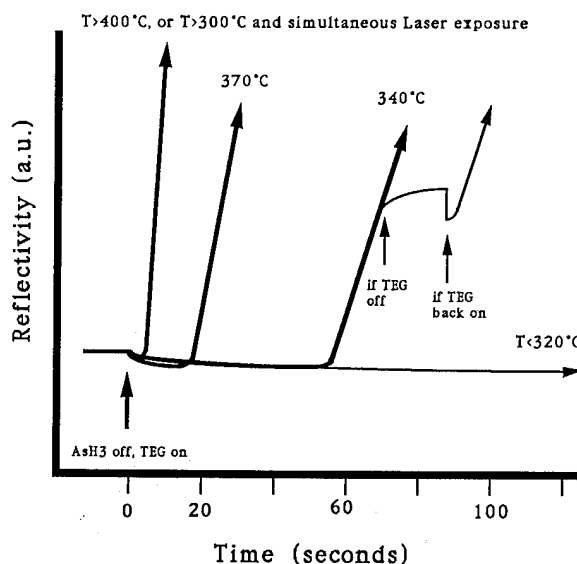


Fig. 5. SPA signals obtained from As-terminated GaAs during exposure to TEG. Substrate temperatures range from 300 to 400 °C.

laser irradiation, Ga deposition from TEG decomposition started after only a few seconds and continued to occur until the TEG supply was stopped. For temperatures from 320 to 400 °C, an initial signal decrease owing to alkylgallium deposition was apparent before Ga deposition commenced. The time lag before Ga deposition started in this temperature region increased with decreasing temperature down to 300 °C, where Ga deposition was never observed thermally. This seems to indicate that the adsorbed alkylgallium species go through a series of surface reactions on the way to leaving Ga metal on the surface. Lastly, as shown for the 340 °C case, it was observed that the surface reached a steady state 10–15 s after the TEG supply was stopped. If TEG is then reintroduced at this point, Ga deposition would be reinitiated after only a few seconds of alkylgallium deposition. This result shows a catalytic effect of TEG decomposition owing to the presence of Ga metal on the surface, thereby making self-limiting Ga deposition impossible while the TEG supply remains on. Therefore, any ALE growth using TEG must involve self-limiting deposition of some alkylgallium species on the surface, which then undergo a subsequent surface reaction to leave Ga.

Figure 6 shows three SPA traces from an As-terminated GaAs sample held at 340 °C and exposed to TEG for different durations before being exposed to arsine. In the top trace, a decrease in the signal is apparent

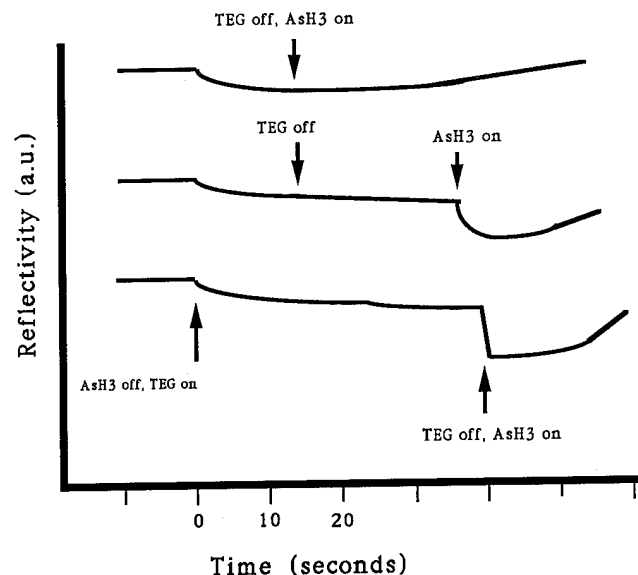


Fig. 6. Schematic diagram of SPA signals obtained from As-terminated GaAs at 340 °C during exposure to TEG for various time durations. Upper curve is from a TEG pulse of 15 s immediately followed by arsine introduction. Middle curve is from a TEG pulse of 15 s followed by a delay of 20 s before arsine introduction. Lower curve is from a TEG pulse of 40 s immediately followed by arsine exposure.

during exposure for 12 s to TEG, as some alkylgallium species cover the surface. When  $\text{AsH}_3$  is turned on 1 s after stopping the TEG flow, no immediate change in the SPA signal is apparent and the surface slowly recovers to an As-terminated surface over 2 min. This seems to indicate that either no surface reaction has occurred between the  $\text{AsH}_3$  and the surface, or that any reaction that has occurred could not be detected by SPA.

In the middle trace, the TEG is again turned on for 12 s but the subsequent arsine dose is delayed for 15 s. In this case, a sudden drop and then a recovery in the reflectivity is observed once the  $\text{AsH}_3$  is turned on, indicating that some drastic change in the surface condition has occurred. This same type of SPA trace could be obtained for TEG pulses ranging in duration from 1 to 24 s at this temperature, provided that the arsine flow was started 25 s after the TEG flow had been initiated. This indicates that whatever alkylgallium initially adsorbs on the surface, it undergoes a further decomposition reaction that takes 24 s to occur on the GaAs surface at 340 °C. This necessary reaction time was shorter at higher temperatures and longer at lower temperatures.

In the final trace, TEG was supplied to the surface for over 24 s. In this case, an extremely sharp decrease in the reflectivity was observed when the arsine was turned on and was independent of any delay in the arsine sourcing. This sharp drop looks similar to the signal obtained from the reaction of arsine with the Ga surface seen in the TMG results, and possibly indicates the formation of Ga–As bonds. Because the reflectivity does not recover to the original As-terminated surface level, many alkyl species still must be present on the surface. Similar traces were obtained when using longer TEG exposures, up to the Ga deposition limit, stressing that any self-limiting deposition must involve an alkylgallium species.

In summarizing these results, it is apparent that TEG undergoes a step-by-step decomposition to Ga on the As-terminated GaAs surface within the temperature range 300–400 °C. Unfortunately, single-wavelength SPA cannot identify the surface species present in this decomposition pathway or the number of monolayers present, but three different surfaces were detected with one obviously being a Ga surface. Since Ga was shown to decompose TEG catalytically, Ga metal is probably absent from the surface until the reflectivity signal is seen rising. TEG has also been shown to decompose dissociatively on the surface [23]. This leaves diethylgallium (DEG) as the initially present alkylgallium species, with DEG decomposing to monoethylgallium (MEG) after sufficient time passes. Then, once the MEG starts to decompose to Ga, all the alkyl species reaching the surface decompose to Ga.

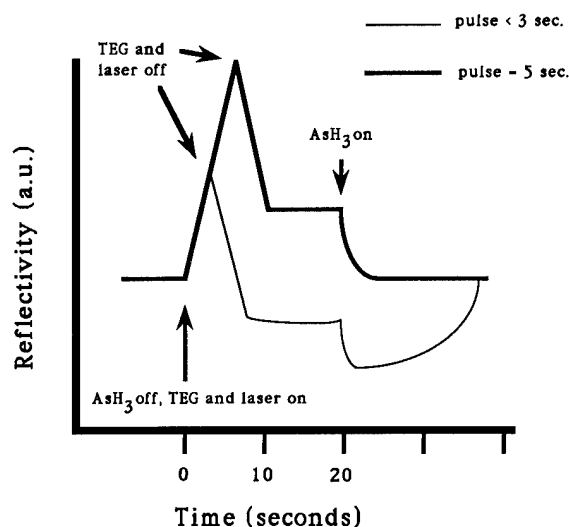


Fig. 7. Schematic diagram of SPA signals obtained from GaAs during LALE processing at 340 °C.

A recent report showed the ALE growth behavior from thermal decomposition of TEG and arsine at a substrate temperature of 320 °C [24] and can be explained by the above results. This growth was accomplished using TEG exposure times of 20–30 s followed by purges of 20–30 s before arsine introduction. From the above observations, this growth is accomplished by dosing the surface with TEG and then waiting for all the adsorbed species to decompose to MEG before supplying the arsine pulse.

LALE growth using TEG also can be explained by self-limiting alkylgallium on the surface. Figure 7 shows a comparison of simultaneous TEG and laser pulses directed at an As-terminated surface for two different durations. Successful LALE growth has been reported for pulse durations of 1 s under these process conditions [1, 7]. It can be seen that an alkylgallium surface is detected after simultaneous TEG and laser pulse exposure of less than 3 s, and that this surface quickly reacts with arsine. Here, Ga metal formation scarcely occurs within a short TEG exposure, since the saturation level after the initial spike of the SPA signal is lower than the Ga metal level and similar to the alkylgallium level. For simultaneous TEG and laser pulses of 5 s, a Ga surface is detected. Successively greater exposure times yielded greater amounts of Ga being detected on the surface, similar to the thermal TEG case.  $\text{Ar}^+$  laser irradiation is considered to enhance the decomposition pathway from TEG to alkylgallium adsorbates. This model can explain the self-limiting LALE growth using TEG; however, surface processes involved in LALE growth using TEG are not completely clear at the present stage and further work should be done.

#### 4. Conclusions

The SPA reflectivity technique was shown as an effective method of monitoring GaAs surface changes during both thermal ALE and LALE processing conditions. Using this technique, self-limiting decomposition during LALE was discussed.

SPA traces showed the existence of three distinct surfaces during various stages of laser-assisted TMG decomposition on As-terminated GaAs surfaces at temperatures from 340 to 390 °C. Initially, TMG dissociatively adsorbs on the surface. Then, under laser exposure, the surface proceeds to a different alkylgallium surface that is in equilibrium with the gas-phase alkylgallium species. Upon stopping the TMG flow at this point, the alkylgallium species remaining on the surface desorb leaving a self-limited deposit of Ga on the surface. This process is analogous to the 'flux-balance' mechanism that has been proposed earlier [11].

When using TEG for either LALE or thermal ALE, no self-limiting Ga deposition was detected, but self-limiting deposition of alkylgallium on the surface was observed. This alkylgallium surface could react with arsine and was shown to be present before arsine introduction under actual LALE growth conditions. Therefore, it is proposed that the self-limiting deposition of alkylgallium on the surface during LALE using TEG is responsible for the successful ALE growth.

#### Acknowledgment

This work was supported in part by a Grant-in-Aid for Scientific Research from the Ministry of Education, Science and Culture.

#### References

- 1 S. Iwai, T. Meguro, A. Doi, Y. Aoyagi and S. Namba, *Thin Solid Films*, 163 (1988) 405.
- 2 Q. Chen, J. S. Osinski, C. A. Beyler, M. Cao and P. D. Dapkus, *Mater. Res. Soc. Symp. Proc.*, 222 (1991) 109.
- 3 J. Nishizawa, T. Kurabayashi, H. Abe and A. Nozoe, *Surf. Sci.*, 185 (1987) 249.
- 4 M. A. Tischler and S. M. Bedair, *Appl. Phys. Lett.*, 48 (1986) 1681.
- 5 M. Ozeki, K. Mochizuki, N. Ohtsuka, and K. Kodama, *Appl. Phys. Lett.*, 53 (1988) 1509.
- 6 S. P. DenBaars, P. D. Dapkus, C. A. Beyler, A. Hariz and K. M. Dzurko, *J. Cryst. Growth*, 93 (1988) 195.
- 7 Y. Aoyagi, A. Doi, S. Iwai and S. Namba, *J. Vac. Sci. Technol. B*, 5 (1987) 1460.
- 8 H. Ohno, S. Ohtsuka, H. Ishii, Y. Matsubara and H. Hasegawa, *Appl. Phys. Lett.*, 54 (1989) 2000.
- 9 J. R. Creighton and B. Banse, *Mater. Res. Soc. Symp. Proc.*, 222 (1991) 15.
- 10 J. R. Creighton, *Surf. Sci.*, 234 (1990) 287.
- 11 M. Yu, N. Buchan, R. Souda and T. F. Keuch, *Mater. Res. Soc. Symp. Proc.*, 222 (1991) 3.

- 12 J. Nishizawa and T. Kurabayashi, *J. Cryst. Growth*, **93** (1988) 98.
- 13 J. A. McCaulley, R. S. Schul and V. M. Donnelly, *J. Vac. Sci. Technol., A* **9** (1991) 2872.
- 14 J. R. Creighton, *J. Vac. Sci. Technol. A*, **9** (1991) 2895.
- 15 U. Memmert and M. Yu, *Appl. Phys. Lett.*, **56** (1990) 1883.
- 16 K. Kodama, M. Ozeki, K. Mochizuki and N. Ohtsuka, *Appl. Phys. Lett.*, **54** (1989) 656.
- 17 I. Kamiya, H. Tanaka, D. E. Aspnes, L. T. Florez, E. Colas, J. P. Harbison and R. Bhat, *Phys. Rev. Lett.*, **68** (1992) 627.
- 18 D. E. Aspnes, E. Colas, A. A. Studna, R. Bhat, M. A. Koza and V. G. Keramidas, *Phys. Rev. Lett.*, **61** (1988) 2782.
- 19 N. Kobayashi and Y. Horikoshi, *Jpn. J. Appl. Phys. Lett.*, **30** (1991) L319.
- 20 A. Doi, S. Iwai, T. Meguro and S. Namba, *Jpn. J. Appl. Phys.*, **27** (1988) 795.
- 21 N. Kobayashi and Y. Horikoshi, *Jpn. J. Appl. Phys. Lett.*, **28** (1989) L1880.
- 22 Y. Horikoshi, M. Kawashima and N. Kobayashi, *J. Cryst. Growth*, **111**, (1991) 200.
- 23 V. M. Donnelly and J. A. McCaulley, *Surf. Sci.*, **238** (1990) 34.
- 24 S. Goto, K. Higuchi, J. Ishizaki, T. Fukui and H. Hasegawa, *39th Spring Meet. of the Japan Society of Applied Physics, 1992*, Extended abstracts, p. 305.

# *In situ* optical characterization of GaAs and InP surfaces during chloride atomic layer epitaxy

Kenichi Nishi, Akira Usui and Hiroyuki Sakaki

Quantum Wave Project, ERATO, Research Development Corporation of Japan (JRDC), 34 Miyukigaoka, Tsukuba, Ibaraki 305 (Japan)

## Abstract

In this paper, the results of *in situ* surface photo-absorption (SPA) measurements on GaAs and InP surfaces under an alternating supply of GaCl and AsH<sub>3</sub> or InCl and tertialybutylphosphine (TBP) in chloride atomic layer epitaxy (ALE) are presented. It was found that the reflection intensity varied by several per cent, depending on the source gas supply sequence. This reflection intensity was constant during the GaCl and InCl supply from both the GaAs and InP surfaces, probably corresponding to the self-limiting mechanism of chloride ALE. Reflection spectra from a GaAs surface during and after GaCl supply were found to be similar. They showed anisotropic spectral structures according to the incidence azimuth of light. This anisotropy is considered to originate from the existence of surface dimers. Thus, a GaAs surface under GaCl supply is assumed to be covered by Ga. In contrast, the spectra from an InP surface during InCl supply were isotropic and different from the anisotropic spectra measured from an In-stabilized surface formed by P desorption. Accordingly, it is assumed the Cl adsorbs on an InP surface during InCl supply and prevents the formation of dimers. The different behavior of Cl on GaAs and InP may be due to a different reaction rate with H<sub>2</sub>.

## 1. Introduction

Atomic layer epitaxy (ALE) is known as an efficient epitaxial growth method, in which the layer thicknesses can be precisely controlled by the number of operational cycles. This technique was first developed for II–VI compound semiconductors [1] and then for III–V semiconductors, such as GaAs [2–4]. There exists an ALE ‘window’, depending on the substrate temperature and source gas supply, that allows one monolayer per cycle growth. ALE using a chloride source gas for group III material is known to have a wide window [5, 6]. It is important to understand the mechanism of chloride ALE to achieve ALE growth for other material systems under a wider range of ALE growth conditions. An understanding of the surface reactions in chloride ALE also will make it possible to control microscopic structure growth, such as one atomic line per cycle at the step edges of a vicinal substrate.

To analyse the surface chemistry in ALE, *in situ* optical measurements are suitable because growth is usually performed in an H<sub>2</sub> ambient, where electron-beam-related characterization methods, such as reflection high energy electron diffraction (RHEED), cannot be used during growth. There already exist sophisticated characterization methods using optical reflection measurements: reflectance difference spectroscopy (RDS) [7–9] and surface photo-absorption (SPA) [10,

11]. RDS measures the difference between the reflectances along two crystallographic axes, which cancel out the bulk contribution. SPA uses p-polarized light incident at the Brewster angle, which minimizes reflection from the substrate. The self-limiting mechanism of Ga deposition in ALE with organometallic sources, such as trimethylgallium (TMGa), has been investigated using both methods [9, 11]. GaAs surfaces under an alternating supply of GaCl and AsH<sub>3</sub> were also studied by SPA spectroscopy [12].

Here we report the *in situ* measurements of optical reflection from (100) GaAs and InP substrate surfaces by SPA under an alternating supply of GaCl and AsH<sub>3</sub> or InCl and tertialybutylphosphine (TBP) during chloride ALE. The reflected light intensity varied by several per cent in the SPA measurements, which was large enough to detect with a high signal-to-noise ratio. This method is also reported to be able to detect bonds perpendicular to the surface [10]. Optical reflection spectra were also measured during each source gas supply with different incidence azimuths ([011] and [0 $\bar{1}$ 1] for (100) substrates). From the change in reflection intensity during and after source gas supply, the stability of the surface adsorption states was estimated. These adsorption states were also discussed relative to the optical reflection spectra. In particular, differences between the reflection spectra during and after the source gas supply were studied.

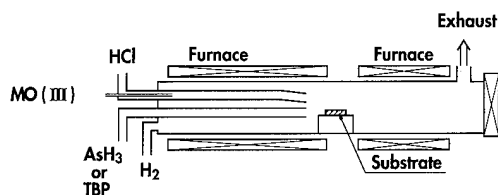


Fig. 1. Schematic drawing of metallorganic chloride ALE growth system.

## 2. Experimental details

The growth system consists of a quartz reactor, two separate furnaces and gas inlet tubes, as shown in Fig. 1. In the experiments on GaAs, the supplied group III source gases were diethylgalliumchloride (DEGaCl) and triethylgallium (TEGa). When DEGaCl was used, the upstream part of the reactor was heated to about 680 °C. At this temperature, DEGaCl is known to decompose thermally into GaCl and hydrocarbons, such as  $C_2H_4$  [13]. Accordingly, the actual group III source gas is believed to be GaCl. During the supply of TEGa, the upstream part was kept at about 150 °C. TEGa was carried to the GaAs surface without decomposition and, on the surface, decomposed to Ga. In the experiments on InP, the supplied source gases for group III were trimethylindium (TMIn) and HCl. These gases were introduced through separate inlet tubes, as shown in Fig. 1. In this case, the actual group III source gas is believed to be InCl, which was formed through the reaction between TMIn and HCl in the upstream part of the reactor heated to about 630 °C. In the reaction, methyl radicals would change into stable hydrocarbons, such as  $CH_4$ . During the experiment, the total  $H_2$  flow was about  $8\text{ l min}^{-1}$  and the reactor pressure was about 760 Torr for the DEGaCl supply. The pressure was 380 Torr when supplying TEGa and during the experiments on InP in order to obtain a high gas velocity to prevent the gas phase decomposition of TEGa. In the experiments on GaAs, the flow rates and the partial pressures of GaCl, TEGa and  $AsH_3$  were 1 sccm ( $9.5 \times 10^{-2}$  Torr), 0.04 sccm ( $1.9 \times 10^{-3}$  Torr) and 4 sccm ( $1.9 - 3.8 \times 10^{-1}$  Torr) respectively. In the experiments on InP, the flow rates and the partial pressures of TMIn, HCl and TBP were 1.5 sccm ( $7.1 \times 10^{-2}$  Torr), 0.8 sccm ( $3.8 \times 10^{-2}$  Torr) and 6 sccm ( $2.9 \times 10^{-1}$  Torr) respectively.

The optical measurement apparatus is shown in Fig. 2. An Xe lamp was used as a light source. When the change in the reflected light intensity was measured, a chopped and monochromatized, p-polarized light of wavelength 488 nm irradiated the substrate at an angle of 75°, which is nearly equal to the Brewster angle. The reflected light was detected by a photomultiplier using a

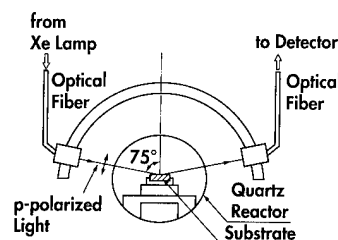


Fig. 2. Schematic drawing of the SPA measurement apparatus.

phase-locking technique. For the spectral measurements, all the light from the lamp was focused on the sample and detected by a combination of a monochromator and a 1024-channel detector array. It should be noted that, in order to cancel out the spectral dependence of the optical system, the reflection spectrum under group V gas supply ( $R_V$ ) was measured first. Then the difference spectrum ( $\Delta R = R - R_V$ ) was normalized by  $R_V$  to obtain the normalized difference spectra  $\Delta R/R_V$ .

GaAs (100) and InP (100) wafers with exact orientation were used as the substrates. Prior to loading, the GaAs and InP substrates were degreased, etched for 1.5 min in 3:1:1 or 3.5:1:1  $H_2SO_4:H_2O_2:H_2O$  solution and rinsed in deionized water. Before starting the experiments, the substrates were kept above 600 °C in an  $H_2$  ambient to remove surface oxide layers.

The substrate temperature was measured by an optical pyrometer that was calibrated using the Al-Si eutectic temperature and the melting point of InSb.

## 3. Results and discussion

### 3.1. Results for GaAs ALE

Figure 3 shows the changes in the reflection intensity from a GaAs surface during an alternating supply of GaCl and  $AsH_3$  at a substrate temperature ( $T_s$ ) of 450 °C with a [011] incidence azimuth. The reflected intensity steeply decreased as the surface was exposed to GaCl and kept constant during the GaCl supply. This intensity remained unchanged for a few minutes,

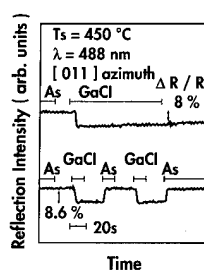


Fig. 3. Changes in reflection intensity from a GaAs surface depending on source gas, using p-polarized light of wavelength 488 nm with a [011] incidence azimuth. Substrate temperature ( $T_s$ ) was 450 °C.

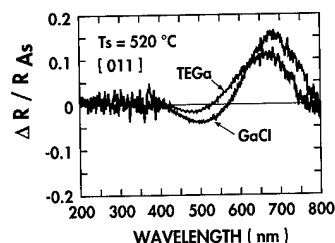


Fig. 4. Normalized difference spectra from GaAs during GaCl supply and after one monolayer of TEGa exposure with [011] incidence azimuth ( $T_s = 520^\circ\text{C}$ ). The difference spectra  $\Delta R$  were normalized by the spectra  $R_{As}$  which was measured during  $\text{AsH}_3$  supply. These spectra show very similar characteristics, which reveals that the surface during GaCl supply was a Ga-stabilized surface.

even after the GaCl supply was stopped. These tendencies were reproducibly observed in other experiments. As shown in the lower part of Fig. 3, the reflection intensity recovered when  $\text{AsH}_3$  was supplied. The intensity difference normalized by the intensity during  $\text{AsH}_3$  supply was approximately 8% in this experimental condition, which was large enough to detect with a high signal-to-noise ratio. The saturation of the reflection intensity change during the GaCl supply is due to the self-limiting mechanism in chloride ALE.

Measurements of the reflection spectra were also conducted. To characterize a GaAs surface under GaCl supply, the reflection spectra from a GaAs surface under GaCl and  $\text{AsH}_3$  supplies were measured at  $520^\circ\text{C}$ . As reference spectra of a Ga-stabilized surface, the normalized difference spectra between TEGa and  $\text{AsH}_3$  at the same temperature were used. In Fig. 4, the reference normalized spectrum  $\Delta R/R_{As}$  and the spectrum corresponding to the surface during GaCl supply measured at  $520^\circ\text{C}$  from a [011] incidence azimuth are shown. The TEGa supply duration was strictly controlled to form one monolayer of Ga. The spectrum measured during the GaCl supply was found to have very similar characteristics to those of the Ga-terminated surface. This was also true for the spectra measured from a [0 $\bar{1}$ 1] incidence azimuth. Accordingly, the GaAs surface under GaCl supply at  $520^\circ\text{C}$  is believed to be identical to a Ga-stabilized surface [12]. Both spectra showed anisotropic spectral structure, from which the existence of surface Ga dimers is suggested.

Figure 5 shows the normalized difference spectra  $\Delta R/R_{As}$  corresponding to the surface during and after GaCl supply at  $520^\circ\text{C}$  from a [011] incidence azimuth. The spectrum during the GaCl supply is marked by 'A' in the figure. The spectra corresponding to the surfaces 5 and 15 min after GaCl supply are marked by 'B' and 'C' respectively. Almost no difference was observed between the A and B spectra. It can be concluded that, at least for 5 min after GaCl supply, the optical properties of the surface remained almost unchanged. In the

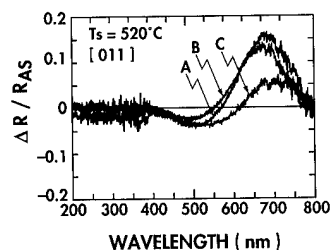


Fig. 5. Normalized difference spectra from GaAs during and after GaCl supply with [011] incidence azimuth ( $T_s = 520^\circ\text{C}$ ). Spectrum marked by 'A' corresponds to the surface during GaCl supply. Spectra marked 'B' and 'C' correspond to the measurements performed 5 and 15 min after GaCl supply respectively.

spectrum marked by 'C', a decrease in the peak intensity around 700 nm was observed. The peak at 1.8 eV is attributed to be due to Ga dimers from RDS measurements at around  $500^\circ\text{C}$  [14]. Also in the SPA measurements, we can expect that the peak positions in the measured spectra are related to the surface dimers. It was considered that some contamination changed the surface reconstruction formed by Ga dimers, which resulted in the intensity decrease of the Ga-dimer-related peak around 700 nm (1.8 eV) in spectrum C.

### 3.2. Results for InP ALE

The characterization of InP surfaces under an alternating supply of InCl and TBP is reported in this section. In Fig. 6, the temperature dependence of the InP growth rate is shown. The data shown by black circles were obtained by Kato *et al.* [15] using a dual-chamber ALE reactor, where InCl was formed by the reaction between In metal and HCl. The data obtained in our experiments are shown by triangles and squares. It was found that growth temperatures less than  $400^\circ\text{C}$  were required to achieve the one monolayer per cycle growth. ALE growth was possible down to about  $300^\circ\text{C}$ , below which the stable supply of InCl became difficult, probably owing to the formation of  $\text{InCl}_3$  in the gas phase.

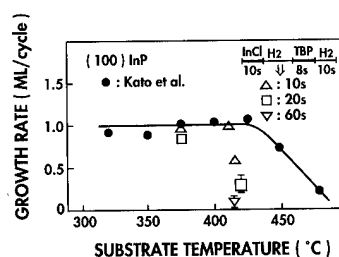


Fig. 6. The substrate temperature dependence of (100) InP growth rate in chloride ALE. Data shown by black circles were obtained by Kato *et al.* [15].

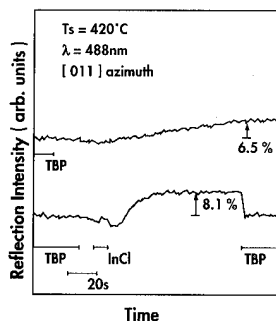


Fig. 7. Changes in reflection intensity from InP surfaces depending on source gas, using p-polarized light of wavelength 488 nm with  $[011]$  incidence azimuth. Substrate temperature ( $T_s$ ) was  $420^\circ\text{C}$ .

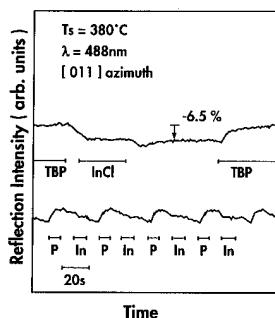


Fig. 8. Changes in reflection intensity from InP surfaces at  $380^\circ\text{C}$ . Other conditions were the same as those of Fig. 7.

The changes in the reflection intensity from an InP surface at a  $[011]$  incidence azimuth are shown in Fig. 7 and Fig. 8 at substrate temperatures of  $420^\circ\text{C}$  and  $380^\circ\text{C}$  respectively, during an alternating supply of InCl and TBP. As can be seen from the upper curve in Fig. 7, the reflection intensity gradually increased after TBP supply. It is estimated that the InP surface became an In-stabilized surface without the TBP supply. The desorption of P is estimated to be of the order of 10 s at this temperature [16] and most probably is the reason for the increasing reflection intensity. In the lower part of Fig. 7, the reflection change after InCl supply is shown. After InCl supply, the reflection intensity first slightly decreased and then increased to a higher value, which was almost the same level as that obtained without the TBP supply. This indicates that the surface also was changed to an In-stabilized surface. When TBP was supplied, the reflection intensity rapidly recovered to the lower level. From Fig. 7, it can be understood that an InP surface under InCl and TBP supply is not stable at around  $420^\circ\text{C}$ .

In contrast, in the upper part of Fig. 8, the reflection intensity after InCl supply was found to be stable compared with the data in Fig. 7. After InCl supply, the intensity first showed a small transient decrease and then increased very slowly. The stable reflection intensity during the InCl supply is considered to be due to

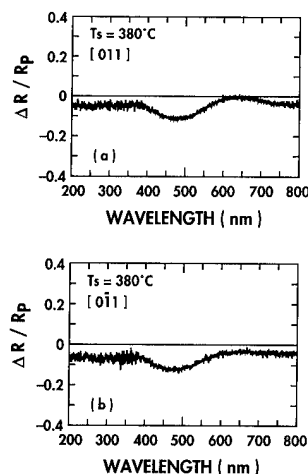


Fig. 9. Normalized difference spectra  $\Delta R/R_p$  from InP during InCl supply with (a)  $[011]$  incidence azimuth and (b)  $[0\bar{1}1]$  incidence azimuth ( $T_s = 380^\circ\text{C}$ ). The spectra obtained are found to be similar, revealing the isotropic surface adsorption state.

the self-limiting mechanism in chloride ALE of InP. Also, it was found that, after the TBP supply was stopped, the reflection intensity increased, as shown in Fig. 7, but very slowly and saturated after about 30 min. This suggested that the InP surface was relatively stable even after stopping the source gas supply. In the lower part of Fig. 8, the reflection intensity oscillation, according to an alternating gas supply, is shown during the ALE growth.

Figure 9 shows the spectra corresponding to the surface during InCl supply. The substrate temperature was  $380^\circ\text{C}$ . The spectra measured under different incidence azimuths ( $[011]$  and  $[0\bar{1}1]$ ) are almost identical. This fact means that an InP surface under InCl supply has isotropic optical properties. This differs from the case of GaAs surface under GaCl supply, where we concluded the existence of Ga dimers from the anisotropic spectra. In the case of InCl supply, In dimers may not be formed on the InP surface during InCl supply.

Figure 10 shows the spectra from the InP surface about 1 min after the InCl supply. Large differences between the two spectra can be observed depending on the incidence azimuth. In Fig. 11, the reference spectra from an In-stabilized InP surface formed by P desorption measured at  $420^\circ\text{C}$  are shown. Although the base-lines are somewhat different, the spectra in Figs. 10 and 11 are found to be similar in anisotropic characteristics and in the peak positions. Thus, the surface after InCl supply probably changes into an In-stabilized surface, while some adsorbates exist on the InP surface during InCl supply.

### 3.3. Discussion of chloride ALE mechanism

In this section, we discuss the surface adsorption state, which closely relates to the self-limiting mecha-



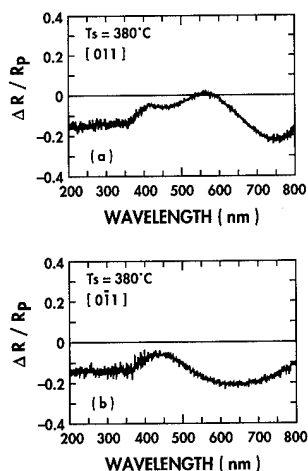


Fig. 10. Normalized difference spectra from InP about 1 min after InCl supply. Large differences in the spectra depending on the incidence azimuth can be observed.

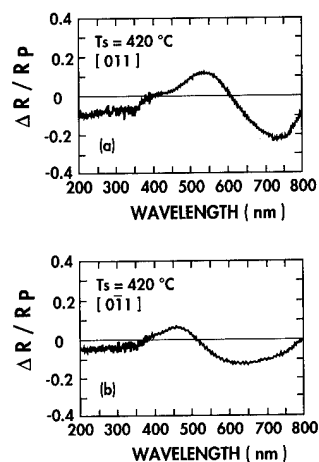


Fig. 11. Reference spectra from an In-stabilized InP surface formed by P desorption at 420 °C. Although the base-lines are somewhat different, these spectra are very similar to the spectra shown in Fig. 10 in anisotropic characteristics and in the peak positions.

nism of chloride ALE. There are some reports about the adsorption state when  $\text{DEGaCl}$  was supplied to an As-stabilized GaAs surface [5, 17]. Mori *et al.* [5] assumed that  $\text{DEGaCl}$  decomposed to GaCl on the substrate surface and that GaCl adsorbed on the As-stabilized surface. In contrast, in the *in situ* X-ray photoelectron spectroscopy (XPS) measurements, no appreciable amount of Cl was detected on the GaAs surface after the  $\text{DEGaCl}$  exposure [17]. This suggested the decomposition reaction of  $\text{DEGaCl}$  to Ga on the As-stabilized surface.

In our experiments, the actual source gas for group III was GaCl made by the thermal decomposition of  $\text{DEGaCl}$  in the upstream part of the reactor. Accordingly, the reaction of GaCl on the surface should explain the self-limiting mechanism. From the results

described in Section 3.1, the GaAs surface is assumed to be covered by one monolayer of Ga under GaCl supply. Furthermore, when the surface is completely covered by one monolayer of Ga, no additional Ga deposition is expected owing to the saturation of the growth rate to one monolayer per cycle. This mechanism is consistent with the calculated surface residence time of GaCl using the surface adsorption energy.

Sasaoka *et al.* [18] reported that the GaCl adsorption energy on As- and Ga-stabilized surfaces were 38 kcal mol<sup>-1</sup> and 32 kcal mol<sup>-1</sup>, respectively, based on temperature-programmed desorption (TPD) measurements. With these values, even on an As-stabilized surface, an extremely short surface residence time of GaCl (less than 10<sup>-2</sup> s at 520 °C) was obtained. This result suggests that GaCl should change to a much more stable species, such as Ga, for ALE growth to occur. Furthermore, the GaCl surface residence time on an As-stabilized surface is calculated to be about 50 times longer than that on a Ga-stabilized surface at 520 °C. This large difference will enhance the selective decomposition of GaCl on the As-terminated surface.

The adsorption state of InP is found to be unstable under InCl supply. From the isotropic properties of the spectra during the InCl supply, the surface is considered to be covered by isotropic adsorbates—probably InCl. Adsorbed Cl will prevent the formation of dimers by terminating the In dangling bonds. This may be due to the stable bond between the In and Cl or due to residual HCl in the ambient. After InCl supply, the surface was found to change gradually to an In-stabilized surface. The different behavior of Cl extraction between GaAs and InP may be due to the different reaction rate with H<sub>2</sub>. By the study of the InCl adsorption energy and the surface reconstruction phase diagram of InP, it may be possible to understand the surface adsorption state of InP and, consequently, the growth mechanism of InP ALE.

#### 4. Summarizing remarks

In summary, *in situ* measurements of optical reflection from GaAs and InP surfaces were performed under an alternating supply of GaCl and AsH<sub>3</sub> or InCl and TBP in chloride ALE. The reflection intensity changed by several per cent as the source gases were switched. During the supply of GaCl or InCl, the reflection level stayed almost constant, which was considered to be due to the self-limiting adsorption of ALE. For GaAs, we considered that the surface was covered by one monolayer of Ga, even under GaCl supply, from the coincidence of the normalized difference spectra of GaCl and Ga supply. This result suggests that the self-limiting mechanism in GaAs ALE originates from the difference

in residence time and/or in the Cl extraction reaction probability of GaCl between As-stabilized and Ga-stabilized surfaces. For InP, the surface is assumed to be covered by InCl during InCl supply. After the InCl supply, the surface was found to change to an In-stabilized surface. This can be explained by the bond stability between In and Cl in an  $H_2$  ambient.

### Acknowledgments

The authors are very grateful to Chiaki Sasaoka, Yoshitake Kato, Jouni Ahopelto, Haruo Sunakawa and A. Atsushi Yamaguchi for their comments and discussion. They are also grateful to Hiroyuki Kano for his encouragement throughout this work.

### References

- 1 T. Suntola and M. J. Antson, *US Patent 4058430* (1977).
- 2 J. Nishizawa, H. Abe and T. Kurabayashi, *J. Electrochem. Soc.*, **132** (1985) 1197.
- 3 A. Usui and H. Sunakawa, *Jpn. J. Appl. Phys.*, **25** (1986) L212.
- 4 A. Usui, H. Sunakawa, F. J. Stützel and K. Ishida, *Appl. Phys. Lett.*, **56** (1990) 289.
- 5 K. Mori, M. Yoshida, A. Usui and H. Terao, *Appl. Phys. Lett.*, **52** (1988) 27.
- 6 Y. Jin, R. Kobayashi, K. Fujii and F. Hasegawa, *Jpn. J. Appl. Phys.*, **29** (1990) L1350.
- 7 D. E. Aspnes, J. P. Harbison, A. A. Studna and L. T. Florez, *Phys. Rev. Lett.*, **59** (1987) 1687.
- 8 E. Colas, D. E. Aspnes, R. Bhat, A. A. Studna, M. A. Koza and V. G. Keramidas, *J. Cryst. Growth*, **94** (1989) 613.
- 9 B. Y. Maa and P. D. Dapkus, *Appl. Phys. Lett.*, **58** (1991) 2261.
- 10 N. Kobayashi and Y. Horikoshi, *Jpn. J. Appl. Phys.*, **28** (1989) L1880.
- 11 N. Kobayashi, T. Makimoto, Y. Yamauchi and Y. Horikoshi, *J. Cryst. Growth*, **107** (1991) 62.
- 12 K. Nishi, A. Usui and H. Sakaki, *Appl. Phys. Lett.*, **61** (1992) 31.
- 13 C. Sasaoka, M. Yoshida and A. Usui, *Jpn. J. Appl. Phys.*, **27** (1988) L490.
- 14 I. Kamiya, D. E. Aspnes, H. Tanaka, L. T. Florez, J. P. Harbison and R. Bhat, *Phys. Rev. Lett.*, **68** (1992) 627.
- 15 Y. Kato, H. Shimawaki and A. Usui, *49th Autumn Meet. of the Japan Society of Applied Physics, 1988*, Extended abstracts, p. 200 (in Japanese).
- 16 N. Kobayashi and Y. Kobayashi, *Jpn. J. Appl. Phys.*, **30** (1991) L1699.
- 17 H. Ohno, H. Ishii, K. Matsuzaki and H. Hasegawa, *Appl. Phys. Lett.*, **54** (1989) 1124.
- 18 C. Sasaoka, Y. Kato and A. Usui, *Jpn. J. Appl. Phys.*, **30** (1991) L1756.

# Study of self-limiting growth mechanism in chloride ALE

A. Usui

Fundamental Research Laboratories, NEC Corporation, 34 Miyukigaoka, Tsukuba, Ibaraki 305 (Japan)

## Abstract

The growth process of chloride atomic layer epitaxy (ALE) using GaCl is studied using the temperature programmed desorption method (TPD), the surface photo-absorption (SPA) method and *ab initio* molecular orbital calculations. From the TPD measurements, the GaCl adsorption energy is calculated to be 32 kcal mol<sup>-1</sup> and 38 kcal mol<sup>-1</sup> for Ga-terminated and As-terminated surfaces respectively. In the absence of H<sub>2</sub>, the Ga–Cl bond appears to be very stable in the adsorption state. Process simulation using a simple cluster model of (AsH<sub>2</sub>)<sub>2</sub>–GaCl indicates that adsorption is completed by forming  $\sigma$  and  $\pi$  covalent bonds, and that there is hardly any self-dissociation of the Ga–Cl bond. From SPA measurements in the ALE system with ambient H<sub>2</sub>, a strong similarity is found between the spectra of the GaCl-supplying surface and the Ga-covered surface. Based on these results, a model of the chemical process in chloride ALE is proposed where adsorbed GaCl molecules can react immediately with hydrogen and Cl is released from the surface as HCl. A self-limiting mechanism results from the very short residence time of GaCl ( $\sim 10^{-3}$  s at 450 °C) on the Ga-terminated surface.

## 1. Introduction

Atomic layer epitaxy (ALE) [1] is a crystal growth process which effectively utilizes gas–solid chemical interaction to form crystals a monolayer at a time. This process is significantly different from molecular beam epitaxy (MBE), which is a physical process because the surface migration of adsorbed molecules dominates the growth process. By using gas–solid chemical interaction, self-limiting monolayer growth has been reported for various kinds of materials such as semiconductors and dielectric films [2, 3]. Recently, ALE has attracted significant attention from III–V researchers due to its great potential to fabricate nanometer scale quantum effect structures, which are expected to realize high-speed devices and highly efficient optical devices. The first report on the ALE of III–V compound semiconductors was published by Nishizawa *et al.* [4], who called this method molecular layer epitaxy (MLE). They demonstrated the self-limiting characteristics of monolayer/cycle growth using metal-organic (MO) sources of Group III elements and hydrides of Group V elements, such as trimethylgallium (TMGa) and triethylgallium (TEGa), and arsine (AsH<sub>3</sub>) in an MOMBE type vacuum chamber. We have developed an ALE system using chloride source gases of Group III elements, such as GaCl and InCl for III–V compound materials.

Chloride gases have strong thermal stability, which is a useful property for obtaining a wide ALE deposition temperature range. However, it was necessary to design a growth apparatus in which GaCl is generated inside

the reactor, because GaCl exists preferably at high temperature and cannot be transported by the carrier gas from outside of the reactor. The first chloride ALE of GaAs was carried out using a dual chamber reactor with a substrate transfer mechanism for hydride vapor phase epitaxy (VPE) [5]. GaCl was formed by the reaction between Ga metal and HCl gas upstream of the reactor. Mori *et al.* [6] developed a diethylgallium chloride (DEGaCl) ALE system using a horizontal MOVPE reactor, where GaCl was generated by the thermal cracking of DEGaCl at approximately 400–500 °C. This method was very convenient because the treatment of DEGaCl is as easy as TMGa or TEGa. However, carbon contamination of the grown layers was observed. Recently, a new reactor system was developed by the authors where TEGa and HCl gas was used. These gases were mixed in the low temperature region ( $\sim 200$  °C) of the reactor and generated GaCl in the high temperature region ( $\sim 700$  °C). This method is considered to enhance the thermal cracking of TEGa by the hot wall reactor, as compared with the MOVPE reactor. It is expected, hence, to reduce carbon contamination by suppressing the generation of hydrocarbon radicals at the substrate surface region. Using this type of chloride ALE apparatus, the growth rate saturation at one monolayer/cycle was obtained over a wide temperature range of 400–600 °C for GaAs and 320–425 °C for InP [7].

Recently, the ALE mechanism has been discussed by many researchers. Two different chemical processes for the formation of a Ga-related monolayer in metal–organic ALE (MOALE) using TMGa or TEGa, and

AsH<sub>3</sub>, have been reported so far. One model is a molecular layer adsorption model, proposed by Nishizawa *et al.* [8]. By examining the thermal desorption spectrum from a TMGa-exposed As surface using quadruple mass spectroscopy (QMS), they concluded that the adsorbate is a monomethylgallium (MMGa) in the growth rate saturation range. Due to the short residence time of Ga-containing species on the first adsorption layer, further adsorption was considered to be prevented. The other model is based on a site-selective reaction, which was proposed by Doi *et al.* [9]. They examined ALE growth procedure using a low-pressure MOVPE type system with Ar-laser irradiation. According to the model, TMGa or TEGa molecules preferentially decompose on As sites leading to a Ga-covered surface by the assistance of the laser irradiation. The self-limiting mechanism was considered to be caused by the short residence time of Ga-containing species on Ga sites.

In chloride ALE, Ohno *et al.* [10] discussed the surface reaction of DEGaCl ALE which was carried out in an MOMBE chamber. They reported that one monolayer of Ga atoms was formed on the DEGaCl-supplied surface because no appreciable amount of Cl was detected by *in situ* XPS measurements. Sasaoka *et al.* [11], who examined the surface reaction of DEGaCl on Si surfaces by XPS, also confirmed that Cl did not exist on the surface. They suggested that atomic hydrogen generated during the composition of DEGaCl on the surface would extract Cl and desorb as HCl. However, this model can be applied only to DEGaCl ALE in the MOMBE system, where undecomposed DEGaCl is supplied to the substrate surface. Koukitu *et al.* [12] recently reported *in situ* optical reflection measurements surface photo-absorption (SPA) method [13] under GaCl and AsH<sub>3</sub> with H<sub>2</sub> carrier gas. However, they did not give enough results, such as spectral characteristics or measurements under various growth temperatures, to discuss the growth mechanism in chloride ALE.

In this paper, we report on the study of the GaCl adsorption/desorption process on GaAs substrate using the temperature programmed desorption (TPD) method [14] and SPA measurements [15]. This paper also describes the theoretical analysis of the GaCl adsorption process onto an As dangling bond site by *ab initio* molecular orbital calculation [16]. Based on these results, the growth mechanism of chloride ALE is discussed.

## 2. Experimental details

To investigate the adsorption/desorption process of GaCl on GaAs substrate, the TPD method was used by Sasaoka *et al.* [14]. Experiments were conducted in a vacuum chamber. A new type GaCl gas cell was devel-

oped to produce a pure GaCl molecular beam from Ga metal and Cl<sub>2</sub> gas. At a cell temperature of 800 °C, the beam contained only GaCl molecules as detected by QMS. No other species such as GaCl<sub>2</sub>, GaCl<sub>3</sub> and unreacted free Cl<sub>2</sub> were observed. The substrate was exposed to the GaCl beam of 4 Langmuir at about 100 °C. After that, the substrate temperature was raised at a constant rate of 0.8 °C s<sup>-1</sup>. Desorbing species were detected by using QMS. In addition, RHEED (reflection high energy electron diffraction) observation was made simultaneously with TPD experiments. From the peak temperature of TPD spectrum, the adsorption energy of the adsorbed species was calculated.

We also carried out an *in situ* optical reflection measurement using the SPA method in an actual chloride ALE reactor [15]. To analyze the surface chemistry under such a gas atmosphere, the optical reflection method is a powerful tool. The growth was carried out by using DEGaCl and AsH<sub>3</sub> under the H<sub>2</sub> carrier gas in a hot wall reactor. The upstream of the reactor was heated to about 680 °C. Therefore, DEGaCl is considered to completely decompose to GaCl and hydrocarbons [17]. The reactor pressure was 760 Torr. The flow rates of DEGaCl, AsH<sub>3</sub> and total H<sub>2</sub> carrier gas were 1, 4 and 8,000 cm<sup>3</sup> min<sup>-1</sup> respectively. In the present experiments, p-polarized light from an Xe lamp was irradiated onto the substrate at an angle of 75°, which is close to the Brewster angle. This paper reports, in particular, on the SPA spectral comparison between GaCl-supplied surface and Ga-covered surface to determine the surface state during GaCl supply.

*Ab initio* molecular orbital calculation is nowadays acceptable as a useful tool to determine surface chemical reactions because of their reliable energetics and the detailed information about the electronic structures. This method has already been used in crystal growth simulation by Ohshita *et al.* for the analysis of SiCl<sub>2</sub> adsorption [18] and Cl extraction on Si crystal [9]. In the present system, CASSCF (complete active space self-consistent field) calculations were carried out to obtain the potential energy curve of GaCl adsorption onto a hollow As dangling bond site. A cluster used here was (AsH<sub>2</sub>)<sub>2</sub>-GaCl. This model is the simplest one, but is useful to illustrate the orbital interactions in the GaCl adsorption process on the As site.

## 3. Results and discussion

In the TPD measurement, the 2 × 4 As-stabilized and 4 × 6 Ga-stabilized surfaces of GaAs (100) substrate were exposed to a GaCl molecular beam of 4 Langmuir at about 100 °C and heated at a constant rate of 0.8 °C s<sup>-1</sup>. Figure 1 shows the typical TPD spectra obtained by the desorption. The only desorbed species

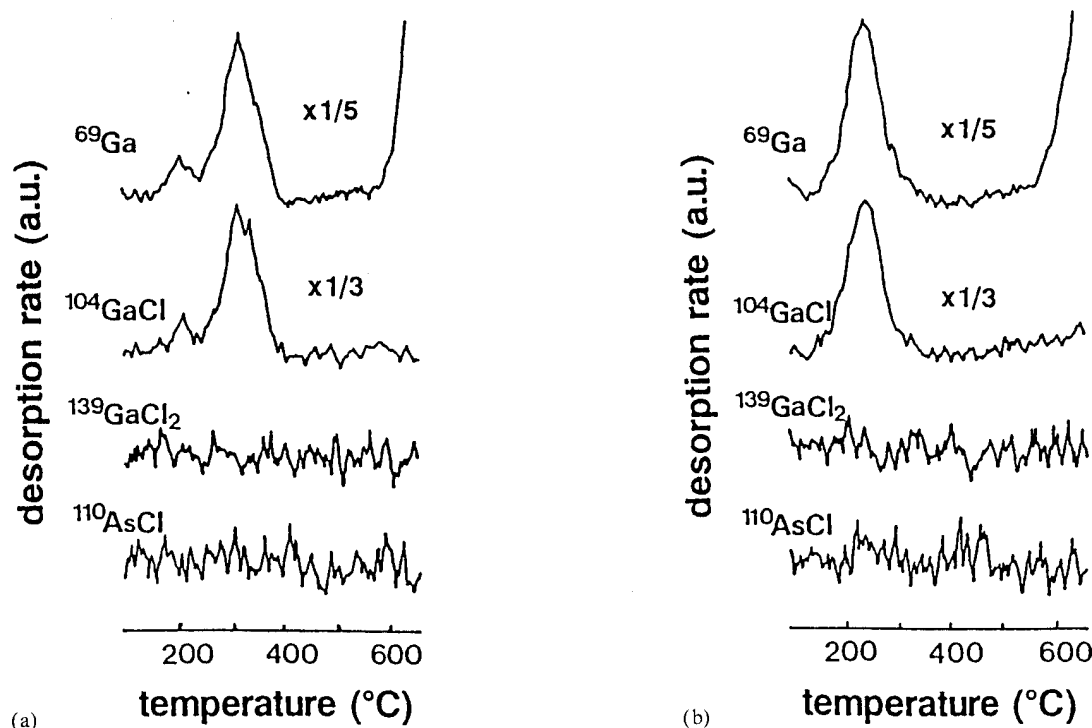


Fig. 1. TPD spectra of GaCl adsorbed on GaAs (100) after 4 Langmuir GaCl exposure (a) for  $2 \times 4$  As-stabilized surface; (b) for  $4 \times 6$  Ga-stabilized surface [14].

detected by QMS was  $^{104}\text{GaCl}^+$ . The  $^{69}\text{Ga}^+$  signal was found to be a fragment of GaCl due to ionization in QMS. Other species, such as  $^{104}\text{GaCl}_2^+$  and  $^{110}\text{AsCl}^+$ , were not detected. The peak temperature  $T_p$  of desorption from the  $2 \times 4$  As-stabilized surface appeared at  $330^\circ\text{C}$ . By further increasing the substrate temperature, the surface reconstruction changed from  $1 \times 4$  to  $2 \times 4$ . This indicates that the surface recovered to an As-stabilized one. When desorption from the  $4 \times 6$  Ga-stabilized surface was investigated,  $T_p$  appeared at  $220^\circ\text{C}$ , which was about  $110^\circ\text{C}$  lower than that from the As-stabilized surface. This indicates that the GaCl adsorption on a Ga-stabilized surface is weaker than that on an As-stabilized surface. After GaCl desorption, the surface recovered to a  $4 \times 6$  Ga-stabilized surface. Because  $T_p$  was found to be independent of the surface coverage, the desorption rate can be described by a first order reaction. Using the equation  $r = \nu \theta \exp(-E_{\text{ad}}/RT)$  ( $r$  = adsorption rate,  $\nu$  = vibration frequency  $= 2.19 \times 10^{13} \text{ s}^{-1}$ ,  $E_{\text{ad}}$  = adsorption energy), the adsorption energy of GaCl  $E_{\text{ad}}$  was calculated to be  $38 \text{ kcal mol}^{-1}$  and  $32 \text{ kcal mol}^{-1}$  for the  $2 \times 4$  As-stabilized and for  $4 \times 6$  Ga-stabilized surfaces respectively.

By the *ab initio* molecular orbital method, the GaCl adsorption process was theoretically analyzed. The cluster used here is shown in Fig. 2. The computational procedure is based on the correlated wavefunctions which ensure a proper description of the system with

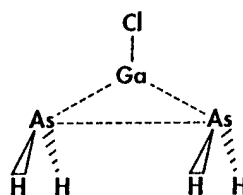


Fig. 2. Structure of the  $(\text{AsH}_2)_2\text{-GaCl}$  cluster model used for computer simulation of the adsorption process [16].

reasonable energetics. The potential energy curve was calculated against the Ga-As bond length. In Fig. 3, the adsorbed bonding state between GaCl and As is shown, which gives the lowest potential energy. Although GaCl usually had a lone pair on Ga in the ground state  $X^1\Sigma^+$ , the valence excited state  $a^3\Pi$  which resulted from the  $4s \rightarrow 4p\pi$  intra-Ga transition was preferable for the adsorption. Mixing of the GaCl excited state with the valence excited state of the As dangling bond  $^3B_1(\sigma^1\pi^1)$  occurred in the  $\sigma$ -orbital and  $\pi$ -orbital. As a result, singlet spin couplings in both orbitals were formed and led to the  $^1A_1$  ground state. Overlap charges between Ga and Cl atoms for free ground state GaCl and adsorbed GaCl were 0.51 and 0.70 respectively. It should be noticed that the overlap charge increased with adsorption on the As-surface. This indicates that self-dissociation of Cl hardly occurs. The GaCl adsorption energy was estimated to be

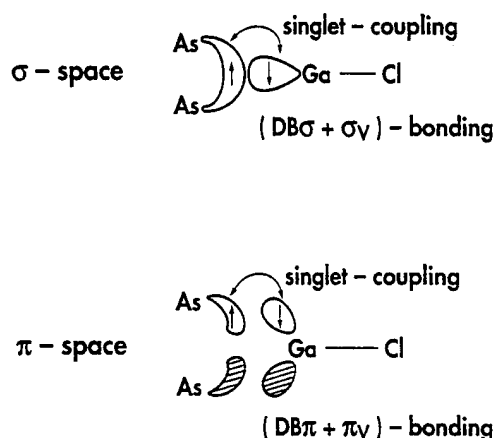


Fig. 3. Adsorbed bonding state of  $\sigma$ -space and  $\pi$ -space between GaCl and the As dangling bond [16].

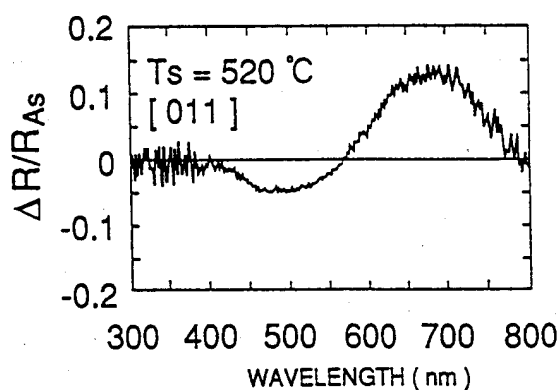
60 kcal mol<sup>-1</sup> including dynamic correlation and reconstruction energy [16]. When this value is compared with 38 kcal mol<sup>-1</sup> obtained from a TPD experiment on an As-stabilized surface, the difference seems to be large. However, such a discrepancy may be acceptable because the present calculation used so small a cluster. The use of a large cluster model would lead to improved values.

TPD results and theoretical analysis showed adsorbed GaCl is stable and the Ga-Cl bond does not break before the desorption. Actually, ALE growth was attempted by using GaCl beam and a solid arsenic source in vacuum without H<sub>2</sub> at 300 °C. Although a GaCl adsorption layer was formed at this temperature, growth was never observed. This result clearly indicates that the Ga-Cl bond needs to be broken in order for growth to occur.

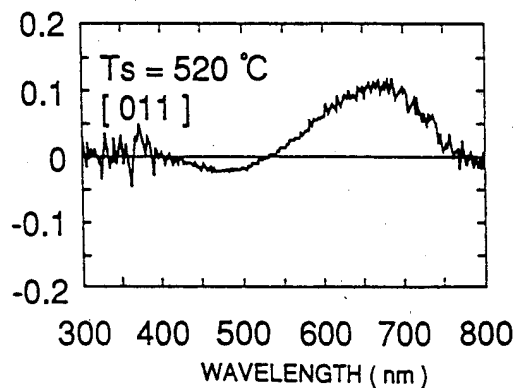
In order to study the growing surface in the actual chloride ALE system, *in situ* optical reflections were observed by the SPA method. The reflected light inten-

sity changed when alternating the gas supply from GaCl to AsH<sub>3</sub>. When (100) GaAs substrate was used and the beam incidence azimuth was [011], the reflected intensity dropped steeply with GaCl exposure and was saturated immediately. The intensity remained unchanged even after the GaCl supply was stopped. When AsH<sub>3</sub> was supplied, the intensity recovered to a level which would indicate an As-stabilized surface. This oscillation continued during ALE growth and was observed in a wide temperature range of 400–600 °C. Figure 4 shows spectra obtained from GaCl-supplied and Ga-supplied surfaces at 520 °C. The vertical axis represents normalized spectra ( $\Delta R(=R - R_{As})/R_{As}$ ), calculated using the spectra ( $R$ ) obtained by supplying GaCl or Ga, and the spectra obtained ( $R_{As}$ ) by supplying AsH<sub>3</sub>. The Ga surface was prepared by supplying TEGa, where the duration of TEGa supply was carefully controlled to cover the surface with one monolayer of Ga by the decomposition of TEGa. The similarity of the two spectra regarding peak positions and their magnitudes was clearly seen. This indicates that the surface under GaCl exposure was identical to a Ga-stabilized surface. The shape of the spectra was almost the same in the temperature range of 400–600 °C. In both spectra, two peaks at  $\sim 700$  nm ( $\sim 1.8$  eV) and  $\sim 500$  nm ( $\sim 2.5$  eV) were observed. The origins of these peaks have not been clearly understood, but Aspnes *et al.* [20] reported that optical transitions occur at 1.8 eV for Ga dimers and at 2.6 and 4.1 eV for As dimers from tight binding calculations. The obtained peak positions agreed well with these theoretical values, although the peak at 4.1 eV was not clearly seen.

Based on these results, a model for the surface reaction when GaCl is supplied under ambient H<sub>2</sub> to an As-stabilized surface is proposed, as shown in Fig. 5. Because the Ga-Cl bond has a considerable high binding energy of 113.8 kcal mol<sup>-1</sup> [21], self-dissociation in



(a) GaCl-supplying surface



(b) Ga-covered surface

Fig. 4. SPA spectra obtained (a) from GaCl-supplying surface and (b) Ga-covered surface at 520 °C with [011] incidence azimuth [15]. The Ga surface was prepared by supplying TEGa.

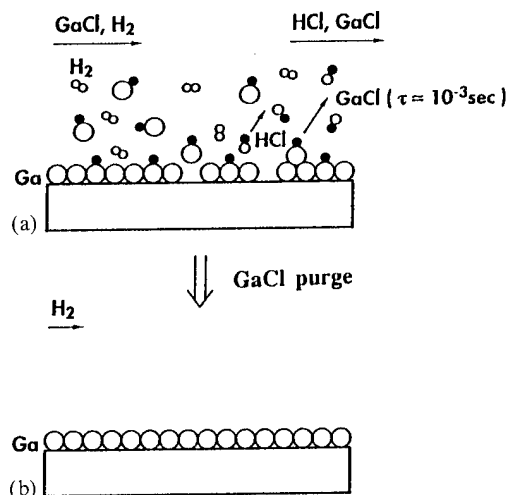


Fig. 5. Schematic representations of (a) the surface reaction when GaCl molecules are supplied with H<sub>2</sub> carrier gas, and (b) a Ga-covered surface after GaCl purge. In (a), the adsorbed GaCl molecules react with H<sub>2</sub> and release Cl as HCl. The GaCl residence time on the Ga layer is as short as 10<sup>-3</sup> s at 450 °C.

the gas phase can be ignored. When GaCl reaches the surface, a large amount of H<sub>2</sub> simultaneously impinges on the surface. GaCl is considered to release Cl as HCl and form Ga atoms by the reaction between adsorbed GaCl and H<sub>2</sub> gas. In this mechanism, H<sub>2</sub> plays a very important role. As mentioned previously, growth was not observed between the GaCl beam and the arsenic solid source in a vacuum chamber without H<sub>2</sub>. In chloride VPE using an AsCl<sub>3</sub> + Ga metal system, it was reported that the growth rate was proportional to the H<sub>2</sub> partial pressure, as shown in Fig. 6 [22]. The total reactor pressure was maintained at 1 atm by injecting inert gases such as He, N<sub>2</sub> and Ar to compensate for the reduction of H<sub>2</sub> partial pressure. The extrapolated growth rate reached almost zero at an H<sub>2</sub> pressure of zero. These results strongly support the necessity of hydrogen in the chloride growth system. As a linear relationship was obtained between H<sub>2</sub> partial pressure and growth rate in Fig. 6, this process can be described as a first order reaction. We can neglect the possibility that the H<sub>2</sub> dissociation reaction is involved in this process. Accordingly, the Eley-Readel reaction scheme, where adsorbed GaCl molecules react directly with H<sub>2</sub> gas and HCl is formed, is considered to be the most probable process.

To maintain monolayer coverage by Ga atoms throughout the GaCl supply, a self-limiting mechanism is necessary to suppress further deposition of Ga atoms. We calculated the residence time of GaCl species using adsorption energies obtained from the TPD measurements and using the relation  $\tau = \nu \exp(-E_{ad}/kT)$ , where  $k$  is the Boltzmann constant and  $T$  is the substrate temperature. The  $\tau$  value at 450 °C, which is the

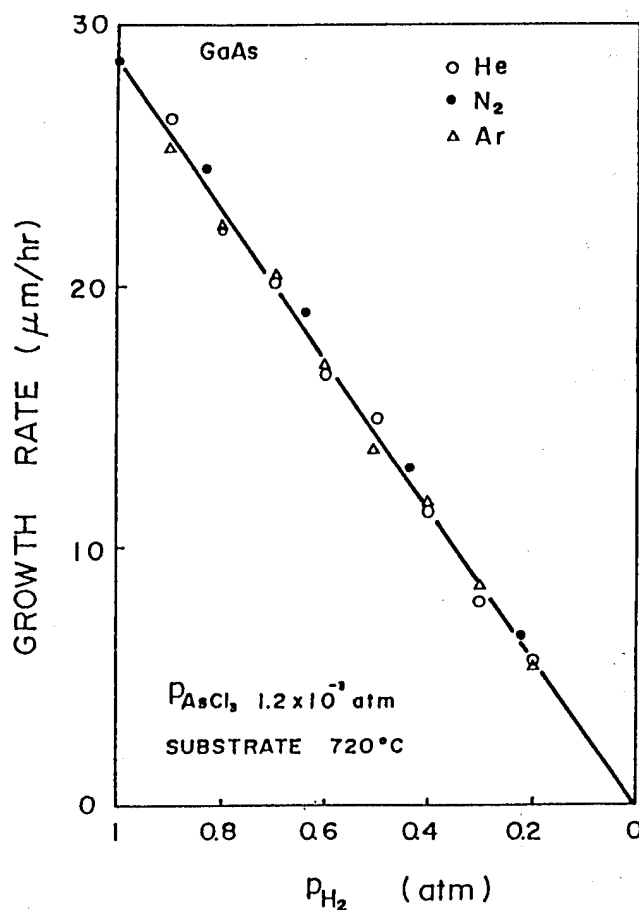


Fig. 6. Growth rate of GaAs versus H<sub>2</sub> partial pressure in chloride VPE using AsCl<sub>3</sub> and Ga metal source [22].

typical GaAs ALE growth temperature, was approximately 10<sup>-1</sup> s and 10<sup>-3</sup> s for the 2 × 4 As-stabilized and 4 × 6 Ga-stabilized surfaces respectively. This short residence time of 10<sup>-3</sup> s for GaCl on a Ga-stabilized surface is considered to suppress the reaction probability between GaCl and H<sub>2</sub>. The calculated  $\tau$  was short even on the As-stabilized surface at ALE growth temperatures. However, an extreme excess number of GaCl molecules of over 10<sup>4</sup>–10<sup>5</sup> times the number of surface adsorption sites is usually supplied to the surface in chloride ALE [23], and accounts for the reaction for Cl extraction proceeding. Another possible reason for the self-limiting growth is considered to lie in the reaction rates for Cl extraction being different between the Ga-GaCl and As-GaCl surfaces.

#### 4. Summary

The adsorption, desorption and reaction processes of GaCl, which is used as a source material in chloride ALE, were discussed. The experimental tools used were temperature programmed desorption (TPD) and sur-

face photo-absorption (SPA) methods. Furthermore, *ab initio* molecular orbital calculation was used to analyze theoretically these processes. From TPD measurements, GaCl molecules were found to adsorb on a GaAs substrate. The adsorption energies obtained were 32 kcal mol<sup>-1</sup> and 38 kcal mol<sup>-1</sup> for Ga-terminated and As-terminated surfaces respectively. Without H<sub>2</sub>, GaAs growth hardly occurred even if the As beam was irradiated onto the GaCl-adsorbed surface in the vacuum chamber. This result indicates that the Ga-Cl bond is very stable in the adsorption state. *Ab initio* molecular orbital calculation using a simple cluster model of (AsH<sub>2</sub>)<sub>2</sub>-GaCl indicated that the adsorption is completed by forming  $\sigma$  and  $\pi$  covalent bonds. The simulation also confirmed the above experimental assumptions that self-dissociation of the Ga-Cl bond hardly occurs. SPA measurements were carried out to study the surface chemistry in the ALE system in ambient H<sub>2</sub>. By comparing the spectrum of the GaCl-supplying surface with that of the Ga-covered surface, we found a strong similarity between the two spectra. Based on these experimental and theoretical results, a model for ALE growth using GaCl was proposed as follows. Adsorbed GaCl molecules can react immediately with hydrogen because GaCl is supplied with H<sub>2</sub> carrier gas in the ALE system, and Cl is released from the surface as HCl. Further dissociation of GaCl by H<sub>2</sub> on a Ga-covered surface could be suppressed by a very short residence time of GaCl ( $\sim 10^{-3}$  s at 450 °C) on the Ga-terminated surface. Although we believe that the present results greatly assist in understanding the growth mechanism of chloride ALE, further investigations are necessary to clarify the chloride ALE process including the detailed mechanism for Cl extraction by H<sub>2</sub> and the reaction between Ga and the As source gas.

### Acknowledgments

The author wishes to express deep appreciation to C. Sasaoka who carried out TPD measurements, K. Nishi who conducted SPA measurement and to Y. Mochizuki who carried out the calculation of GaCl adsorption processes. The author wishes to thank T. Takada, H.

Sunakawa and T. Kato for valuable discussions. The author also thanks Drs H. Watanabe, R. Lang, J. Sone and Professor H. Sakaki for their continuous encouragement and advice.

This work was partly supported by Sakaki Quantum Wave Project of ERATO, the Research Development Corporation of Japan.

### References

- 1 T. Suntola and J. Antson, *US Patent* 4 058 430, 1977.
- 2 C. H. L. Goodman and M. Pessa, *J. Appl. Phys.*, **60** (1986) R25.
- 3 T. Suntola, *Mater. Sci. Rep.*, **4** (1989) 261.
- 4 J. Nishizawa, H. Abe and T. Kurabayashi, *J. Electrochem. Soc.*, **132** (1985) 1197.
- 5 A. Usui and H. Sunakawa, *Jpn. J. Appl. Phys.*, **25** (1986) L212.
- 6 K. Mori, M. Yoshida, A. Usui and H. Terao, *Appl. Phys. Lett.*, **52** (1988) 27.
- 7 A. Usui and H. Watanabe, *Ann. Rev. Sci.*, **21** (1991) 185.
- 8 J. Nishizawa, T. Kurabayashi, H. Abe and A. Nozoe, *Surf. Sci.*, **185** (1988) 249.
- 9 A. Doi, Y. Aoyagi and S. Namba, *Appl. Phys. Lett.*, **49** (1986) 785.
- 10 H. Ohno, H. Ishii, K. Matsuzaki and H. Hasegawa, *Appl. Phys. Lett.*, **54** (1989) 1124.
- 11 C. Sasaoka, Y. Kato, A. Usui, H. Hirayama and T. Tatsumi, *Appl. Phys. Lett.*, **57** (1990) 1733.
- 12 A. Koukitu, H. Ikeda, H. Suzuki and H. Seki, *Jpn. J. Appl. Phys.*, **30** (1991) L1712.
- 13 N. Kobayashi and Y. Horikoshi, *Jpn. J. Appl. Phys.*, **28** (1989) L1880.
- 14 C. Sasaoka, Y. Kato and A. Usui, *Jpn. J. Appl. Phys.*, **30** (1991) L1756.
- 15 K. Nishi, A. Usui and H. Sakaki, *Appl. Phys. Lett.*, **61** (1992) 31.
- 16 Y. Mochizuki, T. Takata and A. Usui, *Jpn. J. Appl. Phys.*, in press.
- 17 C. Sasaoka, M. Yoshida and A. Usui, *Jpn. J. Appl. Phys.*, **27** (1988) L490.
- 18 Y. Ohshita, A. Ishitani and T. Takada, *Phys. Rev.*, **B41** (1990) 12 720.
- 19 Y. Ohshita, A. Ishitani and T. Takada, *J. Cryst. Growth*, **108** (1991) 499.
- 20 D. E. Aspnes, Y. C. Chang, A. A. Studna, L. T. Florez, H. H. Farrell and J. P. Harbison, *Phys. Rev. Lett.*, **64** (1990) 192-195.
- 21 D. W. Shaw *J. Phys. Chem. Solids*, **36** (1975) 111.
- 22 O. Mizuno and H. Watanabe, *J. Cryst. Growth*, **30** (1975) 240-248.
- 23 H. Watanabe and A. Usui, in W. T. Lindley (ed.), *Proc. Gallium Arsenide and Related Compounds, Las Vegas, Nevada*, 28 Sept.-1 Oct. 1986, Institute of Physics Conference Series No. 83, Institute of Physics, Bristol, 1987, pp. 1-8.



# The impact of short exposure times on the ALE self-limiting process: potential mechanisms

K. G. Reid, A. F. Myers, N. A. El-Masry and S. M. Bedair

Department of Electrical and Computer Engineering, North Carolina State University, Raleigh, NC 27695 (USA)

## Abstract

Atomic layer epitaxy (ALE) of GaAs using metal–organic precursors and arsine ( $\text{AsH}_3$ ) has been reported by many researchers for the past several years in a limited temperature range and with a high background of carbon doping. Most reactor designs involve a vent-run configuration which requires long exposure times of several seconds to achieve surface coverage. The rotating susceptor and reactor design used in our laboratory allow exposure times of less than one second and high precursor flux. Such short exposure times have resulted in the successful ALE growth at temperatures as high as 700 °C and low carbon background doping (in the  $10^{15} \text{ cm}^{-3}$  range). We will discuss the advantages of a susceptor design that allows the TMGa gas stream to remain at  $T < T_{\text{substrate}}$  until the substrate is rotated into the gas stream for a given exposure time. A potential ALE self-limiting mechanism will be presented based on the lifetime of adsorbed species and the relevance of this short exposure times approach.

## 1. Introduction

Atomic layer epitaxy (ALE) of GaAs has been investigated for several years achieving success in the ability to grow thin layers with a self-limiting monolayer per cycle growth rate. There remain, however, several challenges for the implementation of ALE GaAs grown with trimethylgallium (TMGa): (1) indications of very low growth rates; (2) narrow windows in both temperature and reactor flux; and (3) high background carbon behaving as an acceptor. Most of these problems can be minimized by special reactor design that allows short exposure times to TMGa. The kinetics of the reaction leading to ALE GaAs from TMGa are given later in the paper, but it should be mentioned that the surface reaction rates are of the order of a few ms at typical growth temperatures, so if the flux is sufficient for monolayer coverage exposure times can be short. There are two types of reactors currently used to grow GaAs using TMGa by ALE: the MOVPE which operates at atmospheric or reduced pressure (760–20 Torr) and the MBE which operates under UHV conditions. Table 1 gives a summary of reported ALE growth conditions for both reactor types. From this table it can be seen that we report a comparatively wide range of growth temperature (450–700 °C), extending over 100 °C higher than any other group [1]. We have demonstrated the importance of high growth temperatures and short exposure times to the TMGa flux to reduce background carbon thought to originate from the methyl groups of the TMGa molecule. For example, the carrier concentrations for a one second expo-

sure to TMGa at 500 °C and 600 °C are  $p = 10^{19} \text{ cm}^{-3}$  and  $p = 10^{16} \text{ cm}^{-3}$  respectively. Also at 500 °C carrier concentrations of  $p = 10^{20} \text{ cm}^{-3}$  and  $p = 10^{16} \text{ cm}^{-3}$  were measured for 2 and 0.2 s exposures respectively. In this paper we draw upon data from our laboratory [1, 2], ALE studies [3–10], and research on the decomposition of TMGa at the surface [11, 12] to propose an explanation of the ALE self-limiting mechanism and address the importance of short TMGa exposure times.

## 2. Experimental details

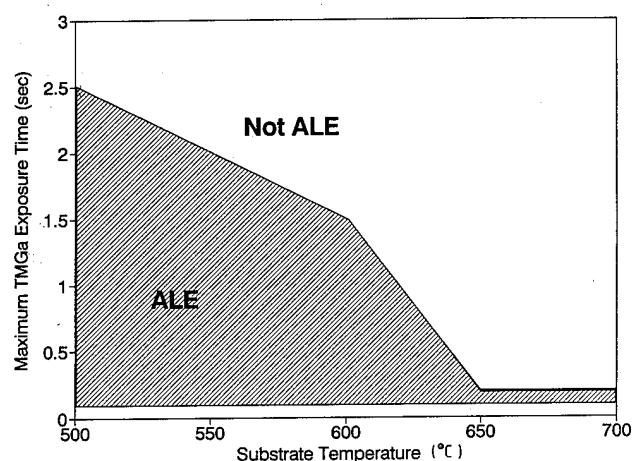
We use an atmospheric pressure, modified MOCVD reactor with three gas inlets; one for TMGa, a center line for hydrogen and one for arsine ( $\text{AsH}_3$ ). The graphite susceptor is heated by an RF coil and the temperature is measured by a thermocouple imbedded in the graphite susceptor. The rotating susceptor allows controlled exposures to the precursors by rotation under windows in a stationary top plate. The clearance of the substrate under the stationary top plate is 0.5 mm which removes most of the gaseous boundary layer. The substrates were semi-insulating (001) 2° toward [110] GaAs. Growth proceeded in cycles where one cycle consisted of a single rotation under the  $\text{AsH}_3$  window and the TMGa window.

## 3. Results and discussion

Figure 1 shows our reported maximum exposure times to TMGa for 500, 550, 600, 650 and 700 °C

TABLE 1. Summary of reported ALE growth conditions for GaAs with TMGa used as the gallium precursor

Type of system pressure (Torr)	Temperature range (°C)	Exposure time (s)	Reference
Vertical MOVPE rotating susceptibility (760 Torr)	450–700	0.2–3/0.2 TMGa/AsH <sub>3</sub>	1
Vertical MOVPE rotating susceptibility (30 Torr)	550–650	0.2–0.6/0.8/0.4/0.8 TMGa/Purge/AsH <sub>3</sub>	2
Vertical chimney MOVPE (20 Torr)	430–560	1–30/1–10 TMGa/AsH <sub>3</sub>	3
Vertical H <sup>+</sup> plasma rotating susceptibility (20 Torr)	430–500	3/2/2/2 TMGa/Purge/AsH <sub>3</sub> /Purge	4
Horizontal MOVPE (100 Torr)	500	3/2/4–8/2 TMGa/Purge/AsH <sub>3</sub> /Purge	5
Horizontal MOVPE vent/run (100 Torr)	$T < 460$	1/1/1/1 TMGa/Purge/AsH <sub>3</sub> /Purge	6
Horizontal MOVPE vent/run (760 Torr)	450	0.6/1.5/1.5/0 TMGa/Halt/AsH <sub>3</sub> /H <sub>2</sub> Purge	7
MOVPE (70 Torr)	490–500	1/3/1/3 TMGa/Purge/AsH <sub>3</sub> /Purge	8
UHV MOMBE	470	15–50/10/10/10 TMGa/Evac/AsH <sub>3</sub> /Evac	9
UHV MOMBE	500	4/3/20/3 TMGa/Evac/AsH <sub>3</sub> /Evac	10

Fig. 1. Exposure time range to TMGa for ALE growth of GaAs with  $0.08 \mu\text{mol}^{-1} \text{s}^{-1}$  TMGa flow.

growth temperatures for monolayer (ML)  $(\text{cycle})^{-1}$  growth. Exposure times longer than those given in Fig. 1 resulted in more than 1 ML  $(\text{cycle})^{-1}$ . From this data it is evident that very short exposures to the TMGa flux are required at  $T > 600^\circ\text{C}$ . Figure 2 confirms the self-limiting mechanism over a range of TMGa integrated flux (flow rate  $\times$  exposure time) at these high growth temperatures.

It is useful to examine the proposed mechanisms and the basic studies of ALE to understand the requirement of short exposure times. The three dominant theories of the self-limiting mechanism are summarized in Fig. 3.

(1) The *selective adsorbate* model [13] states that TMGa will not decompose on an atomic Ga-rich surface. It was supported by XPS surface studies showing no carbon on TMGa dosed surfaces. However, XPS requires cooling and transport from the growth chamber

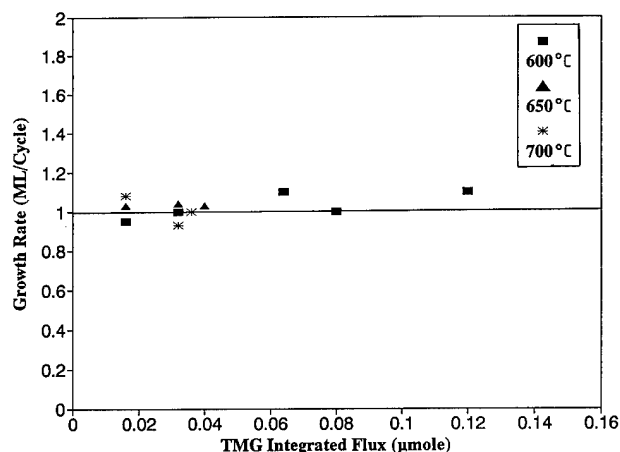


Fig. 2. Growth rate saturation at 1 ML (cycle)<sup>-1</sup> for 600, 650 and 700 °C.

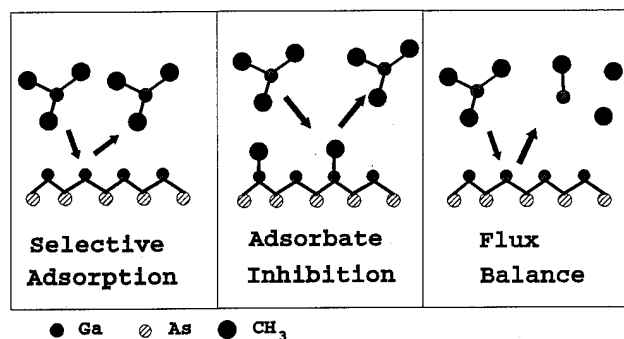


Fig. 3. Summary of three models of ALE of GaAs using TMGa and AsH<sub>3</sub>: *Selective adsorption* allows no TMGa decomposition on a Ga-covered surface. *Adsorbate inhibition* prohibits TMGa decomposition on a methyl covered surface. The *flux balance* requires a balance of adsorbing and desorbing methylgallium species.

to the XPS chamber which is a significant change in the environment for the substrate. This model has been completely excluded by a study demonstrating TMGa decomposition on a Ga surface [14].

(2) The *adsorbate inhibition* model will not allow decomposition of TMGa on a methyl-gallium species covered surface [15]. It is supported by temperature programmed desorption (TPD) studies showing the lifetime of the methyl radicals under UHV conditions. This is not the complete picture, however, since at higher growth temperatures the methyl lifetimes are much too short to explain our ability to maintain ML (cycle)<sup>-1</sup> growth.

(3) The *flux balance* model [16] requires a balance to be maintained between desorbing monomethylgallium (MMGa) and adsorbing MMGa during the TMGa exposure. This seems to be an obvious requirement, but one which had been previously overlooked. There must be a compensation for desorbed MMGa from the surface, otherwise less than a ML (cycle)<sup>-1</sup> growth will

result. However, the upper temperature limit of ALE growth has always been reported by growth rates exceeding the ML (cycle)<sup>-1</sup>, thus the flux balance model is not complete either.

These models cannot completely explain the collection of ALE GaAs data presented in Table 1, nor can they specifically address why our atmospheric pressure reactor can maintain ALE at temperatures far exceeding that of the UHV reactors [9, 10] where the gas decomposition is insignificant. In the following we will discuss the main gas phase and surface reactions and try to explain why our approach can sustain ALE at higher temperatures based upon a flux balance of methyl radicals near the substrate surface.

### 3.1. Gas phase reactions

It is important to examine the gas phase decomposition of TMGa in H<sub>2</sub> for an understanding of ALE in an MOVPE reactor. The region above the hot substrate where temperatures are hot enough for decomposition of TMGa to occur is the chemical boundary layer [17]. Reactor conditions leading to the complete decomposition of TMGa in the gas phase represent the absolute limit of ALE in the MOVPE environment. Therefore, the characteristics of this chemical boundary layer and the time an incoming TMGa molecule spends in it are important reactor design issues.

The chemical boundary layer for TMGa would be established by the gas phase temperature at which it decomposed to Ga and has been proposed to begin at 400 °C [18]. The thermal profile in the hydrogen carrier for the TMGa above the hot substrate is therefore critical for atomic layer epitaxy in the MOVPE reactor. Since the rotating susceptor in our reactor cuts into a relatively cool H<sub>2</sub>/TMGa gas stream and then begins to heat this gaseous layer up to the substrate temperature, the thermal profile is transient. Estimates of these transient thermal profiles were made for substrate temperatures of 500, 600 and 700 °C, by solving the heat conduction equation for a flat plate at a given substrate temperature, heating H<sub>2</sub> at a given height above the substrate ( $y$ ) as a function of time. The boundary conditions are:  $T_{\text{Hydrogen}} = T_{\text{Substrate}}$  at the interface ( $y = 0$ ) and  $T_{\text{Hydrogen}} = 0$  °C as  $y \rightarrow \infty$ . The transient profiles are shown in Fig. 4 for substrate temperatures of 500, 600 and 700 °C. Pertinent TMGa exposure times are included to indicate the strong dependence of the gas phase thermal profile on exposure time increases of fractions of a second at high substrate temperatures. At a substrate temperature of 500 °C, for example, as shown in Fig. 4, for a 0.2 s exposure to TMGa the gas phase temperature where  $T_{\text{Hydrogen}} \geq 400$  °C has developed to 0.25 cm above the substrate. As the substrate temperature is increased, the thermal profile expands and the chemical boundary layer gets thicker for the

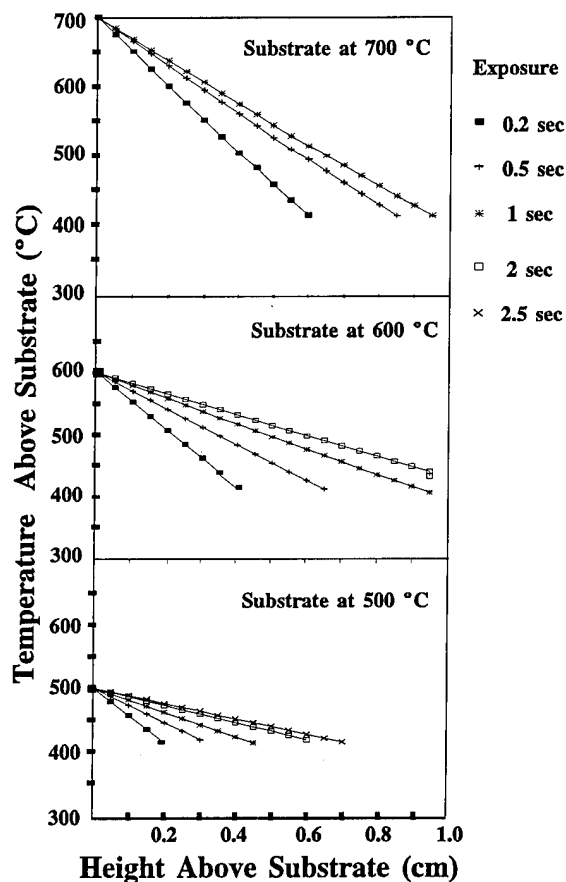


Fig. 4. Transient thermal profile in the  $H_2$  above the hot substrate for a substrate temperature of 500, 600 and 700 °C for several TMGa exposure times.

same exposure time to the TMGa/ $H_2$  stream. Another example is for a substrate temperature of 700 °C as shown in Fig. 4. At this substrate temperature the thickness of the chemical boundary layer where  $T_{Hydrogen} \geq 400$  °C has increased to 0.65 cm for a 0.2 s TMGa exposure. Therefore, the volume where gas phase decomposition of the TMGa molecule is more likely has increased, and the self-limiting characteristics at higher growth temperatures exhibits a narrower window of exposure times in the order of fractions of a second to the TMGa/ $H_2$  stream. However, in most other MOVPE reactors the effective TMGa exposure is one second or longer making high temperature ALE difficult, as shown in Table 1.

From the gas phase decomposition of TMGa arguments alone, the ALE temperature range in the UHV reactor should extend beyond that of the MOVPE. On the contrary, the UHV data demonstrate a narrower ALE temperature window than MOVPE and this has been explained by the limitations established by the lifetime of surface-adsorbed  $CH_3$ , referred to in Section 3.2.

### 3.2. Surface reactions

The TMGa dosed surface has recently received attention by several groups using techniques such as temper-

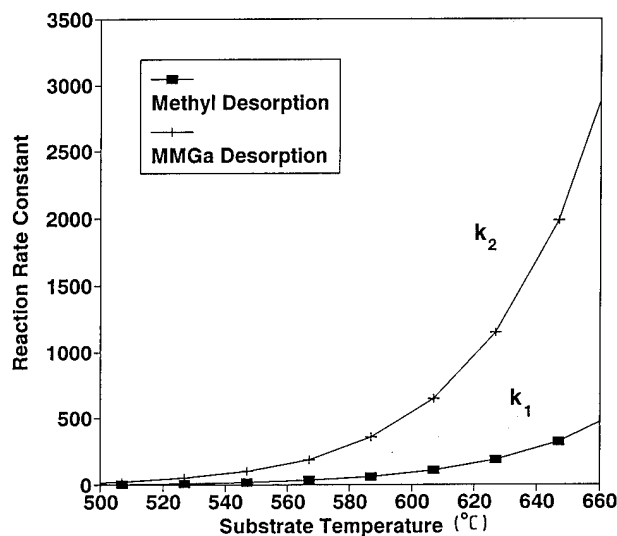
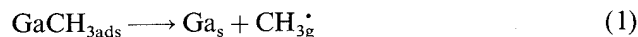


Fig. 5. Reaction rate constants for  $k_1$ , desorption of  $CH_3$  from an MMGa covered surface, and  $k_2$ , desorption of MMGa from the surface as a function of substrate temperature.

ature programmed desorption (TPD) to quantify the lifetime of methyl radicals on the surface as follows [19]:



$$k_1 = 10^{13} \exp[(-44.1 \text{ kcal mol}^{-1})/RT]$$

The desorption of MMGa from the surface was described by Mountziaris and Jensen [11] as:



$$k_2 = 10^{14} \exp[(-45 \text{ kcal mol}^{-1})/RT]$$

A plot of these reactions, shown in Fig. 5, indicates at low temperatures where ALE is observed in UHV reactors [9, 10], the desorption of methyl radicals and the desorption of monomethylgallium are relatively low. However, at  $\approx 600$  °C the methyl desorption becomes more significant leaving more uncovered gallium which is not self-limiting to TMGa.

Based upon the system dependent ALE temperature ranges and the above-mentioned gas phase and surface reactions, we propose the *methyl radical balance* as the self-limiting ALE mechanism. The surface must be stabilized with mono- or di-methylgallium molecules which are selective against chemisorption of TMGa. However, a balance between desorption of the methyl radicals from the monomethylgallium (MMGa) molecules at the surface and adsorption of methyls from the gas phase for the MOVPE type reactor is required during the TMGa exposure. The self-limiting ALE can be lost by two means, which may be a function of reactor type (pressure), growth temperature and gas flux.

(1) Complete gas phase decomposition of incoming TMGa molecules leads to a surface covered with atomic gallium during the TMGa exposure, the surface of atomic gallium will not be self-limiting to further Ga or TMGa chemisorption.

(2) Methyls at the surface desorb faster than they can be replaced from the gaseous boundary layer, opening up sites of atomic Ga upon which TMGa can chemically adsorb. The desorption of MMGa is not a problem as long as there is a flux of TMGa to replace it, and as has been suggested, there is probably a balance of adsorbing MMGa and desorbing MMGa [16].

For the high vacuum case, the self-limiting state is determined by the lifetime of methyl radicals adsorbed at the surface in the mono- or di-methylgallium. There is no boundary layer to provide a source of replacement of methyl radicals and desorbing methyl radicals are not likely to return to the surface since their mean free path is large. If MMGa desorbs it can simply be replaced by the incoming flux of TMGa. If a methyl desorbs from the surface MMGa molecule, however, the resulting Ga atom is no longer self-limiting against the incoming TMGa flux and the growth rate exceeds ML cycle<sup>-1</sup>. Thus ALE in the UHV environment probably has a temperature limit from the surface kinetics that cannot be circumvented.

MOVPE type reactors, however, should be able to extend the ALE temperature range by decreasing the TMGa exposure time to minimize gas phase decomposition and increasing the TMGa flux to achieve surface saturation faster.

#### 4. Conclusions

Several studies agree that self-limitation depends on a surface saturated by MMGa. The lifetime of these methyls at the surface has been shown to be too short to explain the self-limiting conditions at high temperatures. The concept of a methyl flux balance of desorbing CH<sub>3</sub> and gas phase supplied adsorbing CH<sub>3</sub> can explain: the limited range of ALE at low pressure, the

limited range of ALE for long exposures to TMGa, and the wider range of ALE at higher pressures and short exposures to the TMGa.

#### References

- 1 K. G. Reid, H. M. Urdianyk and S. M. Bedair, *Appl. Phys. Lett.*, **59** (1991) 2397.
- 2 P. C. Colter, S. A. Hussien, A. Dip, M. U. Erdogan, W. M. Duncan and S. M. Bedair, *Appl. Phys. Lett.*, **59** (1991) 1440.
- 3 M. Ozeki, K. Mochizuki, N. Ohtsuka and K. Kodama, *J. Vac. Sci. Technol. B*, **5** (1987) 1184.
- 4 M. de Keijser and C. van Opdorp, *Appl. Phys. Lett.*, **58** (1991) 1184.
- 5 A. Usui and H. Watanabe, *Third Int. Conf. on Modulated Semiconductor Structures, Montpellier, France, 1987, J. Phys. (Paris), C5* (1987) 21.
- 6 S. DenBaars, A. Hariz, C. Beyler, B. Maa, Q. Chen and P. Dapkus, *Mater. Res. Soc. Symp. Proc.*, **102** (1988) 527.
- 7 E. Colas, R. Bhat and B. Skromme, *Appl. Phys. Lett.*, **55** (1989) 2769.
- 8 H. Yokoyama, M. Shinohara and N. Inoue, *Appl. Phys. Lett.*, **59** (1991) 2148.
- 9 A. Watanabe, T. Isu, M. Hata, T. Kamijoh and Y. Katayama, *Jpn. J. Appl. Phys.*, **28** (7) (1989) L1080.
- 10 J. Nishizawa, H. Abe and T. Kurabayashi, *J. Electrochem. Soc.*, **132** (1985) 1197.
- 11 T. Mountziaris and K. Jensen, *J. Electrochem. Soc.*, **138** (1991) 2426.
- 12 M. L. Yu, N. I. Buchan, R. Souda and T. F. Kuech, in T. F. Kuech, P. D. Dapkus and Y. Aoyagi (eds.), *1991 Spring MRS Meeting, Anaheim, CA, 1991, Mater. Res. Soc. Symp. Proc.*, Vol. 222, Materials Research Society, Pittsburgh, PA, 1991, p. 3.
- 13 K. Kodama, M. Ozeki, K. Mochizuki and N. Ohtsuka, *Appl. Phys. Lett.*, **54** (1989) 656.
- 14 J. R. Creighton, K. R. Lykke, V. A. Shamamian and B. D. Kay, *Appl. Phys. Lett.*, **57** (1990) 279.
- 15 J. Nishizawa and T. Kurabayashi, *J. Cryst. Growth*, **93** (1988) 98.
- 16 M. L. Yu, U. Memmert, N. I. Buchan and T. F. Kuech, in L. V. Interrante, K. F. Jensen, L. H. Dubois and M. E. Gross (eds.), *Chemical Perspectives of Microelectronic Materials II*, Materials Research Society Proceedings, Vol. 204, Pittsburgh, PA, 1991.
- 17 M. H. J. M. de Croon and L. J. Giling, *J. Electrochem. Soc.*, **137** (1990) 2867.
- 18 J. Nishizawa and T. Kurabayashi, *J. Electrochem. Soc.*, **130** (1983) 413.
- 19 J. R. Creighton, in T. F. Kuech, P. D. Dapkus and Y. Aoyagi (eds.), *Spring 1991 MRS, Anaheim, CA, 1991, Mater. Res. Soc. Symp. Proc.*, Vol. 222, Materials Research Society, Pittsburgh, PA, 1991, p. 15.

# Atomic layer epitaxy of InP using trimethylindium and tertiarybutylphosphine

N. Pan, J. Carter, S. Hein, D. Howe, L. Goldman, L. Kupferberg and S. Brierley

*Raytheon Company, Research Division, 131 Spring Street, Lexington, MA 02173 (USA)*

K. C. Hsieh

*Department of Electrical and Computer Engineering, University of Illinois at Urbana-Champaign, Urbana, IL 61801 (USA)*

## Abstract

Atomic layer epitaxy (ALE) growth of InP was investigated using trimethylindium (TMI) and tertiarybutylphosphine (TBP) in a horizontal atmospheric reactor. The studied growth parameters were exposure times, TMI and TBP fluxes, and growth temperature. Self-limiting ALE growth of InP was achieved at a growth temperature of 340 °C. Substantial increases in the TMI flux and higher growth temperatures exceeding 340 °C resulted in growth rates exceeding 1 monolayer per cycle. Uniform ALE InP layers were verified by cross-sectional transmission electron microscopy and sputtered Auger profiling. The application of thin ALE InP layers (15 Å) on GaAs surfaces was investigated using X-ray photoelectron spectroscopy, 77 K photoluminescence, and 300 K photoreflectance. The absence of arsenic oxide and an increase in the photoluminescence intensity by a factor of 2 were observed after InP passivation.

## 1. Introduction

The precise control of the thickness in ultrathin layers of compound semiconductors has generated significant interest in the growth of these layers in the atomic layer epitaxy (ALE) or flow rate modulation modes. The ALE process is also desirable for certain device structures which require low growth temperatures in order to reduce temperature-dependent diffusion processes. InP is very attractive for high power devices at high frequencies because of its large  $\Gamma$ -L separation (0.52 eV), high saturated velocity, high thermal conductivity, high breakdown voltage, and low surface recombination velocity. There have been numerous reports on the growth of InP in the ALE and flow rate modulation modes using conventional sources such as trimethylindium (TMI) and phosphine [1–4]. Thin layers of InP grown by ALE have been used as buffer layers to improve the X-ray linewidth of InP on GaAs [5]. Improvements in the heterointerface quality of InAs/InP strained layer superlattices have been shown by using the flow rate modulation process [6]. While the ALE process of InP has been demonstrated using TMI and phosphine, there has not been any report of ALE growth using TMI and tertiarybutylphosphine (TBP). TBP is an attractive alternative to phosphine because of its lower toxicity and a lower V/III ratio is required for InP growth owing to its lower pyrolysis temperatures. In this paper, the growth conditions for the realization of InP ALE with monolayer saturation are described

using a conventional atmospheric metalorganic chemical vapor deposition (MOCVD) reactor. The application of ultrathin (15 Å) InP layers for the passivation of GaAs surfaces resulting in a lower surface recombination velocity is also presented.

## 2. Experimental details

ALE growth was performed in a horizontal atmospheric pressure MOCVD reactor [7]. TMI and TBP were used as the source materials. The TMI bubbler was maintained at 20.0 °C and the TBP bubbler at 10.0 °C. The TMI density was monitored using an EPISON gas density analyzer in order to account for the bubbler efficiency at different TMI flows. 99 cycles of InP ALE layers were typically grown on a thin (1000 Å) lattice-matched InAlAs layer (MOCVD grown) on an iron-doped InP substrate oriented 2° off the (100) direction towards the (110). The slight difference in the index of refraction between InAlAs and InP provides reasonable contrast for the layer thickness measurements using grazing incidence X-ray diffraction [8]. The switching of the gases was performed using 4-way Nupro pneumatic valves with a minimum switching time of 1 s. Each source line was designed with separate vent lines enabling visualization of the gas switching process. The reactor pressure was maintained at slightly above atmospheric pressure using an MKS pressure controller. The switching sequence consisted of

a TMI exposure time, an  $H_2$  purge, a TBP exposure time, and an  $H_2$  purge. The TMI cycle was varied from 3 to 6 s and the TMI mole fraction was varied from  $0.5$  to  $3.0 \times 10^{-4}$ . The  $H_2$  purge time was kept at 3 s. The TBP cycle was varied from 8 to 16 s and the mole fraction was  $1.2 \times 10^{-2}$ . The total gas flow in the reactor ranged from  $20 \text{ l min}^{-1}$  to  $31 \text{ l min}^{-1}$ .

ALE InP layer thicknesses were primarily measured using grazing incidence X-ray diffraction. A two-layer model was used to fit the experimental results. Sputtered Auger profiling followed by a surface profilometer scan was used to determine the uniformity of the elemental composition and to confirm the layer thickness. Sputtered Auger profiling and X-ray photoelectron spectroscopy (XPS) were performed using a Perkin-Elmer model 570 multitasking machine. An argon ion beam with an energy of 3 keV ( $I = 0.1 \mu\text{A}$ ) was used for the sputtering. The sputter rate for InP was about  $300 \text{ \AA min}^{-1}$ . 300 K photorefectance (PR) and 77 K photoluminescence (PL) were used to characterize the GaAs layers before and after InP ALE passivation. PR was performed with a monochromatic light source and an argon ion laser. A silicon photodetector and conventional lock-in techniques were used to measure the modulated reflectance. 77 K PL was performed in a liquid helium cryostat in a strain-free mount. The luminescence was dispersed through a double 1.0 m spectrometer and collected by a GaAs photomultiplier tube. The PL spectra were taken with an excitation intensity of  $1 \text{ W cm}^{-2}$ .

### 3. Results and discussion

#### 3.1. Atomic layer epitaxy growth

Figure 1 shows the thickness per cycle of ALE growth as a function of the number of TMI moles per cycle. The ALE cycle consisted of a 3 s TMI exposure, a 3 s  $H_2$  purge, an 8 s TBP exposure, and a 3 s  $H_2$  purge (3/3/8/3). The total flow rate was  $31 \text{ l min}^{-1}$ . The TMI mole fraction was adjusted to reflect the decrease in bubbler efficiency at the higher TMI flow rates. Monolayer saturation is observed at the higher TMI mole fractions as expected since the growth proceeded in the ALE growth mode. The growth rate would be linear as a function of the TMI mole fraction without a self-limiting process if the growth proceeded by the MOCVD growth mode. The TBP flow rate was 200 standard  $\text{cm}^3 \text{ min}^{-1}$  corresponding to a mole fraction of  $1.2 \times 10^{-2}$ . The TBP flow rate was not optimized but the typical surface morphology of the layers was highly reflective and specular (Fig. 2). ALE growth was also investigated at total flow rates up to  $20 \text{ l min}^{-1}$ . At the higher total flow rates, very high flow rates of TBP (greater than 500 standard  $\text{cm}^3 \text{ min}^{-1}$ ) were required in

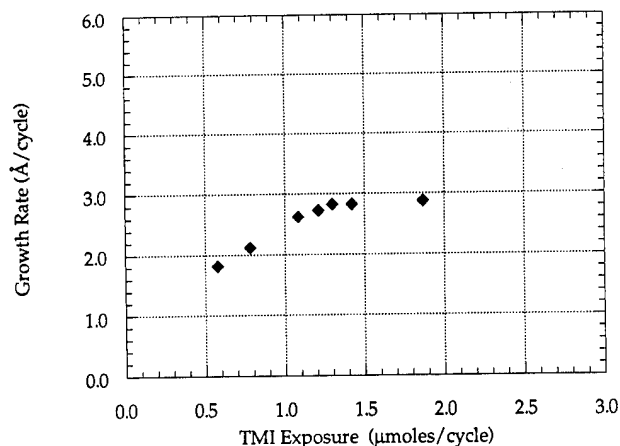


Fig. 1. The thickness per cycle of ALE growth as a function of the number of TMI moles per cycle is shown. The ALE cycle was 3 s TMI, 3 s purge, 8 s TBP, 3 s purge. The growth temperature was  $340^\circ\text{C}$ . Self-limiting growth with monolayer saturation is observed.

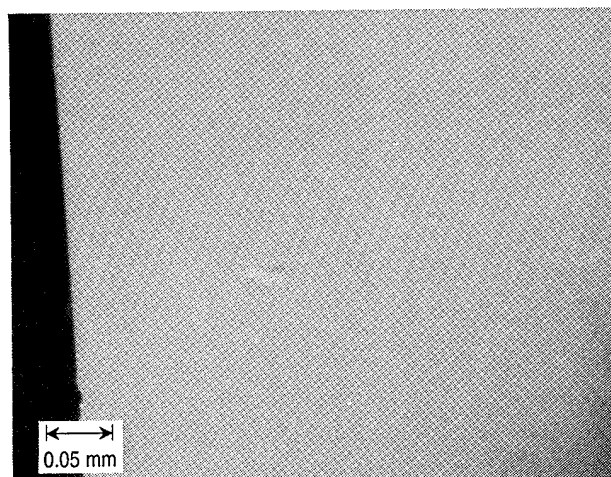


Fig. 2. Surface morphology of an InP ALE layer ( $1200 \text{ \AA}$ ) grown at  $340^\circ\text{C}$  is shown. The surface morphology is excellent at high magnification.

order to preserve the surface. The surface became very dull and indium droplets were clearly visible with the naked eye when the TBP flow was not sufficient. Owing to the high cost of TBP, it was chosen to perform ALE growth at a lower total flow rate in order to maintain a reasonable consumption of TBP. As the total flow rate is reduced, it is expected that the gas velocity would decrease, resulting in longer residence times which may cause problems of intermixing of TBP and TMI. However, the results showed that monolayer saturation is attainable at low total flow rates, indicating that the growth was primarily in the ALE growth mode.

Figure 3 shows the thickness per cycle of ALE growth as a function of the number of TMI moles per cycle at a longer TMI injection time (6 s). The ALE

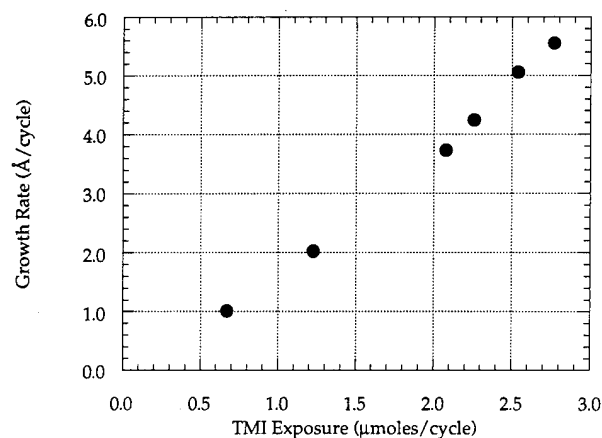


Fig. 3. The thickness per cycle of ALE growth as a function of the TMI moles per cycle is shown. The ALE cycle was 6 s TMI, 3 s purge, 8 s TBP, 3 s purge. The growth temperature was 340 °C. Saturation of the growth rate is not observed for this particular TMI exposure time.

cycle was 6/3/8/3. The growth rate increases with increasing TMI mole fraction but a plateau is not observed. It is possible that the higher number of TMI moles per cycle (more than 2.0 μmol per cycle) and the longer TMI exposure times may result in three-dimensional growth minimizing the self-limiting ALE growth mode. The effects of growth temperature on the growth rate are shown in Fig. 4. The number of TMI moles per cycle was  $2.1 \times 10^{-6}$ . The ALE cycle was 6/3/16/3. Monolayer growth is observed at about 340 °C which is consistent with previous ALE InP results [1, 2, 4]. At higher growth temperatures, the self-limiting ALE process is not evident owing to the increased gas phase decomposition. Previous work has shown that TMI decomposition started at about 300 °C and was completed at 380 °C [9].

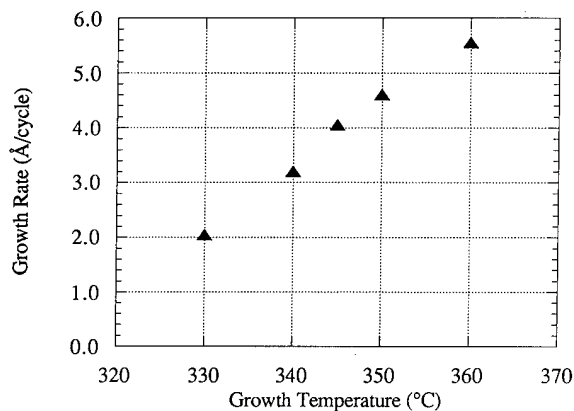


Fig. 4. The thickness per cycle of ALE growth as a function of the growth temperature is shown. The ALE cycle was 6 s TMI, 3 s purge, 16 s TBP, 3 s purge. The number of TMI moles per cycle was  $2.1 \times 10^{-6}$ . 1 monolayer per cycle of ALE growth is obtained around 340 °C.

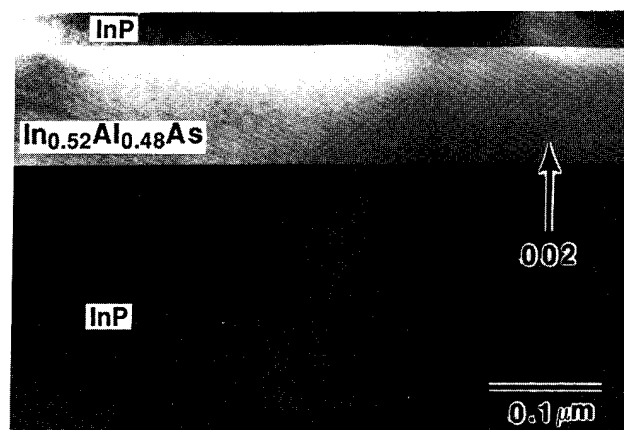


Fig. 5. TEM of an InP ALE (320 Å) layer grown on top of a lattice-matched InAlAs layer (1000 Å) is shown. The interfaces are very clean and distinct. The presence of microtwins is clearly seen at the surface.

### 3.2. Material characterization

A cross-sectional transmission electron micrograph (TEM) of an InP ALE layer grown on top of a lattice-matched InAlAs layer is shown in Fig. 5. Lattice matching of the InAlAs layer was verified by double-crystal X-ray diffraction and 300 K PR. The interfaces are very clear and distinct. The InP layer is uniform, indicating that the growth was two-dimensional. However, there are some microtwins which start at the surface and propagate downwards. The presence of microtwins suggests that the ALE InP layer may not be perfectly stoichiometric at this particular growth condition. A sputtered Auger profile is shown in Fig. 6. The presence of indium and phosphorus is clearly shown.

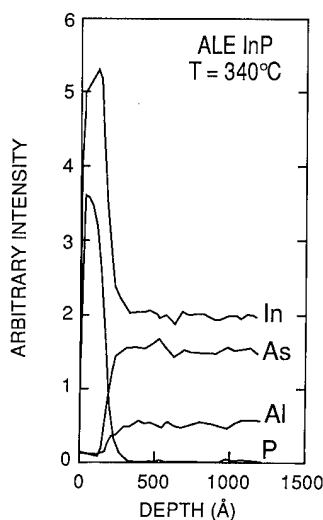


Fig. 6. A sputtered Auger profile of an InP ALE layer (300 Å) grown on top of a lattice-matched InAlAs layer is shown. Indium and phosphorus are present at the surface. The heterojunction is abrupt as shown by the sharp features at the interface.



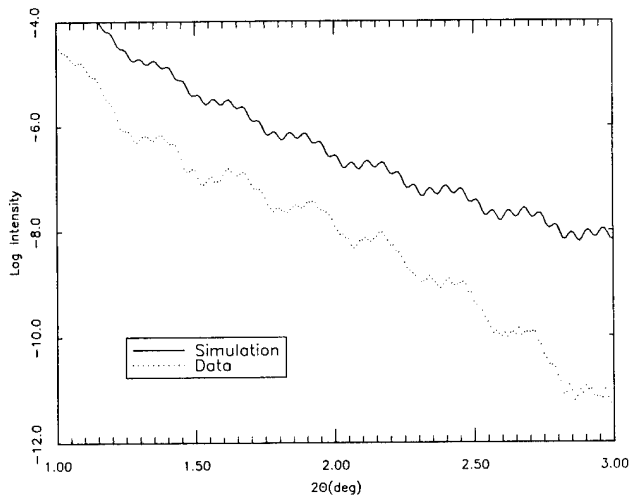


Fig. 7. A grazing incidence X-ray diffraction scan of an InP ALE layer grown on top of a lattice matched InAlAs layer is shown. The simulation results of a two-layer model are also shown. The simulation results are in good agreement with the diffraction scan. The InP layer thickness is 320 Å and the InAlAs layer thickness is 1100 Å.

The interface is abrupt as shown by the sharp features at the interface. An estimate of the InP layer thickness is about 300 Å as measured by surface profilometry of the sputtered crater. The majority of the thickness measurements were performed by grazing incidence X-ray diffraction [8]. The high resolution of this technique ( $\pm 10$  Å) is ideal for these types of heterostructures. A typical scan along with the simulation results is shown in Fig. 7. The superimposed shows the presence of very fine oscillations superimposed with a broader oscillation. The period of the very fine oscillations corresponds to the total layer thickness consisting of both the InAlAs and the InP ALE layer thickness. The period of the broader oscillation corresponds to the InP ALE layer. An InP layer thickness of 320 Å and an InAlAs layer thickness of 1100 Å were determined. The thickness was in excellent agreement with the value obtained from the TEM for this particular sample.

### 3.3. Device applications

The lower surface recombination velocity of InP is very attractive for many device applications. The use of thin layers of InP for passivating GaAs may improve the GaAs surface since its surface recombination velocity is very high. Recent work has shown that thin lattice-matched InGaP layers (200 Å) improved the PL intensity of GaAs by a factor of 25 and are stable at 800 °C for 10 min [10]. Because of the lattice mismatch (3.8%) between GaAs and InP, pseudomorphic passivating layers are desirable in order to avoid the generation of dislocations. A very thin ALE InP (15 Å) layer corresponding to 5 monolayers was investigated on both an undoped GaAs substrate and an ion-implanted

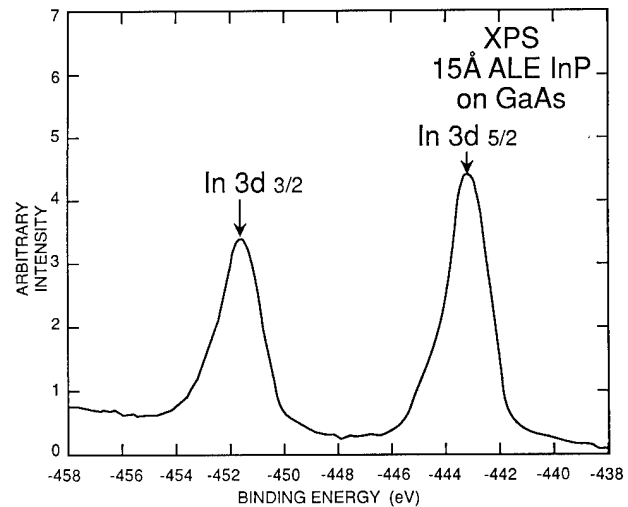


Fig. 8. An XPS spectrum of a GaAs surface that has been passivated with a 15 Å layer of InP ALE. The In 3d signal confirms the presence of indium on the surface.

( $3 \times 10^{17} \text{ cm}^{-3}$ ) GaAs metal semiconductor field effect transistor (MESFET) structure. XPS of the GaAs substrate surface is shown in Figs. 8–10. The presence of indium, phosphorus, and phosphorous oxide is clearly shown. Arsenic is present but arsenic oxide is not detected. The absence of arsenic oxide has been shown to be desirable for improvements in the GaAs surface defect density [11, 12]. 77 K PL spectra of the substrate before and after passivation are shown in Fig. 11. The peaks correspond to the energy gap of GaAs. An improvement in the PL intensity (factor of 2) is observed, indicating a reduction in the effective surface recombination velocity [13]. 300 K PR spectra for an

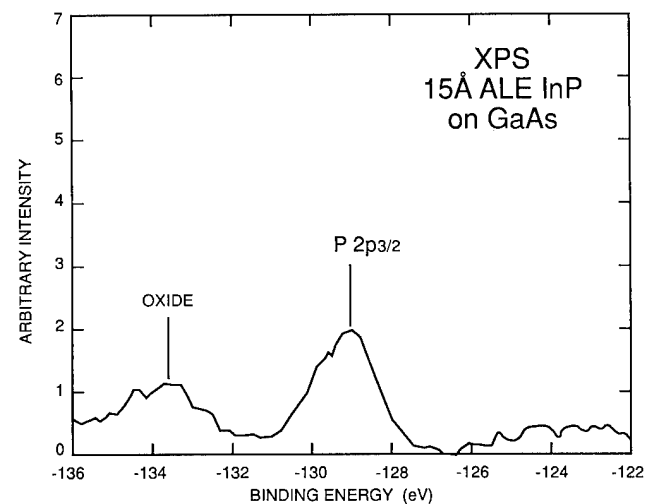


Fig. 9. An XPS spectrum of a GaAs surface that has been passivated with a 15 Å layer of InP ALE. The presence of phosphorus and phosphorous oxide is clearly shown.

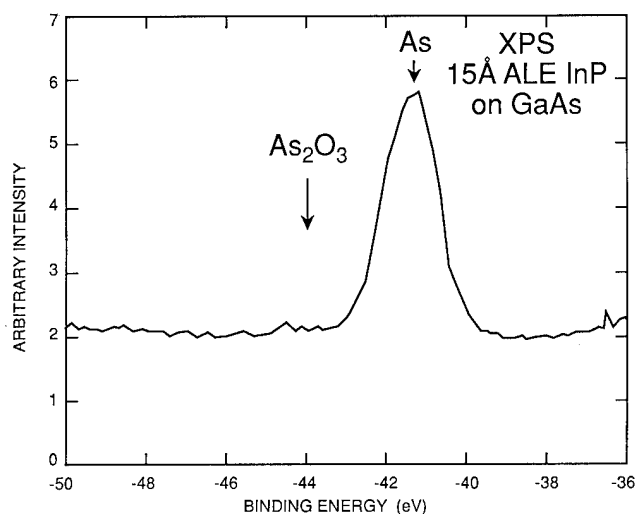


Fig. 10. An XPS spectrum of a GaAs surface that has been passivated with a 15 Å layer of InP ALE. The presence of arsenic and the absence of arsenic oxide are evident.

ion-implanted GaAs MESFET before and after passivation are shown in Fig. 12. The surface electric field which is determined from the Franz-Keldysh oscillations (features above the GaAs energy gap) did not change as the GaAs MESFET was passivated. The preservation of the surface electric field after passivation indicates that the built-in potential remained the same. The absence of arsenic oxide, the increase in PL intensity, and the preservation of the built-in potential suggest the potential of ultrathin ALE InP layers in devices.

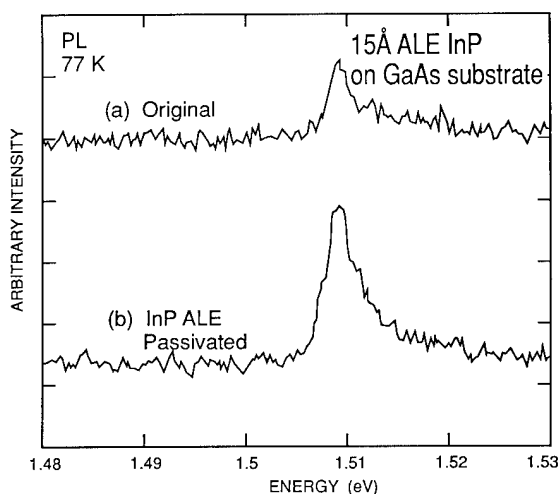


Fig. 11. 77 K PL spectra of an undoped GaAs substrate before and after InP ALE (15 Å) passivation. The peak corresponds to the energy gap of GaAs. An increase in the PL intensity by a factor of 2 is observed after passivation.

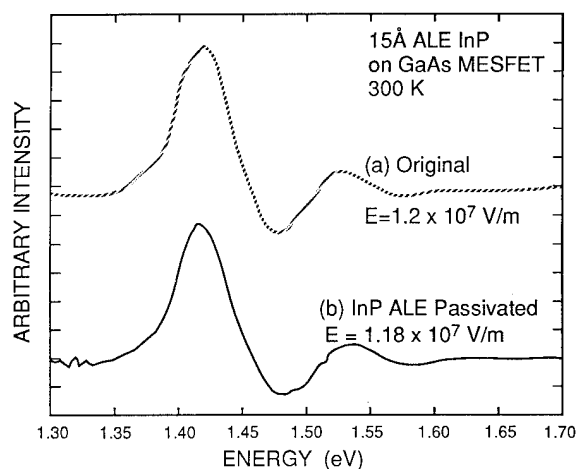


Fig. 12. 300 K spectra of an ion-implanted GaAs ( $3 \times 10^{17} \text{ cm}^{-3}$ ) MESFET structure before and after InP ALE (15 Å) passivation. The surface electric field extracted from the Franz-Keldysh oscillations remained the same after passivation.

#### 4. Conclusions

Self-limiting ALE growth of InP was observed using TMI and TBP at a growth temperature of 340 °C. The use of low total flow rates which required reasonable TBP flows yielded monolayer saturation. Substantial increases in the TMI fluxes and increases in growth temperatures beyond 340 °C resulted in growth rates exceeding 1 monolayer per cycle. Uniform growth of InP was verified by TEM and sputtered Auger profiling. The use of thin (15 Å) ALE InP layers as GaAs passivating layers showed the promise of these layers for device applications. The absence of arsenic oxide along with increases in PL intensity and the preservation of the built-in potential were observed with these passivating layers.

#### Acknowledgments

The authors are grateful to H. Statz and D. Masse for their unconditional support of the MOCVD research effort. Technical assistance in the preparation of the manuscript from S. Fischer and M. Stock is greatly appreciated.

#### References

- 1 Y. Sakuma, K. Kodama and M. Ozeki, *Jpn. J. Appl. Phys.*, 27 (1988) L2189.
- 2 W. K. Chen, J. C. Chen, L. Anthony and P. Liu, *Appl. Phys. Lett.*, 55 (1989) 987.
- 3 A. J. Neuhaufen and B. W. Wessels, *J. Appl. Phys.*, 71 (1992) 281.

- 4 D. Bertone, *J. Electron. Mater.*, 21 (1992) 265.
- 5 W. K. Chen, J. F. Chen, J. C. Chen, H. M. Kim, L. Anthony, C. R. Wie and P. L. Liu, *Appl. Phys. Lett.*, 55 (1989) 749.
- 6 R. P. Schneider, Jr. and B. W. Wessels, *Appl. Phys. Lett.*, 57 (1990) 1998.
- 7 W. E. Hoke, N. Pan and J. Carter, *US Patent 5077875*.
- 8 C. A. Lucas, P. D. Hatton, S. Bates, T. W. Ryan, S. Miles and B. K. Tanner, *J. Appl. Phys.*, 63 (1988) 1936.
- 9 C. A. Larsen and G. B. Stringfellow, *J. Cryst. Growth*, 75 (1986) 247.
- 10 F. Hyuga, T. Aoki, S. Sugitani, K. Asai and Y. Imamura, 1991 *MRS Fall Meet, Boston, MA, Abstracts*, MRS, Pittsburgh, PA, 1991, p. 209.
- 11 S. D. Offsey, J. M. Woodall, A. C. Warren, P. D. Kirchner, T. I. Chappell and G. D. Pettit, *Appl. Phys. Lett.*, 48 (1986) 475.
- 12 P. Viktorovitch, M. Gendry, S. K. Krawczyk, F. Kraft, P. Abraham, A. Bekkaoui and Y. Monteil, *Appl. Phys. Lett.*, 58 (1991) 2387.
- 13 H. Hasegawa, T. Saitoh, S. Konishi, H. Ishii and H. Ohno, *Jpn. J. Appl. Phys.*, 27 (1988) L2177.

# Laser-assisted atomic layer epitaxy of GaP in chemical beam epitaxy

Masahiro Yoshimoto, Atsushi Kajimoto\* and Hiroyuki Matsunami

Department of Electrical Engineering, Kyoto University, Sakyo, Kyoto 606-01 (Japan)

## Abstract

A new atomic layer epitaxy using a photo-process without alternate gas supply in chemical beam epitaxy is proposed. The effects of ultraviolet-laser irradiation on GaP growth at low substrate temperatures were studied in detail using triethylgallium (TEGa) and  $\text{PH}_3$ . The growth rate of GaP was enhanced by ultraviolet light emitted from an  $\text{N}_2$  laser. The growth rate increased with photon number and saturated above  $\sim 10^{17}$  photons  $\text{cm}^{-2}$  pulse. Under enough light intensity ( $2.7 \times 10^{17}$  photons  $\text{cm}^{-2}$  pulse), the growth rate was kept constant in a certain range of TEGa flow rate by  $\text{N}_2$  laser irradiation. This result opens monolayer growth by UV-irradiation under a simultaneous supply of source gases.

## 1. Introduction

Atomic layer epitaxy (ALE) of III–V semiconductors has been studied mainly in vapor phase epitaxy (VPE) [1–6]. It has suffered from a low growth rate. The main reason is due to an approach based on alternating supply of each reactant (Group III and V sources and a purge gas) with valve switching. The switching time of valves and the residence time of reactants in a reactor always limit the growth rate. Optimization of a reactor for ALE is one of the measures to increase the growth rate. In organometallic VPE using a specially designed reactor without switching gas supply, growth rates in the range of  $0.4\text{--}0.7 \mu\text{m h}^{-1}$  have been realized in the ALE mode [1].

Modification of the surface reaction by photo-irradiation is another measure to realize reasonable growth rate in ALE. Chemical beam epitaxy (CBE) promises to be an attractive technique for the growth of III–V semiconductors owing to excellent controllability of Group V sources with high vapor pressure. In CBE without cracking Group III metal–organics, the decomposition of metal–organics takes place only on a heated substrate, which brings about crystal growth dominated by surface reactions. The surface reactions of metal–organics are expected to be modified by photo-irradiation. We have achieved efficient photo-enhancement of GaP growth by  $\text{N}_2$ -laser irradiation in CBE [7]. The modification of the surface reaction will open a new mode in ALE.

In this report, we propose a new ALE process in CBE. Under simultaneous supply of source gases, de-

composition of adsorbed Group III metal–organics on a growing surface in a high vacuum is triggered by photo-irradiation with a short laser pulse ( $\sim 10$  ns). Following decomposition, the reaction of Group V on the growing surface leads to a layer-by-layer growth. Thus, an alternate gas supply may not be necessary in the new ALE.

## 2. Experimental details

The CBE system is shown in Fig. 1. The growth chamber with liquid  $\text{N}_2$  shrouds was evacuated to  $\sim 5 \times 10^{-10}$  torr with a diffusion pump before growth. Triethylgallium (TEGa) and  $\text{PH}_3$  were used as source gases. The temperature of TEGa was kept constant in a thermostat. The flow rates of TEGa ( $F_{\text{TEGa}}$ ) were pre-

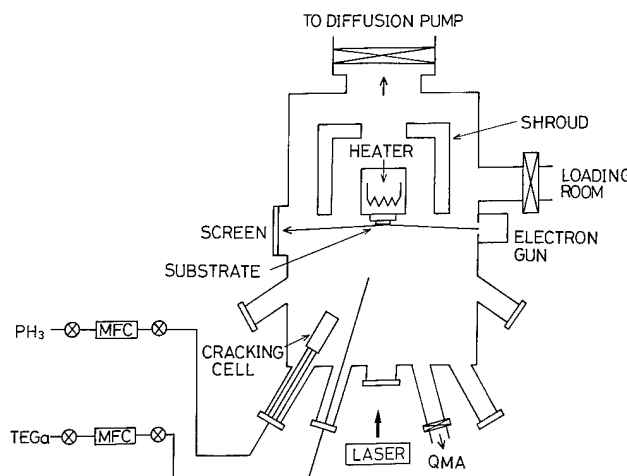


Fig. 1. Schematic diagram of growth system.

\*On leave from Nisshin Steel Co. Ltd, 3-5-3 Akebono, Tachikawa, Tokyo 190, Japan.

cisely controlled between 0.015 and 0.100 sccm by a mass-flow controller without  $H_2$  carrier gas.  $PH_3$  with a flow rate ( $F_{PH_3}$ ) from 0.06 to 1.0 sccm was precracked in a thermal cracking cell. In the cell, the cracking efficiency is estimated to be around 60% from the reduction rate in the peak intensity of 34 amu ( $PH_3$ ) in the mass spectrum detected by a quadrupole mass analyzer. The pressure of the chamber during epitaxy was maintained in the order of  $10^{-5}$  torr. The substrate temperature was varied between 290 and 500 °C. GaP with orientation of (100) or (111) was used as a substrate.

An  $N_2$  laser used for photo-irradiation was operated in pulse mode with a repetition rate of less than 20 Hz and a maximum power of 2 mJ. The ultraviolet light (337 nm) emitted from the laser was focused to change the irradiation intensity. The viewing port in the growth chamber for photo-irradiation was kept transparent during a series of growths. Since TEGa shows no absorption for wavelengths longer than 310 nm [8], TEGa has essentially no absorption in the gas phase for the  $N_2$  laser. The UV light is thought to be adsorbed by TEGa on a growing surface.

### 3. Results and discussion

#### 3.1. Photo-irradiation effects in GaP epitaxy

Without photo-irradiation, the growth rate in GaP epitaxy on a GaP (100) substrate decreases with decreasing temperature below 390 °C as shown in Fig. 2. The flow rates of TEGa and  $PH_3$  were kept at 0.020 and 0.20 sccm respectively. At lower substrate temperatures (320–360 °C), the growth rates of GaP are enhanced with UV light emitted from the  $N_2$  laser. As shown in Fig. 2, the growth rate of GaP reaches a certain value of  $0.40 \mu m h^{-1}$  with photo-irradiation, which is limited by the supply of TEGa.

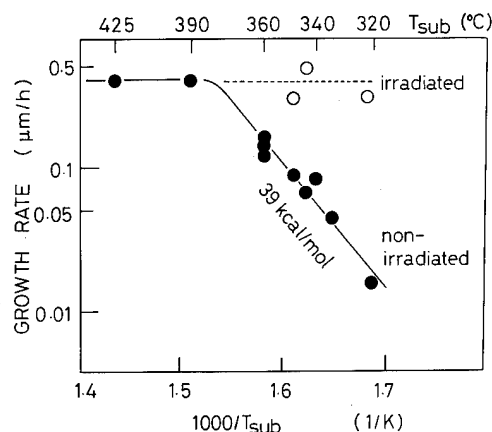


Fig. 2. Growth rate of GaP and its photo-irradiation effect.  $F_{TEGa} = 0.020$  sccm and  $F_{PH_3} = 0.20$  sccm.

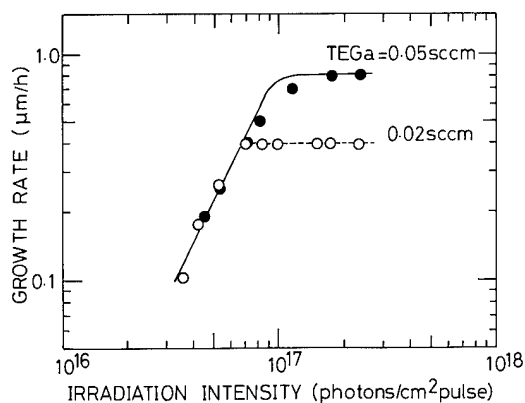


Fig. 3. Growth rate by photo-irradiation as a function of photon number.  $F_{PH_3}/F_{TEGa} = 10$ , substrate temperature = 350 °C, repetition rate of  $N_2$  laser = 7 Hz.

The growth enhancement increases with the irradiated photon number below  $\sim 1 \times 10^{17}$  photons  $cm^{-2}$  pulse (Fig. 3). The photon number was calculated by dividing the incident photon flux on a growing surface by the photo-enhanced area, assuming that the laser beam is spatially uniform. The repetition rate of the  $N_2$  laser was kept at 7 Hz. GaP (111) was used for substrates. Above the photon number, the enhancement is saturated at  $0.43 \mu m h^{-1}$  for  $F_{TEGa} = 0.020$  sccm. In Fig. 3, the saturated value of the growth rate becomes larger ( $0.81 \mu m h^{-1}$ ) in the case of  $F_{TEGa} = 0.050$  sccm.

The growth rate of  $0.81 \mu m h^{-1}$  on GaP (111) was obtained even for 1 Hz repetition by irradiation with  $1.0 \times 10^{17}$  photons  $cm^{-2}$  pulse. Then, the value of  $0.81 \mu m h^{-1}$  corresponds to  $0.71$  monolayers  $s^{-1}$  based on the monolayer thickness of  $3.15 \text{ \AA}$  on GaP (111) derived from the lattice constant ( $5.45 \text{ \AA}$ ). The number of Ga atoms per unit area of GaP (111) monolayer is estimated to be  $7.78 \times 10^{14}$  atoms  $cm^{-2}$  using the lattice constant. Thus, the number of Ga atoms deposited on a growing surface was calculated to be  $5.5 \times 10^{14}$  atoms  $cm^{-2} s^{-1}$  from the growth rate of  $0.81 \mu m h^{-1}$ . If the photo-enhancement efficiency is defined as the ratio of the number of deposited Ga atoms to the irradiating photon number per unit area per unit time, the efficiency is estimated to be around  $5.5 \times 10^{-3}$ .

A transient increase in the surface temperature under laser irradiation was calculated to be 40 °C at most, based on a calculation for one-dimensional heat conduction [9–11]. The time for heating by irradiation is of the same order as the pulse width of the laser ( $\sim 10$  ns), and the average surface temperature is not increased by irradiation. Also, GaP was deposited even at 200 °C with the same growth rate at 350 °C. Thereby, the enhancement of growth rate by  $N_2$  laser irradiation is believed to be due to photochemical reactions. Since TEGa in the gas phase shows no absorption for longer wavelengths than 310 nm, adsorbed TEGa on a

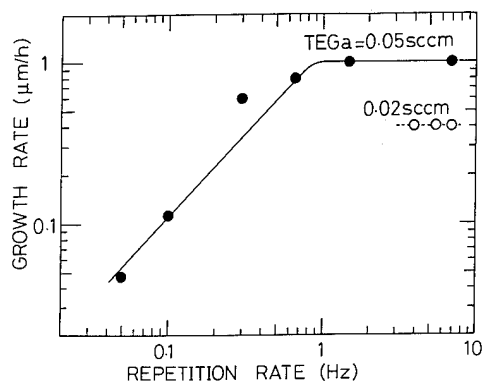


Fig. 4. Growth rate by photo-irradiation as a function of repetition of  $N_2$  laser.  $F_{TEGa}=0.050$  and  $0.020$  sccm,  $F_{PH_3}/F_{TEGa}=10$ , substrate temperature =  $350^\circ\text{C}$ , photon number =  $1.5 \times 10^{17}$  photons  $\text{cm}^{-2}$  pulse.

growing surface may absorb UV light, which brings growth enhancement.

### 3.2. Applicability to atomic layer epitaxy

Figure 4 shows the growth rate on GaP(111) at  $350^\circ\text{C}$  as a function of the repetition rate of the  $N_2$  laser. The growth rate increases linearly with the repetition rate below 1 Hz, which shows that the growth rate per laser pulse is constant. The slope in Fig. 4 corresponds to  $0.71$  monolayer growth per pulse based on a monolayer thickness of  $3.15 \text{ \AA}$  on GaP (111). Above 1 Hz, the growth rate was kept constant. A time of around 1 s is a critical value for the photo-process.

A TEGa flow rate of  $0.050$  sccm gives a TEGa supply of  $2.2 \times 10^{16}$  molecules  $\text{s}^{-1}$  using Avogadro's number. The TEGa gas spreads on the substrate with a diameter of around  $4\text{--}6$  cm ( $13\text{--}28 \text{ cm}^2$ ), estimated from the thickness distribution of the grown layer. The number of TEGa molecules coming onto the growing surface per unit time is calculated to be  $0.80\text{--}1.7 \times 10^{15}$  molecules  $\text{cm}^{-2} \text{ s}^{-1}$  by dividing  $2.2 \times 10^{16}$  molecules  $\text{s}^{-1}$  by the above areas. The number of Ga atoms on the (111) surface of GaP is  $7.78 \times 10^{14} \text{ cm}^{-2}$ . If the sticking probability of TEGa on GaP is close to unity, it takes  $0.5\text{--}1$  s to complete one monolayer adsorption of TEGa. For growth under laser irradiation with a repetition rate higher than 1 Hz, the growth rate per pulse is thought to be limited by the adsorption and/or desorption process of TEGa.

Based on the above argument for the result in Fig. 4, the growth rate per unit time by irradiation with a repetition rate of 7 Hz seems to be the same as that with 1 Hz. Thereby, the values of  $0.43$  and  $0.81 \mu\text{m h}^{-1}$  with 7 Hz in Fig. 3 can be obtained even with 1 Hz. By dividing the growth rate per unit time by the total number of laser pulses ( $3600 \text{ shots h}^{-1}$ ), the values of  $0.43$  and  $0.81 \mu\text{m h}^{-1}$  correspond to  $0.38$  and  $0.71$  monolayer growth per pulse based on the monolayer thickness of GaP (111).

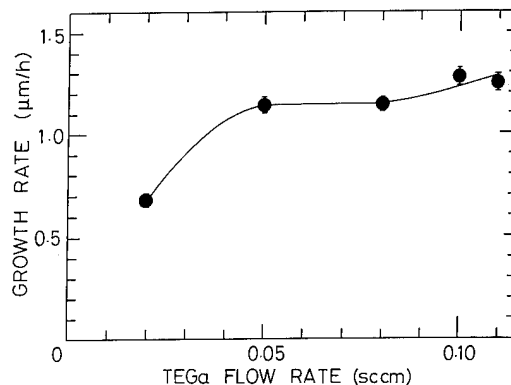


Fig. 5. Growth rate by photo-irradiation as a function of TEGa flow rate.  $F_{PH_3}/F_{TEGa}=10$ , substrate temperature =  $350^\circ\text{C}$ , repetition rate of  $N_2$  laser = 7 Hz, photon number =  $2.7 \times 10^{17}$  photons  $\text{cm}^{-2}$  pulse.

Figure 5 shows the growth rate per unit time as a function of TEGa flow rate at a substrate temperature of  $350^\circ\text{C}$ . The  $F_{PH_3}/F_{TEGa}$  ratio was maintained at 10 with a photon number of  $2.7 \times 10^{17}$  photons  $\text{cm}^{-2}$  pulse. The number of  $2.7 \times 10^{17}$  photons  $\text{cm}^{-2}$  is enough to saturate the growth rate to a value limited by the supply of TEGa as shown in Fig. 3. Cross-sectional images of epilayers by a secondary electron microscope indicated that the growth rate in the non-irradiated area was less than  $0.05 \mu\text{m h}^{-1}$ . The growth rate in the irradiated area was kept constant at  $1.16 \mu\text{m h}^{-1}$  in the flow rate region between  $0.050$  and  $0.080$  sccm. The constant growth rate corresponds to around one-monolayer growth per pulse. Although the mechanism of saturation in the growth rate is not clear, this result indicates the feasibility of a new photo-process to ALE. In this process, monolayer growth can be obtained with simultaneous supply of both Group III and V sources, which gives higher throughput in ALE.

## 4. Conclusions

The effects of ultraviolet-light irradiation on GaP epitaxy have been investigated in CBE using TEGa and thermally cracked  $\text{PH}_3$ . The growth rate of GaP was enhanced by ultraviolet light emitted from an  $N_2$  laser with a photon number of  $\sim 10^{17}$  photons  $\text{cm}^{-2}$  pulse. The growth rate was kept constant in a certain range of TEGa flow rate by  $N_2$  laser irradiation. This preliminary result will open a new ALE mode by UV-laser irradiation without an alternating gas supply in CBE.

## Acknowledgment

This work was partially supported by The Grant-in-Aid on Priority Area Research on 'Photo-Excited Process' promoted by the Ministry of Education, Science and Culture, Japan.

## References

- 1 P. C. Colter, S. A. Hussien, A. Dip, M. U. Erdogan, W. M. Duncan and S. M. Bedair, *Appl. Phys. Lett.*, 59 (1991) 1440.
- 2 J. Nishizawa and T. Kurabayashi, *J. Cryst. Growth*, 93 (1988) 98.
- 3 S. P. Denbaars, P. D. Dapkus, C. A. Beyler, A. Hariz and K. M. Dzurko, *J. Cryst. Growth*, 93 (1988) 195.
- 4 K. Mori, M. Yoshida, A. Usui and H. Terao, *Appl. Phys. Lett.*, 52 (1988) 27.
- 5 K. Kodama, M. Ozeki, Y. Sakuma, K. Mochizuki and N. Ohtsuka, *J. Cryst. Growth*, 99 (1990) 535.
- 6 A. Doi, Y. Aoyagi and S. Namba, *Appl. Phys. Lett.*, 49 (1986) 785.
- 7 M. Yoshimoto, K. Ozasa and H. Matsunami, *J. Appl. Phys.*, 70 (1991) 5708.
- 8 H. Okabe, M. K. Emadi-babaki and V. R. McCrary, *J. Appl. Phys.*, 69 (1991) 1730.
- 9 H. S. Carslaw and J. C. Jaeger, *Conduction of Heat in Solids*, Oxford University Press, 2nd edn., London, 1959, pp. 78, 304.
- 10 J. F. Ready, *Effects of High Power Laser Radiation*, Academic Press, London, 1971, p. 67.
- 11 W. W. Duley, *Laser Processing and Analysis of Materials*, Plenum Press, New York, 1983, p. 85.

# Atomic layer epitaxy of AlAs and $(\text{AlAs})_n(\text{GaAs})_n$

M. Ishizaki\*, N. Kano, J. Yoshino and H. Kukimoto

Imaging Science and Engineering Laboratory, Tokyo Institute of Technology, 4259 Nagatsuda, Midori-ku, Yokohama 227 (Japan)

## Abstract

An overview is given of the recent achievements of self-limiting growth for AlAs by metal–organic vapor phase epitaxy using dimethylaluminumhydride and arsine as source materials, and its application in  $(\text{AlAs})_n(\text{GaAs})_n$  short-period superlattices. There is a discussion of the possible Al configurations for two monolayers of self-limiting growth, the problems of carbon incorporation in the layers and the instability of dimethylaluminumhydride.

## 1. Introduction

Atomic layer epitaxy (ALE) of III–V compound semiconductors, especially of GaAs, has been extensively studied by a variety of growth methods including metal–organic vapor phase epitaxy (MOVPE), molecular beam epitaxy (MBE), metal–organic molecular beam epitaxy (MOMBE) and hydride vapor phase epitaxy. In promoting research in this field it is essential to establish the ALE growth of other materials, which are to be combined with GaAs for fabricating novel heterostructures such as short-period superlattices, quantum wires and dots by taking advantage of the attractive features of ALE. To this effect, the ALE growth of AlAs can be regarded as most important.

ALE growth of AlAs has already been studied by several research groups. Ozeki *et al.* [1] observed self-limiting AlAs growth at two monolayers per cycle using an alternate supply of trimethylaluminum (TMAI) and arsine at 500 °C. DenBaars *et al.* [2] and Meguro *et al.* [3] achieved one monolayer self-limiting growth using TMAI at 460 °C, and triethylaluminum (TEAI) at 350–400 °C under laser irradiation respectively.

In view of these results in the literature, we have come to believe that the self-limiting growth of AlAs depends largely on the reactor geometry and Al source used for growth since ALE is a surface-kinetic limiting growth. Using a growth system capable of fast gas introduction and dimethylaluminum hydride (DMAIH) as the Al source, we have observed one and two monolayer self-limiting growths of AlAs depending on the DMAIH supply and growth temperature [4]. Taking advantage of the temperature range where self-limiting growth for AlAs overlaps with that for GaAs, we have fabricated

$(\text{AlAs})_n(\text{GaAs})_n$  short-period superlattices entirely by ALE, for the first time, at a constant growth temperature [5].

First, we will present the features of our growth system which we believe are influential in the resultant growth. Next, we will show characteristic behavior of the ALE growth of AlAs using DMAIH and arsine, and its application for  $(\text{AlAs})_n(\text{GaAs})_n$  short-period superlattices. Finally, discussion is made on the possible growth mechanisms and the issue of carbon incorporation.

## 2. Growth system

The growth system consisted of a horizontal cold wall quartz reactor, as shown in Fig. 1, with a rectangular cross-section of 72 mm<sup>2</sup>, width of 24 mm and height of 3 mm, and with a tapered region of about 180 mm length for stabilizing gas flow. A typical flow velocity of about 90 m s<sup>−1</sup> was attained at a hydrogen flow rate of 5 l min<sup>−1</sup> under a pressure of 10 Torr by operating a large capacity mechanical booster pump. For the growth of GaAs or AlAs by conventional MOVPE techniques, no unwanted deposition was observed on the inner wall of the reactor at the upper stream of the substrate, implying that decomposition of source materials outside the boundary layer on the substrate and back flow of the reactant gases were minimized. The source materials were supplied using a vent-and-run system which ensures automatic pressure control and a small dead-space manifold operated by a digital sequence controller.

It has been confirmed that ALE growth of GaAs using trimethylgallium and arsine can be successfully achieved by this growth system as shown in Fig. 2(a).

## 3. Growth of AlAs and $(\text{AlAs})_n(\text{GaAs})_n$

Using this growth system, we tried to grow AlAs by an alternate supply of TMAI and arsine. However, no

\*Present address: Technical Research Institute, Toppan Printing Co., Ltd, 4-2-3 Takanodai-Minami, Sugito-machi, Kita-Katsushikagun, Saitama-ken 345, Japan.



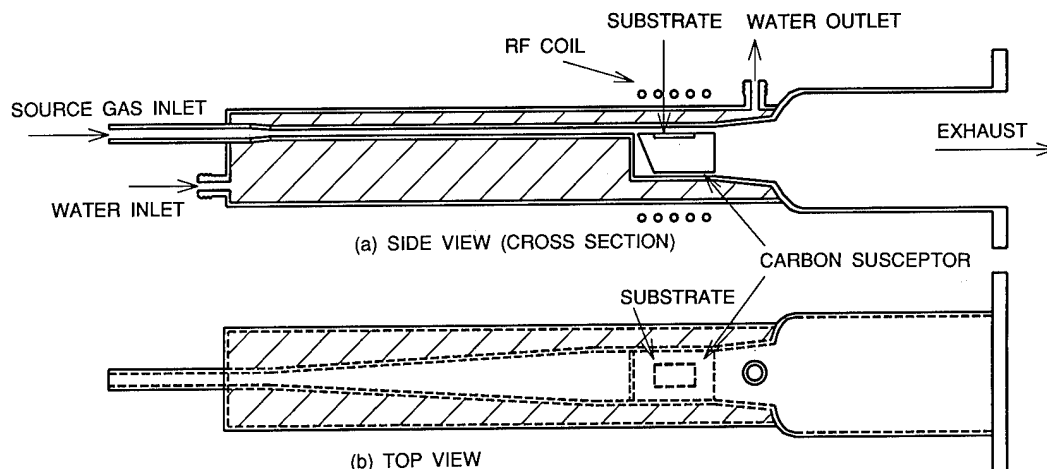


Fig. 1. Side and top views of the reactor.

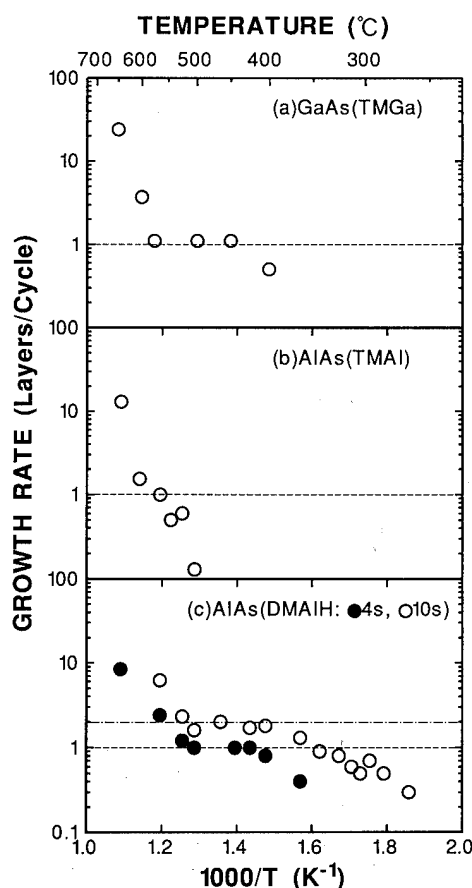


Fig. 2. Growth rate as a function of growth temperature for (a) GaAs grown using TMGa, (b) AlAs grown using TMAI and (c) AlAs grown using DMAIH.

self-limiting growth was observed at the growth temperatures investigated as shown in Fig. 2(b), which is contrary to the result obtained by Ozeki *et al.* [1]. We thought that this discrepancy was due to the different growth system or different TMAI used in our study. We

were trying to investigate the preparation and purification processes of TMAI, when we happened to find out that a specially treated TMAI source containing DMAIH contributes to the enhanced growth of AlAs at low temperatures.

The result of AlAs grown using DMAIH shows one and two monolayer self-limiting growth as shown in Fig. 2(c). It is noted that the temperature range of self-limiting growth is fairly wide and overlaps with that of GaAs. These self-limiting growths were also evidenced by growth rate behavior upon changing pulse width and flow rate of DMAIH [4, 5].

Taking advantage of this observation, we fabricated short-period superlattices of (AlAs)<sub>n</sub> (GaAs)<sub>n</sub> with  $n = 3, 5$  and 10 on GaAs substrates at a growth temperature of 470 °C. The formation of superlattices was confirmed by the observation of X-ray diffraction satellite peaks as shown in Fig. 3.

#### 4. Discussion

The observed behavior of one and two monolayer self-limiting growth can be reasonably explained as given below. For Al deposition on an As-stabilized AlAs (100) surface, an Al atomic layer is first formed so that Al atoms occupy the Al sites of the AlAs lattice resulting in one monolayer self-limiting growth. This would be the case in our relatively low supply of DMAIH and also for the growth condition used by Yokoyama *et al.* [6], where they achieved one monolayer growth of AlAs using thermally decomposed TMAI to form DMAIH in a MOVPE reactor. For more than one monolayer per cycle Al deposition, there are two possibilities which are depicted in Fig. 4. One is that the (100) plane of the Al metal lattice, which is lattice matched to AlAs when it is rotated by 45°, is

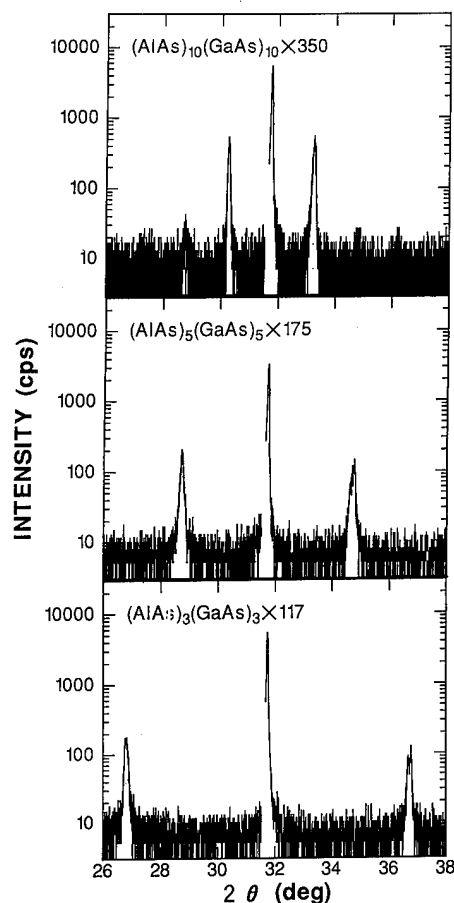


Fig. 3. X-ray diffraction patterns of (AlAs)<sub>n</sub> (GaAs)<sub>n</sub> superlattices ( $n = 3, 5$  and  $10$ ).

formed by accommodating Al atoms to as many as twice the number of Al sites in the AlAs lattice, as shown in Fig. 4(a). The other is that Al atoms also occupy the As site of the AlAs lattice to form a second Al atomic layer as shown in Fig. 4(b). Any of these would result in two monolayer self-limiting growth in the case of relatively high DMAIH supply. According to the proposed Al configurations a question may arise as to whether intermediate self-limiting growths such as 1.5 monolayer per cycle are also possible. However, we believe that the Al configurations responsible for such a possibility are energetically unstable in view of the fact that the two monolayer growth immediately follows the one monolayer growth with increasing Al source supply.

As described above, ALE of AlAs was successfully achieved over a wide temperature range by using DMAIH as the Al source. However, a few problems still exist with its device application. One is the incorporation of carbon in the AlAs layer. Figure 5 shows X-ray diffraction patterns of AlAs layers grown by MOVPE and ALE. The diffraction peak of AlAs layers

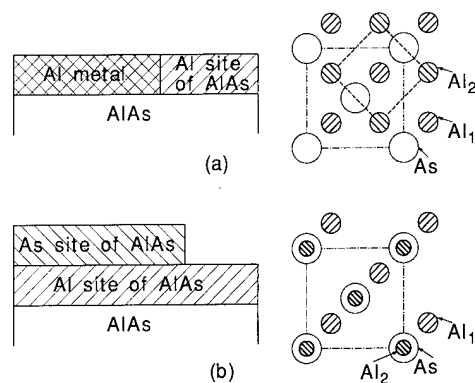


Fig. 4. A possible mechanism of one and two monolayer AlAs growth.

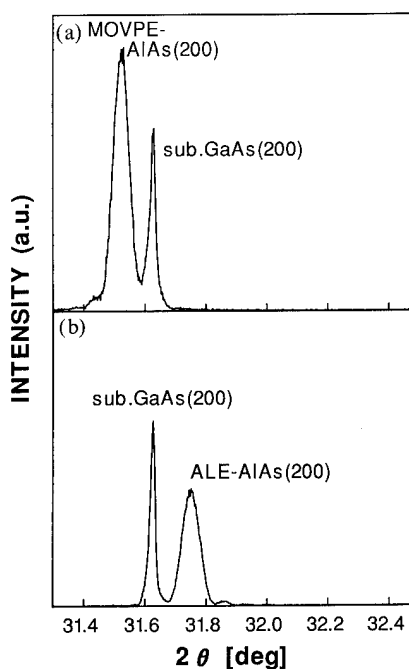


Fig. 5. X-ray diffraction patterns of AlAs layers grown on GaAs substrates by (a) MOVPE and (b) ALE.

grown by MOVPE appears at a diffraction angle lower than that of GaAs substrate as shown in Fig. 5(a) since the MOVPE-grown AlAs lattice is slightly larger than the GaAs lattice. However, the diffraction peak of the AlAs grown by ALE appears at the opposite side as shown in Fig. 5(b), implying that the AlAs layer has a smaller lattice constant. Such a curious phenomenon can be explained by assuming that carbon incorporation in the layer resulted in a decrease in the average lattice constant of AlAs. The estimated carbon concentration of mid  $10^{20} \text{ cm}^{-3}$  was also confirmed by the analysis of secondary ion mass spectroscopy. Several efforts have been made to reduce the carbon content, which include an increase in growth temperature, an increase in pressure, a decrease in DMAIH supply and

an increase in arsine supply. As a result, it has been found that the carbon incorporation is reduced to some extent by high temperature one monolayer ALE growth, which is achieved by decreasing the DMAIH supply, and the increase of AsH<sub>3</sub> supply. Further study is necessary to dramatically reduce the carbon content.

Another problem is the instability of DMAIH over many long growth runs. It is well known that DMAIH can be in the form of dimers, trimers and much larger molecules. During the introduction of hydrogen carrier gas into the DMAIH container, its structure would change resulting in a change of growth conditions. Further studies yet to be done would include the replacement of hydrogen carrier gas by inert gases and the use of alternative Al sources.

## 5. Summary

After presenting the features of our growth system, which we believe are influential in the resultant growth,

we have shown the characteristic behavior of ALE growth of AlAs using DMAIH and arsine, and its application to (AlAs)<sub>n</sub> (GaAs)<sub>n</sub> short-period superlattices. Finally, there was a discussion of the possible Al configurations for the observed one and two monolayer self-limiting growth, and the issues of carbon incorporation in ALE-grown AlAs layers and the long-term instability of the DMAIH source.

## References

- 1 M. Ozeki, K. Mochizuki, N. Ohtsuka and K. Kodama, *J. Vac. Sci. Technol. B*, **5** (1987) 1184.
- 2 S. P. DenBaars, P. D. Dapkus, C. A. Beyler, A. Hariz and K. M. Dzurko, *J. Cryst. Growth*, **93** (1988) 195.
- 3 T. Meguro, S. Iwai, Y. Aoyagi, K. Ozaki, Y. Yamamoto, T. Suzuki, Y. Okano and A. Hirata, *J. Cryst. Growth*, **99** (1990) 540.
- 4 M. Ishizaki, N. Kano, J. Yoshino and H. Kukimoto, *Jpn. J. Appl. Phys.*, **30** (1991) L428.
- 5 M. Ishizaki, N. Kano, J. Yoshino and H. Kukimoto, *Jpn. J. Appl. Phys.*, **30** (1991) L435.
- 6 H. Yokoyama, M. Shinohara and N. Inoue, *Appl. Phys. Lett.*, **60** (1992) 377.

# Study of photocatalytic growth-rate enhancement in MOMBE of GaAs on ZnSe by surface photoabsorption

Akihiko Yoshikawa, Akiyoshi Iguchi and Shigeki Yamaga

*Department of Electrical and Electronics Engineering, Faculty of Engineering, Chiba University, 1–33 Yayoi-cho, Inage-ku, Chiba-shi 263 (Japan)*

## Abstract

In order to lower the epitaxy temperature of GaAs on ZnSe, the effect of photoirradiation on the growth and/or reaction mechanism in the initial growth stage in MOMBE of GaAs has been studied by utilizing the surface photoabsorption technique. It has been found that excess carriers photoinduced in ZnSe can contribute to the decomposition of TEGa on ZnSe, but those photoinduced in GaAs cannot. This has been attributed to the photocatalytic effect of the decomposition of TEGa on the ZnSe surface. It has been confirmed that photoirradiation is effective for enhancing the growth rate at low temperatures, resulting in decreased epitaxy temperature of GaAs on ZnSe.

## 1. Introduction

Strained layer superlattices (SLSs) consisting of wide-gap II–VI compound barriers and III–V compound wells have attracted considerable attention as a new material for short-wavelength optoelectronic devices. In particular, ZnSe/GaAs SLSs are promising because their energy bandgap covers wavelengths from the blue/green to red region [1, 2]. Further, the lattice mismatch between ZnSe and GaAs is quite small.

One of the difficulties in realizing high quality ZnSe/GaAs SLSs with atomically abrupt interfaces is the difference in the optimum growth temperature; the growth temperature for GaAs (500–600 °C) is much higher than that for ZnSe (250–350 °C). This results in difficulty in growing high quality GaAs and ZnSe layers at the same growth temperature. Further, the growth of GaAs on ZnSe at such high temperatures is quite difficult because the probability of the As precursors adhering to ZnSe is quite small [3, 4]. Therefore, a reduction in the growth temperature of GaAs on ZnSe is worthy of investigation. Decreased growth temperature is also favorable for reducing cross-diffusion at the interface.

In this paper, we investigate how to lower the epitaxy temperature of GaAs on ZnSe. Thus growth and/or reaction kinetics in the initial growth stage of photoassisted metal–organic molecular beam epitaxy (MOMBE) of GaAs on ZnSe has been studied using a surface photoabsorption (SPA) technique [5]. It will be shown that the photoinduced excess carriers can contribute to the decomposition of Ga precursors, resulting in decreased growth temperatures.

## 2. Experimental details

MOMBE was used as a growth method, and both GaAs and ZnSe layers were grown in the same growth chamber. Dimethyl zinc (DMZn) and hydrogen selenide ( $\text{H}_2\text{Se}$ ) were used as sources for ZnSe, and triethyl gallium (TEGa) and diethyl arsine hydride (DEAsH) were used for GaAs. If necessary, DMZn,  $\text{H}_2\text{Se}$ , and DEAsH were thermally cracked in a cracking cell before reaching the substrate. Semi-insulating (001) GaAs was used as a substrate.

An argon (Ar) ion laser was used as an excitation light source because it has several emission lines whose energies are below and above the energy bandgap of ZnSe at growth temperatures of 250–400 °C [6]. The photon energy of the 488 nm emission line is well above the bandgap of ZnSe and that of the 514.5 nm line is below the bandgap, though it becomes almost the same as the bandgap of ZnSe at 400 °C. Taking this into account, the 488 nm line was used mainly as an excitation light source. The laser line was normally incident on the substrate surface and its typical power intensity was kept as low as 40 mW cm<sup>-2</sup> compared with conventional laser-assisted ALE of GaAs [7].

First, a thin ZnSe layer of thickness 130 nm was grown on GaAs at 300 °C using thermally cracked DMZn and  $\text{H}_2\text{Se}$  sources [8]. Following this, the substrate temperature was increased up to that for GaAs growth. In order for the ZnSe layer surface to be Zn-terminated until just before the growth of GaAs, the DMZn flow was kept unchanged until the growth of GaAs began. Further, TEGa and DEAsH were alternately supplied to the ZnSe layer surface, and their

decomposition mechanism both with and without photoirradiation has been investigated by using the SPA technique. A 632.8 nm line from a He-Ne laser was used as a probe light for SPA and the incident angle was set at  $70^\circ$  toward  $[110]$ . The SPA signals were acquired and analyzed by a computer system.

### 3. Results and discussion

#### 3.1. Effect of photoirradiation on the decomposition of TEGa and DEAsH

Figure 1 shows how photoirradiation (488 nm) affects the SPA signals for the alternate supply of TEGa and DEAsH on a Zn-terminated ZnSe surface at  $400^\circ\text{C}$ ; Fig. 1(a) and (b) are the cases without and with photoirradiation respectively. In this experiment, DEAsH was not thermally cracked and the source-gas supply was initiated by DEAsH. It is shown in Fig. 1(a) (*i.e.* the case without photoirradiation) that no significant signal change is observed. When irradiated with photons, however, it is clearly shown that the SPA signal is greatly affected especially during the TEGa-supply cycle.

The notable features shown in Fig. 1(b) are:

- (1) for the first TEGa-supply, the SPA signal decreases at first but it soon begins to increase;
- (2) for the second TEGa-supply, the SPA signal increases continuously;
- (3) no significant signal change is observed during the DEAsH-supply cycle.

According to the results reported previously for SPA signals of the epitaxy of GaAs [9], it is known that

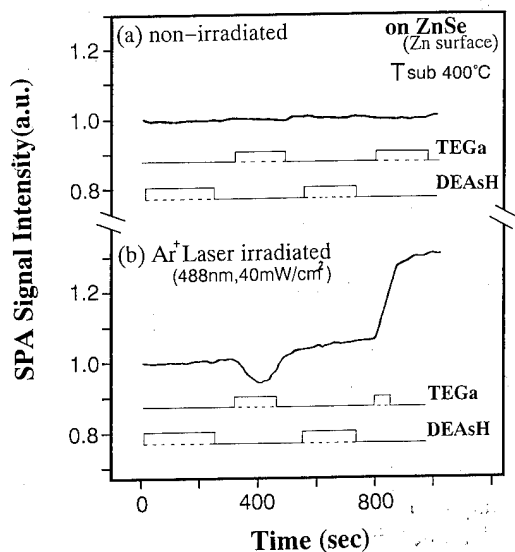


Fig. 1. The effect of photoirradiation (488 nm) on the SPA signals for the alternate supply of TEGa and DEAsH to a Zn-terminated ZnSe surface at  $400^\circ\text{C}$ : (a) non-irradiated; (b) Ar<sup>+</sup> laser irradiated.

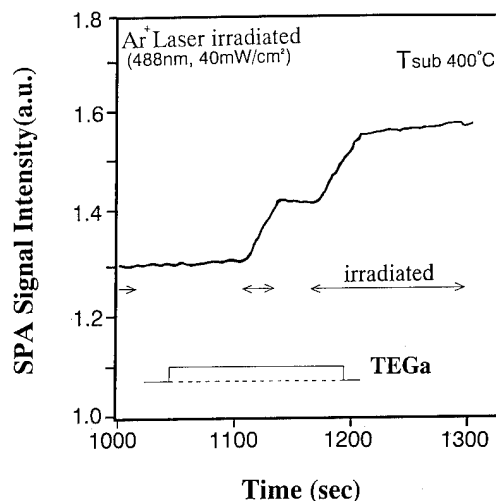


Fig. 2. The effect of intermittent photoirradiation on the SPA signal during TEGa supply. The experiment was performed in succession to that shown in Fig. 1(b).

under the experimental conditions stated above, the intensity of the SPA signal for a Ga-terminated surface is lower than that for As-terminated. It is also known that the SPA signal begins to increase if the surface of the layer is covered by high-density small Ga droplets (*i.e.* excess Ga atoms of more than one monolayer). Therefore, it has been found that TEGa can be decomposed on a ZnSe surface by irradiating with a 488 nm Ar laser line. Further, the results shown in Fig. 1 indicate that DEAsH cannot be decomposed at  $400^\circ\text{C}$  even under photoirradiation. In fact, no deposition of a GaAs layer could be observed when using uncracked DEAsH even under photoirradiation, though GaAs layers could be grown when using thermally cracked DEAsH.

In order to confirm further that TEGa can be decomposed by irradiation with photons, the effect of intermittent photoirradiation on the SPA signal during the TEGa-supply was investigated. In succession to the experiment shown in Fig. 1(b), TEGa was supplied to the same sample and the 488 nm line was irradiated intermittently as indicated in Fig. 2. It can be seen clearly that the SPA signal increases only when both the TEGa supply and Ar ion irradiation are coincident. This also indicates that TEGa can be decomposed by photoirradiation. The reason why the SPA signal still increases slightly after termination of the TEGa supply is attributed to incomplete gas flow termination.

#### 3.2. Effect of As precursors on the decomposition of TEGa

As shown in Fig. 1, when using uncracked DEAsH, no SPA signal change was observed apart from that due to photoirradiation. In order to investigate the

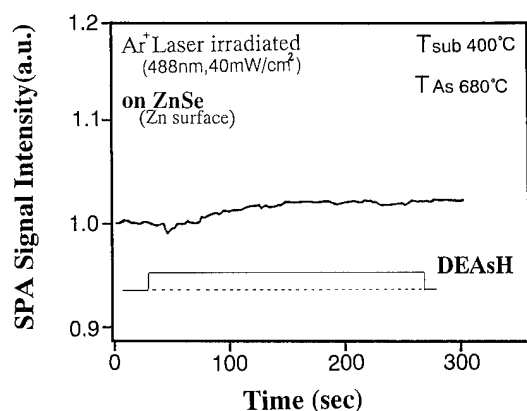


Fig. 3. SPA signal when thermally cracked DEAsH was supplied to Zn-terminated ZnSe.

effect of As precursors on the SPA signal, experiments using thermally cracked DEAsH were performed.

Figure 3 shows how the SPA signal changes when DEAsH cracked at 680 °C is supplied to Zn-terminated ZnSe. It can be seen that the SPA signal intensity increases when cracked DEAsH is supplied and it tends to saturate quite soon. This indicates that an As monolayer can be formed on the surface. This is quite different from the result shown in Fig. 1. It was found that only when DEAsH was thermally cracked could GaAs layers be grown, and when cracked DEAsH and TEGa were supplied alternately, SPA signal-intensity oscillations corresponding to layer-by-layer growth of GaAs were observed.

On supplying TEGa in succession to the formation of an As layer, it was confirmed that the SPA signal intensity began to decrease just after the TEGa supply. This is similar to the case shown in Fig. 1. These results indicate that TEGa can be decomposed on photoirradiation in both cases where cracked and/or uncracked DEAsH are on ZnSe. In order to investigate the effect of As precursors on the decomposition of TEGa on ZnSe, TEGa was supplied directly to Zn-terminated ZnSe and the corresponding SPA signals were observed; the result is shown in Fig. 4. Unlike the cases in which As precursors were supplied at first, the SPA signal intensity is kept unchanged in the beginning and begins to increase after a considerable amount of "incubation" time. It should be noted that no decrease in the SPA signal was observed in this case. This indicates that a Ga monolayer cannot be formed and high-density small Ga droplets are formed from the beginning. Comparing the results shown in Figs. 1 and 4, it was found that As precursors on the ZnSe formed by using both cracked and uncracked DEAsH affect the decomposition of TEGa on ZnSe. Although the mechanism is not clear at present, we suppose the presence of As precursors on ZnSe to affect the adsorption of TEGa on the surface.

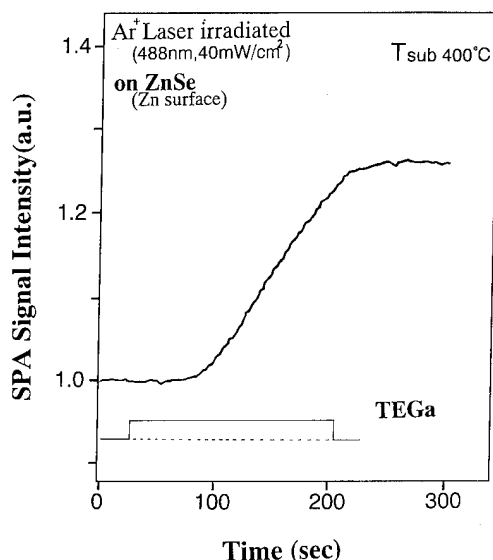


Fig. 4. SPA signal when TEGa was supplied directly to Zn-terminated ZnSe.

### 3.3. Effect of ZnSe layer on the decomposition of TEGa

Finally, the effects on the decomposition of TEGa of (1) the presence of a ZnSe layer and (2) photoirradiation were investigated.

First, in order to investigate how the ZnSe layer affects the decomposition of TEGa, the source gases were supplied directly onto GaAs substrate at 400 °C, and the SPA signal was observed. Although DEAsH and TEGa were supplied alternately onto GaAs under photoirradiation, no change in the SPA signal was observed. This indicates that photoinduced excess carriers in GaAs cannot contribute to the decomposition of TEGa. Therefore, it has been found that the presence of a ZnSe layer is essential for the decomposition of TEGa under photoirradiation.

Next, in order to investigate how photoirradiation affects the decomposition of TEGa, a 514.5 nm line from an Ar ion laser was used as an excitation light instead of the 488 nm line, and SPA signals were observed. The results are shown in Fig. 5. Unlike the case using the 488 nm line, however, no change in the SPA signal was detected during the TEGa supply when using the 514.5 nm line. As already stated, the photon energy of the 514.5 nm line is almost the same as the bandgap energy of ZnSe at the growth temperature, resulting in insufficient photoabsorption by ZnSe layers as thin as 130 nm. This indicates that photoinduced excess carriers in ZnSe play an important role in the decomposition of TEGa under photoirradiation.

The results mentioned in this section are very similar to those observed in the photoassisted MOVPE of ZnSe [10], where growth rate enhancement by photoirradiation was observed.

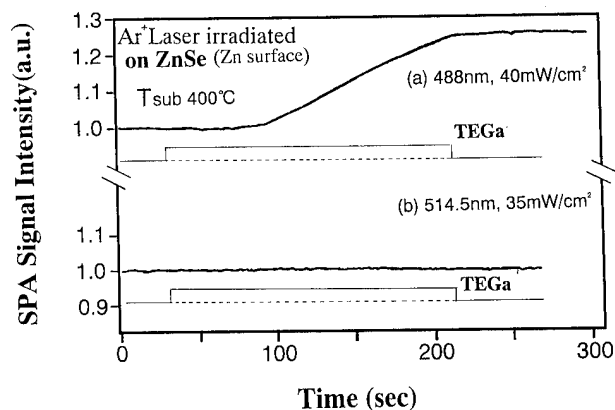


Fig. 5. The effect of photon energy on the decomposition of TEGa on ZnSe. The photon energy of the 488 nm line is well above the energy bandgap of ZnSe at the growth temperature, resulting in sufficient photoabsorption by the ZnSe layer. However, the energy of the 514.5 nm line is almost the same as the bandgap, resulting in insufficient photoabsorption by ZnSe layers as thin as 130 nm.

radiation is attributed to the photocatalytic phenomena of photoinduced excess carriers (probably holes) on ZnSe. Therefore, we believe that the decomposition of TEGa resulting in growth rate enhancement of GaAs at low temperatures will also be attributed to photocatalysis by the photoinduced excess carriers (probably excess holes) on ZnSe.

#### 4. Conclusion

In order to lower the epitaxy temperature of GaAs on ZnSe, the effect of photoirradiation on the growth and/or reaction mechanism in the initial growth stage of MOMBE of GaAs has been studied utilizing the

SPA technique. It has been found that excess carriers photoinduced in ZnSe can contribute to the decomposition of TEGa on ZnSe, but those photoinduced in GaAs cannot. This has been attributed to the photocatalytic effect on the decomposition of TEGa on the ZnSe surface. It has been confirmed that photoirradiation is effective for enhancing the growth rate at low temperatures, resulting in a decreased epitaxy temperature for GaAs on ZnSe.

#### Acknowledgments

This work was partly supported by Grants-in-Aid for Scientific Research and for Scientific Research on Priority Areas from The Ministry of Education, Science and Culture of Japan.

#### References

- 1 M. Kumagai and T. Takagahara, *Phys. Rev. B*, **40** (1989) 12 359.
- 2 J. Shen, J. D. Dow and S. Y. Ren, *J. Appl. Phys.*, **67** (1990) 3761.
- 3 N. Kobayashi and Y. Horikoshi, *Jpn. J. Appl. Phys.*, **29** (1990) L236.
- 4 Sg. Fujita, P. A. Murawara, S. Maruo, O. Tsuji and Sz. Fujita, *Jpn. J. Appl. Phys.*, **28** (1991) L78.
- 5 N. Kobayashi and Y. Horikoshi, *Jpn. J. Appl. Phys.*, **28** (1989) L1880.
- 6 A. Yoshikawa, T. Okamoto, T. Fujimoto, K. Onoue, S. Yamaga and H. Kasai, *Jpn. J. Appl. Phys.*, **29** (1990) L225.
- 7 Y. Aoyagi, M. Kanazawa, A. Doi, S. Iwai and S. Nanba, *J. Appl. Phys.*, **60** (1986) 3131.
- 8 H. Oniyama, S. Yamaga, A. Yoshikawa and H. Kasai, *J. Cryst. Growth*, **93** (1988) 679.
- 9 N. Kobayashi, T. Makimoto, Y. Yamaguchi and Y. Horikoshi, *J. Cryst. Growth*, **107** (1991) 62.
- 10 T. Okamoto and A. Yoshikawa, *Jpn. J. Appl. Phys.*, **30** (1991) L156.

# Determining lattice mismatch or the composition of a single ultra thin GaInAs layer grown on InP

Fumiyuki Ohsawa, Hiromasa Fujita, Toshio Obitsu, Hirokazu Ikeda and Hideo Kawanishi

*Department of Electronic Engineering, Kohgakuin University, Nakano-cho 2665-1, Hachioji-shi, Tokyo 192 (Japan)*

## Abstract

A high resolution measuring method to determine lattice mismatch or the composition for a single ultra thin  $\text{Ga}_x\text{In}_{1-x}\text{As}$  ternary layer is discussed. The maximum errors of lattice mismatch and composition  $x$  depend strongly on the uncertainty of band-offset and are, respectively,  $\pm 0.10\%$  and  $\pm 0.01$  in the case of a two-monolayer GaInAs single quantum well for band-offset uncertain at a conduction band of  $\Delta E_c = 0.42 \pm 0.02$  eV. The accuracy of this method is also calibrated using an X-ray diffraction technique for multiple quantum well structures of two-monolayer thick wells grown by digital epitaxy. This method may also be applied to GaInAsP quaternary.

## 1. Introduction

Determining the lattice match conditions of a substrate or the composition of an ultra thin single GaInAs epitaxial layer is an important technique for reproducible fabrication and/or device fabrication. However, although X-ray diffraction has been a powerful detection tool for relatively thicker epitaxial layers or multiple quantum well structures, the detection or measurement of these parameters becomes very difficult in the case of a single quantum well a few monolayers thick [1].

On the other hand, an actual lattice image obtained by high resolution transparent electron microscopy (TEM) could be a promising technique for counting the number of atomic layers of (Ga + In), In, As or P, or GaInAs monolayers [2]. However, contrast of the TEM image between the GaInAs and InP layers becomes weak at high magnification and this TEM technique cannot be applied to the measurement of the composition of the GaInAs epitaxial layer.

In this paper, a high resolution method of measuring lattice mismatch or the composition of a single ultra thin GaInAs ternary layer is proposed. For this purpose, fundamental parameters such as effective masses of electrons and holes, band-offsets at the heterojunctions, and energy gaps of GaInAs and InP are calibrated using the values of blue shift measured by the photoluminescence technique for fine single GaInAs quantum wells grown by digital epitaxy. The accuracy of the layer number determined by the photoluminescence technique is also checked by a high resolution TEM image obtained from the same sample. The resolution limit of this measuring method and the application of this technique to GaInAsP quaternary are also discussed.

## 2. Digital epitaxy of monolayer GaInAs on InP by metal–organic molecular beam epitaxy

In order to realize an atomically flat GaInAs epitaxial layer across the epitaxial substrate, an atomically flat substrate surface has to be prepared before digital epitaxy. For this purpose, an InP buffer layer and a thick GaInAs layer were grown on the InP substrate as the first step. This process is very important for the epitaxial growth of spatially flat GaInAs of two-monolayer thickness on a commercially available InP substrate, normally in atomic steps. Then a single GaInAs ternary layer of two-monolayer thickness and an InP barrier were grown by metal–organic molecular beam epitaxy (MOMBE), in which atomic sources such as TMI, TEG and  $\text{AsH}_3$  in the case of GaInAs epitaxy, or TMI and  $\text{PH}_3$  for InP, were injected not alternately but simultaneously onto the epitaxial surface.

Another key growth condition for digital epitaxy is the growth temperature. If the growth temperature is selected above  $500 \pm 5^\circ\text{C}$ , epitaxial growth becomes digital as reported earlier [3]. The typical growth time was 0.2–0.7 s for a two-monolayer, and 1.6–2.7 s for a three-monolayer deposit respectively in digital epitaxy. Figure 1 shows the TEM lattice image of a two-monolayer GaInAs/InP quantum well grown by digital epitaxy. Another wide range TEM image indicates that there was no atomic step in the GaInAs epitaxial layer of length 90 nm.

However, the PL peak wavelength, which is measured from the ultra thin GaInAs epitaxial layer, was scattered sometimes in a range of a few nanometers. This fluctuation originates not from thickness variations, but from small fluctuations of the composition in



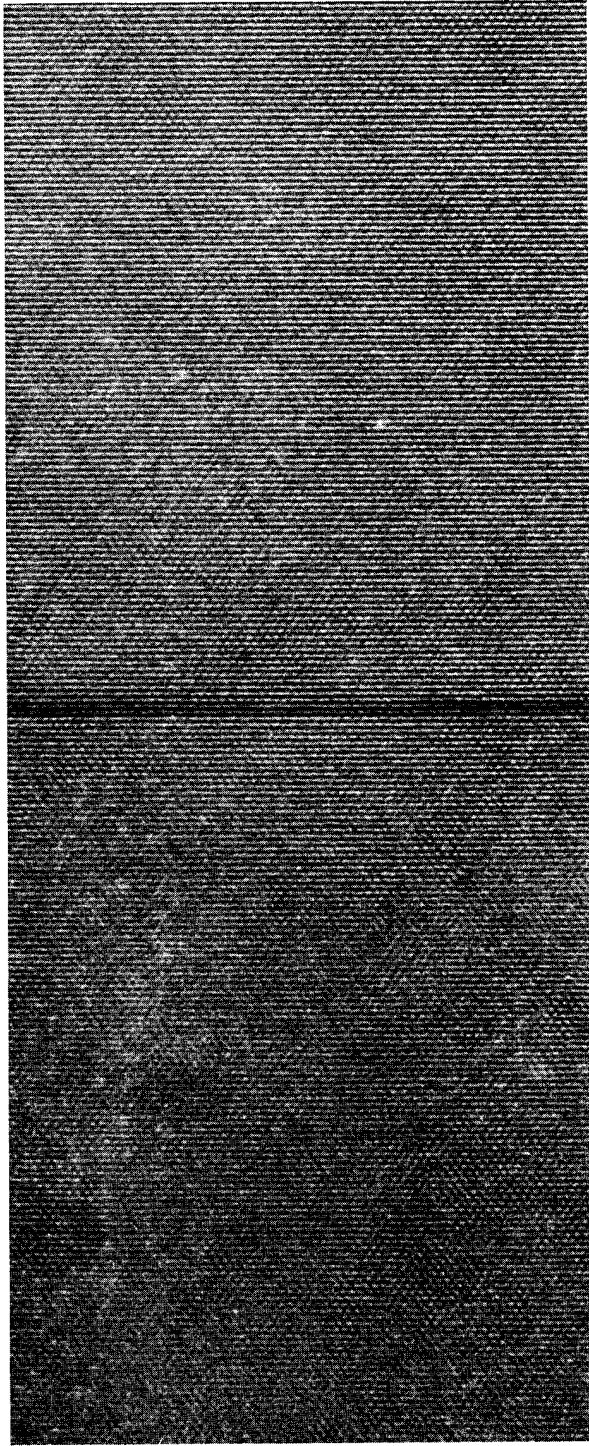


Fig. 1. High resolution (011) cross-sectional TEM image for a single ultra thin GaInAs layer grown by digital epitaxy, with a single PL spectrum originated from two-monolayer GaInAs. In this figure, the darker regions around the lighter pattern correspond to hexagons of the atomic arrangement on the (011) surface in the zinc blende structure.

the ultra thin GaInAs ternary layer, as scattering originating from thickness variations is larger, as discussed in Section 3.1 (See Fig. 2).

### 3. Theory of blue shift in GaInAs/InP quantum wells

#### 3.1. Calculation of blue shift

When we measure the photoluminescence of the GaInAs/InP quantum well structure, the peak wavelength is shifted to a higher energy site. This phenomenon is ordinarily called a blue shift. The theoretical value of the blue shift, which originated from the quantum size effect, was calculated by a simplified effective mass approximation theory using some physical parameters, such as band-offsets in a conduction band or valence band, and effective masses of electrons and holes [4].

Figure 2 shows the calculated blue shift for the range of thickness from one- to ten-monolayer GaInAs quantum wells for an InP barrier width of 20 nm. In this calculation, the conduction band-offset was 42% of the bandgap difference between InP and GaInAs [5], the electron effective mass was  $0.041m_0$  [6], and the heavy hole mass was  $0.470m_0$  for GaInAs [7], where  $m_0$  is the electron mass in free space.

In this monolayer region, the blue shift changes digitally or step-wise, as shown in Fig. 2, and the number of monolayers can be determined by using this digital-like blue shift. The accuracy of this measurement depends strongly on the accuracy of the physical parameters, and increases with a decrease in the number of monolayers. Therefore, if we can decide directly the number of monolayers by a suitable technique, for example, a high resolution TEM image, then we can calibrate these physical parameters and determine the absolute value of the blue shift for lattice matched, as well as lattice mismatched, GaInAs quantum well to InP.

#### 3.2. Calculation of the relation between peak wavelength shift and lattice mismatch or composition $x$ of $Ga_xIn_{1-x}As$

The calculated relation between the peak wavelength shift (the difference in the blue shift for the GaInAs lattice matched to InP) and the lattice mismatch ( $\Delta a/a$ ) or composition  $x$  for  $Ga_xIn_{1-x}As$  is illustrated in Fig. 3 for two- to six-monolayer thicknesses, where the lattice constant of InP was assumed to be  $a(\text{InP}) = 0.586875 \text{ nm}$  [8]. The blue shift for lattice-matched GaInAs is calculated by using the following parameters: the measured bandgaps of GaInAs and InP,  $E_g(\text{GaInAs}) = 0.810 \text{ eV}$ , which is equal to an earlier report [9] and  $E_g(\text{InP}) = 1.332 \text{ eV}$  at 77 K; the band-offset of the conduction band at the hetero barrier of  $(\Delta E_c/\Delta E_g) = 0.42$ ; and the effective masses of electrons and heavy holes of  $(m_e^*/m_0) = 0.041$  and  $(m_{hh}^*/m_0) = 0.470$ ; where  $\Delta E_g$  is defined as  $\Delta E_g = \{E_g(\text{InP}) - E_g(\text{GaInAs})\}$ , respectively. The calculated blue shift for lattice-matched GaInAs has been fitted completely to

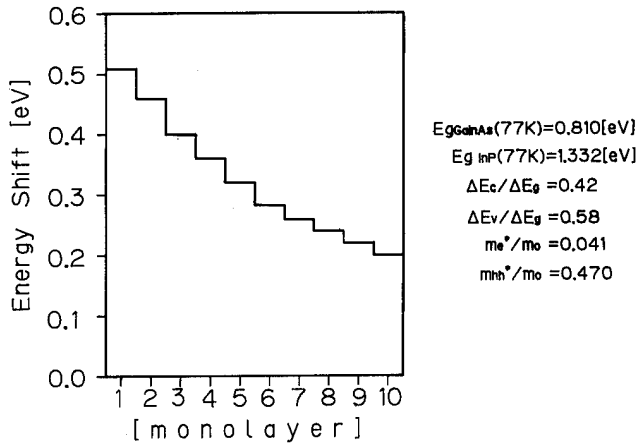


Fig. 2. Theoretical calculation of the blue shift calculated by simplified effective mass theory.

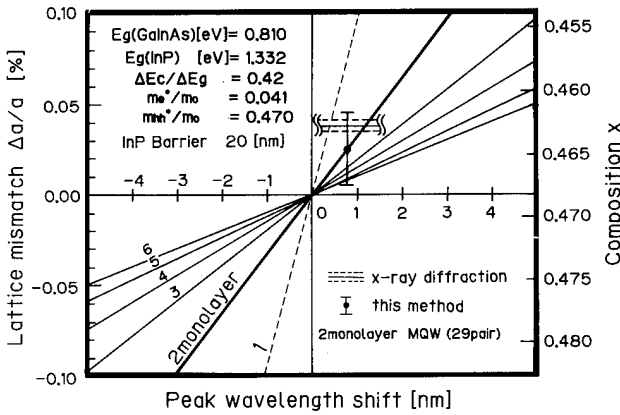


Fig. 3. The calculated relation between the peak wavelength shift and the lattice mismatch  $\Delta a/a$  or composition  $x$  for  $\text{Ga}_x\text{In}_{1-x}\text{As}$  for two-monolayer to six-monolayer thickness. The experimental result for a GaInAs ternary multiple quantum well of two-monolayer thickness is plotted as a closed circle with an error bar.

that obtained from the experimental results for two- to five-monolayer thick GaInAs quantum wells grown by digital epitaxy using the MOMBE technique. In Fig. 3, the zero point of the peak wavelength shift is equal to the blue shift corresponding to the lattice-matched GaInAs layer.

The theoretical fluctuations originating from the uncertainty in the reported physical parameters are summarized in Table 1. The maximum errors in the measured lattice mismatch  $\Delta(\Delta a/a)$  and composition  $\Delta x$  originate from the uncertainty in the band-offset ( $\Delta E_c/\Delta E_g$ ) for the two-monolayer thickness [5], and become  $\Delta(\Delta a/a) = \pm 0.10\%$  and  $\Delta x = \pm 0.01$  respectively. Other theoretical fluctuations due to thicker epitaxial layers of three-monolayer and four-monolayer are also summarized in Table 1 and have smaller values.

Calibration of these physical parameters becomes possible by checking the absolute value of the blue shift of a single quantum well. As a result, these physical parameters, which are used for the theoretical calculation, are summarized as true values in Table 1. The calculated blue shifts using these physical parameters fit the experimental results for two-monolayer to five-monolayer thick GaInAs single quantum wells.

#### 4. Experimental results

The usefulness of this method was demonstrated for bulk GaInAs (relatively thick epitaxial layer of 234 nm). The experimental results are shown in Fig. 4, where the peak wavelength shift from the lattice-matched GaInAs layer is plotted as a closed circle with an error bar. On the other hand, lattice mismatch measured by X-ray diffraction is also indicated in Fig. 4 as lines parallel to the horizontal axis and these data are completely fitted to each other. These experimental results shows the accuracy of the physical parameters used in our theoretical calculation.

The value of the blue shift measured for a multiple quantum well structure (with 29 pairs of GaInAs quantum wells two-monolayer thick and an InP barrier of 20 nm) at 77 K is also compared with the theoretical one. The measured blue shift for a two-monolayer GaInAs quantum well lattice matched to InP was 0.444 eV, which is almost the same as the theoretical one but differs slightly from the value of 0.445 eV for a lattice-matched GaInAs layer of two-monolayer thickness by only 0.001 eV.

TABLE 1. Summary of calculated possible errors corresponding to uncertainties in the physical parameters

Parameter	True $\pm$ error	$\pm \Delta a/a(\%)$			$\pm x_{\text{Ga}} (=0.468)$		
		2ML	3ML	4ML	2ML	3ML	4ML
$\Delta E_c/\Delta E_g$	$0.42 \pm 0.02$	0.1	0.09	0.09	0.01	0.01	0.01
$E_g(\text{InP})$ (eV)	$1.332 \pm 0.001$	0.02	0.01	0.007	0.003	0.002	0.001
$E_g(\text{GaInAs})$ (eV)	$0.810 \pm 0.001$	0.006	0.006	0.006	0.001	0.001	0.001
$m_e^*/m_0$	$0.041 \pm 0.003$	0.004	0.006	0.009	0.001	0.001	0.001
$m_{hh}^*/m_0$	$0.470 \pm 0.001$	0.003	0.002	0.002	0.000	0.000	0.000

InP barrier 20 nm.

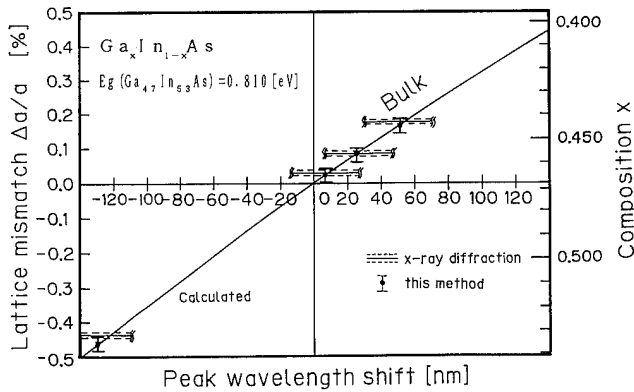


Fig. 4. The calculated relation between the peak wavelength shift and the lattice mismatch  $\Delta a/a$  or composition  $x$  for bulk  $\text{Ga}_x\text{In}_{1-x}\text{As}$ . The experimental results for bulk GaInAs are plotted as closed circles with error bars.

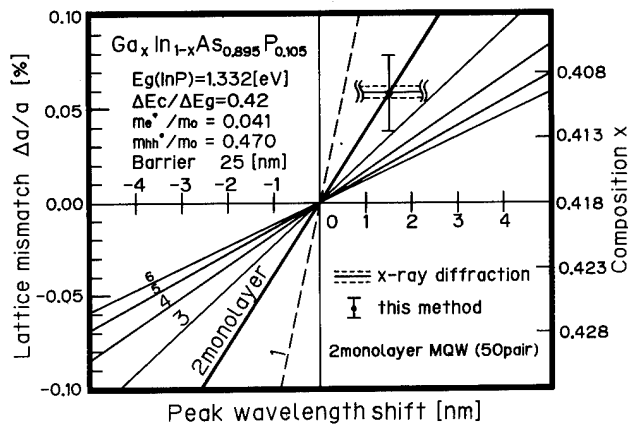


Fig. 5. Experimental result for GaInAsP multiple quantum well of two-monolayer thickness. The experimental result for a multiple quantum well of two-monolayer thickness is plotted as a closed circle with an error bar.

The difference in PL peak (peak wavelength shift in Fig. 3) between the lattice-matched GaInAs quantum well and the lattice-mismatched GaInAs of two-monolayer thickness was measured. By using Fig. 3, we can determine the lattice mismatch and composition  $x$  of an epitaxially grown  $\text{Ga}_x\text{In}_{1-x}\text{As}$  fine layer. The lattice mismatch measured by this method becomes  $(\Delta a/a) = 0.03 \pm 0.02\%$ , and composition of  $x = 0.464 \pm 0.003$ . This data is plotted as a closed circle with an error bar in Fig. 3.

For comparison, the lattice mismatch of the multiple quantum wells with 29 pairs of GaInAs wells was also measured by X-ray diffraction, and became  $(\Delta a/a) = 0.038 \pm 0.003\%$ . The measured lattice mismatch is indicated as a horizontal solid line in Fig. 3. As shown in Fig. 3, these two data are fitted to each other in a permissible error range.

Figure 5 shows the experimental result for GaInAsP quaternary. By adapting this method to the quaternary, lattice mismatch and composition  $x$  and  $y$  in  $\text{Ga}_x\text{In}_{1-x}\text{As}_y\text{P}_{1-y}$  are determined to be  $0.006\%$ ,  $x = 0.410$  and  $y = 0.105$ , respectively, for a multiple GaInAsP quantum well structure with 50 pairs of quantum wells grown by digital epitaxy, see Fig. 5.

## 5. Conclusions

A high resolution measuring method for lattice mismatch or the composition of a single ultra thin GaInAs ternary is proposed. For this purpose, fundamental physical parameters were calibrated by measuring the absolute value of the blue shift for the spatially uniform fine structure single GaInAs quantum well grown by digital epitaxy. The accuracy of this method was also verified by X-ray diffraction from the multiple quantum well structure of two-monolayer thickness. The maximum errors in lattice mismatch and composition determined by this method are  $\pm 0.10\%$  and  $\pm 0.01$  for a two-monolayer GaInAs single quantum well.

## References

- 1 J. M. Vandenberg, S. N. G. Chu, R. A. Hamm, M. B. Panish and H. Temkin, *Appl. Phys. Lett.*, **49** (1986) 1302.
- 2 J. C. H. Spence, *Experimental High Resolution Electron Microscopy*, University Press, Oxford, 1981.
- 3 H. Kawanishi and F. Ohsawa, *Proc. 3rd Int. Conf. on ICCBE-3*, Oxford, Sept. 1-5, 1991.
- 4 R. M. Smith, *Wave Mechanics of Crystalline Solid*, Wiley, New York, 1961, Chapter 4.
- 5 D. V. Lang, M. B. Panish, F. Capasso, A. Allan, R. A. Hamm, A. M. Sergent and W. T. Tsang, *Appl. Phys. Lett.*, **50** (1987) 736.
- 6 J. C. Portal, C. Houlbert, P. Perrier and T. P. Pearsall, *Appl. Phys. Lett.*, **34** (1979) 492.
- 7 P. C. Morais, H. M. Cox, P. L. Bastos, D. M. Hwang, J. M. Worlock, E. Yablonovitch and R. E. Naholy, *Appl. Phys. Lett.*, **54** (1989) 442.
- 8 G. Giesecke and H. Pfister, *Acta Crystallogr.*, **11** (1958) 369.
- 9 H. Temkin, V. G. Keramidas, M. A. Pollack and W. R. Wagner, *J. Appl. Phys.*, **52** (1981) 1574.

# Conditions for light-induced short-time growth of GaAs and InP by chloride epitaxy

K. Tempelhoff

KAI-e.V., Hausvogteiplatz 5-7, O-1086 Berlin (Germany)

## Abstract

The advantages of traditional chloride epitaxy are well known; the growth of thin layer sequences, however, involves manifold difficulties. Moreover, use of the V chlorides renders the classical ALE process quite impossible. The V chloride process was developed to a low temperature, light-induced epitaxy. Inhibition of growth — by coverage of the surface with chlorine atoms at low temperatures below 500 °C — is intermittent with the use of light pulses. The light energy breaks the chlorine bonds and leads to growth during the pulse time. The growth behavior of InP on InP and GaAs on GaAs was examined with respect to layer thickness on the atomic scale in the low temperature region using equipment designed appropriately. Growth rates of  $0.5 \text{ Å s}^{-1}$  (GaAs) and  $1 \text{ Å s}^{-1}$  (InP) have been achieved. The abrupt decrease of the growth rates to zero appears at temperatures of 473 °C GaAs and 458 °C InP.

## 1. Introduction

The advantages of traditional V trichloride epitaxy are commonly accepted (low toxic level, high purity, low costs); but the high growth rate, which is one of the reasons for the high productivity and low costs, is the essential reason for the uselessness of the trichloride method for thin layer growth. Moreover, with the use of V trichlorides application of the classical ALE method is excluded because of the simultaneous appearance of Group III and V elements in the deposition zone. The motivation for employing the trichloride method is that the range of low temperatures ( $T_{\text{dep}} < 500 \text{ °C}$ ) and low partial pressures of chlorides ( $p < 10^{-4} \text{ atm}$ ) have not been investigated until now.

New experimental arrangements and reactor design have been developed to also realize the growth of thin layers on the atomic scale by trichloride epitaxy. Following the accepted model of Cadoret [1] which proposes full coverage of the surface with chlorine atoms at temperatures below 600 °C, we include in our considerations the fact that the reactive desorption of chlorine atoms of adsorbed GaCl by hydrogen may be the growth rate limiting step. Therefore it is expected that during the kinetically determined zero growth at still lower temperatures, a pulse of energy (light) should break the chlorine bonds and lead to growth during the pulse time. With the intention of growing full GaInAsP, we performed preliminary investigations of the pure processes for GaAs and InP growth.

## 2. Experimental details

The main problems associated with low temperature/low partial pressure trichloride epitaxy at present are control and reproducibility of the low partial pressures. Therefore specially formed rods of solid GaAs and InP were used as the sources for Ga/In chlorides (Fig. 1(a)). The rods preserve a constant surface area for the generation of III chlorides during a great number of epitaxial processes. To ensure a constant V chloride partial pressure in the  $\text{H}_2/\text{V}$  chloride mixture for the source reaction, rectifiers were installed behind the V chloride ( $\text{AsCl}_3/\text{PCl}_3$ ) bubblers. The temperature difference between the rectifiers (20 °C) and the bubblers (25 °C) was kept constant.

The experimental reactor system used for the growth of GaAs and InP layers is shown in Fig. 1(b). The small reactor (length of quartz tube: 30 cm) is heated in the source zone and behind the deposition zone with *in situ* transparent gold-coated furnaces. Two types of furnaces were in use for the deposition zone:

- (a) a three-hole oven for outside light irradiation and spectroscopic measurements in a horizontal beam across the deposition zone (Fig. 1(c));
- (b) compact oven with light heating, and irradiation of the sample surface by UV and visible light from inside (Fig. 1(d)).

The temperature gradient set up intentionally along the substrates (almost 50 mm) in the deposition zone was measured and controlled by a thermocouple. The

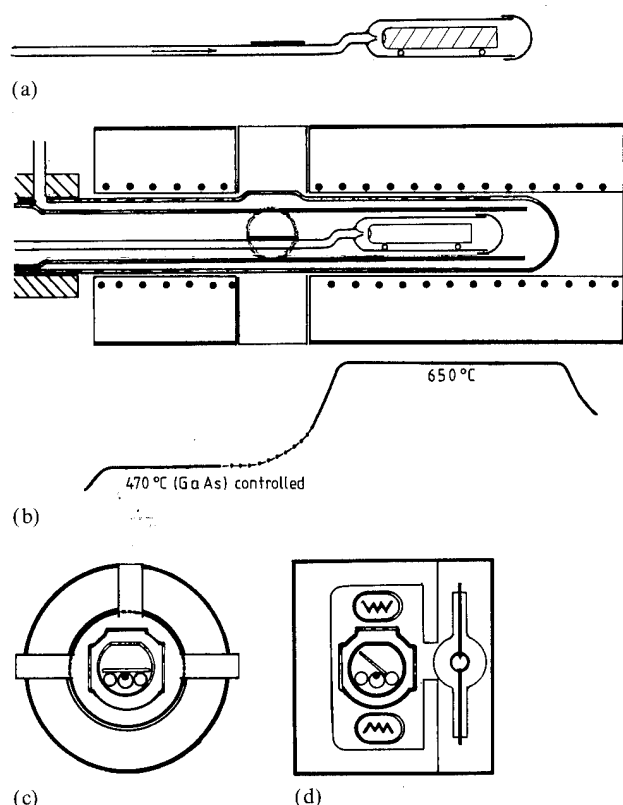


Fig. 1. Schematic diagram of source arrangement (a), reactor (b) and heaters of the deposition zone for light irradiation to the samples (c, d).

total flow rate was regulated to a constant value of  $690 \text{ cm}^3 \text{ min}^{-1}$  taking account of the variation of reactant flow rates. The small quantities of  $\text{H}_2/\text{V}$  chloride mixtures were transported from the bubbler to the reactor by a  $\text{H}_2$ -carrier stream. The well-defined temperature gradient over a  $20^\circ\text{C}$  difference along the

substrate allowed relatively precise determination of the relations between growth behavior and temperature. Layer thickness and carrier concentration profiles were measured by capacitance/voltage (CV) in small steps along the sample.

### 3. Results and discussion

Figure 2 shows different states of deposits in the low temperature region which are observable in this kind by CV measurements. The zero growth in the left (F) is in

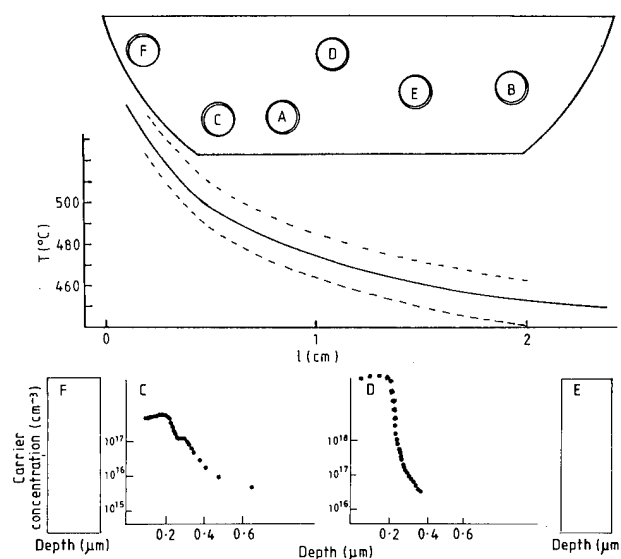


Fig. 2. CV measurements along the temperature gradient of the substrates. States of GaAs growth in the temperature region  $450\text{--}540^\circ\text{C}$  ( $p_{\text{GaCl}}: 7 \times 10^{-5} \text{ atm}$ ) in results of CV measurements: F, zero growth (etching); C, growth of ordered GaAs; D, growth of disordered phase; E, zero growth.

TABLE 1. Parameters of grown epitaxial layers

	GaAs	InP
Ordered phase		
Carrier concentration*	$10^{16} - 10^{18} \text{ cm}^{-3}$	$10^{16} - 10^{18} \text{ cm}^{-3}$
Surface	mirror-like	mirror-like
$\mu$ ( $300^\circ\text{C}$ )	$2000 \text{ cm}^2 \text{ V}^{-1} \text{ s}^{-1}$ ( $n = 5 \times 10^{17}$ )	—
Disordered phase		
Carrier concentration	$> 10^{19}$ (CV ?)	$10^{19}$ (CV ?)
Surface	mirror-like without defects	mirror-like without defects
$\mu$ ( $300^\circ\text{C}$ )	$500 \text{ cm}^2 \text{ V}^{-1} \text{ s}^{-1}$	—
PL spectra	deep levels (bandgap luminescence decreases rapidly)	—

The constitution of the disordered phase is quite unknown, the CV measured (including electrolytic etch) values shows erroneous carrier concentrations (CV measurements by solid contacts give concentrations in the order of  $10^{17} \text{ cm}^{-3}$ ).

\*Carrier concentration depends on the partial pressure of GaCl and results from unintentional doping.

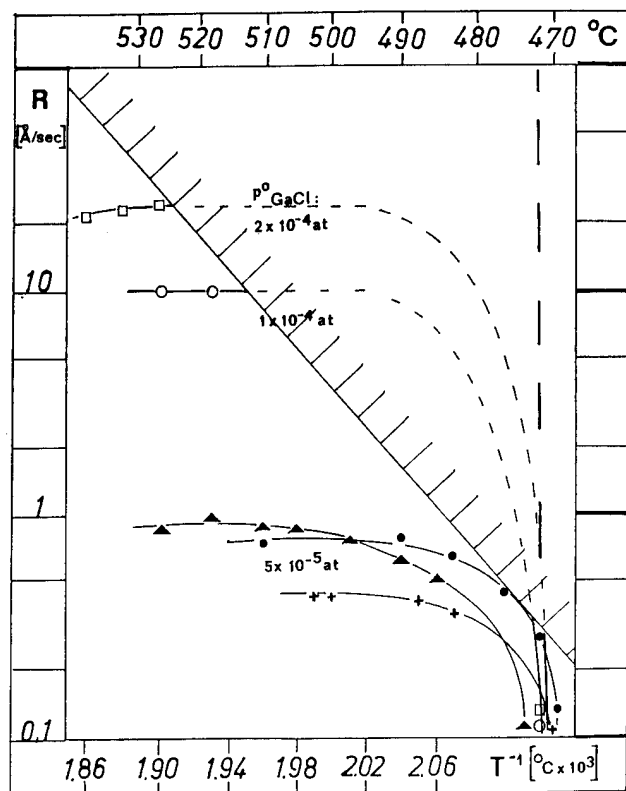


Fig. 3. Growth rates of GaAs layers versus deposition temperature (disordered growth above the hatched line).

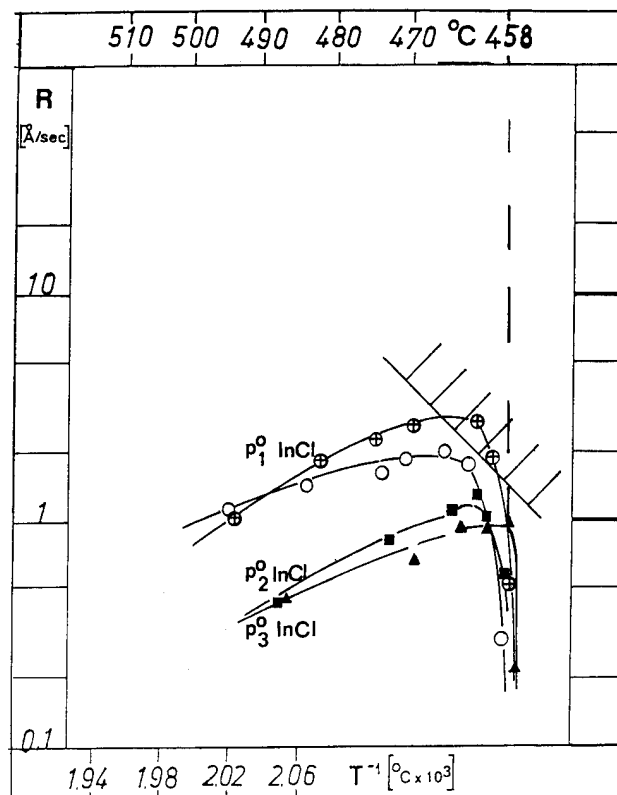


Fig. 4. Growth rates of InP layers versus deposition temperature (disordered growth above the hatched line).

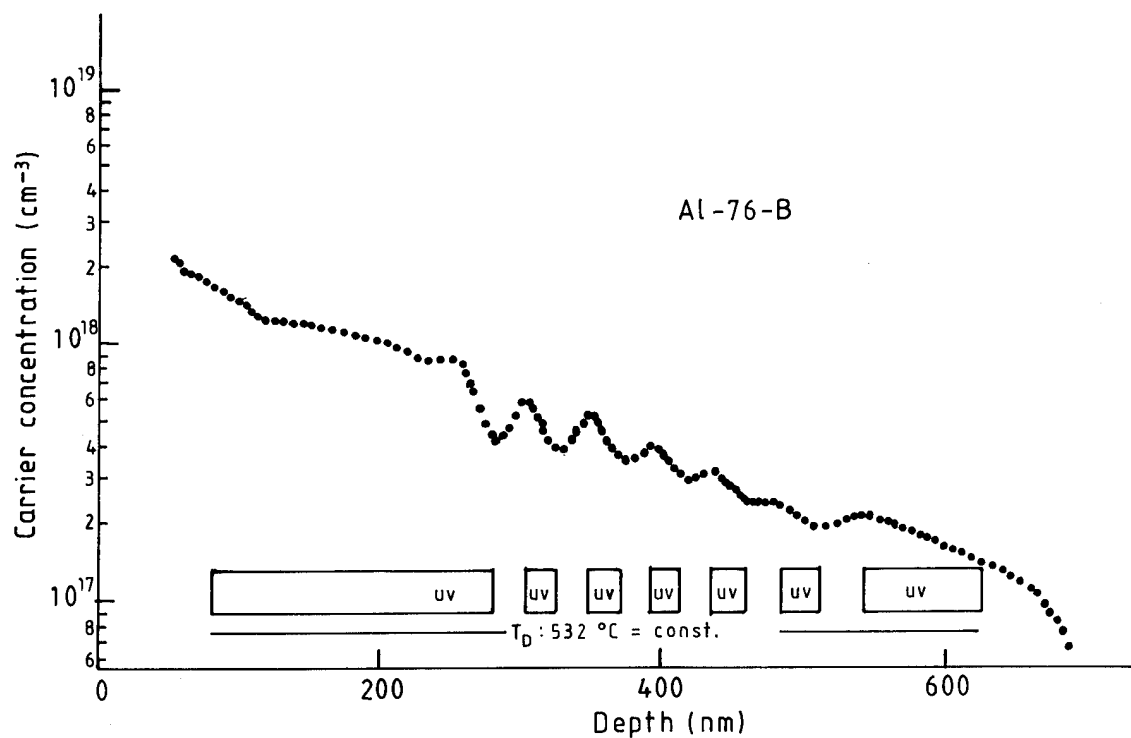


Fig. 5. CV profile of a GaAs layer with modulation of the carrier concentration by UV irradiation (sections which were grown during radiation time are marked (UV); pulse time = break time = 4 min in the middle).

reality the thermodynamically induced etching of the sample. At lower temperatures normal growth appears (C), which changes at sufficiently high partial pressures to the deposition of an obviously disordered phase of GaAs (D) (this we conclude from photoluminescence spectra and from Hall measurements, Table 1).

The zero growth in position (E) indicates the presence of kinetic hindrance to growth between the temperatures at positions (D) and (E).

Figures 3 and 4 represent the detailed results of the temperature dependence of growth rate and growth behavior in the low temperature region for GaAs and InP, respectively. The sharp temperature limits between the growth and zero growth measured in both cases, as well as a nearly vanishing temperature dependence of growth rates above the temperature limit, are essential to our intentions. The very low growth rates obtained of  $0.5 \text{ \AA s}^{-1}$  (GaAs) and  $1.0 \text{ \AA s}^{-1}$  (InP) supposes V chloride epitaxy in the atomic scale range. In order to avoid the disordered phase low partial pressures ( $< 5 \times 10^{-5}$  atmospheres in the case of GaAs) must be realized.

The grown surfaces were all mirror-smooth, Hall measurements and photoluminescence (PL) spectra give results comparable to perfect layers grown in the high temperature region (Table 1).

As we will use light pulses in order to change between the regions of zero growth/ordered growth, the influence of irradiation by Hg lamps (UV) and halogen lamps (hal.l) on growth behavior was examined. The effect of UV radiation is shown by the carrier concentration modulation within the GaAs layer in Fig. 5. The peaks in the curve were related to the light pulses; from it follows an increase of carrier concentration during

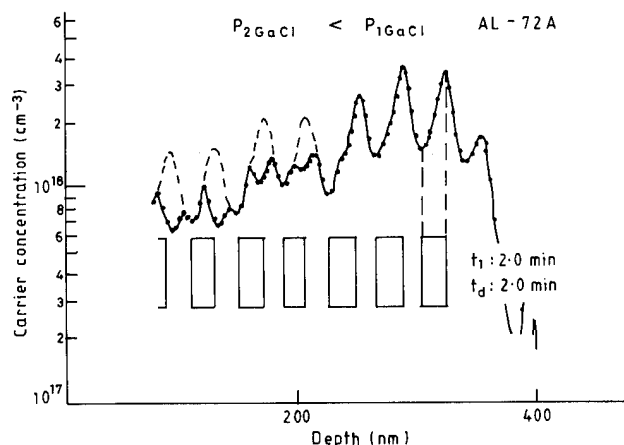


Fig. 6. CV profile of a GaAs layer with modulation of the carrier concentration by light irradiation—inversion of the effect by increase of GaCl partial pressure (sections which were grown during radiation time are marked by rectangles; broken lines: if  $p_{2\text{GaCl}} = p_{1\text{GaCl}}$ ,  $T_{\text{dep}} = 555^\circ\text{C}$ ).

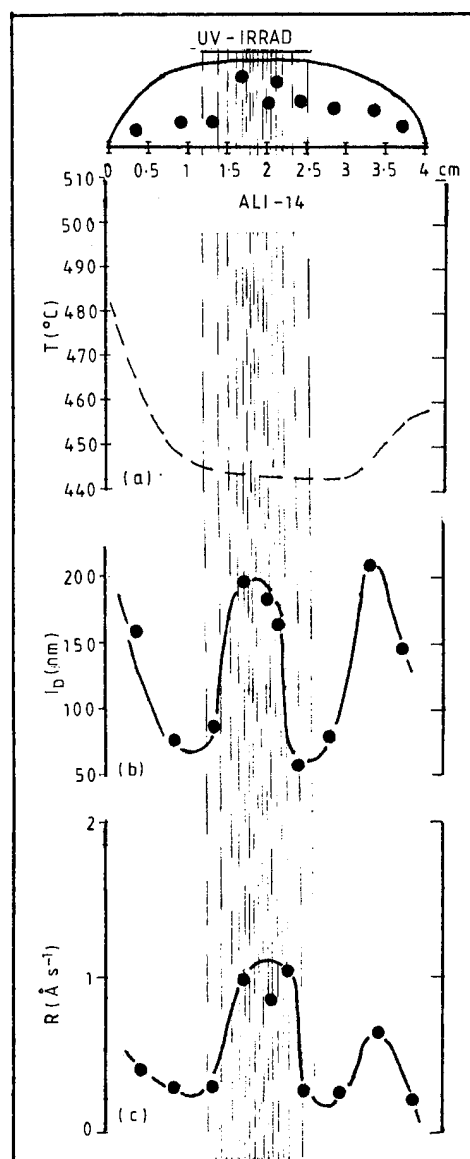


Fig. 7. Growth rates of InP generated by UV irradiation at the temperature level for zero growth: (a) temperature distribution in the deposition zone; (b) depths of out-diffusion of sulfur from the InP substrate along the deposition zone; (c) growth rate variation along the deposition zone.

pulse time. No changes in growth rate were observed, as expected. Similar results were obtained in the other three cases: UV/InP, hal.l/GaAs, and hal.l/InP.

At lower temperatures or higher partial pressures of the reactants respectively, inversion of this effect (decrease of carrier concentration during irradiation) is observable, as shown in Fig. 6. This fact may be explained by a partial appearance of the disordered phase.

Whereas at temperatures above the growth limit no pronounced light-induced growth rates are observed, at temperatures below the limit in the deposition zone the growth rate increases from zero to a considerable value

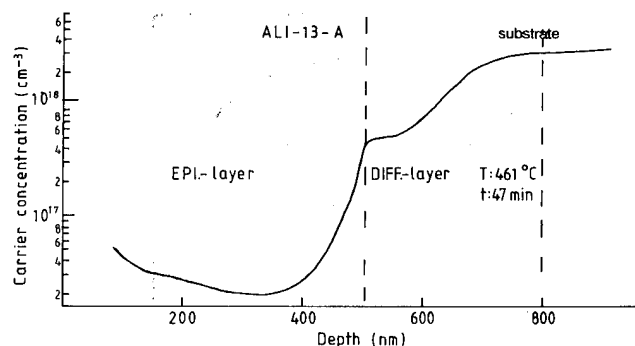


Fig. 8. CV measured diffusion profile on the interface InP epitaxial layer/InP substrate ( $3 \times 10^{18} \text{ cm}^{-3}$  at S-doped).

on light-irradiated parts of the substrate surface (Fig. 7(c)).

The light-induced growth on the sample part below the growth temperature ( $0.5 \text{ cm} > l > 3.5 \text{ cm}$ ; Fig. 7(a)) may be a photocatalytic, photochemical or thermal effect by surface heating. But the evaluation of the diffusion behavior of sulfur on the boundary InP-substrate (S doped:  $3 \times 10^{18} \text{ at cm}^{-3}$ )/epitaxial layer (undoped) allows an estimation of the true temperature distribution directly on the surface of the sample, which is not measurable by the arranged thermocouple.

The depth of carrier out-diffusion below the original substrate surface (diffusion layer in Fig. 8) is determined by temperature and gives satisfactory information about the temperature differences across the

substrate surface. The depths of out-diffusion ( $l_D$ ; Fig. 7(b)) in the UV irradiated sample are compared with the growth rates (Fig. 7(c)).

The coincidence between growth rate changes and depths of out-diffusion of sulfur on the slice (Figs. 7(b) and 7(c)) is evidence of a thermally stimulated growth process from surface heating.

#### 4. Conclusions

- (1) Sufficient absorption of light on GaAs and InP surfaces allows a short heating of the growth face.
- (2) The sharp temperature boundary between growth/zero growth, and the nearly temperature-independent growth rate at partial pressures  $< 10^{-5}$  (Ga/InCl), will result in the growth of layers of uniform thickness.
- (3) The growth rates  $< 1 \text{ Å s}^{-1}$  at low partial pressures in the low temperature region  $480^\circ\text{C}$  (GaAs),  $460^\circ\text{C}$  (InP) make the V chloride process viable for atomic scale epitaxy.
- (4) The preliminary electrical and structural parameters of the layers are hopeful for device application.

#### Reference

- 1 R. Cadoret, in E. Kaldis (ed.), *Current Topics in Material Science*, Vol. 5, North-Holland, Amsterdam, 1980, Chapter 2, p. 220.



# Wavelength dependence of photoenhanced organometallic chemical vapor deposition

J. Salzman, O. Kreinin and E. Maayan

Department of Electrical Engineering and Solid State Institute, Technion-Israel Institute of Technology, Technion City, Haifa 32000 (Israel)

## Abstract

Photoenhanced epitaxial growth of GaAs was investigated by using a fiber-coupled illumination system. The growth rate dependence on illumination intensity and wavelength, and on trimethylgallium partial pressure is reported. The experimental results are consistent with a model in which surface recombination of photogenerated free carriers assists in the decomposition of the adsorbed trimethylgallium.

## 1. Introduction

Photoenhanced organometallic chemical vapor deposition (PE-OMCVD) of GaAs and related compounds [1, 2] is a powerful technique for the implementation of atomic layer epitaxy (ALE). ALE of III–V compounds involves the alternate exposure of the substrate to different precursors, with photoenhancement obtained when exposure to the type III precursor is simultaneous with illumination of the substrate by an intense laser beam [3]. The simpler case of *continuous* exposure to all gas precursors with focused laser illumination also attracted considerable attention because of its potential for selective, localized epitaxial growth with no need of previous masking or patterning of the substrates [4].

In spite of the impressive experimental achievements in PE-OMCVD [4, 5] and efforts to model the photoenhancement mechanisms [6, 7], the details of growth pathways are not yet fully understood. The growth of GaAs from  $\text{Ga}(\text{CH}_3)_3$  (trimethylgallium, subsequently called TMG) and  $\text{AsH}_3$  is one of the best studied systems. Here, it is well established that for high V to III ratio in gas flow, the incorporation of Ga atoms to the surface is the limiting rate, and that illumination enhances this rate. The adsorption, desorption and reaction rates for TMG on GaAs surfaces at  $T \sim 400^\circ\text{C}$ , was studied by Aspnes *et al.* [8].

The wavelength dependence of photoenhancement in crystal growth has not yet been investigated. Photon energy dependence of growth enhancement is expected to provide information related to the basic photochemical or photocatalytic mechanisms of PE-OMCVD. Here, we study the photoenhanced growth rate of GaAs as a function of wavelength  $\lambda$  in the visible and near-infrared range, and photon flux. A simplified

model of the effect of illumination on the adsorbed TMG reaction pathways, consistent with the experimental data, is discussed.

## 2. Experimental details

The epitaxial growth was performed in a conventional horizontal reactor, in which an optical flat window was incorporated. The output beam of an  $\text{Ar}^+$  laser or a Ti:sapphire laser was coupled into a multi-mode optical fiber, from which maximum optical power of  $\sim 400\text{ mW}$  could be extracted and focused onto a  $\sim 50\text{ }\mu\text{m}$  diameter spot. The fiber end-connector and the focusing optics were attached to a motorized  $X$ – $Y$  table and aligned to perform its scanning motion in a plane parallel to the GaAs substrate (see Fig. 1). In a typical experiment, the optical spot was scanned back and forth with a velocity of  $500\text{ }\mu\text{m s}^{-1}$  along a  $1000\text{ }\mu\text{m}$  long line at a growth time of 600 s.

Although we performed the actual PE-OMCVD growth at  $T \leq 400^\circ\text{C}$ , it was found that an initial deoxidation step at  $700^\circ\text{C}$  for 300 s in an  $\text{AsH}_3$  atmosphere was necessary in order to obtain a reproducible photoenhanced growth at low temperatures. These high temperature steps were the main factors in the slow coating of the reactor walls, and the degradation of the optical window transmissivity. With this limitation, 10–15 growth experiments were performed before cleaning the reactor walls, with a total of 20–30 h of photoenhanced growth.

In order to establish the growth selectivity conditions, initial experiments were performed on partially masked GaAs substrates. At atmospheric pressure we found evidence of low-rate growth in the non-illuminated areas. The total reactor pressure was then re-

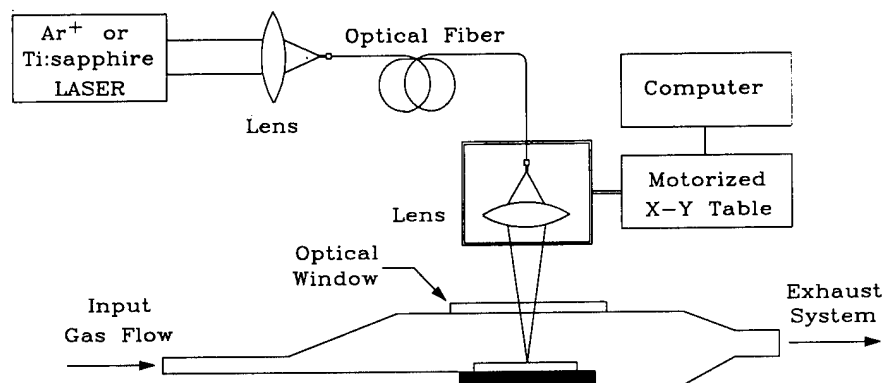


Fig. 1. Fiber-coupled illumination system for PE-OMCVD.

duced to 40 Torr, and the gas flow of the reactants adjusted until the background growth was reduced below our measuring resolution. With these growth parameters, we performed up to seven experiments in a single run, by interrupting the TMG flow, moving the spot to an adjacent area (to a new 'line'), and changing a single parameter.

The growth enhancement in the illuminated lines were measured by using a Tencor  $\alpha$ -step stylus, with each lateral profile measured at several points along the line, normalized for variations in the width, and averaged. The growth features were characterized by spectroscopic methods in order to determine their crystal quality and suitability for heterostructure devices. These measurements will be reported elsewhere [9].

### 2.1 Experimental results

The growth enhancement rate was previously reported to be non-linear with an increase of photon flux [2]. In order to further test and quantify this effect, the growth rate as a function of illuminating intensity was systematically measured by using the  $\text{Ar}^+$  laser source in a multimode operation. The results are presented in Fig. 2. A clear superlinear dependence of the growth rate on the laser intensity is obtained. The wavelength dependence of the growth rate is shown in Fig. 3. The large deviations in the experimental points are due to the slow fluctuations in the fiber-coupled laser power that induce large variations in growth rate due to its intensity dependence (Fig. 2). The absence of any sharp feature in Fig. 3, and the increasing behavior of the

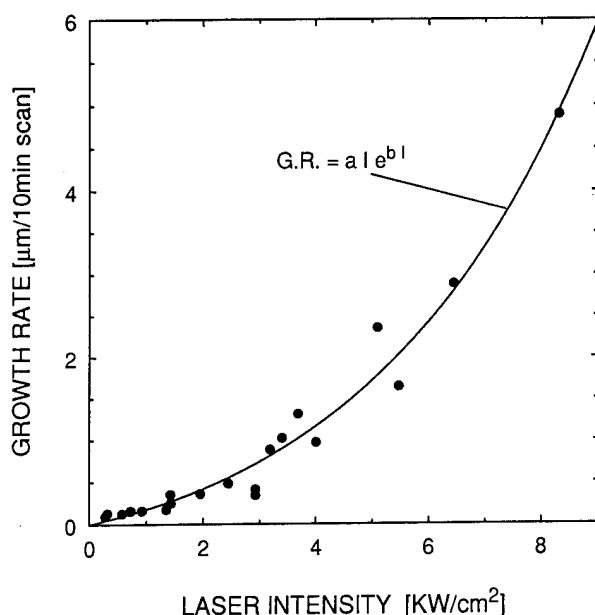


Fig. 2. Growth rate vs. illumination intensity.

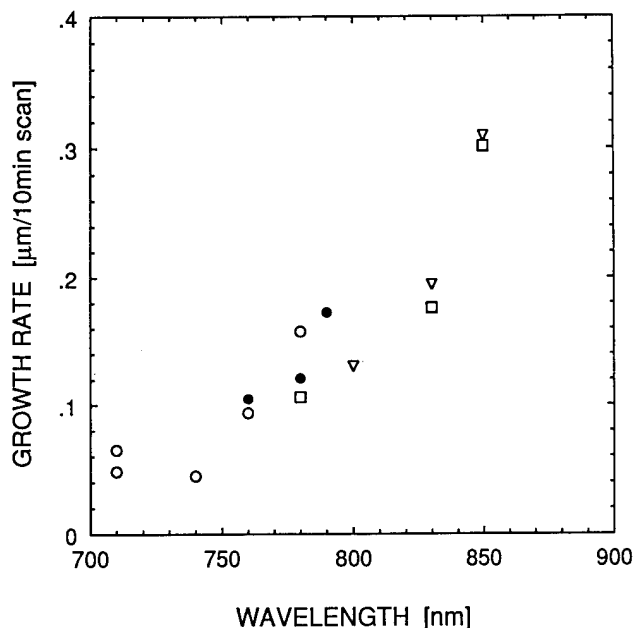


Fig. 3. Growth rate vs. wavelength (Ti:Sa laser source).

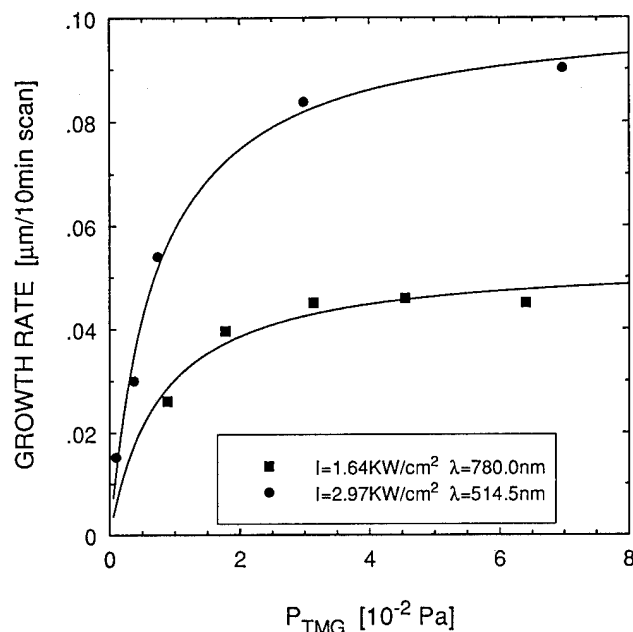


Fig. 4. Growth rate vs. partial pressure of TMG.

growth enhancement with wavelength, contradicts previous expectations.

Finally, Fig. 4 shows the photoenhanced growth rate vs. the partial pressure of TMG ( $P_{TMG}$ ). The saturation of the growth rate at  $P_{TMG} \geq 2-4 \times 10^{-2}$  Pa is in clear contrast with conventional OMCVD experiments, in which a linear, increasing rate was measured for values as high as  $P_{TMG} > 10$  Pa [8].

### 3. Kinetic model

The experimental results shown above, when combined with previous reported results, can be interpreted in the framework of a simplified kinetic model for PE-OMCVD.

Here, we summarize the experimental facts.

(a) Photoenhancement is weakly dependent on the substrate doping, with semi-insulating material exhibiting the smallest effect [3].

(b) The photoenhanced growth saturates with increasing  $P_{TMG}$ .

(c) The photoenhancement is highly superlinear with the photon flux.

(d) The activation energy of the photoenhanced growth rate is independent of photon flux [10].

(e) The photoenhancement increases with wavelength (above substrate bandgap).

We consider the following mechanism for the incorporation of a Ga atom into an As-rich surface: TMG is first physisorbed to the GaAs surface, forming the weakly adsorbed species  $[S^*-TMG]$ . In the absence of light, the

surface coverage and reaction rate are assumed to be dictated by a detailed balance between the sticking rate  $S$ , desorption rate  $E$ , and the decomposition rate  $D$ , as in ref. 8. The premature saturation behavior ((b) above) suggests an increase in the surface fractional coverage by illumination. This effect cannot be explained by a photoinduced increase in  $D$ , as previously assumed [6]. On the other hand, a photoactivated decomposition of  $Ga(CH_3)_3$  to form  $Ga(CH_3)_2$  (dimethylgallium, DMG), or  $Ga(CH_3)$  (monomethylgallium, MMG) cannot explain facts (a), (c) and (e) without surface effects. The incident photons are expected to induce two effects on the GaAs surface: a slight increase in surface temperature  $\Delta T$  and photoexcitation of excess free carriers [11]. We consider the free-carrier assisted probability that the  $[S^*-TMG]$  particle reacts to form a new chemisorbed species, for example  $[S^*-TMG] + [\Delta n, \Delta p] \rightarrow [S^*-DMG]$ . Since there is no reliable information on the new chemisorbed species, we will consider a general scheme as shown in Fig. 5. Particle I is supposed to be  $[S^*-TMG]$  and particle II can be a new electronic configuration, or any of its decomposition products [12]. We assume that  $E^{II} < E^I$  and  $D^{II} > D^I$ .

Let  $\theta$  be the fractional surface coverage of adsorbates of both types (I and II);  $k_{ad}^{(i)}$ ,  $k_{des}^{(i)}$  and  $k_r^{(i)}$  ( $i = I, II$ ) the adsorption, desorption and reaction coefficients of particle ( $i$ ), respectively, and  $\kappa_{I, II}$  the excess-carrier-induced rate of transition of particles from I to II. By solving the corresponding rate equations, we found the steady-state surface coverage:

$$\theta = \frac{P_{TMG} k_{ad}^I}{P_{TMG} k_{ad}^I + (1 - \eta)(\kappa_{I, II} + k_{des}^I)} \quad (1)$$

In eqn. (1),  $\eta = \theta^{II}/\theta$  is the fraction of adsorbed particles of type II, and its equilibrium value is given by

$$\eta = \frac{\kappa_{I, II}}{\kappa_{I, II} + k_{des}^{II}} \quad (2)$$

The transition rate  $\kappa_{I, II}$  is thermally activated. In the absence of light, its activation energy is the energy needed to cleave the  $[S^*-TMG]$  particle,  $E_a^*$

$$\kappa_{I, II}^0 \sim \kappa_0 \exp(-E_a^*/k_B T) \quad (3)$$

where  $k_B$  is the Boltzman constant and  $T$  the temperature. The carrier-assisted transition rate can be evalu-

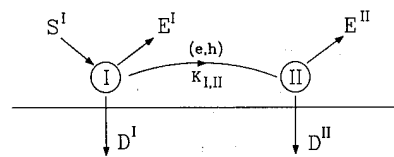


Fig. 5. Kinetic model;  $S^I$ , sticking rate;  $E^I$  and  $E^{II}$ , desorption rates;  $D^I$  and  $D^{II}$ , reaction rates.

ated by calculating the joint probability of excess electron-hole pair recombination at the [S\*-TMG] site, and large energy fluctuations of the adsorbate particle [13]. The surface recombination rate is proportional to the photon flux  $N_{ph}$  [11], we then obtain

$$\kappa_{I, II}(N_{ph}) \sim \kappa'_0 N_{ph} \exp\left(-\frac{E_a^* - \delta E}{k_B T}\right) \quad (4)$$

where  $\delta E$  is the energy released by the recombination event (of the order of the substrate energy bandgap  $E_g$ ). Equation (4) should be modified to include the 'macroscopic' temperature rise  $\Delta T$ . We approximate

$$\kappa_{I, II}(N_{ph}) \sim \kappa'_0 N_{ph} \exp\left(-\frac{(E_a^* - \delta E)\left(1 - \frac{\Delta T}{T}\right)}{k_B T}\right) \quad (5)$$

The temperature rise is, to first order, proportional to the incident optical power  $P = (h\nu)N_{ph}$  ( $h\nu$ —the photon energy). Thus, we write  $\Delta T/T = Ah\nu N_{ph}$  ( $A$  is a proportionality factor) and replace this in eqn. (5) to obtain

$$\kappa_{I, II}(N_{ph}) \sim \kappa'_0 N_{ph} \exp\left(-\frac{E_a^* - \delta E}{k_B T}\right) \exp(b_1 N_{ph}) \quad (6)$$

with  $b_1 = h\nu(E_a^* - \delta E)/(A k_B T)$ . Analogous corrections in all thermally activated rates ( $k_{des}^{(i)}$  and  $k_r^{(i)}$ ) accounting for the temperature rise in the illuminated region should be accounted for. The growth rate,  $R$ , can be calculated as

$$R = \theta[(1 - \eta)D^I + \eta D^{II}] \quad (7)$$

where  $D^{(i)} = B(m^{(i)})k_r^{(i)}$  and  $m^{(i)}$  is the number of sites sheltered by particle ( $i$ ), regulating steric hindrance, and  $B(m^{(i)})$  is a geometrical proportionality factor. According to the model, eqn. (7), with eqns. (1), (2) and (6) completely describe the PE-OMCVD process.

#### 4. Discussion

Here, we address the experimental facts (a)–(e) listed at the beginning of the previous section and show how they can be interpreted in terms of the model:

(a) The doping type and doping level influence on PE-OMCVD have not yet been investigated in a quantitative way. However, it is clear that the doping will regulate the steady-state carrier excess and therefore, change the proportionality factor  $\kappa'_0$  in eqn. (6) thus,  $\kappa_{I, II}$  is doping dependent.

(b) The saturation behavior of  $P_{TMG}$  indicates an increase in the fractional coverage of adsorbates  $\theta$ . This effect is predicted by eqn. (1): an increase in  $\kappa_{I, II}$  with  $N_{ph}$  causes an increase in  $\eta$  (eqn. (2)) and therefore a reduction of the denominator in eqn. (1). The physical picture is that the desorption of particles is retarded by the appearance of the new chemisorbed species II.

(c) The superlinear behavior of the growth rate enhancement is evident from eqns. (6) and (7). As an example, we assume the limit of a highly saturated surface ( $\theta \rightarrow \theta_{max}$ ) and  $D^{II} > D^I$ . Thus,  $R \rightarrow \eta\theta D^{II} \sim \kappa_{I, II} k_r^{II}$ , which includes a linear dependence on  $N_{ph}$  and an exponential factor  $\exp(b_1 + b_2) N_{ph}$ , with  $b_1$  given in eqn. (6) and  $b_2 = h\nu(E_r^{II} A/k_B T)$  ( $E_r$  is the activation energy of  $k_r^{II}$ ).

(d) The kinetic model presented here predicts a correction term in the measured activation energy for PE-OMCVD given by the heating effect  $\Delta E \sim h\nu N_{ph}(E_a^* - \delta E + E_r^{II})A$ . This factor, when calculated from Fig. 2 and applied to the intensities used in Ref. 10 results in negligible values ( $\Delta E \geq 0.02$  eV). Thus, nearly constant activation energies are expected, in agreement with the reported experiments.

(e) The experiments reported here were performed by varying the source wavelength, at constant optical power. Thus,  $N_{ph}$  increases linearly with  $\lambda$ . The large scattering of the experimental points prevents any quantitative comparison with the model. However, if the photon energy would be directly transferred to the [S\*-TMG] adsorbate, one would expect a clear decrease of the photoenhancement with increasing  $\lambda$ . In contrast, our experiments show an increase of the growth rate with  $\lambda$ . This is consistent with the surface recombination-assisted process, where the relevant accelerating energy is that of an electron-hole recombination event ( $\delta E \sim E_g$ ).

#### 5. Conclusions

The growth rate of GaAs at low temperatures from TMG and AsH<sub>3</sub>, and its dependence on the intensity and wavelength of the optical source, was studied. The intensity dependence is found to be exponential with a linear pre-factor. An increase in the growth rate with an increasing wavelength is found. Finally, the growth rate saturates with the increase of the TMG partial pressure. A model invoking photogeneration of free carriers and their surface recombination at the TMG adsorbate sites, leads to a functional dependence of the growth rate on the various parameters, in good agreement with the experimental results.

#### Acknowledgments

This work was performed in the Advanced Optoelectronics Center, and was partially supported by the Israel Ministry of Science and Technology. We would like to thank E. Finkman for his experimental help. Useful discussions with A. Thon and U. Sivan are highly appreciated.

## References

- 1 A. Aoyagi, S. Masuda, S. Namba and A. Doi, *Appl. Phys. Lett.*, **47** (1985) 95.
- 2 N. K. Karam, N. A. El-Masry and S. M. Bedair, *Appl. Phys. Lett.*, **49** (1986) 880.
- 3 A. Doi, Y. Aoyagi and S. Namba, *Appl. Phys. Lett.*, **48** (1986) 1787.
- 4 H. Liu, J. C. Roberts, J. Ramdani, S. M. Bedair, J. Farari, J. P. Vilcot and D. Decoster, *J. Cryst. Growth*, **107** (1991) 878.
- 5 U. Sudarsan, T. Dosluoglu, N. W. Cody and R. Solanki, *J. Cryst. Growth*, **94** (1989) 978.
- 6 A. Doi, S. Iwai, T. Meguro and S. Namba, *Jpn. J. Appl. Phys.*, **27** (1988) 795.
- 7 P. D. Dapkus, B. Y. Moca, Q. Chen, W. G. Jeong and S. P. Den Baars, *J. Cryst. Growth*, **107** (1991) 73.
- 8 D. E. Aspnes, E. Colas, A. A. Studna, R. Bhat, M. A. Koza and V. G. Keramides, *Phys. Rev. Lett.*, **61** (1988) 2782.
- 9 E. Maayan, O. Kreinin, G. Bahir, J. Salzman, A. Eyal and R. Beserman, *IC-MOVPE VI Conference, Boston, June 8-11, 1992*.
- 10 N. H. Karam, H. Liu, I. Yoshida, B. L. Jiang and S. M. Bedair, *J. Cryst. Growth*, **93** (1988) 254.
- 11 K. A. Bertness, C. E. McCants, T. T. Chiang, P. H. Mahowald, A. K. Wahi, T. Kendelewicz, I. Lindau and W. E. Spicer, *Photon, Beam, and Plasma Stimulated Chemical Processes at Surfaces Symp, Boston, December 1-4, 1986*.
- 12 T. J. Mountziaris and K. F. Jensen, *J. Electrochem. Soc.*, **138** (1991) 2426.
- 13 Yu. Khait, J. Salzman and R. Beserman, *Appl. Phys. Lett.*, **53** (1988) 2135.

# Cost-effective processing by atomic layer epitaxy

Tuomo Suntola

*Microchemistry Ltd., Box 45, SF-02151 Espoo (Finland)*

## Abstract

Atomic layer epitaxy (ALE) has been developed for more than 15 years. In spite of an increased research activity in recent years, ALE is still considered a new technology for the growth of thin films and layered crystalline structures. The ALE process is digital in its nature, as are often the expectations of the process. Process control on an atomic level creates an image of piling up perfect crystals from complete crystal faces. At the same time it often creates an image of an expensive and time-consuming way of producing materials. In this paper we review the major factors of the cost efficiency of the ALE process in different application types and for different materials, and make a cost comparison between ALE and some conventional techniques.

## 1. Introduction

Cost efficiency can be defined as the ratio between the value of process performance and the manufacturing cost:

$$\text{cost efficiency} = \frac{\text{value of process performance}}{\text{manufacturing cost}}$$

The value of process performance is related to the effect of process performance on the value of the final product. For example, in the manufacture of integrated circuits, a process which reduces the linewidth increases the number of unit cells on a wafer and accordingly increases the value of the wafer. Reproducibility to tight tolerances, high utilization factor of the processing equipment and high yield are key process performance parameters in any process.

An inherent feature of the atomic layer epitaxy (ALE) process is self-control of monolayer formation due to a saturating surface reaction [1]. While this self-control is a key to well-controlled material characteristics, it is also a key to reducing the production costs. The digital build-up of the material eliminates the need for thickness control, thus reducing the complexity and cost of the processing equipment. In ALE, the uniformity of the flux of the precursor on different parts of the substrate is not critical. A “travelling wave” reaction is an effective way of utilizing the self-control of the material build-up.

In ALE, sequencing of the precursors eliminates gas phase reactions. This allows the use of highly reactive precursors which in turn leads to high material efficiency. The elimination of gas phase reactions also has an important quality effect through the elimination of powder formation in the gas phase.

## 2. Atomic layer epitaxy in different applications

The conditions and demands for cost efficiency are strongly application related. In all cases the control of the process and the material is referred to as the link to desired device performance. The most important condition for good inherent control of the ALE process is a combination of precursors which react “effectively” on the surface. For an “effective” reaction the following conditions must be satisfied.

(1) The activation energy of each surface reaction should be low compared with the energy of the bond formed (this demand is equal to that of a reasonable processing window).

(2) Strong surface reconstructions should not be formed (a strong surface reconstruction increases the activation energy for the next surface reaction).

## 3. Surface reconstruction

A surface is a discontinuity of the bulk. An energetically optimized surface layer (surface reconstruction [2]) may not have an atomic arrangement similar to an ideal cleavage of the bulk (Fig. 1). Surface reconstruction is dependent on the temperature of the surface. In ALE, a monolayer is related to the surface reconstruction of a particular precursor on a particular surface at a particular temperature.

In ALE of II–VI compounds a typical monolayer density of the metal component is about 1/3 of an “ideal full monolayer”. This is the case when the elements themselves are used as the precursors. For CdS it has been shown [3] that the 1/3 monolayer of Cd can be changed to a full monolayer of Cd by replacing the elemental Cd

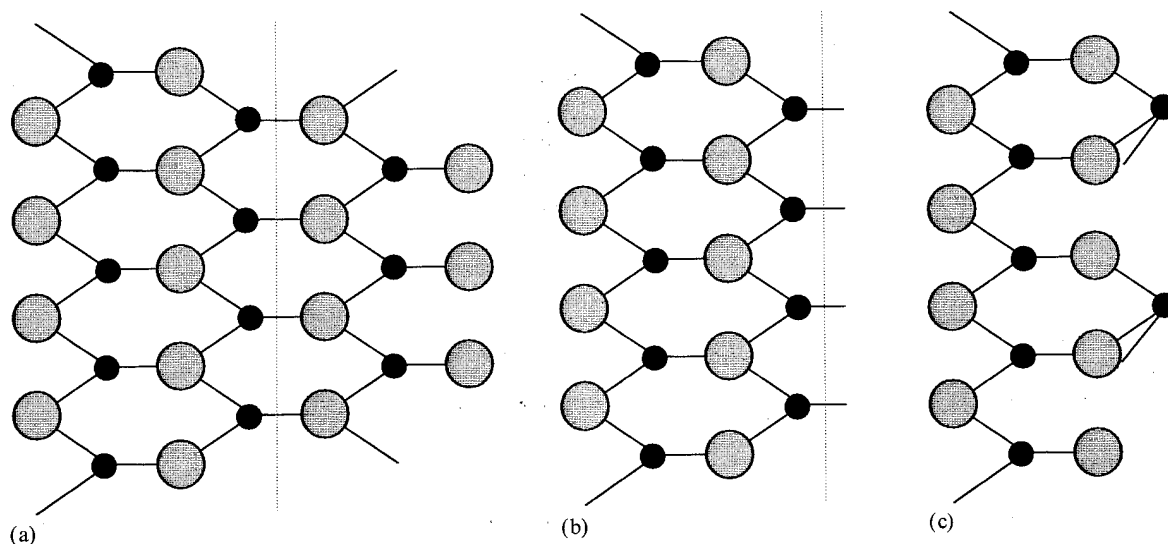


Fig. 1. (a) Internal crystal face in the bulk. (b) Surface formed as an ideal cleavage of the bulk has dangling bonds corresponding to the bonds of the missing crystal face. (c) On a surface formed in an ALE sequence, the dangling bonds may become compensated by a surface reconstruction which minimizes the free surface energy. This may be viewed as a reduced monolayer density.

precursor with  $\text{CdCl}_2$ . One can conclude that the Cl atoms of  $\text{CdCl}_2$  molecules terminate the dangling bonds of a Cd monolayer surface of CdS (Fig. 2).

Temporary termination of the dangling bonds of a monolayer by a ligand of the precursor may be one approach to reduced surface reconstruction effects. This emphasizes the importance of the understanding of the surface chemistry related to the ALE process.

#### 4. Processing equipment

ALE equipment can be classified into two main categories.

##### 4.1. Open or semiopen systems

(1) Typically these are high vacuum systems such as molecular beam epitaxy (MBE) equipment with Knudsen cell sources for low vapour pressure precursors and gas inlets for volatile precursors (Fig. 3(a)).

(2) Thermal equilibrium between the precursors and the substrate surface is not established. Desorbed surface species are collected on the cold walls of the systems or in the vacuum pump without making another collision with the surface.

(3) Both fixed and rotating substrate holders are used. The whole substrate area should be visible from the injection point of the precursor.

(4) The productive efficiency is comparable with that of MBE.

##### 4.2. Closed or semiclosed systems

(1) Typically these are inert gas flow systems such as low pressure chemical vapour deposition equipment. Precursors are supplied to the substrates in thermal

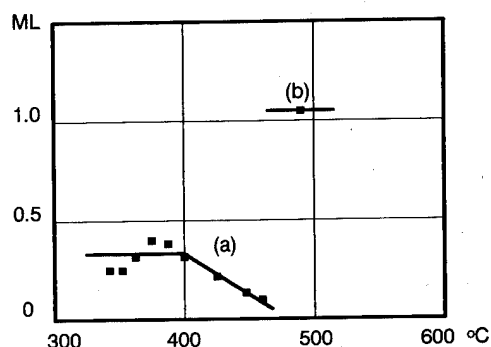


Fig. 2. Processing window of ALE reactions for (a)  $\text{Cd} + \text{S}_x \rightarrow \text{CdS}$  and (b)  $\text{CdCl}_2 + \text{H}_2\text{S} \rightarrow \text{CdS} + 2\text{HCl}$ . In the case of elemental reactions, the Cd surface configuration is determined by reconstruction; Cd monolayer density is 1/3 of an "ideal bulk cleavage" density. In the case of the chloride reactant, chlorine termination reduces the surface reconstruction.

equilibrium (Fig. 3(b)). Purging between ALE sequences is enhanced by an inert gas flow.

(2) Both fixed and rotating substrate holders are used. Because of the thermal equilibrium condition (a hot wall system), multisubstrate cassettes with narrow flow spacings between the substrates can be used.

(3) Material efficiency and the throughput of the equipment can be made high, which leads to a high productive efficiency.

Open reactors have several advantages in the research of ALE growth. First of all, almost any MBE equipment can be used as an open ALE reactor. Open reactors are suitable mainly for single substrates. *In situ* surface analysis in an open reactor is easy, and a variety of different precursors can be used. The limitations of open reactors are mainly their poor productive efficien-

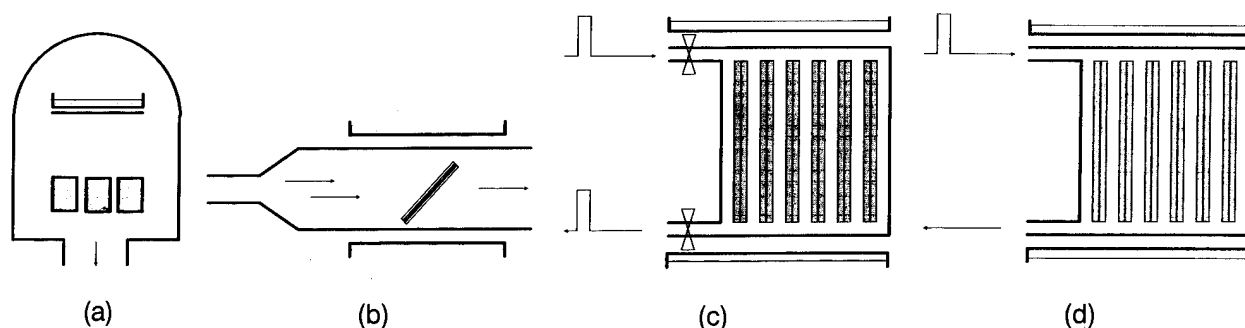


Fig. 3. Schematic diagrams of open and closed ALE reactors. (a) Open reactor, high vacuum. Collision density of the precursor molecules is determined by the molecular flux from the source. Only a single collision of a molecule with the substrate is possible. (b) Semiopen reactor, transfer of the precursor is enhanced with an inert gas flow. Primarily single collisions of the precursor. (c) Closed reactor, all walls are at the same temperature. Collision density of the precursor molecules is determined by the partial pressure of the precursor. (d) Semiclosed, travelling wave, reactor. Precursor molecules make multiple collisions with the substrates while a travelling wave of the precursor passes the surfaces.

cies. Both the throughput of the equipment and the material utilization efficiency are poor.

Closed or semiclosed reactors give a major advantage over the open reactors in productive efficiency. They operate in a thermal equilibrium state which utilizes a multiple collision mode between the precursor molecules and the surface. In a semiclosed "flow-through" or "travelling wave" reactor the multiple collision feature is based on a big difference between the thermal velocity of the molecules and the travelling speed of the precursor wave. In contrast to open systems, not only the throughput of the equipment but also the material utilization efficiency are higher.

For sufficiently complete monolayer saturation, sufficient overdosing of the precursor is one essential demand. In a travelling wave reactor an "effective overdosing condition" on the substrate surface is created by the multiple collisions of the precursor without an increased total dose in the reaction sequence. Thickness uniformity in a travelling wave reactor is strongly dependent on the perfection of the saturation. Even more important than the physical conditions for complete saturation are the effects of the chemistry of the surface.

A travelling wave reactor is an effective tool for

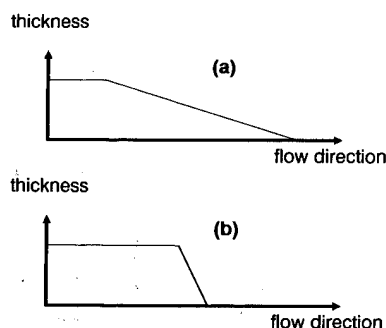


Fig. 4. Thickness profiles in  $\text{TiO}_2$  made in a travelling wave reactor. (a)  $\text{TiCl}_4$  is underdosed: shallow thickness profile reflects a poor reactivity of  $\text{TiCl}_4$  on the surface. (b)  $\text{H}_2\text{O}$  is underdosed: steep thickness profile reflects a good reactivity of  $\text{H}_2\text{O}$  on the surface.

observing the reaction chemistry. The reactivity of each precursor can be observed in the thickness profile in the exhaust end of the substrate in an underdosing condition of the precursor (Fig. 4). Possible desorption of a formed monolayer can be seen as a thinner film in the input end of the substrate. In a travelling wave reactor, a mass spectrometer can be used for *in situ* observation of the reaction results in each sequence [4]. A great advantage of process development in a travelling wave reactor is that processes developed are directly scalable to production reactors.

## 5. Summary

Cost efficiency of ALE is strongly related to the completeness of saturation in the reaction sequences. This is important to the inherent self-control of the process which is the key to unique material features as well as to economical scalability of the process. For desired material and interface characteristics not only the completeness of the saturation is necessary, but also a knowledge of the mechanism of saturation which is related to reaction kinetics and surface reconstructions. The unique features of ALE are emphasized in very thin material layers and interfaces. In such applications the relatively low growth rate, due to sequencing, is not a major cost factor. In thin film applications on large substrates the rate of growth can be effectively compensated by large batches in high density cassettes which lead to a high production efficiency. To take full advantage of ALE, there is a need for theoretical and experimental work on the chemistry of the surface reactions.

## References

- 1 T. Suntola, *Mater. Sci. Rep.*, 4 (1989) 261.
- 2 G. A. Somorjai, *Chemistry in Two Dimensions: Surfaces*, Cornell University Press, Ithaca, NY, 1981.
- 3 A. Rautiainen, Y. Koskinen, J. Skarp and S. Lindfors, *Microchemistry Ltd.*, unpublished results.
- 4 T. Suntola and J. Hyvärinen, *Annu. Rev. Mater. Sci.*, 15 (1987) 177.



# Atomic layer epitaxy for resonant tunneling devices

A. C. Seabaugh, J. H. Luscombe and J. N. Randall

*Texas Instruments Incorporated, Central Research Laboratories, Dallas, TX 75265 (USA)*

P. C. Colter, A. Dip, G. M. Eldallal and S. M. Bedair

*Electrical and Computer Engineering Department, North Carolina State University, Raleigh, NC 27695-7911 (USA)*

## Abstract

We report the first demonstration of an AlGaAs/GaAs resonant tunneling diode (RTD) grown by atomic layer epitaxy (ALE) which features room temperature negative differential resistance. The ALE growth is obtained in a rotating susceptor system with trimethylgallium, trimethylaluminum and arsine sources. Wafer mapping of the RTD properties indicates that monolayer thickness control can be achieved by this technique. In addition to vertical resonant tunneling, we also describe the application of ALE to realize *lateral* tunneling heterostructures and propose one such embodiment, a lateral heterojunction resonant tunneling transistor in a configuration offering room temperature operation.

## 1. Introduction

For circuits using quantum electron devices, precise control of the voltage and current thresholds depends on achieving wafer-scale monolayer thickness control. As device miniaturization proceeds, three-dimensional control of conformal overgrowth processes is also anticipated. Atomic layer epitaxy (ALE) [1] is the only growth technique with the capability for both monolayer thickness control and conformal overgrowth.

In the exploration of ALE growth techniques a number of device demonstrations have been reported including the delta-doped field effect transistor (FET) [2–4], Npn [5] and Pnp [6] heterojunction bipolar transistors (HBT), and the AlAs/GaAs resonant tunneling diode (RTD) [7]. The strongest motivation for the development of ALE is for quantum well devices such as quantum well lasers and detectors, and resonant tunneling devices such as RTDs and resonant tunneling transistors [8, 9] where uniformity depends significantly on the control of quantum well and tunnel barrier dimensions. The resonant peak voltage in an RTD is approximately  $2E_1/q$  where  $E_1$  is the energy of the first quantum well eigenstate (in eV) and  $q$  is the fundamental charge. For high tunnel barriers,  $E_1$  is primarily dependent on the quantum well width  $w$ , so the threshold voltage variation depends on the ability to control the well dimension,  $\Delta V_{th} \approx (4E_1/q)(\delta w/w)$ , where  $\delta w$  is the variation in well width [8]. As an example, consider an  $Al_{0.3}Ga_{0.7}As/GaAs$  quantum well of width  $w = 4$  nm. For this case, the change in resonance voltage with quantum well width is approximately  $26$  meV monolayer<sup>-1</sup>.

Conventional molecular beam epitaxy (MBE) is typically capable of approximately  $\pm 1$  monolayer (ML) thickness control in the growth of a single quantum well [10]. Even given  $\pm 1$  ML thickness uniformity across a wafer, this presents an undesirable limitation on certain resonant tunneling devices such as vertically integrated resonant tunneling diodes [11], where the peak voltage variation sets a limit on the separation between voltage peaks. For these reasons monolayer thickness control is needed to set precisely the device threshold voltage.

In resonant tunneling devices, the peak current density exhibits a greater dependence on monolayer thickness variations than does the peak voltage. For narrow transmission resonances, the peak current density  $J_p$  is given by [12]  $J_p \approx (qm^*E_F/4\pi\hbar^3)\Gamma$ , where  $m^*$  is the electron effective mass,  $\hbar$  is Planck's constant,  $E_F$  is the Fermi energy defined with respect to the conduction band minimum, and  $\Gamma$  is the full width at half-maximum of the transmission coefficient. Shown in Fig. 1 is the computed transmission coefficient for a 5/5/5 nm thick  $Al_{0.3}Ga_{0.7}As/GaAs$  double barrier resonant tunneling diode. The results for the three structures are displayed, differing symmetrically by a single monolayer in the tunnel barrier thickness ( $1 \text{ ML} = 2.827 \text{ \AA}$ ). The transmission resonance width varies by nearly a factor of two for a  $\pm 1$  ML difference, implying that a comparable current density variation is to be expected for this heterojunction system. Wafer mapping of RTD properties has previously shown such a variation in current density across a wafer for MBE-grown materials [10]. The flexibility given to circuit designs utilizing resonant tunneling devices will depend significantly on

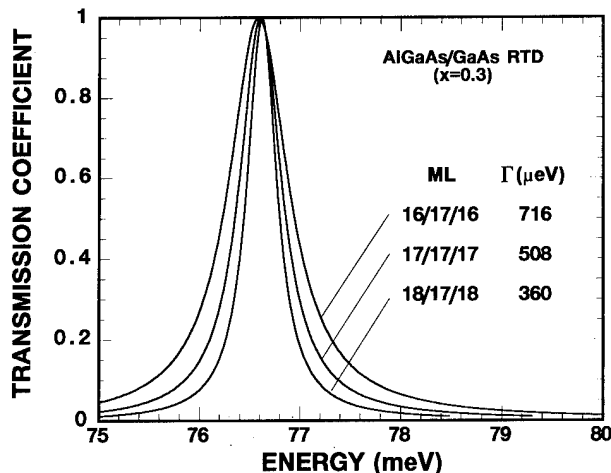


Fig. 1. Computed transmission coefficient for three symmetric  $\text{Al}_{0.3}\text{Ga}_{0.7}\text{As}/\text{GaAs}$  double barrier resonant tunneling diodes differing in tunnel barrier thickness by a single monolayer (ML);  $\Gamma$  ( $\mu\text{eV}$ ) is the full width at half-maximum of the transmission coefficient.

the ability to control dimensions at the monolayer scale.

## 2. Resonant tunneling diodes

The ALE reactor design used in this study is based on the rotating susceptor concept where the wafer is swept between regions containing Group III and Group V reactant gas streams [13]. This concept was used to specially modify a commercial MOCVD reactor to permit operation in the ALE mode [14]. Saturated growth at 30 Torr was then obtained for the GaAs/AlGaAs material system over a temperature range of 550–650 °C. The GaAs material used in the RTDs was deposited at 650 °C with a 1.1 second exposure to trimethylgallium (TMG). Similarly, the optimum AlGaAs growth was obtained at 650 °C with a 2.2 s exposure to TMG + TMA (trimethylaluminum). Hall background carrier concentrations as measured by the Van der Pauw method were found to be below  $10^{15} \text{ cm}^{-3}$  and  $2 \times 10^{17} \text{ cm}^{-3}$  for the GaAs and AlGaAs respectively when grown under these conditions. The background density in AlGaAs is p-type and attributed to carbon. A 1000 ppm silane source was used as the n-type dopant source.

A p-type background carrier density of carbon is typically obtained in the growth of AlGaAs by ALE. The current–voltage ( $I$ – $V$ ) characteristics of an ALE AlGaAs/GaAs RTD measured at room temperature and 77 K are shown in Fig. 2. This structure was grown on an  $n^+$  substrate in the following sequence: 300 nm GaAs ( $6 \times 10^{17}$ – $9 \times 10^{17} \text{ cm}^{-3}$ ), 30 nm GaAs spacer (undoped), 3/5/3 nm  $\text{Al}_{0.3}\text{Ga}_{0.7}\text{As}/\text{GaAs}$  double

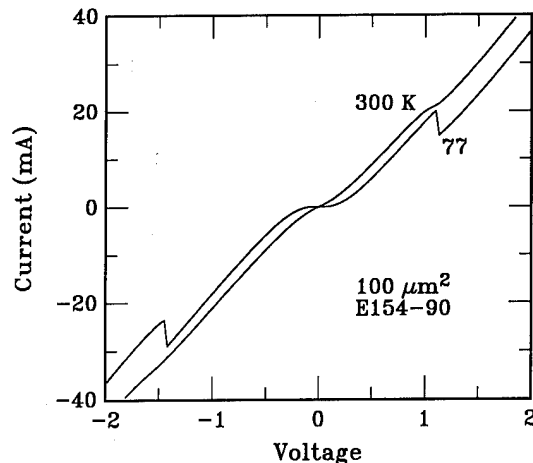


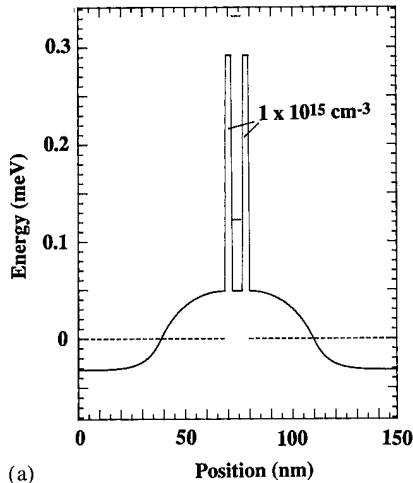
Fig. 2. Current–voltage characteristics of an  $\text{Al}_{0.3}\text{Ga}_{0.7}\text{As}/\text{GaAs}$  resonant tunneling diode grown by atomic layer epitaxy.

barrier, 30 nm GaAs spacer (undoped), and a 300 nm GaAs contact layer ( $6 \times 10^{17}$ – $9 \times 10^{17} \text{ cm}^{-3}$ ). The thin 3 nm tunnel barrier was used to minimize the total acceptor density in the double barrier structure.

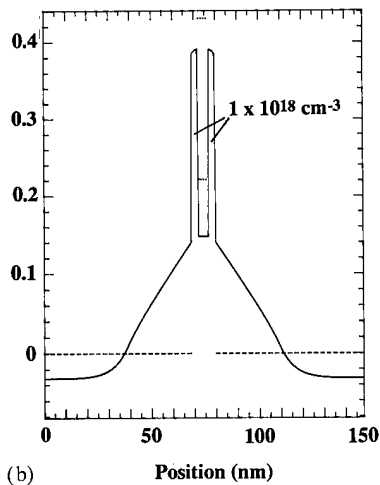
Devices were fabricated using conventional optical lithography and AuGe/Ni/Au ohmic metallization. Dry etching with  $\text{BCl}_3$  was used to form the mesa device structures. A simpler wet-chemically etched process using sulfuric acid/peroxide/water solutions was not used in these materials, due to an enhanced etch rate at the metal/GaAs interface, not observed in comparable MBE-grown structures.

Clear negative differential resistances (NDR) are observed at 77 K for both bias polarities at a voltage of greater than 1 V. To understand this  $I$ – $V$  characteristic, we have computed the potential profile of the device and solved for the quasi-bound states [15]. In Fig. 3(a) the band diagram for this double barrier is shown for the case in which the background doping in the undoped layers is  $1 \times 10^{15} \text{ cm}^{-3}$ , n-type. For this case the quantum well ground state is approximately 120 meV above the emitter Fermi energy, therefore the resonant peak voltage is expected to occur at approximately twice this value, or 240 meV neglecting carrier depletion. Experimentally, we observe in Fig. 2 that the resonance peak voltage is observed at approximately 1.1 V for the positive bias polarity which is significantly higher than expected.

The higher resonance voltage is a consequence of the unintentional carbon doping. Shown in Fig. 3(b) is the energy band diagram with the tunnel barriers doped p-type at a density corresponding to the density expected for these growth conditions,  $1 \times 10^{18} \text{ cm}^{-3}$ . In this case the ionized carbon acceptors act to increase the potential height of the double barrier relative to the neutral n-type regions of the device. The observation



(a)



(b)

Fig. 3. Computed energy band diagrams for the  $\text{Al}_{0.3}\text{Ga}_{0.7}\text{As}/\text{GaAs}$  resonant tunneling diode of Fig. 2 with 30 nm spacer layers, contact doping of  $6 \times 10^{17} \text{ cm}^{-3}$ , and (a) impurity density of  $1 \times 10^{15} \text{ cm}^{-3}$ , n-type, or (b)  $1 \times 10^{18} \text{ cm}^{-3}$ , p-type, in the AlGaAs barriers.

of resonant tunneling at a bias of 1.1 V is consistent with this band diagram.

The effects of carbon doping in the AlGaAs on the resonant peak voltage can be effectively reduced by utilizing an AlGaAs growth temperature of 650 °C. The  $I$ - $V$  characteristic of a typical low effective carbon AlGaAs/GaAs RTD is shown in Fig. 4. In this structure the peak voltage of 275 mV is comparable with that obtained by MBE and the expected value of approximately 240 mV for the zero carbon doping case of Fig. 3(a). This structure was also grown on an  $n^+$  GaAs substrate in the sequence: 300 nm GaAs ( $4 \times 10^{18} \text{ cm}^{-3}$ ), 50 nm GaAs ( $5 \times 10^{17} \text{ cm}^{-3}$ ), 20 nm GaAs spacer (undoped), 5/5/5 nm  $\text{Al}_{0.3}\text{Ga}_{0.7}\text{As}/\text{GaAs}$  double barrier, 20 nm GaAs spacer (undoped), 50 nm GaAs ( $5 \times 10^{17} \text{ cm}^{-3}$ ) and a 300 nm GaAs contact layer ( $6 \times 10^{18} \text{ cm}^{-3}$ ).

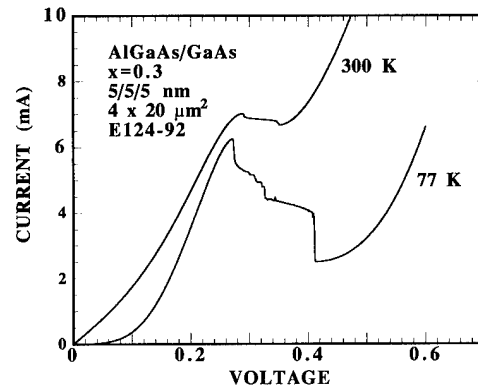


Fig. 4. Room temperature and 77 K current-voltage characteristics of an AlGaAs/GaAs ALE-grown resonant tunneling diode.

Room temperature negative differential resistance in the ALE-grown RTD is observed for the first time in this device, Fig. 4. The low resonant peak voltage suggests that the background carbon density is effectively negated in this growth mode, however, estimates based on growth calibrations for these conditions still indicate a p-dopant density of  $2 \times 10^{17} \text{ cm}^{-3}$ . While these results are not superior to conventional MBE growth of AlGaAs/GaAs RTDs, the ALE RTDs are comparable with previously reported metal-organic chemical vapor deposition grown [16] RTDs. We attribute the difference between MBE and ALE RTDs to the high background carrier densities in the tunnel barriers as grown by ALE which leads to an increase in leakage current at the off-resonance bias.

### 3. Wafer mapping

For the device shown in Fig. 4, we have mapped the uniformity of the resonant peak voltage, the peak current, and the peak-to-valley current ratio (PVR) across the wafer. These results are shown in Fig. 5. A uniform growth region is obtained over the outer radial portion of the growth susceptor, where the isolation of reactants is most complete. Over the uniform part of the wafer the voltage uniformity is within 5% of the average peak voltage over the wafer, and the current density, which is more sensitive to monolayer fluctuations, is within 18% of the average peak current. The lithographic uniformity of device areas has been measured; device areas differ by as much as 8% over the diameter of the 5 cm wafer half. The overall uniformity is comparable with, or slightly better than, what we have previously observed by MBE, and is expected to improve with further optimization of growth conditions, such as temperature, gas inlet jetting and injector flow rates. For the present results, uniformity optimization

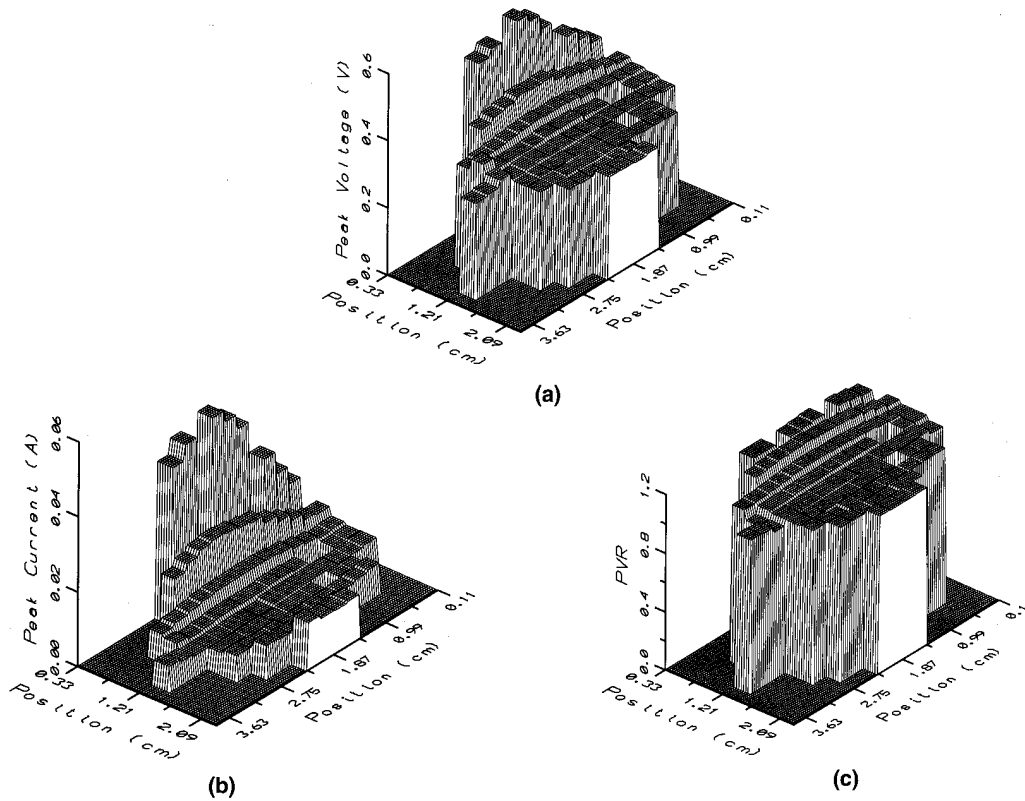


Fig. 5. Wafer maps of the RTD resonant peak voltage (a), peak current density (b), and peak-to-valley current ratio (PVR) (c) for the ALE-grown RTD of Fig. 4 (wafer E124-92, 300 K,  $4 \times 20 \mu\text{m}^2$ ).

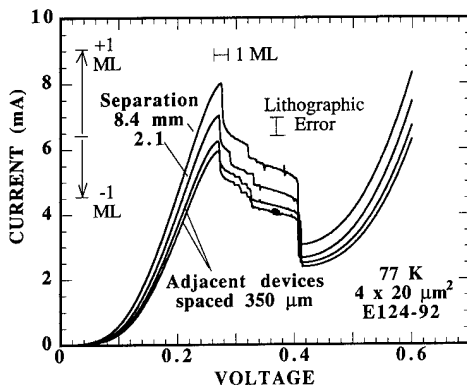


Fig. 6. Comparison of four ALE-grown resonant tunneling diodes along the row corresponding to the fourth row in from the edge of the wafer of Fig. 5 and corresponding to the uniform area of the wafer.

of the reactant gas injectors was not done after the present chamber was modified for ALE growth. As a result, thickness nonuniformities due to gas injector variations of the order of 20–40% exist under conventional MOCVD operation where almost none would be observed for ALE operation under similar growth conditions.

In Fig. 6, we show four  $I$ – $V$  characteristics of this same wafer taken along the fourth row in a line parallel with the cleaved flat. Adjacent devices differ slightly in peak current density, but by less than the lithographic uncertainty. Current increase or decrease by approximately 50% is expected for a single monolayer fluctuation. Since the observed variation (18%) is less than this, the growth of tunnel barriers is reasoned to be controlled to within a fraction of a monolayer. Growth steps [17] and interface roughness [18] in the double barrier structure account for the fact that the observed variations in peak current density and peak voltage are not discrete.

#### 4. Lateral heterojunction resonant tunneling transistor

The ability of ALE to provide conformal overgrowth on etched [19] or selectively grown [20] crystalline facets offers an added degree of freedom for device engineering. This technology offers the possibility of significantly raising the operating temperature of several lateral quantum devices, such as those which use depletion-defined electrostatic barriers formed in the plane of a two-dimensional electron gas to define the

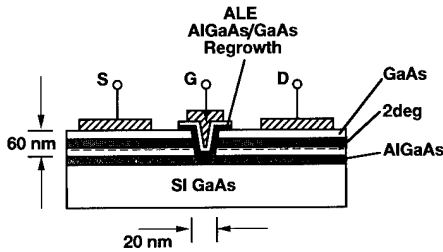


Fig. 7. Proposed lateral heterojunction resonant tunneling transistor formed by conformal atomic layer epitaxial overgrowth.

device geometry. In such systems, the tunnel barriers are both relatively low and relatively wide, which leads to low operating temperatures. By replacing the depletion barriers with lateral heterojunctions, the size of the device can be reduced and the barrier heights increased. This leads to an increase in the quantized state splitting and thereby the temperature of operation.

One such device, the lateral resonant tunneling transistor (LRTT) is shown schematically in Fig. 7. The low temperature multiple NDR characteristics of the LRTT have been demonstrated previously, using depletion-defined tunnel barriers [21–23]. In the proposed device a single trench of order 20 nm width is selectively etched, or otherwise formed, through the two-dimensional electron gas of a modulation doped heterostructure. Lateral heterojunctions formed on the sidewalls by ALE provide dual resonant tunneling barriers between source and drain contacts to the two-dimensional electron gas. Unlike the vertical RTD, in this heterostructure the quantum well region is one-dimensional and the relative alignment between quantized states in the well and the electron source distribution can be controlled by a gate electrode.

The current through the device is the sum over all the current conduction paths through the double barrier,  $I_p \propto (e/h) \sum_i \Gamma_i T_i$ , where  $\Gamma_i$  is the energy width of the  $i$ th tunneling resonance and  $T_i$  is the value of the transmission coefficient at the resonance peak. Simulations of this structure at room temperature indicate that channel current can be modulated by a factor of 50 or more by application of a gate bias. Further reduction in the device dimension normal to the plane of the schematic diagram of Fig. 7 promises still higher modulation factors as the electron gas dimensionality of the source, drain and gate regions is reduced. In addition multiple trench formation allows the realization of multi-input devices to further increase the device function.

## 5. Discussion

We have outlined the characteristics of RTDs grown by ALE, demonstrating both room temperature opera-

tion and monolayer thickness control. We have also proposed a lateral heterojunction resonant tunneling transistor which utilizes the conformal overgrowth of tunnel barriers to raise the transistor operating temperature. For future applications, monolayer dimensional control allows the precise epitaxial definition of quantum device switching voltages and currents. This ability to control the switching thresholds is analogous to the specification of semiconductor bandgaps in conventional device technologies. Further development of the ALE growth method is needed to exploit fully the unique capabilities of ALE over conventional MBE and MOMBE systems for high uniformity and three-dimensional device engineering.

## Acknowledgments

The technical assistance of R. K. Aldert and P. F. Stickney is gratefully acknowledged. The TI authors also thank E. A. Beam, W. M. Duncan, G. A. Frazier, Y.-C. Kao and A. H. Taddiken for useful discussions. This work was sponsored in part by SDIO/IST, ONR/DARPA and AFWL.

## References

- 1 A. Usui and H. Watanabe, *Ann. Rev. Mater. Sci.*, **21** (1991) 185; P. D. Dapkus, B. Y. Maa, Q. Chen, W. G. Jeong and S. P. Denbaars, *J. Cryst. Growth*, **107** (1991) 73, and references cited therein.
- 2 A. Usui and H. Watanabe, *J. Phys. C*, **5** (1987) 21.
- 3 M. Hashemi, J. Ramdani, B. T. McDermott, K. Reid and S. M. Bedair, *Appl. Phys. Lett.*, **56** (1991) 964.
- 4 H. Tian, K. W. Kim, M. A. Littlejohn, S. M. Bedair and L. C. Witkowski, *IEEE Trans. Electron Dev.*, **39** (1992) 1998.
- 5 R. Bhat, J. R. Hayes, E. Colas and R. Esagui, *IEEE Electron Dev. Lett.*, **9** (1988) 442.
- 6 T. Henderson, B. Bayraktaroglu, S. Hussien, A. Dip, P. Colter and S. M. Bedair, *Electron. Lett.*, **27** (1991) 692.
- 7 N. Inoue, H. Yokoyama, M. Shinohara and T. Murashita, *Surf. Sci.*, **267** (1992) 34.
- 8 F. Capasso, S. Sen and F. Beltram, in S. M. Sze (ed.), *High Speed Semiconductor Devices*, Wiley, New York, 1990, p. 465, and references cited therein.
- 9 A. C. Seabaugh and M. A. Reed, in N. G. Einspruch and W. R. Frensley (eds.), *Heterostructure and Quantum Devices*, Academic Press, Orlando, FL, in press.
- 10 A. C. Seabaugh, J. H. Luscombe and J. N. Randall, *Future Electron Dev. J., Japan*, **3** (1992) 16.
- 11 A. C. Seabaugh, Y.-C. Kao and H.-T. Yuan, *IEEE Electron Device Lett.*, **13** (1992) 479.
- 12 H. C. Liu and D. D. Coon, *Appl. Phys. Lett.*, **50** (1987) 1246.
- 13 M. A. Tischler and S. M. Bedair, *Appl. Phys. Lett.*, **48** (1986) 1681.
- 14 P. C. Colter, S. A. Hussien, A. Dip, M. U. Erdogan, W. M. Duncan and S. M. Bedair, *Appl. Phys. Lett.*, **59** (1991) 1440.
- 15 J. H. Luscombe and W. R. Frensley, *Nanotechnology*, **1** (1990) 131.

- 16 S. Ray, P. Ruden, V. Sokolov, R. Kolbas, T. Boonstra and J. Williams, *Appl. Phys. Lett.*, **48** (1986) 1666.
- 17 N. Ikarashi, M. Tanaka, H. Sakaki and K. Ishida, *Appl. Phys. Lett.*, **60** (1992) 1360.
- 18 J. D. Bruno and J. S. Hurley, *Superlattices Microstructures*, **11** (1992) 23.
- 19 Y. Idle, B. T. McDermott, M. Hashemi, S. M. Bedair and W. D. Goodhue, *Appl. Phys. Lett.*, **53** (1988) 2314.
- 20 A. Usui, H. Sunakawa, F. J. Stützel and K. Ishida, *Appl. Phys. Lett.*, **56** (1990) 289.
- 21 S. Y. Chou, D. R. Allee, R. F. W. Pease and J. S. Harris, Jr., *Appl. Phys. Lett.*, **55** (1989) 176.
- 22 K. Ismail, D. A. Antoniadis and H. I. Smith, *Appl. Phys. Lett.*, **55** (1989) 589.
- 23 A. C. Seabaugh, J. N. Randall, Y.-C. Kao, J. H. Luscombe and A. M. Bouchard, *Electron. Lett.*, **27** (1991) 1832.

# GaAs/AlGaAs atomic layer epitaxy in a commercial MOCVD reactor

H. Liu, P. A. Zawadzki and P. E. Norris

Emcore Corporation, 35 Elizabeth Avenue, Somerset, NJ 08873 (USA)

## Abstract

Issues facing large area growth of GaAs by atomic layer epitaxy (ALE) are discussed. We have used a movable X-shaped mechanical barrier to divide the growth chamber into four zones. Alternate zones either supply source gas or mask the wafer from exposure to source gases. The substrate rotating beneath the barrier is alternately exposed to Group III and Group V sources. The thickness uniformity is affected by both the spatial variation of the TMG flux and the range of TMG flux in which self-limited growth is valid. Carbon incorporation can be reduced by using TBA and increasing TBA or AsH<sub>3</sub> exposure time. GaAs epitaxial layers with hole concentration lower than 10<sup>17</sup> cm<sup>-3</sup> and thickness uniformity less than 2% over a 50 mm diameter wafer grown at 580 °C have been obtained. Preliminary 300 K photoluminescence measurement of ALE Al<sub>0.34</sub>Ga<sub>0.66</sub>As grown at 560 °C has shown strong emission intensity which compares with no emission from MOCVD AlGaAs grown at 560 °C.

## 1. Introduction

ALE is an attractive growth technique due to its desirable attributes such as improved thickness and doping uniformity, and digital thickness control. Current problem areas include low growth rate (typically 0.05 μm h<sup>-1</sup> using the alternating gas switching approach), high carbon background and narrow process parameter windows for ALE growth. Several research groups [1–3] have suggested that gas phase decomposition is the major cause of excess surface gallium which limits the extent of the ALE process window. At high temperature and high TMG flux, excess Ga on the surface can lead to greater than one monolayer per cycle ALE growth rate. Ozeki *et al.* [1] have also shown that the removal of the boundary layer is crucial to obtaining the ALE growth mode over a wide process window. The high carbon background has been attributed to insufficient thermal decomposition of trimethylgallium since the temperature range for ALE growth is usually lower than that of conventional MOCVD. Approaches using high temperature and high V/III ratios to reduce the carbon concentration in GaAs and AlGaAs have also been reported [2, 4]. In order to address the problem of low growth rate, an approach has been utilized by Tischler and Bedair [5], which employed a rotating sample holder with adjustable clearance (of the order of <1 mm) under a stationary top plate, alternately exposing the sample to each source gas. Between exposures the sample is rotated under the top plate and the boundary layer is removed before the next exposure. A much higher growth rate of about 0.5 μm h<sup>-1</sup> was obtained due to the elimination of gas switching and the

reduced minimum TMG exposure time (0.25 s) at higher temperatures.

In this work we will discuss issues facing large area growth using ALE such as thickness uniformity and background carbon concentration. Also, preliminary AlGaAs results will be presented.

## 2. Experimental details

Details of the reactor design have been reported elsewhere [6]. A modified EMCORE GS/3300 MOCVD system was used for these ALE studies. The growth chamber is a vertical, cold wall reactor made of stainless steel and incorporates a rotating, resistance-heated Mo wafer carrier. The wafer carrier is capable of holding six 50 mm or three 75 mm wafers. Source gases (and bubbler temperatures) used are trimethylgallium (TMG, -10 °C, tertiarybutylarsine (TBA, 30 °C) and arsine (AsH<sub>3</sub>, 100%).

A top view of the reactor is shown in Fig. 1. The column III and column V precursors are transported to individual dividing flow manifolds (injectors) mounted 180° apart. The injectors are stainless steel tubes with an array of orifices. A movable X-shaped mechanical barrier divides the chamber into four zones. The TMG zone occupies 20% of the total area. The two purging zones are covered by metal plates which prevent exposure to the source gas mixture, which has been a problem within these zones. In order to further isolate individual gas zones, a secondary source of H<sub>2</sub> carrier flows through a tube in the center of the X-shaped barrier down to the center of the wafer carrier. The

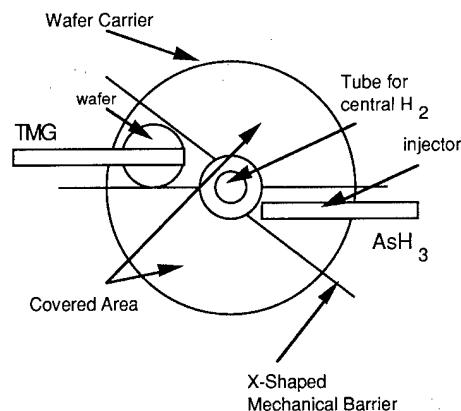


Fig. 1. Top view of the ALE reactor with the dividing barrier.

barrier can be positioned about 0.5 mm away from the wafer carrier and therefore can efficiently shear off most of the hydrodynamic boundary layer. This layer was calculated to be about a few centimeters thick using the equation  $d = 4(\nu/\bar{\omega})^{1/2}$  [7], where  $d$  is the velocity boundary layer thickness,  $\nu$  is the kinematic viscosity and  $\bar{\omega}$  is the angular velocity of the rotating disk. The substrate is rotating beneath the gas streams and thus is alternately exposed to the column III and V precursors. The exposure times of Group III and V precursors can be controlled by changing the rotation speed or pausing the DC servo motor at the respective source zone. In the ALE mode, one revolution consists of one monolayer of column III atoms followed by one monolayer of column V atoms, which results in one monolayer of epitaxial growth (2.83 Å for (100) GaAs). Therefore the total layer thickness is determined only by the lattice constant of the material and the total number of cycles and may be easily controlled by simply counting the number of rotations ('digital epitaxy').

### 3. Results and discussions

Initial results are shown in Figs. 2 and 3 for the growth rate saturation of GaAs (one monolayer per cycle) over a range of TMG flow rates (Fig. 2), and for a range of rotation speeds (exposure time) (Fig. 3). Saturation is observed in both cases indicating that an ALE growth mode has been obtained. The thickness uniformity was found to improve at lower rotation speed and longer exposure times. The reason is not clear, but may be due to insufficient time for surface reconstruction at high rotation (short exposure time). Also, 15% of the wafer area close to the edges (both close to the center of rotation and the edge of wafer carrier) is thinner and may be due to uneven temperature distribution. The best, reproducible thickness uniformity result obtained was  $\pm 1\%$  over 85% of a 50 mm diameter wafer.

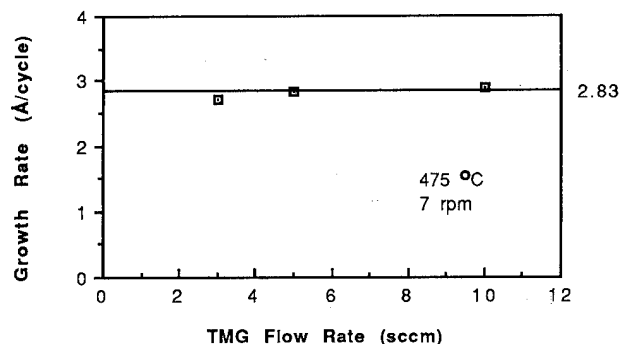


Fig. 2. ALE growth rate vs. TMG flow rate.

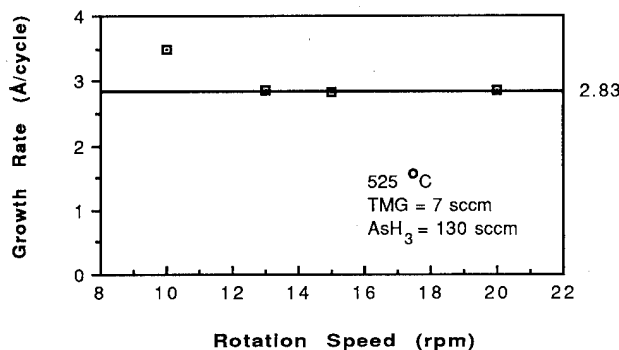


Fig. 3. ALE growth rate vs. rotation speed (exposure time).

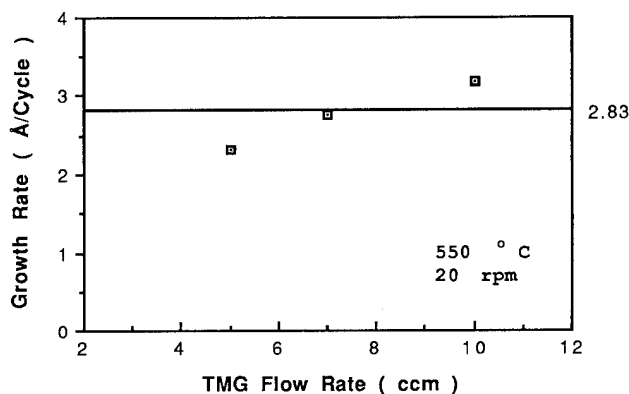


Fig. 4. Growth rate vs. TMG rate at 550 °C.

Figure 4 shows the growth rate vs. TMG concentration characteristic at 550 °C, indicating a non-saturated growth rate. This implies that the ALE growth window has narrowed or completely disappeared. More experiments are needed to further confirm this point. However, Reid *et al.* [8] have observed that in the higher temperature range, self-limiting growth only occurs for a narrow range of TMG exposure times. Colter *et al.* [2] also reported that self-limiting growth was observed only in a narrow range of TMG flow rates at 550 °C in a similar, modified EMCORE reactor. These results have important implications for the ALE growth of



TABLE 1. Temperature effect of thickness uniformity for two injector hole patterns

Run No.	Growth temperature (°C)	Growth rate (monolayer cycle <sup>-1</sup> )	Uniformity (%)
Hole pattern: equal size = 0.03 in.			
345	540	1	3
350	580	0.9	36
359	600	0.9	43
Hole pattern: 0.04 in. for the first four holes, 0.03 in. for the rest			
310	550	1	2.3
312	580	1	2

large area, uniform films since the exposure time and range of Group III flux over the wafer surface have to be within the respective ALE process windows. This argument is supported by the data in Table 1. At high growth temperature, 600 °C, the growth rate at one end of the wafer is lower than one monolayer per cycle and the thickness uniformity is poor, 43%. This indicates a non-uniform TMG flux along the TMG injector. However, this non-uniform flux does not affect the thickness uniformity at 540 °C since the ALE growth process window is wide enough for the variation in TMG concentration to accommodate this variation. When we varied the orifice pattern on the TMG injector, we obtained a uniform film even at 580 °C.

The electrical properties of these films shows heavily p-type conductivity. The hole concentration is typically greater than  $10^{18} \text{ cm}^{-3}$ . The source of the acceptors is likely to be the Group III precursor, TMG. The reduction of carbon incorporation can be enhanced by efficiently removing the methyl group, which can be accomplished by increasing the growth temperature and using high  $\text{AsH}_3$  flux [2, 4]. However, high growth temperature can make uniform films difficult to obtain and high  $\text{AsH}_3$  flux can create difficulties such as cross-contamination between source zones. Therefore, we have investigated the use of an arsenic source which decomposes at a lower temperature than  $\text{AsH}_3$  such as TBA. In addition, a controlled pause was employed beneath the Group V source to increase the exposure

time in order to reduce carbon incorporation. In this way, low temperature ALE growth with low carbon doping may be obtained. The preliminary results are shown in Table 2. Comparing Run No. 345 vs. 369 and 348 vs. 370, we can see that TBA provides higher arsenic overpressure (a hazy surface indicates insufficient arsenic or excess gallium) and higher efficiency of carbon removal (a factor of 3). Also, when the exposure time for the Group V source is increased, the hole concentration is reduced. This has been speculated as due to further methyl group removal by the additional supply of atomic hydrogen from the decomposition of Group V precursors. We have obtained a hole concentration lower than  $10^{17} \text{ cm}^{-3}$  at 580 °C with a V/III of 244 (molar flow rate ratio) and arsine exposure time of 1.4 second.

ALE and MOCVD growth of AlGaAs have been performed at growth temperature as low as 560 °C. Preliminary room temperature photoluminescence results have shown strong emission from the ALE sample (34% of Al) and no emission from the MOCVD sample (21% of Al). Efforts in reducing the carbon incorporation in the AlGaAs film are currently underway.

#### 4. Conclusion

Issues facing large area growth of GaAs by atomic layer epitaxy (ALE) are discussed. The thickness uniformity is affected by the spatial variation of the TMG flux and the range of TMG flux over which self-limiting growth is valid. Uniform thickness films are more difficult to achieve at high growth temperature due to the decreased width of the ALE process window. Carbon incorporation can be reduced by using TBA and increased exposure time (TBA or  $\text{AsH}_3$ ). GaAs films with hole concentration lower than  $10^{17} \text{ cm}^{-3}$  with thickness uniformity less than 2% over a 50 mm diameter wafer grown at 580 °C have been obtained. Preliminary 300 K photoluminescence data for  $\text{Al}_{0.34}\text{Ga}_{0.66}\text{As}$  grown by ALE at 560 °C have shown strong emission intensity as compared with no emission from comparable AlGaAs grown by MOCVD at 560 °C.

TABLE 2. Group V precursor and exposure time effect of background hole concentration

Run No.	TMG (ccm)	TBA (ccm)	Arsine (ccm)	TMG exposure (s)	Group V exposure (s)	Growth temperature (°C)	Hole concentration ( $\text{cm}^{-3}$ )
345	7	80		0.56	0.56	540	$1.4 \times 10^{19}$
348	7	80		0.56	3.85	540	$2.4 \times 10^{18}$
369	7		35	0.56	0.56	540	Hazy
370	7		35	0.56	3.85	540	$7.4 \times 10^{18}$
319	7		80	0.45	0.45	580	$5.5 \times 10^{18}$
350	7		63	0.56	3.85	580	$1.4 \times 10^{17}$

### Acknowledgments

This research was supported by SDIO and monitored by the Office of Naval Research under contract number N00014-90-C-0023. We also thank the valuable discussions with Dr. A. Dip, Dr. K. G. Reid and Dr. S. M. Bedair.

### References

- 1 M. Ozeki, N. Ohtsuka, Y. Sakuma and K. Kodama, *J. Cryst. Growth*, 107 (1991) 102–110.
- 2 P. C. Colter, S. A. Hussian, A. Dip, M. U. Erdogan, W. M. Duncan and S. M. Bedair, *Appl. Phys. Lett.*, 59 (12) (1991) 1440–1442.
- 3 P. D. Dapkus, B. Y. Maa, Q. Chen, W. G. Jeong and S. P. DenBaars, *J. Cryst. Growth*, 107 (1991) 73–82.
- 4 A. Dip, P. C. Colter, G. M. Eldallal and S. M. Bedair, *Proc. SPIE Symp. on Compound Semiconductor Physics and Devices*, Somerset, NJ, March 1992, Vol. 1676, p. 65.
- 5 M. A. Tischler and S. M. Bedair, *Appl. Phys. Lett.*, 48 (24) (1986) 1681–1683.
- 6 H. Liu, P. A. Zawadzki and P. E. Norris, *Proc. SPIE Symp. on Compound Semicond. Phys. and Devices*, Somerset, NJ, March 1992, Vol. 1676, p. 20.
- 7 G. B. Stringfellow, *Organometallic Vapor-Phase Epitaxy, Theory and Practice*, Academic Press, San Diego, 1989, p. 217.
- 8 K. G. Reid, H. M. Urdianyk and S. M. Bedair, *Appl. Phys. Lett.*, 59 (19) (1991) 2397.

# Atomic layer epitaxy of AlAs and $\text{Al}_x\text{Ga}_{1-x}\text{As}$ for device application

A. Dip, G. M. Eldallal, P. C. Colter and S. M. Bedair

North Carolina State University, Department of Electrical and Computer Engineering, Raleigh, NC 27695-7911 (USA)

## Abstract

Atomic layer epitaxy (ALE) of the  $\text{Al}_x\text{Ga}_{1-x}\text{As}$  material system for  $0 \leq x \leq 1$  has been demonstrated on a converted commercial reactor. A second-generation chamber design allows a broadened ALE region of operation over a wide temperature (550–650 °C) and reactant flow range. ALE of device quality GaAs and AlGaAs has been achieved and ALE growth of AlAs has been obtained for the first time. Background doping levels varied from high resistivity to  $10^{20} \text{ cm}^{-3}$  and depended strongly on aluminum content  $x$ , growth temperature and V:III ratio. Also, uniformity results obtained from photoluminescence emissions of AlGaAs/GaAs quantum wells grown by ALE will be presented and discussed.

## 1. Introduction

The ever-increasing demands on the semiconductor industry for better and faster integrated circuits will demand ever-smaller device dimensions. Submicron device geometries and operation of electron devices in the quantum realm will necessitate thickness control on the atomic scale. Additionally, acceptance of III–V semiconductors as a practical successor to silicon will demand high yields over large area substrates. Atomic layer epitaxy (ALE) holds great potential as a growth technique capable of providing such control for III–V semiconductors. Other appealing features of ALE include selective area growth [1], built-in high p-type doping and well-behaved side-wall deposition [2] not possible by normal chemical vapor deposition (CVD) means.

The design of the ALE chamber used for this study is based on one developed previously in our laboratory [3]. The two reactant gas streams (*e.g.* trimethylgallium (TMG) and arsine) are run simultaneously through the chamber separated by both mechanical gas barriers. The substrate is then rotated from the TMG to the arsine stream to complete one cycle of growth.

In recent reports of various device structures, GaAs/AlGaAs lasers [4] and GaAs/AlGaAs heterojunction bipolar transistors (HBTs) [5] were grown using conventional ALE or laser-assisted ALE [6]. In those cases only the GaAs layer was grown by ALE. ALE was not used for deposition of the AlGaAs epilayers, but metal–organic CVD (MOCVD) was used instead. This is chiefly due to the difficulties in depositing ALE AlGaAs films with low background carbon levels. However, we believe that some of the shortcomings of

the ALE growth technique with high band gap materials such as the AlGaAs material system are being overcome. Indeed, we have previously reported on the growth of HBTs entirely by ALE and now report on the ALE growth of additional GaAs/ $\text{Al}_x\text{Ga}_{1-x}\text{As}$  device structures and AlAs material on GaAs substrates.

## 2. Experimental details

The reactor used in this investigation is a modified Emcore 3200 system which has been previously described [7]. The chamber is subdivided into six equally spaced compartments by the quartz partitions which separate the reactant gases and shear off a part of the boundary layer above the substrate. The partition's height above the substrate can be finely controlled for improved confinement of reactant gases and boundary layer shearing. The distance away from the substrate is adjusted via a mechanical feed-through and was set to 1 mm for this study. A growth cycle is composed of an exposure to TMG (and/or trimethylaluminum (TMAI)), flushing by  $\text{H}_2$ , an exposure to  $\text{AsH}_3$  (100%), and flushing by  $\text{H}_2$ . This sequence is carried out by rotating the substrate. All experiments were conducted at a system pressure of 30 Torr. A 1000 ppm silane source (n type) and carbon (p type) from the metal–organic sources were used as the dopants.

First, we will present the results obtained for the GaAs and AlAs binary systems. Then, the results obtained for the ternary AlGaAs alloy system will be presented and followed by a brief review of device application of the GaAs/AlGaAs system.

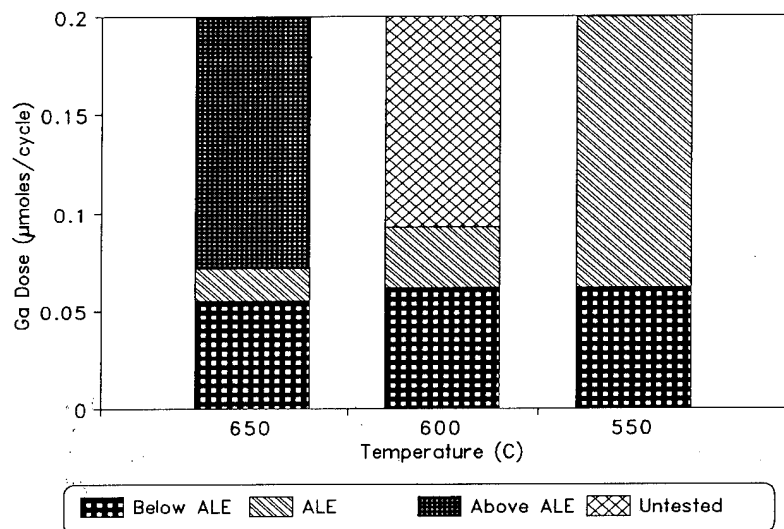


Fig. 1. The ALE region of operation for various temperatures as a function of TMG dose.

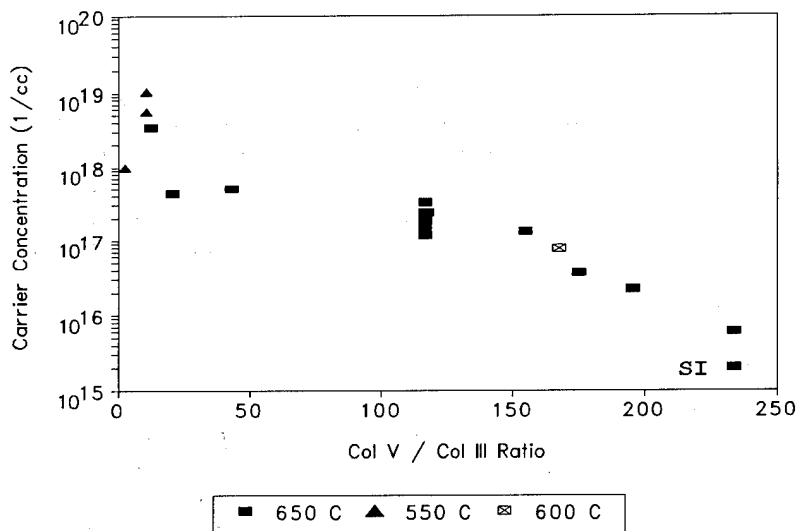


Fig. 2. Background carbon doping of ALE grown GaAs as a function of V:III ratio.

### 2.1. Gallium arsenide

ALE growth of GaAs was achieved over a broad range of temperatures and exposure times to the TMG flux. Figure 1 summarizes the different regions of behavior for a given dose of TMG. The dose was normalized by multiplying the input gallium flux in micromoles per second by the exposure time to TMG per cycle. For example, a rotational rate of 24 rev min<sup>-1</sup> corresponds to a growth rate of 0.4 μm hr<sup>-1</sup> and an exposure time of 0.42 s cycle<sup>-1</sup>. Data points used in generating Fig. 1 were obtained from rotational rates of 18 and 24 rev min<sup>-1</sup>, using both the one- and two-injector configurations for column III sources. From empirical results obtained we can see that the region of self-limited growth exhibits a strong dependence on the growth temperature. Particularly, the 650 °C region of

saturation is narrower than that obtained at 600 or 550 °C.

It was also observed that the background carbon concentration has a strong dependence on the V:III ratio. Figure 2 shows the background p-type carbon doping for several temperatures and V:III ratios. Measured carrier concentrations were obtained from Van der Pauw Hall measurements on films of 0.3 μm or thicker. The point labeled SI in Fig. 2 designates a sample where no Hall measurement could be obtained for a 0.8 μm thick film because of depletion effects. Therefore, this film's background doping level can be estimated [8] to be below  $1 \times 10^{15}$  cm<sup>-3</sup>.

In general, low background doping levels were obtained for high V:III ratios. It was observed for an equivalent dose of TMG (flux multiplied by exposure

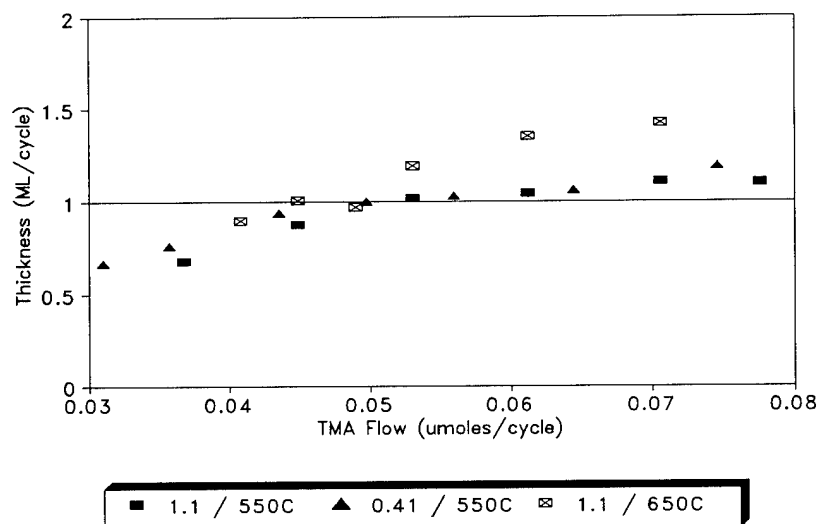


Fig. 3. Growth curve for AlAs; also displayed in the legend is the exposure time to TMAI (in seconds) and growth temperature.

time per cycle), longer exposures at lower fluxes provided a lower background doping level than a higher TMG flux for a shorter exposure time, while keeping the column V flow constant. A longer exposure to the column III element requires a lower column III flow, thus increasing the effective V:III ratio. To prevent possible mixing of the reactant gases, lower TMG fluxes were preferred over high arsine flows for growth of depleted films that required high V:III ratios.

## 2.2. Aluminum arsenide

The saturated growth of aluminum arsenide (AlAs) was also achieved over a wide temperature and exposure range. Saturated growth was observed at both 550 and 650 °C. Figure 3 shows AlAs growth saturating at 1 monolayer (ML) cycle<sup>-1</sup> over the input flux range studied. As expected, the region of saturated growth shrinks as the growth temperature is increased. At 650 °C the ALE region is confined to a 10% input flux variation; although small, this is the highest temperature reported for saturated growth of AlAs.

The regions of saturated growth for both GaAs and AlAs were found to overlap over the same temperature ranges, exposure times and column III reactant input fluxes. The AlAs films exhibited a much higher background carbon concentration than the GaAs. Attempts to reduce the background carbon while maintaining saturated growth results in mid 10<sup>19</sup> cm<sup>-3</sup> carbon doping.

The AlAs films deposited over a TMAI input reactant range near the onset of saturation were observed to have smooth surfaces with excellent specularly. However, as the input flux of TMAI was increased even further, hazing of the films was found to occur. This is believed to be a result of increasing carbon incorporation into

the films. ALE-deposited AlAs/GaAs quantum wells were found to luminescence at 77 K; blue-shifted emission peaks had full widths at half-maximum (FWHM) of about 35 meV.

## 2.3. Aluminum gallium arsenide

A curve showing the self-limited growth of the  $\text{Al}_{0.3}\text{Ga}_{0.7}\text{As}$  is shown in Fig. 4. The region of saturated growth of Fig. 4 appears more related to the AlAs growth curve than to that of GaAs. This implies that the reaction(s) taking place which result in saturated growth have a higher sensitivity to the TMAI precursor than the TMG. This is in good agreement with other published data where difficulty in obtaining saturated growth at 1 ML cycle<sup>-1</sup> of AlAs with TMAI as a precursor was encountered [9]. Since the AlGaAs saturated growth region appears to be dominated by the AlAs saturated growth region, it is desirable to have the latter as broad as possible. Pre-cracking [10] the TMAI and the use of other aluminum precursors [11] are methods recently reported in obtaining saturated growth of AlAs. These techniques may be useful for improving the region of AlAs saturated growth on future experiments.

The variation of background doping was also examined and found to increase with increasing TMG + TMAI flux. This is in agreement with other studies [12], and is due to a higher level of carbon incorporation in the film from the organometallic reactant gases. Background doping levels from low 10<sup>17</sup> to mid 10<sup>19</sup> are possible by changing the conditions under which saturated growth is obtained, such as temperature or column III flow. Background doping levels are controllable over a much wider range by more dramatic changes to the V:III ratio or exposure times to the

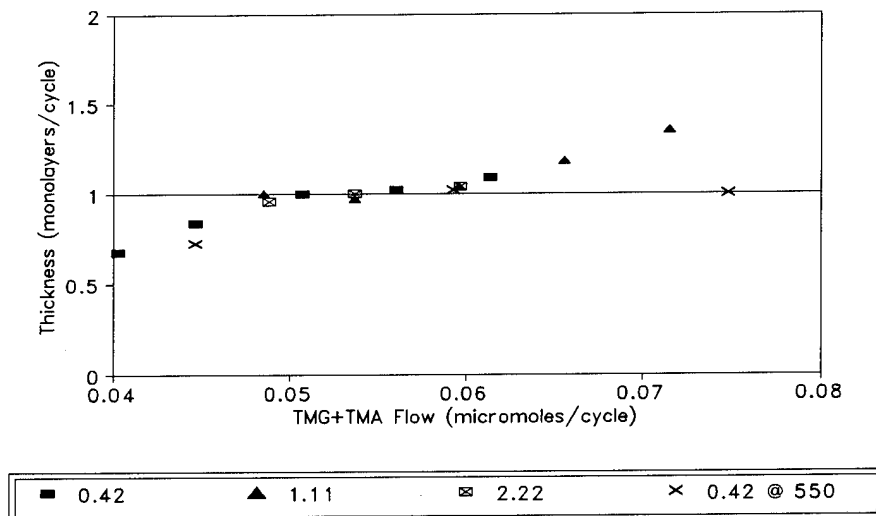


Fig. 4. Self-limited behavior of  $Al_{0.3}Ga_{0.7}As$ : exposure times (in seconds) to column III reactants are given in the legend; growth temperature was 650 °C except where noted.

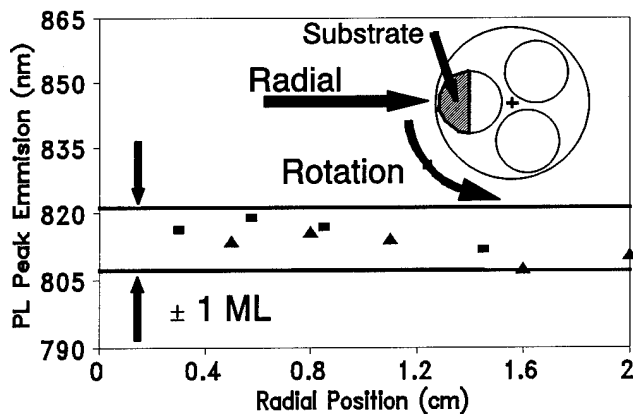


Fig. 5. Room temperature emission observed for 50 Å QW structures grown at 650 °C. The bracketed region corresponds to a 1 ML variation in well thickness.

column III flux, without loss of saturated growth. The highest p-type background carbon level measured was about  $2 \times 10^{20} \text{ cm}^{-3}$ .

The  $Al_{0.3}Ga_{0.7}As$  epilayers also demonstrated good optical properties. Intense photoluminescence (PL) emissions from GaAs/AlGaAs quantum wells (QWs) were obtained at room temperature. These structures used  $Al_{0.3}Ga_{0.7}$  grown at 650 °C as the barrier material. The FWHM of the emissions at room temperature was about 70 meV. The deviation in the peak emissions of the QWs taken at several locations along the substrate's radial direction are shown in Fig. 5. The radial direction is used as a figure of merit for uniformity, since measurements along a track normal to the radial are expected to be uniform resulting from rotation of the susceptor. Shifts in peak energies correspond to radial thickness variations of less than 1 ML across a 2 cm

region. This region of good uniformity is indicated in the schematic of the susceptor plan view in Fig. 5 by the hatched region labeled as "substrate". The reactant gas injection system provides the necessary flux for saturated growth along an outer annular ring of the rotating susceptor. The central region of the susceptor is avoided by the gas inlet jets as much as possible in order to reduce or eliminate any potential reactant gas mixing in or near the center. This results in submonolayer growth for the inner region of the susceptor. Optical measurements made on bulk GaAs films by the groove and stain method [13] with a Philtec 2015-C sectioning system in the radial direction correlated well with the PL emission uniformity results. As expected, virtually no variation in thickness was observed by optical thickness measurements in directions normal to the radial direction.

n-type doping of the  $Al_{0.3}Ga_{0.7}As$  with 1000 ppm silane in  $H_2$  was done. Figure 6 shows the resulting n-type carrier concentrations as a function of the silane flow rate. The  $Al_{0.3}Ga_{0.7}As$  for the n-type doping experiments was deposited at 650 °C with a total column III input flux of about  $0.055 \mu\text{mol cycle}^{-1}$ . These conditions gave a background carbon doping level of about  $2 \times 10^{17} \text{ cm}^{-3}$ . n-type saturation at about  $1 \times 10^{18} \text{ cm}^{-3}$  is found to occur with increases in silane only resulting in a drop in the mobility. This would tend to indicate that increases in dopant flows result in an increased impurity incorporation, and thus the drop in mobility. However, compensation effects may be limiting the upper n-type doping level.

Room temperature Hall mobility for the silicon-doped  $Al_{0.3}Ga_{0.7}As$  films varied from  $1250 \text{ cm}^2 \text{ V}^{-1} \text{ s}^{-1}$  to  $1600 \text{ cm}^2 \text{ V}^{-1} \text{ s}^{-1}$ , for n-type carrier concentrations of about  $1 \times 10^{18} \text{ cm}^{-3}$  and  $3 \times 10^{17} \text{ cm}^{-3}$  respectively.

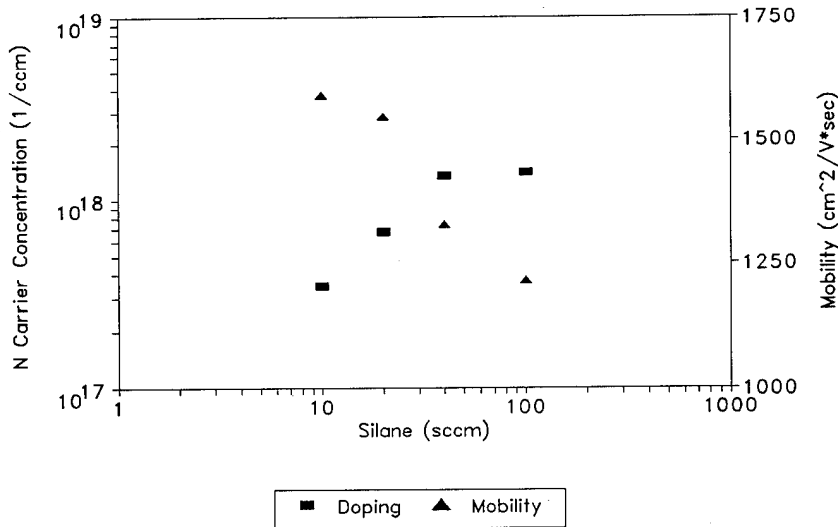


Fig. 6. n-type doping of  $\text{Al}_{0.3}\text{Ga}_{0.7}\text{As}$  with silane at 650 °C; also shown are the mobilities obtained for each experiment.

These mobilities compare favorably with that reported [14] for silicon-doped MOCVD films of about  $220\text{--}2400\text{ cm}^2\text{ V}^{-1}\text{ s}^{-1}$ , and for those reported previously for similar doping concentrations using tellurium [15] and selenium [16] as n-type dopants, of about  $1000\text{--}1800\text{ cm}^2\text{ V}^{-1}\text{ s}^{-1}$ .

We have previously reported use [17] of the GaAs/AlGaAs material system for p-n-p HBTs. More recently we have also grown structures for application as resonant tunneling diodes (RTDs). The RTDs have been generally composed of a 50 Å GaAs well sandwiched by 50 Å  $\text{Al}_{0.3}\text{Ga}_{0.7}\text{As}$  barriers. The entire structure was grown at 650 °C under conditions that gave self-limited growth. A more detailed discussion of the RTD's performance will be presented elsewhere [18].

### 3. Summary

ALE growth of AlAs,  $\text{Al}_{0.3}\text{Ga}_{0.7}\text{As}$  and GaAs was achieved over a wide range of growth conditions on large area substrates in a specially modified commercial reactor. By varying the V:III ratio, exposure times to reactant gases and/or the growth temperature, the background carbon level in these films was controlled from high resistivity to  $p = 2 \times 10^{20}\text{ cm}^{-3}$ . Also, PL results of the undoped  $\text{Al}_{0.3}\text{Ga}_{0.7}\text{As}$ /GaAs and AlAs/GaAs QWs showed the material to be of high quality.

These films were also doped n type with silane as the impurity source. Doping concentrations as high as  $n = 7 \times 10^{18}\text{ cm}^{-3}$  for GaAs and  $n = 1.5 \times 10^{18}\text{ cm}^{-3}$  for  $\text{Al}_{0.3}\text{Ga}_{0.7}\text{As}$  were achieved. Application of the

ALE grown GaAs/AlGaAs system has been demonstrated on RTDs that exhibited good uniformity and performance characteristics.

### Acknowledgments

We gratefully acknowledge support from ONR-SDIO, the NREL and the National Science Foundation which made this work possible.

### References

- 1 A. Usui and H. Sunakawa, *Jpn. J. Appl. Phys.*, 25 (1986) L212.
- 2 S. M. Bedair, B. T. McDermott, Y. Ide, N. H. Karam, H. Hashemi, M. Timmons, M.A. Tishler, J. C. L. Tarn and N. El-Masry, *J. Cryst. Growth*, 93 (1988) 182–189.
- 3 S. M. Bedair, M. A. Tischler, T. Katsuyama and N. A. El-Masry, *Appl. Phys. Lett.*, 47 (1985) 51.
- 4 S. P. DenBaars, C. A. Beylar, A. Hariz and P. D. Dapkus, *Appl. Phys. Lett.*, 51 (1987) 1530.
- 5 R. Bhat, J. R. Hayes, E. Colas and R. Esagui, *IEEE Electron Device Lett.*, 9 (1988) 442.
- 6 Q. Chen, J. S. Osinski and P. D. Dapkus, *Appl. Phys. Lett.*, 57 (14) (1990) 1437.
- 7 P. C. Colter, S. A. Hussien, A. Dip, M. U. Ergogan, W. M. Duncan and S. M. Bedair, *Appl. Phys. Lett.*, 59 (12) (1991) 1440.
- 8 A. Chandra, C. E. C. Wood, D. W. Woodward and L. F. Eastman, *Solid State Electron.*, 22 (1979) 645.
- 9 M. Ishizaki, N. Kano, J. Yoshino and H. Kukimoto, *Jpn. J. Appl. Phys. Lett.*, 51 (1991) L428.
- 10 H. Yokoyama, M. Shinohara and N. Inoue, *Appl. Phys. Lett.*, 60 (3) (1992) 377–379.
- 11 M. Ishizaki, N. Kano, J. Yoshino and H. Kukimoto, *Jpn. J. Appl. Phys. Lett.*, 51 (1991) L435.

- 12 K. G. Reid, H. M. Urdianyk and S. M. Bedair, *Appl. Phys. Lett.*, 59 (1991) 2397.
- 13 S. Wolf and R. N. Tauber, *Silicon Processing for the VLSI Era*, Vol. 1 *Process Technology*, Lattice, Sunset Beach, CA, 1986, pp. 272–273.
- 14 E. P. Visser, X. Tang, R. W. Wieleman and L. J. Giling, *J. Appl. Phys.* 69 (5) (1991) 3266.
- 15 E. E. Wagner, G. Hom and G. B. Stringfellow, *J. Electron. Mater.*, 10 (1) (1981) 239.
- 16 Y. Mori and N. Watanabe, *J. Appl. Phys.*, 52 (4) (1981) 2792.
- 17 T. Henderson, B. Bayraktaroglu, S. A. Hussien, A. Dip, P. C. Colter and S. M. Bedair, *Electron. Lett.*, 27 (1991) 692.
- 18 A. C. Seabaugh, *2nd Int. Symp. on Atomic Layer Epitaxy, Raleigh, NC, 1992*, *Thin Solid Films* 225 (1993) 99.



# Growth and characterization of device quality GaAs produced by laser-assisted atomic layer epitaxy using triethylgallium

Q. Chen and P. D. Dapkus

National Center for Integrated Photonic Technology, Departments of Materials Science and Electrical Engineering, University of Southern California, Los Angeles, CA 90089-0483 (USA)

## Abstract

Triethylgallium is used in combination with arsine in selective area deposition of GaAs by laser-assisted atomic layer epitaxy with the 514.5 nm line of an Ar ion laser. In addition to the much lower laser intensity required to achieve monolayer self-limiting growth than that using trimethylgallium, an intense room temperature photoluminescence response is observable from the double heterostructures of  $\text{Al}_{0.3}\text{Ga}_{0.7}\text{As}/\text{GaAs}$  with the central GaAs grown by this technique, indicating good quality of the GaAs material and interfaces. The GaAs also exhibits low C contamination levels as is evidenced by capacitance–voltage and secondary ion mass spectrometry measurements. GaAs and Zn-doped p<sup>+</sup>-GaAs grown by laser-assisted atomic layer epitaxy are incorporated in broad area laser devices for the first time. A threshold current density as low as  $544 \text{ A cm}^{-2}$  is obtained on a  $570 \mu\text{m}$  long device under pulsed testing conditions at a 10 kHz repetition rate.

## 1. Introduction

Selective area growth by laser-assisted atomic layer epitaxy (LALE) is an attractive technique for realizing complex layer structures in optoelectronic integration. Both trimethylgallium (TMGa) and triethylgallium (TEGa) have been used in LALE studies [1–4]. A systematic LALE study undertaken by us [5] has led to the growth of device quality GaAs by LALE using TMGa and  $\text{AsH}_3$ . The need for further reduction in C contamination in the epilayers was also indicated. C contamination is not uncommon to the growth techniques involving the use of metal–organics at reduced temperature. This may be the consequence of incomplete decomposition of the group III metal–organics and/or the inefficiency of the group V hydrides at low growth temperatures. Although it has been shown that the growth conditions can be optimized to produce device quality GaAs by LALE using TMGa and  $\text{AsH}_3$  [5], further improvement of the material quality is expected only from a change in the growth chemistry by using different precursors.

In this paper, the use of TEGa as the group III precursor in combination with  $\text{AsH}_3$  as the group V precursor in LALE of GaAs is reported. The low C contamination obtainable from metal–organic chemical vapor deposition (MOCVD) [6] and metal–organic molecular beam epitaxy [7, 8] using TEGa makes it a first candidate in the study aimed at reducing the background impurity levels in the GaAs grown by LALE. Photoluminescence (PL) spectroscopy, capaci-

tance–voltage  $C-V$  measurement, and secondary ion mass spectrometry (SIMS) have been utilized to assess the quality of GaAs grown by LALE using TEGa. Through a correlation of the results from material characterization and the growth control parameters, suitable conditions for achieving monolayer self-limiting LALE growth with device quality GaAs are established.

## 2. Experimental procedures

The LALE growth is performed in a switched flow horizontal reactor operated at atmospheric pressure. The schematics of the set-up and the sequence of ALE operation are shown in Fig. 1. The alternate exposure

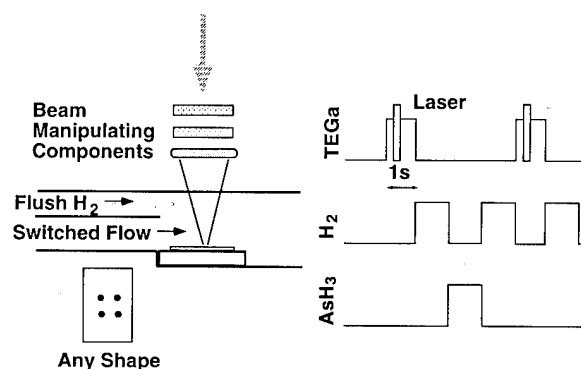


Fig. 1. The schematics of the LALE experimental set-up and the sequence of LALE operations.

of substrates to TEGa and AsH<sub>3</sub> is achieved by temporal switching of the TEGa and AsH<sub>3</sub> into a main carrier H<sub>2</sub> that is flowing continuously through the main chamber of the reactor. The gas handling system and the reactor tube are so designed that both conventional MOCVD and LALE can be performed in a single run of hybridized growth. The optical access is provided by a quartz window situated above the susceptor. A separate stream of H<sub>2</sub> is used to protect the window from fogging. The laser beam from the 514.5 nm line of an Ar ion laser is first expanded and then refocused with a cylindrical lens producing typical beam dimensions of about 10 mm long and about 300  $\mu$ m wide. A chopper mechanism consisting of a beam stop and a computerized stepper motor is utilized to control the timing of laser illumination. Laser pulse durations from 0.03 s to 1 s have been used. It was found previously [9] that the overlap between group III injection and the laser pulse was necessary to obtain monolayer self-limiting growth.

For growth studies, a narrow line is deposited with 300 LALE cycles and the thickness is measured by a stylus profilometer. PL, *C-V*, and SIMS measurements are used to characterize the optical quality and the C contamination. The samples for PL measurement are double heterostructures (DHs) with the central GaAs region (570 Å) grown by LALE using TEGa and the barrier layers grown by conventional MOCVD using TMGa, trimethylaluminum, and AsH<sub>3</sub>. *C-V* measurement was performed with the Schottky contacts formed directly on top of the 0.5  $\mu$ m thick GaAs grown by LALE on either the bare n<sup>+</sup>-GaAs(100) substrates or on the buffer layer of Al<sub>0.3</sub>Ga<sub>0.7</sub>As grown by MOCVD on such substrates. A similar DH structure is used also for SIMS measurement whereby multiple GaAs layers are grown by LALE using a different combination of precursors and the C contamination is studied. LALE was carried out at a substrate bias temperature of about 330 °C. The TEGa source is kept at 20 °C. The accompanying conventional MOCVD growths were carried out at 750 °C.

### 3. Experimental results

Shown in Fig. 2 is the laser intensity dependence of LALE growth rate (in monolayers (MLs) per cycle) for different illumination times. For a given illumination time, the LALE growth rate will depend on the laser intensity at low intensity range before it reaches 1 ML cycle<sup>-1</sup>. At very high laser intensity, on the contrary, LALE growth tends to result in rough morphology with the formation of a polycrystalline deposit. There exists a range of laser intensities with which 1 ML cycle<sup>-1</sup> of LALE growth can be obtained. The onset of the monolayer growth defines a threshold

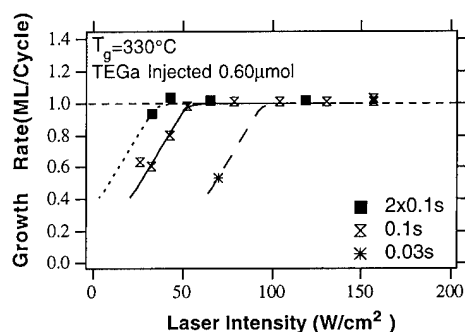


Fig. 2. Laser intensity dependence of LALE growth rate for different illumination times. The lines are drawn to aid the eyes.

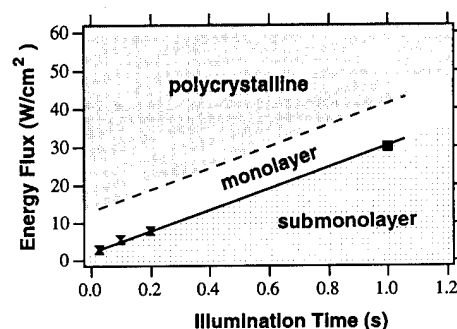


Fig. 3. The illumination for monolayer self-limiting LALE growth. The phase of monolayer LALE operation is obtainable only in the area bounded by the two lines.

intensity for monolayer self-limiting LALE growth at the specific illumination duration. The product of this threshold intensity and the illumination time gives a threshold energy deposit for each LALE cycle (in joules per square centimeter per cycle). Such energy flux for different illumination times is plotted in Fig. 3. The approximate upper bound of LALE monolayer growth is also given by the broken line based on the 0.1 s illumination data in Fig. 2. The point labeled with the square is from work by Meguro and Aoyagi [10]. The plot given in Fig. 3 defines a “phase boundary” of LALE operation within which monolayer LALE growth can be obtained.

Because of the much lower intensity required to achieve monolayer LALE growth in this case than in the case using TMGa, heating effects are greatly reduced. As a result, the lateral definition of the LALE deposit is more abrupt as is shown in Fig. 4 by the full line of the typical cross-sectional profile across LALE stripes as compared with the profile obtained from a stripe grown

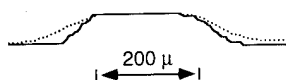


Fig. 4. Typical thickness profiles across LALE stripes grown using TEGa (—) and TMGa (···).

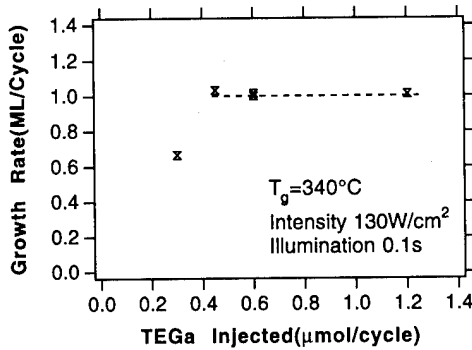


Fig. 5. LALE growth rate as a function of TEGa flux, showing self-limiting growth with respect to TEGa exposure.

using TMGa. This is one of the advantages in using TEGa as the source material.

The LALE growth rate (in monolayers per cycle) as a function of TEGa flux per cycle for the same TEGa exposure time of 1.5 s is plotted in Fig. 5. In contrast to thermal ALE using TEGa where no self-limiting is observable, monolayer self-limiting growth is observed in LALE with respect to TEGa input. This is a strong argument that LALE is not simply the result of localized heating.

Typical room temperature PL spectra from DHs with the central GaAs grown by LALE are shown in Fig. 6 for samples grown using TEGa and TMGa. The intense PL response at room temperature under moderate excitation indicates good quality of the GaAs material and the interfaces. Better PL efficiency is generally obtained in the case of using TEGa despite the lower substrate bias temperature of 330 °C as compared with 380 °C in the case of using TMGa.

In addition, LALE GaAs layers grown to thicknesses up to 0.5 μm were depleted through even at zero bias. A low zero bias capacitance (5 pF) allows us to estimate the background carrier concentration to be  $p \leq 4 \times 10^{15} \text{ cm}^{-3}$  using a built-in potential of 1.4 V. This low

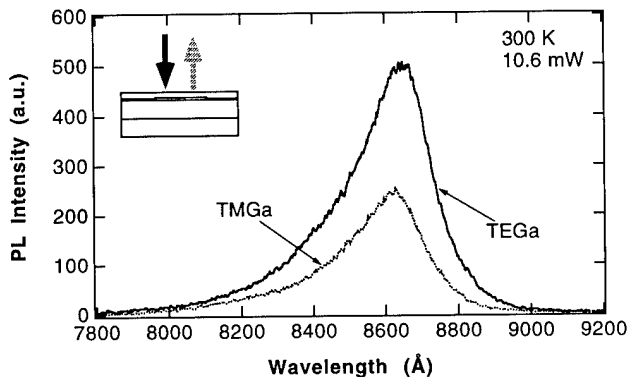


Fig. 6. Room temperature PL spectra from DHs with the central GaAs region grown by LALE using TEGa and TMGa in combination with AsH<sub>3</sub>.

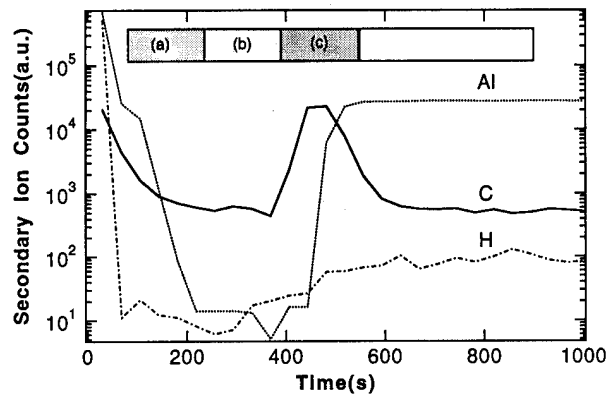


Fig. 7. The SIMS C and Al traces through the structure with the multilayered GaAs region grown by LALE using TEGa and AsH<sub>3</sub> (layer a), TMGa and TBAs (layer b), and TMGa and AsH<sub>3</sub> (layer c).

doping level is accompanied by the fact that Schottky contacts can be formed on top of the GaAs grown by LALE using TEGa with a reverse breakdown voltage as high as 20 V. Direct evidence of C reduction comes from our SIMS measurement as is shown in Fig. 7. The C level in the layer grown using TEGa and AsH<sub>3</sub> (layer a) was not observed above the background level of the Al<sub>0.3</sub>Ga<sub>0.7</sub>As layers used to isolate the LALE GaAs layers. On the contrary, an appreciable amount of C was detected in the layer grown using TMGa and AsH<sub>3</sub>. Growth chemistry is shown to have a substantial influence on the C incorporation in LALE as well as in MOCVD.

The influence of growth conditions on material quality is studied by observing the change in the PL efficiency of the same DH structures grown by LALE under different conditions. The results are summarized in Table 1. First, we see that the PL efficiency is improved by using higher laser intensity. It should be noted here that both intensities listed are within the intensity window for monolayer self-limiting growth. The use of multiple pulses is also seen to improve the PL efficiency. Although the second pulse is triggered 0.5 s after the cut-off of the first pulse and therefore is still overlapping with the 1.5 s TEGa injection pulse, it

TABLE 1. The influence of growth parameters on the photoluminescence efficiency

Growth Parameters	Effect on PL Efficiency
Laser Intensity (76 $\Rightarrow$ 119 W/cm <sup>2</sup> )	Improved
Number of Pulses (0.1 $\Rightarrow$ 2x0.1 s)	Improved
TEGa Exposure (0.45 $\Rightarrow$ 1.3 μmol)	Reduced

causes no additional thickness increase exceeding 1 ML cycle<sup>-1</sup>. Furthermore, the PL efficiency is reduced with increasing TEGa exposure despite the fact that 1 ML cycle<sup>-1</sup> is obtained by virtue of the self-limiting behavior. This suggests that the ranges of TEGa exposure for material of good quality are narrower than those for obtaining monolayer self-limiting LALE growth.

The material characterization data presented above suggest the suitability of the quality of the GaAs material grown by LALE and the interfaces from hybridized growth for device application. We incorporated a single quantum well (QW) of size 100 Å grown by LALE using TEGa into the graded index separate confinement heterostructure (GRINSCH) laser structures. To exploit fully the strength of LALE for *in situ* fabrication, we have also employed Zn-doped p<sup>+</sup>-GaAs (200 Å thick) as the topmost layer to facilitate the alignment in locating the LALE QW region during device processing while providing good ohmic contact between the metal electrodes and the semiconductor. The whole device structure was formed in a single run with four temperature steps. The lower cladding layers (the n side) of the structure were grown first at 750 °C by conventional MOCVD. The substrate temperature was then reduced to 330 °C to carry out the LALE. The top cladding layers (the p side) were again grown at 750 °C. The LALE doping was carried out at 330 °C with the simultaneous injection of TEGa and diethylzinc. The devices were tested at room temperature with no deliberate heat sinking under pulsed conditions at a 10 kHz repetition rate. The device quality of the material and interfaces grown by LALE using TEGa is demonstrated for the first time with a threshold current density as low as 544 A cm<sup>-2</sup> for a cavity length of 570 μm.

#### 4. Discussion

The laser intensity dependence of LALE growth rate shown in Fig. 2 for TEGa is similar to that for TMGa [9] except that the threshold intensity for obtaining 1 ML cycle<sup>-1</sup> is much (about an order of magnitude) lower. At such a low laser intensity as around 100 W cm<sup>-2</sup>, laser induced heating is negligible. The contribution to LALE from localized heating can be ignored. Two other mechanisms are the surface photochemical reaction and the photocatalytic reaction. In a surface photochemical reaction, the molecular orbitals of the surface adsorbates are so modified that their absorption edge is shifted towards lower photon energy than that of the free molecules. For a purely single-photon event, the photons required to produce just 1 ML of surface Ga species should be a constant independent of the manner with which the photons are delivered.

This is not the case as has been shown in Fig. 3. More photons are used to produce 1 ML of surface Ga species when they are delivered at lower intensity for a longer time. In a photocatalytic reaction, the surface electronic states of the semiconductor are so modified that the surface provides one or more reaction pathway(s) for the reacting molecules to pass at a reduced energy barrier. By using an AlAs top layer to isolate the photocatalytic effect due to laser-induced charge transfer, Meguro and Aoyagi [10] showed that LALE can be initiated by the direct absorption of photons by the chemisorbed alkylgallium. In a more general case, both effects may be present as soon as the LALE GaAs becomes thick enough.

The reduction in C incorporation in the GaAs film grown by LALE using TEGa relative to that using TMGa is a result of different reaction mechanisms. The details of TEGa and TMGa decomposition on GaAs surfaces are still being developed. A comparison can be made only by inferring the mechanism from their gas phase decomposition behavior. One of the expected decomposition products from TEGa is C<sub>2</sub>H<sub>4</sub> as opposed to a radical CH<sub>3</sub> in the case of TMGa. The stable C<sub>2</sub>H<sub>4</sub> is much less reactive and less likely to be involved in processes resulting in C incorporation. The β-elimination model of TEGa decomposition leads to Ga species free of C. This is another advantage of using TEGa in LALE. However, because of the low stability of TEGa, the substrate temperature must be low in order to avoid homogeneous decomposition and to obtain selective area growth. This low substrate temperature may eventually become the limiting factor for achieving higher quality materials.

Both an increase in laser intensity and the use of additional laser pulses increase the number of photons irradiating the surface in each cycle. The excess photons, although not inducing further deposition in excess of 1 ML cycle<sup>-1</sup>, are shown to be effective in improving the PL efficiency of the GaAs by LALE. The detailed mechanism for such improvement is not understood, possibly because of enhanced surface species mobility that promotes perfect lattice site registry. Excess TEGa exposure on the contrary causes not only more C to be trapped in the film but also more defects that act as the non-radiative recombination centers. More work is needed to unravel the nature of the defects.

#### 5. Conclusions

LALE using TEGa and AsH<sub>3</sub> as precursors is studied. It is found that much lower intensity is required to achieve monolayer self-limiting LALE growth in this case than that using TMGa. Because of the reduced heating effect at low intensity, LALE using TEGa

results in an abrupt lateral transition in selective area growth. From the fact that the threshold energy flux is dependent on the illumination time, it is suggested that the process is more complex than a surface photochemical reaction through single-photon events.

GaAs grown by LALE using TEGa exhibits low C contamination with a background hole concentration as low as  $4 \times 10^{15} \text{ cm}^{-3}$ . It can also be suggested according to this study that GaAs material of better optical quality can be obtained with reasonably low TEGa exposure, suitably intense laser illumination, and the use of multiple laser pulses. The device quality of the GaAs and the interfaces is demonstrated for the first time by the successful fabrication of broad area GRIN-SCH laser diodes with the single QW grown by LALE using TEGa. A threshold current density as low as  $544 \text{ A cm}^{-2}$  is obtained from a  $570 \mu\text{m}$  long device. The versatility of LALE for *in situ* processing is also explored by employing Zn-doped  $\text{p}^+$ -GaAs as the top-most layer, serving the purpose of precise alignment and ohmic contact.

#### Acknowledgments

This work has been supported by the Strategic Defense Initiative Organization (SDIO-IST) managed by the Army Research Office, the Office of Naval Re-

search, and the National Renewable Energy Laboratory. The authors are thankful to Drs. J. J. Alwan and J. J. Coleman at the University of Illinois for performing the SIMS measurement. Various help and discussions from our colleagues, C. A. Beyler and M. H. MacDougal, are also appreciated.

#### References

- 1 A. Doi, Y. Aoyagi and S. Namba, *Appl. Phys. Lett.*, **49** (13) (1986) 785.
- 2 N. H. Karam, H. Liu, I. Yoshida and S. M. Bedair, *Appl. Phys. Lett.*, **52** (14) (1988) 1144.
- 3 S. P. DenBaars and P. D. Dapkus, *J. Cryst. Growth*, **95** (1989) 195.
- 4 S. Iwai, T. Meguro, A. Doi, Y. Aoyagi and S. Namba, *Thin Solid Films*, **163** (1988) 405.
- 5 Q. Chen, J. S. Osinski and P. D. Dapkus, *Appl. Phys. Lett.*, **57** (14) (1990) 1437.
- 6 T. F. Kuech, E. Veuhoff, T. S. Kuan, V. Deline and R. Potemski, *J. Cryst. Growth*, **77** (1986) 257.
- 7 E. Tokumitsu, Y. Kudou, M. Konagai and K. Takahashi, *Jpn. J. Appl. Phys.*, **24** (1985) 1189.
- 8 N. Pütz, H. Heinecke, M. Heyen and P. Balk, *J. Cryst. Growth*, **74** (1986) 1292.
- 9 Q. Chen, J. S. Osinski, C. A. Beyler, M. Cao, P. D. Dapkus, J. J. Alwan and J. J. Coleman, *Mater. Res. Soc. Symp. Proc.*, **222** (1991) 109.
- 10 T. Meguro and Y. Aoyagi, *Mater. Res. Soc. Symp. Proc.*, **222** (1991) 121.

# Atomic layer manipulation of III–V compounds

Yoshinobu Aoyagi

*The Institute of Physical and Chemical Research (RIKEN), Wako-shi, Saitama 351-01 (Japan), and Extreme Material Research Centre, Osaka University, Toyonaka, Osaka 560 (Japan)*

Kohji Shinmura and Kiyoshi Kawasaki

*Extreme Material Research Centre, Osaka University, Toyonaka, Osaka 560 (Japan)*

Ichirou Nakamoto

*Ishikawajima-Harima Heavy Industries Co. Ltd., Koto-ku, Tokyo 135 (Japan)*

Kenji Gamo and Susumu Namba

*Extreme Material Research Centre, Osaka University, Toyonaka, Osaka 560 (Japan)*

## Abstract

A subtraction process of atomic layer manipulation was achieved in GaAs by alternately feeding an etchant of Cl and applying a low energy Ar ion beam to the GaAs substrate. The etching rate saturates exactly at one molecular layer per cycle and is independent of etchant feeding rate and the energetic ion beam flux. The etched profile is extremely smooth and the number of defects induced by the etching is very small in comparison with that of conventional etching techniques.

## 1. Introduction

Atom manipulation, that is, removal and/or addition of any atom from or on a substrate, has recently become possible by scanning tunnelling microscopy. This atom manipulation makes it possible to fabricate atomic scale devices and to observe new phenomena in the artificially manipulated materials. In the same sense it is possible to have a concept of atomic layer manipulation, removal and/or addition of any atomic layer from or on a substrate. This atomic layer manipulation makes it possible to fabricate new artificial materials in a selected area which have different components in each atomic layer. In achieving atomic layer manipulation, a self-limited layer-by-layer process is indispensable.

The atomic layer epitaxy technique developed recently (e.g. ref. 1) is an additive process of atomic layers on substrates with a self-limiting mechanism. To realize atomic layer manipulation we must have available a technique of layer-by-layer subtraction (etching) from the substrate with a self-limiting mechanism.

This self-limiting etching stops automatically after exactly one molecular layer has been etched from the substrate, and the etch rate is independent of etching parameters such as feeding rate of etchant and flux of the energetic beam used to assist the etching. The etched depth is exactly proportional to the number of cycles of the etching procedure necessary to achieve 1 monolayer etching (one molecular layer per cycle). The

layer-by-layer subtraction may make it possible to etch down the quantum well with a remaining thickness of 1 or 2 monolayers and may flatten the substrate in the atomic scale.

In this paper a subtraction process of atomic layer manipulation, that is ideal molecular layer etching (MLE) with self-limiting at one monomolecular layer, is reported, in which the etching rate saturates at one molecular layer per cycle as a function of the etchant feeding rate and incident energetic beam flux. The characteristics of the etched surface are also examined.

## 2. Experimental procedure

In our experiment, an ultrahigh vacuum electron cyclotron resonance (ECR) plasma system coupled to an X-ray photoemission spectroscopy (XPS) analyser was used as shown in Fig. 1. The ECR system with a background pressure of  $5 \times 10^{-9}$  Torr allows us to transfer the sample in vacuum directly from the ECR etching chamber to the XPS chamber, and to analyse the surface without any exposure to air. A continuous ECR discharge is maintained during the experiment by introducing Ar gas into the ECR discharge chamber.  $\text{Cl}_2$  gas from a mass flow controller is introduced into the discharge chamber through a vent-and-run system for keeping pressure balance in the chamber.

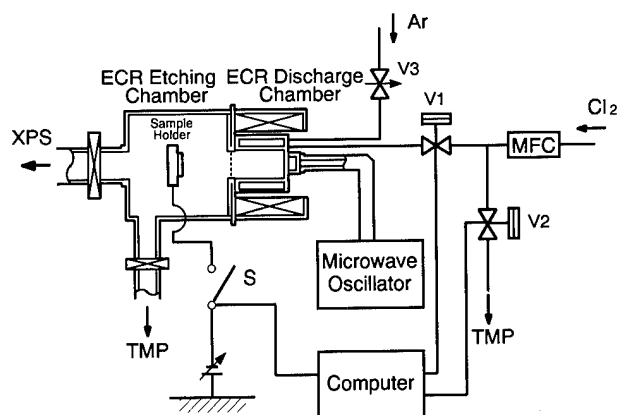


Fig. 1. Schematic diagram of the molecular etching system.

The time sequences and schematic model of MLE are described in Fig. 2. After  $\text{Cl}_2$  gas is fed into the discharge chamber and a purging interval for excess  $\text{Cl}_2$ , a bias voltage is applied to the substrate. While the  $\text{Cl}_2$  gas is fed into the discharge chamber,  $\text{Cl}$  radicals are generated in the chamber and diffuse to the sample surface. After purging, monolayer adsorption of  $\text{Cl}$  radicals is achieved as shown schematically in Fig. 2.

By applying a voltage of 20 eV to the sample holder, a low energy Ar ion beam is extracted from the discharge chamber and irradiates the sample surface, breaking the back bond of every surface atom (sub-surface Ga-As bond) that  $\text{Cl}$  has adsorbed to. Ga-Cl compounds are released from the surface by the beam irradiation, and monolayer etching is completed after the purging of

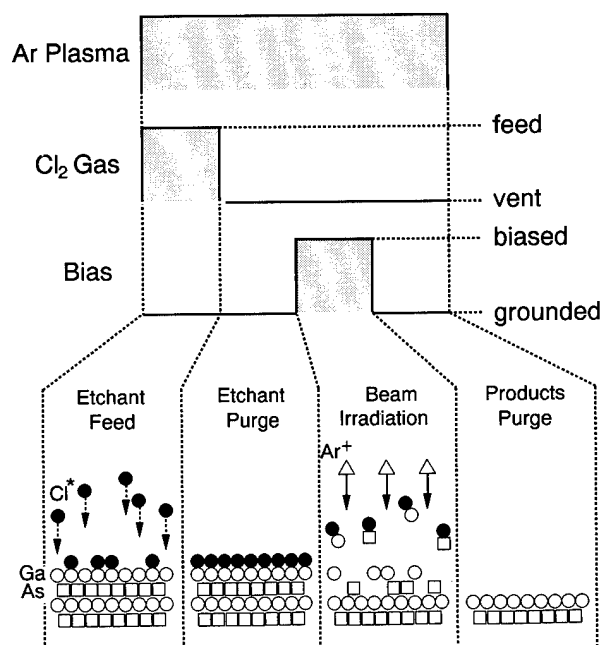


Fig. 2. Time sequences of gas feed, purging and sample biasing for MLE and conceptual view of the procedure of MLE.

these compounds. It was confirmed that the ion current to the sample holder without the acceleration voltage was negligibly small in this system.

The acceleration voltage of 20 eV was chosen so as not to induce physical etching by the Ar ion beam irradiation. It was confirmed that no etching occurs without the acceleration voltage with continuous  $\text{Cl}_2$  feeding, and with an acceleration voltage without  $\text{Cl}$  feeding.

Samples used were n-type GaAs(100) with carrier concentrations of  $5 \times 10^{18} \text{ cm}^{-3}$  and covered with 10  $\mu\text{m}$  line and space Ni masks used for estimating the etching depth. Before etching was started, the oxide layer of the GaAs surface was chemically removed and slightly pre-sputtered by a continuous Ar ion beam with an acceleration energy of 50 eV. It is confirmed by XPS measurement that the oxide layer is completely removed from the surface before the etching starts.

The etching depth is observed by using a Dektak mechanical stylus with an experimental error of about  $\pm 10 \text{ \AA}$ . The etching rate per cycle is determined by dividing the etching depth by the number (60) of etching cycles. The depth of etching caused by pre-sputtering of the oxide layer, which is determined from depth measurements, is subtracted from the measurement.

### 3. Results and discussion

In achieving the monomolecular layer etching condition, it was found that the use of a monolayer adsorption condition of the  $\text{Cl}$  radicals on the GaAs surface was absolutely necessary.

From an analysis of the  $\text{Cl}(2p)$  XPS intensity, the coverage of  $\text{Cl}$  on the GaAs substrate can be determined [2]. Figure 3 shows the amount of  $\text{Cl}$  adsorption on the GaAs surface determined by XPS analysis as a

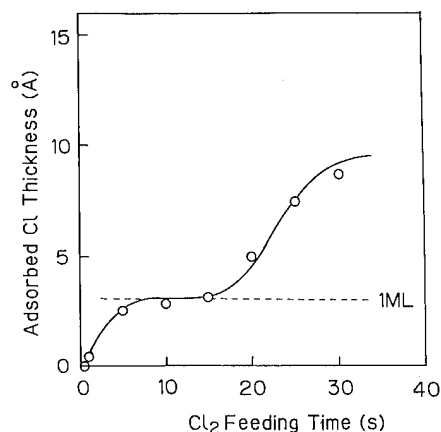


Fig. 3.  $\text{Cl}$  radical adsorption on GaAs surface determined by XPS as a function of  $\text{Cl}_2$  gas feeding time.

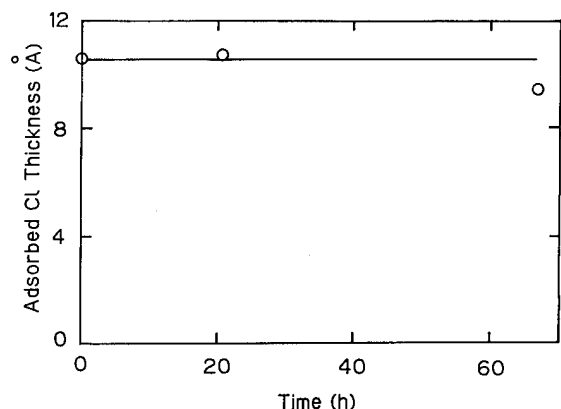


Fig. 4. XPS intensity of adsorbed Cl as a function of time.

function of  $\text{Cl}_2$  gas feeding time into the discharge chamber. From this figure, it is clear that Cl adsorption saturates at 1 monolayer for feeding times between 7 and 15 s. To obtain monolayer etching, the monolayer adsorption condition shown in this figure should be used. In our experiment, a 10 s feeding time of  $\text{Cl}_2$  was used.

It is confirmed that the adsorbed Cl radical on the sample is very stable as shown in Fig. 4. No change in the  $\text{Cl}(2p)$  XPS signal intensity is observed even after the sample has been kept in vacuum for 20 h.

Figure 5 shows the etching rate as a function of  $\text{Cl}_2$  feeding time with a sequence of 100 s for the purging time and successive 20 s Ar ion irradiations with an energy of 20 eV. The etching rate clearly saturates at one molecular layer per cycle for feeding times between 5 and 15 s.

For feeding rates larger than 20 s, the etching rate decreased and had a strong correlation with the thickness of adsorbed Cl atoms on the GaAs surface. It is clear that 1 monolayer etching is achieved for the 1

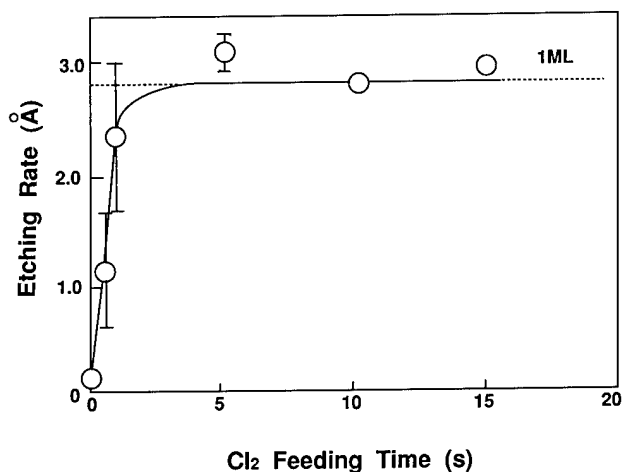


Fig. 5. Etching rate as a function of  $\text{Cl}_2$  feeding time.

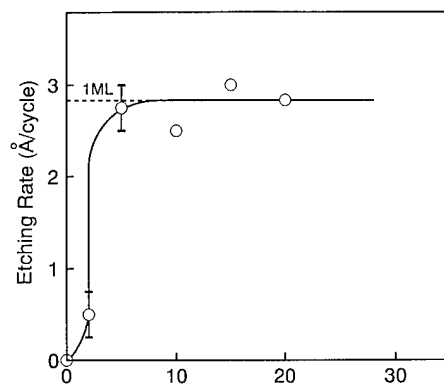


Fig. 6. Etching rate of GaAs as a function of irradiation time of the Ar ion beam.

monolayer adsorption condition of Cl. Under a multiple layer adsorption condition of Cl, the etching rate decreased. This result seems to be due to a stopping effect on Ar ion penetration by the multiple layer absorption of Cl atoms.

Figure 6 shows the etching rate of GaAs as a function of irradiation time of the Ar ion beam. As shown in this figure, the etching rate per cycle is independent of the irradiation time and saturates at a value of one molecular layer per cycle. Figure 7 shows a typical etching profile of MLE compared with normal reactive ion etching. The etched profile is very smooth and flat in the case of MLE but some roughness is observed in the case of conventional etching. This result shows that MLE is advantageous for obtaining a flat profile.

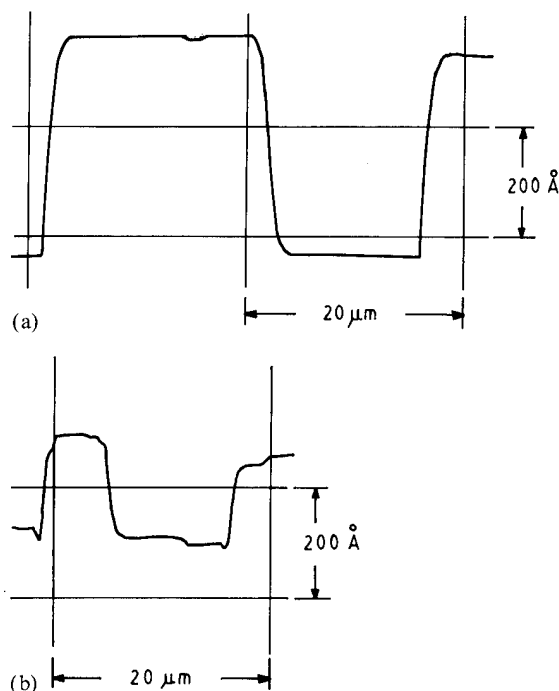


Fig. 7. Etched profile by (a) MLE and (b) normal reactive etching.



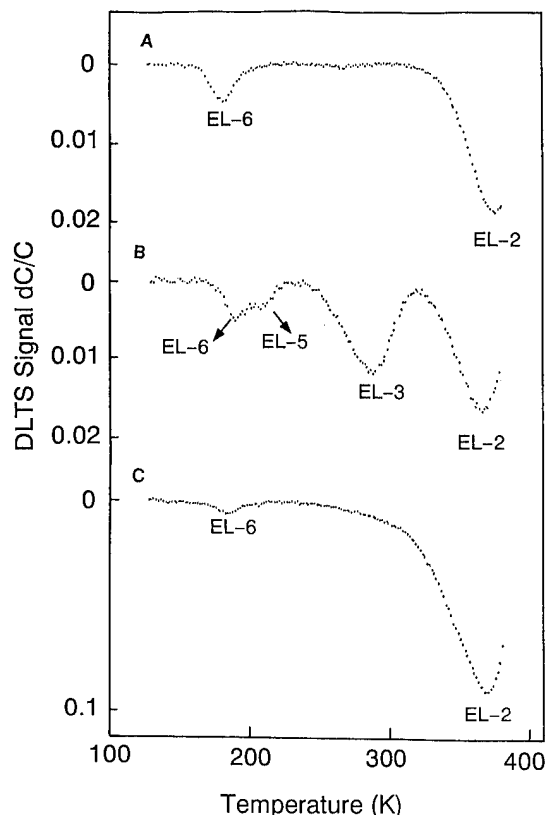


Fig. 8. DLTS spectra of GaAs: spectrum A, control sample, n type,  $5.0 \times 10^{16} \text{ cm}^{-3}$ ; spectra B and C, samples etched by conventional reactive ion beam etching with energy of 20 eV (spectrum B) and MLE (60 cycles) (spectrum C).

Figure 8 shows the deep level transient spectroscopy (DLTS) spectrum of an MLE sample (spectrum C) in comparison with that of a control sample (spectrum A) and that of the sample (spectrum B) etched by conventional Cl reactive ion etching with an ion energy of 20 eV. Peaks EL-2 and EL-3 are due to intrinsic defects and their intensities are sample dependent. The EL-3 signal corresponds to some defects induced during the etching. In conventional etching, the EL-3 peak is observed clearly but is very weak in the case of MLE. Figure 9 shows the photoluminescence intensity of an

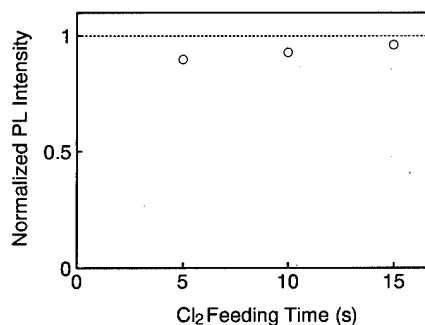


Fig. 9. Photoluminescence intensity of the sample etched by MLE as a function of the  $\text{Cl}_2$  feeding time.

etched sample normalized by the intensity of the control sample observed at liquid  $\text{N}_2$  temperature as a function of  $\text{Cl}_2$  feeding time. The intensity is almost equal to that of the control sample. These results show that MLE is a damage-free process in contrast to the conventional processes.

#### 4. Conclusions

MLE is achieved as a subtraction process of atomic layer manipulation. It is emphasized that monomolecular layer self-limiting etching of GaAs can be achieved under monolayer adsorption conditions of Cl. The etching is independent of both the feeding time of  $\text{Cl}_2$  and the exposure time of the energetic Ar ion beam. The profile of the GaAs surface etched by the MLE technique is very smooth and less damage is induced in comparison with conventional etching techniques. This layer-by-layer self-limiting etching technique makes atomic layer manipulation possible in conjunction with atomic layer epitaxy.

#### References

- 1 T. Suntola, in *Extended Abstracts of Int. Conf. on Solid State Devices and Materials, Kobe, 1984*, Business Centre for Academic Societies of Japan, Tokyo, 1984, p. 647.
- 2 T. J. Chuang, *J. Appl. Phys.*, **51** (1990) 2614.

# Digital etching study and fabrication of fine Si lines and dots

Jiro Yamamoto, Takashi Kawasaki, Hiroyuki Sakaue, Shoso Shingubara and Yasuhiro Horiike

Department of Electrical Engineering, Hiroshima University, 1-4-1 Kagamiyama, Higashi-Hiroshima 724 (Japan)

## Abstract

For the goal of damage-free microfabrication, digital etching in which one or a few atomic layers are removed with minimum reaction energy has been studied. The atomic layer etching of Si(100) was achieved by the precise control of F atom adsorption. To evaluate sidewall etching damage, conductance for lines fabricated on SIMOX was measured at 4.2 K. Lines fabricated by the digital method exhibited no appreciable damage, contrary to the 0.2  $\mu\text{m}$  line fabricated by magnetron reactive ion etching. In a 0.1  $\mu\text{m}$  line subjected partly to an exposure of hydrogen plasma, non-linearity in the  $I$ - $V$  relationship was observed at 4.2 K. The fabrication of Si dots with 20–100 nm diameter was successfully achieved by both an adequate electron beam dose and  $\text{Ar}^+$  irradiation time. Photoluminescence measurements revealed that a significant plastic deformation was generated in oxidized Si dots on SIMOX substrate.

## 1. Introduction

There has been a great deal of effort expended on basic researches in nano-scaled Si devices beyond present Si ultralarge-scale integration circuits. Micro-fabrication of such devices requires higher energy systems in both lithography and etching to achieve high resolution. In particular, reactive ion etching (RIE) which employs energetic ions causes a variety of damage to irradiated surfaces as well as side walls. The etching occurs fundamentally by three simultaneous processes: (1) chemisorption or physisorption of reactive gas such as F or Cl on the surface, (2) energetic beam (e.g. ion, photon, electron) induced reaction between adsorbates and the surface and (3) the desorption of the reaction products. For the goal of damage-free reaction, digital etching which is carried out layer by layer by repeating the fundamental three processes at atomic level with a minimum energy has been studied [1, 2]. In this paper, a study of the F–Si surface reaction in digital etching is reported briefly, and the fabrication of fine Si wires and dots employing this method as well as an electrical and optical evaluation are described.

## 2. Digital etching

Details of the digital etching have been reported in ref. 2. To realize low energy Si etching, the chemistry of F with the highest electronegativity was employed. Figure 1 shows the experimental set-up. A Si(100) wafer was attached on a rotatable disk in a vacuum chamber through a load-lock system. First, F atoms which are

generated by a remote microwave discharge of  $\text{He} + 5\% - 0.2\% \text{F}_2$  in an  $\text{Al}_2\text{O}_3$  tube adsorb on a cooled Si substrate. The exposure time was fixed at 1 s. The adsorption chamber was differentially exhausted. The Si substrate was cooled down to  $-110^\circ\text{C}$  at which the spontaneous reaction hardly occurs. After fluorine exposure, the Si wafer was transferred to another chamber by rotating the substrate table. Next, the surface was irradiated with  $\text{Ar}^+$  ions produced by a downstream electron cyclotron resonance (ECR) plasma at a pressure of  $1 \times 10^{-3}$  Torr, promoting the desorption of the reaction products. The  $\text{Ar}^+$  ion energy was estimated to be 20 eV by the probe measurement, and the measured physical sputtering rate of Si with  $5\%\text{F}_2$ -He and  $0.2\%\text{F}_2$ -He are shown in Fig. 2 as a function of the  $\text{Ar}^+$  ion irradiation time, where the digital etch rate is defined as the total etched depth divided by the

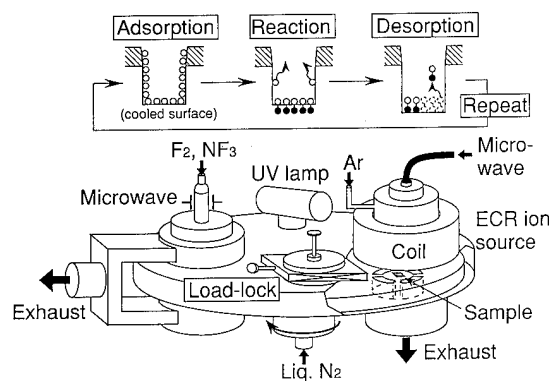


Fig. 1. Schematic illustration of the digital etching method.

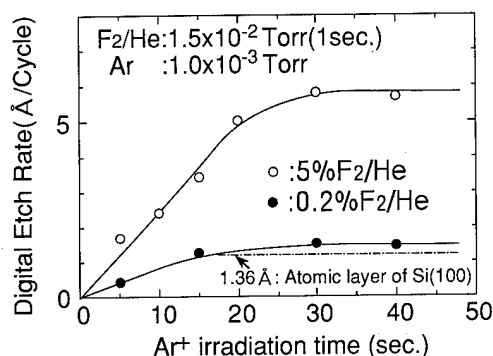


Fig. 2. Digital etch rate of Si with F atoms *vs.* Ar<sup>+</sup> ion irradiation time for a remote plasma of F<sub>2</sub>-He. Two cases of 5%F<sub>2</sub>-He and 0.2%F<sub>2</sub>-He at a pressure of 1.5 × 10<sup>-2</sup> Torr are shown. The substrate temperature was -110 °C.

number of cycles. The etch rate first increases and then reaches a plateau region with an increase in Ar<sup>+</sup> ion irradiation time. The saturated etch rate is 5.7 Å cycle<sup>-1</sup> for 5%F<sub>2</sub>-He at a pressure of 1.5 × 10<sup>-2</sup> Torr. It should be noted that the etching of just one atomic layer of Si(100) takes place in the discharge of 0.2%F<sub>2</sub>-He and the adsorption of a trace amount of F atoms (0.2%) can lead to its monolayer reaction with the Si surface atoms. However, this results indicates that self-limiting characteristics in which the etch rate is independent of parameters such as ion energy and flow rate are difficult to achieve in the case of F chemistry. In the case of Cl chemistry, one Cl atom combines with one dangling bond of Si(100), but the residual oxygen present at the ultimate pressure of 5 × 10<sup>-7</sup> Torr oxidized the Si surface after removal of the Si-Cl layer, thereby reducing the digital etch rate [2].

In order to enhance the very low Si digital etch rate, the reaction chamber was irradiated by a low pressure Hg lamp to promote the F-Si reaction. Nevertheless, the digital etch rate decreased with Hg lamp irradiation time [2]. This implied that the 253.7 nm (about 5 eV)

photon from the lamp desorbed the adsorbed fluorine species from the Si surface. In other words, F is not in a chemisorbed state but rather in a physisorbed state on the cooled Si surface. As soon as F atoms adsorb on the Si surface, they are likely to be recombined through a three-body process to produce condensed molecular fluorine. Accordingly, the etching occurs only when ions impinge onto the physisorbed F on Si through ion-induced F-Si reactions. Hence, in the plateau region in Fig. 2, after a certain amount of F<sub>2</sub> was consumed by reaction with Si, the Si etching was stopped.

### 3. Damage evaluation of fine Si lines

Side wall damage of the etched fine Si lines was evaluated. For this purpose, heavily P-doped (2 × 10<sup>19</sup> cm<sup>-3</sup>) SIMOX (separation by implanted oxygen) substrates (Si(1000 Å)/SiO<sub>2</sub>(5000 Å)/Si) were used. Electron beam (EB) lithography (JEOL JBX 5D-II) with chemical amplification resist (Shipley SAL 601) was used for the delineation of fine wires.

Firstly, a relationship between conductance and wire width was measured for wires fabricated with digital etching or magnetron RIE (MRIE) employing Cl<sub>2</sub> at an r.f. power of 0.4 W and a self-bias  $V_{DC} = -120$  V. The conductance at room temperature (RT; 20 °C) linearly decreased with narrowing wire width for both cases in the width range between 2000 nm and 100 nm. Thus no etching damage was detected in either case in RT measurements. Then, low temperature conductance measurements were carried out for each case. Temperature dependences of the resistance for digital etching and MRIE are shown in Figs. 3(a) and 3(b) respectively. The tendency of the resistance to decrease with lowering temperature is negligibly small in the case of MRIE at a wire width of 200 nm, while it is very large for the 500 nm and 200 nm wires formed by digital

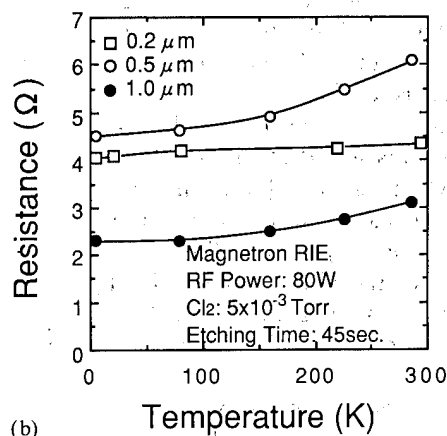
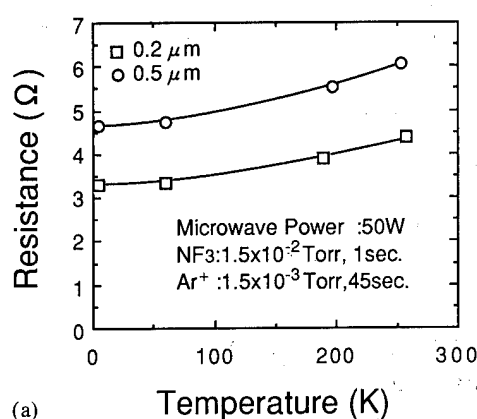


Fig. 3. Temperature dependence of wire resistance for varying wire width: (a) digital etching; (b) RIE.

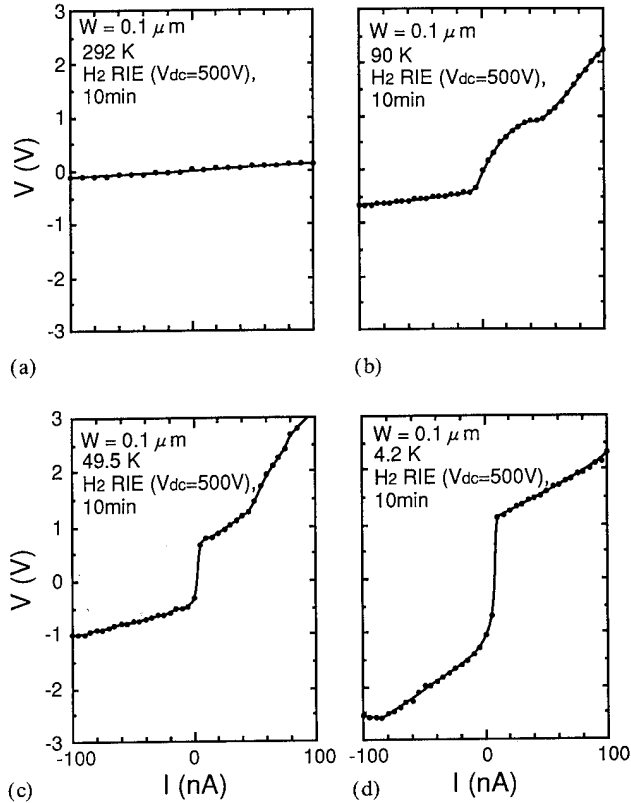


Fig. 4.  $I$ - $V$  characteristics of a 100 nm wire partially exposed to  $H_2$  RIE at various temperatures: (a) 292 K; (b) 90 K; (c) 49.5 K; (d) 4.2 K.

etching. This indicates that the effect of electron scattering by impurities on the resistance is much larger in 200 nm wire in MRIE than in other cases, and it is deduced that a damaged layer was formed at the side wall in MRIE.

Secondly, the effect of  $H_2$  RIE was investigated by exposing to  $H^+$  ions a part of 200  $\mu m$  long wires which were patterned by digital etching. Before the exposure to  $H^+$  ions, the whole area of the wire was covered by a photoresist, and a 20  $\mu m$  wide window was opened by the photolithographic technique. Then, the sample was exposed to  $H_2$  RIE at a self-bias  $V_{DC} = -500$  V for 10 min. The  $I$ - $V$  characteristics for the 100 nm wire measured at various temperatures are shown in Fig. 4. A non-linear  $I$ - $V$  relation was found at low temperature and the non-linearity was enhanced with decreasing temperature to 4.2 K, while a linear relation was observed at RT. On the contrary, a non-linear behaviour was not observed for the 100 nm wire without  $H_2$  RIE treatment even at 4.2 K (Fig. 5). The 200 nm wire exposed to  $H_2$  RIE did not exhibit non-linear behaviour either.

These results strongly suggest that some damage by  $H^+$  ion bombardment was induced not only on the surface but also on the side walls. An elastic recoil

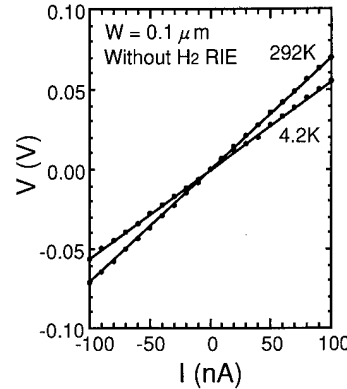


Fig. 5.  $I$ - $V$  characteristics of a 100 nm wire without  $H_2$  RIE fabricated by digital etching at 292 K and 4.2 K.

detection experiment with H atoms and 2 MeV  $He^+$  ions indicated that H atoms distributed in a range of a few tens of nanometres from the surface. The H atom was reported to passivate donor impurities [3], so that it is most probable that an  $n-n^+-n$  structure was formed in the 100 nm wire. It is speculated that a potential barrier formed at the interface between the  $n$  region and the  $n^+$  region plays an essential role in the non-linearity of the  $I$ - $V$  relationship.

#### 4. Fabrication of fine Si dots

Fine Si dots were fabricated by the use of EB lithography with 200 nm thick chemical amplification resist (SAL 601-ER7). In fabricating 40 nm diameter Si dots, the process windows of  $Ar^+$  ion irradiation time for digital etching as well as the EB dose for resist patterning were much narrower than for the wire cases. A comparison of the residual thickness of resist after digital etching between 100 nm dots and wires is shown in Fig. 6, as a function of  $Ar^+$  ion irradiation time. In the case of dots, resist etching was enhanced with an increase in  $Ar^+$  ion irradiation time, and scarcely any resist remained when the irradiation time exceeded 15 s.

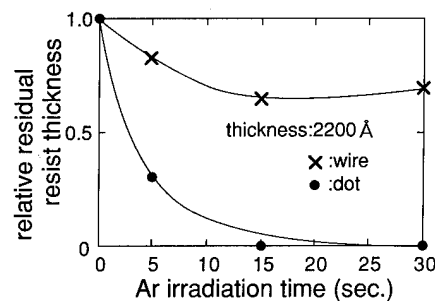


Fig. 6. Relative residual resist thickness as a function of  $Ar$  irradiation time in digital etching for dots and wires.

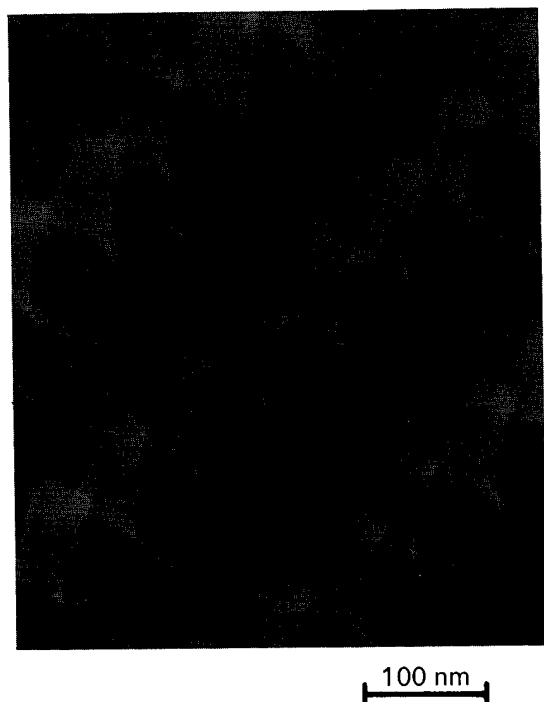


Fig. 7. SEM photograph of 40 nm dots fabricated by digital etching.

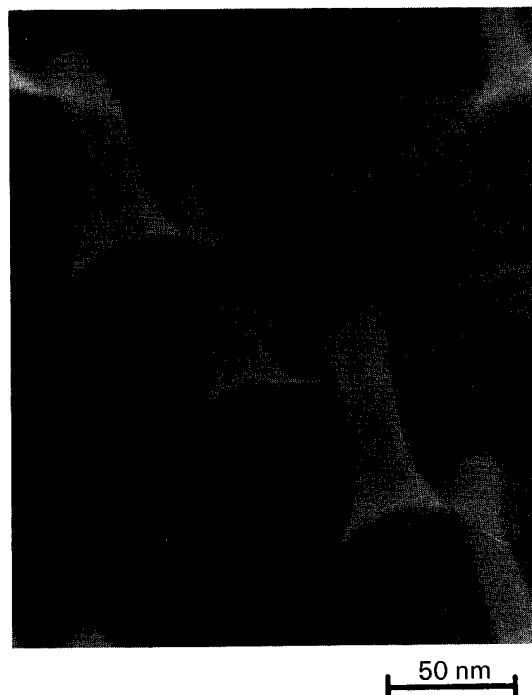


Fig. 8. SEM photograph of fine dots thinned by oxidation and subsequent removal of  $\text{SiO}_2$ .

On the contrary, 65% resist remained even after 30 s irradiation in the case of wires. The difference is ascribed to a heating effect of resist dot patterns during  $\text{Ar}^+$  ion irradiation. The acceptable range of EB dose which was needed for the patterning of an isolated dot with a steep side wall was 26–28  $\mu\text{C}$ . When the EB dose was less than 25  $\mu\text{C}$ , delineated dots fell down, and the bases of the dots crossed each other owing to a backscattered electron proximity effect when the EB dose was more than 30  $\mu\text{C}$ .

Thus, fine Si dot patterns with an average size of 40 nm were successfully fabricated; a typical scanning electron microscopy (SEM) microphotograph is shown in Fig. 7. In order to fabricate even finer dots, dry oxidation of Si and subsequent removal of  $\text{SiO}_2$  by HF wet etching were investigated, and finer dots between 10 nm and 20 nm could be formed (Fig. 8).

Photoluminescence (PL) measurements were carried out for these Si dots by the use of the  $\text{Ar}^+$  ion laser 514.5 nm excitation line at 11 K. A peak at 1130 nm ( $\text{X}_{\text{TO}}$ ) corresponding to bulk free excitonic recombination was observed in 40 nm diameter dots. However, after dry oxidation at 950 °C for 20 min, a significant reduction in the 1130 nm peak and more intense peaks of longer wavelength were observed. In the case of dots formed on the SIMOX substrate, a broad peak was observed at 1330 nm as shown in Fig. 9(a). On the contrary, an intense spectrum consisting of 1180 and 1240 nm peaks was observed in the case of dots formed

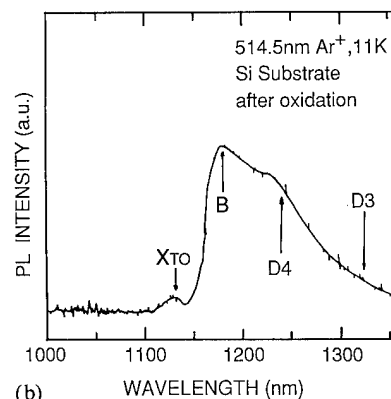
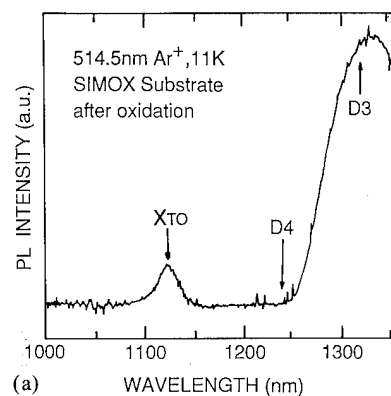


Fig. 9. PL spectra for Si dots after oxidation (900 °C, 20 min) formed on (a) SIMOX and (b) Si substrates.

on a p-Si(100) substrate (see Fig. 9(b)). These observations indicated that a large plastic deformation took place during thermal oxidation, since peaks at 1330 nm and 1240 nm could be identified as D3 (1323 nm) and D4 (1244 nm) emissions of relaxed dislocations [4, 5] respectively. The peak at 1180 nm (B) is identified as transverse optical phonon assisted recombination radiation by B [6], and it suggested that a large accumulation of B occurred near the Si surface during oxidation. These emissions indicative of plastic deformation were scarcely observed in the unpatterned substrate subjected to oxidation. A generation of compressive stress in Si due to volume expansion accompanied by Si oxidation is well known. Concentration of the stress occurs at a curved corner, and its degree is enhanced with decreasing curvature. Hence, it is most likely that an order of magnitude larger compressive stress was generated in 50 nm size dots than in bulk material, and it caused the large plastic deformation. The reason for the difference in the PL spectrum between dots formed on SIMOX and p-Si substrates has not yet been understood clearly, and it may arise from a difference in dislocation types. A large accumulation of B as indicated by the 1180 nm peak may also be caused by a large stress gradient generated near dots during oxidation.

After the removal of  $\text{SiO}_2$  by HF wet etching and subsequent annealing (750 °C, 60 min,  $\text{N}_2$ ), drastic reductions in D3 and D4 peak intensities and a recovery of the free excitonic peak at 1130 nm were observed in dots on both SIMOX and p-Si substrates, as shown in Figs. 10(a) and 10(b) respectively.

The quantum confined size effect in the PL spectrum has been observed in porous Si [7, 8] and microcrystalline Si:H [9]. Although a quantum size effect has not yet been observed, our study would be the first attempt to fabricate Si nanometre dots by lithographic techniques and dry etching. The reported size of microcrystalline Si:H was 2.0–3.0 nm, which was much smaller than the Si dots of the present study. Theoretical work on the three-dimensional size effect on excitons by Kayanuma [10] predicted that the energy level shift from bulk value became apparent when the dot size is smaller than 2–3 Bohr radii  $R_B$  of the bulk free exciton ( $R_B$  is about 5.0 nm for Si [11]), so that the dots of the present work should be of a marginal size to exhibit the quantum size effect.

A broad peak in the PL at around 1004 nm was several times observed in our experiments by the excitation of Ar (514.5 nm) and/or Ar (488 nm) lines; however, the reproducibility of measurements was not sufficiently good. A little surface contamination might delicately affect PL properties. By fabrication of finer dots, less than 10 nm, with a careful control of oxidation and a thorough annealing out of dislocations, the quantum confined effect in the dots should be observable.

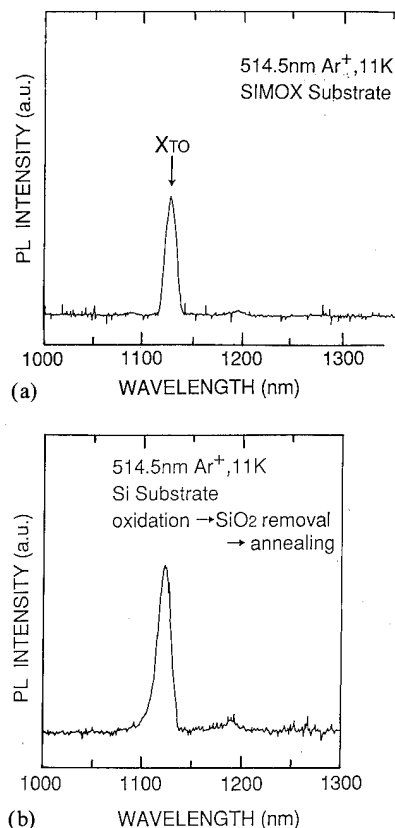


Fig. 10. PL spectra for Si dots after removal of oxide and subsequent annealing (700 °C, 60 min).

## 5. Conclusions

For damage-free microfabrication, digital etching was studied. There was no discernible damage in wires fabricated by digital etching, while damage was detected in MRIE by the low temperature conductance measurement. A non-linear  $I$ - $V$  relationship was observed at low temperature for a 100 nm wire which was partly irradiated by  $\text{H}_2$  RIE. The fabrication of 40 nm Si dots was carried out by digital etching, and they were thinned to 20 nm by the oxidation technique. Considerable dislocation generation was observed in the PL spectrum for the dots owing to oxidation. Sweep out is possible by annealing after  $\text{SiO}_2$  removal. The PL spectrum of fine Si dots less than 40 nm in diameter exhibited a peak at 1004 nm, indicative of a quantum confined effect. However, the reproducibility was poor. Efforts to find the quantum effect by reducing dot size will be made in the future.

## Acknowledgments

The authors would like to express gratitude for Prof. C. Hamaguchi and Prof. K. Taniguchi, as well as Prof. T. Inone and Dr. M. Koyano, for helpful discussions.

## References

- 1 H. Sakaue, S. Iseda, K. Asami, J. Yamamoto, M. Hirose and Y. Horiike, *Jpn. J. Appl. Phys.*, **29** (1990) 2648.
- 2 H. Sakaue, K. Asami, T. Ichihara, S. Ishizuka, K. Kawamura and Y. Horiike, *Mater. Res. Soc. Sym. Proc.*, **222** (1991) 195.
- 3 K. Murakami, H. Suhara, S. Fujita and K. Masuda, *Phys. Rev. B*, **44** (1991) 3409.
- 4 M. Suezawa and K. Sumino, *Phys. Status Solidi*, **78** (1983) 639.
- 5 S. T. Davey, J. R. Davis, K. J. Peeson and P. L. F. Hemment, *Appl. Phys. Lett.*, **52** (1988) 465.
- 6 J. I. Pankove, *Optical Processes in Semiconductors*, Dover Publications, New York, 1975, Chap. 6.
- 7 L. T. Canham, *Appl. Phys. Lett.*, **57** (1990) 1046.
- 8 S. Gardelis, J. S. Rimmer, P. Dawson, B. Hamilton, R. A. Kubiak, T. E. Whall and E. H. C. Parker, *Appl. Phys. Lett.*, **59** (1991) 2118.
- 9 S. Furukawa and T. Miyasato, *Phys. Rev. B*, **38** (1988) 5726.
- 10 Y. Kayanuma, *Solid State Commun.*, **59** (1986) 405.
- 11 J. P. Wolfe, *Phys. Today*, **35** (March 1982) 46.

# Atomic layer epitaxy: chemical opportunities and challenges

Lauri Niinistö and Markku Leskelä\*

Laboratory of Inorganic and Analytical Chemistry, Helsinki University of Technology, SF-02150 Espoo (Finland)

## Abstract

The atomic layer epitaxy (ALE) technique has in ten years established a position as one of the methods capable of controlled processing of thin films. A major part of the 500 studies published has dealt with II–VI and III–V semiconductors and with insulating or conducting oxides. The practically unlimited chemical possibilities of ALE should offer possibilities for widening the scale of materials processed so far. In addition to giving a status report, in this review we discuss some obvious future research trends as well as problems involved in the processing of new materials. To illustrate the difficulties in processing thin films of complicated chemical composition the case of  $\text{YBa}_2\text{Cu}_3\text{O}_{7-x}$  is presented

## 1. Introduction

The earliest atomic layer epitaxy (ALE) publications from the period of the late 1970s to early 1980s demonstrated the basic principle of ALE by describing flow-type reactor constructions [1, 2] and the processing of II–VI semiconductor thin films from the elements and simple inorganic compounds [3, 4]. The original impetus for developing ALE was the need for a better deposition technique in the fabrication of stable thin films for large area thin film electroluminescent (TFEL) devices. As an a.c.-operated TFEL device consists of a dielectric–phosphor–dielectric stack of thin films, research was directed, as well as to II–VI-based phosphors and their doping (e.g.  $\text{ZnS:Mn}^{2+}$ ,  $\text{SrS:Ce}^{3+}$ ), also to the processing of dielectric films ( $\text{Al}_2\text{O}_3$ , Al–Ti oxide) [5]. Another area where ALE research has been active and successful since the middle of the 1980s involves the III–V semiconductors [6]. Several academic and industrial groups in the USA and Japan are studying the processing of III–V semiconductors as shown by recent conference proceedings [7, 8]. Almost exclusively, ALE research has dealt with gas phase deposition and only a few papers on liquid phase or electrochemical ALE have been published [9, 10].

Altogether some 500 publications have been published on ALE including original research papers, reviews, patents and one monograph[11]. It appears that more than 30 groups are actively utilizing the ALE technique for thin film deposition. After an exponential growth in 1985–1988, the number of publications has

TABLE 1. Atomic layer epitaxy publications in the past year

Topic	Number of publications
Ga arsenide	24
Patents	17
Reviews	15
II–VI compounds	8
III–V superlattices, quantum wells	7
Ternary III–V systems	6
Other III–V	5
II–VI superlattices	4
Superconductors	3
<i>In situ</i> diagnostics	3
Al oxide	2
Electrochemical ALE	2
Si	1
Total	97

Source: *Chemical Abstracts* database covering Vols. 114–115 (1991).

levelled off to approximately 100 annually (Fig. 1). As shown in Table 1, semiconductors, especially the III–V compounds, dominate the list of materials with amazingly low activity in other areas.

In the following the chemical opportunities of ALE are discussed with regard to the processing of new materials and material combinations.

## 2. The chemical limits of atomic layer epitaxy

The ALE process is mainly a chemical process [12] which increases in complexity with the increasing bulkiness of the source chemicals undergoing the exchange reaction or sequence of reactions leading to the desired

\*Permanent address: Department of Chemistry, University of Helsinki, SF-00100 Helsinki, Finland.



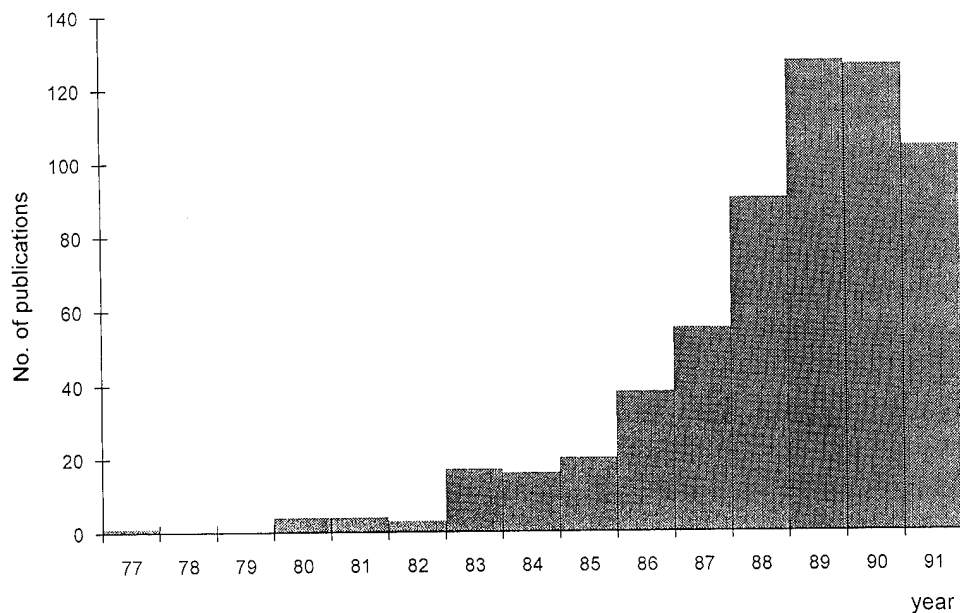


Fig. 1. Publications on ALE 1977–1991. Source: *Chemical Abstracts*.

thin film composition. As well as the source materials and their volatility and stability, the reaction thermodynamics and kinetics need to be considered.

### 2.1. Source materials

Because of insufficient vapour pressure at the ALE operating temperature, the use of elements as source materials is limited to some favourable cases such as Zn and S or to ultrahigh vacuum (UHV) operating conditions (molecular beam epitaxy in ALE mode) where volatility is enhanced. The diatomic gases ( $H_2$ ,  $O_2$ ,  $N_2$ ) are ineffective towards chemisorption and exchange reactions but may be activated by laser and plasma, for instance. On the contrary, the use of inorganic compounds, metal complexes with organic ligands or pure organometallics (containing a metal–carbon bond by IUPAC definition) offers nearly endless possibilities for skilful synthetic chemists.

As to the inorganic compounds, the halides generally have vapour pressures much higher than the corresponding elements [12]. This is true particularly for the covalently bound halides of the transition metals. However, even the halides do not offer suitable starting materials for gas phase transport in the case of rare earth elements where the fluorides, chlorides and bromides have low volatility at the normally used growth temperatures (below 700 °C) and the iodides are not stable enough. The covalently bound halides of the non-metals such as  $SiCl_4$  are also problematic but for another reason: these compounds are inert owing to the strength of the covalent bond between the non-metal and the halogen.

Metal complexes with organic ligands or organometallics usually have higher vapour pressures but this is achieved at the expense of their thermal stability. Trialkylgallium compounds are organometallics which have an established position as GaAs precursors in both the chemical vapour deposition (CVD) and the ALE techniques. As to metal complexes, the  $\beta$ -diketonates offer a possibility to volatilize the alkaline earth and rare earth metals. The synthetic possibilities have not yet been fully explored. For instance, the introduction of F atoms into the  $\beta$ -diketonates increases the volatility. In the 1970s these complexes were extensively studied in connection with gas chromatographic separation and determination of metals and this literature offers useful hints for possible precursors and their chemical modifications [13, 14]; useful further sources are the CVD literature [15, 16] and specialized monographs, for instance metal  $\beta$ -diketonates are discussed in ref. 17.

The source materials may introduce impurities into the films. In the case of metal chlorides it has been demonstrated that chlorine residues are commonly left and these may be detrimental to the films as regards their function and lifetime. In III–V semiconductor films prepared by metal–organic ALE, the C residues pose a serious problem. While the halide residues in thin films can be determined quantitatively at the parts per million level by etching and subsequent spectrophotometry or directly after quantification by secondary ion mass spectrometry [18], their speciation is not straightforward. There are chemical reasons to believe that in the case of alumina films produced from  $AlCl_3$

the Cl residues are associated with O, forming the AlOCl and related phases [19].

In the case of metal complexes, it appears that one needs also to consider the difference in the chemical affinity (bond strength) between the metal and the ligand donor atom in the precursor molecule and, in addition, that between the metal and its neighbour in the resulting thin film. If the affinity in the precursor molecule is large, the metal–donor bond is not (completely) broken in the ALE process and donor atom residues are left in the film. This may explain why, for instance, ZnS films, which are doped with  $\text{Tb}^{3+}$  using the  $\beta$ -diketonate complexes, contain O in the environment of terbium as revealed by extended X-ray absorption fine structure [20].

Finally, a precursor property which requires careful consideration is its toxicity. Many of the existing ALE reactors are non-commercial and lack built-in safety measures such as containment with reduced pressure and continuous monitoring of toxic gases.

## 2.2. Reaction mechanism and energetics

The ALE process can be most simply described as being based on the difference between chemisorption and physisorption (adsorption). The true situation is more complicated and various surface processes such as collisions, bond formation, desorption, surface migration and surface reconstruction take place before the chemisorption sites representing the potential energy wells are occupied. However, this is one of the main advantages of ALE: weak bonds are eventually eliminated because of the energy minimum requirements. Another useful model to describe the operating conditions of the process is the concept of the “ALE window” [21] (Fig. 2).

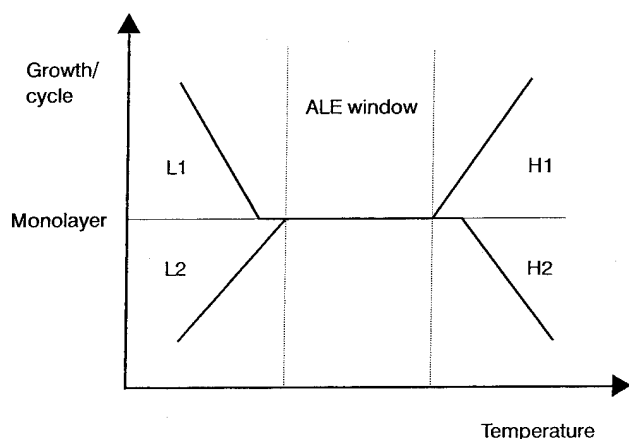


Fig. 2. The concept of the ALE temperature window [21]. L1 and L2 refer to condensation and incomplete reaction while H1 and H2 denote decomposition and re-evaporation respectively. The window indicates the temperature range where self-controlled layer-by-layer growth takes place.

There have been a few theoretical approaches to explain the surface states and reaction mechanisms in an ALE process. ZnS provides an interesting case because experimental data on growth rates as well as on surface and gas phase compositions are available for comparison. On the basis of various surface models and experimental data on the uptake and release of the reactant and product gases, a possible reaction pathway has been suggested for the ALE process  $\text{ZnCl}_2 + \text{H}_2\text{S} \rightarrow \text{ZnS} + 2\text{HCl}$  [22, 23]. The same researchers have also studied possible ALE processes leading to the formation of silicon from silanes and chlorosilanes [24]. In spite of the interesting results obtained by Pakkanen *et al.* it appears that the practical value of theoretical studies in predicting actual reaction pathways is still limited. The *ab initio* valence calculations are very tedious and require compromises, especially when heavier atoms are involved. Furthermore the choice of the surface model is crucial for the reliability [23].

When bulky organometallics or metal chelates with organic ligands are employed as starting materials the difficulties in elucidating the reaction mechanisms, experimentally or theoretically, are almost impossible to overcome. These compounds have complicated structures (Fig. 3) and they may decompose and recombine in the gas phase in an unpredictable manner which leads to a mixture of oligomers and dissociation fragments in addition to the original complex as revealed, for instance, by the mass spectrometric studies of  $\text{Ca}(\text{thd})_2$  and  $\text{Ce}(\text{thd})_4$  ( $\text{thd} \equiv 2,2,6,6$ -tetramethyl-3,5-heptanedione) [25, 26]. Probably owing to steric factors the growth rate with the bulky thd chelates is low, *e.g.* only  $0.5\text{--}0.6 \text{ \AA cycle}^{-1}$  for SrS from  $\text{Sr}(\text{thd})_2$  and  $\text{H}_2\text{S}$ . Furthermore, the surface state is unstable and changes with temperature: when the substrate (reactor)

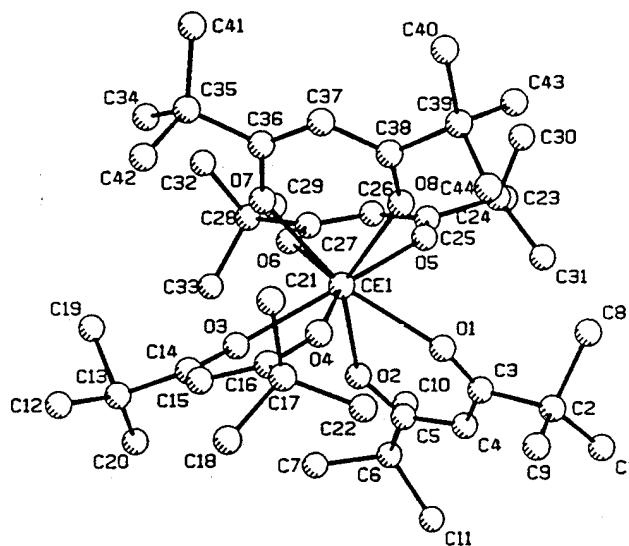


Fig. 3. Structure of the  $\text{Ce}(\text{thd})_4$  molecule in the solid state [26].

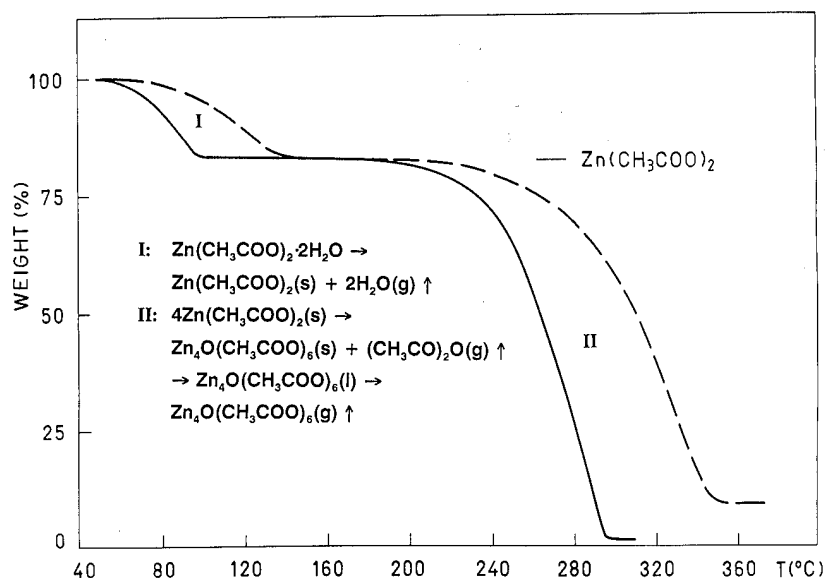


Fig. 4. Thermogravimetric curves in flowing nitrogen showing dehydration (region I) and the thermally induced conversion of Zn acetate into a tetrameric volatile complex (region II). Results for slow (5 °C min<sup>-1</sup>; —) and fast (40 °C min<sup>-1</sup>; ---) heating rates are shown [28].

temperature increases above 400 °C another competing reaction mechanism appears [5, 27].

However, there are examples where bulky complexes containing several metal atoms can be used as precursors for controlled growth at high rates. This requires that the complex is volatile, stable enough and contains the metals in a favourable geometrical arrangement for the formation of a surface layer of the desired product. These requirements are fulfilled in the case of the  $\text{Zn}_4\text{O}(\text{CH}_3\text{COO})_6$  molecule formed from  $\text{Zn}(\text{CH}_3\text{COO})_2$  (Fig. 4) [28] which gives in the growth of ZnS thin films a significantly higher growth rate than  $\text{ZnCl}_2$  [29]. A similar but not yet fully characterized system is the  $\text{Pb}_4\text{O}(\text{OBu})_6$  complex for the growth of PbS thin films [30].

When thin film growth of covalently bound compounds or elements ( $\text{Si}_3\text{N}$ , B, Si etc.) is attempted, temperature alone is not enough to activate the precursors but additional energy is needed in the form of UV or laser radiation, for instance, in order to produce and activate reactive radicals. Only very recently has progress been made in this area [8, 31]. For instance, Greene *et al.* have studied the mechanism and kinetics of photostimulated silicon deposition by ALE using  $\text{Si}_2\text{H}_6$  as a precursor [32].

### 2.3. An illustrative example: $\text{YBa}_2\text{Cu}_3\text{O}_{7-x}$

Probably the most exciting group of new materials discovered during the second half of this century is the new oxide-based high temperature superconductors first reported in 1986 [33]. A major part of the applications-oriented research has been focused on the processing of thin films from  $\text{YBa}_2\text{Cu}_3\text{O}_{7-x}$  (1-2-3 phase) which

has a layered perovskite-type structure and a critical temperature  $T_c = 90$  K. Requirements of high  $T_c$  superconducting thin films for electronic applications include, in addition to  $T_c = 90$  K (above the boiling point of  $\text{N}_2 + 10$  K), that the critical current  $J_c$  is at least  $1 \text{ MA cm}^{-2}$  and the surface resistance  $R_s$  is below  $10^{-4} \Omega$ , the latter values being measured at 77 K, 20 GHz. The surface of the films should be smooth ( $\pm 100 \text{ \AA}$ ) and the relatively large substrates (2 in wafers or larger) should be covered on both sides. A further desirable process parameter is *in situ* growth at low temperatures (below 900 K) in order to achieve compatibility with existing very-large-scale integration technology.

While good quality high  $T_c$  superconductor thin films can be grown by several methods [34] it is the requirement of uniformity over a large substrate area which makes ALE (and CVD) an attractive choice for *in situ* growth [35].

From the chemical point of view, the thin film growth of the new superconductors by ALE represents a challenge. For the gas phase growth of  $\text{YBa}_2\text{Cu}_3\text{O}_{7-x}$ , a copper precursor can easily be found but yttrium and especially barium are problematic if one works outside the UHV range. In the CVD growth of  $\text{YBa}_2\text{Cu}_3\text{O}_{7-x}$ , metal halides ( $\text{YCl}_3$ ,  $\text{BaI}_2$ ,  $\text{CuCl}$ ) have been employed [36] but most groups have chosen the  $\beta$ -diketonate chelates as precursors [35]. Unfortunately, Ba forms the most unstable thd complex of all alkaline earths and it exists as an oligomer already in the solid state fractionating then in the gas phase [37]. Furthermore, as the system contains C the relatively stable Ba carbonate (decomposes above 800 °C) is readily formed when ozone or another active form of O is introduced. Because

the susceptor temperature cannot be changed, a major obstacle is also to find a compromise for the ALE temperature window satisfying simultaneously the deposition conditions for all three metal oxides.

CVD-grown thin films of  $\text{YBa}_2\text{Cu}_3\text{O}_{7-x}$  have good critical values [35] and promising results have also been obtained by layer-by-layer type growth [38]. A fundamental problem remains, however, in that the 1–2–3 phase is not thermodynamically stable with respect to assemblages containing combinations of  $\text{Y}_2\text{BaCuO}_5$ ,  $\text{Y}_2\text{Cu}_2\text{O}_5$ ,  $\text{BaCuO}_2$ ,  $\text{Y}_2\text{O}_3$  and  $\text{CuO}$  [39]. Therefore the so-called 1–2–4 compounds or Bi-containing phases may be better choices but their production also is not without problems.

### 3. New materials by atomic layer epitaxy

Currently only a limited number of materials have been prepared by ALE (Table 2). The research has been focused on areas where potential and needs of the electronic and optoelectronic applications are the greatest. In addition to the III–V and II–VI compounds for semiconductors and electroluminescent applications, a considerable research effort is now being directed to the processing of group IV elements and compounds [8, 31].

As regards oxides, Table 1 indicated activity only in the case of alumina and the high  $T_c$  superconductors. It is expected that other oxide materials will and can be processed by ALE for optical applications or for buffer and substrate layers. ALE offers in many cases a possibility that several layers of different compositions and functions can be made in an integrated process, thus minimizing contamination etc. The inherent slow growth rate, which is one of the disadvantages of ALE, can be partially overcome by precursor design as in the case of ZnS growth from  $\text{Zn}_4\text{O}(\text{CH}_3\text{COO})_6$  [28] or by reactor design [40].

TABLE 2. Thin films grown by atomic layer epitaxy

II–VI compounds
ZnX (X = S, Se, Te, O), MS (M = Ca, Sr, Ba)
Doping with Mn, rare earths, Pb
PbS, CdTe
III–V compounds
GaAs, InP etc., also multilayers
Oxides
$\text{Al}_2\text{O}_3$ , $\text{SnO}_2$ , $\text{TiO}_2$ , $\text{CeO}_2$ , Al–Ti oxide, $\text{In}_2\text{O}_3$ , $\text{Ta}_2\text{O}_5$
Transition metal nitrides
TiN, TaN, NbN etc.
Superconductors
$\delta\text{-NbN}$ , $\text{YBa}_2\text{Cu}_3\text{O}_{7-x}$ , Bi-containing phases
Elements
Si, Ge, C (?)
Other
GaN, $\text{La}_2\text{S}_3$

Areas where ALE activity is almost non-existent include the deposition of metals and covalently bound hard materials (borides, carbides, nitrides). A preliminary study of the transition metal nitride phases [41] indicates that good quality thin films with interesting properties can be grown.

In order to be able to produce the new materials there is a need in some cases for improved reactor designs. Also, the limited availability of *in situ* characterization techniques outside the UHV range has slowed the development.

### 4. Conclusions

In comparison with other thin film deposition methods, it is the chemical versatility of ALE together with the method's inherent advantages which offer wide, but still only partly explored, opportunities. Provided that suitable source materials are available or can be synthesized and that the kinetics and thermodynamics of the exchange reaction are favourable, a variety of new materials can be prepared.

The advantages of ALE include controlled thin film growth with uniform thickness over large substrate areas of varying geometrical shape. The doping is straightforward, at least in the concentration level of a few atomic per cent, and the number and type of layers is in principle unlimited. There is also a possibility to tailor the interfaces and to grow the film stacks in a continuous process without exposing them to the air.

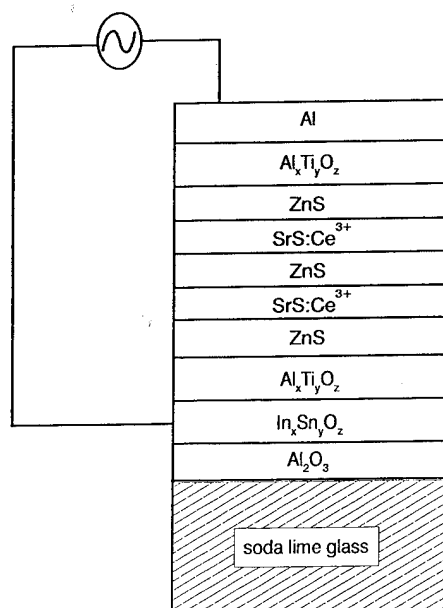


Fig. 5. An advanced TFEL structure where all layers can be deposited and doped (except for the upper Al electrode) by ALE in a continuous process, if necessary.

An example from the TFEL technology is shown in Fig. 5. The disadvantages of the method, especially the slow growth rate, can be partly compensated by precursor and reactor design. While for binary compounds the process parameters can in most cases be found and optimized the processing of thin films with more complicated structures remains a challenge in the ALE technique.

### Acknowledgments

The authors wish to thank the members of the ALE group at the Helsinki University of Technology for stimulating discussions and help in preparing the manuscript. The research project is partly financed by Technology Development Centre (TEKES) through Grant 02114-4.

### References

- 1 T. Suntola and J. Antson, *US Patent 4,058,430*, 1977.
- 2 T. Suntola, A. Pakkala and S. Lindors, *US Patent 4,389,973*, 1983.
- 3 C. H. L. Goodman and M. V. Pessa, *J. Appl. Phys.*, **60** (1986) R65.
- 4 T. Suntola and J. Hyvärinen, *Annu. Rev. Mater. Sci.*, **15** (1985) 175.
- 5 M. Leskelä and L. Niinistö, in V. P. Singh and J. C. McClure (eds.), *Proc. 6th Int. Workshop on Electroluminescence, El Paso, TX, 1992, Electroluminescence*, Cinco Puntos Press, El Paso, TX, 1992, p. 249.
- 6 M. A. Tischler and S. M. Bedair, in T. Suntola and M. Simpson (eds.), *Atomic Layer Epitaxy*, Blackie, Glasgow, 1990, p. 110.
- 7 L. Niinistö (ed.), *Proc. 1st Int. Symp. on Atomic Layer Epitaxy, Helsinki, 1990*, in *Acta Polytech. Scand., Ser. Chem. Technol.*, **195** (1990).
- 8 S. M. Bedair (ed.), *Proc. 2nd Int. Symp. on Atomic Layer Epitaxy, Raleigh, NC, 1992, Thin Solid Films*, **225** (1993).
- 9 Y. F. Nicolau, *Appl. Surf. Sci.*, **22-23** (1985) 1061.
- 10 B. W. Gregory and J. L. Stickney, *J. Electroanal. Chem. Interfacial Electrochem.*, **300** (1991) 543.
- 11 T. Suntola and M. Simpson (eds.), *Atomic Layer Epitaxy*, Blackie, Glasgow, 1990.
- 12 M. Leskelä and L. Niinistö, in T. Suntola and M. Simpson (eds.), *Atomic Layer Epitaxy*, Blackie, Glasgow, 1990, p. 1.
- 13 G. Guichon and C. Pommier, *Gas Chromatography in Inorganics and Organometallics*, Ann Arbor Science Publishers, Ann Arbor, MI, 1973.
- 14 G. Schwedt, *Chromatographic Methods in Inorganic Analysis*, Hüthig, Heidelberg, 1981.
- 15 L. A. Ryabova, *Curr. Top. Mater. Sci.*, **7** (1981) 587.
- 16 G. B. Stringfellow, *Organometallic Vapor Phase Epitaxy, Theory and Practice*, Academic Press, Boston, MA, 1989, p. 15.
- 17 R. C. Mehrotha, R. Bohra and D. P. Gaur, *Metal  $\beta$ -Diketonates and Allied Derivatives*, Academic Press, London, 1978.
- 18 H. Antson, M. Grasserbauer, M. Hamilo, L. Hiltunen, T. Koskinen, M. Leskelä, L. Niinistö, G. Stinger and M. Tammenmaa, *Fresenius Z. Anal. Chem.*, **322** (1985) 175.
- 19 L. Hiltunen, H. Kattelus, M. Leskelä, M. Mäkelä, L. Niinistö, E. Nykänen, P. Soininen and M. Tiitta, *Mater. Chem. Phys.*, **28** (1991) 379.
- 20 Y. Charreire, A. Marbeuf, G. Tourillon, M. Leskelä, L. Niinistö, E. Nykänen, P. Soininen and O. Tolonen, *J. Electrochem. Soc.*, **139** (1992) 619.
- 21 T. Suntola, *Mater. Sci. Rep.*, **7** (1989) 261.
- 22 T. A. Pakkanen, V. Nevalainen, M. Lindblad and P. Makkonen, *Surf. Sci.*, **188** (1987) 456.
- 23 P. Hirva, *Ann. Acad. Sci. Fenn., Ser. A2*, **239** (1992) 1.
- 24 P. Hirva and T. A. Pakkanen, *Surf. Sci.*, **220** (1989) 137.
- 25 M. Leskelä, L. Niinistö, E. Nykänen, P. Soininen and M. Tiitta, *Thermochim. Acta*, **176** (1991) 91.
- 26 M. Leskelä, R. Sillanpää, L. Niinistö and M. Tiitta, *Acta Chem. Scand.*, **45** (1991) 1006.
- 27 M. Leskelä, L. Niinistö, E. Nykänen, P. Soininen and M. Tiitta, *Mater. Res. Soc. Symp. Proc.*, **222** (1991) 315.
- 28 L. Hiltunen, M. Leskelä, M. Mäkelä and L. Niinistö, *Acta Chem. Scand. A*, **41** (1987) 548.
- 29 M. Tammenmaa, T. Koskinen, L. Hiltunen, M. Leskelä and L. Niinistö, *Thin Solid Films*, **124** (1985) 125.
- 30 E. Nykänen, J. Laine-Ylijoki, M. Leskelä, L. Niinistö, P. Soininen and L. G. Hubert-Pfalzgraf, *J. Mater. Chem.*, to be published.
- 31 J. Nishizawa and H. Sakuraba, *Surf. Sci. Rep.*, **15** (1992) 137.
- 32 J. E. Greene, R. Tsu, D. Lubben, T. R. Bramblett, D.-S. Lin and T.-C. Chiang, *Thin Solid Films*, in press.
- 33 J. G. Bednorz and K. A. Müller, *Z. Phys. B*, **64** (1986) 189.
- 34 R. D. McConnell and R. Noufi (eds.), *Science and Technology of Thin Film Superconductors*, Vol. 2, Plenum, New York, 1990.
- 35 M. Leskelä, H. Mölsä and L. Niinistö, *Acta Chem. Scand.*, to be published.
- 36 M. Ottosson, A. Hårsta and J.-O. Carlsson, *J. Cryst. Growth*, **96** (1989) 1019.
- 37 S. B. Turnipseed, R. M. Barkley and R. E. Sievers, *Inorg. Chem.*, **30** (1991) 1164.
- 38 M. Kanai, T. Kawai and S. Kawai, *Appl. Phys. Lett.*, **58** (1991) 771.
- 39 Z. Zhou and A. Navrotsky, *J. Mater. Sci.*, (1992), to be published.
- 40 S. M. Bedair, *Acta Polytech. Scand., Ser. Chem. Technol.*, **195** (1990) 17.
- 41 L. Hiltunen, M. Leskelä, M. Mäkelä, L. Niinistö, E. Nykänen and P. Soininen, *Thin Solid Films*, **166** (1988) 149.

# Surface processes in digital etching of GaAs

T. Meguro

*RIKEN Institute of Physical and Chemical Research, Hirosawa, Wako, Saitama 351-01 (Japan)*

M. Ishii

*Faculty of Engineering Science, Osaka University, Toyonaka, Osaka 560 (Japan)*

K. Kodama

*College of Engineering, Hosei University, Kajinocho, Koganei, Tokyo 184 (Japan)*

Y. Yamamoto

*Research Centre of Ion Beam Technology, Hosei University, Kajinocho, Koganei, Tokyo 184 (Japan)*

K. Gamo

*Faculty of Engineering Science, Osaka University, Toyonaka, Osaka 560 (Japan)*

Y. Aoyagi

*RIKEN Institute of Physical and Chemical Research, Hirosawa, Wako, Saitama 351-01 (Japan)*

## Abstract

The self-limited etching characteristics and the surface processes in digital etching of GaAs employing a Cl radical–Ar ion system are described. In the case that the self-limiting mechanism is involved in the digital etching procedure, the etch rate saturates at the same value for both Cl<sub>2</sub> feed time and Ar ion irradiation time. Excessive Cl accumulation at the surface is considered to prevent the surface from etching, leading to a gradual decrease in etched depth during repetition of the digital etching cycles.

## 1. Introduction

Many investigations on atomic-scale additive modification techniques such as atomic layer epitaxy (ALE) have been carried out, but few reports have been made on atomic-scale subtractive techniques. We have demonstrated a digital etching technique, in which etchants are introduced in sequence with a necessary purge period between the subsequent etchant pulse and energetic beam pulse [1, 2]. In digital etching a reaction column is restricted at the surface and a self-limited etching nature is expected. The self-limiting nature is a key mechanism and plays an important role in obtaining precise controllability. In the digital etching of GaAs, self-limiting characteristics are obtained using a sequential incidence of Cl radicals and low energy Ar ions [3, 4].

In this paper, surface processes in digital etching of GaAs are described and the self-limiting mechanism and unique characteristics in digital etching are discussed, using a Cl radical pulse and sequential low energy Ar ion irradiation. In particular, the origin of the suppression of the digital etching performance with short Ar<sup>+</sup> irradiation is discussed here.

## 2. Experiment

The digital etching study described in this paper was carried out in an electron-beam-excited plasma system [5]. The details of the apparatus are described in previous reports [3, 5]. The digital etching sequence differs from the conventional etching techniques and is divided into four steps as follows.

(i) *Etchant adsorption (0.3–0.7 s)*. Cl radicals generated in the Cl<sub>2</sub> glow discharge are adsorbed on the GaAs surface. To avoid irradiation of the surface, the shutter placed before the sample stage is closed.

(ii) *Etchant purge (10 s)*. An excess of Cl radicals in the vapour phase is purged.

(iii) *Beam irradiation (1.0–18 s)*. An Ar ion beam extracted from the Ar glow discharge plasma irradiates the surface; an appropriate bias voltage is applied to the sample after the immediate opening of the shutter and the etching occurs. In this experiment, the energy of incident Ar ions was maintained at 25 eV.

(iv) *Product purge (3.0 s)*. The purge of etching products completes 1 cycle of the digital etching process.

The GaAs samples used were (001)  $\pm 0.5^\circ$  oriented, n-type, Si-doped GaAs wafers patterned by SiO<sub>2</sub> (1–

5  $\mu\text{m}$  line-and-space patterns). Before  $\text{SiO}_2$  deposition, samples were etched by a chemical solution of  $4\text{H}_2\text{SO}_4:1\text{H}_2\text{O}:1\text{H}_2\text{O}_2$ , followed by patterning with a photolithographic technique, and were set on the water-cooled sample stage. The operating temperature was kept at 300 K during the entire experiment.

Etch rates were determined by measuring etched depth by a surface profiler after typically 500 repetitions of the digital etching cycle, and were also estimated by calculation using rate equations. The calculation method has been reported in detail in a previous paper [4].

### 3. Results and discussion

Figure 1(a) shows the variation in etch rate as a function of the Ar ion irradiation time for various  $\text{Cl}_2$  feed times with 25 eV bombardment energy. As a whole, it was found that the etch rate increases with increasing Ar ion irradiation time until finally saturating. For the case of 0.3 s of  $\text{Cl}_2$  feeding, etching arises without any onset irradiation time. The etch rate at saturation is higher for the longer  $\text{Cl}_2$  feed time. For a longer  $\text{Cl}_2$  feed time, the etching starts after a certain lag time, with the onset of saturation taking longer for increased  $\text{Cl}_2$  feed time. The saturation level is independent of Ar ion irradiation time. These results show that etch rate is independent of both Ar ion irradiation time and  $\text{Cl}_2$  feed time when the Ar ion irradiation time is long enough, indicating that the self-limiting mechanism is involved in the digital etching procedure. Here regions I, II and III are defined as shown in Fig. 1(b); in region I no etching occurs, the etching rate increases

with Ar ion irradiation in region II and the etch rate saturates independently of Ar ion irradiation time in region III where self-limiting etching is obtained.

We assumed that Cl adsorbed only within a critical thickness can contribute to etching and that excess of Cl accumulation suppresses the etching performance to explain the self-limiting property in digital etching. These assumptions are consistent with the experimental results reported by Asakawa [6].

It is easily understood that the saturation of the etch rate is given by the amount of Cl within the critical thickness. As mentioned above, the presence of the onset is considered to result from the gradual Cl accumulation since the adsorbed Cl radicals are not completely removed from the surface owing to excess  $\text{Cl}_2$  feeding and/or insufficient Ar ion irradiation. However, to discuss the origin of onset with large  $\text{Cl}_2$  feed time, it might be taken into account whether the residual contaminants in the etching column ( $\text{O}_2$ , water vapour etc.) induce the onset, because the interval between sequential Ar ion irradiation is relatively long in the digital etching sequence as described in Section 2.

Here we discuss the origin of the onset from etching linearity. It is confirmed that the etched depth linearly increases with number of etching cycles and the etching linearity is kept in region III. However, if a surface oxide layer is formed during this long interval between Ar ion irradiation sequences, the oxide layer prevents the GaAs surface from etching and there should be a time loss to etch the oxide layer at the beginning of the subsequent Ar ion irradiation because of its slower etch rate. The etched depth is smaller than that with no oxide layer but should be the same in each sequence, so

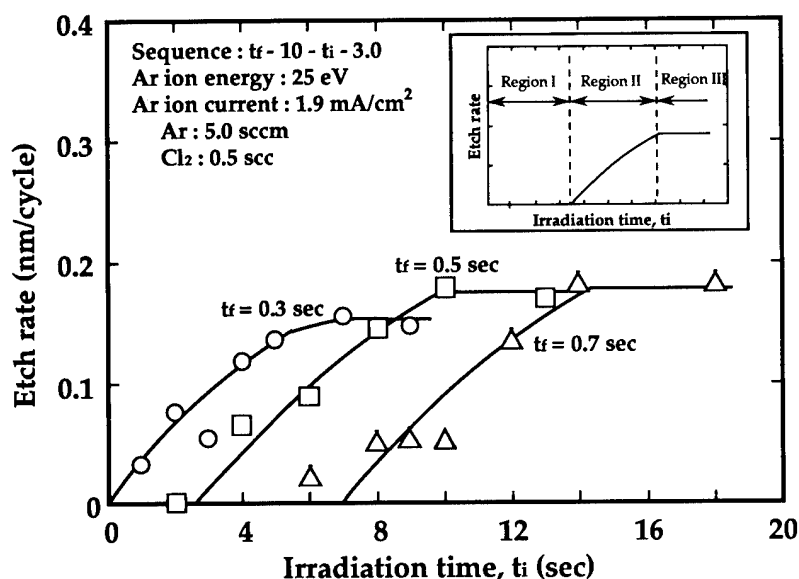


Fig. 1. Etch rate of GaAs vs. Ar ion irradiation time at a various  $\text{Cl}_2$  feed times. The inset shows the definition of regions I, II and III.

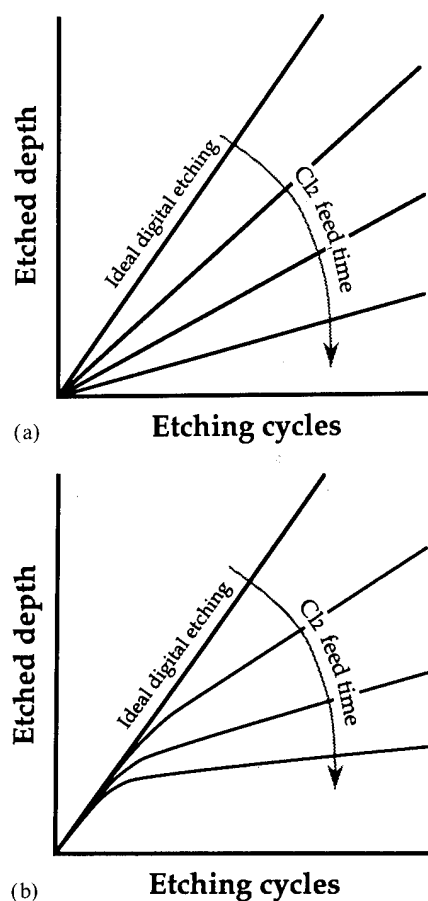


Fig. 2. Schematic illustrations of expected variations in etched depth vs. number of etching cycles; (a) the case of surface contamination; (b) Cl accumulation prevents the surface from etching.

that the etched depth has a linear dependence on the number of etching cycles. Therefore the etched depth dependence on the number of etching cycles in region III at a certain Ar ion irradiation time is expected to exhibit the tendency described in Fig. 2(a).

In contrast, if the surface is free from oxides during the etching procedure and the presence of onset Ar ion irradiation time is mainly caused by the accumulation of Cl radicals as described before, the variation in etched depth as a function of the number of etching cycles is estimated as shown in Fig. 2(b) from the calculated results using rate equations. In this case, since the Cl accumulation increases in the first several tens or hundreds of cycles, the slope of this curve gradually becomes gentle and then, after further cycles, the slope of the curve will be finally linear owing to the balance of feeding and desorption of Cl radicals at the surface.

Figure 3 shows a typical example of the dependence of etched depth on the number of etching cycles in region II. This curve reveals a good agreement with Fig. 2(b). Therefore the surface process that the oxide layer

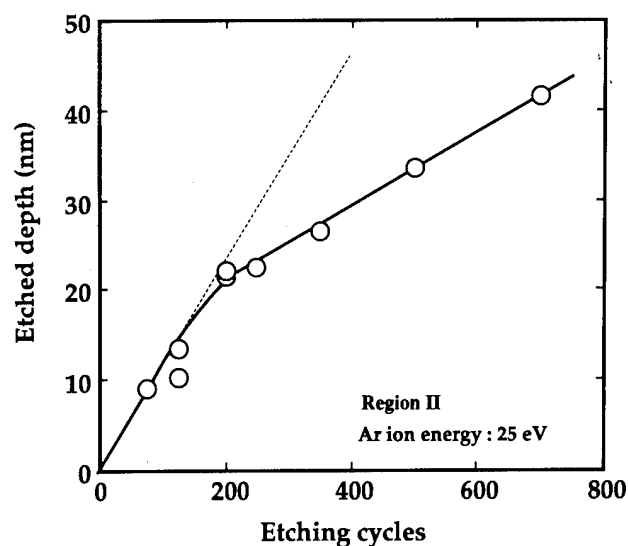


Fig. 3. Typical example of etched depth vs. number of etching cycles.

acts as the origin of onset can be ruled out and consequently it is considered that Cl radicals also act as the blocking layer against the etching in the case of excessive Cl<sub>2</sub> feeding.

From these results, the surface process during one etching cycle of digital etching is considered to be as schematically shown in Fig. 4. Figure 4(a) shows the initial substrate surface before the etching sequence and Figs. 4(b)–4(d) indicate the variation in Cl adsorption depending on the Cl<sub>2</sub> feed time. With thinner Cl adsorption than the critical thickness (Fig. 4(b)), etching occurs without any onset of the Ar ion irradiation time and the process takes place in region I (from Fig. 4(b-1) to Fig. 4(b-3)). The saturated etch rate in region III becomes higher with larger Cl<sub>2</sub> feed time, since the saturated etch rate is decided by the initial Cl coverage. On the contrary, when the adsorbed Cl is thicker than the critical thickness (Fig. 4(d)), etching arises after the removal of the excessive adsorption layer of Cl through the physical sputtering process (from Fig. 4(d-1) to Fig. 4(d-3)). Etching in such a case proceeds only after the Ar ion irradiation clears excess Cl. The saturated etch rate is independent of the thickness of adsorbed Cl. In region III, no Cl remains at the surface after one cycle of etching because Ar ion irradiation is sufficient to remove Cl and the initial surface condition is retained in the digital etching procedure in the ideal case. Thus the etch rate is independent of both Cl<sub>2</sub> feed time and Ar ion irradiation time, and the self-limiting etching nature is obtained (indicated as "self-limited" in Fig. 4).

By fitting results from the rate equation analysis, the reaction time constant is determined to be about 2.5 s, which is estimated to be approximately 2–3 orders of magnitude slower than that in ordinary reactive ion



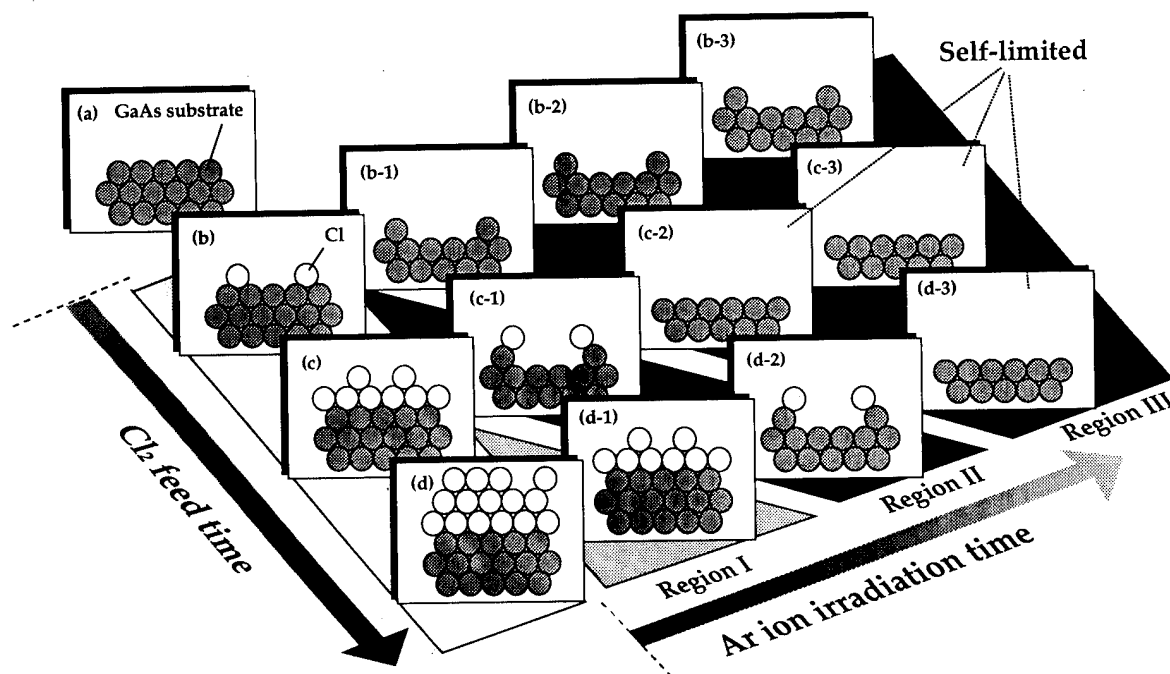


Fig. 4. Plausible model of surface processes in one etching cycle of digital etching.

beam etching [4]. At the present stage, the critical thickness is considered to correspond to monolayer adsorption.

#### 4. Summary

Surface processes in the digital etching of GaAs have been discussed using sequential exposure of the sample to Cl radicals and low energy Ar ions. The self-limited etching characteristics are obtained within both the Ar ion irradiation time and the Cl<sub>2</sub> feed time of the etching cycle. It is confirmed from experimental and calculated results that self-limited etching is induced by the Cl adsorbed only within a critical thickness, which causes the etching of GaAs, and that unexpected Cl accumulation leads to the presence of onset with a short Ar ion irradiation. In addition, the possibility that surface oxides cause the presence of the onset of etching with a short Ar<sup>+</sup> irradiation is ruled out, on the basis of results from rate equation analysis.

#### Acknowledgments

The authors would like to thank S. Hara, K. Ozasa and K. Ishibashi of RIKEN for their fruitful discussions. This work was supported in part by a Grant-in-Aid for Scientific Research from the Ministry of Education, Science and Culture.

#### References

- 1 T. Meguro, H. Hamagaki, S. Modaressi, T. Hara, M. Ishii and Y. Yamamoto, *Appl. Phys. Lett.*, **56** (1990) 1552.
- 2 T. Meguro, M. Ishii, H. Kodama, M. Hamagaki, T. Hara and Y. Aoyagi, *Jpn. J. Appl. Phys.*, **26** (1990) 2216.
- 3 T. Meguro and Y. Aoyagi, *Mater. Res. Soc. Symp. Proc.*, **222** (1991) 121.
- 4 M. Ishii, T. Meguro, H. Kodama, Y. Yamamoto and Y. Aoyagi, *Jpn. J. Appl. Phys.*, **31** (1992) 2212.
- 5 Y. Z. Yu, T. Hara, M. Hamagaki, Y. Yoshinaga, Y. Aoyagi, K. Gamo and S. Namba, *J. Vac. Sci. Technol. B*, **6** (1988) 1626.
- 6 K. Asakawa and S. Sugata, *J. Vac. Sci. Technol., A*, **4** (1986) 677.

# Comparison of $\text{Cl}_2$ and $\text{HCl}$ adsorption on $\text{Si}(100)-(2 \times 1)$

Q. Gao and C. C. Cheng

*Surface Science Center, Department of Chemistry, University of Pittsburgh, Pittsburgh, PA 15260 (USA)*

P. J. Chen and W. J. Choyke

*Department of Physics, University of Pittsburgh, Pittsburgh, PA 15260 (USA)*

J. T. Yates, Jr.

*Surface Science Center, Department of Chemistry, University of Pittsburgh, Pittsburgh, PA 15260 (USA)*

## Abstract

The chemisorption and reaction of  $\text{Cl}_2$  and  $\text{HCl}$  on  $\text{Si}(100)-(2 \times 1)$  have been studied using Auger electron spectroscopy, high resolution electron energy loss spectroscopy (HREELS), digital electron-stimulated desorption ion angular distribution (ESDIAD), and temperature programmed desorption. At 100 K, both  $\text{Cl}_2$  and  $\text{HCl}$  dissociatively chemisorb on the dangling bonds of  $\text{Si}(100)$ . At saturation coverage, following an exposure of the  $\text{Si}(100)$  surface to  $\text{Cl}_2$ , the surface concentration of Cl is about one Cl atom per Si atom while  $\text{HCl}$  can produce a Cl coverage only about one-fourth of that achieved with  $\text{Cl}_2$ . This is the first report of a self-site-blocking effect in adsorption on a semiconductor surface. HREELS spectra indicate that both  $\text{Cl}_2$  and  $\text{HCl}$  adsorption at 100 K give a monochloride surface species with an Si–Cl stretching frequency of about  $550\text{--}600\text{ cm}^{-1}$ . Digital ESDIAD measurements reveal that the Si–Cl bond angle for the monochloride from both  $\text{Cl}_2$  and  $\text{HCl}$  adsorption is oriented on the vertical plane containing the Si–Si dimer bond and is inclined from the surface normal by  $25^\circ \pm 4^\circ$ . The etching products of  $\text{Si}(100)$  by  $\text{Cl}_2$  at elevated temperatures are  $\text{SiCl}_2$  at about 800 K and a small amount of  $\text{SiCl}_4$  at about 500 K. For  $\text{HCl}$ , the only observed etching product is  $\text{SiCl}_2$ .

## 1. Introduction

It is important to understand the basic chemistry of Cl chemisorption and reaction on semiconductor surfaces, since Cl-containing molecules, such as  $\text{SiH}_2\text{Cl}_2$  [1] and  $\text{GaCl}_3$  [2], have been used as precursor molecules for atomic layer epitaxy processes, and  $\text{Cl}_2$  molecules have been used in the ion [3–5] or photon [6–8] assisted etching processes.

In this report, the saturation coverage and vibrational spectrum of Si–Cl and Si–H bonds derived from  $\text{Cl}_2(\text{g})$  and  $\text{HCl}(\text{g})$  adsorption are compared on  $\text{Si}(100)$ . In addition,  $\text{Cl}^+$  electron-stimulated desorption ion angular distribution (ESDIAD) patterns from Si–Cl bonds on  $\text{Si}(100)$  are reported, giving information about the Si–Cl bond direction. All adsorption experiments are carried out at 100–120 K in order to study the primary kinetic processes which occur. Heating experiments then reveal subsequent activated surface processes.

## 2. Experimental details

Experiments were carried out in two ultrahigh vacuum (UHV) chambers. The first was equipped with a digital ESDIAD–low energy electron diffraction

(LEED) apparatus, an Auger electron spectrometer, a quadrupole mass spectrometer for line-of-sight temperature programmed desorption (TPD), and an additional quadrupole mass spectrometer for ion mass analysis in ESD. The second UHV chamber housed a high resolution electron energy loss spectrometer, LEED equipment, an Auger electron spectrometer and a quadrupole mass spectrometer for TPD. The primary beam energy used for the high resolution electron energy loss spectroscopy (HREELS) study was 4.2 eV and the full width at half-maximum of the elastic beam was about  $65\text{ cm}^{-1}$ . Flux-calibrated microcapillary-collimated gas dosers [9, 10] were used in both chambers for control of the  $\text{Cl}_2$  or  $\text{HCl}$  exposure. The  $\text{Si}(100)$  single crystal was cleaned by  $\text{Ar}^+$  sputtering and subsequent annealing at 1173 K. The crystal temperature was measured by a chromel–constantan thermocouple enclosed in a double Ta foil envelope which was inserted into a slot on the crystal edge [9].

## 3. Results and discussion

### 3.1. Adsorption of $\text{Cl}_2$ and $\text{HCl}$

The saturation coverage of the Cl layer was determined from measurements of the kinetics of the

adsorption of  $\text{Cl}_2$  or HCl on  $\text{Si}(100)$  at 100 K. Figure 1 is a plot of the development of the  $\text{Cl}(a)$  coverage as a function of exposure using the two molecules to deposit Cl. It is noticed that above  $3 \times 10^{14}$  molecules  $\text{cm}^{-2}$  exposure, both the  $\text{Cl}_2$  and HCl adsorption rates have dramatically decreased. The reduction in the adsorption rate for  $\text{Cl}_2$  is due primarily to the lack of available surface dangling bonds since at this breakpoint most sites are used up for the chemisorption. (Cross-calibrations of surface Cl coverage from  $\text{Cl}_2$  adsorption on  $\text{Si}(100)$  with the saturation coverage of monohydride from atomic H adsorption indicate that the surface Cl coverage is about 0.8 at the breakpoint of the  $\text{Cl}_2$  Auger electron spectroscopy (AES) uptake curve.) On the basis of the crystal structure of Si, the perfect  $\text{Si}(100)-(2 \times 1)$  surface exposes  $6.8 \times 10^{14}$  dangling bonds  $\text{cm}^{-2}$ . Thus, at a  $\text{Cl}_2$  exposure of about  $3 \times 10^{14}$   $\text{Cl}_2$   $\text{cm}^{-2}$ , saturation of the dangling bonds is expected to occur (near the breakpoint in the curve), assuming a sticking probability of unity in the initial adsorption region. Beyond the breakpoint at about  $3 \times 10^{14}$   $\text{Cl}_2$   $\text{cm}^{-2}$ , the coverage continues to rise slowly as the  $\text{Cl}_2$  exposure is increased. For the same exposure (about  $3 \times 10^{14}$  molecules  $\text{cm}^{-2}$ ), the saturation effect is also observed for HCl adsorption. The saturation surface Cl coverage from HCl adsorption is only about one-fourth of that achieved by  $\text{Cl}_2$  adsorption, as obtained from the  $\text{Cl}(\text{LMM})/\text{Si}(\text{LMM})$  AES intensity ratio in Fig. 1. The  $\text{Cl}_2$  molecules are composed of two Cl atoms which give a Cl coverage of nearly one Cl atom per dangling bond

at the breakpoint. In comparison, HCl is composed of one Cl atom and one H atom. If the surface dangling bonds were all occupied by H(a) and Cl(a) from HCl adsorption, a Cl surface coverage of about 0.5 would be expected. However, at the breakpoint only about one-fourth of the surface dangling bonds are occupied by Cl from HCl adsorption at 100 K. The surface therefore has about one-half of the dangling bonds which are not accessible for HCl adsorption. Furthermore, after a saturation exposure of HCl is achieved, exposure of this prepared surface to  $\text{Cl}_2$  leads to increased Cl coverages as measured by AES, indicating that the dangling bonds inaccessible for HCl adsorption are active for  $\text{Cl}_2$  adsorption. Thus, the HCl adsorption on  $\text{Si}(100)$  is a self-site-blocking process. To our knowledge, this is the first report of such a self-site-blocking adsorption process on a semiconductor surface. The immediate conclusion from this result is that HCl will be a less effective etchant than  $\text{Cl}_2$  because of its limited surface coverage on  $\text{Si}(100)$ . The explanation of this self-site-blocking adsorption phenomenon is not well understood at present.

### 3.2. Vibrational studies of $\text{Cl}_2$ and HCl adsorption

Deeper insight into the Cl surface chemistry can be obtained from the vibrational characterization of the surface species formed during the chemisorption and reaction. Figure 2 shows the vibrational spectra after either  $\text{Cl}_2$  or HCl adsorption on  $\text{Si}(100)-(2 \times 1)$  at 100 K. It is noticed that only one strong Si-Cl stretching mode,  $\nu(\text{SiCl})$ , is observed at about  $600 \text{ cm}^{-1}$  and at about  $550 \text{ cm}^{-1}$  for  $\text{Cl}_2$  and HCl adsorption respectively (refs. 11, p. 132, and 12). For HCl adsorption, an additional vibrational feature is observed at about  $2120 \text{ cm}^{-1}$  (Fig. 2, spectrum b) which is due to the SiH stretching mode [13]. The lack of an HCl stretching mode near about  $3000 \text{ cm}^{-1}$  (ref. 11, p. 101) and the appearance of  $\nu(\text{SiCl})$  and  $\nu(\text{SiH})$  modes indicate that HCl is dissociated on adsorption at 100 K.

The vibrational spectra (Fig. 2) indicate that higher surface chloride species, such as  $\text{SiCl}_2(a)$ ,  $\text{SiCl}_3(a)$  or  $\text{SiCl}_4(a)$ , are not observed following either  $\text{Cl}_2$  or HCl adsorption at 100 K. These chlorides should exhibit an asymmetric stretching mode ( $\nu_a(\text{SiCl})$ , about  $533-617 \text{ cm}^{-1}$ ) and a symmetric stretching mode ( $\nu_s(\text{SiCl})$ , about  $376-465 \text{ cm}^{-1}$ ). In addition, a bending vibrational mode should be present ( $\delta(\text{Si-Cl})$ , about  $164-261 \text{ cm}^{-1}$ ) (refs. 11, p. 132, and 12). There is no prominent evidence for these modes in the spectra observed. This is consistent with the dissociative adsorption of HCl and  $\text{Cl}_2$  forming surface monochloride species. For  $\text{Cl}_2$  adsorption at 100 K, the mode at  $295 \text{ cm}^{-1}$  has been assigned to an  $\text{Si}_2\text{Cl}$  stretching mode for a bridge-bonded Cl species, a minority species [14].

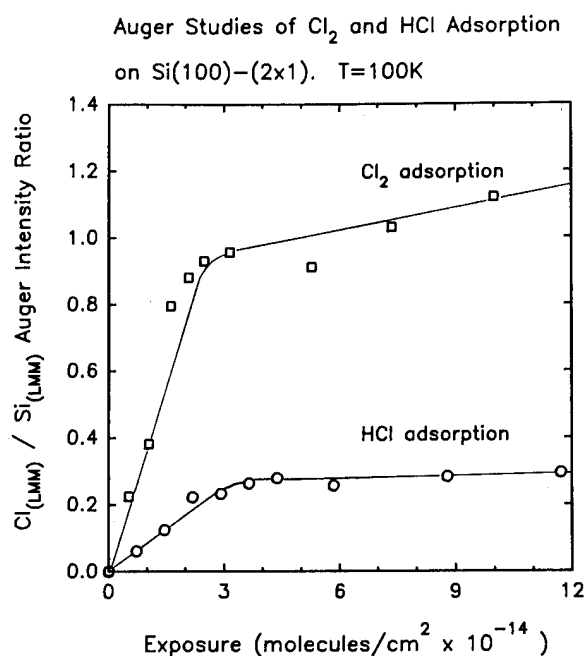


Fig. 1. Rate of Cl coverage increase for  $\text{Cl}_2$  and HCl adsorption on  $\text{Si}(100)-(2 \times 1)$  at 100 K using Auger spectroscopy.  $V_e = 2.0 \text{ kV}$ .

### Comparison of the Vibrational Spectra for $\text{Cl}_2$ and HCl Adsorption on $\text{Si}(100)$

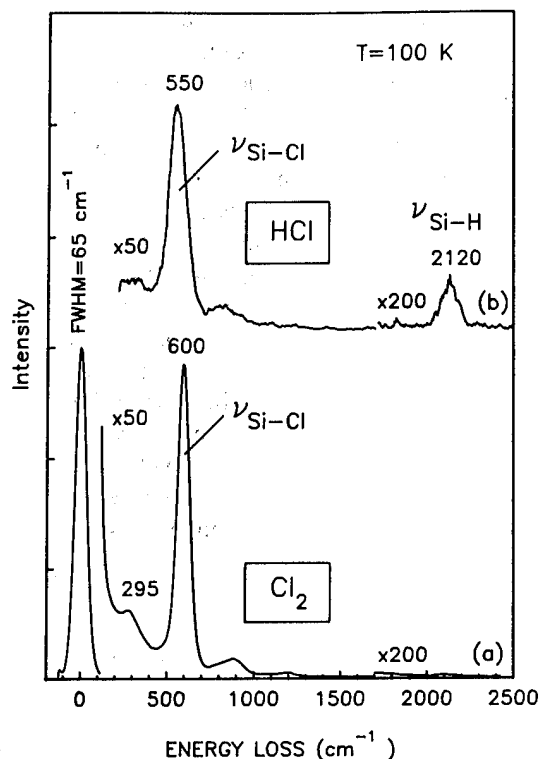


Fig. 2. HREEL spectra of  $\text{Cl}_2$  and HCl adsorption on  $\text{Si}(100)-(2 \times 1)$  at 100 K: spectrum a,  $\text{Cl}_2$  exposure of  $7.4 \times 10^{14}$  molecules  $\text{cm}^{-2}$ ; spectrum b, HCl exposure of  $8.7 \times 10^{14}$  molecules  $\text{cm}^{-2}$ .

### 3.3. Electron-stimulated desorption ion angular distribution studies of Si-Cl bonding on $\text{Si}(100)$

The ESDIAD method has been employed to study the bonding of Cl(a) to  $\text{Si}(100)$  using both  $\text{Cl}_2$  and HCl as adsorbates. In this method, the adsorbed layer is bombarded by electrons ( $V_e = 120$  eV in this case) and the angular distribution of  $\text{Cl}^+$  ions is detected by an ion counting technique. The ejection angle of the  $\text{Cl}^+$  ions is determined primarily by the orientation of the Si-Cl bond being broken [15–17] in the electronic excitation. This angle is modified by final state effects involving the  $\text{Cl}^+$  interaction with its image charge as well as by  $\text{Cl}^+$  reneutralization near the surface [18, 19].

The surface monochloride species produced from HCl or  $\text{Cl}_2$  adsorption give four off-normal  $\text{Cl}^+$  emission beams observed from the ESDIAD measurements, shown in Fig. 3. The  $\text{Cl}^+$  ions are ejected at a tilt angle of  $25^\circ \pm 4^\circ$  (corrected for all final state effects) in planes perpendicular to the crystal surface but parallel to the surface Si-Si dimer bond axes, as confirmed from the comparison of the ESDIAD pattern with the  $(2 \times 1)$  LEED patterns of the substrate surface. Slight misalignment of the Si single crystal from the (100) direction results in a stepped surface with Si-Si dimer rows

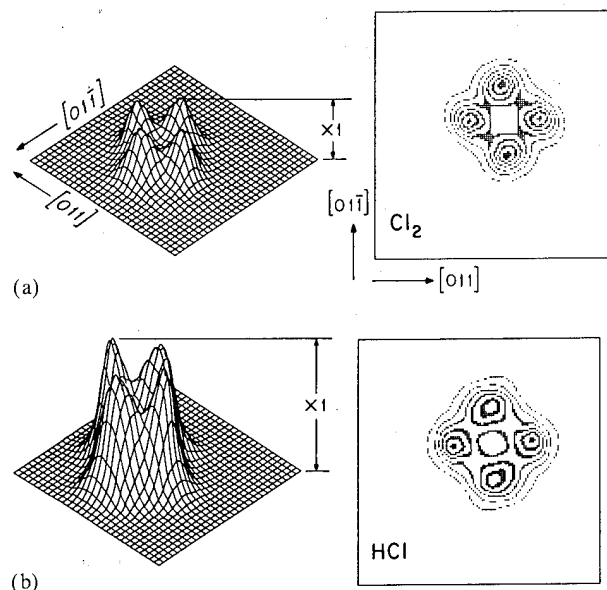


Fig. 3.  $\text{Cl}^+$  ESDIAD patterns of (a)  $\text{Cl}_2$  (after annealing to 673 K to obtain a sharp monochloride pattern) and (b) HCl (120 K adsorption) on  $\text{Si}(100)-(2 \times 1)$ . Near-saturation coverages were achieved for  $\text{Cl}_2$  and HCl adsorption prior to these measurements.  $V_e = 120$  eV. Contour profiles are plotted by an increment of 1/6 of their peak maxima.

oriented alternately in orthogonal directions, forming  $(1 \times 2)$  and  $(2 \times 1)$  domains of reconstructed surface. The inclined Cl bonds of the surface monochloride species from both types of domains produce the four off-normal  $\text{Cl}^+$  ion beams. A single domain surface would give two off-normal  $\text{Cl}^+$  ion beams with the opposite polar angle with respect to the surface normal.

### 3.4. Thermal desorption studies

The thermally activated etching reaction was investigated by TPD measurements. The results (Fig. 4) indicate that Cl(a) from both  $\text{Cl}_2$  and HCl chemisorption etches the  $\text{Si}(100)$  surface, producing  $\text{SiCl}_2(\text{g})$  with a desorption peak temperature at about 820 K for the  $\text{Cl}_2/\text{Si}(100)$  system and at 840 K for the HCl/ $\text{Si}(100)$  system. A small amount of  $\text{SiCl}_4$  desorption (monitored by its major mass spectrometer cracking product,  $\text{SiCl}_3^+$ ,  $m/e = 133$  amu) is also observed for the  $\text{Cl}_2/\text{Si}(100)$  system at monolayer or higher exposures. This is consistent with the previous  $\text{Cl}_2/\text{Si}(100)$  TPD results [6, 14, 20]. These measurements indicate that  $\text{SiCl}_2$  is the main etching product for both  $\text{Cl}_2$  and HCl adsorption, and that the etching process involving  $\text{SiCl}_2$  occurs near 840 K. Species such as  $\text{SiH}_4$  (monitoring  $m/e = 30$  amu) or  $\text{SiH}_3\text{Cl}$  (monitoring  $m/e = 31$  amu),  $\text{SiH}_2\text{Cl}_2$  (monitoring  $m/e = 99$  amu) and  $\text{SiHCl}_3$  (monitoring  $m/e = 133$  amu) were not detected in the TPD spectra, showing that the surface H atom was not involved in the etching process when HCl was employed.

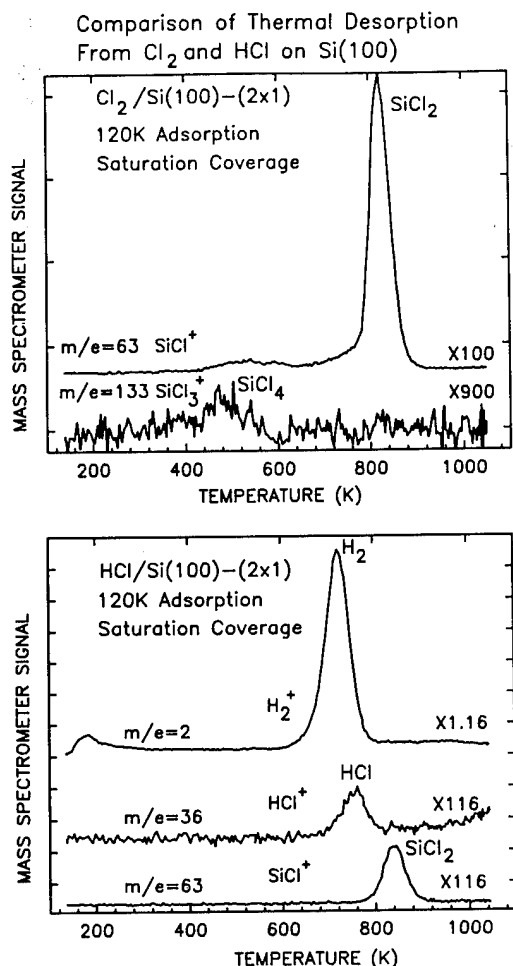


Fig. 4. TPD from layers produced from  $\text{Cl}_2$  and HCl adsorption to saturation coverage on  $\text{Si}(100)-(2 \times 1)$ . Heating rate is about  $3.6 \text{ K s}^{-1}$ .

Following the adsorption of  $\text{Cl}_2$  on  $\text{Si}(100)$ , HREELS was utilized to determine whether the  $\text{SiCl}_2(\text{a})$  species could be detected following an increase in the crystal temperature to about 850 K, and subsequent cooling to 100 K. The HREEL spectrum remained essentially the same, exhibiting a single Si-Cl stretching mode of the surface monochloride shown in Fig. 2, spectrum a, with a reduced intensity and a slightly reduced frequency (to about  $570 \text{ cm}^{-1}$ ) as a result of the reduction of surface chlorine coverage. Thus,  $\text{SiCl}_2(\text{a})$  formation is probably the rate-determining step for  $\text{SiCl}_2(\text{g})$  liberation, and cannot be spectroscopically detected on the surface because of its low surface coverage.

#### 4. Conclusions

The following conclusions may be made from these studies of  $\text{Cl}_2$  and HCl chemisorption on  $\text{Si}(100)-(2 \times 1)$ .

(1) Dissociative adsorption of both  $\text{Cl}_2$  and HCl occurs on  $\text{Si}(100)-(2 \times 1)$  at 100 K. The vibrational spectra produced from  $\text{Cl}_2$  and HCl adsorption indicate that Si-Cl bonds are formed in both cases. For HCl chemisorption, the Si-H bond is also observed.

(2) For  $\text{Cl}_2$  adsorption, about one Cl atom per Si dangling bond is produced at saturation coverage. In addition, the saturation coverage of chlorine from  $\text{Cl}_2$  adsorption is about 4 times greater than that from HCl adsorption. This result implies that HCl adsorption involves an adsorption site exclusion process, where neither H(a) nor Cl(a) species can populate one-half of the dangling bond sites exposed on  $\text{Si}(100)-(2 \times 1)$ .

(3) ESDIAD studies indicate that the Si-Cl bonds are inclined  $25^\circ \pm 4^\circ$  away from the surface normal direction along planes perpendicular to the surface containing the Si-Si dimer bonds.

(4)  $\text{SiCl}_2$  is the main etching product observed from thermal desorption studies of  $\text{Cl}_2$  and HCl on  $\text{Si}(100)$ . It desorbs above 800 K in both cases. HREELS studies indicate that  $\text{SiCl}_2(\text{a})$  is not produced in measurable amounts on heating the surface. This indicates that the rate-determining step for  $\text{SiCl}_2(\text{g})$  desorption is the conversion of  $\text{SiCl}(\text{a})$  species to  $\text{SiCl}_2(\text{a})$  species which then desorb.

#### Acknowledgments

This work was supported by the Office of Naval Research. The authors would like to acknowledge Mr. S. R. Lucas for his reference TPD result for  $\text{Cl}_2/\text{Si}(100)$ .

#### References

- 1 J. Nichizawa, K. Aoki and S. Suzuki, *J. Cryst. Growth*, **99** (1990) 502.
- 2 R. Kobayashi, K. Ishikawa, S. Narahara and F. Hasegawa, *2nd Int. Symp. on Atomic Layer Epitaxy, Raleigh, NC, 1992*.
- 3 M. C. Chuang and J. E. Coburn, *J. Vac. Sci. Technol. A*, **8** (1990) 1969.
- 4 J. O. Chinn and E. D. Wolf, *J. Vac. Sci. Technol. B*, **3** (1985) 410.
- 5 P. C. Zalm, A. W. Kolschoten, F. H. M. Sanders and P. Vischer, *Nucl. Instrum. Methods B*, **18** (1987) 625.
- 6 R. B. Jackman, H. Ebert and J. S. Foord, *Surf. Sci.*, **176** (1986) 183.
- 7 W. Sesselmann and T. J. Chuang, *J. Vac. Sci. Technol. B*, **3** (1985) 1507.
- 8 W. Sesselmann, E. Hudeczek and F. Bachmann, *J. Vac. Sci. Technol. B*, **7** (1989) 1284.
- 9 M. J. Bozack, L. Muehlhoff, J. N. Russell, Jr., W. J. Choyke and J. T. Yates, Jr., *J. Vac. Sci. Technol. A*, **5** (1987) 1.
- 10 A. Winkler and J. T. Yates, Jr., *J. Vac. Sci. Technol. A*, **6** (5) (1988) 2929.
- 11 K. Nakamoto, in *Infrared Spectra of Inorganic and Coordination Compounds*, Wiley, New York, 4th edn., 1986.

- 12 M. C. Tobin, *J. Am. Chem. Soc.*, **75** (1953) 1788.
- K. Shimizu and H. Murata, *Bull. Chem. Soc. Jpn.*, **32** (1959) 46.
- L. Burnelle and J. Duchesne, *J. Chem. Phys.*, **20** (1952) 1324.
- J. Lanne, *Spectrochim. Acta A*, **26** (1970) 517.
- 13 H. Wagner, R. Butz, U. Backes and D. Bruchmann, *Solid State Commun.*, **38** (1981) 1155.
- Y. J. Chabal, *Surf. Sci. Rep.*, **8** (1988) 211.
- H. Ibach, H. Wagner and D. Bruchmann, *Solid State Commun.*, **42** (1982) 457.
- 14 Q. Gao, C. C. Cheng, P. J. Chen, W. J. Choyke and J. T. Yates, Jr., *J. Chem. Phys.*, submitted.
- 15 R. D. Ramsier and J. T. Yates, Jr., *Surf. Sci. Rep.*, **12** (1991) 243.
- 16 T. E. Madey, *Science*, **234** (1986) 316.
- 17 J. T. Yates, Jr., M. D. Alvey, M. J. Dresser, M. A. Henderson, M. Kiskinova, R. D. Ramsier and A. Szabo, *Science*, **225** (1992) 1397.
- 18 Z. Miskovic, J. Vukanic and T. E. Madey, *Surf. Sci.*, **169** (1986) 405.
- 19 D. P. Woodruff, *Surf. Sci.*, **124** (1983) 320.
- 20 C. C. Cheng, S. R. Lucas, H. Gutleben, W. J. Choyke, and J. T. Yates, Jr., *J. Am. Chem. Soc.*, **114** (1992) 1249.
- Unpublished results, 1992.

# Group IV atomic layer epitaxy

Max N. Yoder

Electronics Division, Office of Naval Research, Arlington, VA 22217 (USA)

## Abstract

Group IV atomic layer epitaxy (ALE) provides special challenges in that the conventional alternation of anion and cation species is not applicable. New experimental approaches are proposed that synergistically combine to gain real-time, *in situ* information on the surface, its activation energy, reconstruction, and work function so as to choose optimally feedstock molecules. New computer codes in computational chemistry are expected to stimulate further a synergistic approach to group IV ALE.

## 1. Limited options

The traditional atomic layer epitaxy (ALE) approach employed in II–VI and III–V materials employs a cyclic alternation of the cation-containing and anion-containing reactant species. This approach is, of course, without merit in the growth of elemental semiconductors such as tin, germanium, silicon, diamond, or even selenium. The growth of these elemental semiconductors by ALE demands a deeper investigation to delineate the most efficacious aspects of the processes involved. A primary requirement is a self-limiting adsorption process or a process wherein all except a single atomic layer of adsorbate is easily removed prior to enabling further the chemical reactivity of the surface. Compounds and alloys composed solely of group IV elements such as silicon carbide (SiC), Si–Ge, Ge–Sn, and C–Si–Ge are weakly ionic in nature and may be amenable to conventional alternation of cation and anion species, but to date this has not been reported. Alternations between Lewis acid and Lewis base species may be appropriate as are alternations between hydrides and halides [1, 2]. While initial approaches using alternations between halides and hydrides used molecular species, much faster reactions can be ensured by the alternation of radical species of halides and hydrides [3]. Halides and hydrides can be combined into a single reactant such as  $\text{SiCl}_2\text{H}_2$  or  $\text{SiH}_2\text{Cl}_2$  and  $\text{H}_2$  adsorbed at lower temperatures (*e.g.* below 350 °C) followed by “activation” with synchrotron radiation or rapid thermal processing [4, 5]. The presence of halides, however, can wreck havoc with the surfaces of many growth reactors. To circumvent the use of halides, adsorbing hydrides such as  $\text{GeC}_2\text{H}_7$  or  $\text{GeCH}_5$  have been used [6–8]. Unfortunately, extensions of this approach to siliconaceous hydrides resulted in unacceptable carbon contamination. A different siliconaceous hydride

( $\text{Si}_2\text{H}_6$ ), however, can be used to grow silicon layer by layer [9, 10].

This process involves deposition at temperatures between 150 and 550 °C followed by a UV irradiation to desorb hydrogen and to prepare the surface for the subsequent exposure of  $\text{Si}_2\text{H}_6$ . In this approach temperatures rise during UV irradiation, creating temperature transients with unknown consequences. Large area growth may also be difficult using the excimer lasers currently employed. These problems can be overcome by further dissociating the deposited radicals with remotely generated plasmas creating ions impacting the surface with low translational energies [11]. Helium ions were found to be more effective than argon ions in that their mass was closer to that of the hydrogen to be removed.

A major limitation of all the above processes, however, is that they only considered the deposition of radicals or molecules applied with energies on the order of 0.5 to a few  $kT$  where  $T$  seldom exceeds the temperature of the substrate.

## 2. Supersonic jets and atomic layer epitaxy

While many chemical reactions necessary for ALE can be shown to be exothermic in nature, energy barriers can exist that preclude the reaction from occurring at acceptable substrate growth temperatures. This situation arises most frequently when the precursor molecules contain chemical bonds that are significantly stronger than are the bonds within the resultant crystal being deposited. While it is easy to show that frequently the desired chemical reactions can typically be achieved by the use of chemical radicals rather than molecules, the generation of these radicals can be a problem, the radicals tend to be more reactive with reactor walls, and

their presence in the reactor is more likely to lead to unwanted gas phase reactions. Alternative approaches that ensure precursor dissociation only on the growth surface are desirable.

### 2.1. Cluster beam deposition

Supersonic expansion jets for cluster beam deposition gained notoriety in the 1970s. Leading proponents were Yamada and Takagi [12, 13]. Although very high quality films have been made by ionized cluster beams, the cluster sizes typically vary from 500 to 1000 atoms; this approach does not appear amenable to ALE technology. For ALE, the "cluster size" must be absolutely no more or no less than one single molecule. With such restrictions, the apparatus necessary to generate the beams is very different from that required for conventional cluster beam epitaxy. When limited to single molecule sizes for ALE applications, supersonic jet technology has no meaningful relationship with cluster beam technology.

### 2.2. Supersonic molecular beams

Supersonic jets of molecules have been known for years. An excellent introduction and historical summary is provided by Anderson [14]. Supersonic jet epitaxy can be explained in simple terms, yet a great deal of calculation and sophistication has gone into its development. In simple terms, a gas is forced down a tube and exhausted into a lower pressure region. For a given pressure differential, the velocity of the gas molecules is inversely dependent on their molecular weight. On exiting into the lower pressure region, Joule-Thompson cooling occurs. If the exit region is a high vacuum region, the vibrational and rotational energy of the molecules can be reduced to energies equivalent to those of a few kelvins, while the translational kinetic energy is primarily dependent on the pressure differential and can be very accurately controlled. The residual vibrational and rotational energies are primarily dependent on nozzle temperature, molecular weight, and pressure differential. As early as 1954, Becker and Bier observed that, by "seeding" heavier molecules into a lighter gas, the effective beam intensity significantly increased [15]. In this manner light (*e.g.*  $H_2$ ) or light and inert (*e.g.* helium) gases can be used to propel heavier molecules (*e.g.* propene) (diluted to about a 1% mixture) at the speed of the lighter gas rather than at the lower limitation imposed by the pressure differential if only the heavier molecules were used. At any given pressure differential, the effective increase in kinetic translational energy on the target is approximately proportional to the ratio of molecular weights of the heavy and light molecules in the gas. In this manner, the kinetic energy on target can be up to tens of electronvolts per molecule [16]. This is enough

to dissociate the heavy molecule on impact with the surface. (Since the native surface atoms typically are doubly or triply bonded to the underlying substrate, they are seldom removed from their lattice site unless the impacting energy exceeds about five times the band gap of the underlying crystal.) An excellent tutorial on supersonic jet technology is presented by one of its leading advocates, Ceyer [17]. In this article, the technology is explained in two models. The first explains that the molecule being "hurled" at the surface is dissociated as an exclusive function of its translational or vibrational energy. The immediate products of this event are largely independent of surface temperature. The dissociation creates radicals termed precursors that are chemisorbed to the surface. The further dissociation and bonding of this precursor are modeled as being largely independent of the initial impact and are highly dependent on the surface temperature. It has been demonstrated that the energy distribution as expressed by the full width at half-maximum (FWHM) of a seeded  $CCl_4$  molecule in helium gas experiencing a 1 atm pressure drop into a vacuum can be as little as 0.1 eV with a mean energy of 1.6 eV. The FWHM is typically inversely proportional to the Mach number at Mach numbers exceeding 4. This energy distribution compares with only about 11% of the total flux from a conventional thermal effusion cell being within 5% of the mean molecular velocity. The importance of this finding to ALE is that energy on target can be controlled so as to exceed or equal the activation energy necessary for chemisorption, but to have no tail distribution contributing to unwanted physisorption or unwanted bond breaking. Peak flux density can be as much as 2000 times that from an effusion cell. Finally, it should be stated that although most of the supersonic jet epitaxy experiments to date have been conducted in vacuum systems, there is no fundamental reason why the approach cannot be applied to atmospheric pressure systems. Anyone observing an oil well blowout can readily attest to the supersonic jet exhibiting several Mach rings in its stem before "umbrellaing".

### 3. *In situ* characterization

In recent years several new sets of instrumentation have been developed that enable real-time, *in situ* characterization of the growth process. Among them are reflection difference spectroscopy, scanning tunneling microscopy, and its counterpart atomic force microscopy. In addition, there are the electron microscopies. Two are particularly attractive to the observation of single-layer growth and therefore of great interest to the ALE community. Both rely heavily on phase contrast. They are (1) low energy electron microscopy (LEEM)



and its predecessor and closely related cousin photoemission electron microscopy (PEEM) and (2) reflection high energy electron microscopy (RHEEM). Each (in real time) reveal the dynamic microtopographic details of the changing surface. Each can also be quickly "reprogrammed" to image in reciprocal space thereby providing the well-known low energy electron diffraction and reflection high energy electron diffraction (RHEED) patterns to ascertain the crystallinity of the changing surface. A comprehensive tutorial on the LEEM technology has been published by its progenitor and leading advocate, Bauer [18]. Figure 1 depicts four selected frames of a PEEM video descriptive of a monolayer of carbon being deposited on an oxygen-terminated molybdenum surface. The step and terrace on the surface is evident. The length of the step edge is approximately 100  $\mu\text{m}$ . On the terrace is a dust particle (dark) that serves as a nucleating point for symmetrical self-limiting growth of a monolayer of carbon (light) around it. The step edge is also a nucleating place for the carbon. As seen in the series, the monolayer carbon growth from the step edge eventually coalesces with that from the dust particle. This figure was supplied by Dr. Martin Kordesch of Ohio University depicting ongoing work at that institution supported by the Strategic Defense Initiative Organization. Details of the RHEEM technology can be found elsewhere [19, 20]. LEEM-PEEM-RHEEM appear to be ideally suited to observe *in situ*,

in real time, when chemisorption has occurred and (by virtue of their reciprocal space imaging capability) to determine whether that adsorbed layer was deposited in a crystalline, polycrystalline, or amorphous state. As such, they appear ideally suited to ALE instrumentation. Initial *in situ* observations of group IV growth by LEEM are beginning [21]. Here germanium was grown on an arsenic-terminated silicon surface. Each monolayer grown was observed to rotate the surface reconstruction alternating between  $2 \times 1$  and  $1 \times 2$ .

### 3.1. Synergism

Figure 2 is a composite typical of molecular flux distributions from effusion and supersonic jet sources.

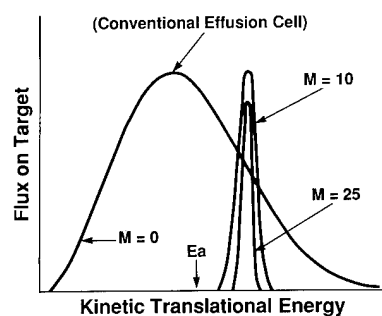


Fig. 2. Unseeded molecular beam flux with Mach number as parameter.

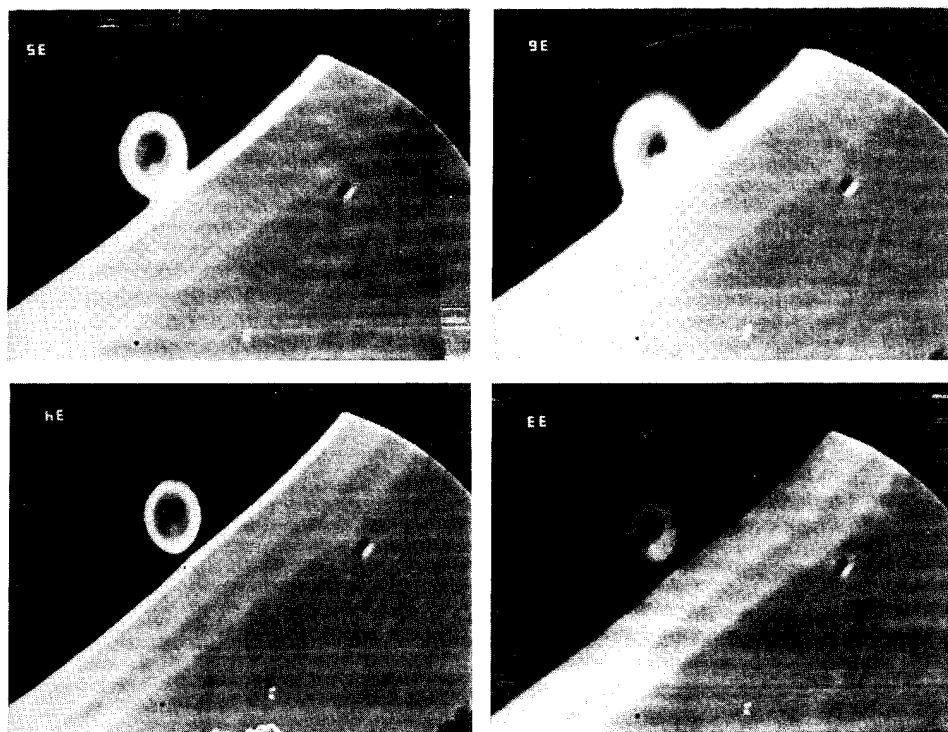


Fig. 1. Sequential PEEM images of carbon monolayer deposition on oxygen-terminated molybdenum.

Of particular note is the relative energy of a typical activation energy associated with a given deposition process. It is apparent that only a limited percentage of the thermal effusion flux is at a sufficient energy to react while the flux energy from the supersonic jet can be controlled so as to exceed that required for chemisorption. If this deposition is done in a pulsed manner (such as would be typical in an ALE process) then, between pulses, LEEM-PEEM-RHEEM imaging can be done. In this manner, the supersonic jet energy can be dynamically adjusted to ensure that it was at least of sufficient magnitude to exceed the activation energy required for chemisorption. More importantly, however, the energy can be controlled to affect maximum efficiency for the process and to ensure that excessive energy was not used. In compound semiconductor growth and in heterojunction growth, the ideal substrate temperature for chemisorbing a given molecule is not the same as that required for a subsequent, but different, molecule. Using a combination of supersonic jet deposition and LEEM-PEEM-RHEEM, substrate temperature can be held constant while impact energy is dynamically adjusted for optimum results.

#### 4. Computational chemistry

Reference 17 describes *inter alia* how  $\text{CH}_4$  was "hurled" at a nickel surface at an energy of  $17 \text{ kcal mol}^{-1}$  and how the surface was then characterized by electron energy loss analysis. The model describing the results indicated that the  $\text{CH}_4$  molecule was first flattened and then lost a hydrogen atom by quantum tunneling in the process of chemisorbing to the nickel surface. These findings are relevant to ALE, of course, because nickel is nearly lattice matched to diamond and ALE is under active pursuit as a means of heteroepitaxially nucleating single-crystal diamond. To verify and refine this model, new *ab initio* calculations have been pursued to permit a more accurate description of this process [22]. Other computational approaches using molecular dynamics have graphically depicted in 0.001 ps intervals the chemisorption (or alternatively the reflection) of molecules on group IV surfaces as a function of impact energy [23]. Later simulations by this group have depicted the impact of radicals at various energies [24]. One particular study has shown that the  $\text{CH}_3$  radical impacting diamond at an energy of about  $0.5kT$  bounces off, but the same radical impacting at 2.0 eV chemisorbs, while an impact energy of 5.0 eV will cause it to bounce off. Computational chemistry may provide the tools to optimize both the choice of reactants and the energy for their self-limiting chemisorption.

#### 4.1. More synergism

While computational chemistry is becoming increasingly capable of calculating the optimized energies for chemisorption, *in situ* characterization results shown in Fig. 1 (and other RHEED studies as well) indicate that crystal growth proceeds primarily at the step edges on slightly vicinal surfaces rather than on the terraces as computed. Working interactively, *in situ* characterization techniques not only can verify predicted chemisorption, but also can provide the data that would lead to more realistically applicable computations (*e.g.* step edge *vs.* terrace growth). Together, a synergetic approach accrues.

#### 5. Discussion

Many new techniques have recently evolved that are each expected to have a significant impact on group IV ALE growth. Taken separately, however, misleading conclusions can be drawn in situations akin to the "blind man and the elephant". Taken together in an integrated system, a new era is dawning that is expected to engender a more scientific approach to crystal growth.

#### References

- 1 M. N. Yoder, Diamond grown by ALE, *Proc. 19th Biennial Conf. on Carbon*, June 25-30, 1989.
- 2 V. B. Aleskovskii and V. E. Drozd, *Acta Polytech. Scand.*, 195 (1990) 155.
- 3 M. P. D'Evelyn, ALE: fundamental studies and new approaches, *SRC Topical Research Conf. on Challenges for GeSi*, Cornell University, Ithaca, NY, May 7-8, 1992.
- 4 Y. Takahashi and T. Urisu, *Jpn. J. Appl. Phys.*, 30 (2A) (1992) L209.
- 5 J. Nishizawa, K. Aoki, S. Suzuki and K. Kikuchi, *J. Cryst. Growth*, 99 (1990) 502.
- 6 Y. Takahashi, H. Ishii and K. Fugunaga, *J. Electrochem. Soc.*, 136 (1989) 137.
- 7 H. Ishii, Y. Takahashi and K. Fukomaga, *Proc. 1st Int. Conf. on Electronic Materials*, Materials Research Society, Pittsburgh, PA, 1989, p. 137.
- 8 Y. Takahashi, Y. Sese and T. Urisu, *Jpn. J. Appl. Phys.*, 28 (1989) 2387.
- 9 J. P. Noel, J. E. Greene, N. L. Rowell, S. Kechang and D. C. Houghton, *Appl. Phys. Lett.*, 55 (1989) 1525.
- 10 D. Lubben, R. Tsu, T. Bramblett and J. Greene, *J. Vac. Sci. Technol. A*, 9 (6) (1991) 3003.
- 11 S. Banerjee, A. Tasch, A. Mahajan, J. Irby, D. Kinoshita, R. Qian and S. Thomas, Silicon ALE using disilane with remote helium plasma bombardment, *SRC Topical Research Conf. on Challenges for GeSi*, Cornell University, Ithaca, NY, May 7-8, 1992.
- 12 I. Yamada and T. Takagi, *IEEE Trans. Electron Devices*, 34 (1987) 1018.
- 13 I. Yamada, *Appl. Surf. Sci.*, 43 (1989) 23.
- 14 J. B. Anderson, Molecular beams from nozzle sources. In P. P. Wegener (ed.), *Molecular Beams and Low Density Gasdynamics*, Dekker, New York, 1974.

- 15 E. W. Becker and K. Bier, *Z. Naturforsch., Teil A*, 9 (1954) 975.
- 16 J. B. Hudson, *Surface Science, an Introduction*, Butterworth-Heinemann, Boston, MA, 1992.
- 17 S. T. Ceyer, *Annu. Rev. Phys. Chem.*, 39 (1988) 479–510.
- 18 E. Bauer, Low energy electron microscopy, *Chemistry and Physics of Solid Surfaces VIII*, Springer Series in Surface Science no. 22, Springer, New York, 1990.
- 19 N. Osakabe, Y. Tanishiro, K. Yagi and G. Honjo, *Surf. Sci.*, 97 (1980) 393.
- 20 K. Takayanagi, K. Yagi, K. Kobayashi and G. Honjo, *J. Phys. E*, 11 (1978) 441.
- 21 R. M. Tromp and M. C. Reuter, *Phys. Rev. Lett.*, 68 (7) (1992) 954.
- 22 H. Yang and J. Whitten, *J. Chem. Phys.*, 96 (7) (1992) 5529.
- 23 R. Mowrey, D. Brenner, B. Dunlap, J. Mintmire and C. White, *J. Phys. Chem.*, 95 (1991) 7138.
- 24 D. W. Brenner, personal communication.

# Atomic H: a reagent for the extraction of chemical species from Si surfaces

John T. Yates, Jr., C. C. Cheng, Q. Gao, M. L. Colaiaanni and W. J. Choyke

Surface Science Center, Department of Chemistry, University of Pittsburgh, Pittsburgh, PA 15260 (USA)

## Abstract

The surface chemistry of adsorbed halogen atoms on Si(100) has been studied using several surface science methods. It has been found that Cl atoms bond to dangling bonds on symmetric Si<sub>2</sub> dimer sites, and that the Si–Cl bond angle is tilted  $25 \pm 4^\circ$  from the normal in the vertical plane containing the Si<sub>2</sub> dimer bond. The covalently bonded halogens Cl, Br, and I have been studied on Si(100) using atomic H bombardment at low substrate temperatures (300–630 K). In all cases, facile elimination of the hydrogen halide occurs, and the coverage of halogen may be driven to zero by moderate exposure to atomic H. The halogen extraction process is almost non-activated, suggesting that the chemical reaction to produce hydrogen halide species is driven by the potential energy carried by the atomic H species. This is an example of an Eley–Rideal reaction process and provides a potentially useful new approach for controlling atomic layer chemistry on semiconductors.

Atomic H driven extraction of adsorbed methyl (CH<sub>3</sub>) species on Si(100) is also observed to occur with lower efficiency than halogen extraction. Thermal desorption studies indicate that the C extraction process occurs as the result of atomic H induced etching of the surface, producing gas phase alkyl silanes such as CH<sub>3</sub>SiH<sub>3</sub>.

## 1. Introduction

The development of low temperature surface processes to manipulate adsorbed species on semiconductor surfaces provides the basis for new methods to produce heterostructure semiconductor devices. Our knowledge of the fundamentals governing chemistry on semiconductor surfaces is in its infancy, and mechanistic understanding of elementary semiconductor surface processes is needed [1]. In this paper, two new classes of surface reactions involving atomic H as a reagent are described. It is expected that the principles governing these two types of atomic H driven surface chemistries will find application in a wide range of semiconductor surface processes.

## 2. Experimental details

The ultrahigh vacuum apparatus and methods used for this research have been described previously [2]. The methods employed include temperature programmed desorption, Auger electron spectroscopy, high resolution electron energy loss spectroscopy (HREELS), and digital ESDIAD electron-stimulated desorption ion angular distribution [3]. Adsorbate gases are adsorbed on the single crystal surface using collimated molecular beam dosers which deliver an absolutely known flux of gas, permitting quantitative exposures and uptake measurements to be made [4].

## 3. Results and discussion

### 3.1. Structure of chemisorbed Cl on Si(100)–(2 × 1)

Figure 1 shows a schematic diagram of the digital ESDIAD apparatus employed for this work [3]. An electron beam excites surface species on the Si(100) single crystal, producing beams of positive ions which are spatially detected by the microchannel plate detector system. The pattern of ion emission angles is closely related to the direction of the surface chemical bonds which are ruptured by the electronic excitation process [5]. These ion emission directions are modified by final state image and reneutralization effects [6], as well as by the electrical bias applied to the crystal for pattern compression. Because the ion emission dynamics is governed by rapid Franck–Condon excitation from the ground state to a repulsive upper state, the statistical summation of millions of ion emission directions from an ensemble of adsorbate species on a single crystal will provide a statistical measurement of the distribution of chemical bond angles caused by thermal disorder at the measurement temperature. This permits digital ESDIAD to be used also as a powerful tool for the study of the dynamical behavior of adsorbates [5].

Figure 2 shows a sequence of Cl<sup>+</sup> ESDIAD patterns from chlorine adsorption on Si(100)–(2 × 1) [7, 8]. At an adsorption temperature of 120 K, a normal Cl<sup>+</sup> beam is observed to overlap an underlying Cl<sup>+</sup> pattern exhibiting four fold symmetry. On annealing the Cl-covered surface to temperatures above 120 K, the central

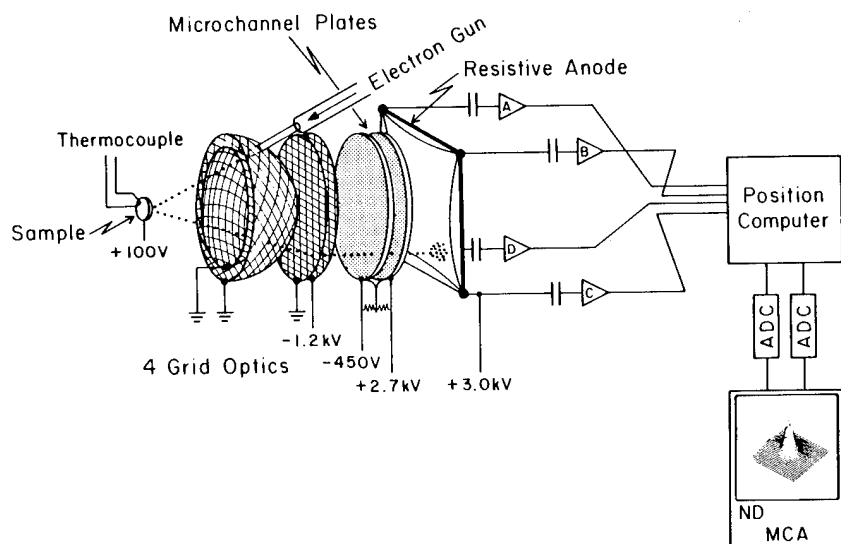


Fig. 1. Digital ESDIAD apparatus for imaging chemical bond directions in adsorbed species.

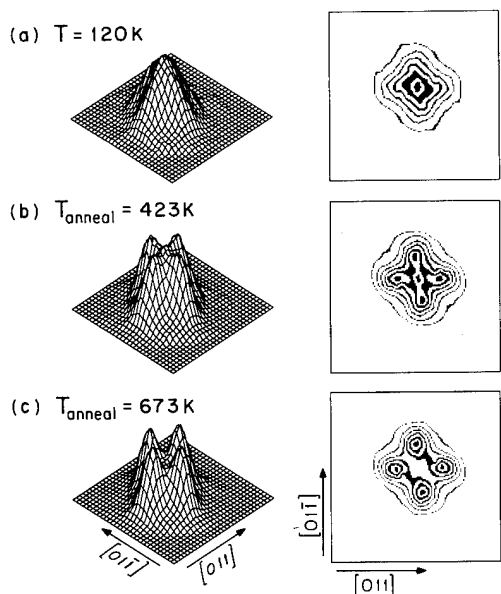


Fig. 2. ESDIAD patterns of  $\text{Cl}^+$  from  $\text{Si}(100)$  as a function of annealing temperature. The initial Cl coverage is near ML.

$\text{Cl}^+$  beam is seen to disappear, revealing the inclined beams which become more pronounced. This process culminates at about 673 K. We believe that the normal  $\text{Cl}^+$  beam is caused by a minority of adsorbed Cl atoms which bridge the symmetric Si dimer sites. These species have a high cross-section for ESD production of  $\text{Cl}^+$ , and the normal emission from these bridged-Cl species therefore dominates the low temperature ESDIAD pattern. As the system is heated, the bridged-Cl species convert to single-bonded Cl species, with the inclined Si-Cl bonds oriented in the vertical plane which includes the  $[011]$  crystallographic axis. This azimuthal plane corresponds to the Si-Si bond directions in the  $\text{Si}_2$  surface dimers on an  $\text{Si}(100)$  terrace. The ortho-

#### HREELS Study of Spectral Changes During Annealing- $\text{Cl}/\text{Si}(100)-(2 \times 1)$

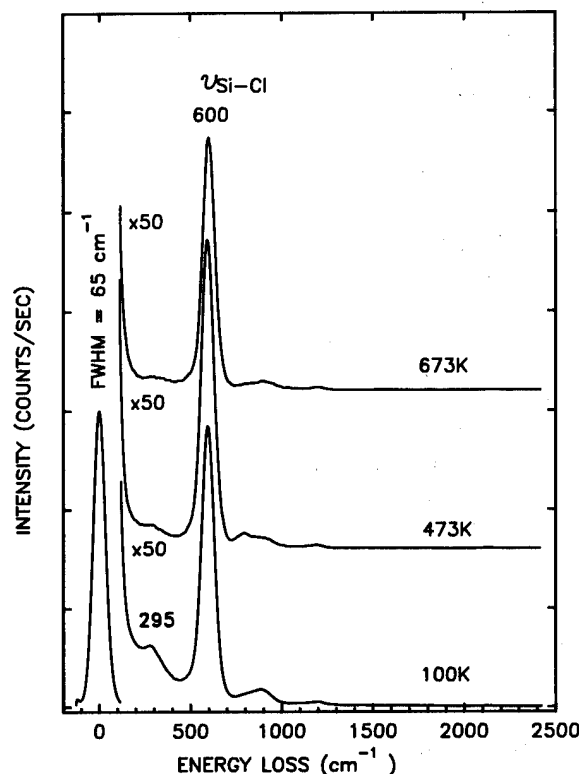


Fig. 3. HREELS study of the spectral changes as a function of annealing temperature.

nal Si-Cl beam directions correspond to inclined Si-Cl bonds (angle  $25 \pm 4^\circ$ ) on the mixture of two types of crystal terraces present on the slightly misaligned  $\text{Si}(100)$  crystal.

Figure 3 shows the vibrational behavior of the surface as a chlorine layer is heated over the same temper-

ature range as used in the ESDIAD experiments [8]. At 100 K, two Cl-related vibrational modes are observed at  $600\text{ cm}^{-1}$  and at about  $300\text{ cm}^{-1}$ . The  $600\text{ cm}^{-1}$  mode is due to the Si-Cl stretching mode of the inclined Si-Cl bonds. Its frequency and intensity remain almost constant as the heating process occurs. The weak mode at about  $300\text{ cm}^{-1}$  is assigned to a bridging-Cl species, linked between two Si atoms in a dimer pair on the Si(100)-(2 × 1) surface. The good analogy to the vibrational frequency of bridging-Cl in compounds such as  $\text{Al}_2\text{Cl}_6$  was employed to make this assignment [9]. The vibrational behavior suggests that the bridging-Cl species is a minority species, since the intensity of the  $600\text{ cm}^{-1}$  mode does not vary significantly during the heating process as the  $300\text{ cm}^{-1}$  mode decreases in intensity. The bridging-Cl species is metastable with respect to the inclined Si-Cl species, which is the most stable species on Si(100). Similar behavior was observed in the theoretical calculations of Wu *et al.* [10] for F on Si(100), except that an energy barrier for the bridge-to-inclined Si-F structure was not predicted theoretically. The large change observed in the  $\text{Cl}^+$  ESDIAD pattern for the heating range 100 K–673 K is related to the high ESD cross-section for  $\text{Cl}^+$  production from the small surface coverage of bridged-Cl which exists below 673 K.

### 3.2. Facile extraction of chemisorbed halogen atoms by atomic H

The Si-Cl bond may be broken easily by bombarding the surface with atomic H, produced on a hot tungsten filament in the ultrahigh vacuum system containing a low pressure of molecular  $\text{H}_2$  [11]. Figure 4 shows the behavior of the Cl surface coverage, together with similar measurements made for adsorbed Br and adsorbed I on Si(100). These measurements have been made in a way in which the small effect of the Auger electron beam on the halogen coverage has no effect on the interpretation. The fitted curves are best fits to first-order kinetics in halogen surface coverage at a

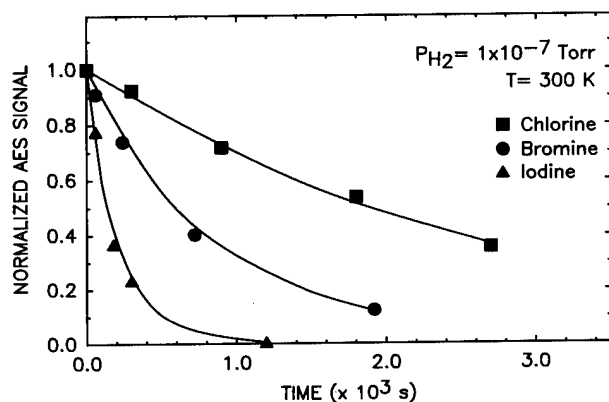


Fig. 4. Atomic H extraction for halogen adsorbates from Si(100).

surface temperature of 300 K. It is seen that the relative rate of halogen extraction is  $\text{I} > \text{Br} > \text{Cl}$ . A similar trend has been observed in gas phase studies for the reaction of atomic H with the methyl halides to produce hydrogen halide species [12].

The bromine extraction rate was studied as a function of the pressure of  $\text{H}_2$  used in the chamber, as seen in Fig. 5. The flux of atomic H is known to be proportional to the  $\text{H}_2$  pressure under these conditions [13]. As the  $\text{H}_2$  pressure is increased, the rate of Br extraction increases at a surface temperature of 430 K; the inset of Fig. 5 shows that the Br extraction rate is linearly proportional to the atomic H flux employed.

The temperature dependence of the atomic H induced extraction of Br was measured as shown in Fig. 6. An activation energy for this process of only  $1.6 \pm 0.2\text{ kcal mol}^{-1}$  was measured over the range 300 K–630 K, as shown in the inset of Fig. 6. Similar studies of the kinetics of extraction of adsorbed Cl gave an activation energy of  $2.1 \pm 0.2\text{ kcal mol}^{-1}$  for Cl/Si(100). These low activation energies are indicative that the thermal excitation of the surface species is of little importance in governing the rate of the halogen extraction process.

Considered together, the kinetic behavior of the halogen extraction process induced by atomic H corresponds to the well-known, but infrequently observed, Eley-Rideal kinetic process [11]. The process involves the use of the potential energy carried by the atomic H to produce the active complex involved in the removal of surface halogen. An active complex,  $\text{Si} \cdots \text{X} \cdots \text{H}$ , is produced when atomic H collides with the covalently bonded halogen atom X. Accommodation of the incoming H atom by the Si surface is not required in this mechanism. The potential energy of the atomic H is  $52\text{ kcal mol}^{-1}$  compared with  $\frac{1}{2}\text{ H}_2(\text{g})$ , and this energy is the primary driver for the halogen extraction process observed.

The Eley-Rideal process observed for atomic H as a reagent is potentially important for a wide range of surface chemistry. Other gas phase free radical species may be expected to be active in similar extraction processes on surfaces, and we will have to await future experiments before knowing the full implications of these first observations involving the most simple free radical species, atomic H. In particular, the use of atomic H extraction procedures for removal of surface halogen ligands (present in atomic layer epitaxy processes involving monolayers of group IV halide species) is expected to be of importance.

### 3.3. Extraction of adsorbed methyl groups with atomic H

The chemisorption of methyl iodide,  $\text{CH}_3\text{I}$ , on Si(100) has been shown to be an efficient way to produce surface methyl groups which are stable up to

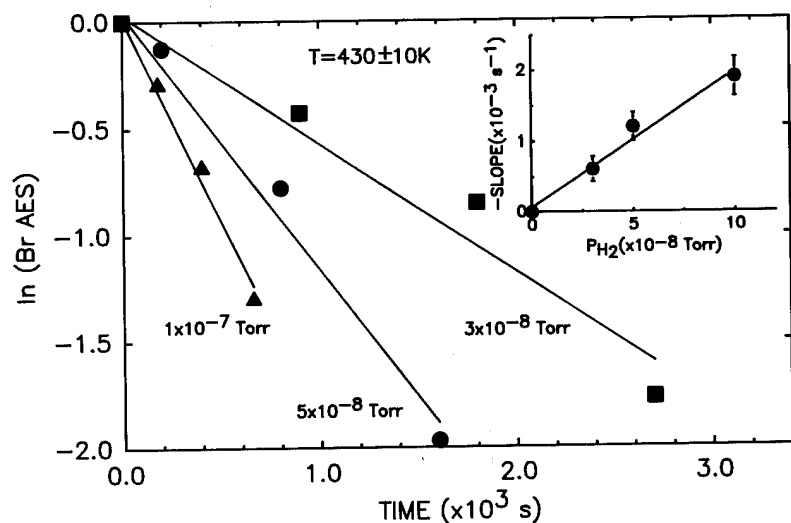
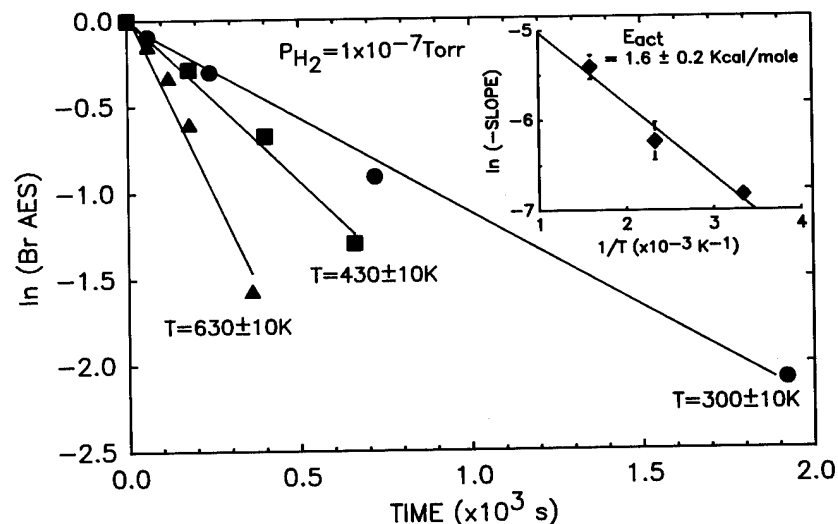
Fig. 5.  $H_2$  pressure dependence of Br extraction rate from Si(100).

Fig. 6. Temperature dependence of Br extraction rate from Si(100).

about 600 K [14, 15]. Therefore, we have employed  $CH_3I$  as a source of  $CH_3(a)$ , and have studied the effect of bombardment by atomic H of the covalently bonded  $CH_3$  groups. Figure 7 shows the surface temperature dependence of the rate of removal of C (as  $CH_3(a)$  species) by means of bombardment by atomic H. Compared with the exposures needed for halogen extraction (Fig. 3), atomic H is much less effective in removing methyl groups from the surface. In addition, the temperature dependence of the rate of the methyl extraction process is opposite to that seen for the halogen extraction process. In the case of methyl extraction, the rate decreases above a surface temperature of about 450 K.

Thermal desorption studies show that  $CH_3SiH_3(g)$  is evolved following atomic H bombardment of  $CH_3(a)$  [15]. In addition,  $SiH_4(g)$  is also evolved in the same temperature range near 600 K. The loss of surface methyl therefore occurs as a result of atomic H etching of the Si(100) surface. The decrease in rate above about 450 K is caused by the reduction in the capacity of the surface to adsorb H at this temperature, and hence to the reduced rate of etching about 450 K.

The comparative rate of removal of surface methyl groups and surface I atoms by atomic H bombardment is also easily seen in Fig. 8, where the vibrational characterization is shown. The vibrational spectrum shows modes related both to the Si-I bond and to the

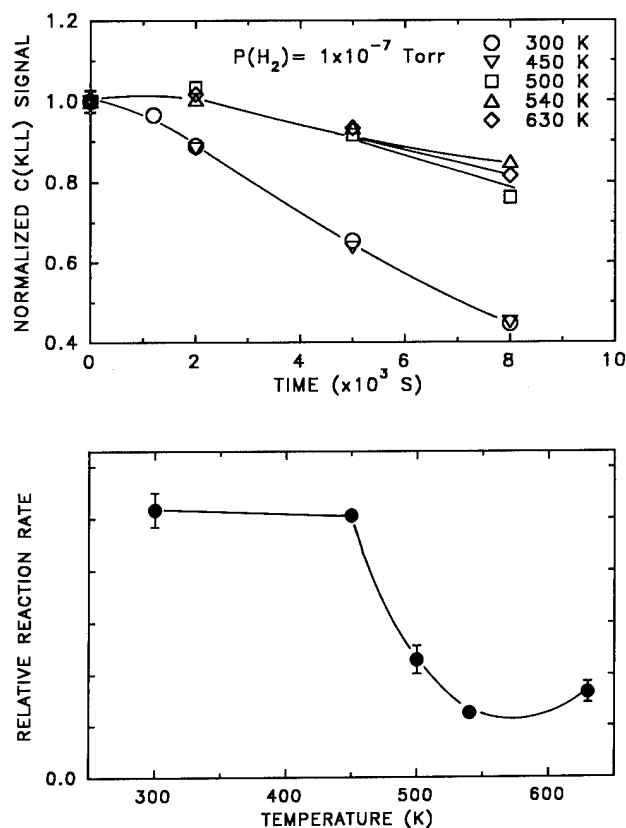


Fig. 7. Temperature dependence of C removal from  $\text{CH}_3/\text{Si}(100)$  by atomic H.

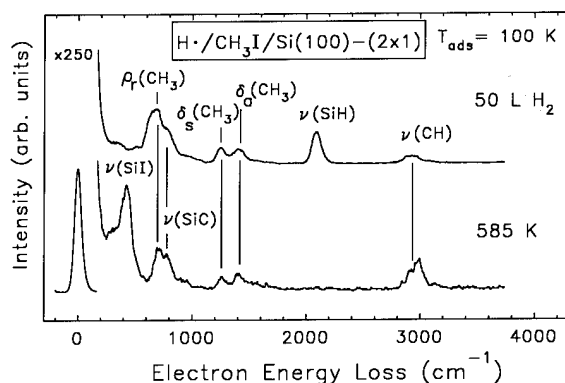


Fig. 8. HREELS study of atomic H extraction of iodine from  $\text{Si}(100)$ .  $T = 585$  K.

$\text{CH}_3(\text{a})$  species produced from dissociative adsorption of  $\text{CH}_3\text{I}$ . Atomic hydrogen efficiently removes the adsorbed iodine Si–I groups first, as seen by the preferential loss of  $\nu(\text{SiI})$  intensity.

#### 4. Summary

This brief review of the use of atomic H as a reagent for inducing surface reactions on Si has dealt with two

entirely different types of elementary surface processes.

(1) Covalently bonded halogen atoms may be efficiently removed by atomic H via an Eley–Rideal process yielding volatile hydrogen halide species. The rate of the Eley–Rideal process is almost temperature independent, indicating that thermal activation from the substrate is of little importance compared with the activation induced by the potential energy of the incident atomic H itself.

(2) Covalently bonded methyl groups are not readily removed from  $\text{Si}(100)$  by atomic H to produce methane. Instead, etching of the Si surface to produce species such as  $\text{CH}_3\text{SiH}_3$  and  $\text{SiH}_4$  is the dominant route for methyl removal.

(3) These two types of extraction processes may be useful in many materials processes such as atomic layer epitaxy.

#### Acknowledgment

We thank the Office of Naval Research for full support of this work.

#### References

- 1 M. E. Gross, J. M. Jasinski and J. T. Yates, Jr. (eds), *Mater. Res. Soc. Symp. Proc.*, 131 (1989).
- 2 C. C. Cheng, R. M. Wallace, P. A. Taylor, W. J. Choyke and J. T. Yates, Jr., *J. Appl. Phys.*, 67 (1990) 3693.
- 3 M. J. Bozack, L. Muehlhoff, J. N. Russell, Jr., W. J. Choyke and J. T. Yates, Jr., *J. Vac. Sci. Technol. A*, 5 (1987) 1.
- 4 J. T. Yates, Jr., M. D. Alvey, K. W. Kolasinski and M. J. Dresser, *Nucl. Instrum. Methods Phys. Res. B*, 27 (1987) 147.
- 5 C. C. Cheng, R. M. Wallace, P. A. Taylor, W. J. Choyke and J. T. Yates, Jr., *J. Appl. Phys.*, 67 (1990) 3693.
- 6 J. T. Yates, Jr., M. D. Alvey, M. J. Dresser, M. A. Henderson, M. Kiskinova, R. D. Ramsier and Z. Szabó, *Science*, 225 (1992) 1397.
- 7 R. D. Ramsier and J. T. Yates, Jr., *Surf. Sci. Rep.*, 12 (1991) 243.
- 8 Z. Misković, J. Vukanic and T. E. Madey, *Surf. Sci.*, 141 (1984) 285.
- 9 Z. Miskovic, J. Vukanic and T. E. Madey, *Surf. Sci.*, 169 (1986) 405.
- 10 C. C. Cheng, Q. Gao, W. J. Choyke and J. T. Yates, Jr., *Phys. Rev. B*, in press.
- 11 Q. Gao, C. C. Cheng, P. J. Chen, W. J. Choyke and J. T. Yates, Jr., *J. Chem. Phys.*, in press.
- 12 E. Maslowsky, *Vibrational Spectra for Organometallic Compounds*, Wiley, New York, 1977, p. 61.
- 13 C. J. Wu and E. Carter, *J. Am. Chem. Soc.*, 113 (1991) 9061.
- 14 C. J. Wu and E. Carter, *Phys. Rev. B*, 45 (1992) 9065.
- 15 P. C. Weakliem, C. J. Wu and E. Carter, *Phys. Rev. Lett.*, to be published.
- 16 C. C. Cheng, S. R. Lucas, H. Gutleben, W. J. Choyke and J. T. Yates, Jr., *J. Am. Chem. Soc.*, 114 (1992) 1249.
- 17 W. E. Jones and J. L. Ma, *Can. J. Chem.*, 64 (1986) 2192.
- 18 A. A. Westenberg and N. deHaas, *J. Chem. Phys.*, 62 (1975) 3321.
- 19 D. Brennen and P. C. Fletcher, *Proc. R. Soc. London, Ser. A*, 250 (1959) 389.
- 20 J. N. Smith, Jr., and W. Fite, *J. Chem. Phys.*, 37 (1962) 898.
- 21 H. Gutleben, S. R. Lucas, C. C. Cheng, W. J. Choyke and J. T. Yates, Jr., *Surf. Sci.*, 257 (1991) 146.
- 22 C. C. Cheng, S. R. Lucas, H. Gutleben, W. J. Choyke and J. T. Yates, Jr., *Surf. Sci.*, 273 (1992) L441.



# Hydrogen–halogen chemistry on semiconductor surfaces

Stephen M. Cohen, Terttu I. Hukka, Yuemei L. Yang and Mark P. D'Evelyn

Department of Chemistry and Rice Quantum Institute, Rice University, Houston, TX 77251-1892 (USA)

## Abstract

The chemistry of coadsorbed H and X ( $X \equiv \text{Cl}, \text{Br}$ ) on semiconductor surfaces is important in epitaxial growth of silicon from chlorosilanes and of  $\text{Si}_x\text{Ge}_{1-x}$  alloys, in hydrogenating–halogenating cycles in atomic layer epitaxy, and also provides an interesting model system, yet has received little attention to date. We have investigated the interaction of H, HCl, and HBr with Ge(100) by temperature-programmed desorption, and find that  $\text{H}_2$ , HCl, and HBr each desorb with near-first-order kinetics near 570–590 K, and that  $\text{GeCl}_2$  and  $\text{GeBr}_2$  desorb with second-order kinetics near 675 K and 710 K respectively. Trends in the chemistry and kinetics can be rationalized by viewing the dimer atoms on clean Ge(100) –  $(2 \times 1)$  as being linked by a strained double bond and adsorption, decomposition, and desorption as being analogous to addition, rearrangement, and elimination reactions of molecular germanium compounds. The near-first-order desorption kinetics are attributed to pairing on surface dimers induced by the  $\pi$  bond on unoccupied dimers. We infer a pairing enthalpy for  $\text{H} + \text{H}$  (approximately the  $\pi$  bond strength of dimerized Ge(100) surface atoms) of approximately  $5 \text{ kcal mol}^{-1}$ .

## 1. Introduction

There is currently great interest in the growth by atomic layer epitaxy (ALE) of the Group IV semiconductors diamond, silicon, and  $\text{Ge}_x\text{Si}_{1-x}$  alloys. Several ALE processes for silicon have been reported, involving alternating halogenated-precursor–hydrogen [1],  $\text{Si}_2\text{H}_6$ –photothermally induced  $\text{H}_2$  desorption [2], or  $\text{Si}_3\text{H}_8$ –thermally induced  $\text{H}_2$  desorption [3] cycles. In addition, chlorosilane chemical vapor deposition (CVD), which involves surface hydrogen and chlorine as intermediates, has been the dominant epitaxial silicon growth technology for 20 years. The surface chemistry of hydrogen and of coadsorbed hydrogen and halogens thus plays a central role in both the ALE and CVD of silicon and of  $\text{Ge}_x\text{Si}_{1-x}$ .

In this paper we investigate the interaction of H, HCl and HBr with Ge(100) by temperature-programmed desorption (TPD) for the first time, focusing on the adsorption kinetics of HCl and HBr and the desorption kinetics of  $\text{H}_2$ , HCl, HBr,  $\text{GeCl}_2$ , and  $\text{GeBr}_2$ .

## 2. Experimental details

Experiments were performed in a custom-built vacuum chamber [4] (base pressure approximately  $1 \times 10^{-10}$  Torr), pumped via a liquid- $\text{N}_2$ -trapped diffusion pump and titanium sublimation pump, and equipped with LEED/ESDIAD optics, an Auger spectrometer (VSW hemispherical analyzer HA-100), IR optics, a VG SXP-400 quadrupole mass spectrometer

(QMS) with a water-cooled shroud mounted on a translation system, a calibrated gas doser [5], an ion gun, and a tungsten filament used for dosing of atomic hydrogen. The sample holder was mounted on a rotatable manipulator capable of translation in the  $x$ -,  $y$ -, and  $z$ -directions.

A Ge(100) sample (Si-Tech, Inc.), cut  $4^\circ$ – $6^\circ$  off the (100) plane towards the [011] direction, 0.25–0.30 mm thick,  $n$ -type,  $\rho = 5$ – $40 \Omega \text{ cm}$ , was cut into a rectangle 13.4 mm  $\times$  13.8 mm. A chromel–alumel thermocouple was cemented into a small hole (approximately 0.5 mm diameter) drilled near one edge, using Aremco 516 high-temperature cement. The sample was mounted between tantalum foil clips attached to a copper block and could be heated resistively to above 873 K and cooled with liquid nitrogen down to 153 K. The active area presented to the doser after mounting was 11.5 mm  $\times$  13.4 mm. After degreasing, the germanium sample was placed in the chamber, and cleaned by several sputter-and-anneal cycles ( $i_{\text{Ar}^+} = 2$ – $3 \mu\text{A cm}^{-2}$ ,  $E_{\text{Ar}^+} = 500 \text{ V}$ ,  $T_{\text{anneal}} = 850 \text{ K}$ ).

Atomic hydrogen exposures were performed by backfilling the ultrahigh vacuum analysis chamber with  $\text{H}_2$  to pressures of  $2 \times 10^{-8}$ – $5 \times 10^{-7}$  Torr and heating a coiled tungsten filament located approximately 3 cm from the sample to 1700–1800 K. For dosing HCl or HBr, the sample was rotated to face the doser and a known amount of gas was admitted to the chamber through a calibrated aperture. Computer calculations of flux [6] show that, for this sample geometry, 17% of the molecules leaving the doser hit the sample, giving a flux during dosing of  $(4.11 \pm 0.23) \times 10^{15} M^{-1/2} P \text{ s}^{-1}$ ,

where  $M$  ( $\text{g mol}^{-1}$ ) is the molecular mass, and  $P$  (Torr) is the pressure upstream of the conductance-limiting orifice [5] during dosing. For Ge(100), one monolayer (ML) is  $6.23 \times 10^{14}$  atoms  $\text{cm}^{-2}$ , and is used below to scale both doses and surface coverages.

All coverages were determined by TPD. A coverage calibration for surface hydrogen was obtained by TPD of  $\text{H}_2\text{S}$ , whose adsorption as  $\text{H} + \text{SH}$  [7] saturates at 0.5 ML [8], and which yields exclusively  $\text{H}_2$  and  $\text{GeS}$  upon heating [9].  $\text{HX}$  ( $\text{X} \equiv \text{Cl}$  or  $\text{Br}$ ) coverages were determined by assuming that both molecules similarly reach a saturation coverage of 0.5 ML of  $\text{H} + \text{X}$ .

After dosing, when the background pressure fell to  $(2-3) \times 10^{-10}$  Torr, the sample was rotated to face the entrance slit of the water-cooled QMS shroud, at a distance of approximately 0.5 cm. The temperature was ramped at a rate of  $2 \text{ K s}^{-1}$ , controlled by a Eurotherm temperature controller, and QMS signals, multiplexed for 1–3 masses, were recorded by an AT-compatible personal computer.

### 3. Results

TPD traces for  $\text{H}_2$  following atomic hydrogen exposures are shown in Fig. 1 for various initial coverages  $\Theta_0$ . The peak desorption temperature  $T_p$  at all initial coverages is about 570 K. The nearly coverage-independent values of  $T_p$ , together with the asymmetric peak shape at initial coverages near 1 ML indicate near-first-order desorption kinetics [10]. However, the slight but readily discernable increase in  $T_p$  and the more symmetric peak shape at lower initial coverages demonstrate a

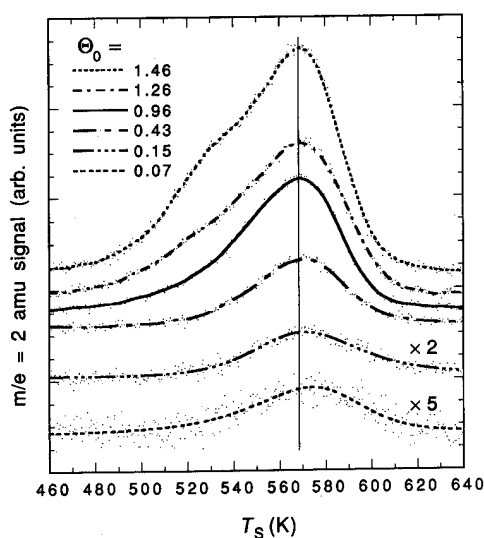


Fig. 1. Temperature-programmed desorption (TPD) data for  $\text{H}_2$  following exposure to atomic hydrogen. The initial hydrogen coverage in monolayers  $\Theta_0$  is indicated for each trace.

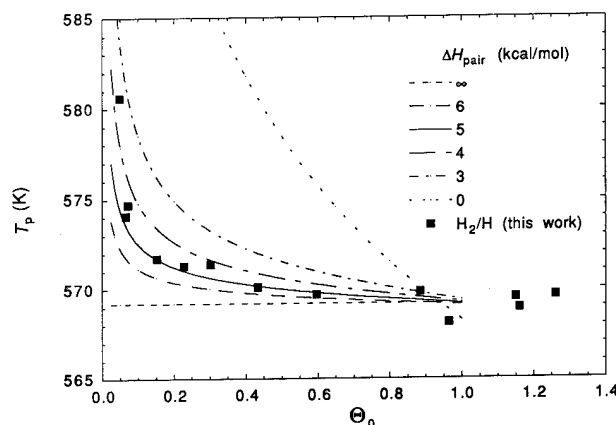


Fig. 2. Dependence of TPD peak temperature of  $\text{H}_2$  on initial hydrogen coverage. Experimental results are supplemented by predictions of the doubly occupied dimer model as a parametric function of  $\Delta H_{\text{pair}}$ .  $T_p$  was calculated using an activation energy of  $42 \text{ kcal mol}^{-1}$  and a pre-exponential factor of  $2 \times 10^{15} \text{ s}^{-1}$  for  $k$  and a heating rate of  $2 \text{ K s}^{-1}$ .

slight departure from first-order kinetics, as also occurs for hydrogen on  $\text{Si}(100)$  [11–13]. The dependence of  $T_p$  on  $\Theta_0$  is shown in Fig. 2 together with theoretical curves which are described in the next section.

At initial hydrogen coverages above 1 ML a shoulder in the desorption curve appears near 525 K (Fig. 1). Hydrogen in the dihydride ( $\text{GeH}_2$ ) configuration, with two hydrogen atoms bonded to a single surface germanium atom, has been shown to decompose at a lower temperature than the  $\text{GeH}$  monohydride state [14]. The dihydride state is also less stable than the monohydride on  $\text{Si}(100)$  [15–18], yielding an  $\text{H}_2$  desorption peak approximately 100 K lower in temperature than the TPD peak from the monohydride [11, 19]. The shoulder in Fig. 1, therefore, almost certainly corresponds to decomposition of surface dihydride. The fact that the onset for the appearance of the shoulder occurs at 1 ML supports the coverage calibration described above, since it is well established that the lower-temperature TPD peak for  $\text{H}_2$  on  $\text{Si}(100)$  begins to appear at an initial coverage of 1 ML.

Three desorption products were observed following exposure to  $\text{HX}$  ( $\text{X} \equiv \text{Cl}$  or  $\text{Br}$ ):  $\text{HX}$ ,  $\text{H}_2$ , and  $\text{GeX}_2$ , as shown in Figs. 3 and 4 for  $\text{HCl}$  and  $\text{HBr}$  respectively. In both cases  $\text{H}_2$  desorption occurs near 570 K after a saturation dose, as for desorption from adsorbed hydrogen alone, with  $T_p$  increasing to around 580 K at initial coverages of approximately 0.05 ML. The dependence of  $T_p$  for the  $\text{H}_2$  and  $\text{HX}$  desorption peaks on initial  $\text{HX}$  coverage is shown in Figs. 5 and 6 for  $\text{HCl}$  and  $\text{HBr}$  respectively.  $\text{HCl}$  and  $\text{HBr}$  desorption occurs near 575 and 580 K at saturation initial coverage respectively, with  $T_p$  increasing by 10–20 K at initial coverages of approximately 0.05 ML. The weak depen-

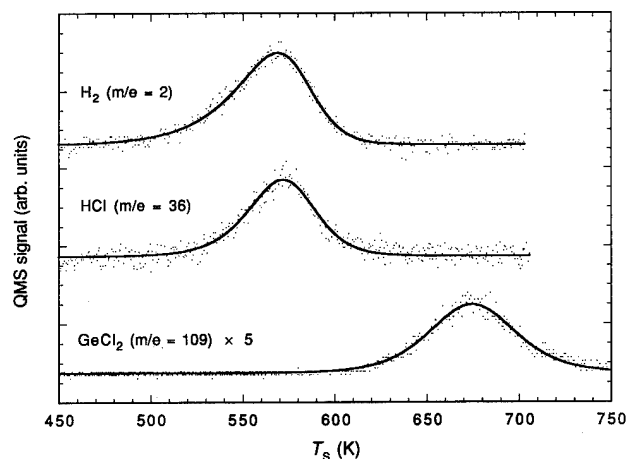


Fig. 3. TPD spectrum of desorption products from Ge(100) following a saturation dose of HCl. Improved signal-to-noise ratio was achieved by monitoring the  $\text{GeCl}^+$  cracking fraction of  $\text{GeCl}_2$ .

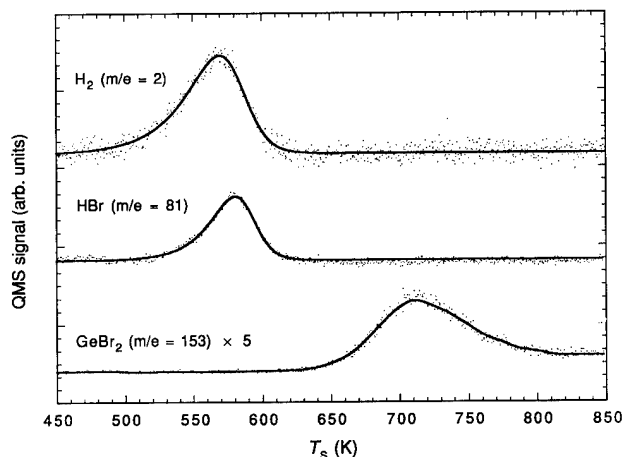


Fig. 4. TPD spectrum of desorption products from Ge(100) following a saturation dose of HBr. Improved signal-to-noise ratio was achieved by monitoring the  $\text{GeBr}^+$  cracking fraction of  $\text{GeBr}_2$ .

dence of  $T_p$  on initial coverage for both  $\text{H}_2$  and  $\text{HX}$  desorption, together with the asymmetric peak shapes (Figs. 3, 4), indicate near-first-order kinetics. The dihalide etch products  $\text{GeCl}_2$  and  $\text{GeBr}_2$  desorb at higher temperatures, 675 and 710 K respectively, following saturation  $\text{HX}$  doses. In contrast to the behavior of the  $\text{H}_2$  and  $\text{HX}$  TPD peaks,  $T_p$  for the  $\text{GeX}_2$  peaks rose by 50–60 K at lower initial coverages, indicating approximately second-order kinetics.

Sticking probabilities for HCl and HBr were obtained from the slopes of coverage *vs.* exposure data. The initial sticking probability  $S_0$  for HCl decreased from 0.6 at 270 K to 0.05 at 400 K, while that of HBr was constant at 0.9 over the same temperature range.

Stoichiometry implies that for every  $\text{H}_2$  molecule that desorbs, the two X atoms remaining from dissociative adsorption of  $\text{HX}$  must desorb as  $\text{GeX}_2$ . The desorp-

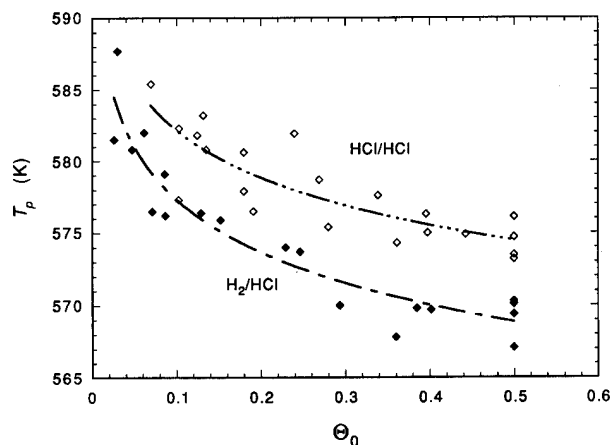


Fig. 5. Dependence of TPD peak temperatures for  $\text{H}_2$  and HCl on initial coverage of HCl.

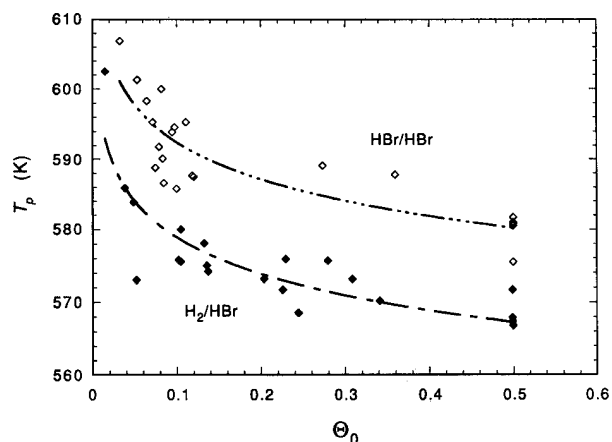


Fig. 6. Dependence of TPD peak temperatures for  $\text{H}_2$  and HBr on initial coverage of HBr.

tion peaks for  $\text{H}_2$  and  $\text{HX}$  have a strong overlap while those of  $\text{GeX}_2$  occur at higher temperature. Therefore, the branching ratio ( $\text{H}_2 + \text{GeX}_2$  *vs.*  $\text{HX}$  desorption) may be usefully described by the fraction of adsorbed hydrogen atoms which desorb as  $\text{H}_2$ . This fraction is nearly coverage independent at 0.6 for HCl, whereas for HBr it increases from 0.66 at saturation initial coverage to approximately 0.9 in the low initial-coverage limit.

#### 4. Discussion

The present results support the paradigm we have proposed [9, 13] for surface chemistry on Group IV (100)–(2 × 1) surfaces: the dimerized surface atoms [20, 21] are analogous to strained digermenes (disilenes or olefins on Si(100) or diamond (100) respectively), and adsorption and desorption are analogous to molecular addition and elimination reactions respectively.

The  $\pi$  bonds on clean surface dimers [22–24] provide a driving force for pairing of adsorbates on the dimers [13, 24]. The enthalpy of pairing  $\Delta H_{\text{pair}}$  is equal to the difference in germanium-atom bond strengths between surface dimers with adsorbed atoms on each germanium atom and dimers with only one adatom. In molecules, where band-structure effects are absent, the difference in the bond strengths to the first and second hydrogen atoms removed from adjacent atoms (which is analogous to the pairing enthalpy for surface hydrogen) is approximately equal to the  $\pi$ -bond strength between the atoms from which the hydrogen atoms are removed [13, 25].

The  $\text{H}_2/\text{H}$  TPD results shown in Fig. 2 are consistent with and may be interpreted using our doubly-occupied dimer model [13], the exact solution to a lattice gas model which incorporates preferential pairing of adsorbates on dimers but neglects interactions between dimers. The coverage of hydrogen which is paired on surface dimers ("doubly-occupied" dimers) is given by [13]

$$\Theta_2 = \Theta - \frac{2\Theta(1-\Theta)}{[1 + 4(1/x - 1)\Theta(1-\Theta)]^{1/2} + 1} \quad (1)$$

where  $\Theta$  is the instantaneous total coverage of hydrogen,

$$x \equiv \exp(-\Delta H_{\text{pair}}/RT) \quad (2)$$

$\Delta H_{\text{pair}}$  is the pairing enthalpy for surface hydrogen,  $R$  is the gas constant, and  $T$  is the temperature. (The form of eqn. (1) is slightly different from that of eqn. (4) of ref. 13 but is algebraically equivalent and better behaved numerically.) We assume that the desorption rate of  $\text{H}_2$  is given by

$$\text{desorption rate} = -\frac{d\Theta}{dt} = k\Theta_2 \quad (3)$$

i.e. that recombinative desorption occurs between H atoms paired on surface dimers [12, 13, 24, 26–28]. Assuming that the pre-exponential factor for  $k$  is  $2 \times 10^{15} \text{ s}^{-1}$ , as was found in a recent study of  $\text{H}_2$  desorption from  $\text{Si}(100)$  which took H-atom pairing into account in the analysis [27], we estimate an activation energy of  $42 \text{ kcal mol}^{-1}$  from the TPD peak temperature [10] at high initial coverage. The dependence of  $T_p$  on  $\Theta_0$  predicted by the model is shown in Fig. 2 for several assumed values of  $\Delta H_{\text{pair}}$ . By comparing the experimental and model results, we estimate  $\Delta H_{\text{pair}}$  to be approximately  $5 \text{ kcal mol}^{-1}$  for H on  $\text{Ge}(100)$ , which is slightly less than the  $6 \text{ kcal mol}^{-1}$  obtained [13, 27] for H on  $\text{Si}(100)$ .

The high sticking probabilities for HCl and HBr imply a negligible activation energy for absorption and suggest four-center transition states, as was suggested previously for  $\text{H}_2\text{S}$  and  $\text{H}_2\text{O}$  on  $\text{Ge}(100)$  [9]. The decrease in  $S_0$  for HCl with surface temperature is

analogous to the behavior seen for  $\text{H}_2\text{O}$  on  $\text{Ge}(100)$  [9, 29] and suggests the existence of a mobile physisorbed precursor state [30]. The larger value of  $S_0$  for HBr than for HCl is explainable by the longer, weaker H–X bond and by transition-state arguments analogous to those comparing the adsorption of  $\text{H}_2\text{O}$  and  $\text{H}_2\text{S}$  on  $\text{Ge}(100)$  [9].

The desorption kinetics of  $\text{H}_2$  from HX are nearly indistinguishable from those of H alone, as well as from  $\text{H}_2\text{S}$  and  $\text{H}_2\text{O}$  [9]. This independence of the desorption kinetics from the presence of coadsorbed chlorine, bromine, oxygen or sulfur implies that desorption is a highly localized process on  $\text{Ge}(100)$ , which contrasts strongly with desorption kinetics on metal surfaces.

The desorption kinetics of HX and  $\text{GeX}_2$  are described in detail elsewhere [31]. The presence of two types of atoms (H, X), three types of pairing (H + H, H + X, X + X), and three desorption channels necessitates a generalization of the doubly-occupied dimer model. Nonetheless, it seems intuitively obvious that the close similarity of the behavior of HX to that of  $\text{H}_2$  (cf. Figs. 2, 5, and 6) can be accounted for by pairing of H and X atoms on surface dimers, implying that preferential pairing of adsorbates on Group IV (100) surfaces is a general phenomenon and is not restricted to hydrogen. The pairing enthalpy for H + X (or for X + X) need not be precisely equal to that for H + H (approximately  $5 \text{ kcal mol}^{-1}$ ), however, because of the possibility of steric and electrostatic interactions and bond polarization effects. Two X atoms must become localized near a Ge atom in order for  $\text{GeX}_2$  to desorb. The identification of the  $\pi$  bond on unoccupied dimers as the driving force for pairing on  $(100) - (2 \times 1)$  surfaces [13, 24] suggests that X + X should also pair preferentially. However, the observed near-second order desorption kinetics for  $\text{GeX}_2$  provides no support for preferential pairing of X + X. This suggests either that  $\Delta H_{\text{pair}}$  for X + X is small or that the doubly occupied dimer model is inapplicable because the  $\pi$ -bonded dimer surface structure is disrupted before or during desorption of  $\text{GeX}_2$ .

## Acknowledgments

The authors acknowledge the Office of Naval Research for support of this work and the National Science Foundation (Grant CHE-8715812) and the Academy of Finland for additional support.

## References

- 1 J. Nishizawa, K. Aoki, S. Suzuki and K. Kikuchi, *J. Electrochem. Soc.*, **137**, (1990) 1898; *J. Cryst. Growth*, **99**, (1990) 502.
- 2 D. Lubben, R. Tsu, T. R. Bramblett and J. E. Greene, *J. Vac. Sci. Technol. A*, **9** (1991) 3003.

- 3 S. Imai, S. Takagi, O. Sugiura and M. Matsumura, *Jpn. J. Appl. Phys.*, **30** (1991) 3646.
- 4 M. P. D'Evelyn, Y. L. Yang, S. M. Cohen and L. M. Ulvick, to be published.
- 5 S. M. Cohen and M. P. D'Evelyn, *J. Vac. Sci. Technol. A*, **9** (1991) 2414.
- 6 V. T. Smith, L. M. Ulvick and M. P. D'Evelyn, to be published.
- 7 K. T. Leung, L. J. Terminello, Z. Hussain, X. S. Zhang, T. Hayashi and D. A. Shirley, *Phys. Rev. B*, **38** (1988) 8241.
- 8 (a) H. J. Kuhr, W. Ranke and J. Finster, *Surf. Sci.*, **178** (1986) 171.  
(b) H. J. Kuhr and W. Ranke, *Surf. Sci.*, **189-190** (1987) 420.
- 9 S. M. Cohen, Y. L. Yang, E. Rouchouze, T. Jin and M. P. D'Evelyn, *J. Vac. Sci. Technol. A*, **10** (1992) 2166.
- 10 P. A. Redhead, *Vacuum*, **12** (1962) 203.
- 11 K. Sinniah, M. G. Sherman, L. B. Lewis, W. H. Weinberg, J. T. Yates, Jr., and K. C. Janda, *J. Chem. Phys.*, **92** (1990) 5700.
- 12 M. L. Wise, B. G. Koehler, P. Gupta, P. A. Coon and S. M. George, *Surf. Sci.*, **258** (1991) 166.
- 13 M. P. D'Evelyn, Y. L. Yang and L. F. Sutcu, *J. Chem. Phys.*, **96** (1992) 852.
- 14 L. Papagno, X. Y. Shen, J. Anderson, G. S. Spagnolo and G. J. Lapeyre, *Phys. Rev. B*, **34** (1986) 7188.
- 15 F. Stucki, J. A. Schaefer, J. A. Anderson, G. J. Lapeyre and W. Göpel, *Solid State Commun.*, **47** (1983) 795. J. A. Schaefer, F. Stucki, J. A. Anderson, G. J. Lapeyre and W. Göpel, *Surf. Sci.*, **140** (1984) 207.
- 16 Y. J. Chabal and K. Raghavachari, *Phys. Rev. Lett.*, **53** (1984) 282.
- 17 K. Oura, J. Yamane, K. Umezawa, M. Naitoh, F. Shoji and T. Hanawa, *Phys. Rev. B*, **41** (1990) 1200.
- 18 J. J. Boland, *Phys. Rev. Lett.*, **65** (1990) 3325.
- 19 C. C. Cheng and J. T. Yates, Jr., *Phys. Rev. B*, **43** (1991) 4041.
- 20 R. J. Hamers, R. M. Tromp and J. E. Demuth, *Phys. Rev. B*, **34** (1986) 5343.
- 21 J. A. Kubby, J. E. Griffith, R. S. Becker and J. S. Vickers, *Phys. Rev. B*, **36**, (1987) 6079.
- 22 J. A. Appelbaum, G. A. Baraff and D. R. Hamann, *Phys. Rev. B*, **14** (1976) 588.
- 23 R. J. Hamers, Ph. Avouris and F. Boszo, *Phys. Rev. Lett.*, **59** (1988) 2071; *J. Vac. Sci. Technol. A*, **6** (1988) 508.
- 24 J. J. Boland, *Phys. Rev. Lett.*, **67** (1991) 1539; *J. Vac. Sci. Technol. A*, **10** (1992) 2458.
- 25 M. W. Schmidt, P. N. Truong and M. S. Gordon, *J. Am. Chem. Soc.*, **109** (1987) 5217.
- 26 K. W. Kolasinski, S. F. Shane and R. N. Zare, *J. Chem. Phys.*, **96** (1992) 3995.
- 27 U. Höfer, L. Li and T. F. Heinz, *Phys. Rev. B*, **45** (1992) 9485.
- 28 J. Sheng and J. Z. H. Zhang, *J. Chem. Phys.*, **97** (1992) 596.
- 29 C. U. S. Larsson and A. S. Flodström, *Phys. Rev. B*, **43** (1991) 9281.
- 30 P. Kisliuk, *J. Phys. Chem. Solids*, **3** (1957) 95; **5** (1958) 78.
- 31 Y. L. Yang, S. M. Cohen, T. I. Hukka, and M. P. D'Evelyn, Adsorption, desorption, and decomposition of HCl and HBr on Ge(100): competitive pairing and near-first-order desorption kinetics, in preparation.

# Dopants on Si(100) surfaces: useful probes of silicon atomic layer epitaxy?

S. M. Gates and D. D. Koleske

IBM T. J. Watson Research Center, Yorktown Heights, NY 10598 (USA)

## Abstract

Submonolayer coverages of N, B, Ge and Sn were studied on Si(100) surfaces using time-of-flight scattering and recoiling spectroscopy. Thin Si layers were grown on top of the dopants, and these layers are designated Si\*. The thermal stability of Si\*/N/Si(100), Si\*/B/Si(100), Si\*/Sn/Si(100) and Si\*/Ge/Si(100) structures is compared here. Attenuation of the elemental dopant signals by Si\* is used to study Si atomic layer epitaxy. The dopant is called an elemental “marker” in this context. Plots of direct recoiling intensity *vs.* incident angle are used to distinguish surface marker layers from marker layers buried under Si\*.

Experimental methods for evaluating precursors used in Si atomic layer epitaxy (ALE) are not well established, owing to the standard problems of studying homoepitaxy. Also, the growth of delta-doped layers by ALE in the Si and Si/Ge systems is of current interest. These reasons motivate our studies of the thermal stability of submonolayer coverages of the dopants N, B, Ge and Sn on the Si(100) surface. Results on the growth of thin Si layers atop these dopants (designated Si\*), and on the thermal stability of the resulting Si\*/dopant/Si(100) structures are summarized here. The studies of B, Ge and Sn have been reported elsewhere [1].

These studies utilize a pulsed 4 keV K<sup>+</sup> ion beam with time-of-flight (TOF) detection to probe the surface. Both scattered K<sup>+</sup> (a sensitive probe of heavy elements), and direct recoil (DR) particles (best for light elements) are detected. Rabalais have reviewed the time-of-flight scattering and recoiling spectroscopy (TOF-SARS) method [2, 3]. Plots of DR intensity *vs.* incident angle  $\alpha$  are used to address qualitatively the location of elemental “marker” layers.

Our comparison of the dopants N, B, Ge and Sn on the Si(100) surface is summarized in Table 1. In each case, we have studied the dopant in an Si\*/dopant/Si(100) structure, with Si\* being approximately 1/3–1/2 monolayer (ML) of new Si deposited in a single self-limiting adsorption of an Si precursor. The precursors Si<sub>2</sub>H<sub>6</sub>, Si<sub>3</sub>H<sub>8</sub> and Si<sub>2</sub>Cl<sub>6</sub> have been used in these studies, and each of these molecules deposits 1/3–1/2 ML of Si\* in a saturation exposure. Thicker Si\* layers are considered later in this paper (see Fig. 3). Other precursors are discussed elsewhere [4]. At present, we have studied primarily the stability with respect to annealing, in order to define the useful range of  $T_s$  for use of these

TABLE 1. Comparison of dopant markers in structures designated Si\*/dopant/Si(100)

Dopant	Decomposition temperature (°C)	Mode of decomposition
N	≥ 500	N diffuses into Si bulk
B	≥ 500	B diffuses into Si bulk
Ge	400	Ge segregates to surface, concurrent with H <sub>2</sub> desorption, if Cl present, GeCl <sub>2</sub> desorption occurs
Sn	400	Sn segregates to surface, concurrent with H <sub>2</sub> desorption

elements as “markers” of the initial Si(100) interface in ALE studies. Structural issues of surface order and lattice quality will be addressed using electron diffraction techniques in future work. We find that Ge and Sn exhibit essentially the same behavior. These Group IV elements migrate to the surface (atop the layer of Si\*) concurrent with H desorption, as shown in Fig. 1. Boron “markers” are stable to at least 500 °C, and possibly higher. Owing to the mass resolution limitations of TOF-SARS, we used Si<sub>2</sub>Cl<sub>6</sub> in our B stability studies to avoid interference of H and B DR signals. As shown elsewhere [1], our investigation of the Si\*/B/Si(100) structure is limited by the desorption of SiCl<sub>2</sub> beginning at 500 °C. We have not yet defined the upper limit of thermal stability for B in this structure in the absence of Cl. Feldman and coworkers have demonstrated the epitaxial growth of Si by molecular beam epitaxy (MBE) on top of an ordered 1/2 ML of B atoms [5]. As shown below in Fig. 3, we find that N marker layers are stable to at least 500 °C. We have some indication that the N marker is stable to higher temperature, and may be useful for Si ALE studies.

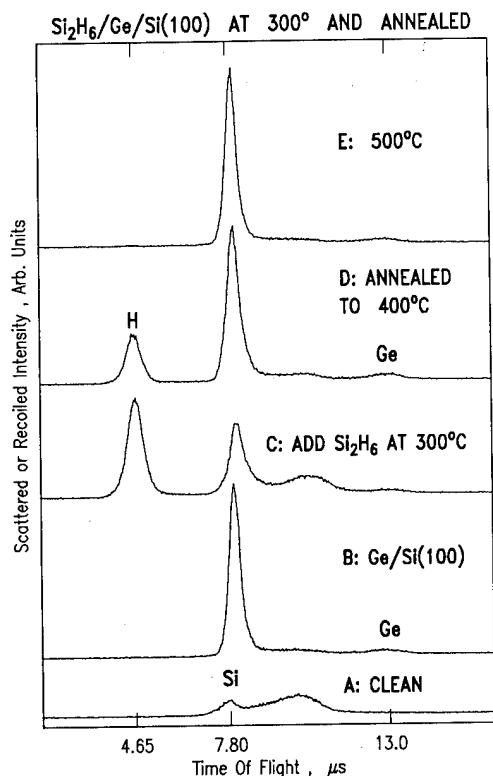


Fig. 1. TOF-SARS spectra using 4 keV potassium ions ( $K^+$ ),  $\alpha = 3^\circ$  angle of incidence with respect to the surface plane, and the detector grid at ground potential. A, clean Si(100) — ( $2 \times 1$ ); B,  $9 \times 10^{17}$   $GeH_4$   $cm^{-2}$  dosed at 500 °C; C, surface in B with  $1 \times 10^{19}$   $Si_2H_6$   $cm^{-2}$  dosed at 300 °C; in D and E, the surface from C was heated to 400 and 500 °C respectively, for 4 min at each temperature.

Figure 1 is an example of our thermal stability studies with a structure designated  $Si^*/Ge/Si(100)$ . Both scattered  $K^+$  ions and DR particles are detected. In spectrum 1A from the clean surface, the feature at 7.8  $\mu s$  is recoiled Si atoms ( $Si_{DR}$ ), and the broad feature from 8–11  $\mu s$  is due to  $K^+$  scattered from Si in the first and second layers ( $K^+ \rightarrow Si$ ). About 1/3 ML of Ge was added by  $GeH_4$  adsorption at 500 °C (the hydrogen desorbs at this temperature) and the result is spectrum 1B. (The Ge coverage was calibrated assuming that a saturation  $GeH_4$  exposure at 100 °C results in 1/4 ML of Ge.) The intense peak at 8.1  $\mu s$  is  $K^+$  scattered from Ge ( $K^+ \rightarrow Ge$ ) and the weak feature at 13.0  $\mu s$  is recoiled Ge atoms ( $Ge_{DR}$ ). After acquiring spectrum 1B at 500 °C, the sample was cooled to 300 °C and saturated with  $Si_2H_6$  before acquiring spectrum 1C. Note that both the  $Ge_{DR}$  and  $K^+ \rightarrow Ge$  features are attenuated compared with spectrum 1B. Virtually identical results are seen using  $Si_3H_8$  [1]. We have measured the  $Ge_{DR}$  signal as a function of  $Si^*$  coverage [1]. The  $Si^*/Ge/Si(100)$  structure is metastable. Annealing to 400 °C (spectrum 1D) results in  $H_2$  desorption and concurrent Ge segregation to the surface. Both the

$Ge_{DR}$  and  $K^+ \rightarrow Ge$  features return to their original levels. Annealing to 500 °C (spectrum 1E) gives a spectrum identical with 1B, before  $Si_2H_6$  adsorption.

The segregation of dopants during MBE Si growth results in poor incorporation of the dopant. We believe that dopant segregation and three-dimensional island growth are related by the common role of open dangling bonds. Island formation can be suppressed using As or Sb as a "surfactant" in Ge on Si(100) and Si on  $GeSi(100)$  growth [6]. Termination of the dangling bonds with As or Sb inhibits island formation [6]. Results such as Fig. 1 prove that termination of the surface dangling bonds with H can prevent Ge segregation. A common role of dangling bonds in these two growth problems is implied, and is under further investigation. Termination of the dangling bonds with H, Cl, As or Sb may relieve lattice strain, decreasing the driving force that causes islanding or dopant segregation. Alternatively, termination of the dangling bonds may reduce a kinetic barrier to atom mobility, allowing segregation or islanding to occur.

The location of a dopant "marker" can be determined qualitatively by changing the incident angle  $\alpha$  of the  $K^+$  beam with respect to the surface plane. Figure 2 shows a schematic diagram of the direct recoiling experiment, including the definition of  $\alpha$ . To study the location of a dopant "marker" layer, direct recoiling spectra are acquired from  $\alpha = 2^\circ$  to  $\alpha = 23^\circ$  in approximately  $3^\circ$  increments. At each  $\alpha$  value, we compute the fraction of the total DR signal appearing as each element, and plot this fraction *vs.*  $\alpha$ . We call such a plot an  $\alpha$  scan. Using surface  $BH_x$  species on the Si(100) surface and B buried in an  $Si^*/B/Si(100)$  structure, we have reported  $\alpha$  scans for B in these two distinct forms [7]. As  $\alpha$  is increased, elements sitting on top of the surface (in the first layer) exhibit a decreasing DR signal. The DR signal of an element with a large concentration in the subsurface region increases as  $\alpha$  is increased. The exact site location cannot be determined from this simple analysis. Subsurface elements can be in any layer (Second, third, etc.) and the simple  $\alpha$  scan does not distinguish these. More refined analysis such as azimuth angle scans and scattering simulations can provide such site determination [3].

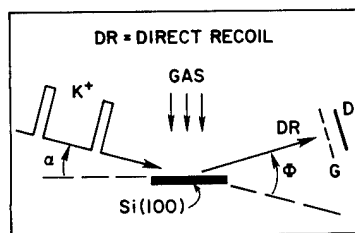


Fig. 2. Schematic geometry of the TOF-SARS experiment.

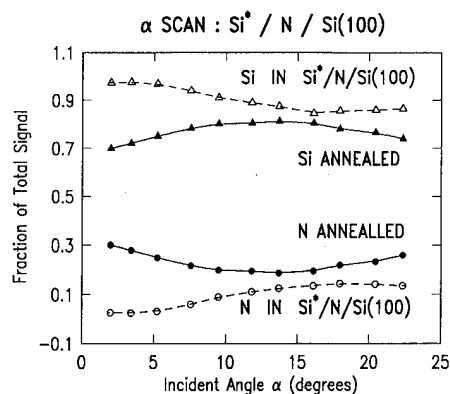


Fig. 3. Incident angle  $\alpha$  scans for N on Si(100) prepared in two ways.  $\blacktriangle$ ,  $\bullet$ , after saturation  $\text{NH}_3$  exposure at 200 °C, and heating to 700 °C;  $\triangle$ ,  $\circ$ , after two full cycles of Si ALE growth at 500 °C ( $\text{Si}_2\text{H}_6$  exposures  $2 \times 10^{19} \text{ cm}^{-2}$ , and  $\text{Si}_2\text{Cl}_6$  exposures  $1 \times 10^{18} \text{ cm}^{-2}$ ). The fraction of the total DR signal contributed by each element is plotted as a function of  $\alpha$  for N and Si. The spectra were measured for 60 s each. Elements located on the surface show a decrease in signal as  $\alpha$  is increased, while elements located below the first surface layer show an increase in signal as  $\alpha$  is increased.

Figure 3 shows  $\alpha$  scans for the elements N and Si in two structures on Si(100). The solid symbols ("annealed") are from approximately 1/2 ML of N below the first layer of the Si(100) surface. To produce this N layer, a saturation coverage of  $\text{NH}_3$  at 200 °C was annealed to 700 °C. This quantitatively causes desorption of H as  $\text{H}_2$ , and migration of N to sites below the first layer, with the exact N site(s) unknown. Note that the N fraction decreases with increasing  $\alpha$ , indicating that the N lies near the surface. The open symbols are from this same surface, with  $\text{Si}^*$  deposited on top of the N. The  $\text{Si}^*$  layer was grown at 500 °C using two full cycles of alternating exposures of  $\text{Si}_2\text{H}_6$  and  $\text{Si}_2\text{Cl}_6$  [7]. The  $\text{Si}_2\text{H}_6$  exposures were  $2 \times 10^{19} \text{ cm}^{-2}$ , and the  $\text{Si}_2\text{Cl}_6$  exposures were  $1 \times 10^{18} \text{ cm}^{-2}$ . Note that the N fraction is smaller than for the N annealed surface (N is attenuated by  $\text{Si}^*$ ) and that the N fraction increases with increasing  $\alpha$ . The increasing N fraction is similar to the increasing Si fraction (a bulk element) for the "annealed" surface. This is the signature of an element located farther beneath the surface. The epitaxial quality of the  $\text{Si}^*$

layers atop N "markers" will be evaluated using electron diffraction methods in subsequent work.

We have illustrated how DR signals from the dopant "marker" elements N, B, Sn and Ge can be used to study the growth of Si by ALE. The stability of  $\text{Si}^*/\text{dopant}/\text{Si}(100)$  structures has been compared. Submonolayer coverages of Ge and Sn present in the structures  $\text{Si}^*/\text{Sn}/\text{Si}(100)$  and  $\text{Si}^*/\text{Ge}/\text{Si}(100)$  are metastable. These structures decompose at about 400 °C by dopant segregation to the surface, if the  $\text{Si}^*$  surface is not terminated with hydrogen. The  $\text{Si}^*/\text{B}/\text{Si}(100)$  structure is observed to decompose at 500 °C, but in this case we have Cl present on the surface and decomposition is by  $\text{SiCl}_2$  desorption. The upper limit of stability for this structure may be higher than 500 °C with a thicker  $\text{Si}^*$  layer and no surface Cl. The  $\text{Si}^*/\text{N}/\text{Si}(100)$  structure is stable to 500 °C (as proven by the data of Fig. 3), but we have not yet studied the epitaxial quality of the  $\text{Si}^*$  layer. We are now comparing B and N with regard to diffusion in the 500–600 °C range. Among the dopants studied, we are unable to state definitively whether N or B is the optimum dopant marker for Si ALE investigations. We hope to resolve this question shortly.

#### Acknowledgments

The authors thank the Office of Naval Research for support under contract N00014-91-C-0080, and Dr. J. A. Schultz for consultation regarding direct recoiling methods.

#### References

- 1 S. M. Gates and D. D. Koleske, *Appl. Phys. Lett.*, **61** (1992) 309.
- 2 J. W. Rabalais, *Science*, **250** (1990) 522.
- 3 J. W. Rabalais, *CRC Crit. Rev. Solid State Mater. Sci.*, **14** (1988) 319.
- 4 D. D. Koleske, S. M. Gates and D. B. Beach, *Thin Solid Films*, **225** (1993) 172.
- 5 R. L. Headrick, B. E. Weir, A. F. J. Levi, D. J. Eaglesham and L. C. Feldman, *Appl. Phys. Lett.*, **57** (1990) 2779.
- 6 M. Copel, M. C. Reuter, M. Horn von Hoegen and R. M. Tromp, *Phys. Rev. B*, **42** (1990) 11682.
- 7 D. D. Koleske, S. M. Gates and D. B. Beach, *J. Appl. Phys.*, **72** (1992) 4073.



# Atomic layer doping for Si

D. A. Grützmacher, K. Eberl, A. R. Powell, B. A. Ek, T. O. Sedgwick and S. S. Iyer

IBM T. J. Watson Research Center, Yorktown Heights, NY 10598 (USA)

## Abstract

We report on initial results of the potential of self-limiting surface reactions for the doping of Si layers using molecular beam epitaxy (MBE) and atmospheric pressure chemical vapor deposition (APCVD). In MBE experiments using Sb as an n-type dopant a self-limiting process is obtained at a coverage of half a monolayer. No evidence of a self-limiting process has yet been found for p-type doping using  $B_2H_6$  above 400 °C. In the case of MBE growth at temperatures below 400 °C the B is only partly activated (10%–20%). In APCVD grown samples B surface coverage leads to significant growth inhibition of the subsequent deposition of Si from  $SiCl_2H_2$ . Finally, preliminary results of atomic layer doping using  $AsH_3$  in APCVD indicate a self-limitation of chemisorption of  $AsH_3$  at about 0.1 monolayer at a temperature of 600 °C; however, subsequent growth of Si leads to a smearing out of the As due to segregation and to the residence time of As in the system.

## 1. Introduction

Conventional Si epitaxy employs ion implantation for the incorporation of dopants. Excellent dosimetry is achieved by monitoring ion currents. However, implant damage removal requires an annealing process that results in diffusion that may not be acceptable or adequate for future generation device technology.

The degree of reproducibility and control obtained by ion implantation might be hard to meet by conventional growth techniques using *in situ* doping, since total doses of often less than 0.1 monolayer (ML) are commonly required to be deposited within a few nanometers and with a reproducibility of a few per cent for modern bipolar technology. Here we explore the possibility of using self-limiting surface reactions (SLSRs) as a method to meter precise dopant doses both for Si epitaxy and as a diffusion source. SLSRs have been proposed for various atomic layer epitaxy schemes [1]. The incorporation of dopants by SLSR processes is attractive, since no self-passivation at exactly 1 ML is mandatory, which is a general problem in Si ALE processes for Si and SiGe [2]. Conceptually an atomic layer doping (ALD) process with self-passivation at a fraction of an ML would lead to the incorporation of a reproducible dose of dopant onto a surface. Figure 1 shows the ALD process schematically. When combined with epitaxy, the epitaxial growth is arrested and the growth surface is exposed to the doping constituents. After surface saturation is reached, an extraction process may be needed to renew the growth surface. Thereafter epitaxy is resumed. This cycle may be repeated until the required dose is attained. Very often, steric hindrance will prevent the adsorption of more than a fraction of an ML. ALD may be

## Atomic Layer Doping

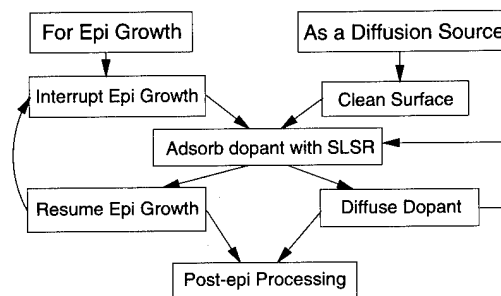


Fig. 1. Schematic diagram of the ALD process.

combined with diffusion as well. Such a process may be used to control source–drain diffusion in complementary metal oxide semiconductor technology. In order to prevent desorption of dopants, a capping layer of silicon nitride or Si may be needed.

## 2. Experimental details

The experiments were performed in a solid source molecular beam epitaxy (MBE) system equipped with a  $B_2H_6$  (1% in  $H_2$ ) gas source and with an atmospheric pressure chemical vapor deposition (APCVD) apparatus using  $SiCl_2H_2$ ,  $B_2H_6$  (0.5% in  $H_2$ ) and  $AsH_3$  (0.2% in He) as reactive gases in an  $H_2$  carrier. In the case of the MBE system the partial pressure of the  $B_2H_6$  is adjusted manually via a leak valve. A remote ion gauge, which is located to avoid  $B_2H_6$  cracking, measures the leak rate. For the ALD experiments  $B_2H_6$  partial pressures of  $10^{-4}$  Pa and 0.13 Pa have been used in the MBE and

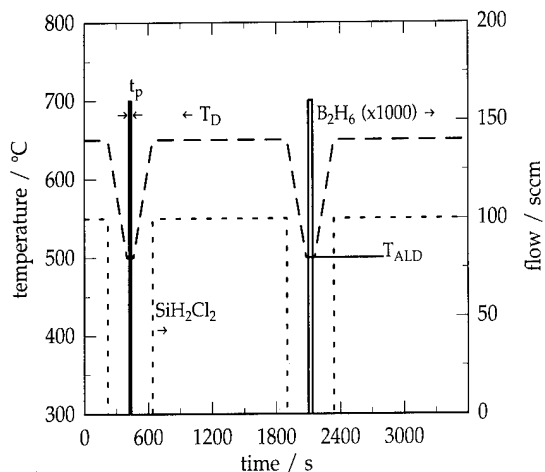


Fig. 2. APCVD temperature and gas flow sequence for ALD using the exposure time  $t_p$  and the temperature  $T_{ALD}$  at time of dopant exposure as parameters.

APCVD respectively. ALD of As by APCVD was performed using an  $AsH_3$  partial pressure of 0.13 Pa.

The following growth cycles were used to study the capabilities of the (1) MBE and (2) APCVD for ALD processes.

(1) After growth of an Si buffer layer the surface was exposed to either  $B_2H_6:H_2$  or Sb during a growth interruption. The growth was interrupted for 30 min, allowing 10 min of pumping on the system before and after the exposure. The structures were then capped by a 100 nm thick Si layer. The exposure time and the growth temperature were chosen as growth parameters.

(2) Figure 2 shows the growth cycle used for the APCVD experiments. After the growth of an Si layer at 650 °C the temperature was dropped within 3 min to the "ALD temperature"  $T_{ALD}$ . At  $T_{ALD}$  the surface was exposed to the dopant and after a purge time of 1 min the temperature was raised again to 650 °C for the Si deposition. During the growth interruptions the reactor was purged with  $H_2$ . Experiments at  $T_{ALD}$  values of 400 °C, 500 °C and 600 °C were performed. This process was cycled a few times varying the exposure time  $t_p$  from 1 to 64 s.

### 3. Results and discussion

#### 3.1. Sb doping in Si molecular beam epitaxy

Elemental Sb is the preferred dopant for n-type doping in Si MBE because of the low vapor pressure. Metzger [3] has studied the adsorption kinetics of Sb on Si(100), Si(111) and Si(110) in great detail. On Si(100) the pertinent observations are described with the help of Fig. 3 adapted from that work. Sb adsorbs in an ordered superstructure on Si(100). As coverage increases to 0.5 ML (1 ML =  $1.2 \times 10^{15} \text{ cm}^{-2}$ ) the frac-

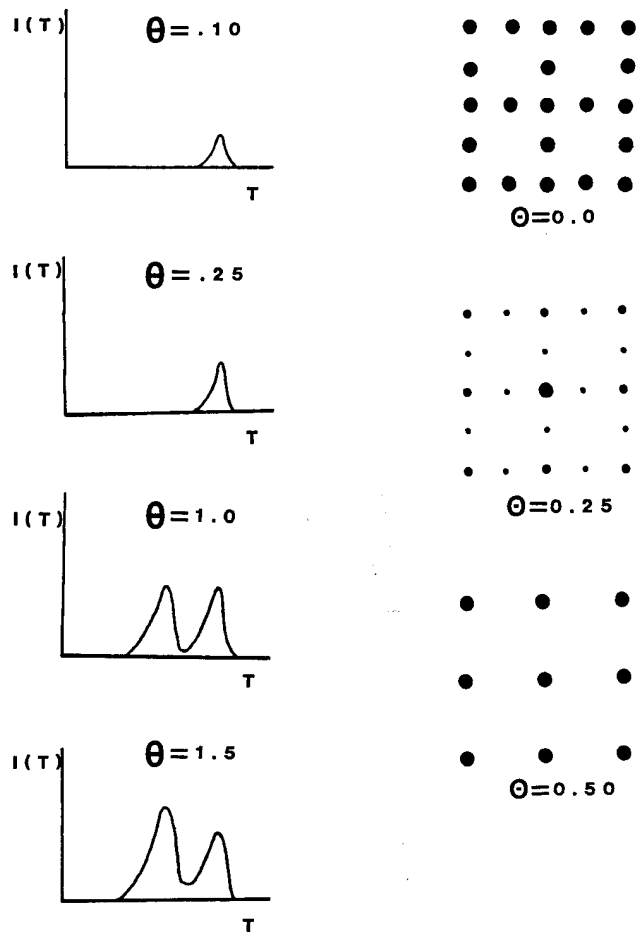


Fig. 3. Sb on Si(100) desorption spectra and surface reconstructions (from ref. 8).

tional order low energy electron diffraction spots are gradually extinguished and a  $1 \times 1$  reconstruction is obtained. Further adsorption of Sb retains this  $1 \times 1$  reconstruction until several MLs of Sb are adsorbed.

Thermal desorption spectroscopy shows that below 0.5 ML a single desorption peak is observed at about 950 °C. However, as the coverage is increased beyond 0.5 ML an additional desorption peak is observed at about 450 °C. All Sb in excess of 0.5 ML desorbs at this temperature.

This suggests that a fixed coverage of exactly 0.5 ML may be easily achieved by exposing the Si(100) surface to an Sb flux in excess of 0.5 ML and desorbing the excess at about 500 °C for several minutes. Monitoring the surface reconstruction until a  $1 \times 1$  reconstruction is obtained and then continuing further exposure for a short time will ensure that the coverage of 0.5 ML is reached. We have used this method to suppress long-range order in SiGe alloys [4]. Alternatively, exposure may be performed at substrate temperatures in excess of 500 °C and the desorption step may be eliminated as coverage will not exceed 0.5 ML.

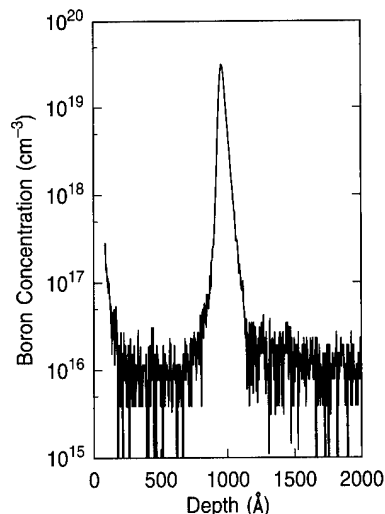


Fig. 4. SIMS profile of a spike deposited at 550 °C from  $B_2H_6$  by MBE.

While we have now a precise doping source, actual epitaxial doping is complicated by the tendency of Sb to segregate to the growing surface [5]. To obviate this problem, subsequent Si growth at extremely low temperatures (below 400 °C) is required. Alternatively, amorphous film deposition followed by solid phase epitaxy is needed [6].

### 3.2. $B_2H_6$ doping in gas source molecular beam epitaxy

Figure 4 shows a  $\delta$ -doped layer obtained by exposing a clean  $2 \times 1$  reconstructed surface to the  $B_2H_6:H_2$  mixture for 10 min at 550 °C. Growth was then resumed after pumping on the system for 10 min. The full width at half-maximum is 4 nm and attests to the sharp profiles possible using this technique. However, no self-limitation of the  $B_2H_6$  adsorption is identified for these growth conditions. Figure 5 shows the B sheet density obtained from secondary ion mass spectroscopy (SIMS) as function of the  $B_2H_6$  exposure in experiments similar to that in Fig. 4. At the low coverage of  $5 \times 10^{11}$ – $5 \times 10^{12}$   $cm^{-2}$  shown in Fig. 5 the dependence appears to be linear; however, at higher coverages the

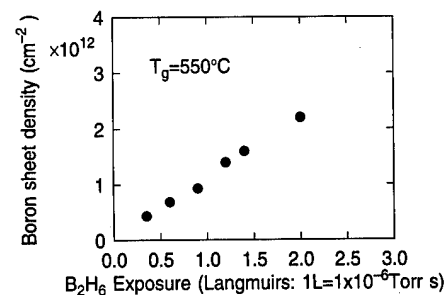


Fig. 5. Dependence of the B sheet density determined by SIMS on the  $B_2H_6$  exposure for MBE grown samples.

TABLE 1. Sticking coefficient  $S$  for different B densities

B density	$S$
$10^9$ $cm^{-2}$	$2.7 \times 10^{-3}$
$10^{11}$ $cm^{-2}$	$1.7 \times 10^{-3}$
$10^{12}$ $cm^{-2}$	$1.5 \times 10^{-3}$
$10^{14}$ $cm^{-2}$	$0.3 \times 10^{-3}$

net incorporated dopant increases sublinearly. This accompanies a reduction in the sticking coefficient as a function of the B coverage which is shown in Table 1. Clearly it decreases with increasing coverage, approaching  $3 \times 10^{-4}$  in agreement with the data of Yu *et al.* [7]. The sticking coefficients were calculated from the total amount of  $B_2H_6$  at the end of the exposure time and the total exposure time; these values may be high, since this calculation averages over the time and does not take the higher sticking coefficient at the beginning of the exposure into account, but nevertheless the sticking coefficient does not approach zero. These results in this temperature range suggest that no self-limiting reaction occurs. Yu *et al.* suggest a self-limiting adsorption at  $10^{14}$   $cm^{-2}$  if the adsorption is carried out at very low temperatures (below 200 °C). At these temperatures the exposure required for achieving this coverage is several thousand langmuirs, which is beyond our current experimental capabilities. However, we did investigate the activation of B in our experiments as a function of temperature. For B incorporated at temperatures above 500 °C, the activation was, within the limits of the measurement, nearly 100%. This number dropped abruptly to below 20% for incorporation at 400 °C. Further annealing at 650 °C for 30 min did not improve this number significantly. Apparently the B is passivated when incorporated at low temperatures. H bound to the B, which appears to be likely at low temperatures, might be the reason for the deactivation. However, H is expected to be removed from the B during the anneal leading to a higher activation, which was not observed in the experiment. Further investigations appear to be necessary for complete understanding of this phenomenon.

### 3.3. $B_2H_6$ doping in atmospheric pressure chemical vapor deposition

In contrast to the experiments using MBE, complex gas phase reactions may occur in APCVD which complicate the interpretation of the data. After the deposition of Si using  $SiCl_2H_2$  the surface is predominantly terminated by  $SiCl_x$  species, most likely  $SiCl$  [2].  $B_2H_6$  is rather unstable and it decomposes in the gas phase; the species arriving at the surface are probably reactive  $BH_x$  components.

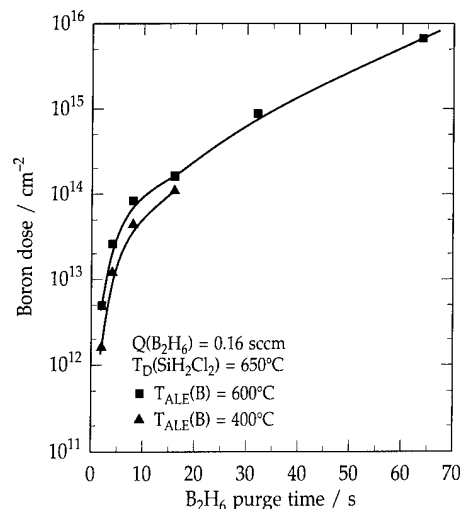


Fig. 6. Dependence of the B sheet density determined by SIMS on the  $B_2H_6$  exposure time for APCVD grown samples.

Figure 6 shows the boron sheet density determined by SIMS as a function of exposure time for  $T_{ALD} = 400^\circ\text{C}$  and  $600^\circ\text{C}$ . There is no indication of a saturation effect; in fact, the sheet density appears to increase superlinearly in the range of exposure times studied to well past ML coverage. For  $t_p = 64\text{ s}$  the amount of B deposited is equal to 5 ML. Apparently, the reactive B species, possibly the radical  $BH_3$ , which arrives at the surface continues to deposit after the first ML. At very low temperatures the gas phase reactions creating these reactive species might be suppressed, but it is possible that the  $B_2H_6$  molecule will not be adsorbed on the SiCl-terminated surface under these conditions.

Figure 7 shows the dependence of the thickness of the Si cap layer on the B sheet density determined by SIMS. The data reveal a significant growth inhibition

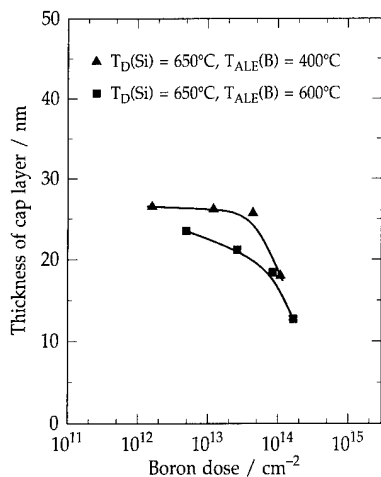


Fig. 7. Effect of the B surface concentration on the thickness of the subsequently grown Si cap layer.

of Si on heavily B-terminated surfaces. This finding suggests that the nucleation of Si from  $SiCl_2H_2$  on the B terminated surface is initially hampered. Surprisingly, this inhibition is found even when the SIMS data reveal a B incorporation of much less than 1M. Indeed, we think, that after the exposure to  $B_2H_6$  for a few seconds, the amount of B on the surface is much larger, and it may be even more than 1 ML. During the subsequent exposure to  $SiCl_2H_2$  initially part of the  $SiCl_2H_2$  is used to remove B rather than to deposit Si. The growth of Si is resumed when either growth nuclei have been formed on the B-terminated surface or the B coverage decreases below 1 ML and the growth starts from Si surfaces. The data evaluated by SIMS after the deposition process are therefore the result of complex adsorption-desorption processes. Further evidence for this model is given by an experiment where the Si source was  $SiH_4$  instead of  $SiCl_2H_2$ . For a B exposure time of 15 s the integrated dose of B in this sample was  $3 \times 10^{15}\text{ cm}^{-2}$ , more than an order of magnitude higher than for the sample where the subsequent layer was grown by  $SiCl_2H_2$ . This indicates that B is removed during the exposure of  $SiCl_2H_2$  and that the Cl plays an important role in the removal. The assumption of B desorption during the initial exposure to  $SiCl_2H_2$  also explains the superlinear increase in the B dose with the exposure time.

However, since no self-limitation has been found, these experiments indicate that  $B_2H_6$  is not a suitable source for a self-limiting ALD process in Si by APCVD at temperatures between 400 and  $600^\circ\text{C}$ .

### 3.4. $AsH_3$ doping in atmospheric pressure chemical vapor deposition

In CVD processes  $AsH_3$  is the typical As dopant source because of the low diffusion coefficient. ALD experiments were performed in the same fashion as for the  $B_2H_6$ . Figure 8 shows the SIMS data for three samples. Each sample was prepared using 5 cycles with 1, 2, 4, 8 and 16 s exposure times of the Cl-H-terminated Si surface to  $AsH_3$ . The temperatures  $T_{ALD}$  of the exposures were 600, 500 and  $400^\circ\text{C}$ . At  $400^\circ\text{C}$  no As was detected by SIMS. Gravimetric techniques established that a 160 nm thick film had grown. Therefore we conclude that no As was incorporated; probably the  $AsH_3$  is not chemisorbed at  $400^\circ\text{C}$  on the Cl- and H-terminated Si surface. Possibly physisorbed  $AsH_3$  on the surface apparently desorbs during the heating to the deposition temperature of  $650^\circ\text{C}$  before it reacts with the surface. At  $500^\circ\text{C}$  no  $AsH_3$  is incorporated for short exposure times whereas SIMS indicates some incorporation for long exposure times (8 and 16 s). For an increase in  $T_{ALD}$  to  $600^\circ\text{C}$  all five As doping spikes are clearly seen in the SIMS spectra. The fact that incorporation occurs must be explained by changes either in the chemical termination of the surface or in the As species

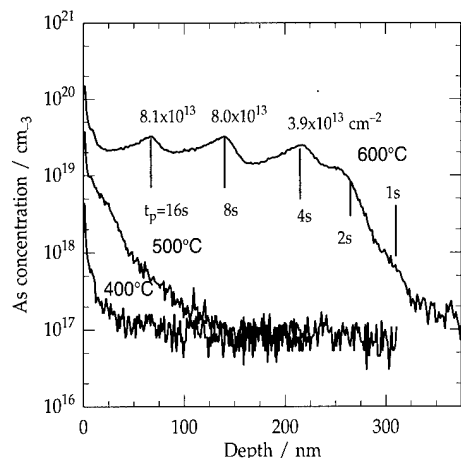


Fig. 8. SIMS profiles of three Si samples exposed to  $\text{AsH}_3$  during growth interruptions at 400, 500 and 600 °C with exposures times of 1, 2, 4, 8 and 16 s for each sample.

arriving at the surface. Cl is released from the surface via  $\text{SiCl}$  at temperatures above 700 °C [2]. Time-of-flight measurements made *in situ* during chemical beam epitaxy indicate that  $\text{H}_2$  desorbs from the surface at temperatures as low as 550 °C [8]; however, the situation at 1 atm of  $\text{H}_2$  in the APCVD reactor is unclear. It is reasonable to assume that the  $\text{AsH}_3$  competes with an equilibrium reaction between desorption and adsorption of H, which might allow  $\text{AsH}_3$  to chemisorb on surface sites. In addition,  $\text{AsH}_3$  starts to decompose at these temperatures. *In situ* measurements of the decomposition of  $\text{AsH}_3$  show that the first step is surface catalyzed and heterogeneous [9]. Clean quartz walls lead to decomposition temperatures as low as 600 °C and wall depositions may even lower that temperature.

At 600 °C the amount of As in the spikes approaches saturation at a level of  $8 \times 10^{13} \text{ cm}^{-2}$  for exposure times longer than 8 s. The low level of the saturation at 0.1 ML is unexpected. It might be correlated to the ratio of the parts of the Si surface terminated with H and with Cl after the growth from  $\text{SiCl}_2\text{H}_2$ . Further experiments using different temperatures for the Si deposition prior to and after the  $\text{AsH}_3$  exposure as well as detailed investigations of the surface chemistry during APCVD from  $\text{SiCl}_2\text{H}_2$  might help to explain this observation.

General factors contribute to the rather poorly resolved (low peak-to-valley ratio) As dopant spikes we have observed. Unfortunately, as in the case of Sb in the MBE experiments, the As tends to segregate leading to a smearing of the As into the subsequently grown Si. In addition, a rather long residence time for As is observed in our APCVD tool. The *in situ* incorporation of As from  $\text{AsH}_3$  into the Si leads to growth rate

enhancement of Si from  $\text{SiCl}_2\text{H}_2$  [10] which accounts for the increase in the thickness of the Si layer between the As spikes. However, the observation of a self-limiting process for As doping has some promise for ALD in CVD techniques to meter precise As doses into Si.

#### 4. Conclusion

We have investigated different methods to incorporate ALD in both MBE and CVD environments. So far we have determined that self-limiting reactions do occur for n-type dopants Sb and  $\text{AsH}_3$ . However, these species also have the problem of surface segregation.  $\text{B}_2\text{H}_6$  was not found to self-limit in the process parameter space explored in the experiments we have described, although at low temperatures it is expected to self-limit. In addition, the experiments permit a new way of looking into surface kinetics for doping in APCVD and gas source MBE which may affect the optimization of growth in the future.

#### Acknowledgments

We would like to acknowledge the support from J. Cotte and F. Cardone, supplying the SIMS data. One of us (S.S.I.) would like to thank R. A. Metzger (Hughes Research, Malibu) for useful discussions. This study was supported by the office of Naval Research contract no. N00014-91-C-0080.

#### References

- 1 J. Nishizawa, K. Aoki, S. Suzuki and K. Kikuchi, *J. Cryst. Growth*, **99** (1990) 502.
- 2 J. A. Yarmoff, D. K. Shuh, T. D. Durbin, C. W. Lo, D. A. Lapiano-Smith, F. R. McFeely and F. J. Himpsel, *American Vacuum Society, Meet. Seattle, WA, November 10–15, 1991*.
- 3 R. A. Metzger, *Ph. D. Dissertation*, 1983.
- 4 F. K. LeGoues, V. P. Kesan, S. S. Iyer, J. Tersoff and R. Tromp, *Phys. Rev. Lett.*, **64** (1990) 2038.
- 5 S. J. Fukatsu, S. Kubo, Y. Shiraki and R. Ho, *J. Cryst. Growth*, **111** (1991) 843.
- 6 L. J. van Ijzendoorn, C. W. Fredriksz, C. van Opdrop, D. J. Gravesatejn, D. E. W. Vandenhoudt, G. F. A. van de Walle and C. W. T. Bulle Lieuwma, *Ion Beam Analysis: 10th Int. Conf., Eindhoven, July 1–5, 1991*, in *Nucl. Instrum. Methods Phys. Res. B*, **64** (1992) 120.
- 7 M. L. Yu, D. J. Vitavage and B. S. Meyerson, *J. Appl. Phys.*, **59** (1986) 4032.
- 8 S. M. Gates and S. K. Kulkarni, *Appl. Phys. Lett.*, **60** (1992) 53.
- 9 W. Richter, P. Kurpas, R. Lückerrath, M. Motzkus and M. Waschbüsch, *J. Cryst. Growth*, **107** (1991) 13.
- 10 P. Agnello, T. O. Sedgwick, M. S. Goorsky and J. Cotte, *Appl. Phys. Lett.*, **60** (1992) 454.

# Atomic layer epitaxy of Si using atomic H

Shigeru Imai, Toshio Iizuka, Osamu Sugiura and Masakiyo Matsumura

Department of Physical Electronics, Tokyo Institute of Technology, 2-12-1 O-okayama, Meguro-ku, Tokyo 152 (Japan)

## Abstract

Atomic H is proposed for the reducer gas in the atomic layer epitaxy (ALE) of Si. Its high reactivity makes it possible to remove surface-terminating adsorbates, which cause the self-limitation of unwanted successive deposition of Si compounds, at low temperature. The ALE growth was attempted by the alternating exposure of the Si(111) substrate to  $\text{SiH}_2\text{Cl}_2$  and H. Ideal monolayer growth was obtained and the growth rate was independent of the gas volumes and the substrate temperature. The lower ALE limit of the substrate temperature was 540 °C, about 250 °C lower than the case of  $\text{H}_2$  as the reducer gas.

## 1. Introduction

Atomic layer epitaxy (ALE), which provides the precise control of grown layer thickness on an atomic level, is one of the most promising technologies for the development of ultrahigh speed devices and optoelectronic devices containing new materials and structures such as superlattices. In particular, ALE of group IV semiconductors is very important because the new materials and structures based on Si, for example Si–Ge superlattices or heterojunction structures, fit Si device technologies much better than the other compound semiconductor materials.

For II–VI or III–V compound semiconductors, ALE growth has been achieved by sequential injections of source gases containing corresponding components of semiconductors, whose heterogeneous reactivities change with surface conditions [1, 2]. On the contrary, group IV semiconductors are constructed with only one component. Therefore, ALE of group IV elements consists of two processes as follows.

The first step of ALE is the monolayer adsorption of partially decomposed source gas molecules over the clean surface. The adsorbate is constructed with an Si (or a Ge) atom and another kind of atom (or group) bonded with Si (or Ge), such as  $\text{SiCl}_x$  (or  $\text{Ge}(\text{CH}_3)_x$ ). The Si (or Ge) atoms in adsorbates terminate the surface dangling bonds and form a grown monolayer, and the atoms (or groups) such as Cl (or  $\text{CH}_3$ ) cover the newly grown layer surface. Therefore, when the whole surface is covered by the adsorbates, monolayer growth is achieved. Further source gas cannot be adsorbed chemically because the surface is completely covered and there are no dangling bonds. As a result, the growth is limited to 1 monolayer, *i.e.* self-limiting growth is achieved.

The second step is the removal of the surface terminating atoms (or groups) in some way. A new clean surface is created on the grown monolayer, and monolayer growth in the next cycle is made possible.

Although many studies of the ALE of compound semiconductors were reported after the proposal of ALE in the 1970s [1], Si ALE has been achieved in the last few years only. The first successful ALE of Si was reported by Nishizawa *et al.* [3, 4] using dichlorosilane ( $\text{SiH}_2\text{Cl}_2$ ) as the source gas and hydrogen ( $\text{H}_2$ ) as the reducer gas.  $\text{SiH}_2\text{Cl}_2$  was decomposed into  $\text{SiCl}_x$ , and  $\text{SiCl}_x$  was adsorbed on the clean Si surface. The clean surface was recovered by the reduction of surface-terminating Cl atoms by  $\text{H}_2$  to HCl. The growth temperature was, however, more than 815 °C for Si(100) and more than 890 °C for Si(111) because Cl atoms bonded strongly to Si atoms are reduced only at high temperature. This temperature is too hot for the fabrication of new materials and structures such as Si–Ge heterojunctions or superlattices because of the interdiffusion of Si and Ge.

Two possible ways to lower the substrate temperature exist. The first is the use of a higher silane as a source gas, where surface-terminating atoms are H atoms instead of Cl atoms. H atoms terminating the Si surface are well known to be thermally desorbed from the Si surface at about 600 °C, which is much lower than for Cl atoms [5]. Therefore, repetition of the injection of a higher silane as the source gas and heating of the substrate for thermal desorption of H atoms can result in ALE.

Suda *et al.* [6, 7] and Lubben *et al.* [8, 9] have achieved UV-photostimulated ALE growth using  $\text{Si}_2\text{H}_6$  as the source gas and KrF laser pulse (20 ns) irradiation. ALE on Si(100) surfaces was obtained for steady-state substrate temperatures from 180 °C to 400 °C. Imai *et*

*al.* [10] have reported temperature modulation ALE using  $\text{Si}_3\text{H}_8$  as the source gas and rapid substrate temperature modulation by an electric current flowing through the substrate. ALE on Si(111) was confirmed at substrate temperature below  $380^\circ\text{C}$  in the adsorption phase and above  $520^\circ\text{C}$  in the desorption phase. However, growth rates obtained in these reports were less than ideal monolayer growth,  $0.4$  monolayers  $\text{cycle}^{-1}$  and  $0.8$  monolayers  $\text{cycle}^{-1}$  respectively.

The second way to lower the ALE temperature is the use of a reducer much more active than  $\text{H}_2$ . We propose here atomic H as the reducer gas instead of  $\text{H}_2$  in Si ALE growth. H atoms can be created easily and without a plasma by decomposition of  $\text{H}_2$  using an incandescent tungsten filament [11, 12]. Si ALE growth by sequential exposures to  $\text{SiH}_2\text{Cl}_2$  as the source gas and H as the reducer gas was attempted. Ideal monolayer growth per cycle has been demonstrated at  $540^\circ\text{C}$ . The system, the experimental conditions, and detailed results are also discussed.

## 2. Experimental details

The ALE system used in our experiment was assembled as shown in Fig. 1. The reaction chamber was a stainless steel cylinder of 95 mm diameter and 220 mm length. The chamber was evacuated by a  $150\text{ l sec}^{-1}$  turbomolecular pump located at the bottom of the chamber to a background pressure of  $3 \times 10^{-9}$  Torr. The gas residence time was shortened to less than 1 s.

A gas nozzle was set at the top of the chamber. The gas supply system had an  $\text{SiH}_2\text{Cl}_2$  line and an  $\text{H}_2$  line. Flow rates of gases were fixed by mass flow controllers (MFCs). Also, a set of computer-controlled valves was placed just above the nozzle and vent line. When one of the gases started to flow, it was passed through the vent line until the MFC operation became stable. After the gas flow became stable, the flow to the vent was changed quickly into the chamber.

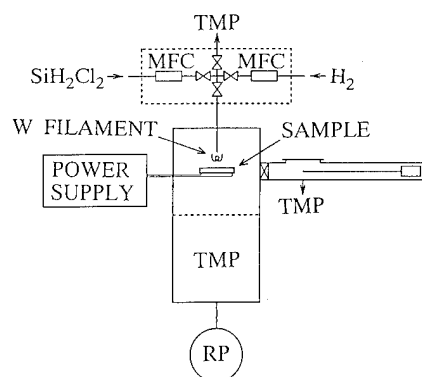


Fig. 1. Schematic view of the ALE system.

A loading system evacuated by a turbomolecular pump was used to load and unload a substrate without breaking the vacuum of the reaction chamber. The substrate measuring  $5\text{ mm} \times 28\text{ mm}$  was transferred to the substrate holder at the opposite side of the loading system. The holder, made of tantalum sheets, picked up the sample at both ends. The substrate was heated by an electric current flow through it. The substrate temperature was fixed by setting the supplied electric power, whose relationship to the temperature had already been determined.

H atoms were created by dissociation of  $\text{H}_2$  at an incandescent tungsten filament set about 1 cm below the gas nozzle in the reactive chamber. The filament was incandescent only while  $\text{H}_2$  was injected into the chamber. The temperature at the incandescent filament was a little less than  $2000^\circ\text{C}$ . It was confirmed by microscopic examination that no change due to the incandescent filament occurred on the substrate surface positioned at the holder. It was also confirmed by *in situ* resistance measurement of the substrate that the temperature increased by less than  $20^\circ\text{C}$  while the filament was on.

The Si(111) substrates, partially covered with thermal oxide, were chemically cleaned by the RCA method and dipped in diluted HF before loading. A substrate was inserted into the chamber and cleaned thermally at  $1000^\circ\text{C}$  for 5 min in high vacuum. After that, 100 cycles of ALE growth were performed.

Si ALE growth using atomic H follows time sequences shown in Fig. 2. The standard set of parameters are tabulated in Table 1. These values were used throughout the experiment unless otherwise mentioned. A diagram of the schematic surface conditions are also shown in Fig. 3. Five phases, *i.e.* (1)  $\text{SiH}_2\text{Cl}_2$  injection, (2)  $\text{SiH}_2\text{Cl}_2$  evacuation, (3)  $\text{H}_2$  injection with the incandescent filament, (4)  $\text{H}_2$  injection without the incandescent filament and (5)  $\text{H}_2$  evacuation, are included in a cycle.  $\text{SiH}_2\text{Cl}_2$  injection corresponds to the first step of ALE, that is the monolayer adsorption of  $\text{SiCl}_x$ . In this phase,  $\text{SiH}_2\text{Cl}_2$  as the source gas injected from the nozzle arrives at the clean surface filled with dangling

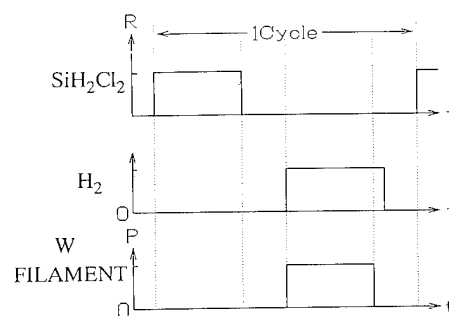
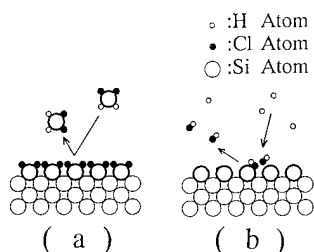


Fig. 2. Time sequences of gas flows and filament power.

TABLE 1. Set of standard atomic layer epitaxy growth parameters

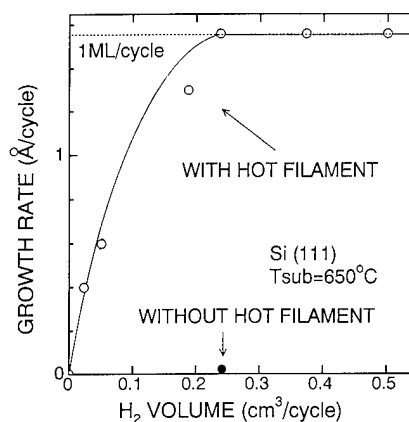
Duration of adsorption interval	10 s
Duration of exhaust interval	30 s
Duration of reduction interval	15 s
Duration of filament cooling interval	10 s
Duration of exhaust interval	30 s
Substrate temperature	650 °C
SiH <sub>2</sub> Cl <sub>2</sub> flow rate	2.6 standard cm <sup>3</sup> min <sup>-1</sup>
H <sub>2</sub> flow rate	1.0 standard cm <sup>3</sup> min <sup>-1</sup>
Filament temperature	<2000 °C
Substrate orientation	(111)
Substrate size	5 mm × 28 mm

Fig. 3. Schematic diagrams of the surface condition: (a) SiCl<sub>x</sub> adsorption; (b) Cl reduction.

bonds and is decomposed into SiCl<sub>x</sub>. SiCl<sub>x</sub> terminates the dangling bonds and makes the adsorption layer. Successive adsorption of SiCl<sub>x</sub> on the SiCl<sub>x</sub> layer cannot occur because there are no dangling bonds on the SiCl<sub>x</sub> layer. Thus, the adsorption is limited to a monolayer. The gas pressure under the standard condition in Table 1 was  $1.5 \times 10^{-3}$  Torr. After monolayer growth, the gas injection is stopped and the excess gas in the chamber is evacuated to a pressure of less than  $10^{-8}$  Torr.

Next, H<sub>2</sub> is injected from the nozzle and then the tungsten filament is turned on; that corresponds to the second step of the ALE, that is the recovery of the clean surface. H<sub>2</sub> molecules arriving at the filament are decomposed into H atoms, and H atoms arriving on the surface reduce Cl atoms on the surface. The H<sub>2</sub> pressure in this phase was  $2 \times 10^{-4}$  Torr. After the reduction, the filament is turned off but H<sub>2</sub> is still injected for a short while to cool the filament. At the end of the cycle, excess H<sub>2</sub> is evacuated. After the H<sub>2</sub> evacuation, the next SiH<sub>2</sub>Cl<sub>2</sub> injection starts again and the cycle is repeated.

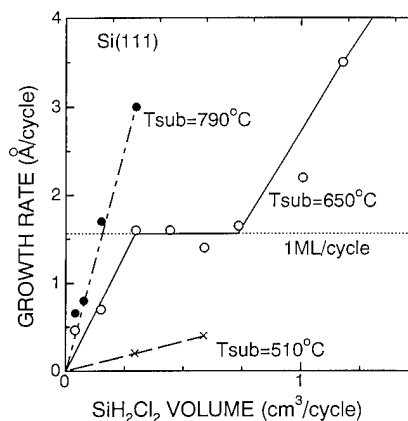
After 100 cycles of ALE growth, the sample was taken out from the chamber and the oxide covering the surface was removed by HF. The grown layer thickness was measured with a Talystep instrument. The crystallinity and the surface morphology of the grown layers were estimated by reflection high energy electron diffraction (RHEED) and scanning electron microscopy (SEM).

Fig. 4. Thickness per unit ALE cycle as a function of the H<sub>2</sub> gas volume within an ALE cycle.

### 3. Results and discussion

Figure 4 shows the growth rate as a function of the injected H<sub>2</sub> gas volume per cycle with a substrate temperature of 650 °C. Only the H<sub>2</sub> gas flow rate was changed and the duration of the reduction interval was kept at the constant values tabulated in Table 1. The case without the incandescent filament is also indicated by a full circle. When the filament was not used, no growth occurred. However, when the filament was used, the growth rate increased with H<sub>2</sub> volume. This means that H atoms were effective for Cl reduction at low temperatures. Reaching 1 monolayer cycle<sup>-1</sup>, the growth rate was saturated, that is ALE growth was achieved in spite of very low substrate temperatures.

Figure 5 shows the growth rate as a function of the SiH<sub>2</sub>Cl<sub>2</sub> gas volume at substrate temperatures of 510 °C, 650 °C and 790 °C. Only the SiH<sub>2</sub>Cl<sub>2</sub> gas flow rate was changed and the duration of the adsorption interval was kept constant as tabulated in Table 1. At

Fig. 5. Thickness per unit ALE cycle as a function of the SiH<sub>2</sub>Cl<sub>2</sub> gas volume within an ALE cycle.



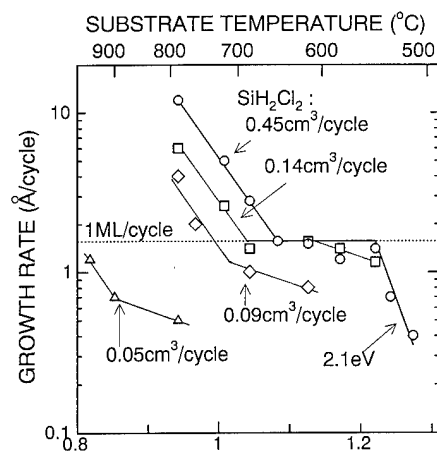


Fig. 6. Thickness per unit ALE cycle as a function of the substrate temperature.

510 °C, the growth rate increased with the gas volume, but was less than 1 monolayer cycle<sup>-1</sup>. The reason will be given later. At 650 °C, the growth rate increased to 1 monolayer cycle<sup>-1</sup> with the gas volume and became saturated. In this saturation region, ALE growth was achieved. However, when the volume increased further the growth rate exceeded 1 monolayer cycle<sup>-1</sup>. This means that the self-limitation of the adsorption was broken. The surface-terminating Cl atoms are assumed to be removed by some reaction with SiH<sub>2</sub>Cl<sub>2</sub> or H<sub>2</sub> generated by SiH<sub>2</sub>Cl<sub>2</sub> decomposition. At 790 °C, the growth rate increased over 1 monolayer cycle<sup>-1</sup> with no clear saturation.

Figure 6 shows the Arrhenius plot of the growth rate with various SiH<sub>2</sub>Cl<sub>2</sub> volumes. With a gas volume of 0.45 cm<sup>3</sup> cycle<sup>-1</sup>, ideal monolayer growth per cycle was obtained over a wide temperature range. Lower and higher limiting temperatures of ALE growth were 540 °C and 650 °C respectively. The growth rate exceeded 1 monolayer cycle<sup>-1</sup> in the regions above 650 °C, where the self-limitation of the adsorption was broken. In the region below 540 °C the growth rate was less than 1 monolayer cycle<sup>-1</sup>. In this region, the activation energy of the growth rate was 2.1 eV. This value is equal to that of the desorption of H atoms from the Si(111) substrate obtained from gas source molecular beam epitaxy using Si<sub>3</sub>H<sub>8</sub> [10]. Moreover, H atoms adsorbed on a Si surface are well known to be desorbed from the Si surface above 600 °C [5]. Therefore, the ALE growth rate was less than ideal monolayer growth below 540 °C not because the surface-terminating Cl atoms were not reduced but because excess H atoms terminated the clean surface which had been recovered by the removal of Cl atoms with the help of H atoms.

When the gas volume decreased, the higher limit of the temperature range of ALE was raised because the rate of reaction breaking the self-limitation of the

growth decreased as shown in Fig. 4. On the contrary, the lower limit of ideal monolayer growth increased and another region appeared where the growth rate was less than 1 monolayer cycle<sup>-1</sup> but the activation energy was much less than 2.1 eV. In this region, insufficient SiCl<sub>x</sub> adsorption decreased the growth rate. The temperature range of ALE narrowed with the decrease in the SiH<sub>2</sub>Cl<sub>2</sub> gas volume. The ALE region vanished at a source gas volume of 0.09 cm<sup>3</sup> cycle<sup>-1</sup>.

Although we carried out no direct investigation of the kinetics of the surface reaction, we are convinced that the ALE processes were executed because the growth rate kept constant at 1 monolayer cycle<sup>-1</sup> and there is no dependence on the gas volumes or the substrate temperature over a wide range of conditions.

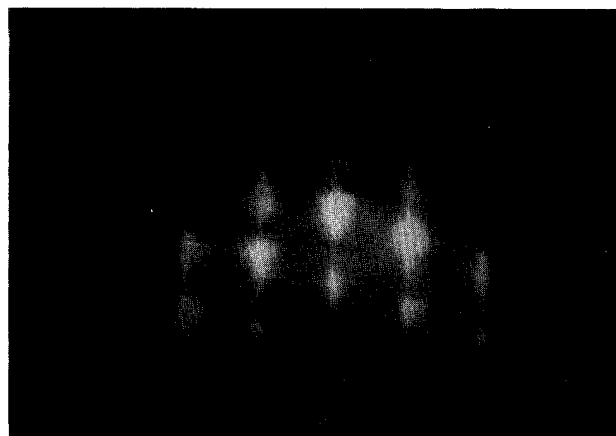


Fig. 7. RHEED pattern of the grown layer.

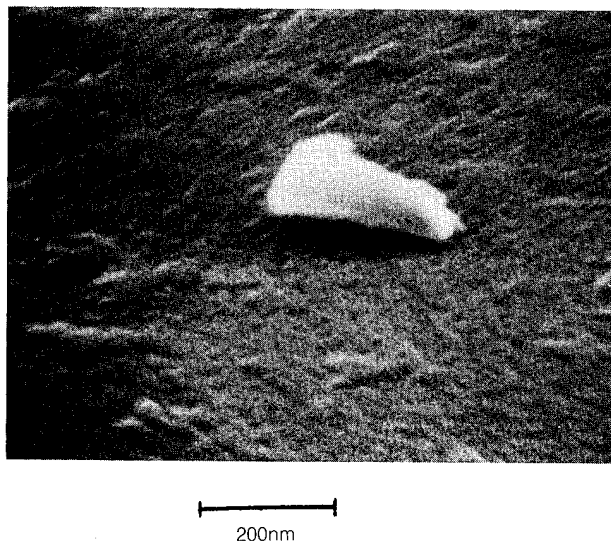


Fig. 8. SEM image of the grown layer. There is a dust particle for focusing at the centre.

The RHEED pattern and SEM image are shown in Figs. 7 and 8, where the chemical cleaning process was changed to the method of Ishizaka and Shiraki [13]. The RHEED pattern had clear spots although the photograph was taken after the sample had been exposed in air. However, the SEM image showed a fine structure on the surface.

#### 4. Conclusions

Si ALE using atomic H has been proposed and demonstrated successfully. The growth rate obtained from the experiment was 1 monolayer cycle<sup>-1</sup>, and the lower temperature limit of the ALE was 540 °C. The lower temperature limit of the ALE was the temperature at which the H atoms started to terminate the clean Si surface. Atomic H is expected to be useful for removing the various self-limiting adsorbates such as F, Cl and CH<sub>3</sub> with lower temperatures and thus this concept will be useful not only for Si ALE but also for Ge ALE and compound semiconductor ALE such as that with GaAs.

#### References

- 1 T. Suntola and M. J. Antson, *US Patent 4,058,430*, 1977.
- 2 J. Nishizawa, H. Abe and T. Kurabayashi, *J. Electrochem. Soc.*, **132** (1985) 1197.
- 3 J. Nishizawa, K. Aoki, S. Suzuki and K. Kikuchi, *J. Cryst. Growth*, **99** (1990) 502.
- 4 J. Nishizawa, K. Aoki, S. Suzuki and K. Kikuchi, *J. Electrochem. Soc.*, **132** (1985) 1197.
- 5 G. Schulze and M. Henzler, *Surf. Sci.*, **124** (1983) 336.
- 6 Y. Suda, D. Lubben, T. Motooka and J. E. Greene, *J. Vac. Sci. Technol. B*, **7** (1989) 1171.
- 7 Y. Suda, D. Lubben, T. Motooka and J. E. Greene, *J. Vac. Sci. Technol. A*, **8** (1990) 61.
- 8 D. Lubben, R. Tsu, T. R. Bramblett and J. E. Greene, *Mater. Res. Soc. Symp. Proc.*, **222** (1991) 177.
- 9 D. Lubben, R. Tsu, T. R. Bramblett and J. E. Greene, *J. Vac. Sci. Technol. A*, **9** (1991) 3003.
- 10 S. Imai, S. Takagi, O. Sugiura and M. Matsumura, *Jpn. J. Appl. Phys.*, **30** (1991) 3646.
- 11 I. Langmuir, *J. Am. Chem. Soc.*, **34** (1912) 860.
- 12 O. Sugiura, T. Shiraiwa, H. Kanoh and M. Matsumura, *Mater. Res. Soc. Symp. Proc.*, **258** (1992), in press.
- 13 A. Ishizaka and Y. Shiraki, *J. Electrochem. Soc.*, **133** (1986) 666.

# Potential Si atomic layer epitaxy processes using halogenated Si precursors

D. D. Koleske, S. M. Gates and D. B. Beach

IBM T. J. Watson Research Center, Yorktown Heights, NY 10598 (USA)

## Abstract

Potential methods for atomic layer epitaxy growth of Si using halogenated silane precursors are discussed. One method uses alternating exposures of  $\text{Si}_2\text{H}_6$  and  $\text{Si}_2\text{Cl}_6$ . This method deposits “new” Si ( $\text{Si}^*$ ) on Si(100) as demonstrated through the attenuation of a boron “marker” layer. Another method uses self-terminating adsorption of  $\text{SiClH}_3$  or  $\text{SiCl}_2\text{H}_2$  at about 500 °C, followed by exposure to atomic H. Only the initial adsorption step of this method is studied here.

## 1. Introduction

Growth of II–VI and III–V semiconductor thin films in a self-limiting, layer-by-layer manner using alternating exposures of precursor gases has been termed atomic layer epitaxy (ALE) [1, 2]. This technique offers the ultimate in control of growth rate and uniformity of film thickness over large areas. For these binary semiconductors, self-limiting gas adsorption and the formation of a partially ionic (polar) bond in the solid are aided by the difference in the elemental electronegativity between the two elements. Also, successful ALE reactions are thermodynamically favorable. In group IV semiconductors this aspect for self-limiting adsorption and partially ionic bond formation does not apply.

Two  $\text{Si}^*$  growth methods are compared here. One strategy for ALE growth is to dose the surface alternately with Si precursors that have atoms of different electronegativities, such as H and Cl [3]. This process deposits “new” Si (which we will represent by  $\text{Si}^*$ ) on the Si substrate through the formation of HCl. Using alternating exposures to  $\text{Si}_2\text{Cl}_6$  and  $\text{Si}_2\text{H}_6$ , we demonstrate isothermal growth of  $\text{Si}^*$  on Si(100) [3]. A different reaction scheme is to terminate fully the surface dangling bonds (DBs) using a halogenated silane and then to remove the surface halogen using atomic H [4, 5]. If the adsorption of precursor is self-limiting, a reproducible quantity of  $\text{Si}^*$  is added for each cycle. However, this second reaction scheme must be implemented at surface temperatures  $T_s$  high enough for  $\text{H}_2$  and HCl desorption to be rapid so that a clean surface exists for the next ALE cycle. The adsorption of  $\text{SiClH}_3$  and  $\text{SiCl}_2\text{H}_2$  is studied here by monitoring in real time the changes in the Cl and H surface concentrations during adsorption.

## 2. Experimental results

The technique used to measure the atomic concentrations during precursor exposure is time-of-flight scattering and recoiling spectroscopy (TOF SARS), which has been described in detail by Rabalais [6, 7] and briefly by us [8, 9]. Both the ion source and the detector TOF leg are attached to a scattering chamber with a base pressure of  $2 \times 10^{-10}$  Torr. The scattering geometry showing how the incident angle  $\alpha$  and the recoil angle  $\Phi$  are defined in Fig. 1 of ref. 6 and also in Fig. 2 of ref. 8. A grid in front of the detector was biased at +4 kV, and therefore the detected signal comprises direct recoil (DR) atoms. Near grazing  $\alpha$  the DR signal is most sensitive to the first layer atomic concentrations [8, 9], because the DR atoms formed from the binary collision with the incident beam must have a line of sight to both the incident beam and the detector [10]. For all TOF spectra shown here, the  $\text{K}^+$  dose per spectrum was less than  $10^{-3}$  ML, with accumulated doses not exceeding  $10^{-2}$  ML in a series of spectra [3].

### 2.1. $\text{Si}_2\text{H}_6$ and $\text{Si}_2\text{Cl}_6$ exchange reaction

The first Si ALE process studied used alternating doses of  $\text{Si}_2\text{Cl}_6$  and  $\text{Si}_2\text{H}_6$ . Precursors were dosed through a quartz glass tube and the pressure was measured with an ion gauge. The amount of  $\text{Si}_2\text{Cl}_6$  needed to exchange the H to a Cl-terminated surface ( $\text{Si}_2\text{Cl}_6 \rightarrow \text{H}$ ) and the amount of  $\text{Si}_2\text{H}_6$  needed to exchange the Cl to an H-terminated surface ( $\text{Si}_2\text{H}_6 \rightarrow \text{Cl}$ ) was monitored in the DR spectra at different  $T_s$ . These exchange reactions are shown in Fig. 1 for  $T_s = 475$  °C and  $\Phi = 39^\circ$ . In Fig. 1, curve A, the Si direct recoil ( $\text{Si}_{\text{DR}}$ ) peak is observed at flight time of 7.80  $\mu\text{s}$ , and this spectrum is representative of a clean

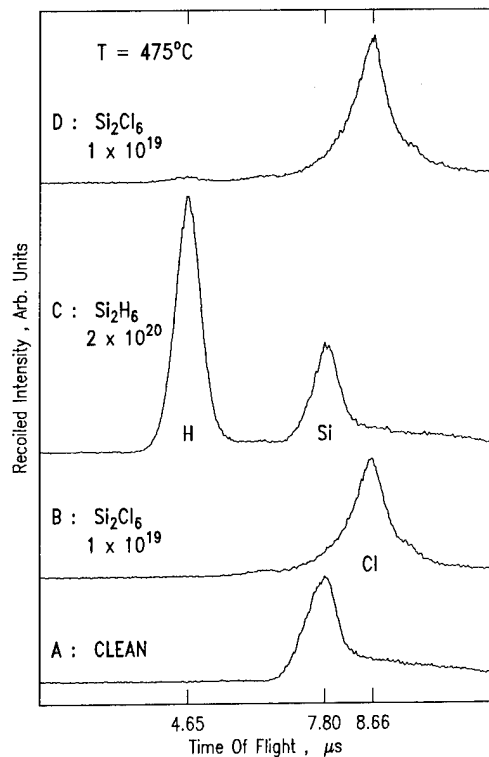


Fig. 1. TOF DR spectra from Si(100)-(2 × 1) surface using a 4 keV  $K^+$  beam, with an incident angle  $\alpha$  of  $3^\circ$  with respect to the surface plane and a recoil angle  $\Phi$  of  $39^\circ$ . This figure shows the  $Si_2H_6$  and  $Si_2Cl_6$  exchange reactions for a surface temperature of  $475^\circ C$ . Spectrum A, TOF spectrum from a clean Si(100) surface where the  $Si_{DR}$  peak appears at  $7.80 \mu s$ . Spectrum B, surface after dosing with  $Si_2Cl_6$  and the  $Cl_{DR}$  peak appears at  $8.66 \mu s$ . Spectrum C, surface after dosing with  $Si_2H_6$  and the  $H_{DR}$  peak appears at  $4.65 \mu s$ . Spectrum D, surface after another dose with  $Si_2Cl_6$ .

surface. In Fig. 1, spectrum B, the clean surface has been exposed to  $10^{19} Si_2Cl_6 cm^{-2}$  (about  $5 \times 10^{-5}$  Torr, for 2 min) at  $475^\circ C$  and then quenched to  $200\text{--}300^\circ C$ . This spectrum shows the  $Cl_{DR}$  peak at  $8.66 \mu s$  which is not totally resolved from the  $Si_{DR}$  peak. This surface should correspond to about 1 ML of monochloride species because only monochlorides have been observed at this  $T_s$  [11]. Desorption of Cl from the surface at  $475^\circ C$  is negligible and this surface is thermally stable for times in excess of 30 min [3]. Next the surface was dosed with  $2 \times 10^{20} Si_2H_6 cm^{-2}$  (about  $2 \times 10^{-4}$  Torr, 10 min) at  $T_s = 475^\circ C$ , quenched to  $T_s = 200\text{--}300^\circ C$  so that no H desorbs, and spectrum C in Fig. 1 was recorded. In Fig. 1, spectrum C, the H DR time is  $4.65 \mu s$  and this signal is clearly separated from the Si and Cl DR signals. It is evident that the Cl-terminated surface has been exchanged for an H-terminated surface. Finally, the H-terminated surface can be converted back to the monochloride surface as shown in Fig. 1, spectrum D, by redosing with  $Si_2Cl_6$ .

The exchange of H to Cl ( $Si_2Cl_6 \rightarrow H$ ) at  $475^\circ C$  is expected to be facile because  $H_2$  desorption creates

vacant DBs for  $Si_2Cl_6$  adsorption on the timescale of 10–15 min. The exchange of Cl to H ( $Si_2H_6 \rightarrow Cl$ ) step is slower because the Cl desorbs as HCl which is about 50–100 times slower than  $H_2$  desorption [3]. As the  $Si_2H_6 \rightarrow Cl$  reaction proceeds and the H concentration increases,  $Si_2H_6$  is adsorbed on DBs vacated from both HCl and  $H_2$  desorption. This means that the  $Si_2H_6 \rightarrow Cl$  reaction is not self-limiting. Extrapolating from the  $Si_2H_6$  growth rate measurements of Mokler *et al.* [12], we estimate additional growth from  $Si_2H_6$  to be about  $0.1 \text{ \AA min}^{-1}$  for  $T_s = 475^\circ C$ . At  $T_s < 475^\circ C$ , more of each reactant is needed to exchange the surface completely, while at  $T_s > 475^\circ C$  smaller exposures are needed [3].

To prove that  $Si^*$  was grown, the initial Si(100) surface was elementally “marked” with B and attenuation of the B DR signal [8, 9, 13] was monitored as the surface was dosed with  $Si_2H_6$  and  $Si_2Cl_6$ . Previously it has been shown for the Si(100) that B atoms are substitutionally incorporated into the outer two surface layers [14], that the surface remains ordered after annealing at  $700^\circ C$  [15], and that epitaxial Si can be grown atop the ordered B layer [15].

The B-doped surface (B/Si(100)) was prepared by dosing a clean Si(100) surface with  $2 \times 10^{16} B_{10}H_{14}$  at  $200^\circ C$  and annealing to  $650^\circ C$ . Dosing and annealing with this amount of B appears to incorporate at least 1/2 ML of B into the outer two surface layers as discussed later; however, it is not known exactly how this B is distributed in the B/Si(100) surface prepared in this manner [14, 15]. A DR spectrum of the resulting surface is shown in Fig. 2, spectrum A, where the  $B_{DR}$  signal is observed at  $5.79 \mu s$ . Each exchange reaction was performed at  $T_s = 400^\circ C$ , using gas exposures similar to those shown in Fig. 1. These results are shown in Fig. 2. Evidence that  $Si^*$  grew on the B/Si(100) surface at  $T_s = 400^\circ C$  is seen by the decrease in the  $B_{DR}$  signal in Fig. 2, spectrum C, which is roughly 1/2 the original  $B_{DR}$  signal in Fig. 2, spectrum A. Because the  $H_{DR}$  and  $B_{DR}$  signals overlap, it is hard to quantify the additional attenuation in Fig. 2, spectrum E; however, the  $B_{DR}$  signal in Fig. 2, spectrum E, is slightly less than in Fig. 2, spectrum C. Growth of  $Si^*$  on a Ge(100) surface by this method has also been demonstrated [16].

As well as providing an initial “marker” layer the substitutional B also has a profound impact on the rate of chemical exchange and hence the  $T_s$  at which the film was grown. The substituted boron weakens the Si–H and Si–Cl bonds and this was confirmed in temperature programmed desorption (TPD) measurement [3]. Both the TPD peaks and leading edges were shifted to lower  $T_s$  on the B/Si(100) surface compared with the clean Si(100) surface [3]. This explains why the exchange reactions succeed on the B/Si(100) surface at  $400^\circ C$ , while on the clean Si(100) surface no exchange

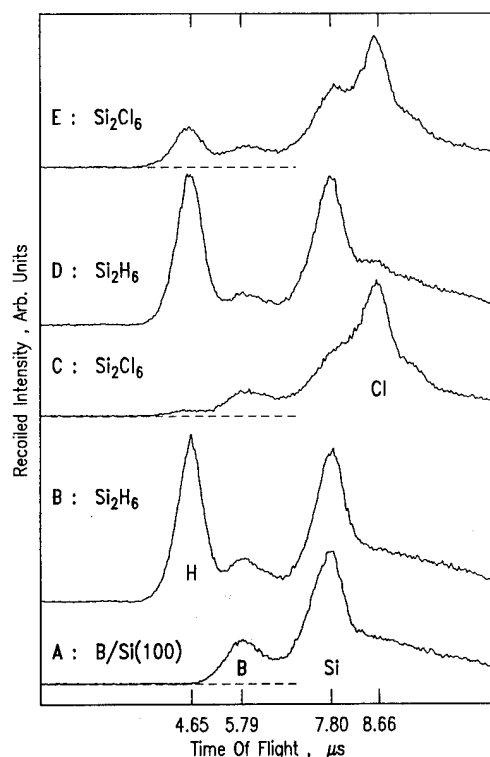


Fig. 2.  $\text{Si}_2\text{H}_6$  and  $\text{Si}_2\text{Cl}_6$  exchange spectra measured for the B-doped Si(100) surface, similar to Fig. 1 (surface temperature,  $400^\circ\text{C}$ ). The  $\text{B}_{\text{DR}}$  peak appears at  $5.79\ \mu\text{s}$ . Spectrum A,  $\text{B}_{10}\text{H}_{14}$  dosed and annealed, giving the B/Si(100) surface. Spectrum B, B/Si(100) surface dosed with  $4 \times 10^{19}\ \text{Si}_2\text{H}_6\ \text{cm}^{-2}$ . Spectrum C, surface of spectrum B, dosed with  $2 \times 10^{19}\ \text{Si}_2\text{Cl}_6\ \text{cm}^{-2}$ . Spectrum D, surface of spectrum C, dosed with  $1 \times 10^{20}\ \text{Si}_2\text{H}_6\ \text{cm}^{-2}$ . Spectrum E, surface of spectrum D, dosed with  $5 \times 10^{19}\ \text{Si}_2\text{Cl}_6\ \text{cm}^{-2}$ .

is possible at such a low temperature [3]. Also, the integrated peak areas for saturation coverages of  $\text{Si}_2\text{H}_6$  and  $\text{Si}_2\text{Cl}_6$  were about 1/2 as large on the B/Si(100) surface compared with the clean surface [3]. This difference in the saturation coverage of H and Cl implies that the substitutional boron renders 1/2 of the Si DBs chemically inactive. The growth of  $\text{Si}^*$  on this interface is strikingly different on this surface compared with clean Si(100) [3, 15].

## 2.2. Evaluation of Si precursors: $\text{SiClH}_3$ and $\text{SiCl}_2\text{H}_2$

The adsorption of two chlorinated silanes,  $\text{SiClH}_3$  and  $\text{SiCl}_2\text{H}_2$  was studied in real time using TOF SIRS while the gas was dosed at elevated  $T_s$ . These precursors were studied since they might deliver about 1 ML or about 1/2 ML of  $\text{Si}^*$  using  $\text{SiClH}_3$  and  $\text{SiCl}_2\text{H}_2$  respectively [17]. This would be true if  $\text{H}_2$  could be the only desorbed product during the adsorption.

Figure 3 illustrates real-time DR measurements of the surface Cl and H concentrations during adsorption of  $\text{SiClH}_3$  and  $\text{SiCl}_2\text{H}_2$  at  $T_s = 450^\circ\text{C}$ . The DR spectra in Fig. 3 were measured under a constant flux of about  $2 \times 10^{17}\ \text{cm}^{-3}\ \text{s}^{-1}$  of  $\text{SiClH}_3$  (Fig. 3(a)) and  $\text{SiCl}_2\text{H}_2$

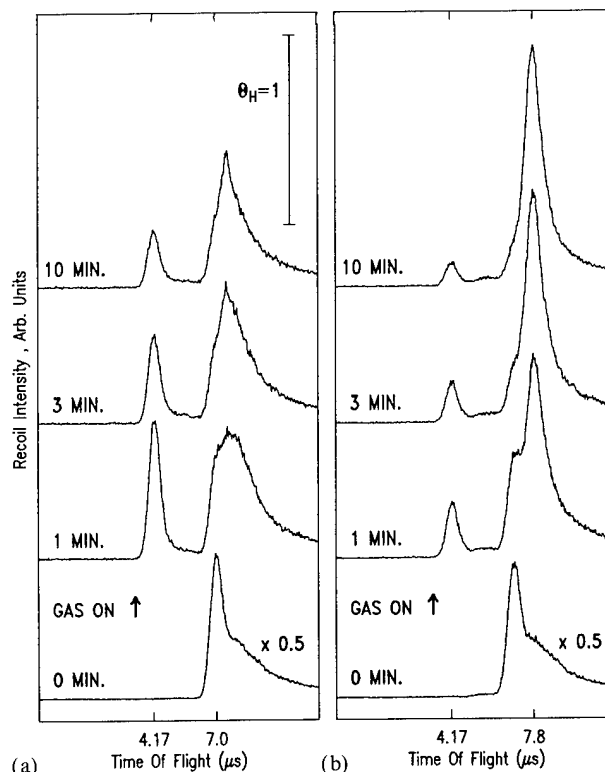


Fig. 3. DR spectra measured during dosing of about  $2 \times 10^{17}\ \text{cm}^{-3}\ \text{s}^{-1}$  with (a)  $\text{SiClH}_3$  and (b)  $\text{SiCl}_2\text{H}_2$  at  $450^\circ\text{C}$ . Here  $\alpha = 9.5^\circ$  and  $\Phi = 30^\circ$ . The spectra were measured for 1 min each and the time reported on the left-hand side of each spectrum corresponds to the last measuring time, i.e. 1 min corresponds to counting from 0 to 1 min. Also shown in the upper right-hand side of (a) is the  $\text{H}_{\text{DR}}$  signal corresponding to  $\theta_{\text{H}} = 1$ .

(Fig. 3(b)). Because  $\Phi$  was changed from  $39^\circ$  to  $30^\circ$ , the DR flight times are shorter compared with Figs. 1 and 2:  $\text{Si}_{\text{DR}}$ ,  $7.0\ \mu\text{s}$ ;  $\text{H}_{\text{DR}}$ ,  $4.17\ \mu\text{s}$ ;  $\text{Cl}_{\text{DR}}$ ,  $7.8\ \mu\text{s}$ . At this  $T_s$ , the adsorbed coverages of H and Cl exhibit a pronounced dynamical change in concentration. This is clearly observed in the  $\text{H}_{\text{DR}}$  signal from  $\text{SiClH}_3$ , which is initially large but then decreases as  $\text{H}_2$  desorbs and more  $\text{SiClH}_3$  adsorbs onto the vacated DB sites. This change in the  $\text{H}_{\text{DR}}$  is also observed in  $\text{SiCl}_2\text{H}_2$  adsorption but to a lesser extent. The initial concentrations of Cl and H reflect the precursor Cl:H concentration of 1:3 ( $\text{SiClH}_3$ ) or 1:1 ( $\text{SiCl}_2\text{H}_2$ ). Eventually the  $\text{H}_{\text{DR}}$  and  $\text{Cl}_{\text{DR}}$  signals reach constant values using both precursors, but only after about 6–8 min. After 8 min of dosing, we estimate Cl coverage ( $\theta_{\text{Cl}} = 0.7$ ) and H coverage  $\theta_{\text{H}} = 0.3$  for  $\text{SiClH}_3$  and  $\theta_{\text{Cl}} = 0.85$  and  $\theta_{\text{H}} = 0.15$  for  $\text{SiCl}_2\text{H}_2$ , with the details given elsewhere [17].

Dynamic adsorption of both gases was also studied at  $T_s = 500^\circ\text{C}$ , as shown in Fig. 4 [17]. The  $\text{H}_{\text{DR}}$  and  $\text{Cl}_{\text{DR}}$  signal from  $\text{SiClH}_3$  (Fig. 4(a)) is constant during the dosing time with  $\theta_{\text{Cl}} = 0.75$ . The  $\text{H}_{\text{DR}}$  signal from  $\text{SiCl}_2\text{H}_2$  (Fig. 4(b)) exhibits a small but noticeable transient behavior, and after 3 min reaches  $\theta_{\text{Cl}} = 1$ . To

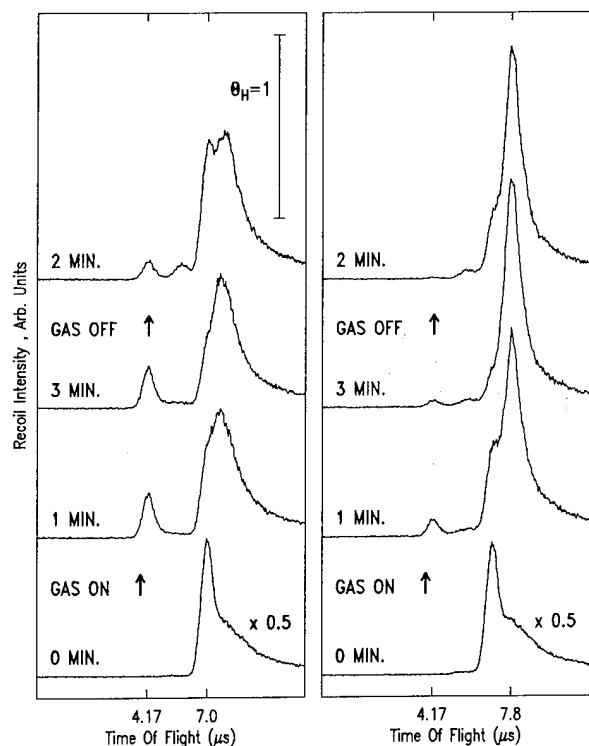


Fig. 4. Same as Fig. 3, except that the surface temperature is 500 °C and that the top spectra were measured 2 min after the dosing gas was turned off.

check for self-terminated adsorption, the dosing gas was turned off and the DR spectrum recorded 2 min later (top spectrum in each part of the figure). Both the  $H_{DR}$  and the  $Cl_{DR}$  signals drop equally in Fig. 4(a) ( $SiClH_3$ ), suggesting HCl desorption. In Fig. 4(b) ( $SiCl_2H_2$ ) the  $Cl_{DR}$  signal remains fixed at  $\Theta_{Cl} \approx 1$ , indicating that a self-terminated Cl layer has formed [17]. At  $T_s \geq 500$  °C, self-limiting adsorption of precursor is not possible, because HCl is readily desorbed from the surface and some  $SiCl_2$  desorption occurs over 100 s [17]. Desorption of  $SiCl_2$  is undesirable since this results in a loss of Si from the surface.

### 3. Discussion and summary

The results presented in this paper have several implications for the growth of Si thin films by ALE. The precursor molecules  $Si_2H_6$  and  $Si_2Cl_6$  can be cyclically dosed at  $T_s = 450$ – $500$  °C to grow thin Si films. At  $T_s = 500 \pm 25$  °C, the  $Si_2Cl_6$  exposure step is self-limiting. It appears that the Cl removal step using  $Si_2H_6$  is thermally activated, is not self-limiting, and is therefore kinetically controlled [3]. While this is not strictly a true ALE process, the film thickness is proportional to the number of growth cycles [16].

The dynamic change in surface Cl and H concentrations while  $SiClH_3$  and  $SiCl_2H_2$  are adsorbed indicates

that self-limiting adsorption of halogenated silanes might not be feasible. At  $T_s$  suitable for  $H_2$  desorption some HCl also desorbs allowing adsorption of more precursor. A fully self-limiting Cl layer using  $SiClH_3$  never forms, rendering this gas useless for ALE. A self-limiting Cl layer is formed using  $SiCl_2H_2$  at  $T_s = 500$ – $550$  °C [17]. However, dosing with  $SiCl_2H_2$  above 500 °C leads to significant  $SiCl_2$  desorption over the dosing time of 100 s [17]. Desorption of HCl and  $SiCl_2$  is significantly reduced if  $SiCl_2H_2$  is dosed at 500 °C. It is not known how much additional  $Si^*$  is deposited from HCl desorption. If the amount of  $Si^*$  deposited per cycle is not important but adsorption of a self-limiting layer is important then fully halogenated silanes should be used.

For both ALE processes presented in this paper, the growth rate of  $Si^*$  is limited by the desorption rate of  $H_2$  and HCl. These desorption rates will govern Si ALE cycle times, the prospect of achieving self-limiting adsorption, and the ALE process temperature.

### Acknowledgment

This work is supported by the Office of Naval Research under Contract N00014-91-C-0080.

### References

- 1 T. Suntola and M. Simpson (eds.), *Atomic Layer Epitaxy*, Chapman & Hall, New York, 1990.
- 2 C. H. L. Goodman and M. V. Pessa, *J. Appl. Phys.*, **60** (1986) R65.
- 3 D. D. Koleske, S. M. Gates and D. B. Beach, *J. Appl. Phys.*, **72** (9) (1992) 4073.
- 4 R. E. Thomas, R. A. Rudder and J. R. Markunas, *Mater. Res. Soc. Symp. Proc.*, **204** (1991) 327.
- 5 C. C. Cheng, S. R. Lucas, H. Gutleben, W. J. Choyke and J. T. Yates, *J. Am. Chem. Soc.*, **114** (1992) 1249.
- 6 J. W. Rabalais, *Science*, **250** (1990) 522.
- 7 J. W. Rabalais, *CRC Crit. Rev. Solid State Mater. Sci.*, **14** (1988) 319.
- 8 S. M. Gates and D. D. Koleske, *Proc. 2nd Int. Conf. on ALE*, in *Thin Solid Films*, **225** (1993) 159.
- 9 S. M. Gates, C.-M. Chiang and D. B. Beach, *J. Appl. Phys.*, **72** (1992) 246.
- 10 S. Chadhury and R. S. Williams, *Surf. Sci.*, **225** (1991) 127.
- 11 L. J. Whitman, S. A. Joyce, J. A. Yarmoff, F. R. McFeely and L. J. Terminello, *Surf. Sci.*, **232** (1990) 297.
- 12 S. M. Mokler, W. K. Liu, N. Ohtani and B. A. Joyce, *Appl. Phys. Lett.*, **60** (1992) 2255.
- 13 S. M. Gates and D. D. Koleske, *Appl. Phys. Lett.*, **61** (1992) 309.
- 14 B. E. Weir, R. L. Headrick, Q. Shen, L. C. Feldman, T. R. Hart, M. Needels, M. S. Hybertson and M. Schluter, to be published.
- 15 R. L. Headrick, B. E. Weir, A. F. J. Levi, D. J. Eaglesham and L. C. Feldman, *Appl. Phys. Lett.*, **57** (1990) 2779.
- 16 S. M. Gates, D. D. Koleske, J. R. Heath and M. Copel, *Appl. Phys. Lett.*, in press.
- 17 D. D. Koleske, S. M. Gates and D. B. Beach, *Appl. Phys. Lett.*, **61** (1992) 1802.

# Si atomic layer epitaxy based on $\text{Si}_2\text{H}_6$ and remote He plasma bombardment

A. Mahajan, J. Irby, D. Kinosky, R. Qian, S. Thomas, S. Banerjee and A. Tasch

Department of Electrical and Computer Engineering, ENS415, University of Texas, Austin, TX 78712 (USA)

T. Picraux

Sandia National Laboratories, Albuquerque, NM 87185 (USA)

## Abstract

Atomic layer epitaxy (ALE) of Si has been demonstrated by using remote He plasma low energy ion bombardment to desorb H from an H-passivated Si(100) surface at low temperatures and subsequently chemisorbing  $\text{Si}_2\text{H}_6$  on the surface in a self-limiting fashion. Si substrates were prepared using an RCA clean followed by a dilute HF dip to provide a clean, dihydride-terminated ( $1 \times 1$ ) surface, and were loaded into a remote plasma chemical vapor deposition system in which the substrate is downstream from an r.f. noble gas (He or Ar) glow discharge in order to minimize plasma damage. An *in situ* remote H plasma clean at 250 °C for 45 min was used to remove surface O and C and to provide an alternating monohydride and dihydride termination, as evidenced by a ( $3 \times 1$ ) reflection high energy electron diffraction (RHEED) pattern. It was found necessary to desorb the H from the Si surface to create adsorption sites for Si-bearing species such as  $\text{Si}_2\text{H}_6$ . Remote He plasma bombardment for 1–3 min was investigated over a range of temperature (250 °C–410 °C), pressures (50–400 mTorr) and r.f. powers (6–30 W) in order to desorb the H and to convert the ( $3 \times 1$ ) RHEED pattern to a ( $2 \times 1$ ) pattern which is characteristic of either a monohydride termination or a bare Si surface. It was found that as He pressures and r.f. powers are raised the plasma potential and mean free paths are reduced, leading to lower He bombardment energies but higher fluxes. Optimal He bombardment parameters were determined to be 30 W at 100 mTorr process pressure at 400 °C for 1–3 min. He was found to be more effective than Ar bombardment because of the closer match of the He and H masses compared with that between Ar and H. Monte Carlo TRIM simulations of He and Ar bombardment of H-terminated Si surfaces were performed to validate this hypothesis and to predict that approximately 3 surface H atoms were displaced by the incident He atoms, with no bulk Si atom displacement for He energies in the range 15–60 eV. The He bombardment cycles were followed by  $\text{Si}_2\text{H}_6$  dosing over a range of partial pressures (from  $10^{-7}$  Torr to 1.67 mTorr), temperatures (250 °C–400 °C) and times (from 20 s to 3 min) without plasma excitation, because it is believed that  $\text{Si}_2\text{H}_6$  can chemisorb in a self-limiting fashion on a bare Si surface as two silyl ( $\text{SiH}_3$ ) species, presumably leading to a H-terminated surface once again. The  $\text{Si}_2\text{H}_6$  dosing pressures and times corresponded to saturation dosing (about  $10^6$  langmuirs). Alternate  $\text{Si}_2\text{H}_6$  dosing and He low energy ion bombardment cycles (about 100–200) were performed to confirm the ALE mode of growth. It was found that the growth per cycle saturates with long  $\text{Si}_2\text{H}_6$  dosing at a level which increases slightly with He bombardment time. At 400 °C, for 2 min He bombardment at 100 mTorr and 30 W, the growth per cycle saturates at about 0.1 monolayers cycle<sup>-1</sup>, while for 3 min He bombardment the Si growth saturates at about 0.15 monolayers cycle<sup>-1</sup>. It was also confirmed that the growth is achieved only by using alternate He bombardment and  $\text{Si}_2\text{H}_6$  dosing. He bombardment alone for a comparable time (3 min  $\times$  100 cycles) causes a negligible change in the Si film thickness (less than 5 Å). Similarly, thermal growth using  $\text{Si}_2\text{H}_6$  under these conditions for (3 min  $\times$  100 cycles) causes negligible deposition (less than 5 Å).

## 1. Introduction

Precise control of doping and heterostructures is extremely important for next-generation Si ultralarge-scale integration devices. Such a capacity can maintain compact doping profiles and fabricate the abrupt hetero interfaces required for “ordered”  $\text{Si}_m\text{Ge}_n$  superlattices which will require “digital” control over layer thicknesses. Delta-doped structures will require atomic plane doping which is possible only by atomic layer epitaxy (ALE) techniques. The basic technique consists of use

of surface chemical reactions for obtaining layer-by-layer growth. ALE of III–V compounds has been widely demonstrated by alternately introducing gaseous reactants into the reaction chamber [1]. ALE of column IV materials poses certain unique difficulties. Passivation of the surface to inhibit adsorption of the species between depositions is required. H coverage is an attractive passivation technique as it is relatively easy to attain and sometimes the only passivation technique obtainable. The H needs to be removed from the surface to open up surface adsorption sites for the next

cycle of deposition. Thermal means have been effectively used for H removal either by heating the whole substrate, as in rapid thermal processing (RTP), or in a localized fashion as in laser-induced thermal desorption (LITD). In the current approach we have used low energy noble gas ion bombardment from an r.f. plasma for H removal from the Si surface.

Ge ALE has been reported by using  $\text{Ge}(\text{C}_2\text{H}_5)_2\text{H}_2$  with the ethyl group as the surface passivating species [2]. Extension of this method to Si is known to create C contamination problems. Si molecular layer epitaxy using RTP with  $\text{SiH}_2\text{Cl}_2$  and  $\text{H}_2$  gases has been reported [3]. This is a high temperature process with transient temperatures rising to as high as 1100 K. In addition, a halogenic approach is incompatible with ultrahigh vacuum (UHV).  $\text{Si}_2\text{H}_6$  has been successfully used as a precursor for ALE, using LITD of H [4]. However, large area growth is difficult with an excimer laser.

In our approach, a remote H plasma clean was used to obtain initially a stable H-terminated Si surface. This H was then removed to create adsorption sites by He ion bombardment from a remote r.f. He plasma. The surface was then dosed with the Si bearing precursor,  $\text{Si}_2\text{H}_6$ , which chemisorbs in a self-limiting manner and restores the H-passivated surface. The H is removed again by He ion bombardment in the next cycle to create adsorption sites.

## 2. Experimental procedure

The schematic of the remote plasma chemical vapor deposition (RPCVD) system used for the *in situ* remote H plasma clean and ALE growth is shown in Fig. 1. The system consists of three interconnected UHV chambers: a load-lock chamber for sample loading with a base pressure of  $3 \times 10^{-9}$  Torr; a surface analysis chamber with a base pressure of  $2 \times 10^{-10}$  Torr equipped with an Auger electron spectroscopy system for *in situ* monitoring of surface contamination, and a process chamber with a base pressure of  $5 \times 10^{-9}$  Torr equipped with an r.f. plasma source in which the remote H plasma clean and epitaxial growth are performed. The deposition chamber is equipped with a residual gas analyzer to allow monitoring of the background levels of oxygen and water in the ambient, as well as to monitor the various species during processing using a differential pumping scheme. A reflection high energy electron diffraction (RHEED) system in the process chamber allows *in situ* diagnostics of surface reconstruction and crystallinity. Ultrahigh purity gases are used in the process, in which the partial pressures of water and oxygen were  $1 \times 10^{-9}$  Torr and  $5 \times 10^{-11}$  Torr respectively. To reduce further the oxygen and water vapor in the process gases, all gas lines are equipped with Nanochem gas purifiers which reduce the oxygen and water vapor to the parts per billion level (Nanochem was

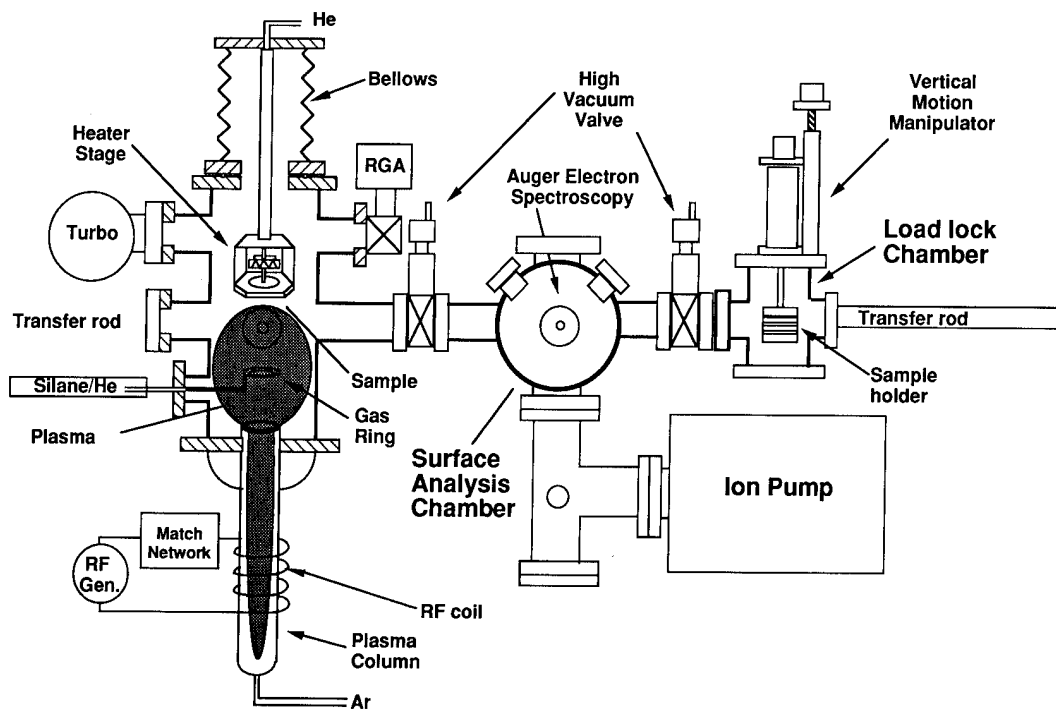


Fig. 1. RPCVD system schematic.



a trademark of Semigas Corp.). The wafers used were 75 mm diameter lightly doped p-type Si(100) substrates. Before wafers were loaded into the system, they were cleaned using a wet chemical treatment consisting of an ultrasonic degrease in TCA, acetone, and methanol. A subsequent ultrahigh purity water rinse was followed by a modified RCA clean for removal of organic and metallic contamination. A 60 s 40:1  $\text{H}_2\text{O}:\text{HF}$  dip was used to remove the oxide grown during the RCA clean. After a final 20:1  $\text{H}_2\text{O}:\text{HF}$  dip for 30 s the wafers were spun dry, and immediately placed in a nitrogen-purged glove-box and loaded into the load-lock chamber. Prior to the process, the wafers were cleaned *in situ* using a remote H plasma clean to remove carbon and oxygen contamination [5]. For a typical clean, 200 standard  $\text{cm}^3 \text{min}^{-1}$  of H is introduced at the base of the plasma column at a pressure of 50 mTorr and inductively excited with 9 W of r.f. power (13.56 MHz). During the clean, which lasts 45 min, the substrate is heated to 250 °C from the back using a boron nitride heater. RHEED analysis of wafers cleaned by the above technique reveals 1/3-order streaks (Fig. 2(a)) indicative of a  $(3 \times 1)$  reconstruction pattern. The  $(3 \times 1)$  reconstruction pattern has been found to be due to alternating monohydride and dihydride termination [6]. This surface was then bombarded with He or Ar ions from the plasma over a range of temperatures (250 °C–410 °C), pressures (50–400 mTorr) and r.f. powers (6–30 W) in order to desorb the H and convert the  $(3 \times 1)$  RHEED pattern to a  $(2 \times 1)$  pattern which is characteristic of either a monohydride termination or a bare Si surface.

The ALE growth was started on this H-passivated surface which consisted of 100–200 repetitions of the deposition cycle. Each cycle consisted of He plasma bombardment to desorb H after which the r.f. power was switched off and  $\text{Si}_2\text{H}_6$  was introduced into the chamber through a gas feed ring at a flow rate and for a time required to produce the required dose. This was

followed by a pumpdown time of 30 s during which the  $\text{Si}_2\text{H}_6$  flow was shut off and was flushed out of the system before starting the next He bombardment cycle.

### 3. Results and discussion

Figure 3 shows the parameter space in which H desorption was obtained by the above method as was evidenced by the change of the  $(3 \times 1)$  RHEED pattern to a  $(2 \times 1)$  pattern. It was seen that there is a certain optimum range of plasma powers for an effective H removal from the Si surface. This range becomes narrower at higher pressures. It was determined from Langmuir probe measurements that as r.f. power is increased the ion flux increases but the plasma potential and hence the bombardment energy decreases. Also, as the pressure is increased, the ion free path decreases and the bombardment energy decreases although the ion density goes up. The inability of He bombardment to desorb H from the surface at low powers was presumed to be due to low ion fluxes at low powers. On the contrary, as the plasma potential decreases with increasing r.f. power, the bombarding ions lack the energy for effective removal of the H from the surface at high r.f. powers. The energy of the bombarding ions also decreases with increasing pressure because of the decreasing mean free path. Thus it was more difficult to remove H from the surface at higher pressures. The optimal plasma power for H desorption at a given process pressure was chosen to be in the middle of the r.f. power range.

For the ALE cycles, the process pressure during the bombardment was chosen to be 100 mTorr, where the optimum range of r.f. plasma powers is rather wide. The temperature was kept constant at 400 °C during the process. This places the temperature below the  $\beta_2$  peak of the temperature programmed desorption

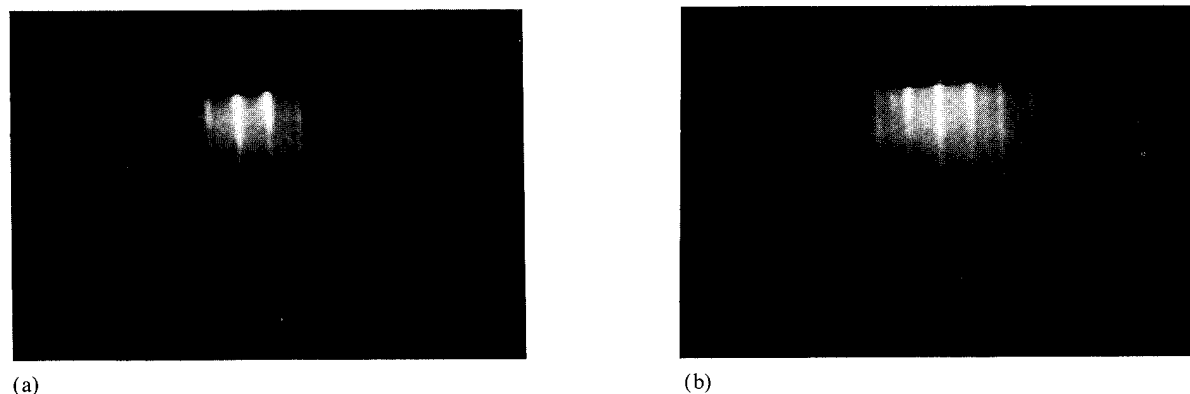


Fig. 2. RHEED analysis showing removal of hydrogen by He ion bombardment: (a)  $(3 \times 1)$  reconstruction after remote H plasma clean; (b) the surface reconstruction has converted to  $(2 \times 1)$  after 1 min of He ion bombardment.

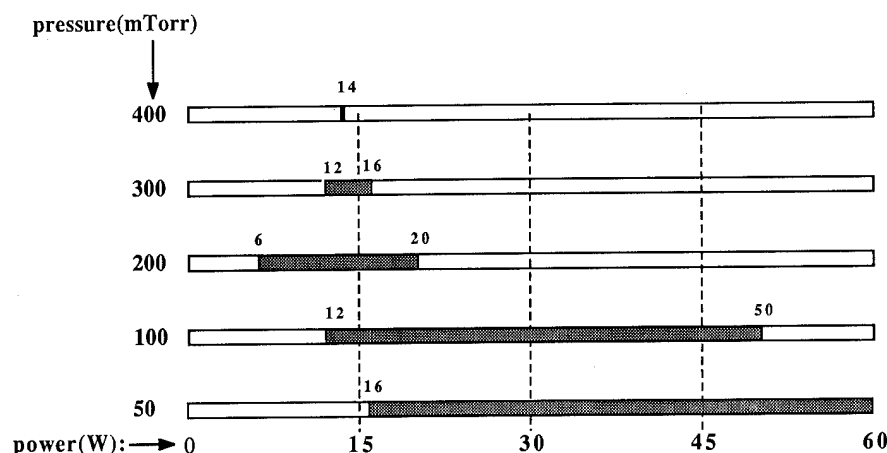


Fig. 3. Darkened areas show range of plasma powers at various pressures for effective removal of H from Si(100) surface at 250 °C for bombardment times of 1–2 min as evidenced by RHEED.

(TPD) curve of H (Fig. 4 [7]), thus ensuring that there was no significant H desorption from the surface during the process by thermal means. 30 W of r.f. power was used to excite the He plasma. The bombardment time was varied from 1 to 3 min with different amounts of dosing for each bombardment duration. The results are shown in Fig. 5. As the  $\text{Si}_2\text{H}_6$  dosing is increased for the same amount of He bombardment, the amount of growth increases initially. In this regime it is believed that the growth is limited by the availability of  $\text{Si}_2\text{H}_6$ . As the  $\text{Si}_2\text{H}_6$  dosing increased, the growth is limited by the extent of H desorption from the Si surface by the He ion bombardment, as evidenced by an increase in the growth rate from 0.06 monolayers cycle<sup>-1</sup> for a dosing of  $9 \times 10^4$  langmuirs to a saturation growth rate of about 0.11 monolayers cycle<sup>-1</sup> at higher doses (for a He bombardment time of 2 min). Thus, the growth rate follows the general trend of saturation at higher doses for a given He bombardment time. Also, the amount of growth in the saturation region increases with the He bombardment time. A plot of the Si growth rate vs. the He bombardment time for a given amount of dosing reveals an increase in the growth rate with the time of

He bombardment (Fig. 6). It can be seen that the saturation growth rate increases from about 0.1 monolayers cycle<sup>-1</sup> for 2 min of He bombardment to about 0.15 monolayers cycle<sup>-1</sup> for 3 min of He bombardment, thus leading to the inference that the amount of H desorption is increased by increasing the He bombardment time. This can be used to control the extent of H desorption and hence the growth rate.

The films grown by ALE are smooth and single crystal. This is indicated by RHEED analysis which shows a streaky ( $2 \times 1$ ) reconstruction pattern after growth (Fig. 7).

It might also be mentioned that it was confirmed that the growth observed in these experiments was not due to purely thermal growth of Si from  $\text{Si}_2\text{H}_6$  or due to sputtering of Si from the chamber wall deposits during He plasma bombardment, both of which resulted in negligible growth (less than 5 Å) for a comparable duration.

Monte Carlo TRIM simulations were performed to estimate the number of H and Si atoms displaced by the incident He and Ar ions [8]. An amorphous Si substrate with a monolayer coverage of H is assumed as the starting material and is bombarded with normal incidence He or Ar ions. No crystallographic information is included in the model. Sharp displacement thresholds for bulk and surface atoms are assumed. The displacement energy is 3 eV for the surface H atoms and 22 eV for the bulk Si atoms. A target atom which receives a recoil energy greater than the displacement energy is assumed to be displaced. He ions are found to be more effective for removal of H atoms from the substrate than Ar ions. The number of H atoms from the surface displaced by ion bombardment increases to about 3 displacements per incident He ion with increasing ion energy in the 10–70 eV range, which corresponds to typical values of the plasma

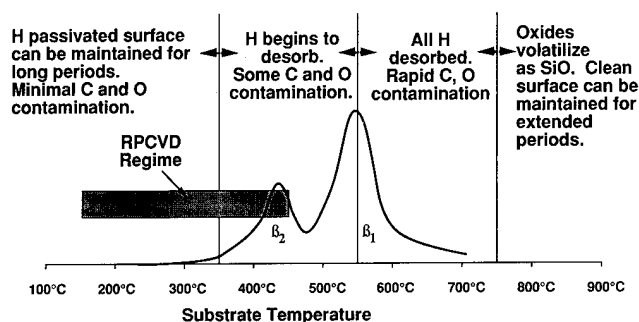


Fig. 4. H passivation as a function of temperature. TPD data from ref. 7.

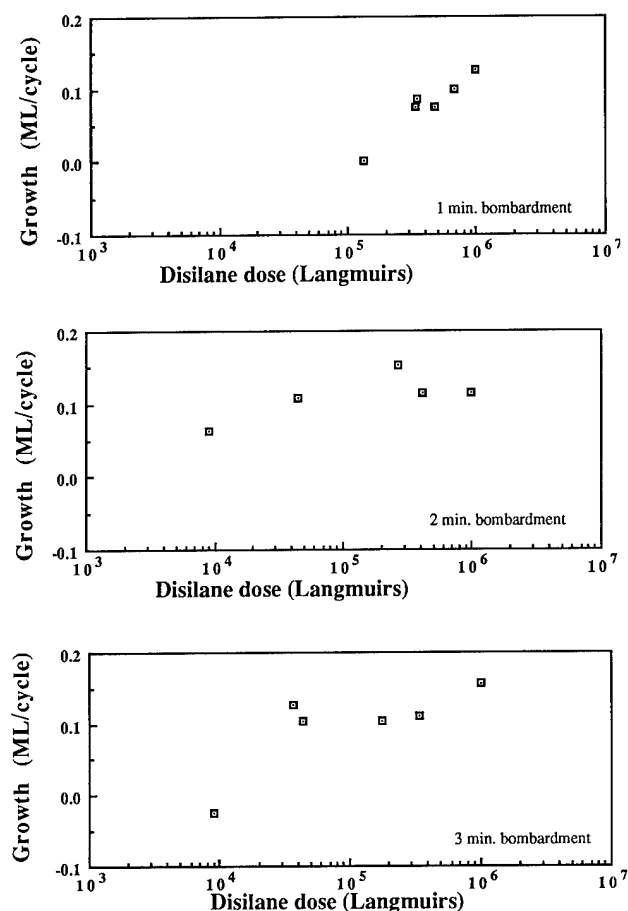


Fig. 5. Plot of growth vs. disilane dose for bombardment times of 1, 2 and 3 min.

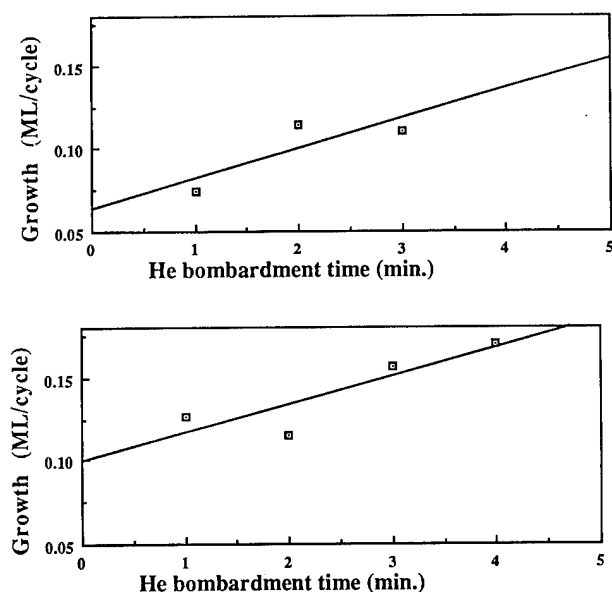
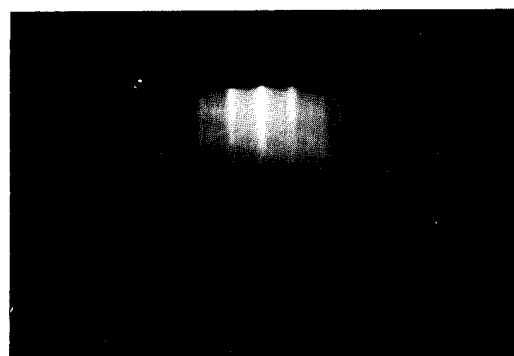


Fig. 6. Plot of growth vs. He bombardment time for disilane doses of (a)  $4 \times 10^5$  langmuirs and (b)  $1 \times 10^6$  langmuirs.



(a)



(b)

Fig. 7. RHEED analysis of films grown by ALE showing that the films are high quality single crystal: (a) pattern before deposition; (b) after 100 cycles of ALE growth at  $400^\circ\text{C}$ , 100 mTorr pressure, 2 min. He bombardment at 30 W plasma power. Disilane dosing was  $1.0 \times 10^6$  langmuirs cycle $^{-1}$ .

potential in RPCVD. The number is lower for Ar ion bombardment (Fig. 8). There is more Si atom displacement in the underlying Si substrate by Ar ions (about 0.11 Si displacements per Ar ion at 45 eV) compared with negligible displacement by He ions (0.003 Si displacements per He ion at 70 eV). This indicates that there is a wider process window for He than for Ar in which H can be desorbed from the Si surface without creating subsurface damage. This is believed to be due to the fact that the He mass is more closely matched to the H mass than Ar, while the mismatch with the Si mass is greater for He.

#### 4. Conclusions

We have demonstrated removal of H from an H-passivated Si(100) surface by low energy (about 50 eV) He ion bombardment. The extent of the removal of H from the surface can be controlled by varying the duration of He bombardment and plasma parameters. This, in turn, means that the growth rate by this method can also be controlled.  $\text{Si}_2\text{H}_6$  was shown to adsorb in a self-limiting manner on the Si(100) surface.

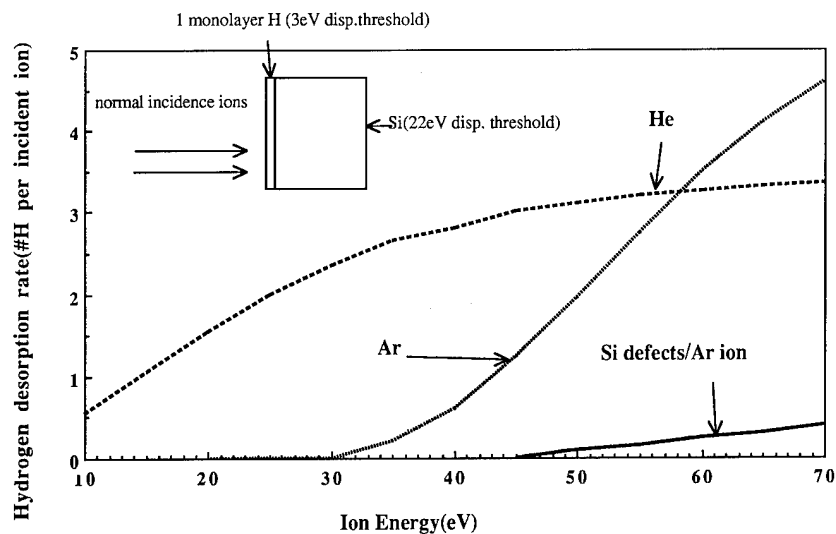


Fig. 8. Monte Carlo TRIM simulations of H displacement rate vs. energy of incident ions (He and Ar).

### Acknowledgments

This work was supported by ONR-SDIO and by the NSF Science and Technology Center at the University of Texas at Austin.

### References

- 1 T. Suntola and M. Simpson (eds.), *Atomic Layer Epitaxy*, Chapman & Hall, New York, 1990.
- 2 Y. Takahashi, Y. Sese and T. Urisu, *J. Electrochem. Soc.*, **136** (6) (1989) 1826.
- 3 J. Nishizawa, K. Aoki, S. Suzuki and K. Kikuchi, *J. Electrochem. Soc.*, **137** (6) (1990) 1898.
- 4 D. Luben, R. Tsu, T. R. Bamblett and J. E. Greene, *J. Vac. Sci. Technol. A*, **9** (6) (1991) 3003.
- 5 T. Hsu, B. Anthony, R. Qian, S. Banerjee and A. Tasch, *J. Electron. Mater.*, **20** (1991) 279.
- 6 J. Boland, *Phys. Rev. Lett.*, **54** (1985) 1055.
- 7 S. Gates, R. Kunz and M. Greenlief, *Surf. Sci.*, **207** (1989) 364.
- 8 J. Biersack and L. Haggmark, *Nucl. Instrum. Methods*, **174** (1980) 257.

# Silicon monolayer growth using dichlorosilane and hydrogen in a near atmospheric pressure chemical vapor deposition reactor

F. G. McIntosh, P. C. Colter and S. M. Bedair

Department of Electrical and Computer Engineering, North Carolina State University, Raleigh, NC 27695-7911 (USA)

## Abstract

Monolayer growth of silicon in a chemical vapor deposition reactor has been investigated in the dichlorosilane (DCS)–hydrogen system. During each deposition cycle the wafer is rotated through the separate DCS and hydrogen streams. A 1 monolayer cycle<sup>-1</sup> plateau in the growth rate was obtained over a fourfold increase in the DCS partial pressure, resulting in a 0.48  $\mu\text{m h}^{-1}$  deposition rate. The experiments were conducted at 825 °C and 50 Torr. The effects of reactant partial pressures and cycle time on the deposition will be discussed, as well as possible mechanisms for this process.

## 1. Introduction

A great deal of effort has been recently focused on the atomic layer epitaxy (ALE) of silicon. Nishizawa *et al.* have demonstrated ALE at 825 °C in the  $10^{-4}$  Torr pressure regime using dichlorosilane (DCS) and molecular hydrogen as the precursors [1]. In order to explore this process further, silicon has been deposited using the same precursors, DCS and hydrogen, at 825 °C. The experiments were conducted at a higher pressure, 50 Torr total pressure, in a chemical vapor deposition (CVD) reactor. This avenue of research has potential practical value as a result of the possibility of high speed ALE with our system design.

## 2. Experimental details

The growth chamber used for silicon deposition is similar in design to vertical reaction chambers used for ALE of III–V compounds in our research group at North Carolina State University [2]. The graphite susceptor design is depicted in Fig. 1. The reactant gases, DCS and hydrogen, pass through the windows on opposite sides of the stationary susceptor. Argon is used as the carrier gas for these reactants and also to form a buffer layer to keep the reactants separated. The silicon wafer, positioned on the lower rotating susceptor, passes through each of these gas streams once during each growth cycle. The two sections of the susceptor are separated by a gap of approximately 1 mm, which helps to remove DCS and hydrogen carried along the boundary layer above the rotating wafer. The high purity reactants and argon are passed through

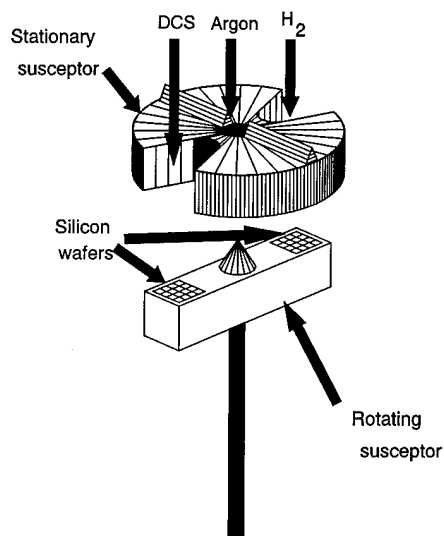


Fig. 1. Graphite susceptor design.

purifiers in order to reduce the oxygen and water contamination levels. In addition, the entire chamber is contained in a nitrogen-filled glove-box to prevent exposure to the outside air.

The Si(100) samples are prepared using the RCA procedure [3] followed by a 15 s dip in 5% HF solution. The samples are then blown dry, transferred quickly into the glove-box, and then loaded onto the susceptor. Prior to growth the chamber is pumped down to below  $10^{-6}$  Torr with a turbo pump to remove residual water and oxygen. The silicon substrate is degassed at 1050 °C under hydrogen for 10 min. The temperature is then lowered to 950 °C and a buffer layer of silicon is

deposited to provide a good surface for low temperature deposition. The temperature and gas flows are then adjusted as desired for the growth experiment. In all cases, a total argon flow rate of  $1.75 \text{ standard l min}^{-1}$  was used for the shroud, which both separates and acts as a carrier gas for the reactants. The thickness of each epitaxial layer is measured using the groove and stain method [4] in order to determine the deposition per cycle. Typical thicknesses for the layers measured range from 0.3 to 0.6  $\mu\text{m}$ .

### 3. Results

Figure 2 shows the growth per cycle as a function of the DCS flow rate, which is proportional to the DCS partial pressure. All of the samples were grown at  $825^\circ\text{C}$  at a rotational speed of  $60 \text{ rev min}^{-1}$  and a pressure of 50 Torr. The upper curve is with DCS flowing through one window and hydrogen through the other. The bottom curve shows results with a DCS stream passing through one window and only argon, *i.e.* no hydrogen, passing through the other. The top curve shows that with a cyclic exposure to DCS and hydrogen a plateau region of 1 monolayer cycle $^{-1}$  is attained over a DCS flow range of 5–20 standard  $\text{cm}^3 \text{ min}^{-1}$ . At DCS flows above 20 standard  $\text{cm}^3 \text{ min}^{-1}$ , however, the deposition per cycle continues to rise above 1 monolayer. Both curves follow the same general trend and reveal an increase in deposition due to hydrogen exposure of approximately 0.3 monolayers cycle $^{-1}$  for all DCS flows examined.

The growth rate *vs.* the hydrogen flow rate is shown in Fig. 3. The two curves are for a 5 standard  $\text{cm}^3 \text{ min}^{-1}$  DCS flow at  $60 \text{ rev min}^{-1}$  and at  $180 \text{ rev min}^{-1}$ . Doubling the hydrogen flow from 50 to 100 standard  $\text{cm}^3 \text{ min}^{-1}$  had little effect on the deposition per cycle, although it does appear to have increased the growth

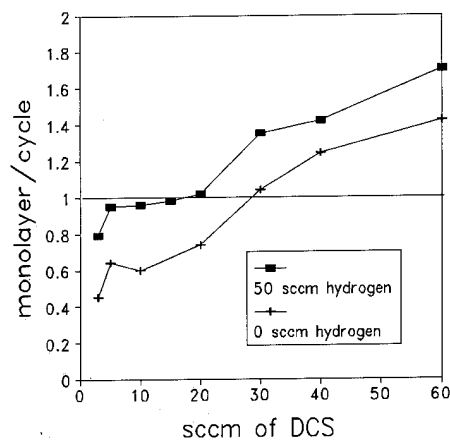


Fig. 2. Deposition per cycle *vs.* DCS flow rate at  $825^\circ\text{C}$  and 50 Torr.

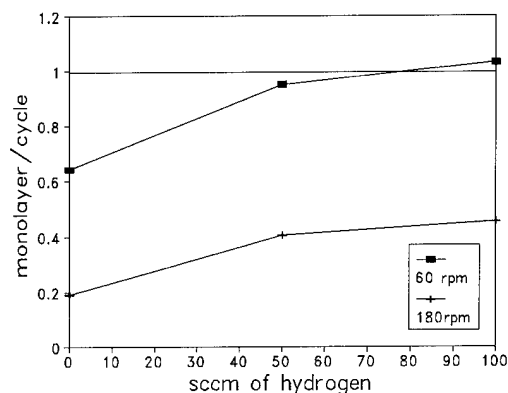


Fig. 3. Deposition per cycle *vs.* hydrogen flow rate at  $825^\circ\text{C}$  and 50 Torr.

rate slightly for the two 5 standard  $\text{cm}^3 \text{ min}^{-1}$  DCS curves. Hydrogen exposure for the  $60 \text{ rev min}^{-1}$  case increased the growth rate by approximately 0.3 monolayers, but for the  $180 \text{ rev min}^{-1}$  cases the hydrogen only increased the deposition by 0.2 monolayers cycle $^{-1}$ . This decrease in the effect of hydrogen on the growth per cycle at  $180 \text{ rev min}^{-1}$  *vs.*  $60 \text{ rev min}^{-1}$  may be due to insufficient time for the surface reactions to proceed at the high speed during the short exposures to the reactants.

Figure 4 shows the effects of exposure time to a 5 standard  $\text{cm}^3 \text{ min}^{-1}$  DCS flux on the deposition per cycle with and without exposure to hydrogen. Because of the symmetry of the susceptor and uniform rotational speed, the wafer is exposed to the  $\text{H}_2$  and DCS for the same length of time over 1 rev. The exposure times were calculated assuming that the wafer is interrupting each reactant gas stream for 15% of each cycle. Times of 0.05 s, 0.075 s, 0.15 s and 0.30 s correspond to rotation speeds of  $180 \text{ rev min}^{-1}$ ,  $120 \text{ rev min}^{-1}$ ,  $60 \text{ rev min}^{-1}$  and  $30 \text{ rev min}^{-1}$  respectively. The upper curve is for growth with hydrogen exposure and the lower is without hydrogen. Again, both curves appear very

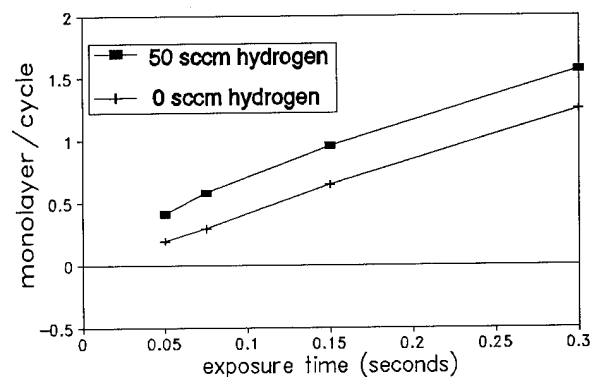


Fig. 4. Deposition per cycle *vs.* exposure time at  $825^\circ\text{C}$  and 50 Torr. The exposure time is the same for both reactants ( $\text{DCS}$  and  $\text{H}_2$ ) and is equal to 15% of the cycle time.

similar, except that for experiments with hydrogen exposure the curve is shifted up by about 0.3 monolayers cycle<sup>-1</sup>. The data for growth with no hydrogen give a very good fit and a *y* intercept near zero, indicating that the deposition per cycle is only dependent on the exposure time to DCS.

#### 4. Discussion

Since our system design and operating pressure make *in situ* analysis difficult, examination of the reaction processes depends partly on investigations by other researchers. The desired mechanism for silicon ALE involves the deposition of a stable chlorinated silicon layer which is reduced to bare silicon by subsequent reaction with hydrogen. The plateau region in Fig. 2 suggests a stable surface species is present, and the data in Figs 2, 3 and 4 for DCS exposure with and without hydrogen indicate that molecular hydrogen is reacting with this surface species.

The most likely surface species may be determined by examining the results from other researchers' investigations. Temperature programmed desorption [5] studies detect the desorption of both SiCl and SiCl<sub>2</sub> from the Si(111) surface under ultrahigh vacuum conditions. X-ray photoelectron spectroscopy (XPS) [6] studies indicate that SiCl is the only stable chlorinated surface species present on Si(100) and Si(111) surfaces at a DCS pressure of  $2 \times 10^{-4}$  Torr and between room temperature and 800 °C. If, as proposed in ref. 5, the SiCl<sub>2</sub> desorption is due to a second-order reaction between surface SiCl groups, then these experiments show that SiCl is the most probable surface species present on silicon after DCS exposure. Both investigations, however, indicate that little or no chlorine should be bound to the silicon surface at the present research temperature of 825 °C. The upper temperature limits of detection of desorbed SiCl and SiCl<sub>2</sub> are at approximately 1000 K (823 °C) and the XPS studies detect no surface chlorine at 800 °C. The higher DCS partial pressure and shorter cycle times for the present research may account for the apparent chlorine effects in the data presented here. High DCS pressures may shift the surface species' concentrations and, assuming that the chlorine has a temperature-dependent lifetime on the silicon surface, the surface chlorine would appear to be stable if the cycle times are much shorter than its lifetime. From these investigations it will be assumed for the remainder of this discussion that the only significant chlorinated surface species is SiCl.

The presence of surface chlorine and its reaction with molecular hydrogen in the data presented here is supported by the effects of adding molecular hydrogen to

the deposition cycle, although it has been concluded in ref. 6 that molecular hydrogen will not react with surface chlorine above 800 °C. This conclusion, however, is based on experiments with molecular hydrogen at 600 °C and assumes no chlorine is present on the surface above 800 °C. Assuming that we are forming chlorinated surface species at 825 °C, the 225 °C temperature increase may be enough to activate the hydrogen reaction on the surface. Figures 2, 3 and 4 show that cyclic exposure to DCS and hydrogen increases the growth rate by approximately 0.3 monolayers cycle<sup>-1</sup> vs. exposure to only DCS under similar conditions. This 0.3 monolayer increase is seen over a twentyfold change in DCS partial pressure, a sixfold change in rotational speed, and a twofold change in hydrogen pressure. If this deposition enhancement due to hydrogen were caused by diffusion to the DCS side, which would result in standard DCS-H<sub>2</sub> CVD, then this consistent difference would not be expected. The difference in deposition per cycle is best explained by reaction of H<sub>2</sub> with SiCl, which partially covers the surface and inhibits further deposition at those sites. Exposure to hydrogen removes the chlorine and makes those sites available for deposition during the next cycle. Assuming that the hydrogen reacts with all of the surface chlorine, then 0.3 monolayers of SiCl are formed on the surface over a wide range of DCS partial pressures and exposure times. This indicates that the SiCl is quickly formed on the surface and, except at very short exposure times, saturates at approximately 0.3 monolayers cycle<sup>-1</sup>. As shown in Fig. 4, this saturation occurs at growth rates varying from 0.5 to 1.5 monolayers cycle<sup>-1</sup>. This limit may be due to surface steric effects of steady state surface reactions. In addition, Fig. 3 shows that increasing the hydrogen flow from 0 to 50 standard cm<sup>3</sup> min<sup>-1</sup> has a dramatic effect on the growth per cycle, but doubling the flow has little effect. Therefore, the molecular hydrogen does react with the majority of the surface SiCl. The slight increase in deposition after doubling the hydrogen flow is probably due to the inefficiency of the H<sub>2</sub> in reacting with any residual SiCl on the silicon surface. For lower temperature deposition, however, it may be necessary to use molecular hydrogen or activate the H<sub>2</sub> in order to remove the surface chlorine.

The presence of SiCl surface species also partially explains the 1 monolayer cycle<sup>-1</sup> plateau observed in Fig. 2. Although SiCl may not be stable under equilibrium conditions at 825 °C, it may be stable enough over the 1 s time domain to passivate the surface in these experiments. This does not fully account for the plateau region, however, since the studies with and without hydrogen indicate that only approximately 30% of the surface is covered by SiCl, while one full monolayer per cycle is deposited. The remaining 70% of each

monolayer may result from reactions with adjacent SiCl groups, such as  $\text{SiCl} + \text{SiCl} \longrightarrow \text{Si} + \text{SiCl}_2$ , where the  $\text{SiCl}_2$  is desorbed and a bare silicon atom is left on the surface. Another possibility is the formation of  $\text{SiHCl}$  on the surface, which would readily decompose to form a deposited silicon atom and gaseous  $\text{HCl}$ .

The increase in deposition rate above 1 monolayer cycle<sup>-1</sup> in Fig. 2 indicates the existence of a DCS pressure dependent surface reaction. At low DCS partial pressures the reaction is not dominant and the surface is effectively passivated by the other processes. The slight positive slope in the plateau region suggests the existence of such a reaction. At higher pressures, above 20 standard cm<sup>3</sup> min<sup>-1</sup> of DCS, this pathway becomes more dominant and the growth rate *vs.* DCS flow rises more dramatically. The possible mechanisms for this reaction are not clear at present, but future research on the orders of the reactions involved may reveal likely reaction pathways.

An alternate pathway for removal of surface chlorine, besides the reaction with  $\text{H}_2$ , must exist since, even over the plateau region in Fig. 2, deposition occurs without the introduction of  $\text{H}_2$  to the system. This may be due to reaction with hydrogen from other sources or to self-desorption of chlorine. Two possible sources of hydrogen are (1) as a byproduct of deposition (*e.g.*  $\text{DCS} \longrightarrow \text{SiCl}_2 + \text{H}_2$ ) and (2) from the gaseous DCS. If the hydrogen were from a deposition reaction, then as the deposition rate increases then the hydrogen concentration should increase and the remaining surface chlorine should decrease. Figure 4, however, indicates that the chlorine coverage is consistent over a large increase in the deposition rate. This figure also suggests that the surface chlorine is stable over the cycle times investigated. As the growth rate is tripled, the exposure time increases by a factor of 6, which means that the time the substrate is not exposed to reactant gases also increases by a factor of 6. If the lifetime of the surface chlorine were on the order of the cycle times, then a drop in chlorine coverage would be expected as the

exposure time is increased. However, the chlorine coverage is consistent over this range, except for a small drop at the shortest exposure time. This small drop is probably due to either insufficient time to form  $\text{SiCl}$  on the surface or insufficient time for the hydrogen to react with the surface chlorine. Therefore, the most likely path for removal of chlorine without using  $\text{H}_2$  is reaction with DCS, or with an unknown surface intermediate formed from DCS.

## 5. Conclusions

A silicon growth rate of 1 monolayer cycle<sup>-1</sup> has been obtained in a rotating susceptor vertical reactor at 825 °C and 50 Torr. The operating temperature is low enough to inhibit rapid self-decomposition of DCS and high enough for molecular hydrogen to react with surface chlorinated species. Control of the exposure time results in a plateau region of 1 monolayer growth cycle<sup>-1</sup> over a DCS flux from 5 to 20 standard cm<sup>3</sup> min<sup>-1</sup>. The growth rate for this region is 0.48 μm h<sup>-1</sup>. Although this is not an ALE process, the system is promising for high speed silicon ALE provided that the reactivity of hydrogen with the surface chlorine may be enhanced at lower growth temperatures.

## References

- 1 J. Nishizawa, K. Aoki, S. Suzuki and K. Kikuchi, *J. Cryst. Growth*, **99** (1990) 502.
- 2 K. G. Reid, H. M. Urdianyk and S. M. Bedair, *Appl. Phys. Lett.*, **59** (1991) 2397.
- 3 W. Kern and D. A. Puotinen, *RCA Rev.*, **3** (June 1970) 187.
- 4 S. Wolf and R. N. Tauber, *Silicon Processing for the VLSI Era*, Lattice, Sunset Beach, CA, 1986, pp. 272–273.
- 5 P. A. Coon, P. Gupta, M. L. Wise and S. M. George, *J. Vac. Sci. Technol., A*, **10** (2) (1992) 324–333.
- 6 J. A. Yarmoff, D. K. Shuh, T. D. Durbin, C. W. Lo, D. A. Lapiano-Smith, F. R. McFeely and F. J. Himpsel, *J. Vac. Sci. Technol., A*, **10** (1992) 2303.



# The chemisorption and reaction of $\text{GeCl}_4$ with $\text{Si}(100)$

D. A. Lapiano-Smith and F. R. McFeely

IBM Thomas J. Watson Research Center, P.O. Box 218, Yorktown Heights, NY 10598 (USA)

## Abstract

The chemisorption of  $\text{GeCl}_4$  on  $\text{Si}(100)$  as a function of substrate temperature was investigated by soft X-ray photoemission spectroscopy. At a substrate temperature of 300 °C,  $\text{GeCl}_4$  chemisorbs dissociatively forming  $\text{GeCl}_2$  and  $\text{GeCl}$  species as well as elemental Ge bonding to Si. At higher temperatures we observe the loss of  $\text{GeCl}_2$ , but trace amounts of  $\text{GeCl}$  remain on the surface until a temperature of about 500 °C is attained. In addition, the decomposition of  $\text{GeCl}_4$  promotes the formation of  $\text{SiCl}$  surface species at all substrate temperatures. A maximum amount of adsorbed Cl has been observed to bond to the Si surface following an exposure at 500 °C.

## 1. Introduction

Interest in atomic layer epitaxy (ALE), namely, the self-limiting, layer-by-layer growth of semiconductor materials by chemical vapor deposition, is due primarily to the potential opportunity to control film growth to very fine atomic layer thicknesses [1, 2]. To date, most ALE investigations have concentrated on the development of group II–VI [3] and III–V [1, 2, 4, 5] compound semiconductor materials and very few research efforts have been directed towards group IV materials. An extensive class of potential source molecules for group IV ALE include a variety of Si and Ge halides, hydrides and halohydrides. To evaluate rationally a specific source gas–substrate system as suitable for ALE, a fundamental understanding of the chemical mechanisms which govern the surface reaction processes in that particular system is in order.

We thus report the results of a soft X-ray photoemission experiment designed to ascertain the surface chemistry involved following the chemisorption and subsequent reaction of germanium tetrachloride ( $\text{GeCl}_4$ ) with the technologically important  $\text{Si}(100)$  surface as a function of the substrate temperature. Following an exposure of the surface to 25 000 L at 300 °C,  $\text{GeCl}_4$  chemisorbs dissociatively forming significant amounts of  $\text{GeCl}_2$  and  $\text{GeCl}$  species as well as elemental Ge bonding to Si. At a substrate temperature of 500 °C no germanium chloride species exist on the surface. The Si surface has been terminated with elemental Ge and a maximum amount of adsorbed Cl primarily in the form of  $\text{SiCl}$  moieties, as shown by the Ge 3d and Si 2p core level spectra respectively.

## 2. Experimental details

The  $\text{Si}(100)$  substrate was prepared by direct ohmic heating to 1050 °C and then by annealing at 850 °C to produce the  $(2 \times 1)$  surface reconstruction [6]. The cleaning process was completed in a preparation chamber with a base pressure of  $3 \times 10^{-10}$  Torr. Exposures of the substrate to  $\text{GeCl}_4$  were completed in a dosing chamber with a base pressure of  $4 \times 10^{-10}$  Torr.  $\text{GeCl}_4$  was introduced into the ultrahigh vacuum (UHV) chamber through a sapphire leak valve in order to achieve pressure control during the exposures. A cold cathode gauge was used to measure the chamber pressure. Following each exposure the sample was transferred via a UHV manipulator transfer system to the spectrometer for surface analysis.

Ge 3d and Si 2p soft X-ray photoemission spectra were measured at beamline U8B of the National Synchrotron Light Source at Brookhaven National Laboratory. The synchrotron radiation was dispersed by a 6 M toroidal grating monochromator. Tunable photons in the energy range from 90 to 225 eV were utilized to excite the electrons of the Ge 3d (about 29 eV binding energy) and Si 2p (100 eV) core levels. An angle-integrating display type electron spectrometer [7] was utilized to analyze the ejected photoelectrons energetically. Ge 3d and Si 2p spectra were obtained with a total instrumental resolution of approximately 0.2 eV.

## 3. Results

The Ge 3d and Si 2p core level photoemission spectra were acquired at a variety of sample temperatures

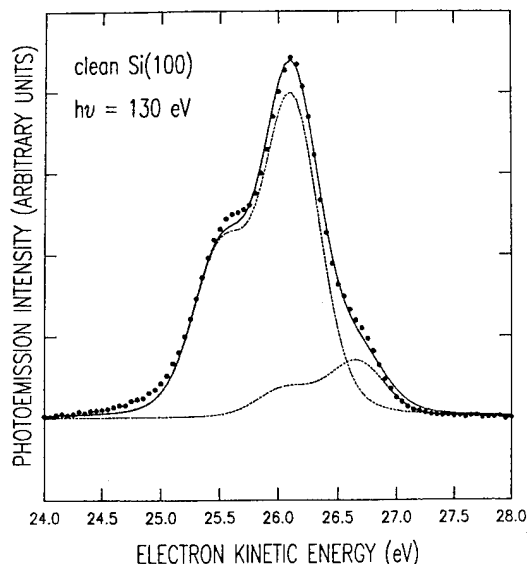


Fig. 1. Si 2p photoemission spectrum from a clean Si(100) surface: ---, empirical decomposition of the Si 2p feature into surface and bulk emission components; •, experimental data; — sum of the surface and bulk components.

between room temperature and 800 °C. As a point of reference, Fig. 1 shows an Si 2p soft X-ray photoemission spectrum characteristic of a clean Si(100) surface. The points in this spectrum, as well as in Fig. 2, represent the experimental data. The analysis of these data, as well as the Ge 3d and Si 2p spectra shown in Fig. 2, is as follows. A background representing the

secondary electron yield was subtracted first from the original data. The Ge 3d spectra, being somewhat more complex in appearance, had the  $3d_{3/2}$  spin-orbit component numerically deconvoluted following the initial background subtraction. The resultant Ge 3d data and the original Si 2p data were then fitted with a least-squares procedure to a sum of gaussian-broadened lorentzian line shapes. The lines in all spectra give the least-squares decomposition of the photoemission feature into its chemical components and the full lines display the sum of these fits.

The Si 2p spectrum shown in Fig. 1 clearly cannot be fitted with just a single, spin-orbit doublet peak. Following the work of Himpsel *et al.* [6] this spectrum was fitted with two gaussian-broadened lorentzian doublet peaks. The Si 2p feature comprises a bulk feature positioned at 26.12 eV and a surface component shifted to higher kinetic energy (lower binding energy) by about 0.55 eV. The energy separation between these two components agrees within 10% with that value previously reported by Himpsel *et al.* [6].

Figure 2 shows the soft X-ray photoemission spectra obtained from Ge 3d and corresponding Si 2p core levels following exposures of the Si(100) surface to  $\text{GeCl}_4$  at elevated temperatures. Figures 2(a) and 2(b) are observed following an exposure of the surface to 25 000 L of  $\text{GeCl}_4$  at a substrate temperature of 300 °C. Figures 2(c) and 2(d) show the same surface following an exposure at 500 °C.

#### 4. Discussion

Figure 2(a) clearly shows that  $\text{GeCl}_4$  chemisorbs readily and dissociatively onto the Si(100) surface following a 25 000 L exposure at a substrate temperature of 300 °C. The dotted line (large points) representing the experimental data shows a poorly resolved, rather broad band that extends for just about 4 eV. The smaller points show the data following the numerical removal of the  $3d_{3/2}$  spin-orbit component. The spin-orbit deconvolution procedure was necessary to discern distinct chemical contributions to the Ge 3d line shape. Although the spin-orbit deconvoluted data also appear to be poorly resolved, indicative of a very disordered surface, three components are assumed to contribute to the line shape. The component fitted to the leading edge of the high kinetic energy side has a binding energy that is approximately that expected for elemental Ge [8]. Thus we interpret this feature to be due to Ge bound to the Si substrate with no Cl atoms attached to it. The rest of the band may be fitted using the assumption that it arises from  $\text{GeCl}$  and  $\text{GeCl}_2$  components. It is assumed that each Ge chloride feature has identical linewidth and that the chemical shifts for each Cl atom

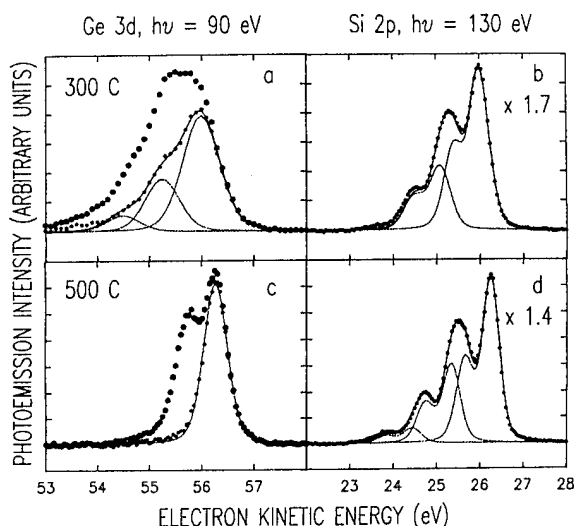


Fig. 2. Photoemission spectra of the Ge 3d and Si 2p core levels showing the results of exposing a clean Si(100) surface to (a), (b) 25 000 L of  $\text{GeCl}_4$  at 300 °C and (c), (d) 25 000 L of  $\text{GeCl}_4$  at 500 °C: •, experimental data in the Ge 3d spectra; •, data following the numerical removal of the  $3d_{3/2}$  spin-orbit component in the Ge 3d spectra; —, decomposition of Ge 3d and Si 2p into its chemical constituents; ---, sum of the component fits.

bound to a Ge atom are additive. With these assumptions, the lines composing the spin-orbit deconvoluted spectrum give the least-squares fit to the data shown and produce a chemical shift per Cl atom of 0.75 eV. This value is about 32% greater than that reported by Schnell *et al.* [9] for Cl adsorption on Ge(100) and Ge(111) surfaces but is in very good agreement with shifts observed in the photoemission spectra of gas phase species [10]. The discrepancy that we observe can be explained by the fact that we are not observing chlorinated Ge surface atoms but rather adsorbed Ge chloride species on an Si substrate.

Figure 2(b) shows the corresponding Si 2p spectrum which results following an exposure of the Si(100) surface to 25 000 L of GeCl<sub>4</sub> at 300 °C. There is one chemically shifted component located 0.91 eV to lower kinetic energy (higher binding energy) with respect to the Si bulk peak. This feature has been previously assigned to SiCl surface species [11]. Referring to the work of Yarmoff *et al.* [12] we estimate the Cl surface coverage to be approximately 0.68 monolayers, keeping in mind that the total surface coverage is somewhat greater because of the chemisorption of Ge and Ge chloride species which also occupy a number of Si surface sites. An upper limit to the amount of Ge deposited on the surface can be approximated. Since four Cl atoms are bonded to each Ge atom in GeCl<sub>4</sub>, and if it is assumed that no Cl desorbs from the surface during the exposure, then we can approximate that about 0.17 monolayers of Ge is deposited on the surface. Thus, the total coverage of the Si(100) surface following an exposure of the substrate to 25 000 L of GeCl<sub>4</sub> at 300 °C is about 0.85 monolayers.

Following an exposure of the same surface shown in Figs. 2(a) and 2(b) to 25 000 L of GeCl<sub>4</sub> at a substrate temperature of 500 °C, the Ge 3d band sharpens considerably, and the higher Ge chloride moieties that were previously observed following an exposure of the surface to 300 °C have been completely eliminated. The spin-orbit deconvoluted Ge 3d<sub>5/2</sub> spectrum is shown as the small-point, dotted line shape. This feature is clearly fitted with a single gaussian-broadened lorentzian line shape, indicating that elemental Ge from the decomposition of GeCl<sub>4</sub>, remains bonded to surface Si sites. While the amount of reduced Ge deposited on the surface is only about 4% greater than that observed in Fig. 2(a), the total Ge 3d intensity has decreased by about 37%.

The corresponding Si 2p spectrum obtained following an exposure of the surface at 500 °C shows the development of an additional chemically distinct feature shifted by 0.9 eV and 1.80 eV to lower kinetic energy (higher binding energy) relative to the SiCl and Si bulk peaks respectively. This feature has been previously assigned to SiCl<sub>2</sub> surface moieties [11]. The photoemission intensity contribution from the SiCl<sub>x</sub> species (where  $x = 1, 2$ ) to

the total Si 2p band has increased by about 42% with respect to that observed in Fig. 2(b), indicating that a maximum amount of Cl bonds to the surface at 500 °C. The Cl surface coverage is estimated to be about 0.81 monolayers at this point. The rise in the Cl-bound-to-Si intensity parallels closely, within the experimental error, the complete loss in intensity of the GeCl<sub>2</sub> and GeCl surface species. This observation indicates that surface Si sites which have become available at elevated temperatures as a result of the rapid desorption of Ge chloride species are readily attacked by Cl atoms which result from the dissociation of GeCl<sub>4</sub>. Although the intensity of the SiCl<sub>x</sub> species decreases at temperatures above 500 °C, Cl remains on the surface to about 800 °C, in agreement with previously reported results [13].

## 5. Conclusions

The chemisorption and reaction of GeCl<sub>4</sub> on Si(100) as a function of substrate temperature has been investigated by using core level photoemission spectroscopy. At a substrate temperature of 300 °C, GeCl<sub>4</sub> chemisorbs dissociatively, forming GeCl<sub>2</sub>, GeCl and elemental Ge bonding to the Si surface as well as Si monochloride surface species. Following a comparison of the results obtained from exposures of Si(100) to GeCl<sub>4</sub> at substrate temperatures from room temperature to 800 °C, we have found that a maximum amount of Ge, GeCl<sub>2</sub> and GeCl is deposited on the surface at 300 °C and we estimate this coverage to be slightly less than 0.2 monolayers. At 500 °C we observe the loss of the GeCl<sub>2</sub> and GeCl species, as elemental Ge remains bonded to the Si surface. In addition, the intensity of the SiCl<sub>2</sub> and SiCl species subsequently increases, as Cl from the thermal decomposition of GeCl<sub>4</sub> binds to available Si surface sites that were not present at lower temperatures.

In order to consider GeCl<sub>4</sub>/Si(100) as a possible system to use for ALE we propose the following. In the first step, GeCl<sub>4</sub> is adsorbed onto the surface at a temperature around 300 °C. This temperature is chosen as it represents the point at which a maximum amount of Ge, GeCl<sub>2</sub> and GeCl species are deposited on the surface. In addition, this temperature is below that at which the intermixing of Si and Ge is observed [14]. In the second step, atomic H, which is known to remove Cl from Si surfaces [15], would be used to remove all Cl from the surface. This would possibly leave behind the newly deposited Ge as well as unterminated Si dangling bonds ready for the next exposure of GeCl<sub>4</sub>. We plan to investigate thoroughly the effectiveness of atomic H in removing Cl from the Si surface as well as from the deposited Ge and these results will be published elsewhere in a comparative report regarding the reaction of GeCl<sub>4</sub> on Si(100) and Si(111) surfaces.

## Acknowledgment

D.L.S. would like to thank Louis J. Terminello.

## References

- 1 A. Usui and H. Sunakawa, *Jpn. J. Appl. Phys.*, **25** (1986) L212.
- 2 A. Doi, Y. Aoyagi and S. Namba, *Appl. Phys. Lett.*, **48** (1986) 1787.
- 3 K. Ohkawa, *J. Cryst. Growth*, **111** (1991) 797.
- 4 J. Nishizawa, H. Abe and T. Kurobayashi, *J. Electrochem. Soc.*, **132** (1985) 1197.
- 5 S. M. Bedair, M. A. Tishler, T. Katsuyama and N. A. El-Masry, *Appl. Phys. Lett.*, **47** (1985) 51.
- 6 F. J. Himpsel, F. R. McFeely, A. Taleb-Ibrahimi and J. A. Yarmoff, *Phys. Rev. B*, **38** (1988) 6084.
- 7 D. E. Eastman, J. J. Donelon, N. C. Hien and F. J. Himpsel, *Nucl. Instrum. Methods*, **172** (1980) 327.
- 8 D. A. Lapiano-Smith and F. R. McFeely, *Proc. Mater. Res. Soc.*, submitted.
- 9 R. D. Schnell, F. J. Himpsel, A. Bogen, D. Rieger and W. Steinmann, *Phys. Rev. B*, **32** (1985) 8052.
- 10 A. Bakke, C. Chen and W. Jolly, *J. Electron Spectrosc. Relat. Phenom.*, **20** (1980) 333.
- 11 L. J. Whitman, S. A. Joyce, J. A. Yarmoff, F. R. McFeely and L. J. Terminello, *Surf. Sci.*, **232** (1990) 297.
- 12 J. A. Yarmoff, D. K. Shuh, T. D. Durbin, C. W. Lo, D. A. Lapiano-Smith, F. R. McFeely and F. J. Himpsel, *J. Vac. Sci. Technol.*, to be published.
- 13 P. Gupta, P. A. Coon, B. G. Koehler and S. M. George, *Surf. Sci.*, **249** (1991) 92.
- 14 A. J. Hoeven, J. Aarts and P. K. Larsen, *J. Vac. Sci. Technol. A*, **7** (1989) 5.
- 15 R. E. Thomas, R. A. Rudder and R. J. Markunas, *Mater. Res. Soc. Symp. Proc.*, **204** (1991) 327.

# Si<sub>2</sub>H<sub>6</sub> adsorption and dissociation pathways on Ge(001)2 × 1: mechanisms for heterogeneous atomic layer epitaxy

R. Tsu, D. Lubben, T. R. Bramblett and J. E. Greene

Materials Science Department, The Coordinated Science Laboratory and The Materials Research Laboratory, University of Illinois, 1101 West Springfield, Urbana, IL 61801 (USA)

## Abstract

Auger electron spectroscopy (AES), electron energy loss spectroscopy (EELS), and reflection high-energy electron diffraction (RHEED) were used to investigate the adsorption, surface dissociation, and thermal desorption of Si<sub>2</sub>H<sub>6</sub> on Ge(001)2 × 1. At room temperature, EELS results show that Si<sub>2</sub>H<sub>6</sub> is dissociatively adsorbed onto Ge dangling bonds and further decomposes to yield a disordered overlayer consisting of SiH<sub>2</sub>, GeH, and undissociated SiH<sub>3</sub>. A saturated coverage of approximately 0.5 monolayers is obtained with Si<sub>2</sub>H<sub>6</sub> exposures greater than or equal to  $1 \times 10^{15}$  cm<sup>-2</sup>. RHEED results indicate that, in contrast to Si<sub>2</sub>H<sub>6</sub>-saturated Si(001), the saturated Ge(001) surface still exhibits a significant fraction of dimerized bonds. H<sub>2</sub> desorption from the silicon dihydride phase occurs during 1 min anneals at  $T_a > 150$  °C while hydrogen desorption from the silicon monohydride phase and Ge surface segregation both occur at significant rates at  $T_a \geq 350$  °C. All hydrogen is desorbed by 450 °C, compared with  $\approx 550$  °C for the saturated Si(001) surface.

Disilane (Si<sub>2</sub>H<sub>6</sub>) is a promising precursor molecule for silicon growth by gas-source molecular beam epitaxy (GS-MBE) [1, 2] and atomic layer epitaxy (ALE) [3, 4]. Compared with silane (SiH<sub>4</sub>), Si<sub>2</sub>H<sub>6</sub> exhibits several orders of magnitude higher sticking probabilities on Si [5, 6], a lower decomposition activation energy for both gas-phase [7, 8] and surface [9] reactions leading to lower desorption temperatures [1–4], and a larger UV adsorption cross-section [10, 11] for photoinduced deposition [12, 13]. Most of the above advantages are related to the fact that the Si–Si bond (3.3 eV) is weaker than the Si–H bond (3.8 eV) [14].

Si<sub>2</sub>H<sub>6</sub> adsorption and thermal decomposition has been investigated using electron energy loss spectroscopy (EELS) [15], temperature-programmed static secondary-ion mass spectrometry (TPSSIMS) [16], reflection high-energy electron diffraction (RHEED) [15], and scanning tunneling microscopy (STM) and spectroscopy (STS) [17, 18] on Si(001)2 × 1 and by temperature-programmed desorption (TPD) [19] and multiple internal reflection IR spectroscopy (MIRS) [20] on Si(111)7 × 7. We have recently shown that silicon single-crystal films can be grown on Si(001)2 × 1 substrates at temperatures as low as 160 °C by UV photostimulated ALE from Si<sub>2</sub>H<sub>6</sub> [4]. The ALE deposition rate  $R$  per growth cycle remained constant and kinetically self-limited at 0.4 monolayers (ML) over a very wide range of deposition parameters. A film growth model, based upon the results of deposition experiments, Monte Carlo simulations, and our previous adsorption–desorption measurements [15], was

used to describe the reaction pathway for the process. Si<sub>2</sub>H<sub>6</sub> is dissociatively adsorbed on Si surface dimers as two silyl (SiH<sub>3</sub>) radicals which subsequently dissociate to silylene (SiH<sub>2</sub>) and H. Site blocking during the adsorption and surface dissociation steps limit the surface coverage to  $2.9 \times 10^{14}$  SiH<sub>2</sub> cm<sup>-2</sup> (hence  $R = 0.43$  ML per cycle). The saturated surface is passive to further Si<sub>2</sub>H<sub>6</sub> exposure. ArF or KrF laser pulses (approximately 20 ns) were used to desorb H, following a Si<sub>2</sub>H<sub>6</sub> exposure, and the growth cycle repeated until the desired film thickness was obtained. Recent STM measurements provide further insights regarding nucleation, surface mobilities, and two-dimensional island growth [17].

By comparison with Si, relatively few data are available concerning Si<sub>2</sub>H<sub>6</sub> interactions on Ge(111) [21] and essentially nothing has been published on Si<sub>2</sub>H<sub>6</sub>–Ge(001) reactions. In this paper, we report the initial results of an investigation, utilizing Auger electron spectroscopy (AES), EELS, and RHEED, of the adsorption and thermally induced dissociation of Si<sub>2</sub>H<sub>6</sub> on Ge(001)2 × 1. This work provides a basis for subsequent film-growth studies of heterogeneous Si ALE on Ge(001).

The experiments were carried out in a three-chamber stainless-steel  $10^{-10}$  Torr load-locked ultrahigh-vacuum (UHV) Si ALE system [3, 4, 15]. Disilane flow was regulated via a precision leak valve and introduced into the chamber through a gas doser directed at the Ge surface from a distance of 2.3 cm. The impingement rate at the sample [22] during disilane exposure was

maintained at either  $2.1 \pm 0.6 \times 10^{11}$  or  $1.0 \pm 0.3 \times 10^{13} \text{ cm}^{-2} \text{ s}^{-1}$ . The RHEED electron accelerating voltage was 20 kV and the beam was adjusted to intercept the substrate at an angle of approximately  $1.5^\circ$ . First-derivative AES spectra were obtained using a primary electron energy  $E_p = 3 \text{ keV}$  and a cylindrical mirror analyzer (CMA) with a modulation voltage  $V_m = 1.87 \text{ V}$ . EELS spectra were acquired in negative second-derivative mode with  $E_p = 100 \text{ eV}$ ,  $V_m$  either 0.50 or 0.63 V, and a primary beam current of less than  $0.3 \mu\text{A}$ .

The  $\text{Ge}(001)$  substrates used in these experiments were  $7 \text{ mm} \times 20 \text{ mm}$  plates cleaved from  $0.4 \text{ mm}$  thick n-type ( $1\text{--}5 \Omega \text{ cm}$ ) wafers. Initial cleaning consisted of degreasing followed by a UV ozone treatment as described in ref. 4. The wafers were degassed at  $250^\circ \text{C}$  for 1 h, and rapidly heated to  $450^\circ \text{C}$  for 5 min to desorb the oxide overlayer. Substrate heating was accomplished resistively by passing current through the sample. Following the *in situ* cleaning procedure, the substrates exhibited sharp  $2 \times 1$  surface reconstruction patterns typical of clean  $\text{Ge}(001)$  surfaces while AES spectra showed no indication of C or O.

The Si LVV 92 eV and Ge LMM 1147 eV peak-to-peak intensities  $I$  were measured as a function of  $\text{Si}_2\text{H}_6$  dose  $\phi$  from 0 (the clean surface) to  $8 \times 10^{16} \text{ cm}^{-2}$  at room temperature.  $I_{\text{Ge}}$  decreased and  $I_{\text{Si}}$  increased with increasing  $\phi$  until saturation was achieved at  $\phi \approx 10^{15} \text{ cm}^{-2}$  with an estimated coverage  $\theta_{\text{Si}}$  of 0.5 ML as determined by AES based upon published values for

the escape depth of Ge 47 eV MNN Auger electrons through a Si overlayer deposited by MBE [23].

An EELS spectrum from a clean  $\text{Ge}(001)2 \times 1$  surface, with peak assignments from ref. 24, is shown in Fig. 1.  $E_1$  ( $3.0 \pm 0.2 \text{ eV}$ ) and  $E_2$  ( $4.4 \pm 0.2 \text{ eV}$ ) are associated with bulk band transitions while  $\hbar\omega_s$  ( $10.7 \pm 0.2 \text{ eV}$ ) and  $\hbar\omega_p$  ( $16.0 \pm 0.2 \text{ eV}$ ) are due to surface and bulk plasmons, respectively. The features  $S_2$  ( $7.9 \pm 0.8 \text{ eV}$ ),  $S'_2$  ( $9.3 \pm 0.8 \text{ eV}$ ), and  $S_3$  ( $14.5 \pm 0.8 \text{ eV}$ ) arise from transitions between backbond states and dangling-bond states in the reconstructed surface. The surface state transition  $S_1$  at  $1.3 \text{ eV}$  [24] is lost in the tail of the elastic peak. The higher-energy loss peaks labeled  $d_s$  ( $29.1 \pm 0.2 \text{ eV}$ ),  $d_1$  ( $30.5 \pm 0.2 \text{ eV}$ ),  $d_2$  ( $32.9 \pm 0.2 \text{ eV}$ ), and  $d_3$  ( $34.5 \pm 0.2 \text{ eV}$ ) have been ascribed to transitions between Ge 3d core levels and empty dangling bond ( $d_s$ ) and conduction band ( $d_1$ ,  $d_2$ , and  $d_3$ ) states, respectively [24].

Typical EELS spectra acquired following  $\text{Si}_2\text{H}_6$  exposures at room temperature (RT) are also shown in Fig. 1. Comparing the spectra for  $\phi = 1.4 \times 10^{13} \text{ cm}^{-2}$  and  $3.4 \times 10^{13} \text{ cm}^{-2}$  with the clean surface spectrum shows that these exposures resulted in sufficient adsorption to reduce the intensities of the surface dangling-bond peaks and decrease  $\hbar\omega_s$  with respect to  $\hbar\omega_p$ .  $E_1$  and  $E_2$  broaden following  $\text{Si}_2\text{H}_6$  exposure and decrease in intensity while a new peak, which we have labeled GSH, begins to emerge at  $8.2 \pm 0.2 \text{ eV}$ . With further increases in  $\text{Si}_2\text{H}_6$  exposure, the surface dangling-bond peaks are no longer observable, the surface plasmon peak continues to decrease with respect to the bulk plasmon peak, and the intensity of the GSH peak grows and shifts to lower energy as the remaining peaks become weaker. For  $\phi > 3 \times 10^{14} \text{ cm}^{-2}$ , the  $E_1$  and  $E_2$  peaks are no longer resolvable as hydrogen-related peaks occurring at 2.8 and 5.1 eV dominate the low-energy region of the spectra. Further increases in  $\text{Si}_2\text{H}_6$  dose above  $\approx 1 \times 10^{15} \text{ cm}^{-2}$  have no observable effect on the EELS spectra.

We have shown previously that during  $\text{Si}_2\text{H}_6$  adsorption on clean  $\text{Si}(001)2 \times 1$ , a loss peak SH attributed to a transition from Si-H bond states, emerges initially at  $8.4 \text{ eV}$  when  $\phi \geq 4 \times 10^{14} \text{ cm}^{-2}$  and shifts to lower energy with higher coverages to reach  $8.0 \text{ eV}$  at saturation exposure [3, 15]. The  $8.0 \text{ eV}$  position is characteristic of a surface which is nearly saturated with  $\text{SiH}_2$ . Surnev and Tikhov [25] reported observing a H-related EELS peak GH at  $8.2 \text{ eV}$  for H coverage on  $\text{Ge}(001)$  equal to 0.75 of the saturated value. Based upon their TPD data, together with previous MIRS [26] and UV photoemission spectroscopy [27] results, they associated the GH EELS peak with the GeH monohydride surface phase. Thus, we attribute the GSH peak in Fig. 1 which emerges at  $8.2 \text{ eV}$  with  $\phi \geq 1.4 \times 10^{13} \text{ cm}^{-2}$  as being a convolution of SH and

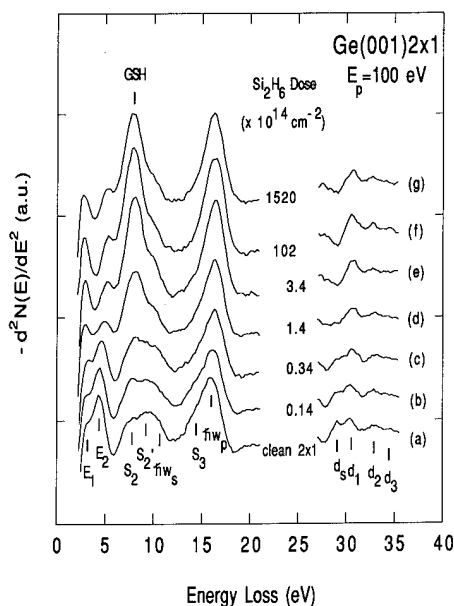


Fig. 1. EELS spectra, obtained using a 100 eV primary electron energy, from a  $\text{Ge}(001)2 \times 1$  surface after exposure at room temperature of an  $\text{Si}_2\text{H}_6$  dose of (a) 0, (b)  $1.4 \times 10^{13}$ , (c)  $3.4 \times 10^{13}$ , (d)  $1.4 \times 10^{14}$ , (e)  $3.4 \times 10^{14}$ , (f)  $1.0 \times 10^{15}$ , and (g)  $1.5 \times 10^{17} \text{ cm}^{-2}$ .

GH peaks due to a mixture of  $\text{SiH}_2$  and  $\text{GeH}$  formed through the surface decomposition reaction  $\text{SiH}_3(\text{ad}) \rightarrow \text{SiH}_2(\text{ad}) + \text{GeH}(\text{ad})$  following the dissociative chemisorption of  $\text{Si}_2\text{H}_6$  on surface dangling bonds. Based upon previous TPSSIMS [16] and ALE [4] data for  $\text{Si}_2\text{H}_6$  adsorbed on  $\text{Si}(001)2 \times 1$  at RT and MIRS [21] results for  $\text{Ge}(111)$ , there is likely to be some undecomposed  $\text{SiH}_3$  present as well. The intensity of the GSH peak in Fig. 1 increased with increasing  $\text{Si}_2\text{H}_6$  exposure owing to continued adsorption while the peak position decreased. At saturation exposure, the GSH peak position was 7.9 eV.

Zero-order Laue zone RHEED patterns along the  $[\bar{1}10]$  azimuth from clean  $\text{Ge}(001)2 \times 1$  substrates show approximately equal intensities in fundamental and half-order diffraction rods. A typical example is shown in Fig. 2(a). The intensity of half-order, with respect to the fundamental rods, decreases with increasing  $\text{Si}_2\text{H}_6$  exposure. For disilane doses  $\phi \geq 2.5 \times 10^{13} \text{ cm}^{-2}$ , both integral and non-integral reflection intensities decreased with respect to the 00 reflection as the diffuse background intensity increased owing to surface disorder resulting from  $\text{Si}_2\text{H}_6$  adsorption at random sites. At saturation exposure, the half-order reflections were still relatively strong as shown in Fig. 2(b). This is quite different from the case of  $\text{Si}_2\text{H}_6$  adsorption on  $\text{Si}(001)2 \times 1$  where the half-order reflections essentially disappeared for  $\phi \geq \phi_{\text{sat}}$ . The saturated  $\text{Ge}(001)$  sur-

face still has a significant fraction of dimerized bonds which have been shown by total energy calculations to be more stable than their Si counterparts owing primarily to differences in the buckling energy [28]. Our results are consistent with the finding that hydrogen-saturated  $\text{Ge}(001)$  remains  $2 \times 1$  while  $\text{Si}(001)$  reverts to  $1 \times 1$  [26, 27]. The average lattice constant obtained from Fig. 2(b) is 0.556 nm compared with 0.565 nm from the clean  $\text{Ge}(001)$  surface in Fig. 2(a).

Clean Ge substrates were exposed to a saturation  $\text{Si}_2\text{H}_6$  dose and then annealed at temperatures  $T_a$  between 150 and 550 °C for 1 min each after which peak-to-peak intensities of the Ge LMM 1147 eV and Si LVV 92 eV AES lines were measured. The Ge intensity was found to increase while the Si intensity was attenuated for  $T_a \geq 350$  °C, signaling Ge segregation to the surface in agreement with Si 2p and Ge 3d core-level photoemission observations of MBE Si layers on Ge [29].

EELS spectra acquired following annealing are shown in Fig. 3. The GSH and  $\hbar\omega_p$  peak intensities both decreased during 1 min anneals at  $T_a = 150$  °C while the GSH peak split into two components with the main peak located at  $7.7 \pm 0.2$  eV and a shoulder peak at  $8.2 \pm 0.2$  eV. The splitting, while small, was quite reproducible. The shoulder peak at 8.2 eV is in good agreement with the reported position for  $\text{GeH}$  [25] while the main peak is at a slightly lower energy than

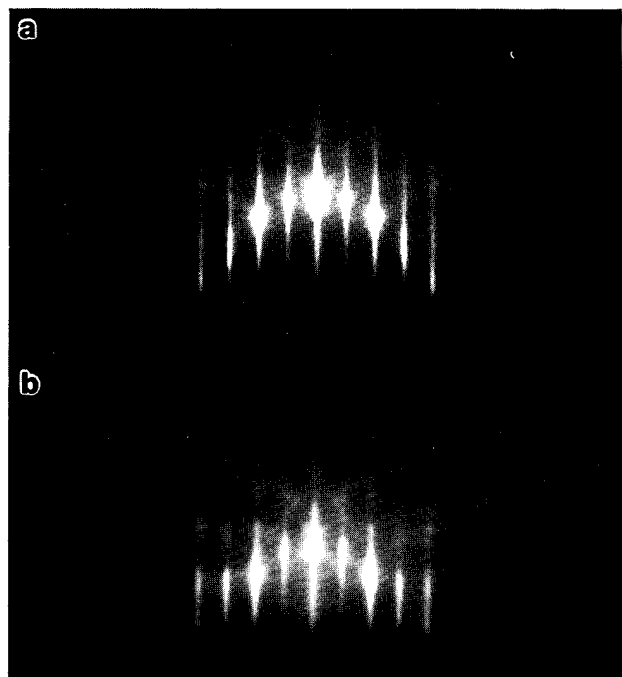


Fig. 2. RHEED patterns from (a) a clean  $\text{Ge}(001)2 \times 1$  surface and (b) after exposure at room temperature to an  $\text{Si}_2\text{H}_6$  dose of  $1.0 \times 10^{16} \text{ cm}^{-2}$ .

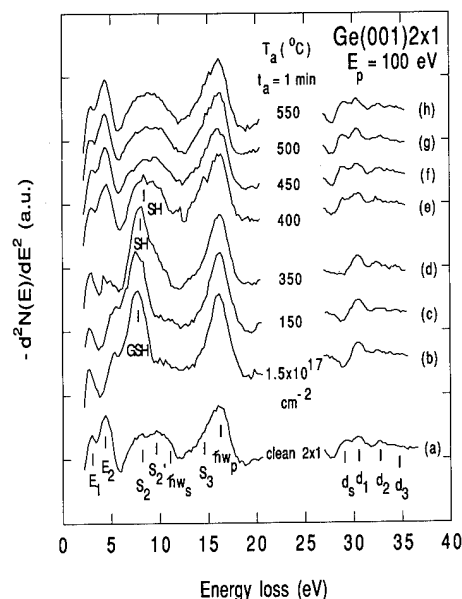


Fig. 3. EELS spectra, obtained using a primary electron energy  $E_p$  of 100 eV, from (a) a clean  $\text{Ge}(001)2 \times 1$  surface and (b) a  $\text{Ge}(001)2 \times 1$  surface after exposure at room temperature of an  $\text{Si}_2\text{H}_6$  dose of  $1.5 \times 10^{17} \text{ cm}^{-2}$  and then annealed for 1 min at (c) 150 °C, (d) 350 °C, (e) 400 °C, (f) 450 °C, (g) 500 °C, and (h) 550 °C.

our previous results for  $\text{SiH}_2$  on Si [15]. These assignments,  $\text{GeH}$  and  $\text{SiH}_2$ , are consistent with the peak splitting being caused by the decomposition of residual  $\text{SiH}_3$ . Previous Si ALE results showed the activation energy for decomposition of  $\text{SiH}_3$  on  $\text{Si}(001)$  to be 0.5 eV with all residual silyl radicals dissociated by  $\approx 180^\circ\text{C}$ . Excess residual  $\text{SiH}_3$  on the  $\text{Si}_2\text{H}_6$  saturated  $\text{Ge}(001)$  surface is also consistent with the RHEED results showing a persistent  $(2 \times 1)$  reconstruction assuming that  $\text{SiH}_3$  dissociation results in dimer breaking.

At  $T_a \geq 350^\circ\text{C}$ , Fig. 3 shows that the GSH integrated intensity has decreased, the splitting is no longer observable, and the peak is due primarily to SH. The  $\text{S}_2'$  back-bond peak, due to hydrogen desorption from the Ge monohydride phase, has reappeared on the high-energy side of GSH and the Ge peak  $\text{E}_2$  is again resolved. At the same time, and consistent with the appearance of the  $\text{d}_s$  dangling-bond peak indicating an increasing concentration of germanium surface dimers, RHEED patterns began to exhibit increased half-order, with respect to fundamental diffraction rod intensities. Taken together, these results show that the mixed dihydride-monohydride surface is converted to a mostly monohydride surface at temperatures less than  $350^\circ\text{C}$  and hydrogen is desorbed from the Si monohydride phase at  $T_a \geq 350^\circ\text{C}$  as significant Ge surface segregation begins to occur.

The dangling-bond peak  $\text{d}_s$  becomes visible at  $T_a \geq 400^\circ\text{C}$  as the GSH peak, which continues to decrease with higher annealing temperatures, shifts up in energy to 8.4 eV. GSH is unobservable above about  $450^\circ\text{C}$  as the remaining hydrogen is desorbed. Annealing at higher temperatures results in EELS spectra which are essentially indistinguishable from the germanium clean-surface spectrum and no further changes are observed. RHEED diffraction rod spacings obtained from  $\text{Ge}(001)$  substrates exposed to  $\text{Si}_2\text{H}_6$  saturation doses and then annealed for 1 min at  $T_a \geq 450^\circ\text{C}$  were essentially identical with the values obtained from the clean substrate surface.

From previous TPD [19] and EELS [15] results, H desorbs from Si monohydride at temperatures greater than or approximately  $450\text{--}500^\circ\text{C}$  while TPD results for H-adsorbed  $\text{Ge}(111)$  [25] show that desorption occurs at  $\approx 300^\circ\text{C}$ . The Si-H binding energy is known to be larger than that of Ge-H ( $\approx 3.6$  [30, 31] and 3.0 eV [27] respectively) [32]. Thus, in the present experiments, the H desorption observed at  $\leq 350^\circ\text{C}$  from  $\text{Si}_2\text{H}_6$ -saturated  $\text{Ge}(001)$  was primarily from Ge monohydride rather than from Si monohydride. We believe that Ge surface segregation, driven by a decrease in surface energy and strain effects [33], then occurred as H on the Si monohydride islands diffused to available Ge dangling bonds. All H was desorbed from the primarily Ge surface by  $450^\circ\text{C}$ .

The overall trends we observe in the present  $\text{Si}_2\text{H}_6/\text{Ge}(001)2 \times 1$  experiments are similar to those for  $\text{Si}_2\text{H}_6$  interactions on  $\text{Si}(001)2 \times 1$  [4, 15, 17]—the Si saturation coverage at room temperature is approximately 0.5 ML and the overlayer is disordered—but important differences exist. The half-order RHEED diffraction rods are still relatively strong on the saturated  $\text{Ge}(001)$  surface, while almost undetectable on saturated  $\text{Si}(001)$ . Hydrogen desorption from Ge monohydride, indicated by the re-emergence of EELS dangling-bond peaks, occurs at temperatures which are approximately  $150^\circ\text{C}$  less than for Si monohydride, and Ge begins to segregate to the surface at  $T_a$  near  $350^\circ\text{C}$  as hydrogen is lost from the Si monohydride phase. All hydrogen is desorbed by  $450^\circ\text{C}$ , compared with  $\approx 550^\circ\text{C}$  for the saturated  $\text{Si}(001)$  surface. These results indicate that the growth parameter window for heterogeneous  $\text{Si}_2\text{H}_6$  ALE on  $\text{Ge}(001)2 \times 1$  will be considerably narrower than on  $\text{Si}(001)2 \times 1$  until steady-state deposition is achieved.

### Acknowledgments

The authors gratefully acknowledge the financial support of the Office of Naval Research, through contract number N00014-90-J-1241 administered by Dr. George Wright, and the Semiconductor Research Corporation during the course of this research.

### References

- 1 H. Hirayama, T. Tatsumi and N. Aizaki, *Appl. Phys. Lett.*, **52** (1988) 1484.
- 2 H. Hirayama, M. Hiroi, K. Koyama and T. Tatsumi, *Appl. Phys. Lett.*, **56** (1990) 2645.
- 3 Y. Suda, D. Lubben, T. Motooka and J. E. Greene, *J. Vac. Sci. Technol. B*, **7** (1989) 1171.
- 4 D. Lubben, R. Tsu, T. R. Bramblett and J. E. Greene, *J. Vac. Sci. Technol. A*, **9** (1991) 223.
- 5 S. M. Gates, *Surf. Sci.*, **195** (1988) 207.
- 6 S. M. Gates, C. M. Greenlief, D. B. Beach and P. A. Holbert, *J. Chem. Phys.*, **92** (1990) 3144.
- 7 K. F. Roenigk, K. F. Jenson and R. W. Carr, *J. Phys. Chem.*, **91** (1987) 5732.
- 8 J. G. Martin, M. A. Ring and H. E. O'Neal, *Int. J. Chem. Kinetics*, **19** (1987) 715.
- 9 F. Mieno, S. Nakamura, T. Deguchi, M. Maeda and K. Inayoshi, *J. Electrochem. Soc.*, **134** (1987) 2320.
- 10 M. Suto and L. C. Lee, *J. Chem. Phys.*, **84** (1986) 1160.
- 11 U. Itoh, Y. Toyoshima and H. Onuki, *J. Chem. Phys.*, **85** (1986) 4867.
- 12 S. Nishida, T. Shiimoto, A. Yamada, S. Karasawa, M. Konagai and K. Takahashi, *Appl. Phys. Lett.*, **49** (1986) 79.
- 13 K. Kumata, U. Ttoh, Y. Toyoshima, N. Tanaka, H. Anzai and A. Matsuda, *Appl. Phys. Lett.*, **48** (1986) 1380.
- 14 P. M. Agrawal, D. L. Thompson and L. M. Raff, *J. Chem. Phys.*, **92** (1990) 1069.
- 15 Y. Suda, D. Lubben, T. Motooka and J. E. Greene, *J. Vac. Sci. Technol. A*, **8** (1990) 61.



- 16 S. M. Gates, C. M. Greenlief and B. B. Beach, *J. Chem. Phys.*, **93** (1990) 7493.
- 17 D.-S. Lin, E. S. Hirschorn, T.-C. Chiang, R. Tsu, D. Lubben and J. E. Greene, *Phys. Rev. B*, **45** (1992) 3494.
- 18 J. J. Boland, *Phys. Rev. B*, **44** (1991) 1383.
- 19 R. Imbihl, J. E. Demuth, S. M. Gates and B. A. Scott, *Phys. Rev. B*, **39** (1989) 5222.
- 20 K. J. Uram and U. Jansson, *J. Vac. Sci. Technol. B*, **7** (1989) 1176.
- 21 J. E. Crowell and G. Lu, *J. Electron Spectrosc. Relat. Phenom.*, **54** (1990) 1045.
- 22 P. Clausen, *Z. Phys.*, **66** (1930) 471.
- 23 P. H. Mahowald, R. S. List, W. E. Spicer, J. Woicik and P. Pianetta, *J. Vac. Sci. Technol. B*, **3** (1985) 1252.
- 24 R. Ludeke and A. Koma, *Phys. Rev. B*, **13** (1976) 739.
- 25 L. Surnev and M. Tikhov, *Surf. Sci.*, **138** (1984) 40.
- 26 Y. J. Chabal, *Surf. Sci.*, **168** (1986) 594.
- 27 J. A. Appelbaum, G. A. Baraff, D. R. Hamann, H. D. Hangstrum and T. Sakurai, *Surf. Sci.*, **70** (1977) 654.
- 28 J. Wang and J. D. Joannopoulos, private communication, 1992.
- 29 A. J. Hoeven, J. Aarts and P. K. Larsen, *J. Vac. Sci. Technol. A*, **7** (1989) 5.
- 30 B. G. Koehler, C. H. Mak, D. A. Arthur, P. A. Coon and S. M. George, *J. Chem. Phys.*, **89** (1988) 1709.
- 31 U. Höfer, L. Li and T. F. Heinz, *Phys. Rev. B*, **16** (1992) 9485.
- 32 S.-M. Jang and R. Reif, *Appl. Phys. Lett.*, **59** (1991) 3162.
- 33 P. C. Kelires and J. Tersoff, *Phys. Rev. B*, **63** (1989) 1164.

# Hydrocarbon surface chemistry on Si(100)

C. C. Cheng, P. A. Taylor\*, R. M. Wallace\*\*, H. Gutleben\*\*\*, L. Clemen†††, M. L. Colaianni, P. J. Chen†, W. H. Weinberg††, W. J. Choyke††† and J. T. Yates, Jr.

*Surface Science Center, Department of Chemistry, University of Pittsburgh, Pittsburgh, PA 15260 (USA)*

## Abstract

The interaction of various hydrocarbon species with the Si(100) surface has been investigated using several surface science techniques. The efficiency of carbon deposition is related to the efficiency of SiC thin film formation. The hydrocarbon species studied include acetylene ( $C_2H_2$ ), ethylene ( $C_2H_4$ ), and the adsorbed methyl group ( $CH_3(a)$ ). In the case of the chemisorption of acetylene and ethylene, the  $\pi$ -bond of the olefinic molecules interacts with the dimer unit ( $Si_2$ ) on the Si(100)-(2 × 1) surface. One monolayer of both acetylene and ethylene on Si(100) has been achieved by saturating the surface at 105 K, and a di- $\sigma$ -bonding structure is proposed for one molecule per  $Si_2$  dimer unit at monolayer coverage. Upon heating, the majority (>95%) of the adsorbed acetylene undergoes dissociation to produce chemisorbed carbon and  $H_2(g)$ . In contrast, chemisorbed ethylene desorbs intact from Si(100) at ~550 K, with approximately 2% of the monolayer undergoing dissociation. The low activation energy for desorption ( $E_d(C_2H_4) = 38 \text{ kcal mol}^{-1}$ ) allows  $C_2H_4$  to desorb prior to significant decomposition.

Investigations of the thermal behavior of  $CH_3(a)$  on Si(100) show that the adsorbed methyl group is stable up to ~600 K. At higher temperatures,  $CH_3(a)$  decomposes to  $CH_x(a)$  ( $x < 3$ ) species, and subsequently liberates  $H_2(g)$ , leaving carbon on the surface. Less than 1% of the adsorbed carbon species ( $CH_x$ ,  $x \leq 3$ ) desorbs in the form of  $C_2$  hydrocarbon species upon heating. This indicates that the methyl group is an efficient source of surface carbon by thermal decomposition.

## 1. Introduction

The mechanism by which a molecule interacts with a crystalline semiconductor surface is of fundamental importance in semiconductor technologies. Various vapor deposition methods and epitaxial growth procedures are largely dependent on the interaction of gaseous molecules with the substrate surface. Knowledge of the nature of the elementary chemical processes at the surface, and the bonding structure as well as the chemical nature of the chemisorbed species, is therefore important.

The adsorption and thermal behavior of hydrocarbon molecules on well-defined silicon surfaces is of considerable interest since such species are used in the formation of SiC thin films [1–10] or in epitaxial

diamond film growth (for a recent review of diamond growth see ref. 11). This paper is a review of our investigations of the interaction of various hydrocarbon species with the Si(100) surface [12–17]. It is known that the reconstructed Si(100) surface consists of parallel rows of  $Si_2$  dimers with one dangling bond on each surface Si atom. As a result of Si dimerization, a (2 × 1) superlattice is observed by low energy electron diffraction (LEED) [18], and by scanning tunneling microscopy (STM) [19]. The study of the chemisorption of a number of hydrocarbon molecules on the Si(100) surface has shown that the  $\pi$ -bond in an unsaturated hydrocarbon is the active center for the reaction of these molecules with a clean Si(100) surface [20]. In contrast, the saturated hydrocarbon molecules, containing only single bonds ( $\sigma$ -bonds) between carbon atoms, do not react with the clean Si(100) surface at low temperatures [20].

The hydrocarbon species studied in this work include acetylene ( $C_2H_2$ ) [12, 15], ethylene ( $C_2H_4$ ) [12–14], and the adsorbed methyl group ( $CH_3(a)$ ) produced by dissociative adsorption of  $CH_3I$  [16, 17]. Various surface science techniques have been employed, including quantitative uptake measurements, temperature programmed desorption (TPD), Auger electron spectroscopy (AES) and vibrational spectroscopy. Both  $C_2H_2$  and  $C_2H_4$  are studied because of the multiple

\*Present address: Laboratory of Applied Physics, Technical University of Denmark, Denmark.

\*\*Present address: Texas Instruments, Inc., Central Research Laboratories, MS147, Dallas, TX 75265, USA.

\*\*\*Present address: Lenzing Ag, A-4800 Lenzing, Austria.

†Present address: Department of Chemistry, Texas A & M University, College Station, TX 77843, USA.

††Present address: Department of Chemical and Nuclear Engineering, University of California, Santa Barbara, CA 93106, USA.

†††Department of Physics, University of Pittsburgh, Pittsburgh, PA 15260, USA.

carbon-carbon bonds in these two molecules and also because both molecules have been used in the growth of SiC films [2-6, 10]. One monolayer of both acetylene and ethylene on Si(100) has been achieved by saturating the surface at 105 K, and a di- $\sigma$ -bonding structure is proposed for one molecule per Si<sub>2</sub> dimer unit at monolayer coverage. Upon heating, the majority (>95%) of the adsorbed acetylene undergoes dissociation to produce chemisorbed carbon and H<sub>2</sub>(g). In contrast, chemisorbed ethylene does not dissociate appreciably on Si(100) and desorbs intact at ~550 K.

The methyl radical is also generally considered as an active species for carbon deposition using plasma sources as well as in high temperature chemical vapor deposition (CVD) reactors [9, 11]. Our investigations of the thermal behavior of CH<sub>3</sub>(a) on Si(100) show that the adsorbed methyl group is stable up to ~600 K. At higher temperatures, CH<sub>3</sub>(a) decomposes to CH<sub>x</sub>(a) ( $x < 3$ ) species. Combining the results from AES and TPD studies, we conclude that the methyl group is an efficient source of surface carbon by thermal decomposition.

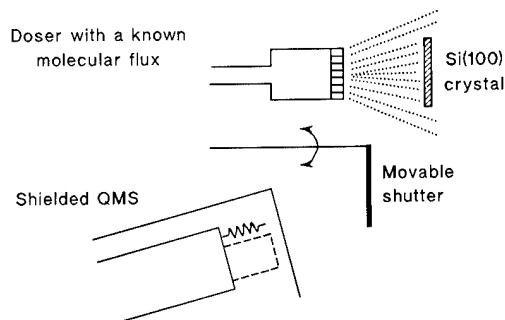
## 2. Experimental details

The ultrahigh vacuum (UHV) system (with a base pressure of  $1 \times 10^{-10}$  Torr) and the Si(100) crystal preparation have been described previously [12-16]; selected aspects will be summarized here. The system is equipped with an Auger electron spectrometer, an argon ion sputtering gun, a collimated and calibrated microcapillary array doser [21], and a multiplexed quadrupole mass spectrometer (QMS) with capabilities for both random flux and line-of-sight detection [22]. Heating of the Si(100) crystal ( $15 \times 15 \times 1.5$  mm<sup>3</sup>; p-type; B-doped; 10  $\Omega$  cm) is provided by a Honeywell programmable temperature controller used to drive a feedback circuit to control the power to the crystal [23].

For the adsorption of molecular species, a calibrated microcapillary array doser was used to deliver the gas molecules onto the Si(100) surface [21] (Fig. 1(A)). The doser contains an internal pinhole aperture (2  $\mu$ m diameter) whose conductance has been calibrated accurately for the molecular species to be studied [12]. The partial pressure change of the molecular species during adsorption was monitored by the mass spectrometer with the shield open and in a random flux detection geometry. Using the same mass spectrometer (differentially pumped), TPD measurements can be made with the shield closed and in a line-of-sight detection geometry.

Surface cleanliness and the relative coverages of adsorbates were verified by AES. All the AES data reported here were obtained by averaging at four or more positions on the prepared surface. In addition, a second UHV chamber, equipped with a high resolution elec-

### (A) Schematic of Uptake Measurement



### (B)

#### ADSORPTION OF C<sub>2</sub>H<sub>2</sub> ON Si(100) SURFACE AT 105K

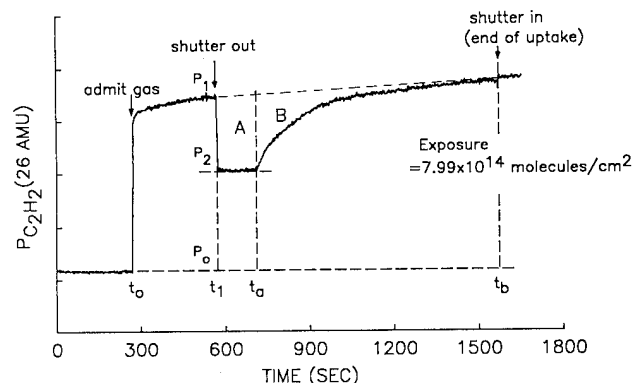


Fig. 1. (A) Schematic diagram of apparatus for quantitative uptake measurements; (B) a typical kinetic uptake measurement for C<sub>2</sub>H<sub>2</sub> on Si(100) at 105 K.

tron energy loss spectrometer (HREELS), is used for the surface vibrational spectroscopy studies [17]. The typical primary beam energy used for HREELS measurements is 4.2 eV with a full width at half-maximum of 65-70 cm<sup>-1</sup>.

## 3. Results and discussion

### 3.1. Absolute coverage measurements for C<sub>2</sub>H<sub>2</sub> and C<sub>2</sub>H<sub>4</sub>

Figure 1(A) shows a schematic diagram of the apparatus employed to measure the absolute coverage of adsorbate during the adsorption process. A collimated beam of molecular species is delivered from a doser containing a microcapillary collimator array. The absolute flux of the collimated beam onto the crystal surface is determined from the calibrated conductance through the internal pinhole aperture [12] and from the calculated angular distribution of the beam [24]. Before the measurement, the cleaned Si(100) crystal is placed in a known position relative to the doser, and a movable

shutter is placed between the doser and the crystal to separate the crystal from the direct beam. After a flux of gas molecules has been established through the doser, the shutter is then moved out of the beam and adsorption begins to take place on the surface. The gas molecules which miss the crystal, or which strike the crystal and do not adsorb, are measured with the shielded QMS which detects only the random flux of non-adsorbed species. For a detailed description of the measurement method, the interested reader is referred to refs. 12 and 25.

A typical adsorption measurement for  $C_2H_2$  on Si(100)-(2 × 1), at a crystal temperature of 105 K, is shown in Fig. 1(B). When the shutter is moved out of the beam, the partial pressure of  $C_2H_2$  detected by the mass spectrometer decreases instantly from  $P_1$  to  $P_2$ , indicating that the adsorption of  $C_2H_2$  onto the Si(100) surface occurs. The fraction of gas molecules striking the surface and adsorbing can be determined by the ratio of  $(P_1 - P_2)/(P_1 - P_0)$ , which is  $0.45 \pm 0.01$  for  $C_2H_2$ . This is in excellent agreement with the calculation which shows that the fraction of the beam intercepted by the crystal is  $0.46 \pm 0.05$ , based on the known doser and crystal geometry [24]. This indicates the initial  $C_2H_2$  sticking probability,  $S(0)$ , is nearly unity at 105 K. Knowing the absolute flux,  $F$ , and the sticking probability,  $S(t)$ , the absolute coverage,  $N(t)$ , in the time interval  $t$  can be determined directly from the kinetic uptake curve (as shown in Fig. 1(B)) according to the following equation,

$$N(t) = F \int S(t) dt$$

With an additional small correction in the low sticking probability region (the region where the adsorption efficiency is beyond the detection limit of the mass spectrometer) [12], we have determined that the saturation coverage of  $C_2H_2$  on the Si(100)-(2 × 1) surface is  $2.5(\pm 0.2) \times 10^{14}$  molecules  $cm^{-2}$ . Using the same measurement, an identical saturation coverage has been determined for  $C_2H_4$  on Si(100) at 105 K. On a perfect reconstructed Si(100)-(2 × 1) surface, the dimer density is  $3.4 \times 10^{14}$   $Si_2$  dimers  $cm^{-2}$ . However, a high density of defects, like missing dimers, is generally seen on an UHV-prepared surface [19]. Missing dimer defects were also suggested to stabilize the Si(100) reconstruction [26]. STM measurements often show a 5–10% defect density on Si(100) surfaces. Since other studies have shown that defects are inactive for olefin adsorption [27], the saturation capacity of Si(100) will be reduced in proportion to the defect density. Assuming a 10% defect density, the saturation coverage on non-defective Si(100) sites is near unity ( $0.8 \pm 0.07$ ), i.e. our measurements suggest that each  $Si_2$  dimer site adsorbs a single  $C_2H_2$  or  $C_2H_4$  molecule. This chemisorption

model, which involves the formation of Si–C bonds between the carbon atom pair of the chemisorbed olefinic molecule and the silicon atom pair in a  $Si_2$  dimer, is supported by the preservation of the (2 × 1) LEED pattern upon chemisorption of  $C_2H_2$  and  $C_2H_4$ , by HREELS measurements [28, 29], and by thermodynamic arguments [14, 15].

### 3.2. Thermal behavior of chemisorbed $C_2H_2$ and $C_2H_4$

Thermal desorption studies for both  $C_2H_2$  and  $C_2H_4$  on Si(100) reveal that the only desorption products are the intact molecules ( $C_2H_2$  and  $C_2H_4$ ) and  $H_2$ . TPD spectra obtained after saturating the Si(100) surface with  $C_2H_2$  and  $C_2H_4$  are shown in Figs. 2(A) and 2(B) respectively. Using the analytical method developed by Chan *et al.* [30], the activation energy for desorption ( $E_d$ ) and the pre-exponential factor ( $k_d$ ) can be determined by using the full width half-maximum of the desorption peaks. This analysis was performed for various initial coverages. Assuming first-order desorption kinetics,  $E_d$  and  $k_d$  in the zero-coverage limit for both molecules are:  $E_d^0(C_2H_2) = 46.1 \pm 2.0$  kcal  $mol^{-1}$ ,  $k_d^0(C_2H_2) = 2 \times 10^{13 \pm 1}$   $s^{-1}$  [15]; and  $E_d^0(C_2H_4) = 38.0 \pm 1.5$  kcal  $mol^{-1}$ ,  $k_d^0(C_2H_4) = 5 \times 10^{13 \pm 0.5}$   $s^{-1}$  [14].

Also measured was the thermal desorption of molecular hydrogen, which is evolved from thermal decomposition of the chemisorbed hydrocarbon molecules (Fig. 2). This desorption feature occurs at  $T \geq 700$  K, which is near that for  $H_2$  desorption from the monohydride phase (H–Si–Si–H) on Si(100). Based on the magnitude of the  $H_2$  desorption signals, the extent to which the chemisorbed hydrocarbon molecules have decomposed on the Si(100) surface during heating can be estimated. By comparing the yield of  $H_2$  desorption from a saturated overlayer of  $C_2H_2$  with that from a saturated monohydride phase (the amount of  $H_2$  desorbed from the saturated monohydride phase corresponding to 1 monolayer (ML) =  $6.8 \times 10^{14}$  H  $cm^{-2}$  [31]), the integrated area of  $H_2$  desorption from decomposition of  $C_2H_2$  is estimated to be ~78% of 1 ML. For a  $C_2H_2$  coverage of  $0.8 \pm 0.07$  ML, this therefore indicates that the major reaction pathway for chemisorbed  $C_2H_2$  on Si(100) is thermal decomposition of  $C_2H_2$  with subsequent hydrogen desorption; and only a small fraction of  $C_2H_2$  desorbs as the intact molecule (Fig. 2(A)). A similar analysis has been done for the thermal desorption of  $C_2H_4$  on Si(100). In contrast to the thermal behavior of chemisorbed  $C_2H_2$ , the measurements indicate that approximately 98% of the chemisorbed  $C_2H_4$  desorbs as intact molecules without decomposition (Fig. 2(B)). Figure 2 is shown for hydrogen-containing hydrocarbons for simplicity. The amount of the decomposed ethylene based on the molecular hydrogen desorption was estimated from measurements using perdeuteroethylene ( $C_2D_4$ ) (see ref. 14).

TPD SPECTRA OF  $C_2H_2$  AND  $C_2H_4$  ON  $Si(100)-(2 \times 1)$   
AT SATURATION COVERAGE;  $dT/dt = 1.0$  K/s

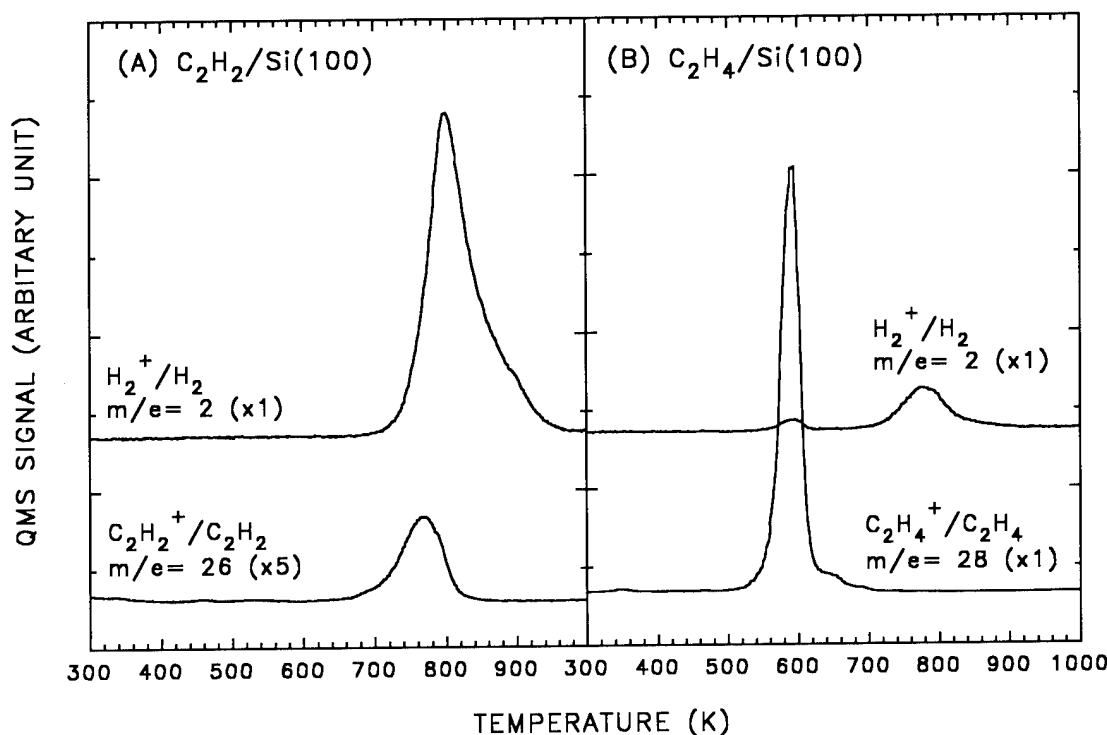


Fig. 2. TPD spectra obtained after saturating the  $Si(100)$  surface with  $C_2H_2$  (A) and  $C_2H_4$  (B). The heating rate for the TPD measurements was  $1.0$  K  $s^{-1}$ . Note that the desorption spectrum of  $C_2H_2^+/C_2H_2$  is amplified by a factor of 5.

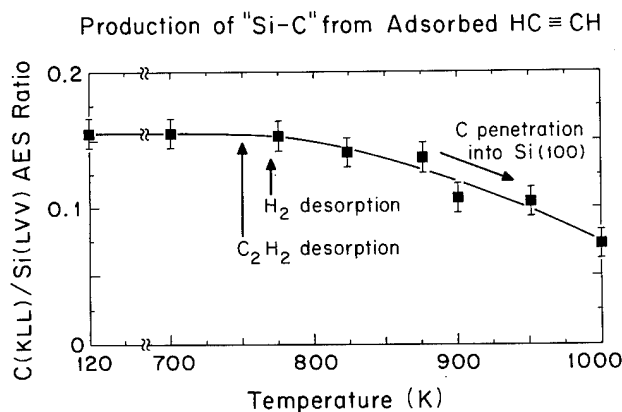


Fig. 3. The change in carbon Auger intensity upon annealing a  $C_2H_2$  adlayer to different temperatures on  $Si(100)$ . The error bars represent  $\pm 1$   $\sigma$  deviation from the average of six AES measurements on the surface.

The conversion of chemisorbed hydrocarbon to surface carbon was also investigated using AES. In Fig. 3, the ratios of C(KLL) to Si(LVV) signals indicate that the amount of carbon retained on the surface is a function of the crystal temperature. Heating of a  $C_2H_2$

saturation overlayer through the  $C_2H_2$  desorption temperature results in a  $\sim 5\%$  decrease of the C/Si Auger intensity ratio as judged by the averaged data in Fig. 3. This confirms the TPD measurements which show that the desorption process is a minor reaction pathway for  $C_2H_2$  on  $Si(100)$ . Heating above  $\sim 800$  K causes the C(KLL) signal to decrease as carbon diffuses into the bulk. Qualitatively, similar results have been reported for the decomposition of the propylene ( $H_2C=CH-CH_3$ ) on  $Si(100)$  with subsequent carbon penetration at higher temperatures [27]. On the other hand, investigation of thermal behavior of  $C_2H_4$  on  $Si(100)$  using AES shows that the carbon coverage decreases distinctly at  $\sim 550$  K, and has dropped to nearly zero by  $\sim 600$  K [14]. This corresponds to the temperature range in which  $C_2H_4$  desorption occurs (Fig. 2(B)).

The information contained in Figs. 2 and 3 shows that chemisorbed  $C_2H_4$  decomposes very inefficiently on  $Si(100)$ , in sharp contrast to chemisorbed  $C_2H_2$  which dehydrogenates nearly completely ( $>95\%$ ). The main difference between the interaction of these two molecules with the  $Si(100)$  surface is the activation energy for desorption:  $E_d^o(C_2H_2) = 46.1 \pm$

$2.0 \text{ kcal mol}^{-1}$ ;  $E_a(\text{C}_2\text{H}_4) = 38.0 \pm 1.5 \text{ kcal mol}^{-1}$ , which produces an  $\sim 160 \text{ K}$  difference in desorption temperature. The low desorption activation energy for  $\text{C}_2\text{H}_4$  allows the adsorbed  $\text{C}_2\text{H}_4$  to desorb at a lower temperature prior to significant decomposition, whereas the high desorption activation energy for  $\text{C}_2\text{H}_2$  causes the adsorbed  $\text{C}_2\text{H}_2$  to be retained on the surface to a higher temperature where dehydrogenation dominates the surface process. In addition, mechanistic studies using the isotopic mixing method ( $^{13}\text{C}_2\text{H}_4$  and  $^{12}\text{C}_2\text{H}_4$ ) have shown that less than 1% isotopic mixing of ethylene occurs in the approximate temperature range of 500 K–950 K where the desorption and decomposition of  $\text{C}_2\text{H}_4$  takes place [13]. This observation excludes the remote possibility that  $\text{C}_2\text{H}_4$  desorption is via the scission of the carbon–carbon bond, followed by recombination of  $\text{CH}_2(\text{a})$  fragments. We therefore conclude that the low probability of SiC film growth at elevated temperatures, as previously reported (the efficiency of SiC formation using  $\text{C}_2\text{H}_4$  is  $\sim 10^{-3}$  per collision at 940 K [3, 13]), is due mainly to non-dissociative behavior and desorption of  $\text{C}_2\text{H}_4$ , rather than to inefficient  $\text{C}_2\text{H}_4$  chemisorption. In fact, studies of the growth of a  $\beta$ -SiC film on Si surfaces have shown that the growth rate obtained using  $\text{C}_2\text{H}_2$  was larger than that obtained using  $\text{C}_2\text{H}_4$  in an UHV environment [10].

### 3.3. Thermal behavior of adsorbed $\text{CH}_3$

The thermal stability of the adsorbed methyl group on Si(100) was studied by using the dissociative chemisorption of methyl iodide ( $\text{CH}_3\text{I}$ ) as a source of  $\text{CH}_3(\text{a})$ . Experimental evidence, based on both quantitative uptake measurements (the method described in Section 3.1) and TPD, indicates that the  $\text{CH}_3\text{I}$  molecule dissociates into a covalently bonded methyl group and an iodine atom upon adsorption at 300 K [16]. Heating causes the decomposition of the adsorbed methyl group. Figure 4 shows typical TPD spectra from  $\text{CH}_3\text{I}$  on Si(100). The main features observed are 2 amu ( $\text{H}_2^+$  from  $\text{H}_2$  desorption) and 127 amu ( $\text{I}^+$  from both HI and I desorption). The desorption of  $\text{C}_2$  hydrocarbon species (data not shown) occurring in the same temperature range as the  $\text{H}_2$  desorption peak was also observed. The amount of the adsorbed carbon species desorbing in the form of  $\text{C}_2$  hydrocarbon species was estimated to be less than 1% [16]. In addition, neither the desorption of methane nor the desorption of  $\text{CH}_3\text{I}$  was observed. These results suggest that  $\text{CH}_3(\text{a})$  on Si(100) is stable up to  $\sim 600 \text{ K}$ . At higher temperatures, the adsorbed methyl group decomposes and liberates  $\text{H}_2(\text{g})$ .

The thermal stability of  $\text{CH}_3(\text{a})$  on Si(100) has also been verified by vibrational spectroscopy using HREELS [17]. Figure 5 shows the vibrational spectra obtained after the  $\text{CH}_3\text{I}$  adlayer on Si(100) was heated

### TYPICAL TPD SPECTRA FROM $\text{CH}_3\text{I}$ ON Si(100)

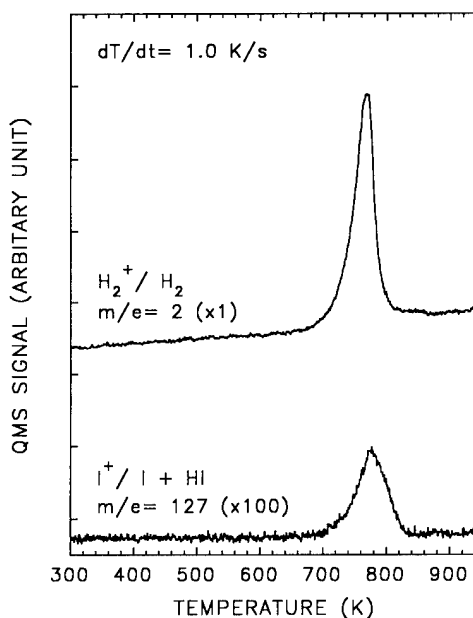


Fig. 4. Typical TPD spectra from  $\text{CH}_3\text{I}$  on Si(100) with a heating rate of  $1.0 \text{ K s}^{-1}$ .

to the temperatures indicated. Characteristic  $\text{C}-\text{H}_x$  ( $3 \geq x \geq 1$ ) vibrational modes are observed in three regions: the C–H stretching modes in the  $2800\text{--}3200 \text{ cm}^{-1}$  region, and the C–H deformation modes in the  $1100\text{--}1600 \text{ cm}^{-1}$  and  $700\text{--}1000 \text{ cm}^{-1}$  regions [32, 33]. The vibrational spectrum shown in Fig. 5(A) was obtained after  $\text{CH}_3\text{I}$  adsorption at 300 K. In addition to the  $\text{CH}_x$  vibrational modes, the presence of the Si–I stretching vibration at  $435 \text{ cm}^{-1}$  and the absence of the C–I stretching mode at  $525 \text{ cm}^{-1}$  confirm that  $\text{CH}_3\text{I}$  dissociates into  $\text{CH}_3(\text{a})$  and  $\text{I}(\text{a})$  at 300 K. Identical spectra were observed by heating the surface up to 600 K. Further heating to 700 K (Fig. 5(C)) causes two pronounced changes in the vibrational spectrum: (1) a large intensification of the Si–H mode at  $2140 \text{ cm}^{-1}$ ; and (2) a new frequency mode developing at  $980 \text{ cm}^{-1}$ . The appearance of the Si–H mode at 700 K suggests that the adsorbed methyl group has begun to decompose to  $\text{CH}_2(\text{a})$  and/or  $\text{CH}(\text{a})$  species. This is also supported by the development of the new vibrational feature at  $980 \text{ cm}^{-1}$  which can be assigned to either a  $\text{CH}_2$  rocking mode [32] or to a C–H deformation mode [33, 34]. The vibrational spectrum recorded after heating to 775 K (Fig. 5(D)) shows that all the  $\text{CH}_3$  and  $\text{CH}_2$  deformation modes in the  $1100\text{--}1600 \text{ cm}^{-1}$  region have disappeared, indicating the decomposition of all the  $\text{CH}_3(\text{a})$  and  $\text{CH}_2(\text{a})$  species. In addition, the presence of  $\text{CH}(\text{a})$  up to 775 K is indicated by the  $\delta(\text{C}-\text{H})$  bending deformation of  $945 \text{ cm}^{-1}$  and the attenuated

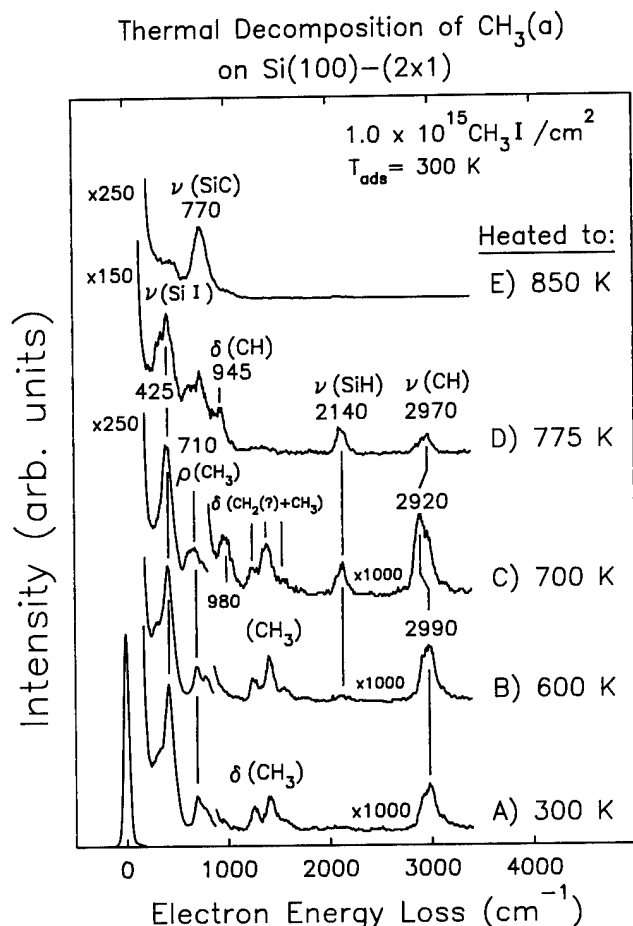


Fig. 5. Vibrational spectra of CH<sub>3</sub>I adsorbed on Si(100) at 300 K, followed by sequential heating to the temperatures indicated with a heating rate of 1 K s<sup>-1</sup>. All HREEL spectra were recorded after cooling to 100 K.

C-H stretching mode at 2970 cm<sup>-1</sup>. By 850 K, only a 770 cm<sup>-1</sup> vibrational loss remains which is due to carbon on the surface [35]. These results provide direct evidence for the thermal stability of CH<sub>3</sub>(a) on Si(100).

The lack of a desorption pathway (<1%) for chemisorbed CH<sub>x</sub>(a) ( $x \leq 3$ ) species suggests that the efficiency for the conversion of the CH<sub>x</sub>(a) species to surface carbon is near unity. Figure 6 shows the thermal effect on both carbon and iodine Auger intensities. The change of carbon Auger intensity is negligible up to ~760 K when a monolayer produced from CH<sub>3</sub>I is examined. At higher temperatures, diffusion of surface carbon into the bulk is observed as shown by the decrease of the carbon Auger intensity. The iodine signal, on the other hand, begins to decrease at ~700 K and becomes undetectable above 900 K. The decrease of iodine Auger intensity is consistent with the thermal desorption of iodine and hydrogen iodide shown in Fig. 4. Combining these results with TPD and HREELS

#### THERMAL EFFECTS FOR CH<sub>3</sub>I ON Si(100) USING AUGER ELECTRON SPECTROSCOPY

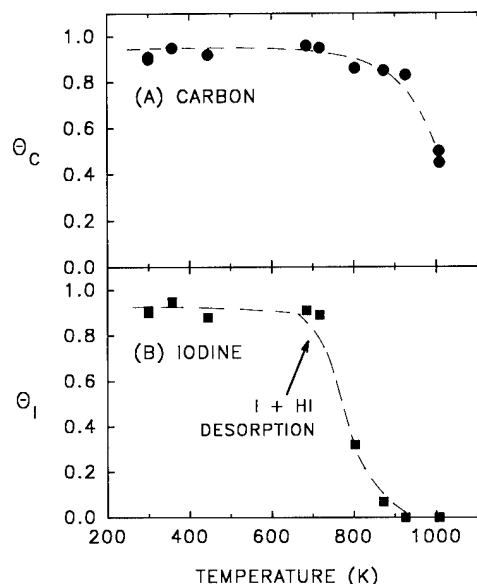


Fig. 6. Thermal effects on adsorbed CH<sub>3</sub>I on Si(100) using AES. The Auger intensities are normalized to the intensities of the saturated adlayer. Lines are drawn to guide the eye.

studies, we therefore conclude that the methyl group is an efficient source for carbon deposition on Si(100).

Finally, the general observation of carbon diffusion at  $T \geq 800$  K (Figs. 3 and 6, and ref. 27) suggests that a supply of surface Si can be achieved by heating during the SiC thin film growth process. In fact, it has been shown, for the reaction of Si(100) with C<sub>2</sub>H<sub>4</sub>, that the formation of a SiC film occurs only at  $T \geq 940$  K [5]. In addition, it was found that the surface of the growing film was covered with an Si layer, indicating that surface aggregation of bulk Si on top of the growing SiC film occurs [5]. Recently, the epitaxial growth of SiC crystals has been achieved from the reaction of Si(100) with a low flux beam of C<sub>2</sub>H<sub>2</sub> ( $< 6 \times 10^{15}$  molecules s<sup>-1</sup> cm<sup>-2</sup>) at 1100–1300 K. These studies also confirmed that the surface under reaction conditions was covered with an Si-rich layer [2].

#### 4. Summary

The adsorption and thermal behavior of various hydrocarbon species (C<sub>2</sub>H<sub>2</sub>, C<sub>2</sub>H<sub>4</sub> and CH<sub>3</sub>(a)) on the Si(100)-(2 × 1) surface have been investigated. The major findings are summarized below:

(1) A quantitative uptake measurement method has been developed using an accurately calibrated beam doser and a shielded QMS for random flux detec-

tion. The results of the  $C_2H_2(C_2H_4)$  chemisorption on Si(100) at 105 K show that the chemisorbed  $C_2H_2(C_2H_4)$  forms a saturated monolayer with one  $C_2H_2(C_2H_4)$  per  $Si_2$  dimer site, producing a di- $\sigma$  surface complex.

(2) Chemisorbed  $C_2H_2$  predominantly undergoes dehydrogenation, leading to carbon deposition. A minor reaction pathway ( $\leq 5\%$ ) involves desorption of  $C_2H_2$  with an activation energy at the zero-coverage limit ( $E_a^0$ ) of 46 kcal mol $^{-1}$ . In contrast, chemisorbed  $C_2H_4$  desorbs predominantly without appreciable dissociation. The relatively low binding energy for  $C_2H_4$ , as suggested from its low activation energy for desorption ( $E_a^0(C_2H_4) = 38$  kcal mol $^{-1}$ ), allows the chemisorbed  $C_2H_4$  to desorb at a lower temperature prior to significant C-H bond activation.

(3) The adsorbed methyl group on Si(100) is stable up to  $\sim 600$  K. At higher temperatures,  $CH_3(a)$  decomposes to  $CH_x(a)$  ( $x < 3$ ) species and subsequently liberates  $H_2(g)$ , leaving carbon on the surface. The lack of a desorption pathway ( $< 1\%$ ) for chemisorbed  $CH_x(a)$  ( $x \leq 3$ ) allows the  $CH_x(a)$  species to decompose completely, suggesting that the methyl group is an efficient source for carbon deposition.

(4) The general observation of carbon diffusion into the bulk at  $T \geq 800$  K (Figs. 3 and 6, and ref. 27) suggests that a supply of surface Si for epitaxial growth of SiC can be achieved by heating during the growth process.

## Acknowledgments

We gratefully acknowledge support of this work by the Office of Naval Research (ONR) and by the Air Force Office of Scientific Research (AFOSR).

## References

- 1 J. A. Powell, J. B. Petit, J. H. Edgar, I. G. Jenkins, L. G. Matus, J. W. Yang, P. Pirouz, W. J. Choyke, L. Clemen and M. Yoganathan, *Appl. Phys. Lett.*, **59** (1991) 333.
- 2 I. Kusunoki, M. Hiroi, T. Sato, Y. Igari and S. Tomoda, *Appl. Surf. Sci.*, **45** (1990) 171.
- 3 P. A. Taylor, M. J. Bozack, W. J. Choyke and J. T. Yates, Jr., *J. Appl. Phys.*, **65** (1989) 1099.
- 4 C. D. Stinespring, A. Freedman and J. C. Wormhoudt, *Mater. Res. Soc. Symp. Proc.*, **131** (1989) 227.
- 5 F. Bozso, J. T. Yates, Jr., W. J. Choyke and L. Muehlhoff, *J. Appl. Phys.*, **57** (1985) 2771.
- 6 P. Liaw and R. F. Davis, *J. Electrochem. Soc.*, **132** (1985) 642.
- 7 A. Addamiano and J. A. Sprague, *Appl. Phys. Lett.*, **44** (1984) 525.
- 8 S. Nishino, J. A. Powell and H. A. Will, *Appl. Phys. Lett.*, **42** (1983) 460.
- 9 Y. Catherine, G. Turban and B. Grolleau, *Thin Solid Films*, **76** (1981) 23.
- 10 I. H. Khan and R. N. Summergrad, *Appl. Phys. Lett.*, **11** (1967) 12.
- 11 J. C. Angus and C. C. Hayman, *Science*, **241** (1988) 913.
- 12 C. C. Cheng, R. M. Wallace, P. A. Taylor, W. J. Choyke and J. T. Yates, Jr., *J. Appl. Phys.*, **67** (1990) 3693.
- 13 C. C. Cheng, W. J. Choyke and J. T. Yates, Jr., *Surf. Sci.*, **231** (1990) 289.
- 14 L. Clemen, R. M. Wallace, P. A. Taylor, M. J. Dresser, W. J. Choyke, W. H. Weinberg and J. T. Yates, Jr., *Surf. Sci.*, **268** (1992) 205.
- 15 P. A. Taylor, R. M. Wallace, C. C. Cheng, W. H. Weinberg, M. J. Dresser, W. J. Choyke and J. T. Yates, Jr., *J. Am. Chem. Soc.*, **114** (1992) 6754.
- 16 H. Gutleben, S. R. Lucas, C. C. Cheng, W. J. Choyke and J. T. Yates, Jr., *Surf. Sci.*, **257** (1991) 146.
- 17 M. L. Colaizzi, P. J. Chen, H. Gutleben and J. T. Yates, Jr., *Chem. Phys. Lett.*, **191** (1992) 561.
- 18 J. A. Appelbaum and D. R. Hamann, *Surf. Sci.*, **74** (1978) 21.
- 19 (a) R. J. Hamers, R. M. Tromp and J. E. Demuth, *Phys. Rev. B*, **34** (1986) 5343.  
(b) R. M. Tromp, R. J. Hamers and J. E. Demuth, *Phys. Rev. Lett.*, **55** (1985) 1303.
- 20 M. J. Bozack, P. A. Taylor, W. J. Choyke and J. T. Yates, Jr., *Surf. Sci.*, **177** (1986) L933.
- 21 M. J. Bozack, L. Muehlhoff, J. N. Russell, Jr., W. J. Choyke and J. T. Yates, Jr., *J. Vac. Sci. Technol.*, **A5** (1987) 1.
- 22 V. S. Smentkowski and J. T. Yates, Jr., *J. Vac. Sci. Technol.*, **A7** (1989) 3325.
- 23 R. J. Muha, S. M. Gates, J. T. Yates, Jr., and P. Basu, *Rev. Sci. Instrum.*, **56** (1985) 613.
- 24 (a) C. T. Campbell and S. M. Valone, *J. Vac. Sci. Technol.*, **A3** (1985) 408.  
(b) A. Winkler and J. T. Yates, Jr., *J. Vac. Sci. Technol.*, **A6** (1988) 2929.
- 25 (a) D. A. King and M. G. Wells, *Surf. Sci.*, **29** (1972) 454.  
(b) T. E. Madey, *Surf. Sci.*, **33** (1972) 355.
- 26 K. C. Pandey, Reconstruction of the Si(100)- $2 \times 1$  surface, in D. J. Chadi and W. A. Harrison (eds.), *Proc. Seventeenth Int. Conf. on the Physics of Semiconductors*, Springer-Verlag, New York, 1985, p. 55.
- 27 M. J. Bozack, W. J. Choyke, L. Muehlhoff and J. T. Yates, Jr., *Surf. Sci.*, **176** (1986) 547.
- 28 J. Yoshinobu, H. Tsuda, M. Onchi and M. Nishijima, *J. Chem. Phys.*, **87** (1987) 7332.
- 29 M. Nishijima, J. Yoshinobu, H. Tsuda and M. Onchi, *Surf. Sci.*, **192** (1987) 383.
- 30 C.-M. Chan, R. Aris and W. H. Weinberg, *Appl. Surf. Sci.*, **1** (1978) 360.
- 31 C. C. Cheng and J. T. Yates, Jr., *Phys. Rev. B*, **43** (1991) 4041.
- 32 R. T. Conley, *Infrared Spectroscopy*, Allyn and Bacon, Newton, 1972.
- 33 L. J. Bellamy, *The Infrared Spectra of Complex Molecules*, Wiley, New York, 1975.
- 34 F. Lee, A. L. Backman, R. Lin, T. R. Gow and R. I. Masel, *Surf. Sci.*, **216** (1989) 173.
- 35 J. A. Strosio, S. R. Bare and W. Ho, *Surf. Sci.*, **154** (1985) 35.



# Chemistry of hydrogen on diamond (100)

Yuemei L. Yang, Lisa M. Struck, Leyla F. Sutcu and Mark P. D'Evelyn

Department of Chemistry and Rice Quantum Institute, Rice University, Houston, TX 77251-1892 (USA)

## Abstract

Hydrogen plays a crucial role in diamond film growth by chemical vapor deposition and is likely to be similarly critical to atomic layer epitaxy, yet the surface chemistry of hydrogen on diamond is only beginning to be understood. We investigated the adsorption of hydrogen and deuterium on diamond (100) by temperature-programmed desorption and by IR multiple-internal-reflection spectroscopy using a natural type IIa diamond internal reflection element. Complementary theoretical studies were carried out using the empirical MM3 molecular mechanics force field, which has a demonstrated high degree of accuracy for many molecules despite computational simplicity.  $H_2$  desorption was observed with a peak temperature of approximately 1250 K and a peak shape suggestive of first-order kinetics, and is assigned to the monohydride surface structure, with one hydrogen atom per surface carbon atom. Assuming a pre-exponential factor of  $10^{13} s^{-1}$ , the activation energy for desorption is estimated as approximately 80 kcal/mol<sup>-1</sup>. IR evidence was seen for the monohydride surface structure, with one hydrogen atom per surface carbon atom ( $\delta_{CD}$  mode at 901 cm<sup>-1</sup>), for the first time on diamond (100). The MM3 calculations predict that the  $(2 \times 1):H$  monohydride phase is the most stable thermodynamically and the dominant phase under typical chemical vapor deposition conditions.

## 1. Introduction

The critical role played by hydrogen in diamond chemical vapor deposition (CVD) is well established [1]. To date only preliminary results have been published on the growth of diamond films by atomic layer epitaxy (ALE) [2], but surface hydrogen plays a crucial role in ALE growth of silicon [3–5], and will certainly be important in diamond ALE processes currently being developed. Despite its obvious importance, the surface chemistry of hydrogen on diamond is only beginning to be understood. Of the two crystal faces which are prevalent in CVD-grown diamond films, the properties of the clean and hydrogenated (111) face are much better understood than those of the (100) face. However, the (100) face is the only low-index orientation where the actual surface of CVD films resembles the nominal orientation (*i.e.* the surface is smooth on the nanometer-to-micrometer scale) [6], and is the orientation most likely to be useful for ALE. Nominally clean diamond (100) has been observed to have a  $(2 \times 1)$  unit cell by low energy electron diffraction [7]. By analogy to the well studied Si(100) and Ge(100) surfaces, the  $(2 \times 1)$  unit cell suggests the formation of dimer bonds between pairs of surface carbon atoms, as illustrated schematically in Fig. 1(a). Hydrogen atoms are known to chemisorb on diamond (100) [8–11], with either a  $(2 \times 1)$  [9, 10] or nominally  $(1 \times 1)$  [9] unit cell. The most transparent assignments for these structures, by analogy to the better studied H/Si(100) system, are a

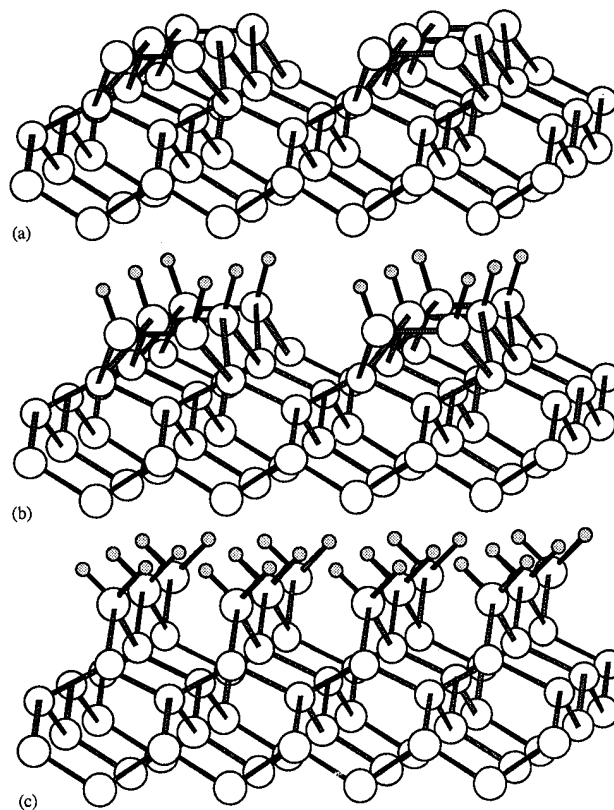


Fig. 1. Schematic illustration of (a) clean diamond (100)-(2 × 1), (b) the (100)-(2 × 1):H monohydride with one hydrogen atom per surface carbon atom, and (c) the (100)-(1 × 1):2H full dihydride with two hydrogen atoms per surface carbon atom.

$(2 \times 1)$ :H monohydride, with one hydrogen atom per surface carbon atom (Fig. 1(b)) and a  $(1 \times 1)$ :2H dihydride, with two hydrogen atoms per surface carbon atom (Fig. 1(c)) respectively.

Hamza *et al.* [9] reported temperature-programmed desorption (TPD) results for hydrogen on diamond (100), with the peak desorption rate occurring at a substrate temperature near 1200 K at low initial coverage. Based on their observation, by electron-stimulated desorption, of the continued presence of surface hydrogen even after annealing to 1400 K and their inability to detect unoccupied surface states, Hamza *et al.* assigned the TPD peak to hydrogen in the  $(1 \times 1)$ :2H dihydride state (Fig. 1(c)) desorbing, leaving hydrogen in the  $(2 \times 1)$ :H monohydride state (Fig. 1(b)). Several aspects of this assignment are troubling, however. First, the structural similarity of diamond and silicon surfaces suggests that the behavior of hydrogen on the two materials will be qualitatively similar even if the energetics are different.  $H_2$  desorbs from the monohydride state on both Si(100) and Si(111) near 800 K, yielding the clean surface, although the details of the desorption kinetics are different on the two crystal faces [12]. On diamond (111), the monohydride, with a  $(1 \times 1)$  near-ideal bulk-terminated structure [13], desorbs upon heating to around 1200 K, yielding a clean surface with a  $(2 \times 1)$  unit cell [14–16]. The similarities in the desorption temperatures of  $H_2$  on diamond (100) and (111) and the analogy to silicon suggest, therefore, that the observed desorption on diamond (100) near 1200 K is taking place from the monohydride rather than from the dihydride. A second difficulty with the desorption assignment is that steric repulsion between hydrogen atoms in the  $(1 \times 1)$ :2H dihydride should be extreme. The corresponding monohydride and dihydride species on Si(100) have a substantial literature and it appears that a full dihydride can only be formed under conditions where  $SiH_3(a)$  is also formed and some etching takes place, and that steric repulsion between the hydrogen atoms is important [17]. The lattice constant of diamond is 34% smaller than that of silicon and hydrogen–hydrogen repulsion will be even more important. If the hydrogen atoms on diamond  $(1 \times 1)$ :2H remained in their ideal  $sp^3$  positions, the distance between neighboring (non-bonded) hydrogen atoms would be only 0.71 Å, less than the H–H bond length in  $H_2$ ! If this structure exists, therefore, one should expect rather dramatic orientational changes in the C–H bonds in order to stabilize the surface. Such changes will cost energy, perhaps enough to make the  $(1 \times 1)$ :2H dihydride thermodynamically unstable with respect to dehydrogenation to the monohydride. Indeed, our calculations [18], along with recent semi-empirical calculations [19], predict that the  $(1 \times 1)$ :2H full dihydride is unstable, although the quantitative reliability of the calculations

is uncertain. A final difficulty with the assignment by Hamza *et al.* [9] is that in subsequent experiments, Thomas *et al.* [10] also observed a hydrogen desorption peak near 1200 K, but observed  $(2 \times 1)$  diffraction patterns both before and after desorption. The latter observation can be explained by a substantial activation barrier for hydrogen-atom attack on the C–C dimer bond in the monohydride (Fig. 1(b)) [9c], and suggests, in accord with the argument presented above, that the desorption peak is due primarily to hydrogen atoms in the monohydride structure and that the diamond surface is essentially clean following desorption.

Although we believe that the  $(1 \times 1)$ :2H full dihydride is not important in diamond CVD under typical growth conditions, dihydride ( $CH_2$ ) structures with hydrogen coverages less than two full monolayers are likely to be important. For example, a  $(3 \times 1)$  structure may be generated by inserting a monohydride dimer between dihydride units at a hydrogen coverage of 1.33 monolayers. The analogous  $(3 \times 1)$ :1.33H structure on Si(100) is well established [17], and steric repulsion is nearly eliminated.

We have investigated the interaction of hydrogen with diamond (100) by TPD, by IR spectroscopy, and by theoretical molecular mechanics calculations. IR spectroscopy should be able to distinguish readily between different forms of surface hydrogen, and we believe that molecular mechanics is very useful for predicting the structure and energetics of surface species on covalent solids such as diamond.

## 2. Experimental details

The TPD and IR spectroscopic experiments were performed in the ultrahigh vacuum (UHV) chamber shown schematically in Fig. 2. The analysis chamber is pumped via a liquid- $N_2$ -trapped diffusion pump and titanium sublimation pump (base pressure approximately  $(1-2) \times 10^{-10}$  Torr), and is equipped with a quadrupole mass spectrometer (UTI 400C), a cylindrical mirror analyzer for Auger electron spectroscopy, homebuilt LEED/ESDIAD optics, and a tungsten filament used for atomic hydrogen dosing [20, 21].

Separate diamond (100) samples were used in the TPD and IR experiments. Type Ia diamond (100) samples,  $6.5 \times 3.5 \times 0.5$  mm<sup>3</sup> in dimension (DRI, Inc.), were used in the TPD experiments. The samples were obtained in as-sawn condition and were polished on a high-speed iron scaife with diamond powder in olive oil [21]. Our initial TPD experiments utilized a tantalum foil holder and heater for the diamond, but this proved to be unsatisfactory as atomic hydrogen dissolves readily in bulk tantalum [22]. We found that TPD spectra taken without the diamond in the holder were indistin-

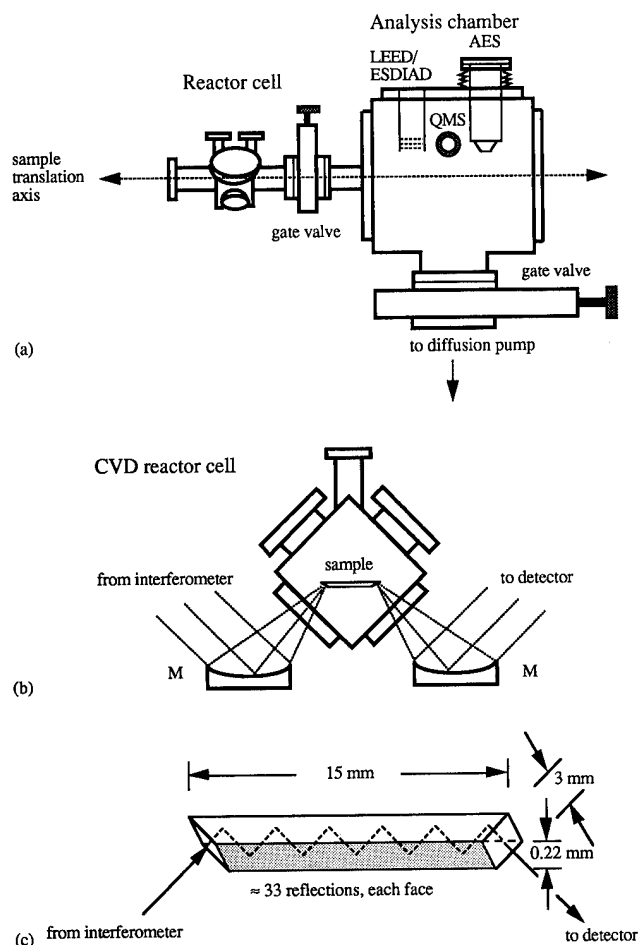


Fig. 2. Schematic diagram of combination CVD reactor and UHV analysis apparatus. (a) Side view of apparatus, with analysis chamber separated from the reactor cell by a gate valve: LEED/ESDIAD, optics for low energy electron diffraction and electron-stimulated desorption ion angular distribution; QMS, quadrupole mass spectrometer; AES, cylindrical mirror analyzer for Auger electron spectroscopy. (b) End view of reactor cell, showing scheme for IR multiple internal reflection spectroscopy. Collimated light from a Fourier transform IR spectrometer is focused from below onto a beveled edge of the diamond (100) crystal sample (S) in the reactor by an  $f/1$  off-axis paraboloidal mirror (M), and the transmitted light is collected and focused onto a remote, liquid-nitrogen-cooled narrow-band HgCdTe detector. (c) Schematic view from below of type IIa natural diamond (100) internal reflection element,  $15 \times 3 \times 0.22 \text{ mm}^3$  in dimension. The IRE has a (100) orientation on the large-area faces, and the end faces are beveled at  $45^\circ$ , providing approximately 33 internal reflections from each long face.

guishable from data taken with the diamond, implying that most of the desorbing hydrogen originated from the bulk of the tantalum foil. (This finding is in agreement with Kubiak and coworkers, who later concluded that the higher-coverage TPD results reported in ref. 9 were spurious, owing to desorption from the tantalum support [23].) A second difficulty with the foil sample holder scheme is that accurate sample temperatures are difficult to obtain. Unlike silicon, diamond is transparent in the visible and well into the IR and UV

and therefore does not glow at temperatures near 1000 K, and so optical and IR pyrometry cannot be used to provide a temperature correction.

The TPD results presented below were obtained using a modified sample holder scheme, which has significant advantages in terms of reduced outgassing and capability for accurate sample temperature calibration. A tungsten film,  $0.5 \mu\text{m}$  thick, was sputter deposited onto the back of the diamond (100) sample. Hydrogen desorbs from tungsten below 600 K [24], and therefore should not interfere with the desorption signal due to the diamond. The sample was held at each end between two sets of tungsten wire clips,  $0.254 \text{ mm}$  in diameter, which in turn were electrically isolated and attached to a cooled copper block. A pair of chromel–alumel thermocouples was placed in direct contact with the sample underneath one of the wire clips. The sample was heated by passing current between the pair of clips through the tungsten film on the back. As the thermal contact between the tungsten film and the sample should be excellent, the temperature of the tungsten should reflect accurately that of the diamond, even if the thermocouple-derived temperature is in error. We performed careful temperature calibrations by optical pyrometry of the tungsten–diamond interface. As the emissivity of the tungsten–diamond interface was not known, we prepared a second diamond sample with a tungsten film on the back and placed it in a tubular furnace within the UHV analysis chamber. We used the second sample, whose temperature should be equal to that of the furnace (measured with a chromel–alumel thermocouple), to calibrate the pyrometer over the temperature range 1000–1473 K [21]. The calibrated pyrometer was then used to measure the temperature of the first diamond sample over the same range. Near temperatures of 1000 K, the thermocouple pressed against the sample was found to be accurate to within 10–20 K, but the temperature error rose to 140 K (with the thermocouple reading too low) at a sample temperature of 1473 K. We estimate that the corrected temperatures are accurate to within about  $\pm 25 \text{ K}$ .

Temperature ramps for TPD were generated using a standard d.c. power supply controlled by a commercial PID temperature controller (Eurotherm 818P) interfaced to an IBM-AT-compatible personal computer. The output of the mass spectrometer was digitized by a data acquisition board in the same computer, allowing acquisition of TPD or residual gas analysis data [21]. A heating rate of  $5 \text{ K s}^{-1}$  was used in the TPD experiments reported here.

Diamond cannot be sputtered and annealed without extensive graphitization [7, 25], but several groups have shown that heating a freshly polished diamond sample in UHV to around 1300 K desorbs oxygen and generates a clean (except possibly for hydrogen) diamond surface [7, 9, 14, 26, 27]. We followed this procedure. Freshly

polished diamond samples were rinsed with hydrogen peroxide, trichloroethylene, acetone, and ethanol and placed in the chamber, which was then evacuated and baked out. The samples were cleaned *in situ* by heating to 1400 K in UHV. Atomic hydrogen exposures were performed by backfilling the UHV analysis chamber with  $H_2$  to pressures of  $5 \times 10^{-7}$ – $5 \times 10^{-5}$  Torr and heating a coiled tungsten filament located approximately 2 cm from the sample to 1700–1800 K. Because of the difficulty in calibrating accurate atomic hydrogen exposures made in this way, we simply report the apparent exposures to molecular hydrogen as Langmuirs ( $1L \equiv 10^{-6}$  Torr s), without an ion gauge correction.

We performed preliminary IR multiple-internal reflection spectroscopy (IMIRS) [28, 29] experiments in the reactor cell shown in Fig. 2(b). IMIRS is a high-sensitivity technique for obtaining high-resolution vibrational spectra of submonolayer quantities of adsorbates on substrates which are transparent in the IR. IMIRS takes advantage of the phenomenon of total internal reflection to gain sensitivity to surface vibrational modes by using many internal reflections. We have a type IIa natural diamond internal reflection element (IRE),  $15 \times 3 \times 0.22$  mm<sup>3</sup> in dimension, with a (100) orientation on the large-area faces. The end faces of the IRE are beveled at 45°, providing approximately 33 internal reflections from each long face, as illustrated schematically in Fig. 2(c). The optical coupling scheme is shown in Fig. 2(b). Collimated light from a Fourier-transform IR spectrometer (Mattson Cygnus 100) is focused by an off-axis paraboloidal mirror through a differentially pumped KBr window onto one bevelled edge of the diamond IRE. Light transmitted through the opposite end of the IRE is collected and focused onto a detector (narrow-band HgCdTe, Graseby Infrared) by two additional off-axis paraboloidal mirrors.

The diamond IRE was assumed to be well polished as received from the vendor, and was placed in the reactor cell after degreasing with acetone and ethanol. For the experiments reported here the IMIRS sample was heated in UHV to only about 250°C (the temperature could not be measured accurately), and therefore the surface was probably partially contaminated by oxygen. Exposures of the diamond (100) IRE to atomic hydrogen or deuterium were made by backfilling the reactor cell with  $H_2$  or  $D_2$  respectively, at pressures between  $1 \times 10^{-7}$  and  $2 \times 10^{-6}$  Torr for up to 2 h, and heating a tungsten filament located approximately 1 cm from the sample to 1700–1800 K.

### 3. Molecular mechanics calculations

The method used to calculate the structures and enthalpies of formation of clean and hydrogenated

diamond (100) has been described in detail previously [18]. The third-generation MM3 force field, with parameters for saturated, unsaturated and conjugated hydrocarbons, has a demonstrated high degree of accuracy (bond lengths approximately  $\pm 0.01$  Å, bond angles between atoms other than hydrogen approximately  $\pm 1^\circ$ , torsional angles approximately  $\pm 4^\circ$ , heats of formation approximately  $\pm 1$  kcal mol<sup>-1</sup>) for small, large, and highly strained molecules and bulk diamond as well [30, 31]. MM3 should be applicable to the description of saturated, unsaturated, and conjugated hydrocarbon species on any crystal face of diamond as long as the bond lengths, bond angles, and distances between non-bonded atoms are within the range of values in structures for which MM3 has demonstrated accuracy. MM3 parameters for radicals are tentative [31], making calculations with open-shell species more uncertain, and MM3 cannot describe surface species with bonding configurations that have not been parameterized in molecules. (Although MM2, the predecessor to MM3, has been applied successfully to alkyl radicals, MM3 has not yet been parameterized specifically for radicals [32].)

Atomic positions were determined by minimizing an empirical potential energy function, the so-called steric energy  $E$  [30, 31], subject to periodic boundary conditions and a substrate lattice constant fixed at the value of bulk diamond [18]. Enthalpies of formation were calculated by adding bond enthalpies  $\Delta H_{\text{bond}}$  and functional-group correction terms  $\Delta H_{\text{struct}}$  to the minimized steric energy for various surface species.

### 4. Results and discussion

TPD results for  $H_2$  desorbing from diamond (100) are shown in Fig. 3. For the reasons discussed above and elsewhere [18], we assign the TPD peak to the monohydride. The peak desorption rate occurs at  $T_p \approx 1250$  K, and the peak has the asymmetric shape characteristic of first-order desorption. Better evidence for first-order desorption may be derived from the independence of  $T_p$  on the initial surface coverage [33, 34]. However, we have not yet been able to establish the dependence of  $T_p$  on coverage owing to poor signal-to-noise ratio. The peak temperature (1250 K with a heating rate of  $5 \text{ K s}^{-1}$ ) agrees reasonably well with those of Hamza *et al.* [9], 1200 K at low coverage (heating rate  $6 \text{ K sec}^{-1}$ ), and of Thomas *et al.* [10], around 1175–1200 K. Thomas *et al.* [10] used a heating rate of  $20 \text{ K s}^{-1}$ , however; at  $5 \text{ K s}^{-1}$  their peak temperature would probably be lower by about 50 K. Assuming a pre-exponential factor of  $10^{13} \text{ s}^{-1}$ , the activation energy for desorption may be estimated from our data as approximately  $79.5 \text{ kcal mol}^{-1}$  [33]. A calculated TPD spec-

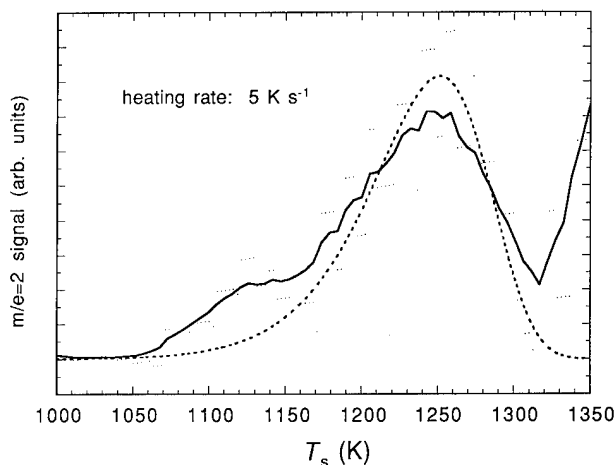


Fig. 3. Temperature-programmed desorption spectrum of  $H_2$  from diamond (100), prepared with a 720 L nominal dose at a sample temperature of 325 K: —, smoothed raw data (points), the rising signal at temperatures above 1320 K is due to desorption from supports; ---, calculated desorption trace assuming first-order desorption, a pre-exponential factor of  $10^{13} s^{-1}$ , and an activation energy of  $79.5 kcal mol^{-1}$ . The heating rate was  $5 K s^{-1}$ .

trum, assuming first-order desorption, a pre-exponential factor of  $10^{13} s^{-1}$ , and an activation energy of  $79.5 kcal mol^{-1}$  is also plotted in Fig. 3. The semiquantitative agreement in the measured and calculated peak shapes supports our assignment of first-order desorption and the approximate value of the pre-exponential factor. The assignment of first-order desorption is in agreement with Thomas *et al.* [10b], who found that  $T_p$  was essentially coverage independent. The “normal” value of the pre-exponential factor for hydrogen desorption indicated by our data contrasts with the results of Hamza *et al.* [9] and of Thomas *et al.* [10] on diamond (100) and of Schulberg *et al.* [35] on polycrystalline CVD-grown diamond films. Each of these authors obtained significantly broader TPD peaks than that shown in Fig. 3, implying apparent pre-exponential factors in the range  $3 \times 10^5$  to  $5 \times 10^7 s^{-1}$  [9, 35]. Differences in sample preparation may be responsible for the disparate results, as desorption from steps and defect sites might occur at slightly different rates and might give rise to anomalously broad TPD peaks.

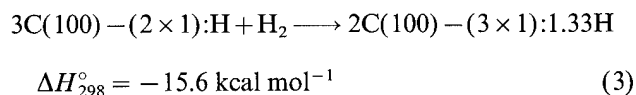
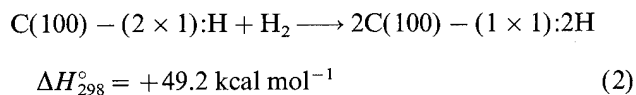
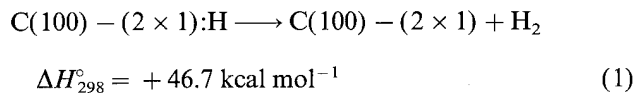
Another intriguing feature of the TPD spectrum is an apparent shoulder near 1125 K, approximately 125 K below  $T_p$ . The limited signal-to-noise ratio makes it impossible to determine whether this is a true shoulder, but it is well established that desorption from dihydride species on silicon ( $SiH_2$  groups) gives rise to a secondary TPD peak about 100 K lower in temperature than the monohydride ( $SiH$ ) peak near 800 K [17e, 36]. On Ge(100), hydrogen adsorption at above one monolayer coverage (implying dihydride formation) gives rise to a shoulder about 40 K below the monohydride peak

desorption temperature at 570 K [37]. If the shoulder in Fig. 3 is real, it may indicate desorption from dihydride species, by analogy to the behavior of hydrogen on silicon and germanium.

The poor signal-to-noise ratio in Fig. 3 is due to background hydrogen desorption from supports, despite the fact that hot surface areas on the sample holder were kept to a bare minimum. The rising background became quite significant above 1200 K. The background can be partially compensated for by taking the differences between TPD spectra obtained after and before hydrogen dosing, and this was done with the data shown in Fig. 3. However, imperfect cancellation is responsible for the sharp rise in the background above 1300 K. A satisfactory solution to the background desorption problem should be achievable by adding differential pumping to the mass spectrometer.

The results of MM3 calculations of the structures of the surface species illustrated in Fig. 1 are summarized in Fig. 4 [18]. The structures are entirely consistent with the qualitative conclusions which might be drawn from simple bond length and van der Waals radius considerations. The dimerized surface atoms on the  $(2 \times 1)$  clean surface (Figs. 1(a), 4(a)) are linked by highly pyramidalized double bonds with a bond length of  $1.46 \text{ \AA}$ , much greater than the typical  $C=C$  bond length of  $1.34 \text{ \AA}$  in organic molecules, and the dihedral angle between the dimer bond and the backbonds to the second-layer atoms is nearly  $60^\circ$ , far from the ideal  $sp^2$  planar geometry. The strain due to the backbonds also increases the  $C-C$  single bond length in the  $(2 \times 1):H$  monohydride structure (Figs. 1(b), 4(b)) from its unstrained value of  $1.54 \text{ \AA}$  to  $1.63 \text{ \AA}$ . Finally, the extreme steric repulsion between neighboring, non-bonded hydrogen atoms in the  $(1 \times 1):2H$  full dihydride structure (Figs. 1(c), 4(c)) causes a reduction in the  $H-C-H$  angle and twisting by some  $26^\circ$  about the surface normal. The extreme steric repulsion of the  $(1 \times 1):2H$  full dihydride is eliminated in the  $(3 \times 1):1.33H$  structure (Fig. 4(d)).

The energetic predictions of the MM3 calculations can be summarized by the following enthalpies of reaction at 298 K, expressed with respect to the  $(2 \times 1):H$  monohydride:



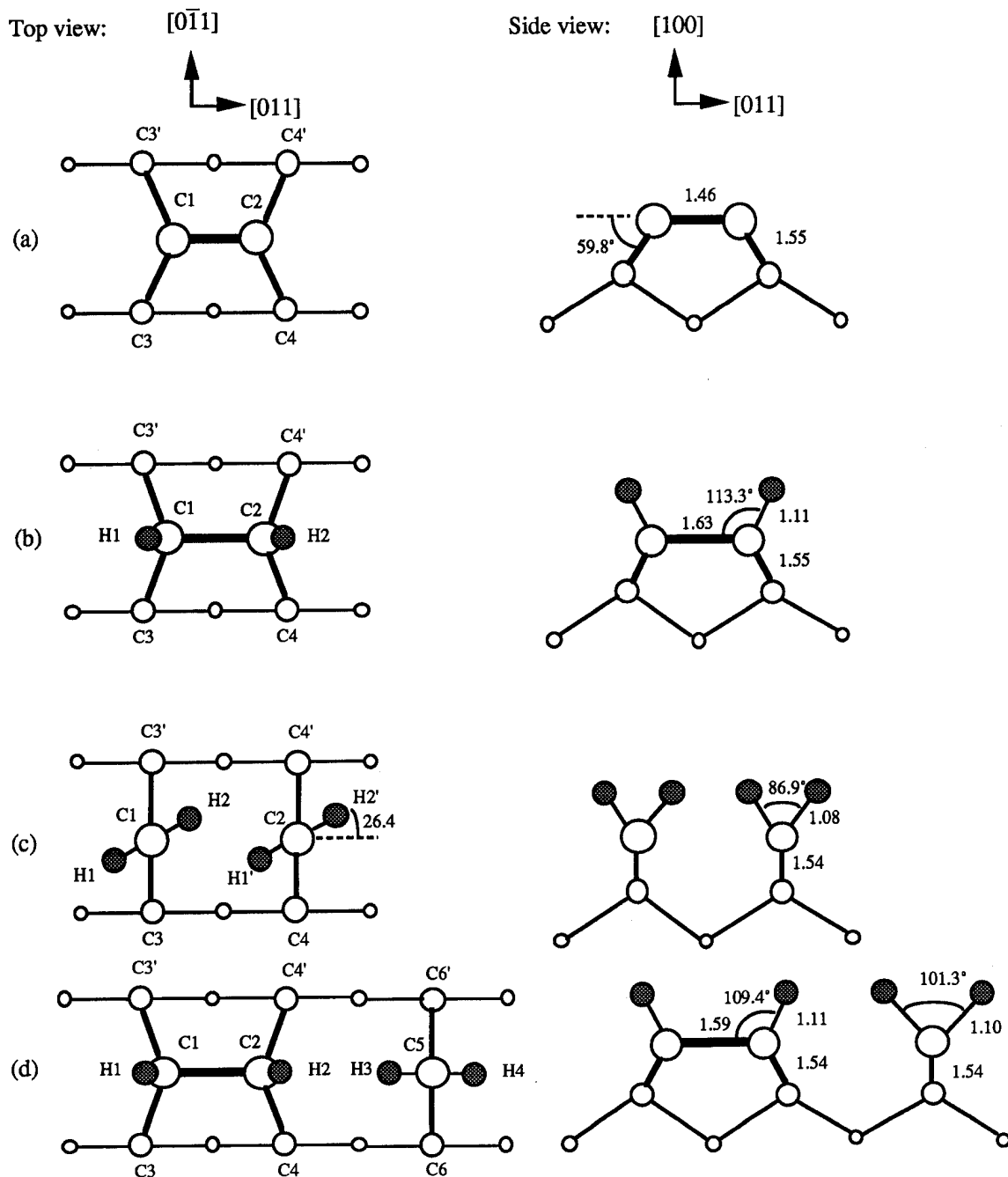


Fig. 4. Top and side views of atomic structures of clean and hydrogenated diamond (100) surfaces: (a)  $(2 \times 1)$ ; (b)  $(2 \times 1):H$ ; (c)  $(1 \times 1):2H$ ; (d)  $(3 \times 1):1.33H$ . Bond lengths are given in ångströms  $\bigcirc$ ,  $\bigcirc$ , and  $\bigcirc$ , carbon atoms in top, second, and third layers respectively;  $\bullet$ , hydrogen atoms.

The implication of the positive heat of reaction for eqn. (2) is that we predict that the  $(1 \times 1):2H$  full dihydride is indeed thermodynamically unstable, as the system may reduce its energy by 49 kcal mol<sup>-1</sup> by desorption of H<sub>2</sub>, producing the monohydride. The bond length and angle strain in the  $(2 \times 1)$  clean surface structure exceeds that in any known organic compounds, making the reliability of both the predicted

bond length and the energetics uncertain. Similarly, the distance between non-bonded hydrogen atoms in the  $(1 \times 1):2H$  full dihydride structure is substantially shorter and the steric repulsion correspondingly greater than that in any known molecule, and the quantitative reliability of the predicted structure and energetics is therefore suspect. Hydrocarbons with strain comparable with that in the  $(2 \times 1):H$  monohydride are known,

however, and MM3 has been shown to be quantitatively accurate, and so this surface structure should be accurate.

We find MM3 to be a computationally convenient yet very powerful tool for calculating the structure and energetics of surface species on diamond. The method makes the clear prediction that the monohydride is the most stable species and that which is likely to predominate under typical CVD conditions. However, because the amount of strain and steric repulsion which is present in the  $(2 \times 1)$  clean and  $(1 \times 1):2\text{H}$  structures on diamond (100) considerably exceeds that in any molecules for which the (empirical) MM3 method has been demonstrated to be quantitatively accurate, comparisons of our results with predictions of high level quantum chemical calculations are needed.

An IMIRS spectrum of diamond (100) following an exposure to atomic deuterium at a sample temperature of about 500 K is shown in Fig. 5. A peak observed at a frequency of  $901\text{ cm}^{-1}$  is assigned to a C-D deformation mode. This assignment is based on the similarity of the frequency of the surface vibrational mode to CC-D bending modes of  $901$  and  $918\text{ cm}^{-1}$  in adamantane- $d_{16}$  [38] and  $(\text{CD}_3)_3\text{C-D}$  [39] respectively. The peak has a full width at half-maximum of approximately  $20\text{ cm}^{-1}$ , comparable with that seen for the C-H stretching mode on diamond (111) [40] and the Si-H stretching mode on flat Si(100) [28(c)]. The linewidth for hydrogen on

flat Si(100) was overwhelmingly due to inhomogeneous broadening [28(c)], which is almost certainly also the source of the linewidth seen here. The diamond (100) IRE sample was "as-polished" when inserted in the chamber, with a standard roughness quoted by the vendor as 40 nm. We recently observed, by atomic force microscopy, that an as-polished diamond (111) sample had a high density of ridges and scratches from the polishing, with most of the features 5–10 nm in height [6b]. If, as seems likely, similar features were present on our (100)-oriented IRE, they probably would not have been removed by a mild anneal and could easily account for the IR linewidth. Several other IR peaks have been observed, including features that may be associated with CH species. However, we have found that trace amounts of hydrocarbon impurities are present in the IR detector and that miscancellation between background and sample scans can lead to spurious CH peaks, and we have not yet been able to distinguish unambiguously the surface peaks from the detector (spurious) peaks.

Our preliminary IMIRS results show evidence for the monohydride, whose bending frequency has been observed here for the first time. The closeness of the peak frequency ( $901\text{ cm}^{-1}$ ) to that of molecular analogs suggests that little, if any, strain is present, which is consistent with the hydrogen being present in the  $(2 \times 1):\text{H}$  structure (Figs. 1(a), 4(a)). The apparent dominance of

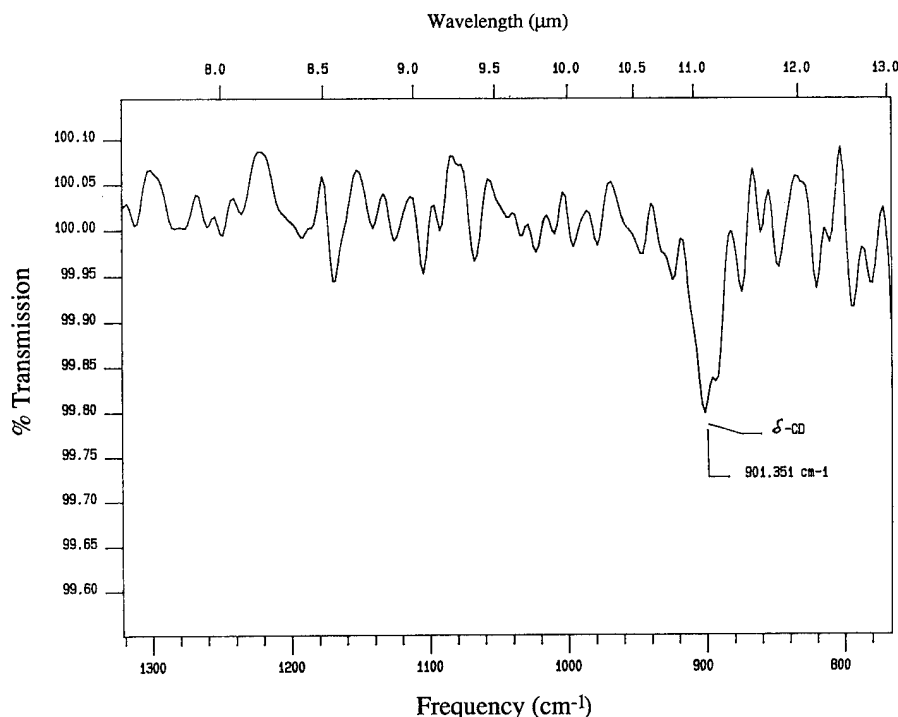


Fig. 5. Infrared multiple internal reflection spectrum, taken at  $4\text{ cm}^{-1}$  resolution with 1024 scans, of CD species on diamond (100). Deuterated surface was prepared with a 7200 L nominal dose of a hydrogenated surface at a sample temperature of 500 K.

the monohydride over dihydride-derived IR features is consistent with the monohydride being the more stable species, as predicted by MM3. We hope to improve the signal-to-noise ratio by modifying the sample holder so as to allow adsorption on both front and back faces and by growing an ultraflat CVD diamond film on the IRE [6]. We plan to determine the thermal stability of the monohydride CH mode and will try to identify conditions under which CH<sub>2</sub> species can be formed.

## Acknowledgments

The authors gratefully acknowledge the National Science Foundation (Grant CHE-8807546) and the Office of Naval Research for support of this work.

## References

- 1 (a) J. C. Angus and C. C. Hayman, *Science*, **241** (1988) 913.  
(b) W. A. Yarbrough and R. Messier, *Science* **247** (1990) 688.  
(c) F. G. Celii and J. E. Butler, *Annu. Rev. Phys. Chem.*, **42** (1991) 643.
- 2 V. B. Aleskovskii and V. E. Drozd, *Proc. 1st Int. Conf. on Atomic Layer Epitaxy*, in *Acta Polytech. Scand.*, **195** (1990) 155.
- 3 J. Nishizawa, K. Aoki, S. Suzuki and K. Kikuchi, *J. Electrochem. Soc.*, **137**, (1990) 1898; *J. Cryst. Growth*, **99** (1990) 502.
- 4 D. Lubben, R. Tsu, T. R. Bramblett and J. E. Greene, *J. Vac. Sci. Technol. A*, **9** (1991) 3003.
- 5 S. Imai, S. Takagi, O. Sugiura and M. Matsumura, *Jpn. J. Appl. Phys.*, **30** (1991) 3646.
- 6 (a) L. F. Sutcu, M. S. Thompson, C. J. Chu, R. H. Hauge, J. L. Margrave and M. P. D'Evelyn, *Appl. Phys. Lett.*, **60** (1992) 1685.  
(b) L. F. Sutcu, C. J. Chu, M. S. Thompson, R. H. Hauge, J. L. Margrave and M. P. D'Evelyn, *J. Appl. Phys.*, **71**, (1992) 5930.
- 7 P. G. Lurie and J. M. Wilson, *Surf. Sci.*, **65** (1977) 453.
- 8 T. E. Derry, C. C. P. Madiba and J. F. P. Sellschop, *Nucl. Instrum. Methods*, **218** (1983) 559.
- 9 A. V. Hamza, G. D. Kubiak and R. H. Stulen, *Surf. Sci.*, **237** (1990) 35.
- 10 (a) R. E. Thomas, R. A. Rudder and R. J. Markunas, in A. J. Purdes, J. C. Angus, R. F. Davis, B. M. Meyerson, K. E. Spear and M. Yoder (eds.), *Diamond Materials*, The Electrochemical Society, Pennington, NJ, 1991, p. 186.  
(b) R. E. Thomas, R. A. Rudder and R. J. Markunas, *J. Vac. Sci. Technol. A*, **10** (1992) 2451.  
(c) R. E. Thomas, R. A. Rudder, R. J. Markunas, D. Huang and M. Frenklach, *J. Chem. Vapor Deposition*, **1** (1992) 1.
- 11 H. K. Schmidt, J. A. Schultz and Z. Zheng, in R. E. Clausing et al. (eds.) *Diamond and Diamond-Like Films and Coatings*, Plenum, New York, 1991, p. 669.
- 12 For example, M. L. Wise, B. G. Koehler, P. Gupta, P. A. Coon and S. M. George, *Surf. Sci.*, **258** (1991) 166.
- 13 W. S. Yang, J. Sokolov, F. Jona and P. M. Marcus, *Solid State Commun.*, **41** (1982) 191.
- 14 (a) B. B. Pate, M. H. Hecht, C. Binns, I. Lindau and W. E. Spicer, *J. Vac. Sci. Technol.*, **21** (1982) 364.  
(b) B. Pate, *Surf. Sci.*, **165** (1986) 83.
- 15 B. J. Wacławski, D. T. Pierce, N. Swanson and R. J. Celotta, *J. Vac. Sci. Technol.*, **21** (1982) 368.
- 16 A. V. Hamza, G. D. Kubiak and R. H. Stulen, *Surf. Sci.*, **206** (1988) L833.
- 17 (a) T. Sakurai and H. D. Hagstrum, *Phys. Rev. B*, **14** (1976) 1593.  
(b) Y. J. Chabal and K. Raghavachari, *Phys. Rev. Lett.*, **54** (1985) 1055.  
(c) J. J. Boland, *Phys. Rev. Lett.*, **65** (1990) 3325.  
(d) K. Oura, J. Yamane, K. Umezawa, M. Naitoh, F. Shoji and T. Hanawa, *Phys. Rev. B*, **41** (1990) 1200.  
(e) C. C. Cheng and J. T. Yates, Jr., *Phys. Rev. B*, **43** (1991) 4041.  
(f) J. E. Northrup, *Phys. Rev. B*, **44** (1991) 1419.  
(g) J. J. Boland, *Surf. Sci.*, **261** (1992) 17.  
(h) Z. H. Lu, K. Griffiths, P. R. Norton and T. K. Sham, *Phys. Rev. Lett.*, **68** (1992) 1343.
- 18 (a) Y. L. Yang and M. P. D'Evelyn, *J. Am. Chem. Soc.*, **114** (1992) 2796; *J. Vac. Sci. Technol. A*, **10** (1992) 978.
- 19 D. Huang and M. Frenklach, *J. Phys. Chem.*, **96** (1992) 1868.
- 20 M. P. D'Evelyn, L. M. Ulvick, L. F. Sutcu, Y. L. Yang, S. M. Cohen, E. Roucouze and T. Jin, Ultrahigh vacuum apparatus for combined surface science and *in situ* studies of chemical vapor deposition, in preparation.
- 21 Y. L. Yang, *PhD Dissertation*, Department of Chemistry, Rice University, 1992 (unpublished).
- 22 S. M. Ko and L. D. Schmidt, *Surf. Sci.*, **42** (1974) 508.
- 23 G. D. Kubiak, paper presented at the *Fourth Chemical Congress of North America*, New York, August 25–30, 1991.
- 24 P. W. Tamm and L. D. Schmidt, *J. Chem. Phys.*, **54** (1971) 4775.
- 25 J. B. Marsh and H. E. Farnsworth, *Surf. Sci.*, **1** (1964) 3.
- 26 G. Vidali and D. R. Frankl, *Phys. Rev. B*, **27** (1983) 2480.
- 27 Y. Mitsuda, T. Yamada, T. J. Chuang, H. Seki, R. P. Chin, J. Y. Huang and Y. R. Shen, *Surf. Sci.*, **257** (1991) L633.
- 28 (a) N. J. Harrick, *Phys. Rev. Lett.*, **4** (1960) 224.  
(b) N. J. Harrick, *Internal Reflection Spectroscopy*, Wiley, New York, 1967.  
(c) Y. J. Chabal, *Surf. Sci.*, **168** (1986) 594 and references cited therein.  
(d) J. R. Swanson, C. M. Friend and Y. J. Chabal, *J. Chem. Phys.*, **87** (1987) 6725.  
(e) U. Jansson and K. J. Uram, *J. Chem. Phys.*, **91** (1989) 7978.  
(f) J. E. Crowell and G. Lu, *Mater. Res. Soc. Symp. Proc.*, **198** (1990) 533.
- 29 M. P. D'Evelyn, Y. L. Yang, S. M. Cohen and L. M. Ulvick, Ultrahigh vacuum apparatus for infrared multiple-internal-reflection spectroscopy studies on semiconductor surfaces, in preparation.
- 30 (a) N. L. Allinger, Y. H. Yuh and J. Lii, *J. Am. Chem. Soc.*, **111** (1989) 8551.  
(b) J. Lii and N. L. Allinger, *J. Am. Chem. Soc.*, **111** (1989) 8566.  
(c) J. Lii and N. L. Allinger, *J. Am. Chem. Soc.*, **111** (1989) 8576.  
(d) N. L. Allinger, F. Li and L. Yan, *J. Comput. Chem.*, **11** (1990) 849.  
(e) N. L. Allinger, F. Li, L. Yan and J. C. Tai, *J. Comput. Chem.*, **11** (1990) 868.
- 31 *MM3(89) Operation Manual*, Quantum Chemistry Program Exchange, University of Indiana, Bloomington, IN 47405, 1989.
- 32 M. R. Imam and N. L. Allinger, *J. Molec. Struct.*, **126** (1985) 345.  
N. L. Allinger, private communication, 1992.
- 33 P. A. Redhead, *Vacuum*, **12** (1962) 203.
- 34 M. P. D'Evelyn, Y. L. Yang and L. F. Sutcu, *J. Chem. Phys.*, **96** (1992) 852.
- 35 M. T. Schulberg, G. D. Kubiak and R. H. Stulen, *Mater. Res. Soc. Symp. Proc.*, **270** (1992) 401.
- 36 (a) S. M. Gates, R. R. Kunz and C. M. Greenlief, *Surf. Sci.*, **207** (1989) 364.



- (b) K. Sinniah, M. G. Sherman, L. B. Lewis, W. H. Weinberg, J. T. Yates, Jr., and K. C. Janda, *J. Chem. Phys.*, **92** (1990) 5700.
- 37 (a) S. M. Cohen, T. I. Hukka, Y. L. Yang and M. P. D'Evelyn, Hydrogen-halogen chemistry on semiconductor surfaces, *Thin Solid Films*, **225** (1993) 154.
- (b) M. P. D'Evelyn, S. M. Cohen, E. Rouchouze and Y. L. Yang, Surface  $\Pi$  bonding and the near-first-order desorption kinetics of hydrogen from Ge(100)( $2 \times 1$ ), *J. Chem. Phys.*, in press.
- 38 R. T. Bailey, *Spectrochim. Acta* **27A** (1971) 1447.
- 39 J. K. Wilmshurst and H. J. Bernstein, *Can. J. Chem.*, **35** (1957) 969.
- 40 R. P. Chin, J. Y. Huang, Y. R. Shen, T. J. Chuang, H. Seki and M. Buck, *Phys. Rev. B*, **45** (1992) 1522.

# Novel method for chemical vapor deposition and atomic layer epitaxy using radical chemistry

Terttu I. Hukka, Robin E. Rawles, and Mark P. D'Evelyn

Department of Chemistry and Rice Quantum Institute, Rice University, Houston, TX 77251-1892 (USA)

## Abstract

A novel method for chemical vapor deposition and atomic layer epitaxy using radical precursors under medium vacuum conditions is being developed. Fluorine atoms are generated by thermal dissociation in a hot tube and abstract hydrogen atoms from precursor molecules injected immediately downstream of the source, generating radicals with complete chemical specificity. The radical precursors are then transported to the growing substrate surface under nearly collision-free conditions. To date we have grown diamond films from  $\text{CCl}_3$  radicals together with atomic hydrogen, generated by injecting  $\text{CHCl}_3$  and  $\text{H}_2$  into the fluorine atom stream at reactor pressures between  $10^{-3}$  and  $10^{-2}$  Torr. This approach should be ideal for low-temperature growth and atomic layer epitaxy: growth rates remain relatively high because activation energies for radical reactions are typically small and because the cycle times for atomic layer epitaxy can be reduced to the millisecond range by fast gas-stream switching, and contamination and segregation are minimized by keeping the surface "capped" by chemisorbed intermediates and working under ultraclean conditions.

## 1. Introduction

Atomic layer epitaxy (ALE) is a powerful technique for growing semiconductor materials one atomic layer at a time [1]. Relative to more conventional growth methods, ALE possesses several distinct advantages which are likely to be critical to development of the next generation of electronic devices: (i) the *digital* nature of the process, *i.e.* growth of a well defined number of monolayers, offering the ultimate in control of film thickness; (ii) the *uniformity* of growth on large-area substrates, since each reaction cycle runs to completion regardless of deviations in reactant fluxes; (iii) intrinsic capability for *atomically abrupt* heteroepitaxial interfaces. In addition, ALE processes are normally carried out at lower temperatures than the corresponding chemical vapor deposition (CVD) process, again allowing smaller and more sharply defined circuit elements to be fabricated.

Originally developed for growth of II–VI materials, ALE has been widely applied to growth of GaAs and other III–V semiconductors [1]. However, ALE is still in its infancy for Group IV semiconductors. Nishizawa *et al.* [2] demonstrated ALE with a growth rate of one monolayer per cycle using alternating fluxes of  $\text{SiH}_2\text{Cl}_2$  and  $\text{H}_2$  at temperatures near 825 °C. Lubben *et al.* [3] obtained a growth rate of 0.4 monolayers per cycle from a process involving alternating  $\text{Si}_2\text{H}_6$  doses and UV laser pulses at substrate temperatures of 180–400 °C, and Imai *et al.* [4] obtained a growth rate of 0.8

monolayers per cycle by adsorbing  $\text{Si}_3\text{H}_8$  at temperatures between 50 and 380 °C and desorbing surface hydrogen at temperatures above 520 °C. Preliminary accounts of ALE on germanium [5] and diamond [6] as well as on silicon [7] have also been reported.

Radical chemistry would be ideal for ALE but has not yet been applied to any ALE process. Dichlorosilane is not highly reactive, thus necessitating high growth temperatures [2]. Disilane and trisilane are more reactive than dichlorosilane but not as reactive as radicals, and adsorption saturates at coverages considerably below one monolayer [3, 4]. The attainment of low growth temperatures is a central goal of current research—interdiffusion is greatly reduced, which is essential in fabricating circuit elements smaller than 0.1  $\mu\text{m}$ , and the effects of differential thermal expansion coefficients in complex layered materials are minimized. However, the use of low temperatures introduces stringent demands on the cleanliness of the process. A process that involves creating a clean surface for adsorption, *e.g.* of  $\text{Si}_2\text{H}_6$ , will be very susceptible to contamination, and segregation, interdiffusion, and three-dimensional island formation in  $\text{Ge}_x\text{Si}_{1-x}$  heterostructures all occur more readily on clean than on covered surfaces [8, 9]. While there is evidence that  $\text{Si}_2\text{H}_6$  can react with hydrogenated silicon surfaces at substrate temperatures above 400 °C [10–12], growth at these temperatures appears not to be self-terminating. An ideal ALE growth process would take place at low temperature and keep the surface covered by protective

groups during the process so as to minimize contamination and segregation. Radical reactants can create their own surface "site" by abstracting adsorbed atoms which stabilize and protect the substrate lattice from less reactive species (*e.g.* contaminants). Radicals thus are conducive to low-temperature growth, as creation of vacant sites by thermal desorption is not necessary, and simultaneously provide an elegant solution to the contamination and segregation problem, *i.e.* capped surfaces. Another advantage of radical precursors is that once adsorbed, radicals are much more likely to decompose (yielding growth) than simply desorb (yielding nothing). This preference for decomposition over desorption is the most likely reason why  $\text{CH}_3$  is a more effective growth precursor for diamond than  $\text{C}_2\text{H}_2$  [13–16].

Performing growth from radical precursors in a high vacuum environment offers several additional advantages. Gas-phase collisions subsequent to radical formation can be minimized, enabling the creation of very specific radicals. Two mechanistic advantages are that the identity of the reactant species responsible for growth is easy to determine, and surface analytical techniques can be more readily applied in order to understand the surface chemistry. Control of contamination is facilitated by an ultraclean, ultrahigh vacuum compatible environment. Finally, in a high vacuum environment ALE reaction cycle times associated with switching gases can in principle be reduced to the millisecond time scale, allowing for substantial growth rates, which is very important if group IV ALE is to become a commercially significant process.

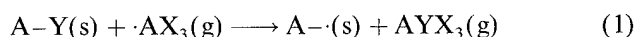
As a general growth technique, remote plasma-enhanced CVD (RPCVD) [17, 18] comes close to the ideal, as it generates reactive species without allowing the plasma to damage the sample by direct contact. However, RPCVD does not selectively produce reactive radicals—interaction of excited atoms, ions and electrons with the molecular growth precursor (*e.g.*  $\text{SiH}_4$ ) can generate a variety of reactive species. For ALE, the difficulty is that two reactive species are produced from each molecular precursor, *e.g.*  $\text{SiH}_3 + \text{H}$ , which complicates and may prevent growth reactions from being self-limiting and reduces the flexibility of the process. Better would be a process where well defined radical species are produced without side reactions.

We are developing a new ALE method for epitaxial growth of diamond, silicon, and germanium, using gas phase radicals under high vacuum conditions (effective pressure above the substrate up to 0.1 Torr, background pressure less than  $10^{-2}$  Torr). Considerations affecting the choice of radical precursors and the apparatus and radical generation scheme are described in the next two sections. Preliminary results on radical generation and film growth of diamond are presented next, followed by a discussion.

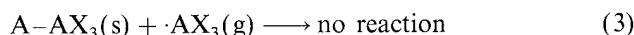
## 2. Radical growth chemistry

For ALE, the radical growth precursor should not be too reactive, or else the reaction will not be self-terminating. In the context of diamond or silicon ALE, for example, carbenes and silylenes ( $\text{CX}_2$  or  $\text{SiX}_2$ ,  $\text{X}=\text{H}$ ,  $\text{F}$ ,  $\text{Cl}$ , etc.) are too reactive to be useful. These species will readily insert into  $\text{C}-\text{H}$  or  $\text{Si}-\text{H}$  bonds, producing  $\text{CX}_2\text{H}$  or  $\text{SiX}_2\text{H}$ , which in turn can undergo another insertion reaction. In addition, a less reactive radical will yield better selectivity, *e.g.* the rate of reaction with tertiary hydrogen atoms will be much greater than the rate with secondary hydrogen atoms.

Monovalent radicals would seem to be ideal for sticking to dangling bonds on Group IV semiconductor surfaces. What types of radicals are well suited for ALE processes? Consider the growth step in a general, ALE-type radical-surface growth process, where  $\text{A}=\text{C}$ ,  $\text{Si}$ , or  $\text{Ge}$ , and  $\text{X}$  and  $\text{Y}$  represent arbitrary functional groups:

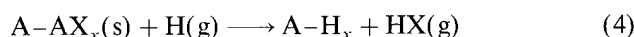


A surface  $\text{Y}$  group is abstracted by an  $\text{AX}_3$  radical; a second  $\text{AX}_3$  radical then adsorbs on the resulting dangling bond site. For reactions (1) and (2) to be self-terminating, the reaction of  $\text{AX}_3(\text{g})$  with  $\text{A}-\text{Y}(\text{s})$  must be faster than the reaction with  $\text{A}-\text{X}(\text{s})$ :



Abstraction of hydrogen atoms is much more facile than abstraction of halogen atoms, for both alkyl [19] and silyl radicals [20]. Thus, the most natural choice is  $\text{Y}=\text{H}$ ,  $\text{X}=\text{halogen}$ . As an example, alternating cycles of  $\text{CCl}_3$  and  $\text{H}$  are likely to be a good choice for ALE of diamond, as self-termination should occur naturally. The reaction of  $\text{CCl}_3$  with a hydrogenated diamond surface will self-terminate because the activation energy for abstraction of  $\text{H}$  by  $\text{CCl}_3$  is lower by at least  $15 \text{ kcal mol}^{-1}$  than the activation energy for abstraction of  $\text{Cl}$  [19]. In contrast, the activation energies for abstraction of  $\text{Cl}$  and primary hydrogen by  $\text{CH}_3$  are nearly the same [19], so that the reaction of methyl radicals with a chlorinated diamond surface is unlikely to self-terminate and cycles of  $\text{CH}_3$  and  $\text{Cl}$  are a poor choice for diamond ALE.

To complete the ALE cycle, a hydrogenated surface can be regenerated from the halogen-terminated surface (produced by adsorption of  $\text{AX}_3$ ) by abstraction and recombination reactions with atomic hydrogen:



where uncertainty in the actual stoichiometry in the surface species is indicated by the  $x$  subscript ( $x = 1, 2$ , or  $3$ ) and stoichiometric coefficients are omitted from

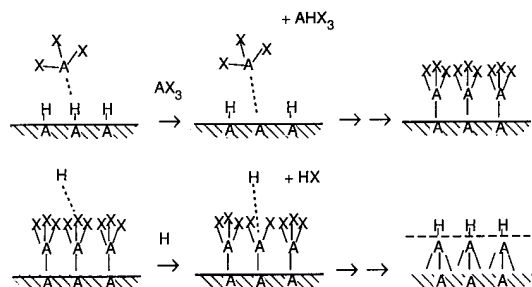


Fig. 1. Schematic representation of radical ALE growth chemistry. In the first "growth" portion of the ALE cycle, trihalo (or dihalo) radicals ( $A\equiv C$  or  $Si$ ) impinge on a hydrogen terminated surface, abstracting hydrogen atoms and creating vacant surface sites. Radicals then quickly adsorb on the vacant site. When the surface becomes halogen terminated the reaction stops, since abstraction rates of halogen atoms are much lower than those of hydrogen atoms. In the "cleaning" or "reactivation" portion of the cycle, hydrogen atoms abstract surface halogen atoms and then stick to the vacant surface sites, regenerating the hydrogen-terminated surface which has been augmented by one monolayer. This illustration is oversimplified, as a full monolayer of trihalide species will not fit on either  $Si(100)$  or diamond (100) surfaces—rearrangements and/or desorption of  $HX$  must take place.

the equation. We have opted to use hydrogen atoms because  $H$  abstracts halogen atoms from carbon much better than do carbon-centered radicals [19]. Recent work by Yates and coworkers has shown that abstraction of  $Cl$ ,  $Br$ , and  $I$  from  $Si(100)$  by atomic hydrogen is quite facile, with activation energies less than or equal to  $2 \text{ kcal mol}^{-1}$  [21]. On silicon,  $SiH_3$  is also an excellent halogen abstractor, and alternating cycles of  $SiCl_3$  and  $SiH_3$  might yield a good ALE process.

To summarize, in our proposed ALE sequence a trihalo radical ( $AX_3$ ) reacts with a hydrogenated surface ( $A-H_x$ ), first by abstraction of surface hydrogen and then by recombination with the vacant site, to yield a halogenated substrate which has been augmented by one monolayer (or perhaps a fraction of a monolayer). Atomic hydrogen is then allowed to react with the halogenated surface, regenerating a hydrogenated surface. This is illustrated schematically in Fig. 1.

The uncertainty in the stoichiometry of the self-terminated surface adlayer ( $A-AX_x$ ) in eqn. (4) reflects an uncertainty in the saturation coverage of this species and, consequently, in the number of monolayers per cycle that would result from this sequence. Neglected in eqn. (2) is the fact that steric repulsion will prevent formation of a complete monolayer of  $A-AX_3$ . Formation of a full  $(1 \times 1):2H$  dihydride surface (*i.e.*  $AH_2$ ), on  $Si(100)$  has until recently been controversial [22] (observation of a  $(1 \times 1)$  diffraction pattern does not prove that a full dihydride has formed), and on diamond (100) the dihydride appears to be too sterically hindered to form under growth conditions [23, 24]. Given the much larger covalent radius for  $Cl$  than  $H$ , it

seems clear that a full monolayer of  $ACl_2$  groups will not fit on either diamond or silicon, and the saturation coverage of  $ACl_3$  would be even smaller.

Two possible resolutions of the saturation coverage question are envisaged. The first is that under growth conditions, the adsorbed  $AX_3$  groups will probably not remain intact. For example,  $SiH_3$  groups on  $Si(100)$  decompose to  $SiH_2 + H$  [25, 26] at temperatures between 200 and 600 K, depending on the surface hydrogen coverage [26]. A second possibility is that some of the surface halogen atoms will react with surface hydrogen and desorb as  $HX$ , and the relatively favorable kinetics of dehydrohalogenation reactions served as an additional motivation for choosing halogen-hydrogen chemistry for the ALE growth chemistry. Reaction of  $X$  atoms might take place with preadsorbed hydrogen left over from the last hydrogenating cycle, or alternatively could be present in the precursor (*i.e.*  $AHX_2$  could be used rather than  $AX_3$ ).

### 3. Experimental details

Our radical CVD-ALE reactor, which has conceptual similarities to a remote-plasma-enhanced CVD reactor but uses thermally dissociated fluorine instead of discharge-excited helium or argon and has an ultrahigh-vacuum-compatible, corrosive-service turbomolecular pump which can handle a heavy load of corrosive gases, is illustrated schematically in Fig. 2. The turbomolecular pump is backed by an integral molecular drag stage and by an oil-free diaphragm pump.  $F_2$  or  $XeF_2$  is injected into an  $MgO$  tube which is wrapped by nickel

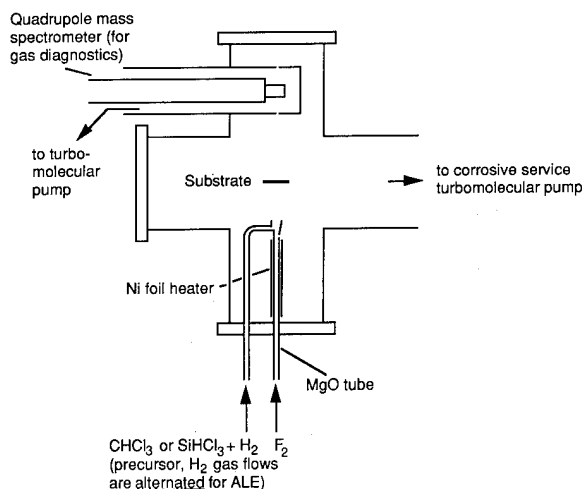


Fig. 2. Schematic diagram of ultrahigh-vacuum-compatible radical ALE growth apparatus. Precursor molecules are injected into a stream of fluorine atoms generated by thermal dissociation in an  $MgO$  tube wrapped by resistively heated nickel foil, producing radicals and  $HF$ . The radicals are then transported to the substrate under nearly collision-free conditions.

foil. The nickel foil acts as a furnace for the MgO tube and is resistively heated to a temperature of 700–800 °C, yielding fluorine dissociation in the range 96%–98% at a pressure of approximately 1 Torr [27]. Undissociated F<sub>2</sub> should be able to react with the radicals produced by H abstraction [28]. MgO is chosen as the wall material because MgF<sub>2</sub>, which will form on the inside wall of the tube, is among the least volatile of all the fluorides (lower than NiF<sub>2</sub>, for example), with a vapor pressure of 10<sup>-8</sup>–10<sup>-6</sup> Torr in this temperature range. The principal advantages of a thermal source relative to a discharge source are simplicity, low cost, and flexibility in the choice of gas pressures and flow rates (maintenance of a plasma discharge requires a substantial pressure and flow rate). For a scaled-up reactor, a plasma fluorine atom source would probably be preferable. The fluorine atoms abstract hydrogen atoms quantitatively from precursor molecules injected in excess downstream from the fluorine source where the gas density is high enough for collisions. The extreme reactivity of fluorine atoms toward hydrogen drives the reaction to completion, producing HF (135 kcal mol<sup>-1</sup> bond energy), which is non-reactive to hydrogen-terminated diamond, silicon, and germanium in the absence of water. The radicals (and HF) formed downstream of the fluorine-atom source flow under nearly collision-free conditions to the substrate. Fluorine-atom-based secondary generation of radicals has been used to etch semiconductor substrates (at rates up to 1000 Å min<sup>-1</sup>) [28] but is being applied to growth for the first time in the present work.

The gas handling system is constructed of stainless steel tubing and fittings, with most of the joints made with Cajon VCR fittings. The flow rates of reactant gases are controlled with piezoelectric valves, which have rapid switching times and hence will be well suited to ALE, and are monitored by mass flowmeters.

Our initial film growth efforts have focused on diamond. Since only a handful of groups have successfully demonstrated diamond film growth at pressures less than 1 Torr [29], we felt it essential to demonstrate growth by CVD (continuous reactant fluxes) before attempting ALE. Preliminary results were obtained using mixtures of H<sub>2</sub> and CHCl<sub>3</sub> as precursor gases. The reagents F<sub>2</sub> (Air Products, 97%), CHCl<sub>3</sub> (Aldrich, 99.9%), and H<sub>2</sub> (Air Products, 99.9995%) were used without further purification. The CHCl<sub>3</sub> was carefully outgassed before use by numerous freeze–evacuate–thaw cycles. Typical flow rates were 1–1.5 standard cm<sup>3</sup> min<sup>-1</sup> F<sub>2</sub>, 4–6 standard cm<sup>3</sup> min<sup>-1</sup> H<sub>2</sub>, and 2–6 standard cm<sup>3</sup> min<sup>-1</sup> CHCl<sub>3</sub>. The chamber pressure rose to 10<sup>-3</sup>–10<sup>-2</sup> Torr during growth.

The substrates were type 2A, (100)-oriented natural diamond windows, 3.0 × 3.0 × 0.22 mm<sup>3</sup> in dimension, purchased from Dubbeldee Harris. Two different sub-

strate holding–heating schemes were employed. The first used 0.025 mm thick platinum foil, heated resistively, as both holder and heater. The sample temperature was measured by a chromel–alumel thermocouple spot-welded to the foil immediately adjacent to the sample. The second sample holder consisted of two graphite rods, 1.6 mm in diameter, with the sample held between them in slots machined in the sides of the rods. The thermocouple was embedded in one of the graphite rods. The latter scheme has the advantage of providing a rigid sample support, which is very helpful for thickness measurements. The samples were held at 850–950 °C during the growth experiments.

Films were characterized by Raman spectroscopy, scanning electron microscopy, and electron-beam microprobe. Film thicknesses were determined by measuring the total thickness of the diamond (100) substrates before and after growth from the fringe pattern in Fourier transform IR transmission spectra [14b].

#### 4. Results

Our initial tests of the radical source focused on demonstration of radical production. Mass spectra of CHCl<sub>3</sub> and of CCl<sub>3</sub> produced by hydrogen abstraction by atomic fluorine are shown in Fig. 3. Mass spectrometry of chlorohydrocarbons is complicated by the existence of both 35 and 37 amu isotopes of chlorine and by electron-impact-induced loss of hydrogen. The latter can be eliminated by reducing the electron energy in the ionizer to just above the ionization threshold. The spectra shown in Fig. 3 were obtained at an electron energy of 15.9 eV, which was found to be

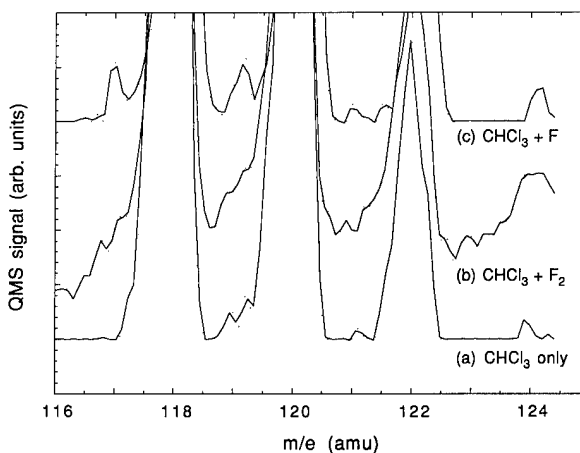


Fig. 3. Threshold ionization mass spectra of (a) CHCl<sub>3</sub> only, (b) CHCl<sub>3</sub> injected into a stream of F<sub>2</sub> (MgO tube at room temperature), and (c) CHCl<sub>3</sub> injected into a stream of fluorine atoms (MgO tube at 750 °C). The mass spectra were obtained at an electron energy of 15.9 eV.

sufficiently low to suppress the hydrogen-loss mass peaks. The mass spectrum of  $\text{CHCl}_3$  injected alone (Fig. 3(a)) shows prominent peaks at  $m/e = 118$ , 120, and 122, with a minor peak at 124 amu, corresponding to the parent ions. The observed intensity ratios correspond well to that expected from the approximately 3:1  $^{35}\text{Cl}$ -to- $^{37}\text{Cl}$  natural isotopic abundance ratio. After heating the MgO tube furnace to 750 °C and injecting  $\text{F}_2$  into it, the mass spectrum shown in Fig. 3(c) was obtained. Small peaks at  $m/e = 117$ , 119, and 121 amu are visible, corresponding to  $\text{CCl}_3$  radicals. The intensity ratios of the  $m/e = 117$ , 119, and 121 peaks are in good agreement with the expected ratios of 3:3:1. In order to eliminate chemistry in the ion source of the mass spectrometer as a spurious source of the radical mass peaks, spectra were also obtained during injection of  $\text{CHCl}_3$  and  $\text{F}_2$  with the MgO tube held at room temperature. A typical result is shown in Fig. 3(b). The absence of peaks corresponding to loss of a hydrogen atom in Fig. 3(b) indicates that the radical peaks seen in Fig. 3(c) are not simply the result of reaction of  $\text{F}_2$  and  $\text{CHCl}_3$  in the ion source.

The low signal-to-noise ratio in Fig. 3 is the result of the low electron energy, together with the fact that a single stage of differential pumping is insufficient to discriminate properly against background gases—considerable recombination of the  $\text{CCl}_3$  radicals takes place within both the reactor and the mass spectrometer chamber. Operation of the mass spectrometer in a partial pressure of  $\text{F}_2$  causes even further degradation of the signal level, which is responsible for the lower signal-to-noise ratio in Fig. 3(b), and prolonged exposure to  $\text{F}_2$  burns out the filaments. Normal operation of the radical source quantitatively converts the fluorine to HF, which is much less reactive.

To date the best evidence we have obtained for diamond growth using the new method is a film grown using  $\text{CHCl}_3$  as the precursor which increased in thickness by 0.9  $\mu\text{m}$  in 12 h, corresponding to a modest growth rate of 0.08  $\mu\text{m h}^{-1}$ . We conservatively estimate the uncertainty in the thickness measurements to be  $\pm 0.2$ –0.5  $\mu\text{m}$ , so the thickness increase appears to be real. A scanning electron micrograph of this film is shown in Fig. 4, and a Raman spectrum obtained after growth is shown in Fig. 5. The micrograph also suggests that growth has occurred: the linear features arranged by 90° with respect to one another on the left-hand portion of the image are highly suggestive of ledge features arising from growth, as the (100) substrate has square symmetry, steps and/or ledges along [011] and [0 $\bar{1}$ 1] are commonly observed in [100]-oriented epitaxy, the as-polished substrate had no such features originally, and etching under high vacuum conditions normally roughens surfaces rather than creating regular features. Deposits of metal fluorides

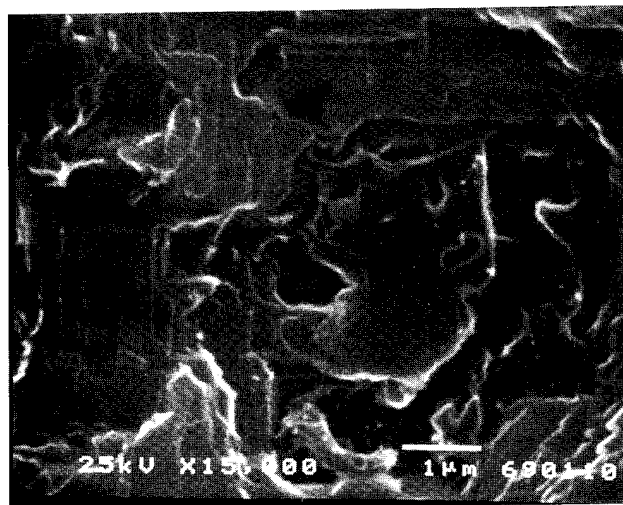


Fig. 4. Scanning electron micrograph of a 0.9- $\mu\text{m}$ -thick film grown in 12 h from  $\text{CCl}_3\text{-H}$  on a diamond (100) substrate.

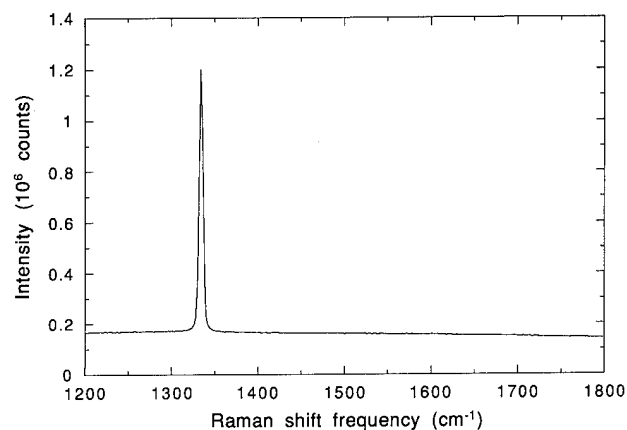


Fig. 5. Raman spectrum of a 0.9- $\mu\text{m}$ -thick film grown in 12 h from  $\text{CCl}_3\text{-H}$  on a diamond (100) substrate.

( $\text{NiF}_2$ ,  $\text{MgF}_2$ ,  $\text{AlF}_3$ ,  $\text{CaF}_2$ , and  $\text{SiF}_2$ ) were sometimes observed on portions of the sample, the sample holder and on the chamber walls, and could be responsible for the globular features on the right-hand portion of Fig. 4. Areas of the sample which were free of visible particulates appeared to be contamination free at the sensitivity of the electron-beam microprobe. Surface contamination may nonetheless have reduced the growth rate. We believe that an initial design for the gas injector was responsible for the  $\text{NiF}_2$  impurities, as  $\text{NiF}_2$  was eliminated following its modification and was not present on the film shown in Fig. 4. We believe that a Macor insulator in the sample holder was the principal source of the remaining contamination, and it is currently being modified. The Raman spectrum indicates that no non-diamond carbon was deposited, to within our sensitivity limit, as no feature near 1550  $\text{cm}^{-1}$  associated with graphitic carbon is visible.

## 5. Discussion

We have proposed a new method for ALE and CVD using radical precursors under high vacuum conditions. We have presented a rationale for the use of cycles of halogenated radicals and atomic hydrogen for growth of the Group IV semiconductors diamond, silicon, and germanium based on well known radical chemistry, and have delineated some of the issues involved in determining the number of monolayers per cycle that can be deposited using this chemistry.

We have chosen to generate the radicals with a secondary source using thermally dissociated fluorine atoms. This approach has several advantages: well defined radical species may be produced without side reactions; a very wide variety of radicals may be produced using standard, commercially available precursor gases; the reactor and process can be readily scaled up without inordinate effort or cost; the basic methodology should be applicable to synthesis of a wide variety of materials; the complexity, cost, and power-consumption of discharge sources are avoided. The principal drawback of the fluorine-atom-abstraction approach is the production of HF. The HF abstraction product necessitates the use of corrosion-resistant pumps and will prevent the growth of materials which are strongly attacked by HF even in the absence of water. For example, in order to grow silicon by this method it will almost certainly be necessary to work at substrate temperatures low enough that the surface hydrogen (or halogen) coverage remains very high throughout the process so as to passivate the surface to HF adsorption. HF adsorbs readily on clean Si(100) [30], and the dominant pathway for surface fluorine removal is likely to be desorption of  $\text{SiF}_2$ , i.e. etching, although abstraction by atomic hydrogen is also a less deleterious possibility. A disadvantage of the thermal dissociation source relative to a discharge source is that material compatibility issues are more stringent. We find, for example, that if a significant fraction of the  $\text{F}_2$  is not consumed by abstraction and the nickel foil has not been carefully passivated, the nickel foil becomes etched and fails within several days.

Further diamond growth experiments are currently underway in our laboratory. We hope to improve several aspects of the experiments, including the reliability of the radical source and the sensitivity of growth rate measurements. Once incontrovertible evidence for diamond growth has been achieved and the approximate parameter values for optimal growth have been identified, we hope to be able to achieve ALE by cycling the reactant fluxes.

## Acknowledgments

The authors gratefully acknowledge the Office of Naval Research for support of this work and the Academy of

Finland for additional support. We also thank Dr Dan Callahan for assistance with the scanning electron microscopy, and Benjamin Bai and Dr Judy Chu for assistance with the Raman spectroscopy.

## References

- 1 T. Suntola, *Mater. Sci. Rep.* **4** (1989) 265.
- 2 J. Nishizawa, K. Aoki, S. Suzuki and K. Kikuchi, *J. Electrochem. Soc.*, **137** (1990) 1898; *J. Cryst. Growth*, **99** (1990) 502.
- 3 D. Lubben, R. Tsu, T. R. Bramblett and J. E. Greene, *J. Vac. Sci. Technol. A*, **9** (1991) 3003.
- 4 S. Imai, S. Takagi, O. Sugiura and M. Matsumura, *Jpn. J. Appl. Phys.*, **30** (1991) 3646.
- 5 (a) Y. Takahashi, H. Ishii and K. Fujinaka, *J. Electrochem. Soc.*, **136** (1989) 1826.  
(b) Y. Takahashi, T. Urisu and Y. Sese, *Jpn. J. Appl. Phys.*, **28** (1989) 2387.
- 6 V. B. Aleksovskii and V. E. Drozd, in *Proc. 1st Int. Symp. on Atomic Layer Epitaxy, Acta Polytech. Scand.*, **195** (1990) 155.
- 7 T. Tanaka, Y. Nagasawa, S. Miyazaki and M. Hirose, *Appl. Phys. Lett.*, **56** (1990) 1445.
- 8 M. Copel, M. C. Reuter, M. Horn von Hoegen and R. M. Tromp, *Phys. Rev. B*, **42** (1990) 11682.
- 9 S. M. Gates and D. D. Koleske, *Thin Solid Films*, **225** (1993) 159.
- 10 S. K. Kulkarni, S. M. Gates, C. M. Greenlief and H. H. Sawin, *J. Vac. Sci. Technol. A*, **8** (1990) 2956.
- 11 J. J. Boland, *Phys. Rev. B*, **44** (1991) 1383.
- 12 S. M. Gates and C. M. Chiang, *Chem. Phys. Lett.*, **184** (1991) 448.
- 13 (a) L. R. Martin and M. W. Hill, *J. Mater. Sci. Lett.*, **9** (1990) 621.  
(b) S. J. Harris and L. R. Martin, *J. Mater. Res.*, **5** (1990) 2313.  
(c) L. R. Martin, High quality diamonds from an acetylene growth mechanism, *J. Mater. Sci. Lett.*, in press.
- 14 (a) C. J. Chu, M. P. D'Evelyn, R. H. Hauge and J. L. Margrave, *J. Mater. Res.*, **5** (1990) 2405.  
(b) C. J. Chu, M. P. D'Evelyn, R. H. Hauge and J. L. Margrave, *J. Appl. Phys.*, **70** (1991) 1695.  
(c) M. P. D'Evelyn, C. J. Chu, R. H. Hauge and J. L. Margrave, *J. Appl. Phys.* **71** (1992) 1528.
- 15 C. E. Johnson, W. A. Weimer and F. M. Cerio, *J. Mater. Res.*, **7** (1992) 1427.
- 16 S. J. Harris and D. N. Belton, *Jpn. J. Appl. Phys.*, **30** (1991) 2615.
- 17 R. Rudder, G. Fountain and R. Markunas, *J. Appl. Phys.*, **60** (1986) 3519.
- 18 B. Anthony, L. Breaux, T. Hsu, S. Banerjee and A. Tasch, *J. Vac. Sci. Technol. B*, **7** (1989) 621.
- 19 J. A. Kerr, in J. K. Kochi (ed.), *Free Radicals*, Wiley, New York, 1973, p. 1.
- 20 J. W. Wilt, in R. A. Abramovitch (ed.), *Reactive Intermediates*, Vol. 3, Plenum, New York, 1983, p. 113.
- 21 C. C. Cheng, S. R. Lucas, H. Gutleben, W. J. Choyke and J. T. Yates, Jr., *J. Am. Chem. Soc.*, **114** (1992) 1249.
- 22 (a) T. Sakurai and H. D. Hagstrum, *Phys. Rev. B*, **14** (1976) 1593.  
(b) Y. J. Chabal and K. Raghavachari, *Phys. Rev. Lett.*, **54** (1985) 1055.  
(c) J. J. Boland, *Phys. Rev. Lett.*, **65** (1990) 3325.  
(d) K. Oura, J. Yamane, K. Umezawa, M. Naitoh, F. Shoji and T. Hanawa, *Phys. Rev. B*, **41** (1990) 1200.  
(e) C. C. Cheng and J. T. Yates, Jr., *Phys. Rev. B*, **43** (1991) 4041.  
(f) J. E. Northrup, *Phys. Rev. B*, **44** (1991) 1419.  
(g) J. J. Boland, *Surf. Sci.*, **261** (1992) 17.  
(h) Z. H. Lu, K. Griffiths, P. R. Norton and T. K. Sham, *Phys. Rev. Lett.*, **68** (1992) 1343.

- 23 Y. L. Yang and M. P. D'Evelyn, *J. Am. Chem. Soc.*, **114** (1992) 2796; *J. Vac. Sci. Technol. A*, **10** (1992) 978.
- 24 D. Huang and M. Frenklach, *J. Phys. Chem.*, **96** (1992) 1868.
- 25 Y. Suda, D. Lubben, T. Motooka and J. E. Greene, *J. Vac. Sci. Technol. A*, **8** (1990) 61.
- 26 S. M. Gates, C. M. Greenlief and D. B. Beach, *J. Chem. Phys.*, **93** (1990) 7493.
- 27 M. W. Chase, Jr., C. A. Davies, J. R. Downey, Jr., D. J. Frurip, R. A. McDonald and A. N. Syverud, *JANAF Thermochemical Tables*, 3rd edn., *J. Phys. Chem. Ref. Data* **14**, Suppl. 1, 1985.
- 28 (a) J. E. Spencer, J. H. Dinan, P. R. Boyd, H. Wilson and S. E. Buttrill, Jr., *J. Vac. Sci. Technol. A*, **7** (1989) 676.  
(b) J. E. Spencer, T. R. Schimert, J. H. Dinan, D. Endres and T. R. Hayes, *J. Vac. Sci. Technol. A*, **8** (1990) 1690.
- 29 (a) J. Suzuki, H. Kawarada, K. Mar, J. Wei, Y. Yokota and A. Hiraki, *Jpn. J. Appl. Phys.* **28** (1989) L281.  
(b) Y. H. Shing, F. S. Pool and D. H. Rich, *Thin Solid Films*, **212** (1992) 150.  
(c) W. Tsai, G. J. Reynolds, S. Hikido and C. B. Cooper III, *Appl. Phys. Lett.*, **60** (1992) 1444.
- 30 (a) A. L. Johnson, M. M. Walczak and T. E. Madey, *Langmuir*, **4** (1988) 277.  
(b) S. A. Joyce, J. A. Yarmoff, A. L. Johnson and T. E. Madey, *Mater. Res. Soc. Symp. Proc.*, **131** (1989) 185.



# Layer-by-layer growth of SiC at low temperatures

J. J. Sumakeris, L. B. Rowland, R. S. Kern, S. Tanaka and R. F. Davis

North Carolina State University, Department of Materials Science and Engineering, Box 7907, Raleigh, NC 27695-7907 (USA)

## Abstract

A novel reactor for layer-by-layer deposition of compound semiconductors has been designed and commissioned for the deposition of SiC. The substrates rested on a heated, rotating platform. They encountered individual fluxes of  $\text{Si}_2\text{H}_6$  and  $\text{C}_2\text{H}_4$  and subsequently paused beneath a hot filament. The filament was used to encourage the surface reaction between silicon adatoms and carbon precursors. Heteroepitaxial films were grown between 850 and 980 °C on Si(100) substrates oriented 3° off-axis toward  $\langle 011 \rangle$ . They were analyzed for composition, crystallinity, growth per cycle, and morphology using depth profiling Auger spectroscopy, reflection high-energy electron diffraction, ellipsometry and transmission electron microscopy. Growth, as measured by ellipsometry and transmission electron microscopy, corresponded to approximately one monolayer per cycle. Monocrystalline films were achieved. Initial growth and characterization results of representative films are presented and discussed.

## 1. Introduction

The extremes in the thermal, mechanical, chemical and electronic properties of the common polytypes of SiC allow the types and numbers of current and conceivable applications of this material to be substantial. SiC exists in over 250 polytypes of which only one is cubic, forming in the zinc blende structure and referred to as  $\beta$  or 3C SiC. All the remaining polytypes are hexagonal or rhombohedral [1] and are referred to collectively as  $\alpha$ -SiC. The most common of the latter polytypes is 6H where the 6 refers to the number of Si/C bilayers of closest packed planes necessary to produce the unit cell and H refers to the hexagonal nature of the crystal. The indirect band gaps at 300 K of these two polytypes are 2.23 eV (3C) and 2.93 eV (6H) [2]. Silicon carbide also possesses high values of saturated electron drift velocity ( $2 \times 10^7 \text{ cm s}^{-1}$  for 6H [3]; a slightly higher value has been predicted [4] for 3C because of reduced phonon scattering), junction breakdown electric field ( $5 \times 10^6 \text{ V cm}^{-1}$  for 6H-SiC [5]) and thermal conductivity ( $3.5 \text{ W cm}^{-1} \text{ }^\circ\text{C}^{-1}$  at 300 K for 6H-SiC) [6]. These attributes taken together make SiC an attractive candidate for high-power, high-temperature and high-frequency devices that are resistant to radiation damage. These superior physical properties are reflected in Johnson's figure of merit which assesses the suitability of a material for discrete high-frequency and high-power devices. The normalized value for 6H-SiC is 26.2 times that of silicon [7]. Discrete devices having the potential for the aforementioned applications have been achieved and characterized in the laboratory [8–10]. A review of this research through 1991 has been published by Davis *et al.* [11]. The high

thermal conductivity of SiC also indicates the potential for high density integration of SiC devices.

Epitaxial SiC films have been grown on a variety of materials, the most common substrate being that of Si(100). However, to accommodate some of the 20% and 8% mismatches in lattice parameters and coefficients of thermal expansion respectively, between silicon and SiC, the former is usually reacted with a carbon-containing gas to produce a thin buffer layer [12]. Subsequently, much thicker films have been grown by chemical vapor deposition (CVD) [13], plasma-assisted CVD [14] and gas source molecular beam epitaxy [2]. Recently Golecki *et al.* have reported the CVD of single-crystal SiC from  $\text{Si}(\text{CH}_3)_3\text{H}_3$  on Si(100) at 750 °C. This is 300 °C lower than most CVD films have been deposited [15].

To build high-technology devices using SiC, it is desirable to grow the material at lower temperatures and in a highly conformal fashion without the necessity of growing a conversion buffer layer. Atomic layer epitaxy (ALE) offers all of these possibilities. The objective of this research is to extend the state-of-the-art regarding SiC thin films via the employment of ALE to deposit the materials onto selected substrates in a layer-by-layer process. The following subsections describe the experimental procedures and discuss the results and conclusions of this research.

## 2. Experimental procedure

### 2.1. Atomic layer epitaxy reactor

In the reactor used in this research, the substrate is alternately exposed to a dose of  $\text{Si}_2\text{H}_6$  equivalent to one monolayer of silicon and an excessive exposure to  $\text{C}_2\text{H}_4$

each revolution during deposition. Figure 1 shows the basic internal components of the ALE system growth chamber including the vane assembly which separates the gases. The substrates rest on a receiver plate that rotates above a heater body and below a vane as shown in Fig. 1. A rotating sample starts at the front zone and rotates clockwise to be exposed to  $\text{Si}_2\text{H}_6$  on the left of the vane. As rotation continues, the sample passes through an intermediate  $\text{H}_2$  purge zone at the back of the vane before exposure to  $\text{C}_2\text{H}_4$  on the right side of the vane. The sample will finally return to the front zone where it will stop and reside under a hot tungsten filament that is used to enhance the surface reaction of the deposited silicon and carbon species. The filament is approximately 0.5 cm above the substrates.

Heteroepitaxial films deposited onto Si(100) substrates oriented  $3^\circ$  off-axis toward the [011] pole have been analyzed on the basis of composition, crystallinity, growth per cycle and morphology using depth profiling Auger, reflection high-energy electron diffraction (RHEED), ellipsometry and transmission electron microscopy (TEM). Growth rate, as measured by ellipsometry and TEM, corresponded to approximately 1 monolayer per cycle. Both single-crystal and highly textured polycrystalline films of  $\beta$ -SiC have been deposited. The potential for the growth of monocrystalline films improved significantly with extended residence time beneath the filament.

## 2.2. Atomic layer epitaxy deposition procedure

A typical experimental run was performed according to the following procedure. Each Si(100) substrate was cleaned, immediately loaded into the system and positioned in the growth chamber within an intermediate zone. The flows of the  $\text{H}_2$  diluent and argon curtain gases were initiated, temperature was increased at  $10^\circ\text{C min}^{-1}$  and samples were baked at the growth temperature for 5 min. The flows of  $\text{Si}_2\text{H}_6$  and  $\text{C}_2\text{H}_4$  were started, the filament heated and sample rotation begun. Typically each sample was rotated  $360^\circ$  before pausing under the filament for 30 s, repeating as required for desired film thickness. Once rotation was finished the

TABLE 1. Ranges of process variables used in SiC deposition

Variable	Range
Sample temperature	820 °C–980 °C
$\text{Si}_2\text{H}_6$ flow	0.2–10 sccm in $\text{O}_2$ ; 75–300 sccm of $\text{H}_2$
$\text{C}_2\text{H}_4$ flow	1.5–20 sccm in $\text{O}_2$ ; 75–200 sccm of $\text{H}_2$
Filament temperature	25 °C; 1450 °C–1700 °C
Time per revolution	0.66–10 s per revolution
Residence time under filament	0–60 s

sample was stopped under a  $\text{H}_2$  purge, the  $\text{Si}_2\text{H}_6$  and  $\text{C}_2\text{H}_4$  flows were stopped and the filament extinguished. The sample was allowed to cool until the sample temperature was less than  $300^\circ\text{C}$  when all gases were turned off and the chamber evacuated to high vacuum.

Films have been grown across a broad range of process variables as shown in Table 1. While most SiC films were highly textured polycrystalline, single-crystal SiC films have recently been achieved on silicon at  $850^\circ\text{C}$  without any preliminary carbonization step.

Characterization of the films employed the analytical techniques of depth profiling Auger spectroscopy, RHEED, ellipsometry and TEM. To reduce the background brightness in the RHEED images the samples were heated before analysis to  $900^\circ\text{C}$  in high vacuum to remove the native oxide.

Initial growth and characterization results and discussion of these results are presented in the following subsections for both the polycrystalline and monocrystalline films.

## 3. Results

### 3.1. Auger spectroscopy

Auger depth profiles for an SiC film and an SiC wafer standard are given in Figs. 2 and 3 respectively. The growth conditions were as follows: sample temperature  $830^\circ\text{C}$ ,  $\text{Si}_2\text{H}_6$  flow rate 3 standard  $\text{cm}^3 \text{min}^{-1}$  in 150 standard  $\text{cm}^3 \text{min}^{-1}$   $\text{H}_2$ ,  $\text{C}_2\text{H}_4$  flow rate 20 standard  $\text{cm}^3 \text{min}^{-1}$  in 150 standard  $\text{cm}^3 \text{min}^{-1}$   $\text{H}_2$ , exposure to each process gas for 2.5 s, 10 s per revolution, filament temperature  $1400^\circ\text{C}$ , no pause time below the filament and 700 revolutions total. Results from the film compared with those for the wafer reveal a very constant stoichiometric SiC film with no detectable impurities within the film.

### 3.2. Reflection high-energy electron diffraction

The residence time below the heated filament caused a notable increase in the degree of preferred orientation of the polycrystalline SiC films to a maximum coinciding with a residence of 30 s as shown in Fig. 4. Other than differing residence times below the filament, all four samples were run under the same

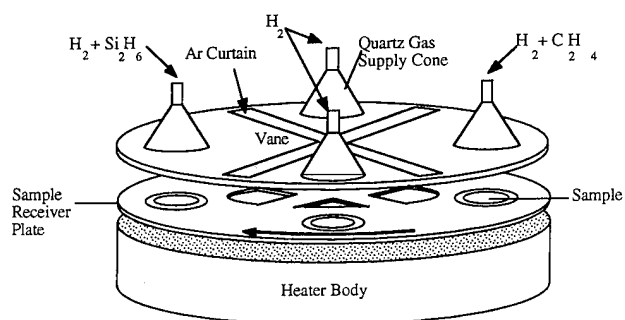


Fig. 1. Internal components of the ALE deposition system.

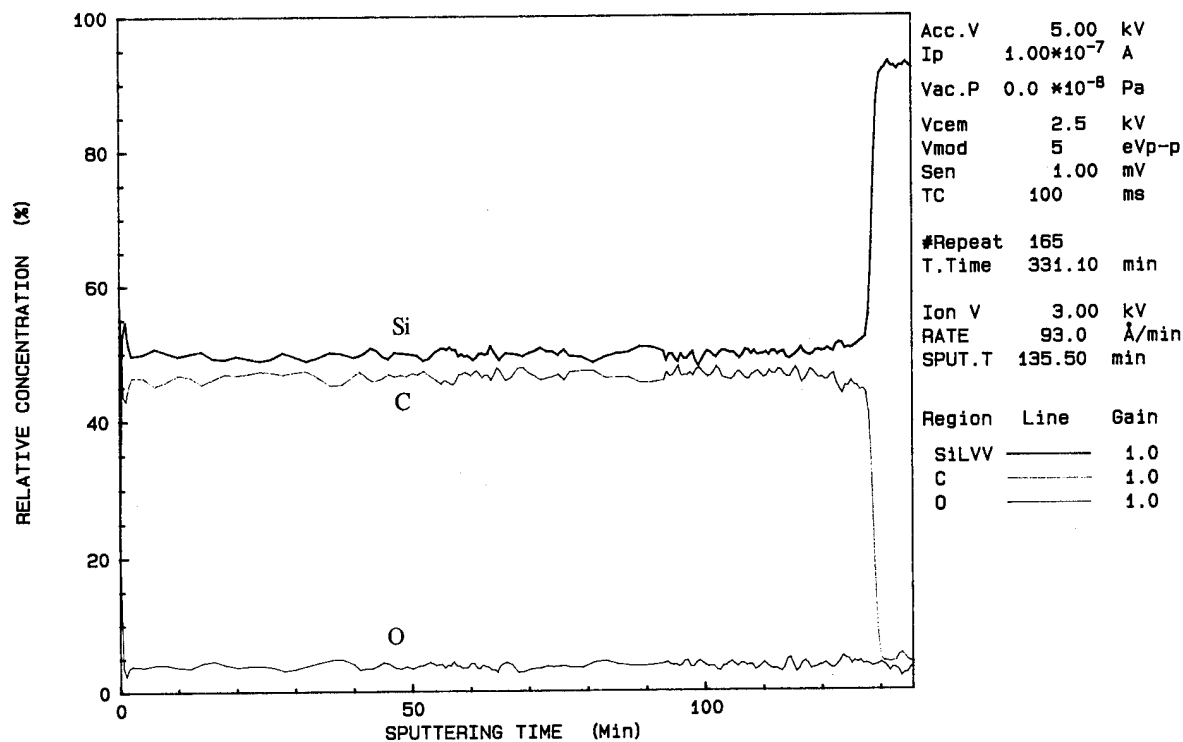


Fig. 2. Auger depth chemical profile of polycrystalline SiC film grown at 830 °C.

conditions: sample temperature 970 °C,  $\text{Si}_2\text{H}_6$  flow rate 3 standard  $\text{cm}^3 \text{min}^{-1}$  in 75 standard  $\text{cm}^3 \text{min}^{-1}$   $\text{H}_2$ ,  $\text{C}_2\text{H}_4$  flow rate 7.5 standard  $\text{cm}^3 \text{min}^{-1}$  in 75 stan-

dard  $\text{cm}^3 \text{min}^{-1}$   $\text{H}_2$ , exposure to each gas stream for 2.5 s, 10 s per revolution, filament temperature 1650 °C and 50 revolutions total.

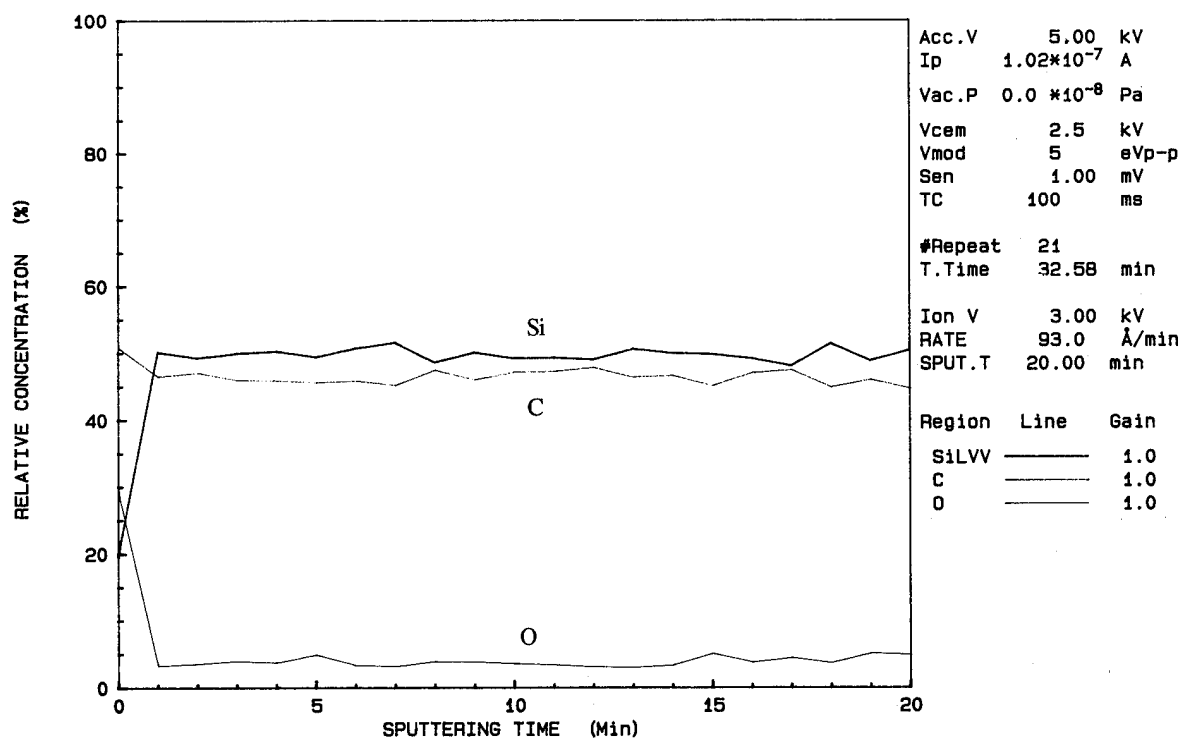


Fig. 3. Auger depth chemical profile of an  $\alpha(6\text{H})$ -SiC wafer cut from a boule grown by Cree Research, Inc., Durham, NC.

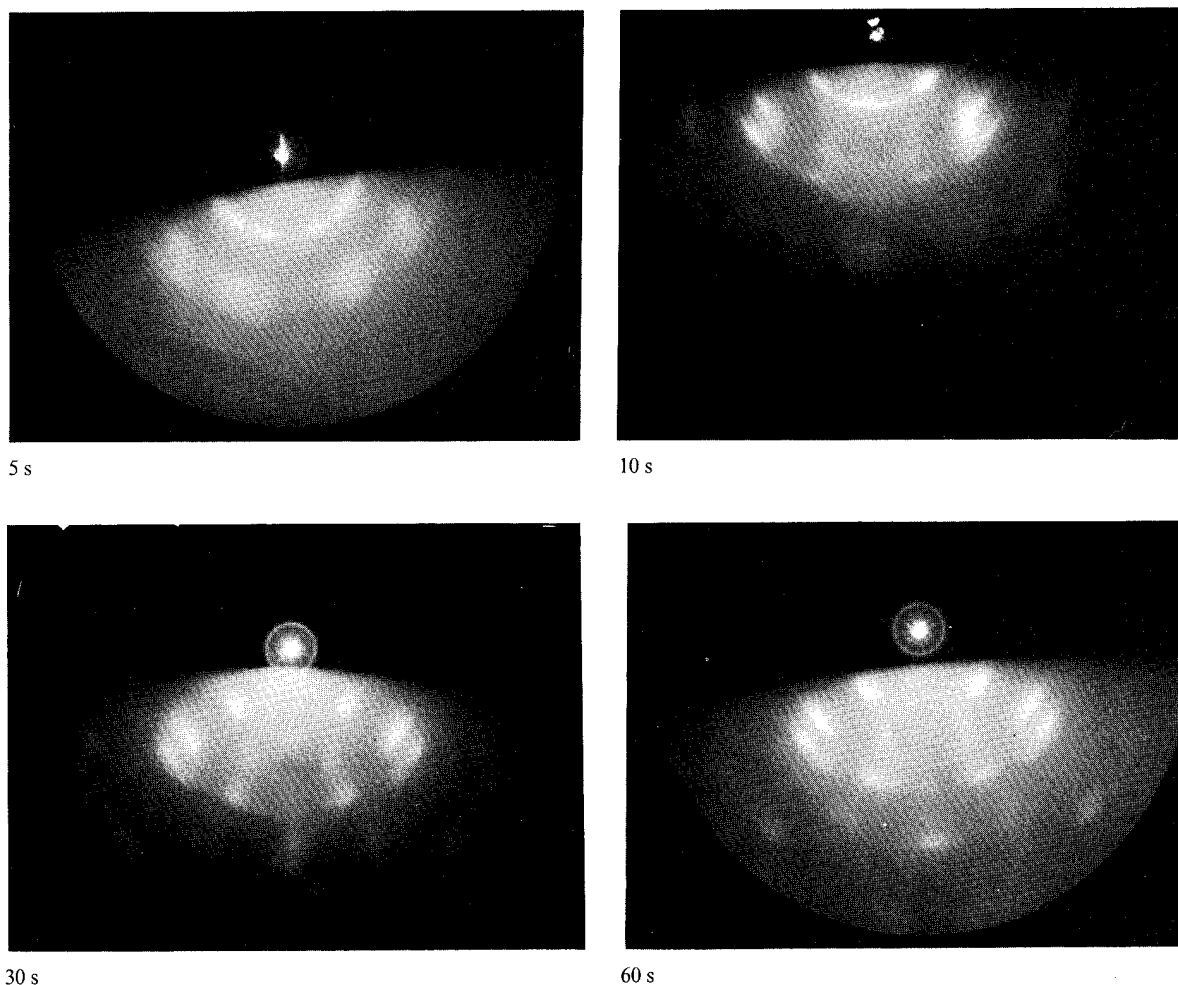


Fig. 4. Improvement in the degree of preferred orientation of the polycrystalline films with residence time below the tungsten filament.

The temperature rise of the sample during exposure to the filament was estimated using convection-radiation-thermal conductivity calculations and confirmed by optical pyrometry as approximately 100 °C. The thickness of all four films, as measured by ellipsometry, was approximately  $265 \text{ \AA} \pm 15 \text{ \AA}$ . The thickness varied by only 6% while the length of the runs varied by a factor of 12. This indicated that there was very good gas separation during the deposition.

Single-crystal films of SiC were grown without using any  $\text{C}_2\text{H}_4$  pre-exposure. Figure 5 shows the RHEED patterns for a single-crystal film of SiC. The growth conditions were as follows: sample temperature 850 °C,  $\text{Si}_2\text{H}_6$  flow rate  $0.8 \text{ standard cm}^3 \text{ min}^{-1}$  in  $300 \text{ standard cm}^3 \text{ min}^{-1}$   $\text{H}_2$ ,  $\text{C}_2\text{H}_4$  flow rate  $2.0 \text{ standard cm}^3 \text{ min}^{-1}$  in  $200 \text{ standard cm}^3 \text{ min}^{-1}$   $\text{H}_2$ , exposure to each process gas for 2.5 s, 10 s per revolution, filament temperature of 1600 °C, pause time below the filament for 30 s and 50 revolutions total. Repeating the above run without heating the filament resulted in the deposition of a polycrystalline film.

### 3.3. Transmission electron microscopy

Figure 6 is a high-resolution TEM image of the SiC film used to obtain the RHEED images in Fig. 5. The TEM image shows the film to be monocrystalline with a relatively flat surface and to contain a high concentration of (111) twin defects. The film is  $107 \text{ \AA}$  thick indicating a deposition of  $2.14 \text{ \AA}$  per Si/C cycle, which is equivalent to the deposition of 98% of a monolayer per exposure.

### 3.4. Role of filament in deposition

In order to clarify the role of the filament in deposition, several growth runs were performed with or without heating the filament and with or without argon flowing across the filament instead of  $\text{H}_2$ . The growth conditions explored were as follows: anti-mixing gas flow of  $200 \text{ standard cm}^3 \text{ min}^{-1}$   $\text{H}_2$ ,  $\text{Si}_2\text{H}_6$  flow rate  $0.8 \text{ standard cm}^3 \text{ min}^{-1}$  in  $300 \text{ standard cm}^3 \text{ min}^{-1}$   $\text{H}_2$ ,  $\text{C}_2\text{H}_4$  flow rate  $2.5 \text{ standard cm}^3 \text{ min}^{-1}$  in  $200 \text{ standard cm}^3 \text{ min}^{-1}$   $\text{H}_2$ , exposure to each process gas for 2.5 s, 10 s per revolution, filament temperature of

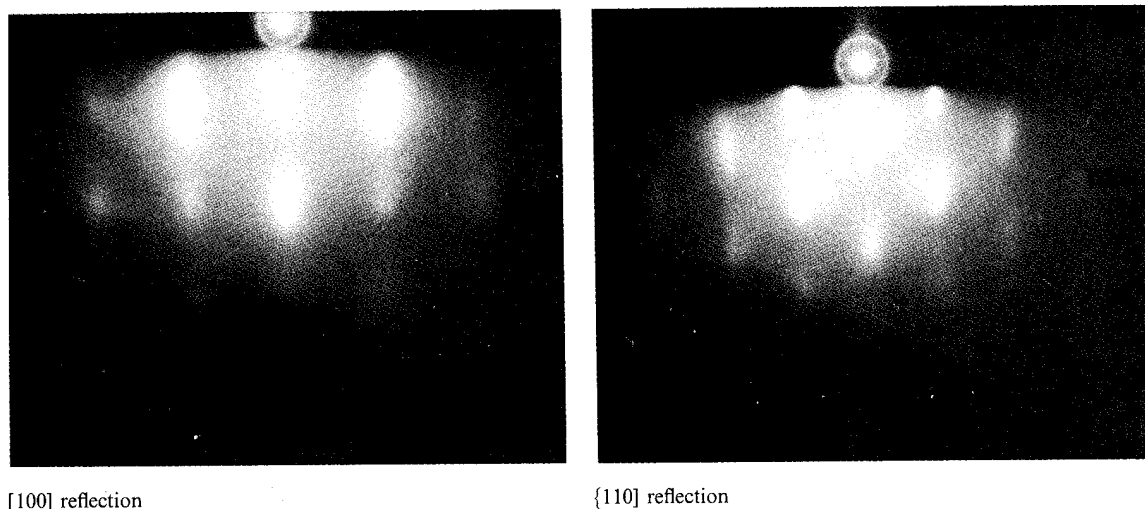


Fig. 5. RHEED patterns for monocrystalline SiC film deposited at 830 °C.

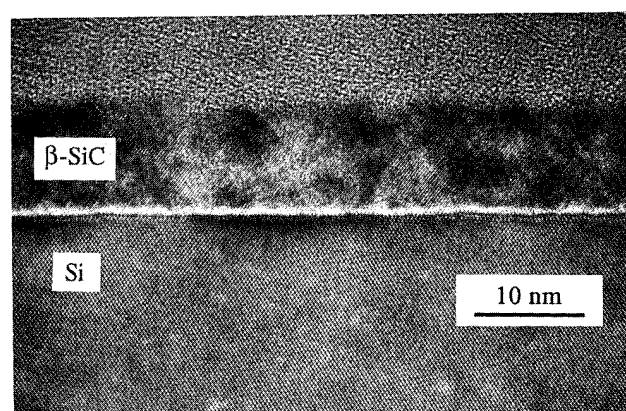


Fig. 6. High resolution TEM image of SiC film.

1600 °C if heated, pause below the filament for 30 s and 50 revolutions total. The previous conditions gave randomly oriented films by RHEED examination when run without a heated filament at sample temperatures of 830 °C, 850 °C and 930 °C. Monocrystalline  $\beta$ -SiC films were achieved consistently when the sample was stopped briefly during deposition below a heated filament across which  $H_2$  flowed. However, if only argon was flowed across the heated filament or if either argon or  $H_2$  was flowed across an unheated filament, all resulting films were randomly oriented polycrystalline  $\beta$ -SiC. Monocrystalline films were achieved only when samples paused during deposition below a heated filament across which  $H_2$  was flowed.

#### 4. Discussion

The philosophy employed in this research was to expose the heated substrate or growing SiC film to an

$Si_2H_6$  flux that was equivalent to approximately one monolayer of silicon followed by an exposure to  $C_2H_4$  to form SiC layers. This is similar to the method employed by Fuyuki *et al.* [16] who deposited cubic SiC by ALE through alternating the flows of source gases while monitoring RHEED reconstruction patterns. It is reported [17, 18] that for the temperature range used in this research,  $Si_2H_6$  will decompose quickly on a silicon surface, resulting in adsorbed  $SiH_2$  fractions which form a multilayer silicon film through the evolution of  $H_2$ . Ethylene may not decompose spontaneously on SiC in the manner of  $Si_2H_6$ . Haq and Learn [19] have reported that no reaction of an unsaturated hydrocarbon occurs on an SiC substrate at 920 °C, but that this hydrocarbon reacts readily with exposed silicon to form SiC under the same conditions. As a result, it is expected that after previously dosing an SiC surface with silicon, exposure to  $C_2H_4$  should result solely in the conversion of adsorbed silicon into SiC and no deposition of graphite. Following exposure to the source gases, the samples were allowed to remain under the filament to promote the reaction of any carbon-containing fragments with the silicon adatoms on the surface.

The initial SiC films produced in this research were randomly oriented polycrystalline  $\beta$ -SiC as a result of high concentrations of reactants in the gas phase impinging on the substrate. By reducing the supply rate of the reactants, highly preferentially oriented polycrystalline films were achieved. As noted in Fig. 4, an extended residence time below the filament increased the preferred orientation in polycrystalline films. By allowing a substantial pause time below the hot filament after each Si/C cycle using the diluted  $Si_2H_6$  and  $C_2H_4$  supply, single-crystal films of  $\beta$ -SiC have been deposited.

The filament had a marked effect on the nature of the deposited films. Under some conditions its use made the difference between the deposition of single-crystal and polycrystalline films. At a sample temperature of 970 °C, the improvement in the film by pausing under the filament was optimized after approximately 30 s.

The optimal growth conditions favored a very dilute supply of Si<sub>2</sub>H<sub>6</sub>, extended residence time below the filament and a sample temperature of less than 930 °C. The preference for a dilute supply of Si<sub>2</sub>H<sub>6</sub> can be explained by considering that the C<sub>2</sub>H<sub>4</sub> supplied after the Si<sub>2</sub>H<sub>6</sub> exposure will only deposit onto exposed silicon. Therefore, if more than one monolayer of silicon is deposited, insufficient carbon will react and a non-stoichiometric silicon-rich film will be deposited. Extended residence time below the filament enhanced the reaction of the deposited C<sub>2</sub>H<sub>4</sub> fractions and improved the opportunities for the growth of monocrystalline films. The preference for a lower sample temperature was due to the occurrence of pitting in the silicon substrates at the higher temperatures.

## 5. Conclusions

Alternating deposition of silicon and carbon species from disilane and ethylene source gases respectively, has been used to deposit polycrystalline and monocrystalline films of stoichiometric β-SiC onto Si(100) substrates within the temperature range 850–980 °C. The degree of preferred orientation of the polycrystalline films improved with increased residence time below a hot tungsten filament. Single-crystal SiC films were difficult to achieve at higher temperatures owing to increased pitting of the substrate. The best monocrystalline films of SiC were grown at 850 °C with extended residence time below the filament. The surfaces of the deposited films were very smooth, as would be expected for a layer-by-layer process. However, the films exhibited substantial twinning, as revealed by TEM.

## Acknowledgments

The authors would like to acknowledge Ms. S. Rogers who performed the Auger analysis presented in this work and to express our appreciation to Professors J. Crowell and J. Yates of the University of California, San Diego and the University of Pittsburgh respectively, and to Dr. C. Wang of North Carolina State University for helpful conversations and insights. This work is supported by the Office of Naval Research through grant # N00014-91-J-1416.

## References

- 1 G. R. Fisher and P. Barnes, *Philos. Mag. B*, 61 (1990) 217.
- 2 T. Yoshinobu, H. Mitsui, I. Izumikawa, T. Fuyuki and H. Matsunami, *Appl. Phys. Lett.*, 60 (1992) 824.
- 3 W. von Muench and E. Pettenpaul, *J. Appl. Phys.*, 48 (1977) 4823.
- 4 P. Das and D. K. Ferry, *Solid-State Electron.*, 19 (1976) 851.
- 5 W. von Muench and I. Pfaffender, *J. Appl. Phys.*, 48 (1977) 4831.
- 6 E. A. Bergemeister, W. von Muench and E. Pettenpaul, *J. Appl. Phys.*, 50 (1979) 5790.
- 7 J. H. Edgar, *J. Mater. Res.*, 7 (1992) 235.
- 8 H. Matsunami, *Optoelectron. Devices Technol.*, 2 (1987) 29.
- 9 G. Kelner, M. S. Shur, S. Binari, K. J. Slegers and H. S. Kong, *IEEE Trans. Electron Devices*, 36 (1989) 1045.
- 10 J. W. Palmour, H. S. Kong and R. F. Davis, *Appl. Phys. Lett.*, 51 (1987) 2028.
- 11 R. F. Davis, G. Kelner, M. Shur, J. W. Palmour and J. A. Edmond, *Proc. IEEE*, 79 (1991) 677.
- 12 H. Matsunami, S. Nishino and H. Ono, *IEEE Trans. Electron Devices*, 28 (1981) 1235.
- 13 H. S. Kong, J. T. Glass and R. F. Davis, *Appl. Phys. Lett.*, 49 (1986) 1074.
- 14 S. Nishino, H. Ishida and J. Saraie, *Electrochem. Soc., Extended Abstracts*, 89-2 (1989) 691.
- 15 I. Golecki, F. Reidinger and J. Marti, *Appl. Phys. Lett.*, 60 (1992) 1703.
- 16 T. Fuyuki, M. Makayama, T. Yoshinobu, H. Shiomi and H. Matsunami, *J. Cryst. Growth*, 95 (1989) 461.
- 17 J. L. Regolini, D. Bensahel and J. Mercier, *J. Electron. Mater.*, 19 (1990) 1075.
- 18 J. J. Boland, *Phys. Rev. B*, 44 (1991) 1383.
- 19 K. E. Haq and A. J. Learn, *J. Appl. Phys.*, 40 (1969) 431.

# Atomic layer epitaxy controlled by surface superstructures in SiC

Takashi Fuyuki, Tatsuo Yoshinobu and Hiroyuki Matsunami

Department of Electrical Engineering, Kyoto University, Yoshidahonmachi, Sakyo, Kyoto 606-01 (Japan)

## Abstract

Novel atomic layer epitaxy controlled by surface superstructures in SiC was demonstrated. An alternating supply of source gases of  $\text{Si}_2\text{H}_6$  and  $\text{C}_2\text{H}_2$  in gas source molecular beam epitaxy induced the transitions of the surface superstructures. When  $\text{Si}_2\text{H}_6$  was supplied, Si atoms generated by thermal decomposition adsorbed on the substrate and constructed superstructures corresponding to the number of constituent Si atoms. When  $\text{C}_2\text{H}_2$  was supplied, the adsorbed Si atoms reacted with the  $\text{C}_2\text{H}_2$  molecules, resulting in crystallization. The growth rate seemed to be regulated by the limited number of Si atoms forming the superstructures. Single-crystalline 3C-SiC was homoepitaxially grown at a low substrate temperature of 1000 °C. Detailed analysis of dynamic reflected high energy electron diffraction observations revealed the proper configuration of the surface superstructures, and the possibility of single monolayer growth of 3C-SiC was presented.

## 1. Introduction

In atomic layer epitaxy (ALE), a limited number of atoms (molecules) are adsorbed on a growing surface by so-called 'self-stopping mechanisms'. Chemical reactions on a surface give rise to layer-by-layer growth regulated at the atomic level [1], which results in high quality crystallinity and interface formation. Many extensive investigations have been carried out in the fields of II–VI and III–V semiconductors [2, 3] using chemical vapor deposition (CVD) or gas source molecular beam epitaxy (MBE) methods, but there have been very few studies on ALE of group IV semiconductors, such as Si and SiC.

We have found a distinct feature in the reconstruction of surface superstructures during crystal growth of 3C-SiC in gas source MBE, using alternating supplies of source gases of disilane ( $\text{Si}_2\text{H}_6$ ) and acetylene ( $\text{C}_2\text{H}_2$ ) [4]. When  $\text{Si}_2\text{H}_6$  is supplied, its thermal decomposition on the substrate surface generates Si atoms which adsorb and construct surface superstructures. The superstructures are reconstructed corresponding to the number of adsorbed Si atoms. When  $\text{C}_2\text{H}_2$  is supplied, the adsorbed Si atoms react with the  $\text{C}_2\text{H}_2$ , forming SiC. Epitaxial growth at as low as 1000 °C could be realized [5, 6], and the growth rate seemed to be regulated by the amount of Si atoms constructing the superstructures.

In this study, a novel mechanism for atomic level control in gas source MBE of SiC is discussed based on the *in situ* analysis of surface superstructures during crystal growth. Dynamic reflected high energy electron diffraction (RHEED) observation can show the various configurations of the superstructures, according to the

number of constituent Si atoms. The crystallinity and surface morphology are also mentioned.

## 2. Experimental details

Experiments were carried out in a commercially available ultrahigh vacuum (UHV) chamber with additional modifications for gas molecular sources described elsewhere [5]. Antiphase-domain-free single crystals of 3C-SiC(001) grown by CVD [7] on Si(001) with a 2° off-orientation towards [110] were used as substrates. Source gases of pure  $\text{Si}_2\text{H}_6$  and  $\text{C}_2\text{H}_2$  were introduced alternately onto the substrate with particular interval times. The chamber pressure during growth was about  $10^{-6}$ – $10^{-5}$  Torr and was maintained by a turbomolecular pump and a liquid nitrogen shroud. The substrate temperature was in the range 1000–1200 °C, and almost all the experiments except the surface cleaning process were carried out at 1000 °C. The typical growth conditions are listed in Table 1.

TABLE 1. Typical conditions for epitaxial growth using an alternating source supply

Substrate Temp.	1000–1200 °C
$\text{Si}_2\text{H}_6$ flow rate	0.2–0.6 sccm
$\text{C}_2\text{H}_2$ flow rate	0.2–1.6 sccm
$\text{Si}_2\text{H}_6$ supply interval	5–15 s 10–50 s
$\text{C}_2\text{H}_2$ supply interval	5–15 s 10–50 s

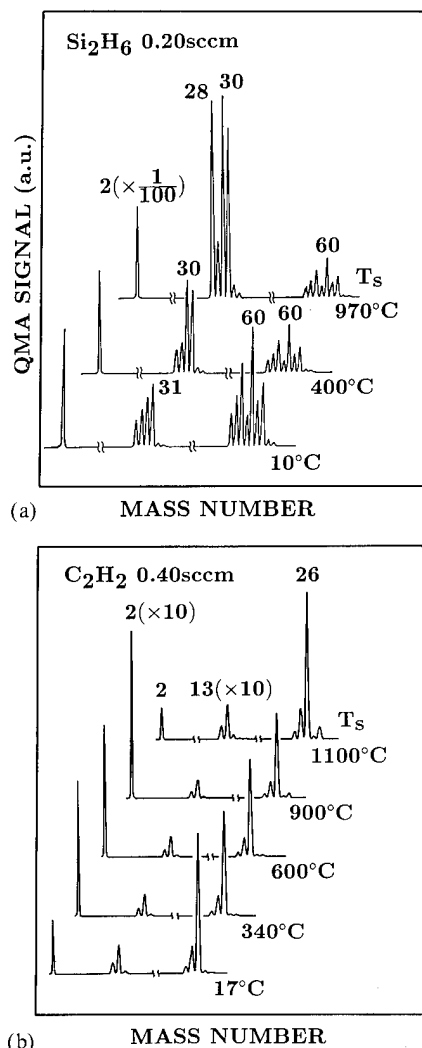


Fig. 1. Typical mass spectra taken at various substrate temperatures for source gases of (a)  $\text{Si}_2\text{H}_6$  and (b)  $\text{C}_2\text{H}_2$ .

Preliminary experiments using quadrupole mass analysis showed the decomposition of the source gases. Typical mass spectra of  $\text{Si}_2\text{H}_6$  and  $\text{C}_2\text{H}_2$  taken at various substrate temperatures are shown in Figs. 1(a) and (b) respectively. In Fig. 1(a), the peaks around  $m/e = 60$ , which originate from  $\text{Si}_2\text{H}_6$ , decrease with increasing temperature; meanwhile the peaks of  $m/e = 28-31$ , corresponding to  $\text{SiH}_n$ , increase with increasing substrate temperature. The  $\text{Si}_2\text{H}_6$  molecules are thermally decomposed at substrate temperatures higher than 600 °C, as was supported by the experimental results of Si deposition when Si was used as the substrate. In contrast, in Fig. 1(b), the peak around  $m/e = 26$  ( $\text{C}_2\text{H}_2$ ) does not show any change up to 1100 °C, which means  $\text{C}_2\text{H}_2$  can hardly be decomposed thermally. No C deposition was observed after a long supply of  $\text{C}_2\text{H}_2$ .

### 3. Results and discussion

#### 3.1. Surface superstructures

The substrate was first heated up to 1100 °C in a high vacuum (better than  $3 \times 10^{-8}$  Torr) which was for oxide removal, and then the substrate temperature was lowered to 1000 °C (at which temperature the experiments were carried out). Just after the oxide removal, the initial surface superstructure was identified to be  $c(2 \times 2)$  by *in situ* and real-time RHEED observation. The same  $c(2 \times 2)$  pattern was reproduced for  $\text{C}_2\text{H}_2$  supply at 1000 °C. No C deposition was observed when the surface was exposed to a  $\text{C}_2\text{H}_2$  beam for a long time, as mentioned above. The  $c(2 \times 2)$  surface is considered to be terminated by a single layer of C atoms without any overlayer, which is also proposed through medium energy ion scattering (MEIS), low energy electron diffraction (LEED) and Auger electron spectroscopy (AES) analyses [8].

When the surface was exposed to an  $\text{Si}_2\text{H}_6$  beam, the superstructures changed successively, as shown in Fig. 2. These superstructures are composed of Si atoms generated by the thermal decomposition of  $\text{Si}_2\text{H}_6$  molecules on the substrate surface. The relationship of the crystallographic direction and the configuration of the surface superstructures has been discussed in detail [9] based on RHEED observations with various incident directions. The number of Si atoms comprising the superstructures is assumed to increase in the order  $(2 \times 1)$ ,  $(5 \times 2)$  and  $(3 \times 2)$ , according to the  $\text{Si}_2\text{H}_6$  supply duration. No further transition from the  $(3 \times 2)$  superstructure was observed for any continuous supply of  $\text{Si}_2\text{H}_6$ .

The change in the superstructures after the formation of  $(3 \times 2)$  superstructures was investigated, keeping the same substrate temperature. The superstructure of  $(3 \times 2)$  was maintained for a few hours in a high vacuum, and it gradually changed to the  $(2 \times 1)$  superstructure. The  $(2 \times 1)$  pattern was maintained for longer than 10 h. The transition from  $(3 \times 2)$  to  $(2 \times 1)$  was caused by the decrease in the amount of constituent Si atoms owing to thermal evaporation. The  $(3 \times 2)$  superstructure is considered not to be as stable as the  $(2 \times 1)$ .

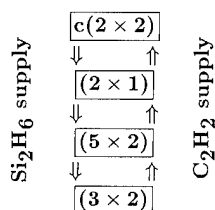


Fig. 2. Transition of surface superstructures during alternating supply of  $\text{Si}_2\text{H}_6$  (downward) and  $\text{C}_2\text{H}_2$  (upward).



When the  $C_2H_2$  was introduced, the adsorbed Si atoms reacted with the  $C_2H_2$ , resulting in a superstructure change from the  $(3 \times 2)$  to the initial  $c(2 \times 2)$ , in the reverse order shown in Fig. 2. By this surface reconstruction sequence, the crystal growth of 3C-SiC was confirmed, as discussed below.

### 3.2. Crystal growth

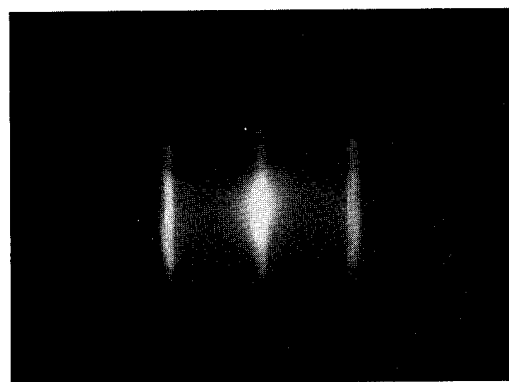
By repeating the surface reconstruction sequence many times, 3C-SiC was epitaxially grown at a substrate temperature of 1000 °C. The growth rate, defined as the number of SiC monolayers (ML) per cycle was controlled in the range 2–6 ML cycle<sup>-1</sup>, relative to the Si–C bond length along the  $\langle 001 \rangle$  direction. Clear streaks were observed in the RHEED pattern for samples with a low growth rate of 2.3 ML cycle<sup>-1</sup>, whereas stacking faults and twins were observed in the samples with higher growth rates, as shown in Fig. 3. The surface morphology showed no change compared with the substrate surface, regardless of growth conditions.

A schematic growth process with an alternating source supply is shown in Fig. 4. During the  $Si_2H_6$  supply, the  $Si_2H_6$  molecules are thermally decomposed on the substrate surface (step (a)) and the Si atoms generated form superstructures (step (b)). During  $C_2H_2$  supply, the adsorbed Si atoms react with the  $C_2H_2$  molecules (step (c)) to form SiC (step (d)). The growth rate is regulated by the number of Si atoms adsorbed on the surface (step (b)). The verification and control of the surface superstructures are indispensable to realize atomic level control in crystal growth.

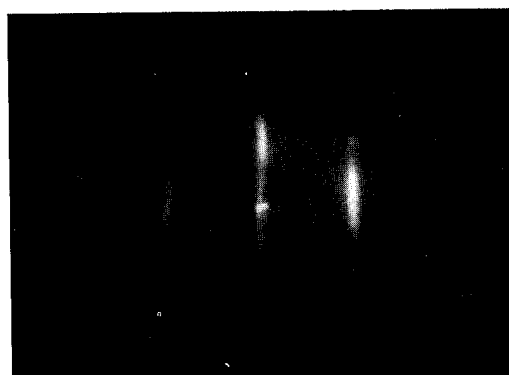
### 3.3. Dynamic analysis of reconstruction

The transition of the superstructures under an  $Si_2H_6$  molecular beam supply was dynamically analysed using an RHEED pattern-monitoring system explained in our previous publication [9]. The relative amount of constituent Si atoms in each superstructure, as mentioned in Section 3.1, was estimated by experimental results on the time evolution of the structure transition, and the exact number of Si atoms constructing the superstructures could be proved, taking various proposed models into account.

In this experiment, the flow rate of  $Si_2H_6$  was set at the minimum value of 0.07 sccm to maintain the accuracy of the time measurement. Typical intensity profiles of the superstructure-related streaks are plotted in Fig. 5 as a function of the  $Si_2H_6$  exposure time. The measured durations required for the transitions  $c(2 \times 2) \rightarrow (2 \times 1)$ ,  $c(2 \times 2) \rightarrow (5 \times 2)$  and  $c(2 \times 2) \rightarrow (3 \times 2)$ , denoted as  $t_{2 \times 1}$ ,  $t_{5 \times 2}$  and  $t_{3 \times 2}$  in the figure, are listed in Table 2 with the relative values of the second two durations normalized to the first duration. The relative values of  $t_{5 \times 2}/t_{2 \times 1}$  and  $t_{3 \times 2}/t_{2 \times 1}$  take the averages of 1.16 and 1.36 with the very small standard deviations of



(a)



(b)



(c)

Fig. 3. RHEED patterns of the layers grown at 1000 °C with growth rates of (a) 5.0 Å cycle<sup>-1</sup> (2.3 ML cycle<sup>-1</sup>), (b) 6.6 Å cycle<sup>-1</sup> (3.0 ML cycle<sup>-1</sup>) and (c) 7.6 Å cycle<sup>-1</sup> (3.5 ML cycle<sup>-1</sup>) ( $\langle 110 \rangle$  azimuth).

0.03 and 0.02 respectively. We can assume that the number of adsorbed Si atoms is proportional to the  $Si_2H_6$  dose, which in turn is proportional to the exposure time. Thus, the experimental results show that the relative quantities of constituent Si atoms in the superstructure are

$$N(2 \times 1) < N(5 \times 2) < N(3 \times 2) \quad (1)$$

and

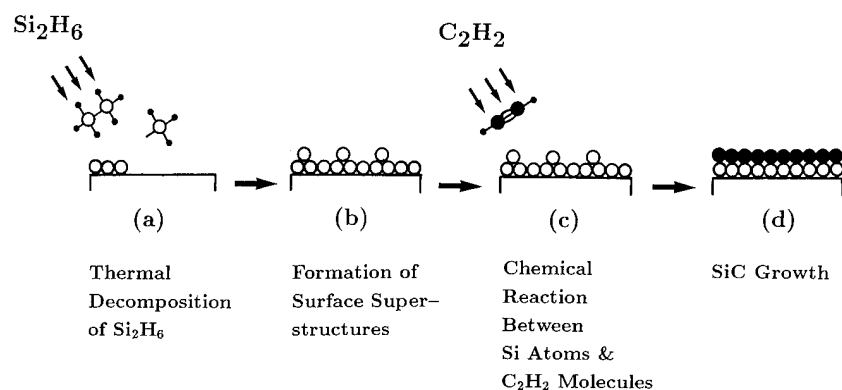


Fig. 4. Schematic growth process using an alternating source supply: (a) thermal decomposition of  $\text{Si}_2\text{H}_6$ ; (b) formation of surface superstructures; (c) chemical reaction between Si atoms and  $\text{C}_2\text{H}_2$  molecules; (d) SiC growth.

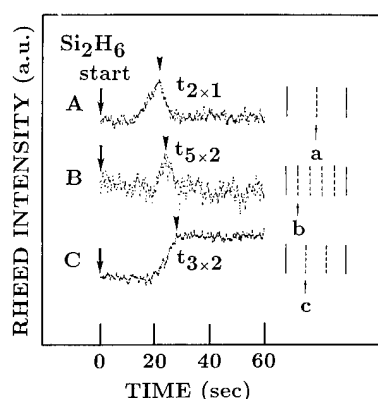


Fig. 5. RHEED intensity of superstructure-related streaks under  $\text{Si}_2\text{H}_6$  beam exposure.

$$N(5 \times 2)/N(2 \times 1) = 1.16 \quad (2)$$

$$N(3 \times 2)/N(2 \times 1) = 1.36 \quad (3)$$

where  $N(2 \times 1)$ ,  $N(5 \times 2)$  and  $N(3 \times 2)$  denote the amounts of constituent Si atoms in each superstructure.

Dayan [10] proposed an adatom model and a missing dimer model for the  $(2 \times 1)$  and  $(3 \times 2)$  superstructures, respectively, based on annealing experiments of oxidized SiC surfaces. Following his models, the numbers of Si atoms  $N(2 \times 1)$  and  $N(3 \times 2)$  were calculated to be 1.50 and 1.67. The number of Si atoms constructing

the  $(5 \times 2)$  superstructure observed in our experiments, though he did not mention it, was estimated to be 1.80, following the calculation using his missing dimer model. Then,  $N(5 \times 2)$  became larger than  $N(2 \times 1)$  or  $N(3 \times 2)$ , and the order of numbers could not satisfy our experimental results of eqn. (1).

Carter [11] carried out energy-minimizing calculations and pointed out that the simple dimer model is more favorable than the adatom model for the  $(2 \times 1)$  superstructure. Hara [8] investigated the transition of superstructures during annealing of Si-rich surfaces, using MEIS, LEED and AES analyses, and proposed the additional dimer model for the  $(5 \times 2)$  and  $(3 \times 2)$  superstructures. Typical configurations of superstructures of  $(2 \times 1)$ ,  $(5 \times 2)$  and  $(3 \times 2)$ , following the models mentioned above, are shown in Figs. 6(a), 6(b)

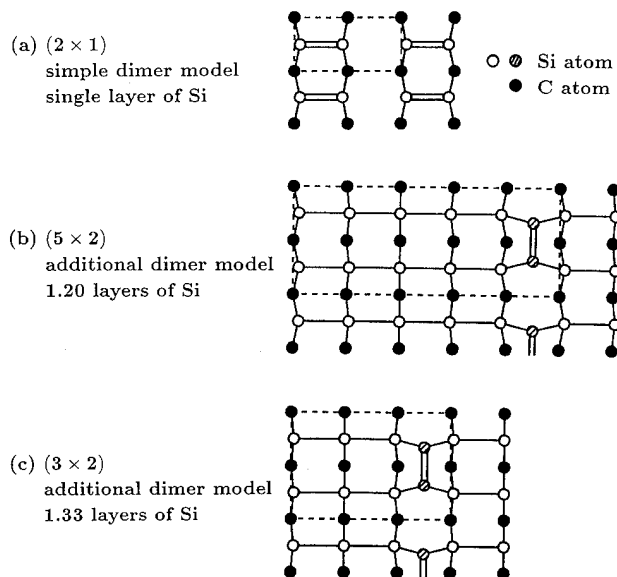


Fig. 6. Proposed models of superstructure configurations: (a)  $(2 \times 1)$  simple dimer model [11]; (b)  $(5 \times 2)$  additional dimer model [8]; (c)  $(3 \times 2)$  additional dimer model [8].

TABLE 2.  $\text{Si}_2\text{H}_6$  exposure time required for the transition of the surface superstructures

	$t_{2 \times 1}$ (s)	$t_{5 \times 2}$ (s)	$t_{3 \times 2}$ (s)	$t_{5 \times 2}/t_{2 \times 1}$	$t_{3 \times 2}/t_{2 \times 1}$
1	21.4	23.8	29.0	1.11	1.36
2	18.4	21.4	25.2	1.16	1.37
3	24.6	29.0	34.2	1.18	1.39
4	24.6	29.2	33.0	1.19	1.34
5	24.8	28.2	33.0	1.14	1.33
Ave				1.16	1.36

and (c) respectively. Theoretically, the expected numbers of Si atoms are 1.00, 1.20 and 1.33 for  $(2 \times 1)$ ,  $(5 \times 2)$  and the  $(3 \times 2)$  superstructures, respectively, and these agreed very well in both their order (eqn. (1)) and their relative amounts (eqns. (2) and (3)). Our experimental results strongly support a simple dimer model for the  $(2 \times 1)$  superstructure and an additional dimer model for the  $(5 \times 2)$  and the  $(3 \times 2)$  superstructures.

In our present experimental situation, relatively high flow rates of  $\text{Si}_2\text{H}_6$  are used in the growth experiments to shorten the required time of one cycle, and the  $(3 \times 2)$  superstructure was observed reproducibly as a result. When the reconstruction sequence via the  $(3 \times 2)$  superstructure was used in crystal growth, a growth rate of  $1.33 \text{ ML cycle}^{-1}$  should be expected, as discussed above. The obtained growth rates of  $2 \sim 6 \text{ ML cycle}^{-1}$  suggested the following: as well as the Si atoms constructing the superstructures, additional Si atoms, which could not be observed by RHEED measurements, might contribute to the crystal growth. The precise control of the  $\text{Si}_2\text{H}_6$  supply to form the  $(2 \times 1)$  structure is needed to realize single monolayer growth of 3C-SiC.

#### 4. Conclusions

Novel ALE controlled by surface superstructures in SiC was demonstrated. An alternating supply of source gases of  $\text{Si}_2\text{H}_6$  and  $\text{C}_2\text{H}_2$  in gas source MBE induced the transitions of the surface superstructures. When  $\text{Si}_2\text{H}_6$  was supplied, Si atoms generated by thermal decomposition adsorbed on a 3C-SiC(001) substrate, inducing the structure change from the initial  $c(2 \times 2)$  to the sequential evolution of  $(2 \times 1)$ ,  $(5 \times 2)$  and  $(3 \times 2)$ , corresponding to the increased amount of constituent Si atoms. When  $\text{C}_2\text{H}_2$  was supplied, the adsorbed Si atoms reacted with the  $\text{C}_2\text{H}_2$  molecules, resulting in the crystallization of the 3C-SiC, and the superstructure showed the initial  $c(2 \times 2)$  pattern.

After repeating the alternating supply for more than 1000 cycles, single-crystalline 3C-SiC was homoepitaxially grown at a low substrate temperature of  $1000^\circ\text{C}$ . Clear streaks were observed in the RHEED patterns for samples grown with a low growth rate of  $2.3 \text{ ML cycle}^{-1}$ , whereas stacking faults and twins were observed for samples grown at higher growth rates.

Detailed analysis of dynamic RHEED observations revealed the proper configuration of the surface superstructures and the possibility of single monolayer growth of 3C-SiC was presented.

#### Acknowledgment

This work was partially supported by Grant-in Aid for Scientific Research on Priority Areas (04205069) from the Ministry of Education, Science and Culture, Japan.

#### References

- 1 T. Suntola, *Mater. Sci. Rep.*, **4** (1989) 261.
- 2 W. Faschinger, H. Sitter and P. Juza, *Appl. Phys. Lett.*, **53** (1988) 2519.
- 3 S. M. Bedair, M. A. Tischler, T. Katsuyama and N. A. El-Masry, *Appl. Phys. Lett.*, **47** (1985) 51.
- 4 T. Fuyuki, M. Nakayama, T. Yoshinobu, H. Shiomi and H. Matsunami, *J. Cryst. Growth*, **95** (1989) 461.
- 5 T. Yoshinobu, M. Nakayama, H. Shiomi, T. Fuyuki and H. Matsunami, *J. Cryst. Growth*, **99** (1990) 520.
- 6 T. Fuyuki, T. Yoshinobu and H. Matsunami, *Mater. Res. Soc. Symp. Proc.*, **222** (1991) 207.
- 7 K. Shibahara, S. Nishino and H. Matsunami, *Appl. Phys. Lett.*, **50** (1987) 1888.
- 8 S. Hara, W. F. J. Slijkerman, J. F. van der Veen, I. Ohdomari, S. Misawa, E. Sakuma and S. Yoshida, *Surf. Sci. Lett.*, **231** (1990) L196.
- 9 T. Yoshinobu, I. Izumikawa, H. Mitsui, T. Fuyuki and H. Matsunami, *Appl. Phys. Lett.*, **59** (1991) 2844.
- 10 M. Dayan, *J. Vac. Sci. Technol. A*, **4** (1986) 38.
- 11 J. N. Carter, *Solid State Commun.*, **72** (1989) 671.

# Atomic level epitaxy of 3C–SiC by low pressure vapour deposition with alternating gas supply

H. Nagasawa and Y. Yamaguchi

Materials Research Laboratory, Hoya Corporation, 3-3-1, Musashino, Akishima, Tokyo 196 (Japan)

## Abstract

The heteroepitaxial growth of 3C–SiC on Si substrates has been studied in a hot-wall-type, low pressure, chemical vapour deposition reactor with an alternating supply of  $\text{SiH}_2\text{Cl}_2$  and  $\text{C}_2\text{H}_2$  in the temperature range of 750–1050 °C. SiC films have been grown only at temperatures above 800 °C. The growth rate of the SiC films increases with temperature above 900 °C, while a constant growth rate ( $4.4 \text{ \AA cycle}^{-1}$ ) is obtained in the temperature range between 800 and 900 °C. The characteristics of the growth rate of the SiC films can be understood by taking into account the decomposition of adsorbed  $\text{SiCl}_2$  on the surface of the substrates. The crystallinity of the SiC layers was affected by the orientation of the Si substrates and the growth temperature. Monocrystalline 3C–SiC has been obtained on the Si(111) face at temperatures above 1000 °C, while polycrystalline 3C–SiC deposits on the (001) face over the range of growth temperature studied.

## 1. Introduction

$\beta$ -SiC (3C–SiC) is a semiconductor material that is useful for high temperature devices. It exhibits several outstanding properties, such as a high thermal stability, high electron mobility (about  $1000 \text{ cm}^2 \text{ V}^{-1} \text{ s}^{-1}$ ), wide bandgap (2.2 eV at 300 K) and high saturated drift velocity [1, 2]. It is necessary for the fabrication of SiC devices to develop a growth technology to deposit high quality 3C–SiC over large areas. Although intensive studies of the large-area heteroepitaxy of 3C–SiC on Si substrates have been performed recently [3, 4], the required growth temperature for chemical vapour deposition (CVD) of approximately 1350 °C is too high to be suitable for device material. A growth temperature for 3C–SiC that is lower than 1000 °C is desirable to reduce the interdiffusion of dopants.

Molecular beam epitaxy (MBE) is one of the prominent methods for the low temperature growth of SiC, and successful results for homoepitaxy of high quality 3C–SiC at 1000 °C have been reported [5]. However, the productivity of MBE is far inferior to that of CVD.

We have attempted to grow heteroepitaxial 3C–SiC on Si substrates by low pressure CVD (LPCVD). To realize an atomic-level-controlled surface reaction by LPCVD, SiC growth has been carried out by alternating the supply of the source gases. In addition, we have conducted growth experiments by changing the growth temperatures to study the SiC growth mechanisms.

We will discuss the growth mechanisms of 3C–SiC using the results of quadrupole mass spectrometry (QMS) measurements.

## 2. Experimental procedure

The quartz reaction tube of the LPCVD reactor was uniformly heated by a surrounding heater. The base pressure of the reaction tube evacuated by a mechanical booster pump was  $1 \times 10^{-3}$  Torr. Acetylene ( $\text{C}_2\text{H}_2$ ) and dichlorosilane ( $\text{SiH}_2\text{Cl}_2$ ) were used as the C and Si source gases, respectively, and  $\text{H}_2$  was used as the carrier gas. Each gas flow rate was precisely controlled by a mass flow controller. To control the pressure in the reaction tube, a butterfly valve was employed between the reaction tube and the mechanical booster pump. Single-crystal Si wafers with a (111) face or a (001) face were used as the substrates. All the wafers were treated with  $\text{NH}_4(\text{OH})\text{:H}_2\text{O}_2\text{:H}_2\text{O}$  and  $\text{HCl:H}_2\text{O}_2\text{:H}_2\text{O}$  solutions, before being loaded into the reaction tube.

A typical SiC growth procedure, as shown in Fig. 1, consisted of two processes: carbonization and growth. First, the carbonization process was carried out to convert the Si surface into a thin epitaxial SiC layer [6]. This carbonized layer is the key to obtaining superior epitaxial SiC on Si substrates.  $\text{H}_2$  and  $\text{C}_2\text{H}_2$  were supplied into the reaction tube from the start of the heating process. The flow rates of  $\text{H}_2$  and  $\text{C}_2\text{H}_2$  were kept at  $500 \text{ cm}^3 \text{ min}^{-1}$  and  $10 \text{ cm}^3 \text{ min}^{-1}$  respectively. The partial pressure of  $\text{C}_2\text{H}_2$  was 2.9 mTorr and the total pressure was kept at 150 mTorr. After carbonization for 90 min at 1000 °C, a mirror-like carbonized layer 80 Å thick was obtained [7] and the temperature of the reaction tube was changed to the desired growth temperature, keeping the  $\text{H}_2$  and  $\text{C}_2\text{H}_2$  flows constant.

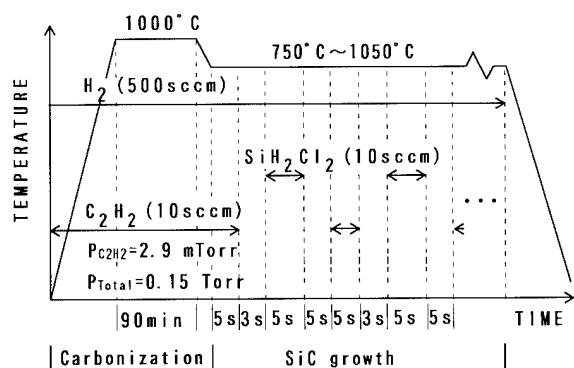


Fig. 1. Growth procedure of SiC.

The growth temperature was varied from 750 to 1050 °C. The  $\text{SiH}_2\text{Cl}_2$  at a flow rate of  $10 \text{ cm}^3 \text{ min}^{-1}$  and the  $\text{C}_2\text{H}_2$  at a flow rate of  $10 \text{ cm}^3 \text{ min}^{-1}$  were alternately introduced into the reaction tube during deposition. Throughout the entire process of SiC growth, the  $\text{H}_2$  carrier gas flow rate was maintained at  $500 \text{ cm}^3 \text{ min}^{-1}$  and the total pressure was held constant at 150 mTorr. The durations of the  $\text{SiH}_2\text{Cl}_2$  flow and  $\text{C}_2\text{H}_2$  flow were fixed at 5 s each. Intervals of 5 s were employed after stopping the  $\text{SiH}_2\text{Cl}_2$  supply, while intervals of 3 s were employed after stopping the  $\text{C}_2\text{H}_2$  supply. The number of cycles of the gas supply was typically about 1500. After the SiC growth process, the reaction tube was cooled down to room temperature without any flow of gases.

QMS measurements were carried out to observe changes in the partial pressures of the various gas species in the reaction tube during growth.

The thickness of the SiC film was calculated from the measured reflectance curve using visible light spectroscopy, with some interference peaks and valleys, and a refractive index value of 2.63. The thickness of the SiC film divided by the number of gas supply cycles gave the growth rate of the SiC. The crystallinity of the SiC films was evaluated by electron channelling pattern (ECP) observations. The surface morphology of the grown SiC films was observed by scanning electron microscopy (SEM).

### 3. Results and Discussion

SiC film growth has been realized for temperatures above 800 °C on both the Si(111) face and the Si(001) face, as shown in Fig. 2. At a growth temperature of 750 °C, continuous SiC films did not form but many whiskers were present on the substrate.

The SiC films grown in the temperature range 800–900 °C have a constant growth rate of  $4.4 \text{ Å cycle}^{-1}$ , as shown in Fig. 3. The rate of  $4.4 \text{ Å cycle}^{-1}$  corresponds

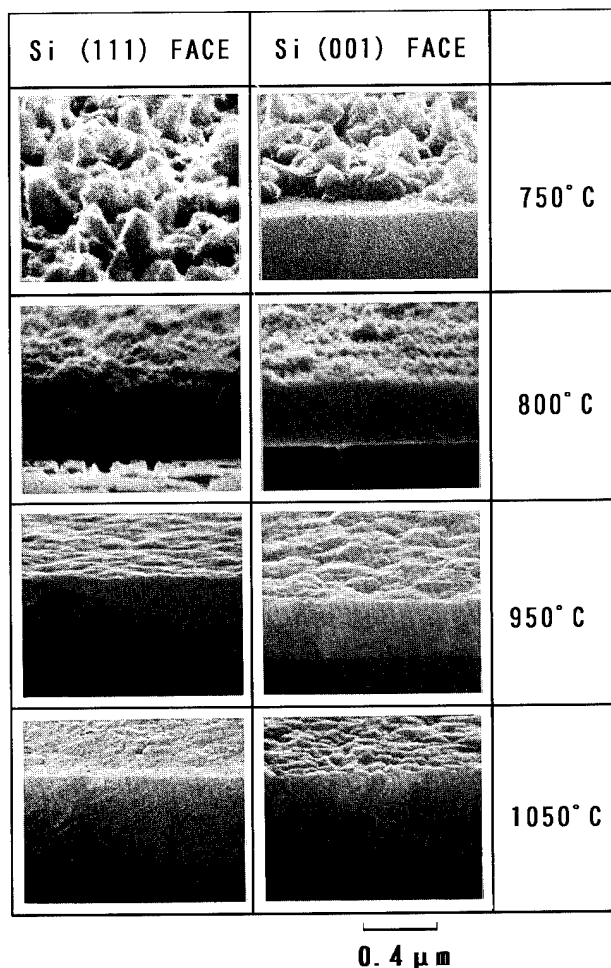


Fig. 2. Cross-sectional SEM micrographs of the SiC films grown on the Si(111) face and Si(001) face at various growth temperatures.

to a 1.8 monolayer (ML) growth of 3C-SiC per cycle. The growth rate of SiC increases with the growth temperature in the range of 900–1050 °C. The discrepancy in the growth rates implies that there may be several different mechanisms active in the growth of SiC.

It is generally recognized that  $\text{SiCl}_2$  molecules are formed by thermal decomposition of  $\text{SiH}_2\text{Cl}_2$  over the temperature range studied [8–13]. The constant growth rate of SiC seems to be determined by a surface reaction below 900 °C, as schematically shown in Fig. 4. The  $\text{SiCl}_2$  molecules are adsorbed on hollow bridge sites of the substrates [11–13]. The  $\text{SiCl}_2$  molecules change into the fairly stable ionized state  $\text{SiCl}_2^- (^2\text{B}_1)$  which has loose bonds between the Si and Cl (Fig. 4(a)). When the metastable layer of  $\text{SiCl}_2$  molecules is exposed to  $\text{C}_2\text{H}_2$  molecules the adsorbed  $\text{SiCl}_2$  is converted to SiC, resulting in a constant growth rate of SiC (Fig. 4(b)) [14, 15]. It is not understood yet why the constant growth rate of SiC is  $1.8 \text{ ML cycle}^{-1}$  rather than  $1 \text{ ML cycle}^{-1}$ .

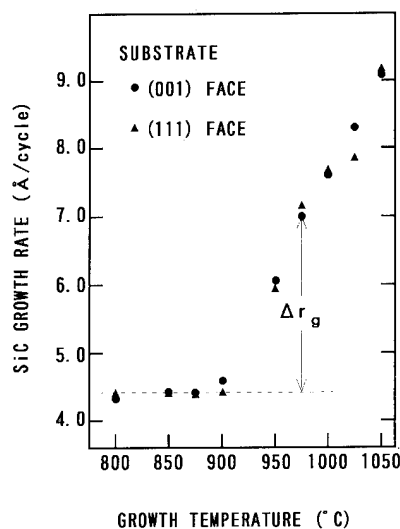


Fig. 3. SiC growth rate as a function of growth temperature.

At growth temperatures above 900 °C, the increase in the SiC growth rate no longer can be accounted for by a stable adsorption layer of  $\text{SiCl}_2$ , as mentioned above. An additional growth mechanism seems to contribute to the SiC growth. The additional growth rate ( $\Delta r_g$ ) was estimated by subtracting the constant growth rate from the total growth rate in Fig. 3, and is displayed as an Arrhenius plot in Fig. 5. The Arrhenius plot of  $\Delta r_g$  shows an activation energy of 26.6 kcal mol<sup>-1</sup> for the

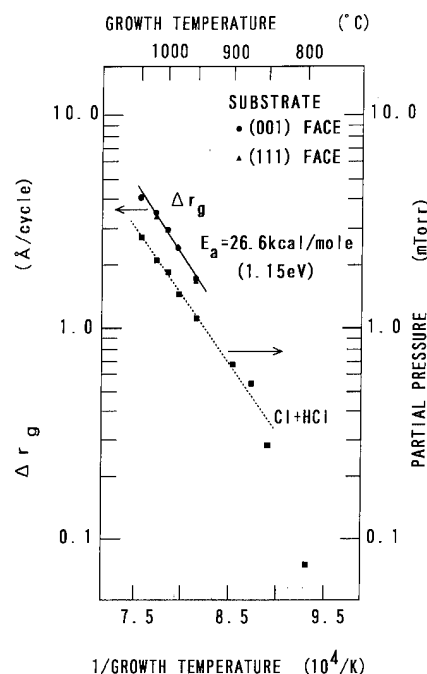


Fig. 5. Arrhenius plot of the additional growth rate of SiC and sum of Cl and HCl partial pressures.

additional growth rate in the temperature range 950–1050 °C.

To clarify the activated process of 26.6 kcal mol<sup>-1</sup>, time variations of the partial pressures of the gas species in the reaction chamber were measured by QMS. Figure 6 shows the typical changes in  $\text{SiH}_2\text{Cl}_2$ ,  $\text{C}_2\text{H}_2$ ,  $\text{SiCl}_2$ ,  $\text{SiCl}$ ,  $\text{HCl}$  and  $\text{Cl}$  partial pressures at 900 °C. All the gaseous species show changes synchronous to the supply periods of the source gases. The Cl and HCl molecules are generally considered to be released by the decomposition of  $\text{SiCl}_2$  on the surface of the substrates [8–10]. Thus, the sum of the partial pressures of Cl and HCl during the supply of  $\text{SiH}_2\text{Cl}_2$  is thought to be proportional to the total amount of Si deposited by

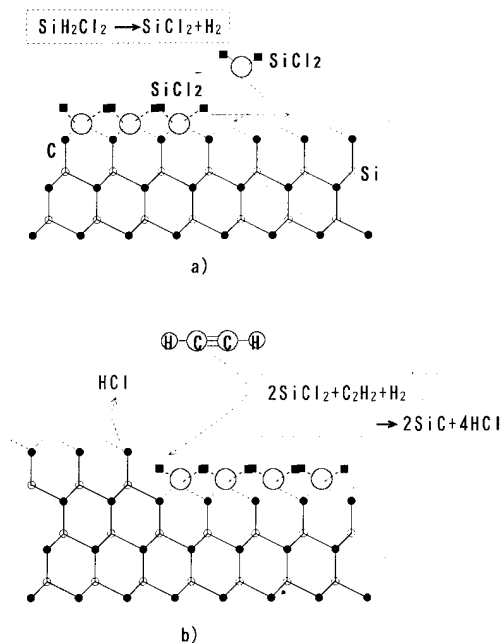


Fig. 4. Model of SiC growth at below 900 °C: (a)  $\text{SiCl}_2$  molecules are adsorbed on hollow bridge sites of substrates and then change into a fairly stable ionized state; (b) the stable  $\text{SiCl}_2$  molecules are exposed to  $\text{C}_2\text{H}_2$  molecules, resulting in the constant growth rate of SiC.

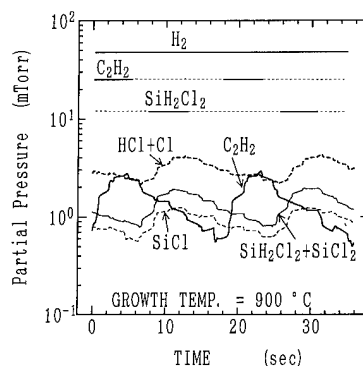


Fig. 6. Change of  $\text{SiH}_2\text{Cl}_2$ ,  $\text{C}_2\text{H}_2$ ,  $\text{SiCl}_2$ ,  $\text{SiCl}$ ,  $\text{HCl}$  and  $\text{Cl}$  partial pressures during growth process at 900 °C.

the decomposition of  $\text{SiCl}_2$  on the surface of the substrates. The sum of the partial pressures of Cl and HCl changes with the growth temperature, which corresponds to the activation energy of  $26.6 \text{ kcal mol}^{-1}$  for the additional growth rate of SiC film, as also shown in Fig. 5.

At a growth temperature above  $900^\circ\text{C}$ , the decomposition of adsorbed  $\text{SiCl}_2$  by  $\text{H}_2$  during the  $\text{SiH}_2\text{Cl}_2$  supply seems to contribute to the additional growth of SiC, as shown in Fig. 7. Cl atoms may be reduced by  $\text{H}_2$  and removed from the surface of a substrate, leaving residual Si atoms to be incorporated into the surface of the substrate (Fig. 7(a)). Subsequently, additional  $\text{SiCl}_2$  molecules will be adsorbed onto the new surface of the substrate during the supply of  $\text{SiH}_2\text{Cl}_2$ . Consequently, excess homoepitaxial Si atom layers may be formed on the surface of substrates at temperatures above  $900^\circ\text{C}$ . The Si atoms in these excess layers will react with the  $\text{C}_2\text{H}_2$  on its introduction into the reaction tube, resulting in additional SiC formation.

The crystallinity of the SiC layer grown was affected by the orientation of the Si substrate and the growth temperature. Single-crystal 3C-SiC films have been obtained on the Si(111) face at temperatures above  $1000^\circ\text{C}$ . Figure 8 shows the ECP patterns of SiC films deposited at various growth temperatures on the Si(111) and the Si(001) faces. The Kikuchi patterns are

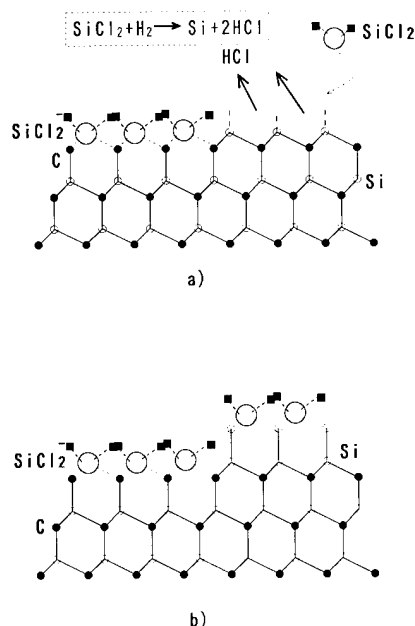


Fig. 7. Model of SiC growth at higher than  $900^\circ\text{C}$ : (a) adsorbed  $\text{SiCl}_2$  molecules are decomposed by  $\text{H}_2$  during  $\text{SiH}_2\text{Cl}_2$  supply, Cl atoms are desorbed from the surface of substrates and the residual Si atoms are incorporated into the surface of the substrates; (b) then, the additional  $\text{SiCl}_2$  molecules are adsorbed on the surface of substrates during  $\text{SiH}_2\text{Cl}_2$  supply.

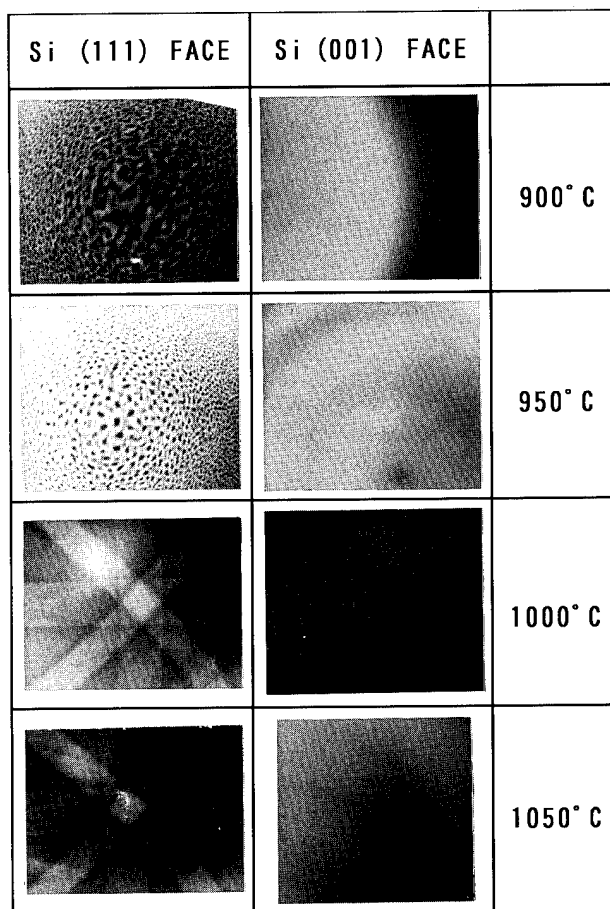


Fig. 8. ECP patterns of SiC films grown at various growth temperatures on the Si(111) and Si(001) faces.

clearly observed from the SiC films grown on the Si(111) face at above  $1000^\circ\text{C}$ . When the growth temperature was lower than  $950^\circ\text{C}$ , insufficient surface migration seems to cause the formation of polycrystalline SiC films [8]. No Kikuchi patterns are observed for the SiC films deposited on the Si(001) face at any of the growth temperatures studied. The higher density of hollow bridge sites on the Si(001) face might explain the polycrystalline structure [11].

The SiC films grown on the Si(111) faces at temperatures above  $1000^\circ\text{C}$  have smoother surfaces ( $R_a = 8 \text{ nm}$ ) than those grown on Si(001) ( $R_a = 15 \text{ nm}$ ), as shown in Fig. 9.

#### 4. Conclusions

The heteroepitaxial growth of 3C-SiC on Si substrates has been realized in a hot-wall-type LPCVD reactor with an alternating supply of  $\text{SiH}_2\text{Cl}_2$  and  $\text{C}_2\text{H}_2$  in the growth temperature range  $800\text{--}1050^\circ\text{C}$ . The growth rate of the SiC films increases with the growth

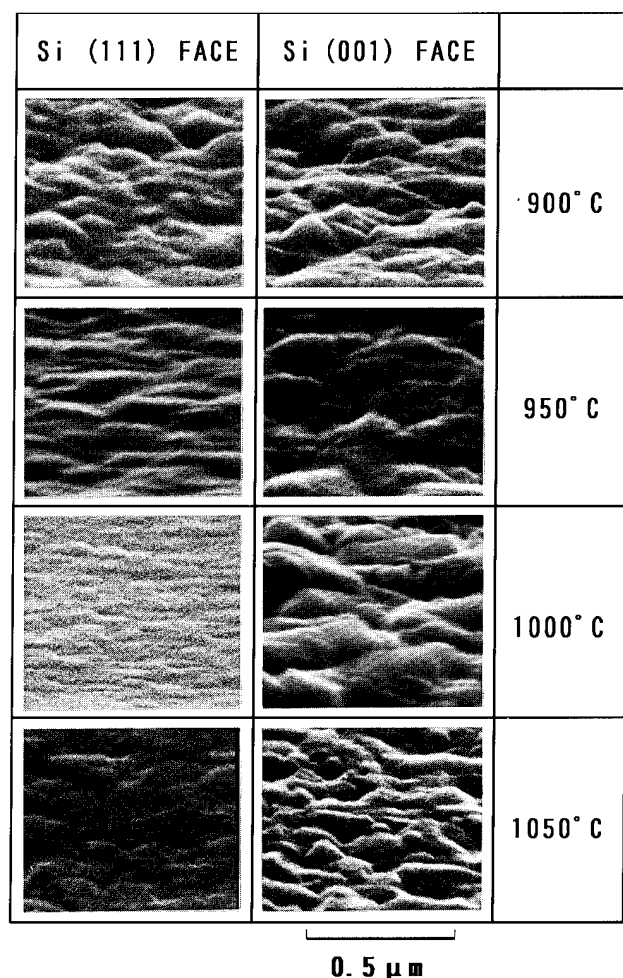


Fig. 9. SEM images of surface of SiC films grown on the Si(111) and Si(001) faces at various growth temperatures.

temperature above 900 °C, while a constant growth rate ( $4.4 \text{ \AA cycle}^{-1}$ ) is obtained in the range 800–900 °C.

The  $\text{SiCl}_2$  molecules formed by the thermal decomposition of  $\text{SiH}_2\text{Cl}_2$  are adsorbed onto the hollow bridge sites of the substrates and change into their stable ionized state. Subsequently, the ionized  $\text{SiCl}_2$  may be

decomposed by introducing  $\text{C}_2\text{H}_2$ , giving rise to SiC growth at the constant rate of  $4.4 \text{ \AA cycle}^{-1}$  in the growth temperature range 800–900 °C. When the growth temperature is above 900 °C, the adsorbed  $\text{SiCl}_2$  may be decomposed on the surface of the substrates by  $\text{H}_2$ , resulting in the additional growth of SiC with an activation energy of  $26.6 \text{ kcal mol}^{-1}$ .

Single-crystal 3C-SiC has been grown on the Si(111) face at growth temperatures above 1000 °C. No growth of monocrystalline 3C-SiC has been realized on the Si(001) face at any of the growth temperatures studied. The higher density of hollow bridge sites on the Si(001) face might cause the polycrystalline structure.

## References

- 1 G. L. Harris and C. Y.-W. Wang (eds.), *Amorphous and Crystalline Silicon Carbide*, Springer Proc. Phys., 34 (1989).
- 2 M. M. Rahmann, C. Y.-W. and G. L. Harris (eds.), *Amorphous and Crystalline Silicon Carbide II*, Springer Proc. Phys., 43 (1989).
- 3 S. Nishino, J. A. Powell and H. A. Will, *Appl. Phys. Lett.*, 42 (5) (1983).
- 4 Y. Furumura, M. Doki, F. Mieno, T. Eshita, T. Suzuki and M. Maeda, *J. Electrochem. Soc.*, 135 (5) (1988) 1255.
- 5 T. Fuyuki, N. Nakayama, T. Yoshinobu, H. Shiomi and H. Matsunami, *J. Cryst. Growth*, 95 (1989) 461.
- 6 C. J. Mogab and H. J. Leamy, *J. Appl. Phys.*, 45 (1974) 1075.
- 7 H. Nagasawa and Y. Yamaguchi, *J. Cryst. Growth*, 115 (1991) 612.
- 8 J. Bloem, L. J. Giling, in S. M. Sze (ed.), *VLSI Technology*, McGraw-Hill, New York, 1983, Ch. 3.
- 9 W. A. P. Classen and J. Bloem, *J. Cryst. Growth*, 50 (1980) 807.
- 10 T. O. Sedgwick, J. E. Smith, Jr., R. Ghez and M. E. Cowher, *J. Cryst. Growth*, 31 (1975) 264.
- 11 Y. Ohshita *et al.*, 47th Autumn Meeting, 1986, The Japan Society of Applied Physics, Extended Abstracts, p. 718.
- 12 A. Ishitani *et al.*, 47th Autumn Meeting, 1986, The Japan Society of Applied Physics, Extended Abstracts, p. 718.
- 13 A. Ishitani, T. Takada, and Y. Ohshita, *J. Appl. Phys.*, 63 (2) (1988) 15.
- 14 S. Motoyama, N. Morikawa, and S. Kaneda, *J. Cryst. Growth*, 100 (1990) 615.
- 15 H. Nagasawa and Y. Yamaguchi, *Proc. 4th Int. Conf. on Amorphous and Crystalline Silicon Carbide and other IV-IV Materials*, Springer Proc. Phys., in press.



# Si heterojunction diodes with a thin $\beta$ -SiC layer prepared with gas layer source molecular beam epitaxy

Kinam Kim, Si-Don Choi and K. L. Wang

Device Research Laboratory, 66-147 Eng. IV, MS: 56-125B, Electrical Engineering Department, University of California at Los Angeles, Los Angeles, CA 90024-1594 (USA)

## Abstract

Recently we have achieved successful growth of thin  $\beta$ -SiC film on Si substrates using gas source molecular beam epitaxy (MBE) at low temperatures around 850 °C. In this work, we have studied the growth of  $\beta$ -SiC film on Si substrate using  $C_2H_2$  gas source MBE. The films grown with  $C_2H_2$  gas were analysed using various *in situ* (Auger electron spectroscopy, reflected high energy electron diffraction) and *ex situ* analysis tools (secondary ion mass spectroscopy X-ray photoelectron spectroscopy, Fourier transform IR, ellipsometry). We also have studied the  $C_2H_2$  gas reaction for potential SiC atomic layer epitaxy (ALE) applications. The  $C_2H_2$  gas shows a useful self-limiting reaction for the ALE process, in that  $C_2H_2$  gas reacts rapidly with the highly reactive Si surface; after forming  $\beta$ -SiC on the Si surface, the reaction of  $C_2H_2$  gas with Si drops rapidly and further reaction of SiC is almost quenched. Finally, to study further these thin  $\beta$ -SiC films, Si heterojunction diodes with a thin  $\beta$ -SiC layer between heavily doped  $n^+$ -type polysilicon and highly doped p-type Si layers were fabricated. The  $I$ - $V$  curve of these diodes shows a reasonably good forward characteristic and an improved breakdown voltage compared with those of devices without the thin  $\beta$ -SiC film.

## 1. Introduction

$\beta$ -SiC has attracted much interest owing to its many outstanding properties, such as high electron mobility ( $1000 \text{ cm}^2 \text{ V}^{-1} \text{ s}^{-1}$ ) [1], high electron saturation velocity ( $2\text{--}2.7 \times 10^7 \text{ cm s}^{-1}$ ) [2], high breakdown electric field ( $2\text{--}3 \times 10^6 \text{ V cm}^{-1}$ ) [3], a wide bandgap (2.2 eV) [4], high thermal conductivity, and good mechanical and chemical stability. Hence,  $\beta$ -SiC is a promising semiconductor for high temperature, high frequency, high power electronic devices and opto-electronic devices.

The successful growth of  $\beta$ -SiC on an Si substrate by chemical vapor deposition (CVD) has been reported by several authors [5, 6]. The electrical properties of  $\beta$ -SiC grown by CVD have been intensively studied, and high temperature electronic devices, such as an SiC metal-oxide semiconductor field-effect transistor [7] and an SiC bipolar transistor [8], were reported. However, the high growth temperature of more than 1000 °C used in the works mentioned above causes the redistribution of dopants in the Si substrate, generation of slip lines, wafer warpage, and contamination from the growth environment. Therefore, this process cannot be adopted in current Si very large scale integration technology. To achieve a lower growth temperature for  $\beta$ -SiC, a clean growth ambient and better control are desirable.

Ultrahigh vacuum molecular beam epitaxy (MBE) appears to be attractive. A clean sample surface can be easily prepared in the MBE environment. Recently a

few groups have reported  $\beta$ -SiC growth with MBE at low temperatures of around 800–1000 °C using an Si-bearing gas source and a hydrocarbon gas source [9], or solid Si and hydrocarbon gas sources [10, 11]. The carbonization process using  $C_2H_2$  gas in gas source MBE also has been reported [12]. Although the successful growth of  $\beta$ -SiC at low temperatures was recently achieved, the electrical properties of these films have not been reported. In this work, the growth of  $\beta$ -SiC on an Si substrate in MBE using a  $C_2H_2$  gas source and a solid Si source is presented. The electrical properties of undoped  $\beta$ -SiC prepared with this growth method was investigated using an  $n^+$ - $p^+$  Si diode with a thin  $\beta$ -SiC layer sandwiched in between.

## 2. Crystal growth

The growth of  $\beta$ -SiC was carried out in a gas source MBE chamber, which has a base pressure of about  $10^{-10}$  Torr. The growth of  $\beta$ -SiC was performed using a two-step growth method. Firstly, a thin buffer layer as formed by surface carbonization with the  $C_2H_2$  gas beam to relieve the large lattice mismatch (about 20%) between SiC (4.36 Å) and Si (5.43 Å). After the carbonization process, the Si molecular beam was turned on under the simultaneous irradiation of the  $C_2H_2$  beam for the MBE SiC growth.

The SiC film was grown under the following conditions: an Si beam flux of  $0.8\text{--}2.5 \text{ Å s}^{-1}$ , a substrate temperature of  $700\text{--}900 \text{ °C}$  and a growth pressure of  $10^{-7}\text{--}5 \times 10^{-6}$  Torr. The growth pressure was mainly determined by the  $\text{C}_2\text{H}_2$  gas flow rate which was controlled by a mass flow controller. The initial buffer layer and subsequent SiC growth were studied using *in situ* reflected high energy electron diffraction (RHEED) and Auger electron spectroscopy (AES), and *ex situ* X-ray photoelectron spectroscopy (XPS), IR absorption measurement and scanning electron microscopy (SEM).

### 2.1. Buffer layer formation (carbonization) process

In the buffer layer formation, the optimal carbonization conditions for the subsequent SiC growth and the reaction behavior of  $\text{C}_2\text{H}_2$  on the Si surface were investigated with the  $\text{C}_2\text{H}_2$  beam irradiation. The importance of a thin buffer layer produced by carbonization as a precondition of the subsequent  $\beta$ -SiC growth was studied in CVD growth [13]. The optimal carbonization conditions in our experiment, as determined by RHEED, were found to be as follows: carbonization time of 10 min, substrate temperature of  $875 \text{ °C}$  and growth pressure  $1.6 \times 10^{-6}$  Torr. Figure 1 shows the evolution of the AES surface C concentration with exposure to  $\text{C}_2\text{H}_2$  irradiation for two substrate temperatures of 875 and  $1000 \text{ °C}$ . As shown in Fig. 1, the ratio of C and Si concentrations (C:Si) in the case of the  $875 \text{ °C}$  carbonization temperature increases linearly from the pure Si surface initially to presumably the formation of SiC (1:1 C:Si ratio) with the increase in the  $\text{C}_2\text{H}_2$  beam exposure. This 1:1 C:Si ratio indicates

an SiC stoichiometric composition. A further increase in the  $\text{C}_2\text{H}_2$  beam irradiation does not seem to change the C:Si ratio. The thickness measurement of the SiC layers using ellipsometry shows the saturation of the film thickness after exposure for 30 min. For example, the film thickness of the SiC layer irradiated for 30 min is almost the same as that for irradiation for 60 min (about  $100 \text{ Å}$  by ellipsometry measurement). From the AES and thickness measurements, it is suspected that the  $\text{C}_2\text{H}_2$  gas rapidly reacts with the highly reactive Si surface. After forming  $\beta$ -SiC on the Si surface, the reaction of the  $\text{C}_2\text{H}_2$  gas with Si drops rapidly and further formation of SiC stops almost completely. This 'self-limiting' reaction of the  $\text{C}_2\text{H}_2$  beam on the Si substrate may be useful for group IV epitaxial growth involving Si, Ge and C. However, this kind of reaction behavior of the  $\text{C}_2\text{H}_2$  gas beam on the Si substrate was not observed at a carbonization temperature of  $1000 \text{ °C}$ . At  $1000 \text{ °C}$ , first, the C:Si concentration ratio seems to increase linearly from the pure Si surface to 1:1, with the increase of the exposure time to the  $\text{C}_2\text{H}_2$  beam. Then, the C concentration drops from the stoichiometric composition with continuous exposure to the  $\text{C}_2\text{H}_2$  beam. This is probably due to the reduced sticking coefficient of the  $\text{C}_2\text{H}_2$  and the enhanced Si diffusion from bulk Si at high temperature. This reduced reaction at high temperature was reported also in the case of  $\text{C}_2\text{H}_4$  exposure on the Si substrate [14].

According to the ellipsometry measurements, the SiC layer obtained in the optimized carbonization process is less than  $100 \text{ Å}$  thick. This thickness is too thin to be useful for device applications. Therefore, we have investigated the SiC growth on the thin carbonized layer using the  $\text{C}_2\text{H}_2$  gas beam and a solid Si source.

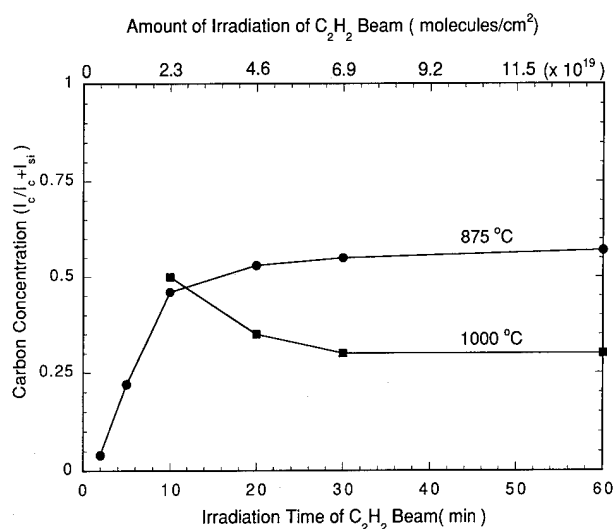


Fig. 1. AES of the C concentration on carbonized surface vs.  $\text{C}_2\text{H}_2$  beam exposure time during the carbonization process. The experiments were conducted at a growth pressure of  $1.6 \times 10^{-6}$  Torr and growth temperatures of 875 and  $1000 \text{ °C}$ .

### 2.2. Growth of SiC

After performing the optimum surface carbonization using the conditions described previously, The Si molecular beam was turned on while the substrate was continuously exposed to the  $\text{C}_2\text{H}_2$  gas in order to obtain thick SiC layers. The properties of the resulting SiC films were studied using RHEED, XPS, X-ray diffraction, IR absorption, and ellipsometry measurements. Figure 2 shows a typical IR absorption spectrum using Fourier transform (FT) for the film grown at  $875 \text{ °C}$ . The other growth conditions are as follows: Si flux of  $0.8 \text{ Å s}^{-1}$ , growth pressure of  $1.6 \times 10^{-6}$  Torr and growth time of 30 min. As shown in Fig. 2, the data show only one strong absorption peak at  $794 \text{ cm}^{-1}$  ( $12.6 \text{ μm}$ ) with a narrow full width at half-maximum (FWHM) of  $28 \text{ cm}^{-1}$ , owing to the Si-C stretching vibration of SiC. The sharp absorption peak at  $794 \text{ cm}^{-1}$  ( $12.6 \text{ μm}$ ) indicates that the film has the stoichiometric composition with no other products being deposited in the reaction between  $\text{C}_2\text{H}_2$  and Si.

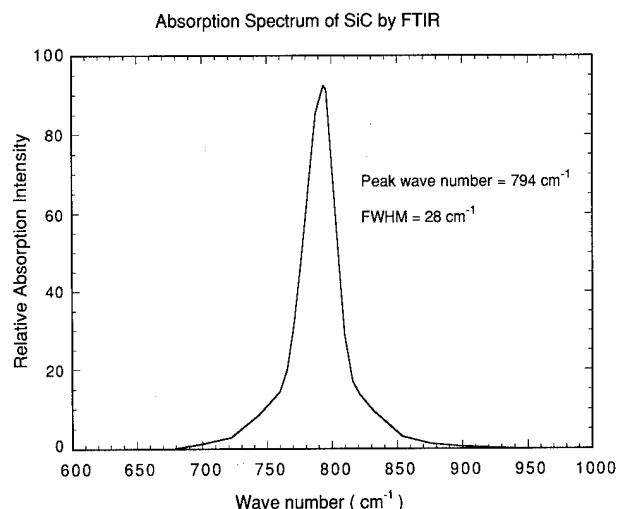


Fig. 2. Typical IR absorption spectrum of  $\beta$ -SiC film obtained by FTIR. The film was grown at a growth temperature of  $875^\circ\text{C}$ , Si flux of  $0.8\text{ Å s}^{-1}$  and growth pressure of  $1.6 \times 10^{-6}$  Torr for a growth time of 30 min.

The crystalline structure was verified by X-ray diffraction measurement and RHEED observation. Figure 3 shows the X-ray spectrum of the sample grown on Si(111) at  $900^\circ\text{C}$  for 30 min with an Si beam flux of  $0.8\text{ Å s}^{-1}$  and a growth pressure of  $1.6 \times 10^{-6}$  Torr. This sample is approximately  $0.1\text{ }\mu\text{m}$  thick as determined by ellipsometry measurements. As shown in Fig. 3, this film is  $\langle 111 \rangle$ -oriented  $\beta$ -SiC and has a narrow FWHM ( $0.40^\circ$ ). The RHEED pattern, X-ray diffraction and IR absorption data support the growth of single-crystalline  $\beta$ -SiC under the conditions mentioned above.

The films grown at a high growth rate resulted in a polycrystalline structure. Figure 4 shows the RHEED patterns of relatively thin SiC ( $2000\text{ Å}$ ) and relatively

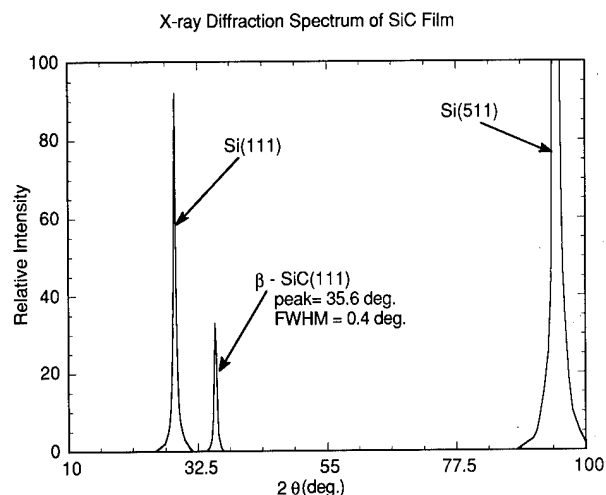
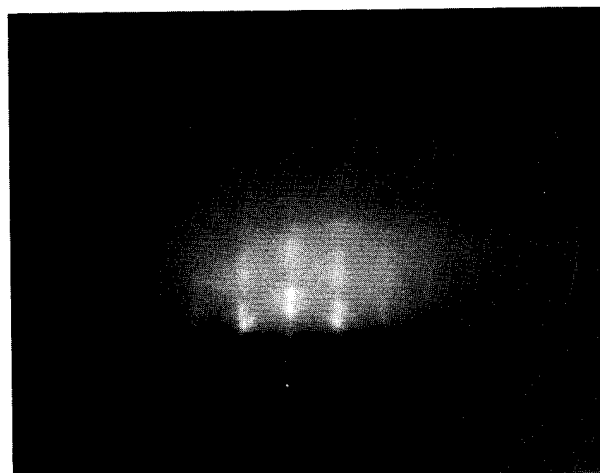
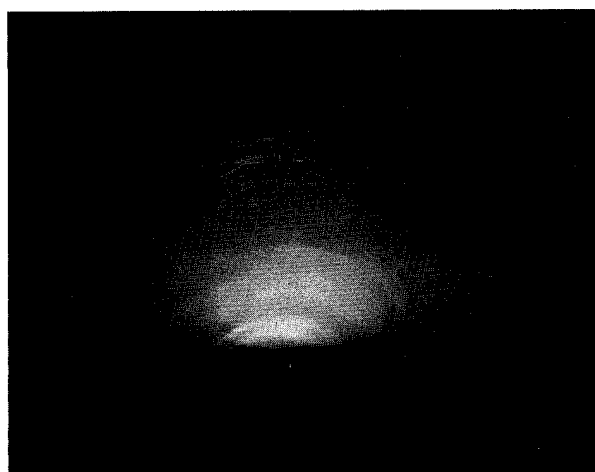


Fig. 3. X-ray diffraction measurement of an SiC film grown at  $900^\circ\text{C}$ .



(a)

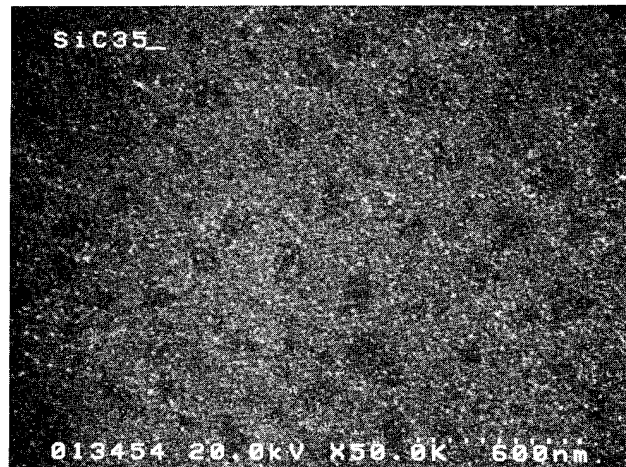


(b)

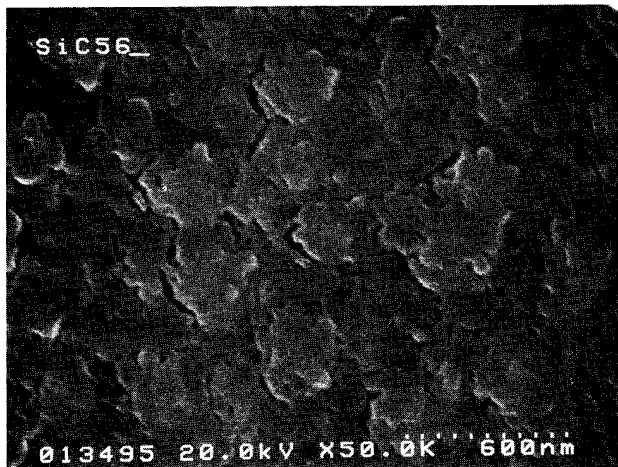
Fig. 4. RHEED patterns of SiC films on an Si substrate: (a)  $2000\text{ Å}$  thick; (b)  $1\text{ }\mu\text{m}$  thick.

thick SiC ( $1\text{ }\mu\text{m}$ ). As shown in Fig. 4, the thin SiC film appears to have maintained the single-crystalline  $\beta$ -SiC structure, while the thick SiC film is polycrystalline. The surface morphology of the samples described in Fig. 4 was obtained with SEM as shown in Fig. 5. The polycrystalline nature of the thick films (about  $1\text{ }\mu\text{m}$ ) is not clear but it is believed to be due to three-dimensional growth arising from the misfits or dislocations which can occur owing to the large lattice mismatch between SiC and Si. To check further whether this polycrystalline film is stoichiometric SiC or an SiC-Si mixture, the composition of the film is evaluated by XPS depth profiling. The results in Fig. 6 clearly show that the polycrystalline film has the stoichiometric SiC composition within experimental accuracy.

The electrical properties of the  $\beta$ -SiC films grown with this technique were characterized using hot thermal probe,  $I$ - $V$  and  $C$ - $V$  measurements. It is well known that an unintentionally doped  $\beta$ -SiC film grown



(a)



(b)

Fig. 5. SEM surface morphology of SiC films corresponding to those in Fig. 4.

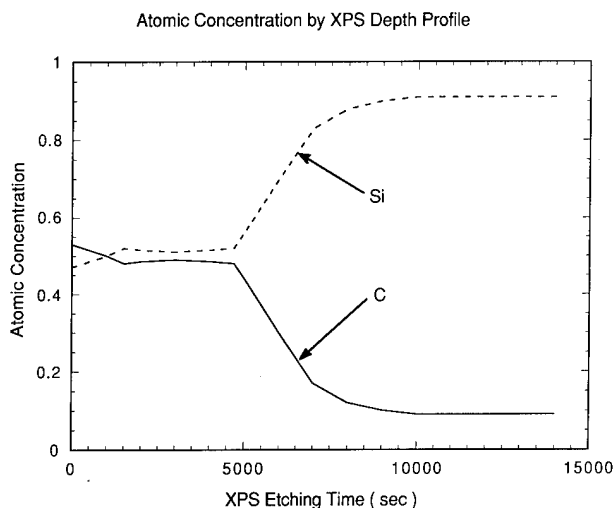


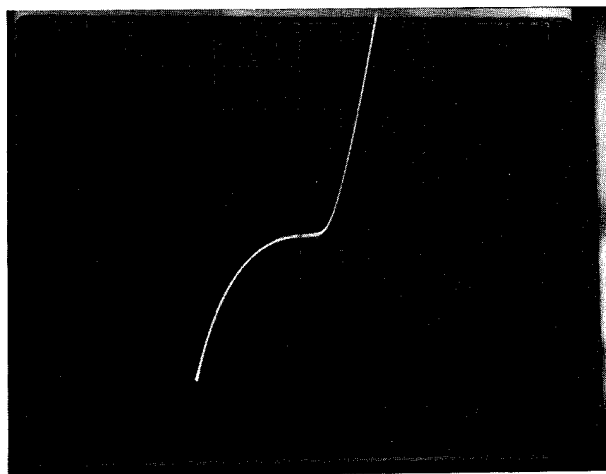
Fig. 6. XPS depth profiling of a thick (3000 Å) polycrystalline SiC film.

on an Si substrate by CVD gives an n-type behavior with a residual donor concentration of around  $10^{16} \text{ cm}^{-3}$ , regardless of the Si substrate doping type [15]. The cause of this unintentional n-type doping in  $\beta$ -SiC is not well established. Residual nitrogen doping from the growth environment of CVD systems or non-stoichiometric defects [16] were suspected. In our case, the unintentionally doped  $\beta$ -SiC films grown during MBE are almost intrinsic with high resistivity although the films grown on a p-type Si substrate have a p-type residual doping as determined by hot thermal probe measurements. Likewise, films grown on an n-type Si substrate have a low residual donor concentration, as determined by  $C-V$  measurements. The detailed electrical properties of undoped SiC films are currently under investigation. To determine the device grade quality of the film, we have fabricated simple  $n^+ - p^+$  diodes with a thin  $\beta$ -SiC layer.

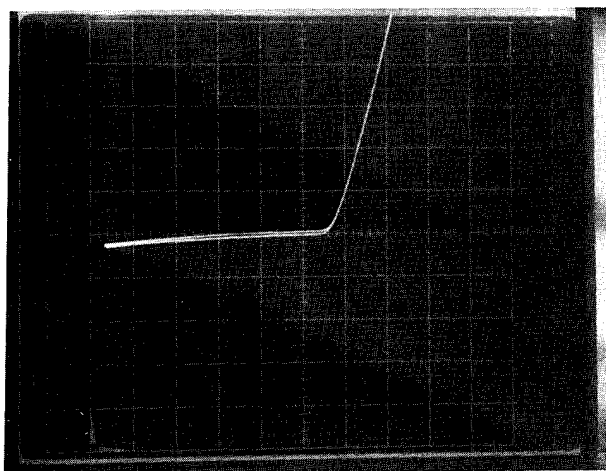
### 3. p-n junction diode with a thin $\beta$ -SiC layer

The current state-of-the-art Si bipolar junction transistor (BJT) used heavily doped  $n^+$  polysilicon as the emitter and a very shallow, highly doped  $p^+$  Si as the base to achieve high speed performance. The improvement in the current gain achieved by inserting a very thin oxide layer between the  $n^+$  polysilicon emitter and the shallow  $p^+$  base in a BJT has been reported [17]. The improvement in the gain in this structure was attributed to the reduction in hole injection owing to the high valence band offset (about 4.0 eV) between Si and  $\text{SiO}_2$ . However, the high emitter resistance of this structure is one of the major drawbacks. Replacing the  $\text{SiO}_2$  with a thin  $\beta$ -SiC layer is a good choice in improving Si BJTs owing to the reduction in hole injection and a small emitter resistance, which can be obtained by using the relatively large valence band offset voltage (about 0.8 eV) and small conduction band offset voltage (about 0.3 eV) [18].

The feasibility of using a thin  $\beta$ -SiC film in Si BJTs was studied by fabricating heterojunction  $p^+ - n^+$  diodes with a thin  $\beta$ -SiC film. For performance comparison, conventional  $p^+ - n^+$  Si diodes without  $\beta$ -SiC also were fabricated using the same growth conditions. The  $p^+$  region is a heavily B-doped Si substrate ( $10^{19} \text{ cm}^{-3}$ ) and the  $n^+$  region is a heavily Sb-doped polycrystalline film deposited after the thin  $\beta$ -SiC film growth. The film thickness of the  $\beta$ -SiC is about 100 Å, as determined by the ellipsometry measurements. Figure 7 shows the  $I-V$  curves of the diode with and without the thin  $\beta$ -SiC film. The forward characteristics of both types of diode (with and without the thin  $\beta$ -SiC layer) are comparable. For the Si diode (without the  $\beta$ -SiC layer), a small reverse breakdown voltage result-



(a)



(b)

Fig. 7.  $I$ - $V$  characteristics of  $n^+$ - $p^+$  diodes without (a) and with (b) the SiC layer in between.  $I$  axis is 0.1 mA/division,  $V$  axis is 1 V/division.

ing from tunnelling between the  $n^+$  polysilicon and the  $p^+$  substrate is observed, as shown in Fig. 7(a). As shown in Fig. 7(b), the reverse breakdown voltage was improved by inserting an undoped  $\beta$ -SiC layer 100 Å thick. The improvement is believed to be due to the increase in the tunnelling barrier width with the insertion of the undoped thin  $\beta$ -SiC. To study further the heterojunction between the Si and  $\beta$ -SiC, other device structures, such as heterojunction bipolar transistors, are being investigated.

#### 4. Conclusions

The growth of single-crystalline  $\beta$ -SiC was performed using a solid Si source and a  $C_2H_2$  gas beam. The carbonization process and subsequent growth of SiC

were studied using various analysis tools. The SiC films grown by this method show that films below 2000 Å thick are single crystalline; however, thick films are polycrystalline. To check the film quality,  $p^+$ - $n^+$  diodes with and without a  $\beta$ -SiC layer were fabricated. In the case of an  $n^+$ (polysilicon)- $p^+$  heterojunction with the thin  $\beta$ -SiC layer, improved reverse  $I$ - $V$  characteristics are observed along with reasonably good forward characteristics when compared with the diode without the thin  $\beta$ -SiC layer. A self-limiting reaction of the  $C_2H_2$  reaction with the Si substrate at around 875 °C is observed and can be useful for group IV ALE applications. Such methods may be applied for the growth of many new material combinations, such as Si/Ge/Si/SiC, etc.

#### Acknowledgment

The authors would like to acknowledge support by an IBM Research Initiated Grant.

#### References

- 1 W. E. Nelson, F. A. Halden and A. Rosengreen, *J. Appl. Phys.*, **37** (1966).
- 2 D. K. Ferry, *Phys. Rev. B*, **12** (1975) 2361.
- 3 W. V. Muench and I. Pfaffender, *J. Appl. Phys.*, **48** (1977) 4831.
- 4 H. P. Phillip and E. A. Taft, in J. R. O'Connor and J. Smiltens (eds.) *Silicon Carbide, A high temperature Semiconductor*, Pergamon, New York, 1960, p. 371.
- 5 S. Nishino, J. A. Powell and H. A. Will, *Appl. Phys. Lett.*, **42** (1983) 460.
- 6 S. Nishino, Y. Hazuki, H. Matsumani and T. Tanaka, *J. Electrochem. Soc.*, **127** (1980) 2674.
- 7 H. Fuma, A. Miura, H. Tadano, S. Sugiyama and M. Takigawa, *Jpn. J. Appl. Phys.*, **27**, (1988) 2143.
- 8 T. Sugii, T. Yamazaki and T. Ito, *IEEE Trans. Electron Devices*, **37** (1990) 2331.
- 9 S. Motoyama, N. Morikawa and S. Kaneda, *J. Cryst. Growth*, **100** (1990) 615.
- 10 T. Sugii, T. Aoyama and T. Ito, *J. Electrochem. Soc.*, **137** (1990) 989.
- 11 K. Kim, S. Choi and K. Wang, *J. Vac. Sci. Technol. B*, **10** (2) (1992) 930.
- 12 T. Yoshinobu, T. Fuyuki and H. Matunami, *Mater. Res. Soc. Symp. Proc.*, **220** (1991) 575.
- 13 A. Addamiano and J. A. Sprague, *Appl. Phys. Lett.*, **44** (1984) 525.
- 14 F. Bozso, J. Yates, W. Choyke and Muehlhoff, *J. Appl. Phys.*, **57** (8) (1985) 2771.
- 15 H. Matsumami, *Mater. Res. Soc. Symp. Proc.*, **97** (1987) 171.
- 16 A. Suzuki, A. Uemoto, M. Shigeta, K. Furukawa and S. Nakajima, *Appl. Phys. Lett.*, **49** (1986) 450.
- 17 H. de Graaff and J. de Groot, *IEEE Trans. Electron Devices*, **ED-26** (1979) 1771.
- 18 K. Sasaki, S. Furukawa and M. Rahman, *Int. Electron Device Meet.*, 294 (1985).

# Microscopic mechanisms of accurate layer-by-layer growth of $\beta$ -SiC

Shiro Hara, T. Meguro, Y. Aoyagi and M. Kawai

*The Institute of Physical and Chemical Research (RIKEN), 2-1 Hirosawa, Wako, Saitama 351-01 (Japan)*

S. Misawa, E. Sakuma and S. Yoshida

*Electrotechnical Laboratory, 1-1-4 Umezono, Tukuba-shi, Ibaraki 305 (Japan)*

## Abstract

Atomic layer epitaxy of cubic SiC was investigated to examine gas reactions on the surface at high temperature using Auger electron spectroscopy and low energy electron diffraction. Self-limiting growth at one and one-third atomic monolayers at 1050 °C was observed for exposure of a carbon-terminated surface to  $\text{Si}_2\text{H}_6$ , and self-limiting growth at just one atomic monolayer was observed for exposure of a silicon-saturated surface to  $\text{C}_2\text{H}_2$ . It was also found that the extra partial silicon layer of the silicon-saturated surface desorbs during  $\text{C}_2\text{H}_2$  exposure. By alternating exposure to  $\text{Si}_2\text{H}_6$  and  $\text{C}_2\text{H}_2$ , accurate layer-by-layer growth is achieved. In this system, the spontaneous atomic layer desorption of silicon which occurs during  $\text{C}_2\text{H}_2$  exposure is consistent with the nature of exact atomic layer epitaxy.

## 1. Introduction

Recent chemical vapor deposition (CVD) techniques for the preparation of silicon carbide using the buffer layer technique [1, 2] produce excellent cubic SiC ( $3\text{C}$ -SiC or  $\beta$ -SiC) epitaxial layers on silicon (001) substrates. The high quality of this epitaxial  $\beta$ -SiC has motivated us to study applications of multi-heteroepitaxy such as  $\text{Si}/\text{SiC}/\text{Si}/\text{SiC} \dots$ ,  $6\text{H}/3\text{C}/6\text{H}/3\text{C} \dots$ , etc. which are new materials with controllable band gaps. However, there are no reports on precisely controlled epitaxy that could provide us with a physical basis for creating these structures.

In general, the simultaneous precursor gas supply used for most CVD growth involves complex mechanism(s) that make understanding the nature of the resultant epitaxy difficult. In contrast, in atomic layer epitaxy (ALE), single or alternating precursor supplies are directed onto a substrate. In terms of growing a multilayer, one of the most important and interesting phenomena is self-limiting growth required for ALE, where growth from each precursor stops at a coverage of one monolayer. When a self-limiting phenomenon is found on a particular surface, then ALE becomes possible. In a material composed of two elements such as SiC, ALE requires self-limiting growth for each gas supply.

Fuyuki *et al.* reported achieving ALE of  $\beta$ -SiC [3]. They demonstrated homoepitaxial growth of  $\beta$ -SiC at 1000 °C by alternating supplies of  $\text{Si}_2\text{H}_6$  and  $\text{C}_2\text{H}_2$  under a partial pressure of  $5 \times 10^{-5}$  Torr. They observed an increase in growth rate per cycle when the

$\text{Si}_2\text{H}_6$  flux was increased. In other words, self-limiting growth was not present.

To investigate one monolayer deposition, knowledge of surface elemental compositions and surface atomic configurations is required. We have reported correlations between low energy electron diffraction (LEED) reconstruction phases and surface compositions of  $\beta$ -SiC(001) [4].  $(2 \times 1)$  and  $c(4 \times 2)$  phases have a full silicon top layer, whereas the  $c(2 \times 2)$  phase has a full carbon top layer. The  $(3 \times 2)$  and  $(5 \times 2)$  phases have additional dimer rows on top of a silicon-terminated crystal.

In this work, we investigate the feasibility of ALE of  $\beta$ -SiC crystals by alternating exposure to  $\text{C}_2\text{H}_2$  and  $\text{Si}_2\text{H}_6$ .

## 2. Experimental details

$\beta$ -SiC samples were grown on an Si(001) wafer by CVD using the buffer layer technique in order to relax strain resulting from the lattice mismatch between the silicon substrate and  $\beta$ -SiC overlayer. The details of such growth have been described elsewhere [5]. The thickness of the heteroepitaxial  $\beta$ -SiC layer was about 2  $\mu\text{m}$ .

The samples were degreased in trichloroethylene, followed by an HF rinse to remove the native oxide. After cleaning, the samples were annealed at 1150 °C for 10 min by direct current heating in an ultrahigh vacuum chamber (base pressure  $5 \times 10^{-10}$  Torr) equipped with LEED and Auger electron spectroscopy (AES) instru-

mentation. After this treatment, a sharp  $c(2 \times 2)$  LEED pattern was always observed at room temperature. In the previous work [4], the  $c(2 \times 2)$  pattern was found to be a full carbon top layer without any contamination and oxygen.

A silicon atomic layer was grown on a carbon-terminated  $c(2 \times 2)$  sample surface at 1050 °C by exposure to  $\text{Si}_2\text{H}_6$  at a partial pressure of  $1 \times 10^{-6}$  Torr. After every 20 s of  $\text{Si}_2\text{H}_6$  exposure, the gas supply was stopped and the sample was cooled down to room temperature to observe the surface reconstruction using LEED and the surface composition using AES. Subsequently, the temperature was again raised to 1050 °C and the gas supply restarted.

A carbon atomic layer was grown at 1050 °C by exposure to  $\text{C}_2\text{H}_2$  at a partial pressure of  $1 \times 10^{-6}$  Torr on the silicon-covered  $(3 \times 2)$  sample prepared by  $\text{Si}_2\text{H}_6$  exposure. The surface characterization procedure was the same as for  $\text{Si}_2\text{H}_6$ .

Not only the presence of self-limiting mechanism(s), but also the feasibility of actual ALE was investigated by alternating exposure to  $\text{Si}_2\text{H}_6$  and  $\text{C}_2\text{H}_2$ .

### 3. Results and discussion

#### 3.1. Silicon self-limiting growth

Figure 1 shows surface composition *vs.*  $\text{Si}_2\text{H}_6$  exposure time on a  $\beta$ -SiC(001)- $c(2 \times 2)$  carbon-terminated surface. The vertical axis indicates the AES peak-to-peak ratio of Si LVV to C KLL. The  $[\text{Si}]/[\text{C}]$  ratio increases from the initial clean  $c(2 \times 2)$  surface to the  $(3 \times 2)$  surfaces with increasing exposure time. The AES energy analyser was set at a relatively shallow angle ( $24^\circ$ ) from the horizontal axis of the sample so that the signals detected were more surface sensitive. The changes in the phases and the  $[\text{Si}]/[\text{C}]$  ratios from the  $c(2 \times 2)$  to the  $(3 \times 2)$  surface correspond to the change in surface composition from a carbon-terminated to a silicon-covered surface. We believe that this change occurred by epitaxial growth of a silicon monolayer on the carbon-terminated surface.

Saturation of the composition in the  $(3 \times 2)$  region is seen in the figure. The LEED pattern did not change in the saturation region. These phenomena are attributed to the self-limiting growth of silicon on the carbon-terminated surface.

The thickness of the deposited silicon film was estimated at about 1.3 ML (atomic monolayer) because the  $(3 \times 2)$  surface consists of a full 1 ML with an additional  $1/3$  ML of silicon on top of the carbon layer [4].

The pattern changes from the initial carbon-terminated  $c(2 \times 2)$  phase to the final silicon-saturated  $(3 \times 2)$  phase through  $(1 \times 1)$  and  $(2 \times 1)$ , which is consistent with our previous work on phase changes at

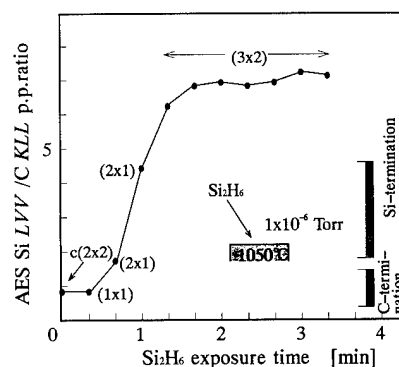


Fig. 1. The transition of elemental composition from the carbon-terminated to the silicon-covered surface by exposure to  $\text{Si}_2\text{H}_6$  at 1050 °C. The initial  $c(2 \times 2)$  surface is carbon terminated. The  $(3 \times 2)$  surface is silicon covered. Saturation of the composition in the  $(3 \times 2)$  region suggests silicon self-limiting growth on the carbon-terminated  $c(2 \times 2)$  surface.

a high temperature using medium ion energy scattering spectroscopy (MEIS), except that a  $(5 \times 2)$  phase between the  $(3 \times 2)$  and the  $(2 \times 1)$  phases was observed in previous experiments [4]. Since the  $(5 \times 2)$  phase requires long-range correlation among additional dimer rows, skipping the  $(5 \times 2)$  phase is probable.

On the Si(001) surface, the silane family ( $\text{SiH}_4$ ,  $\text{Si}_2\text{H}_6$ ,  $\text{Si}_3\text{H}_8$ , etc.) forms epitaxial films without self-limiting growth [6–8]. A significant difference in growth conditions between those used for Si(001) and those for SiC(001) is the growth temperature. Epitaxial growth on Si(001) is usually done at temperatures of 700–800 °C [6, 7], which is considerably lower than our growth temperature of 1050 °C. In general, at a higher temperature, surface atoms tend to dissociate owing to the increase in their kinetic energy, resulting in gas desorption. At the same time, the precursor(s) apparently experience no reaction with the surface. At a lower temperature, surface atoms and the precursor atoms receive insufficient energy to form gaseous products, leading to no reaction (slow growth), polycrystalline or amorphous deposition. The best temperature for ALE growth on  $\beta$ -SiC(001) is about 300 °C higher than that used on the Si(001) surface. At 700–800 °C on the  $\beta$ -SiC(001) surface, silicon deposition may not be self-limiting and may continue after 1 ML of deposition, leading to polycrystalline or amorphous material since the surface dissociation of excess silicon that seems to be the main cause of self-limiting growth hardly occurs, compared with the rate of dissociation at 1050 °C.

#### 3.2. Carbon self-limiting growth

Figure 2 shows the surface composition *vs.*  $\text{C}_2\text{H}_2$  exposure time on a  $\beta$ -SiC(001)- $(3 \times 2)$  silicon-covered surface. The initial silicon-covered  $(3 \times 2)$  phase

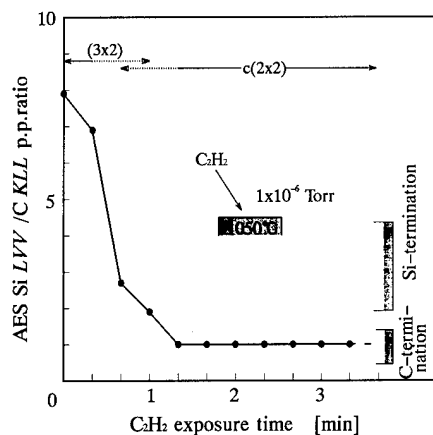
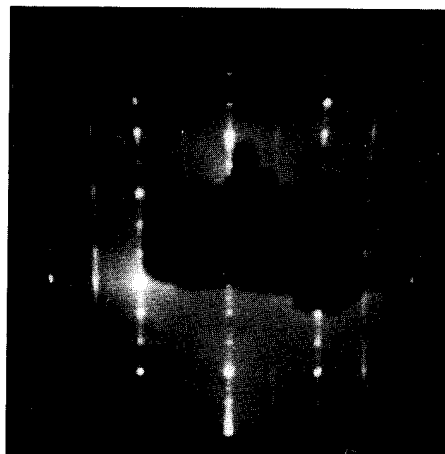


Fig. 2. The transition of elemental composition from the silicon-covered to the carbon-terminated surface by exposure to  $C_2H_2$  at  $1050^\circ C$ . Saturation of the composition in the  $c(2 \times 2)$  region suggests carbon self-limiting growth on the silicon-covered  $(3 \times 2)$  surface. The dotted lines indicate a mixed region of  $(3 \times 2)$  and  $c(2 \times 2)$ .

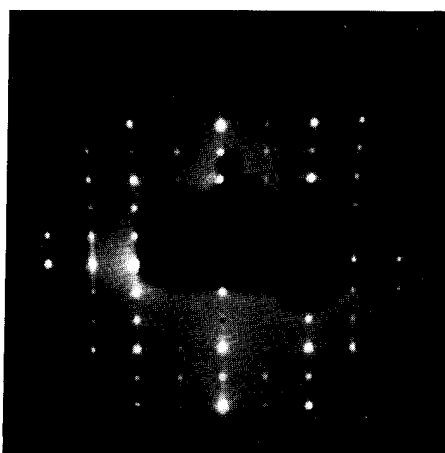
changes into the carbon-terminated  $c(2 \times 2)$  phase after 80 s exposure. The AES peak-to-peak ratio of Si LVV to C KLL decreases with the surface phase transition, subsequently reaching a constant value at the  $c(2 \times 2)$  region. We believe that about 1 ML carbon is deposited epitaxially onto the silicon-saturated  $(3 \times 2)$  surface during the transition, followed by termination of growth. Evidently, the termination of growth is attributed to the self-limiting growth of carbon on the silicon-saturated surface, similar to the silicon self-limiting growth discussed in the previous section.

The straight line without data scattering in the  $c(2 \times 2)$  region suggests that the  $c(2 \times 2)$  phase is a somewhat stabler structure than the  $(3 \times 2)$  structure shown in Fig. 1. We observed that the  $c(2 \times 2)$  phase continues up to 1200 s, followed by a new  $(1 \times 1)$  phase. The  $c(2 \times 2)$  region has a much longer lifetime than the transition region from the  $(3 \times 2)$  to the  $c(2 \times 2)$ , so one can distinguish the  $c(2 \times 2)$  phase from the  $(1 \times 1)$ , much more conveniently for ALE. In other words, the ALE window for the precursor dose is very wide in this system. The  $(1 \times 1)$  phase that appears after the  $c(2 \times 2)$  has been reported by Kaplan [9] and by Parrill *et al.* [10]. From their electron energy loss spectroscopy measurements, they concluded that this  $(1 \times 1)$  phase has the graphite structure. In our experiment, no evidence of this carbon structure was found.

Estimating the carbon growth thickness on the  $(3 \times 2)$  surface is more complicated than for silicon because the initial  $(3 \times 2)$  surface has the additional silicon dimer layer with  $1/3$  ML thickness, which could be an obstruction to growing the next atomically flat  $c(2 \times 2)$  carbon surface. If the additional  $1/3$  layer remained during deposition of the carbon atoms, the resulting surface should have an atomic corrugation



(a)



(b)

Fig. 3.  $(3 \times 2)$  LEED patterns before and after ALE: (a) a disordered  $(3 \times 2)$  surface formed by exposure to atomic hydrogen, followed by an anneal to desorb the hydrogen; (b) a well ordered  $(3 \times 2)$  surface after four cycles of ALE. An improvement in the crystal surface quality is observed as a result of ALE.

with a different atomic configuration from the normal  $c(2 \times 2)$  structure. However, we observed a typical  $c(2 \times 2)$  pattern after 80 s  $C_2H_2$  exposure, as shown in Fig. 2. This is evidence that the resulting  $c(2 \times 2)$  surface has no extra silicon atoms just below the top-most grown carbon layer. This implies that the additional silicon atoms desorb during  $C_2H_2$  exposure at  $1050^\circ C$ . Therefore, we estimate the carbon growth thickness at exactly 1 ML.

### 3.3. Accurate layer-by-layer growth

The feasibility of actual ALE was investigated by several cycles of alternating exposure of an SiC sample at  $1050^\circ C$  to  $Si_2H_6$  and  $C_2H_2$ . The gas partial pressures were  $1 \times 10^{-6}$  Torr. The exposure time for each gas was 3–5 min which is adequate for growth saturation. After each gas exposure, the sample temperature



was reduced to room temperature, and a LEED pattern was observed, before raising the sample temperature up to 1050 °C again. The purge time for each gas was about 5 min, including the LEED observation time, which reduces the pressure to around  $1 \times 10^{-9}$  Torr. We observed repetition of the typical  $(3 \times 2)$  and  $c(2 \times 2)$  LEED patterns during the alternating exposures. This indicates that ALE is achieved under these conditions. This is due to spontaneous desorption of the additional silicon layer during  $C_2H_2$  exposure.

An improvement in surface ordering is observed following several cycles of sequential alternating exposures to the two gases without reducing the temperature as shown in Fig. 3. Figure 3(a) is a LEED pattern before ALE. This surface was formed by exposing a  $(3 \times 2)$  sample to atomic hydrogen at  $1 \times 10^{-6}$  Torr was some minutes, followed by hydrogen desorption at a high temperature around 1150 °C. The streaks observed for all spots correspond to surface atom disordering caused by the hydrogen exposure. Note that the high temperature anneal at 1150 °C does not improve the streaking. As this surface seems to have no hydrogen, the surface disordering is caused by surface silicon disordering itself.

After four cycles of ALE, the surface ordering was improved greatly, as shown in Fig. 3(b) where the streaks disappear entirely. This demonstrates that ALE in this system has the effect of improving the crystal quality. In addition, the growth temperature of  $\beta$ -SiC at 1050 °C is much lower than the usual growth temperature of around 1350 °C CVD. This is another advantage of the ALE method in this system.

The silicon desorption during  $C_2H_2$  exposure may be attributed to weak bonding between the additional silicon atoms and the silicon atoms underneath. Takai et al. [11] found, from numerical calculations, that the Si-Si and the Si-C surface bond energies are 2.817 eV and 3.895 eV respectively. This suggests that Si-Si bonds between the top additional silicon atoms and the silicon atoms in the second layer are considerably weaker than bulk Si-C bonds. This weak adsorption of the additional silicon atoms seems to be the cause of the desorption under  $C_2H_2$  exposure at the high temperature of 1050 °C.

We predict that there will be ALE with spontaneous desorption of an extra layer in other systems. In a stoichiometric compound semiconductor, one constituent atom A tends to bond with the other constituent atom B energetically. Therefore, if an extra

layer of A is present on one monolayer of A, the other constituent B should purge the extra A layer. At the corner of an ALE window with a growth rate of over 1 ML per cycle, it appears that there is often an extra layer A which desorbs during supply of B, resulting in growth of 1 ML per cycle.

#### 4. Conclusions

We have found that the  $\beta$ -SiC(001) surface has self-limiting mechanisms of growth for both the silicon surface and the carbon surface. Silicon growth by  $Si_2H_6$  exposure at 1050 °C under  $1 \times 10^{-6}$  Torr onto the  $c(2 \times 2)$  carbon-terminated surface ends at 1.3 ML growth, producing a  $(3 \times 2)$  silicon-covered surface. Carbon growth by  $C_2H_2$  exposure onto the  $(3 \times 2)$  surface under the same conditions as  $Si_2H_6$  exposure ends at 1 ML growth, producing a  $c(2 \times 2)$  carbon surface.

Further, alternative exposures of  $Si_2H_6$  and  $C_2H_2$  achieve accurate layer-by-layer growth, which is due to the spontaneous atomic layer desorption of silicon during  $C_2H_2$  exposure.

#### Acknowledgment

This work was partially supported by a Grant-in Aid for Scientific Research of the Ministry of Education, Science and Culture, Japan.

#### References

- 1 S. Nishino, J. A. Powell and H. A. Will, *Appl. Phys. Lett.*, **42** (1983) 460.
- 2 A. Suzuki, K. Furukawa, Y. Higashigaki, S. Harada, S. Nakajima and T. Inoguchi, *J. Cryst. Growth*, **70** (1984) 287.
- 3 T. Fuyuki, M. Nakayama, T. Yoshinobu, H. Shiomi and H. Matsunami, *J. Cryst. Growth*, **95** (1989) 461.
- 4 S. Hara, W. F. J. Slijkerman, J. F. van der Veen, I. Ohdomari, S. Misawa, E. Sakumka and S. Yoshida, *Surf. Sci.*, **231** (1990) L196.
- 5 S. Yoshida, K. Sasaki, E. Sakumka, S. Misawa and S. Gonda, *Appl. Phys. Lett.*, **46** (1985) 766.
- 6 J. H. Comfort and R. Reif, *J. Electrochem. Soc.*, **136** (1989) 2386.
- 7 S. M. Gates, *Surf. Sci.*, **195** (1988) 307.
- 8 S. Lian, B. Fowler, D. Bullock and S. Banerjee, *Appl. Phys. Lett.*, **58** (1991) 514.
- 9 R. Kaplan, *Surf. Sci.*, **215** (1989) 111.
- 10 T. M. Parrill and Y. W. Chung, *Surf. Sci.*, **243** (1991) 96.
- 11 T. Takai, T. Halicioğlu and W. A. Tiller, *Surf. Sci.*, **164** (1985) 341.

# Layer-by-layer epitaxial growth of GaN at low temperatures

J. Sumakeris, Z. Sitar and K. S. Ailey-Trent

North Carolina State University, Department of Materials Science and Engineering, Box 7907, Riddick Hall, Raleigh, NC 27695-7907 (USA)

K. L. More

Metals and Ceramics Division, Oak Ridge National Laboratory, Oak Ridge, TN 37831-6064 (USA)

R. F. Davis

North Carolina State University, Department of Materials Science and Engineering, Box 7907, Riddick Hall, Raleigh, NC 27695-7907 (USA)

## Abstract

GaN films have been grown on (0001)<sub>Si</sub> SiC substrates from triethylgallium and ammonia sources using a self-terminating atomic layer epitaxy method, as well as a layer-by-layer technique and a novel reactor design employing hot filaments to decompose the ammonia. The material properties and growth process were strongly dependent on the temperature and exposure time. GaN grew in a self-terminating fashion for temperatures below 120 °C but the films were amorphous. Above this temperature, the films were deposited in a layer-by-layer process giving single-crystal material in the 250–350 °C range. Characterization of the films was conducted using reflection high energy electron diffraction, single-crystal X-ray diffraction, ellipsometry and high resolution transmission electron microscopy.

## 1. Introduction

The potential optoelectronic applications of wide bandgap materials have stimulated considerable research concerned with thin film growth, characterization and device development of the III–V nitrides, namely cubic BN, AlN, GaN and InN. Of this family, GaN has been the most thoroughly studied. Measures of the potential of GaN are revealed by its high Johnson and Keyes figures of merit of  $80.0 \times 10^{11}$  and  $4.2 \times 10^8$ , respectively, compared with  $4.75 \times 10^{11}$  and  $2.39 \times 10^8$  for Si [1]. GaN usually forms in a wurtzite structure with a bandgap of 3.4 eV [2]. However, recently several groups [3–6] have deposited films of the cubic (zinc blende structure)  $\beta$ -GaN which has a smaller bandgap of 3.26 eV. As the wurtzitic polytype of GaN forms continuous solid solutions with both AlN and InN which have bandgaps of 6.2 eV [7] and 1.9 eV [8], respectively, materials with engineered bandgaps may be produced for the construction of optoelectronic devices active from the visible to deep UV frequencies.

A major difficulty in the growth of thin films of GaN is the lack of suitable substrates. The lattice parameters and coefficients of thermal expansion are given in Table 1 for GaN and the most common substrate materials of Si, SiC (6H and 3C), sapphire, ZnO and GaAs. With the possible exception of the basal planes of  $\alpha$ (6H)-SiC and ZnO, none of these materials is suitable for the

two-dimensional epitaxial growth of GaN. However, films have been grown on all these materials by several techniques, including chemical vapor deposition (CVD) [10], metal–organic CVD (MOCVD) [11, 12], reactive molecular beam epitaxy (RMBE) [13] and electron cyclotron resonance (ECR) microwave plasma-assisted MBE [3, 5]. Films deposited on  $\alpha$ (6H)-SiC(0001), sapphire and ZnO normally have the wurtzite structure [3]; films deposited on  $\beta$ -SiC(100) [3], GaAs(100) [6] and Si(100) [5] usually possess the zinc blende structure.

Although atomic layer epitaxy (ALE) was first developed by Suntola and Antson for the deposition of

TABLE 1. Physical properties of GaN and potential substrate materials [9]

Material	Lattice parameter		Coefficient of thermal expansion (K <sup>-1</sup> )
	<i>a</i> (Å)	<i>c</i> (Å)	
GaN	3.189	5.185	$5.59 \times 10^{-6}$ $3.17 \times 10^{-6}$
Si	5.43		$3.59 \times 10^{-6}$
$\alpha$ (6H)-SiC	3.08	15.12	$4.2 \times 10^{-6}$ $4.7 \times 10^{-6}$
$\beta$ (3C)-SiC	4.36		$2.7 \times 10^{-6}$
Al <sub>2</sub> O <sub>3</sub>	4.758	12.991	$7.5 \times 10^{-6}$ $8.5 \times 10^{-6}$
ZnO	3.252	5.213	$2.9 \times 10^{-6}$ $4.75 \times 10^{-6}$
GaAs	5.653		$6.0 \times 10^{-6}$

polycrystalline ZnSe on glass substrates [14], the technique has been adapted from the deposition of II–IV compounds to the III–V and group IV materials to allow ALE of GaAs [15], GaP [16], GaN [17] and Si [18]. One method of ALE employs the adsorption of incompletely decomposed precursor species. In this case, there is a ceiling substrate temperature for any given reactant gas. Because of the relatively low temperatures employed, for example, less than 600 °C for GaAs from trimethylgallium, surface mobility is diminished. This may result in degradation in the film crystallinity, morphology and properties. Alternative ways to supply energy to the growing films have been explored. For example, Nishizawa *et al.* [19] have studied the effect of photo-stimulation on the deposition of GaAs. It was determined that UV irradiation enhances the film morphology and increases film resistivity.

In addition to a decreased surface mobility, another difficulty may be that the source gases used in the ALE of compound materials decompose at greatly different temperatures. As a result, the temperature required to decompose partially the more stable species may completely decompose the less stable species. To surmount these problems, we have employed heated W filaments in the flow path of the more stable gas (NH<sub>3</sub> in this case) to assist in decomposition and to provide a 'temperature spike' to the nearby sample surface to increase the surface mobility. This has allowed the achievement of better films at lower substrate temperatures.

In the following is described the research concerned with the successful ALE of monocrystalline GaN on  $\alpha(6H)$ -SiC(0001). The conditions to achieve self-terminating monolayer deposition and the effects of the filaments, sample temperatures and the exposure time of the substrates to the source gases on the film character are described.

## 2. Experimental procedure

### 2.1. Substrate material

The substrates for all the experiments were pieces of single-crystal  $\alpha(6H)$ -SiC(0001) wafers which previously had been sliced from boules grown by Cree Research, Inc., of Durham, NC. The lattice parameter of this material is relatively closely matched to that of GaN with a linear misfit on the basal plane of 3.5%. All the samples were RCA cleaned and immediately loaded into the reactor for deposition.

### 2.2. Reactor design

The major internal components of the ALE system are depicted in Fig. 1. In general, the substrates reside on a receiver plate and revolve continuously over an SiC-coated graphite heater and below a vane assembly.

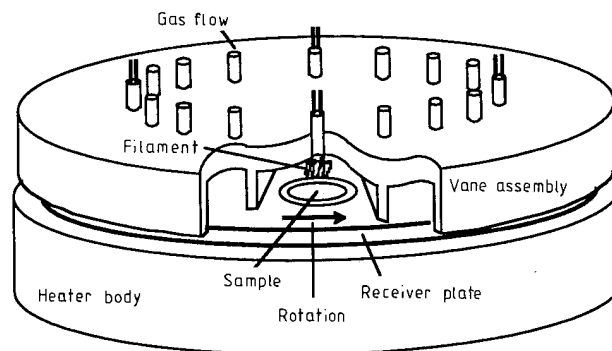


Fig. 1. Major internal components of ALE system. View into group V element supplying zone.

The gases are introduced through the vane assembly which directs the flow of each gas and also is responsible for supporting the hot W filaments. The temperature controller monitors a K-type thermocouple on the heater body; thus, the sample temperature is not measured directly. However, optical pyrometry (samples are visible beneath a sapphire window on the vane assembly) has revealed that, once the heater housing temperature has equilibrated, the sample temperature remains constant within  $\pm 5$  °C. Sample temperatures of over 980 °C can be achieved. Sample rotation is accomplished by a shaft supporting the receiver plate in its center that passes through an internal water-cooled bearing housing to a rotary feedthrough driven by a computer-controlled servomotor.

The reactants used in the growth were NH<sub>3</sub> and Ga(C<sub>2</sub>H<sub>5</sub>)<sub>3</sub> (TEG). An organometallic Ga source was chosen over a chloride source, because higher purity material was available and the transport of the Ga species is easier with organometallics. The preference of triethylgallium (TEG) over trimethylgallium (TMG) was due to a lower decomposition temperature range for TEG, the reduced Ga–(C<sub>2</sub>H<sub>5</sub>) bond energy and the consequent reduction in C incorporation in the growing films [20]. Both the H<sub>2</sub> curtain gas and the NH<sub>3</sub> are of ultrahigh purity grade and were further purified with chemical purifiers.

The introduction and control of the H<sub>2</sub> and NH<sub>3</sub> were achieved via mass flow controllers and appropriate shut-off valves. The TEG was supplied by passing H<sub>2</sub> through a constant pressure bubbler contained in a temperature-controlled bath. The flow rate of TEG was calculated from the determined values of three variables— $P(\text{TEG})$ , the vapor pressure of TEG at the bubbler temperature;  $P(\text{bubbler})$ , the pressure in the bubbler;  $F(\text{H}_2)$ , the flow rate of H<sub>2</sub> carrier gas—and the application of the following expression:

$$F(\text{TEG}) = \{F(\text{H}_2) \times P(\text{TEG})\} / \{P(\text{bubbler}) - P(\text{TEG})\} \quad (1)$$

The pressure in the bubbler was measured with a capacitance manometer. The desired pressure was maintained by setting a manual metering valve on the outlet of the bubbler which controlled the conductance between the bubbler and the reactor.

In each revolution, the samples were alternately exposed to isolated fluxes of TEG and  $\text{NH}_3$  separated by intermediate purge zones. The vane pictured in Fig. 1 has 16 zones; every other zone supplied  $\text{H}_2$  purge gas while the remaining eight zones were evenly divided between TEG and  $\text{NH}_3$ . In this manner, GaN was grown in a layer-by-layer process in the  $\langle 0001 \rangle$  direction, resulting in 10.4 Å film per revolution if a complete monolayer of material was deposited with every exposure.

### 2.3. ALE growth procedure

The RCA-cleaned substrates of  $\alpha(6\text{H})\text{-SiC}$  were loaded immediately into the load-lock and then into the cleaning chamber. Once the vacuum of the cleaning chamber was better than  $10^{-7}$  Torr, the samples were transferred into the growth chamber. The samples were positioned in a zone through which  $\text{NH}_3$  would be supplied, and the flows of  $\text{NH}_3$  and the  $\text{H}_2$  purge gas were then started. The samples were heated to the growth temperature at  $10^\circ\text{C min}^{-1}$ , the TEG flow was initiated and equilibrated, and the filaments heated to about  $1400^\circ\text{C}$ . The sample rotation was then started and maintained for the duration of the deposition. To end the run, the rotation was stopped, the TEG and the filaments shut off, and the samples allowed to cool. At a sample temperature of less than  $200^\circ\text{C}$ , all gas flow was terminated, the ALE chamber evacuated to high vacuum and the samples removed from the system.

The deposition runs were performed using various combinations of process variables. Table 2 shows the ranges of the process variables studied.

TABLE 2. Ranges of process variables

Sample temperature	150–650 $^\circ\text{C}$
ALE chamber pressure	0.5–50 Torr
$\text{NH}_3$ flow	100–300 sccm
$\text{H}_2$ (purge) flow	200–300 sccm
$\text{H}_2$ (TEG carrier) flow	50–100 sccm
TEG bubbler temperature	–10–20 $^\circ\text{C}$
TEG bubbler pressure	400–800 Torr
Time per zone	2–80 s

### 2.4. Film characterization

The sample crystallinity was analysed using reflection high energy electron diffraction (RHEED) and an X-ray diffractometer. The chemical analysis was performed by scanning Auger spectroscopy. The surface morphology and film thickness were determined using scanning electron microscopy (SEM) and automatic ellipsometry, respectively, while additional film characterization employed cross-sectional transmission electron microscopy (TEM).

## 3. Results and discussion

### 3.1. Electron diffraction

The RHEED analysis of the films revealed that both the degree and the nature of the crystallinity were strongly dependent on the temperature. Figure 2 shows the RHEED patterns for a GaN film deposited under the following conditions: sample temperature  $500^\circ\text{C}$ ; chamber pressure 2 Torr;  $\text{H}_2$  purge 200 sccm;  $\text{NH}_3$  flow 350 sccm over  $1200^\circ\text{C}$  filaments; TEG bubbler conditions—800 Torr pressure, TEG temperature  $23^\circ\text{C}$ , 100 sccm of  $\text{H}_2$  carrier and rotation rate of 11 s per zone.

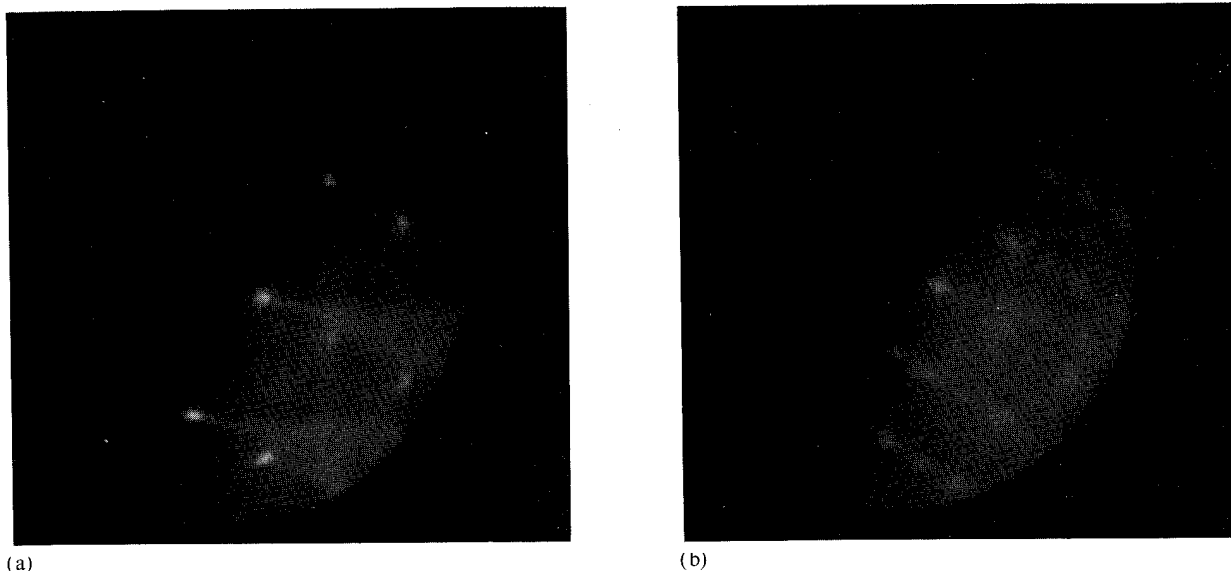


Fig. 2. RHEED patterns for GaN film deposited on  $\alpha(6\text{H})\text{-SiC}$  at  $500^\circ\text{C}$ : (a)  $(2\bar{T}0)$ ; (b)  $(01\bar{T})$ .

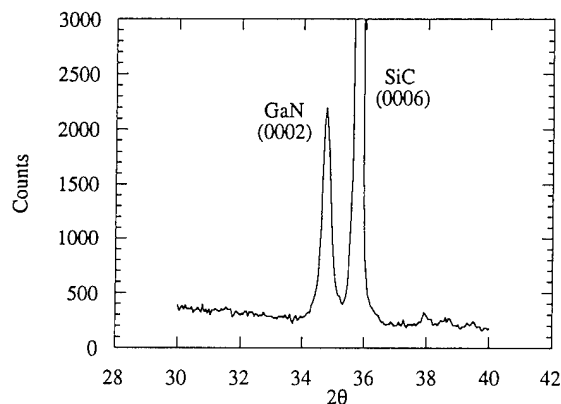


Fig. 3. X-ray diffraction pattern of film about 650 Å thick deposited on  $\alpha(6H)$ -SiC(0001).

Single-crystal RHEED patterns, indicative of the wurtzite structure, were readily achieved for sample temperatures above 350 °C when the heated filaments were employed. A series of films approximately 200 Å thick were grown across a range of sample temperatures from 150 to 550 °C. Films grown at high temperatures showed sharp diffraction spots, indicative of a rough surface, which was confirmed by SEM. Films grown at intermediate temperatures between 350 and 500 °C yielded streaked RHEED patterns with Kikuchi lines, indicative of smooth surfaces and good crystallinity. At lower temperatures, the patterns again become sharp spots. Below 250 °C, the films were no longer monocrystalline but highly textured and oriented with the substrate. However, the RHEED patterns remained as sharp diffraction spots. Films deposited below 200 °C became more randomly oriented and, finally, below 170 °C the films are amorphous. If the filaments were not heated, monocrystalline films could only be grown when sample temperatures were greater than 500 °C.

### 3.2. X-Ray diffraction studies

Each crystalline film with a thickness of 500 Å or more exhibited the (0002) reflection of wurtzitic GaN, indicating an epitaxial relationship with the substrate. Figure 3 shows an X-ray diffraction pattern of a GaN film grown under the following conditions: sample temperature 500 °C; chamber pressure 30 Torr;  $H_2$  purge 200 sccm;  $NH_3$  flow 300 sccm over 1200 °C filaments; TEG bubbler conditions—800 Torr pressure, TEG temperature -10 °C, 100 sccm of  $H_2$  carrier and rotation speed of 4 s per zone. The film thickness was about 650 Å.

### 3.3. Chemical analysis

Figure 4 is an Auger depth profile of the GaN film from which the previous RHEED image was obtained.

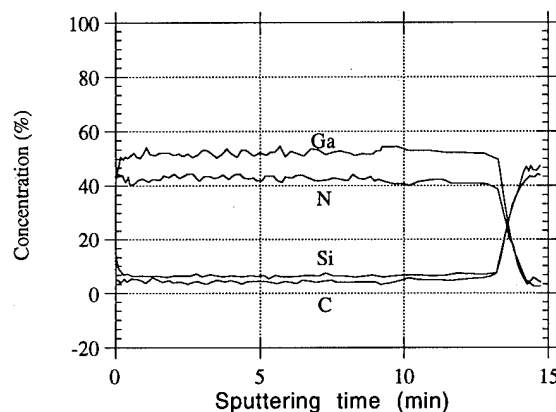


Fig. 4. Auger depth profile of GaN film deposited on  $\alpha(6H)$ -SiC at 500 °C.

The sputter rate for the film during Auger analysis was approximately 100 Å min<sup>-1</sup> using an Ar<sup>+</sup> sputter gun. Neither impurities within the film nor oxygen at the growth interface was detected. The resolution of the instrument is typically about 0.1 at.%. The spectra obtained indicated a stoichiometric film when compared with a GaN standard prepared by MBE.

### 3.4. Ellipsometry

The film thickness was measured by ellipsometry to study the effect of the exposure time to the reactant species on the amount of material deposited per cycle. If a truly self-limiting deposition process was achieved for each element then, at a given temperature and source gas flux, the amount of material deposited per cycle would increase with increasing exposure time until the deposition per cycle saturates at the monolayer or submonolayer level. Figure 5 displays the results of this study performed with several experiments run under

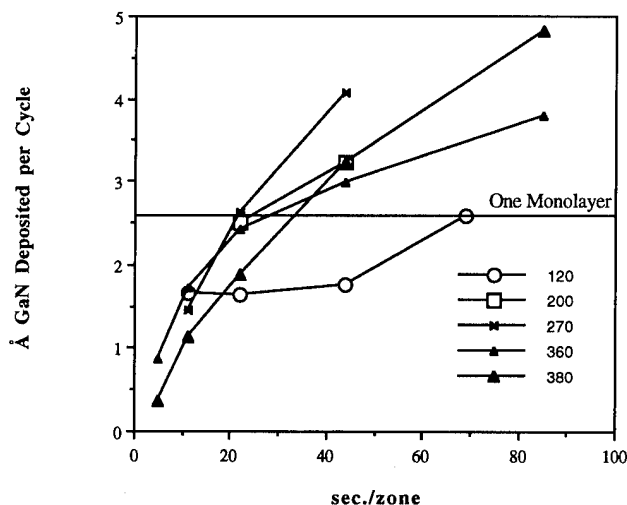


Fig. 5. Deposition thickness of GaN per cycle vs. sample temperature and time per zone.

similar conditions but differing in exposure time. Typical values for film thickness ranged from 200 to 400 Å. The values of the other process parameters were constant as follows: chamber pressure 2 Torr; H<sub>2</sub> purge rate 200 sccm; NH<sub>3</sub> flow rate 350 sccm over 1200 °C filaments; TEG bubbler conditions—800 Torr pressure, TEG temperature 23 °C and 100 sccm of H<sub>2</sub> carrier.

These flow conditions for the bubbler yielded a TEG delivery rate of 0.625 sccm or 28 μmol min<sup>-1</sup>. One can see that, for a sample temperature of 120 °C, an apparent plateau formed at about 7 Å where coverage remained constant with varying exposure time up to about 50 s. The reason for the increase at about 50 s is not yet known. The resultant films were extremely uniform: multiple readings with the ellipsometer across a 1 cm specimen gave a thickness variation of less than ±2%. Wurtzitic GaN has lattice parameters of  $a = 3.19$  Å and  $c = 5.19$  Å. Assuming complete monolayer coverage with each exposure, each cycle would give a film thickness of about 2.6 Å. These results indicated that, at 120 °C, coverage was limited to about 67% of a monolayer. Unfortunately, films grown at this temperature were amorphous.

The crystallinity improved with increasing temperature but the chemically self-limiting growth characteristic disappeared. However, from Fig. 5, one can see, for example, that at 360 °C the coverage per cycle initially increased rapidly with exposure time to a value of about 2.5 Å where the rate of further deposition began to decrease. This behaviour can be exploited to grow films in a layer-by-layer process within the portion of the range where the deposition rate has diminished. Monocrystalline films were grown at temperatures as low as 270 °C in this manner.

### 3.5. Transmission electron microscopy

Figure 6 is a high magnification TEM micrograph of a GaN film grown under the following conditions:

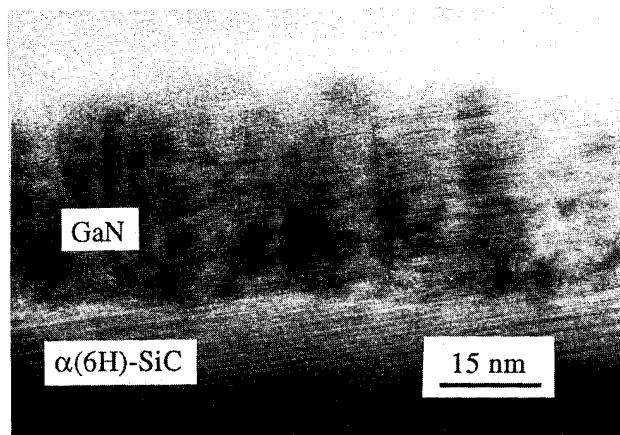


Fig. 6. High magnification TEM image of GaN film deposited on α(6H)-SiC substrate.

sample temperature 380 °C; chamber pressure 2 Torr; H<sub>2</sub> purge rate 200 sccm; NH<sub>3</sub> flow rate 350 sccm over 1200 °C filaments; TEG bubbler conditions—800 Torr pressure, TEG temperature 23 °C, 100 sccm of H<sub>2</sub> carrier and rotation speed of 11 s per zone. The SiC substrate was intentionally cut off-axis by 4.8° towards [11 $\bar{2}$ 0] during its production. One can see lattice fringes in the SiC substrate parallel to those in the film, indicating an epitaxial relationship. The film was 270 Å thick after 120 cycles. This gave a deposition per exposure of 2.25 Å or 87% of a monolayer. In addition, the surface of the film was parallel to the interface with the substrate, as would be expected from a layer-by-layer process.

## 4. Conclusions

A unique reactor for ALE growth of compound semiconductor materials has been designed and commissioned. The design employed hot W filaments to assist in both decomposing the reactants and heating the sample surface to enhance surface mobility. Epitaxial GaN films were grown on 6H-SiC substrates by a self-terminating ALE process and by a time-dependent layer-by-layer process. All the crystalline GaN deposited in this research was of the wurtzitic polytype, as determined from RHEED patterns and X-ray diffraction data. The preferred epitaxial relationship between the GaN films and the 6H-SiC substrate was with basal planes parallel.

This initial research of ALE growth of GaN on SiC using triethylgallium and ammonia as reactants has revealed that, at a sample temperature of 120 °C, an apparent plateau in growth per cycle *vs.* exposure time occurred at a time of about 50 seconds and with saturation at 67% of a monolayer. However, films grown under these conditions were amorphous. At sample temperatures higher than 270 °C, a time-dependent deposition rate can be exploited to grow single-crystal material in a layer-by-layer process. Films grown by the layer-by-layer technique at sample temperatures above 350 °C possessed good crystallinity with smooth surfaces, as evidenced by streaked RHEED patterns.

## Acknowledgments

We would like to extend our appreciation to Satoru Tanaka for helpful advice on preparation of the samples for TEM analysis and to Cree Research Inc (Durham, NC, USA) for the α(6H)-SiC wafers. This work is supported under Grant N00014-86-K-0686 P5, Innovative Science and Technology Office of the Strategic Defense Initiative, Office of the Chief of Naval Research.

## References

- 1 J. H. Edgar, *J. Mater. Res.*, **7** (1992) 235.
- 2 H. P. Maruska and J. J. Tietjen, *Appl. Phys. Lett.*, **15** (1969) 327.
- 3 M. J. Paisley, Z. Sitar, J. B. Posthill and R. F. Davis, *J. Vac. Sci. Technol. B*, **7** (1989) 701.
- 4 S. Strite, J. Ruan, Z. Li, A. Salvador, H. Chen, D. J. Smith, W. J. Choyke and H. Martoc, *J. Vac. Sci. Technol. B*, **9** (1991) 1924.
- 5 T. Lei, M. Fanciulli, R. J. Molnar and T. D. Moustakas, *Appl. Phys. Lett.*, **59** (1991) 944.
- 6 M. Mizuta, S. Fujieda, Y. Matsumoto and T. Kawamura, *Jpn. J. Appl. Phys.*, **25** (1986) L945.
- 7 W. M. Yim, E. J. Stofko, P. J. Zanzucchi, J. I. Pankove, M. Ettenberg and S. L. Gilbert, *J. Appl. Phys.*, **44** (1973) 292.
- 8 J. A. Sajurjo, E. Lopez-Cruz, P. Vogh and M. Cardona, *Phys. Rev. B*, **28** (1983) 4579.
- 9 *Landolt-Bornstein*, Vol. 17, Springer, New York, 1982.
- 10 H. P. Naruska, D. A. Stevens and J. I. Pankove, *Appl. Phys. Lett.*, **22** (1973) 303.
- 11 M. Hashimoto, H. Amano, N. Sawaki and I. Aksasoki, *J. Cryst. Growth*, **68** (1984) 163.
- 12 M. A. Kahn, R. A. Skogman, R. G. Schulze and M. Gershenson, *Appl. Phys. Lett.*, **42** (1983) 430.
- 13 H. Gotoh, T. Suga, H. Suzuki, and M. Kimata, *Jpn. J. Appl. Phys.*, **20** (1981) L545.
- 14 T. Suntola and J. Atson, *US Patent 4 058 430*, November 15, (1977).
- 15 M. A. Tischler and S. M. Bedair, *Appl. Phys. Lett.*, **48** (1986) 1681.
- 16 Y. Sakuma, K. Kodama and M. Ozeki, *Appl. Phys. Lett.*, **56** (1990) 827.
- 17 M. A. Kahn, R. A. Skogman, J. M. Van Hove, D. T. Olson and J. N. Kuznia, *Appl. Phys. Lett.*, **60** (1992) 1366.
- 18 J. Nishizawa, *J. Cryst. Growth*, **99** (1990) 502.
- 19 J. Nishizawa, T. Kurabayashi, H. Abe and N. Sakurai, *J. Vac. Sci. Technol. A*, **5** (1987) 1572.
- 20 N. Kobayashi, T. Makimoto and Y. Horikoshi, *Jpn. J. Appl. Phys.*, **24** (1985) L962.

# Ultra high vacuum atomic layer epitaxy of CdTe

H. Sitter

*Institut für Experimentalphysik and Forschungsinstitut für Optoelektronik, Universität Linz, A-4040 Linz (Austria)*

W. Faschinger

*Institut für Halbleiterphysik, Universität Linz, A-4040 Linz (Austria)*

## Abstract

Ultrahigh vacuum atomic layer epitaxy was successfully applied to grow CdTe on BaF<sub>2</sub> and GaAs. We found a set of growth parameters, the so-called self regulatory regime, where layer-by-layer growth occurs. A thermodynamic model is presented which describes the growth rate as a function of the substrate temperature and leads to the prediction of the stability range of the monolayer growth regime. Reflected high energy electron diffraction intensity measurements allowed a more detailed understanding of the growth process. We also report a Monte-Carlo-based method for the simulation of epitaxial crystal growth in the layer-by-layer-regime.

## 1. Introduction

Atomic layer epitaxy can be realized in chemical vapor deposition or by an ultrahigh vacuum evaporation process [1]. The latter case, which we call ultrahigh vacuum atomic layer epitaxy (UHV-ALE) may be most successfully applied to wide gap II–VI compounds, such as CdTe, ZnTe, ZnSe and ZnS. This is due to the rather high vapor pressures of the elemental species whereas the dissociative evaporation of the compounds is negligibly small. In contrast to other growth methods in ALE there exists a set of growth parameters, the so-called self-regulatory regime, where layer-by-layer growth occurs.

In this paper, we will concentrate on the CdTe system in reporting on the investigations of the growth mechanisms in UHV-ALE. After a short description of the necessary experimental equipment, we present our results on growth rates, which can be described by a model based on thermodynamic calculations.

To support our microscopic picture of the growth process we performed reflected high energy electron diffraction (RHEED) intensity measurements in surface resonance conditions, which make the spots sensitive to either Cd or Te deposition. We show that this new approach is superior to the observation of the specular spot for the measurement of surface coverages and adsorption kinetics.

Finally, we describe our *ab initio* calculation by Monte Carlo simulation of epitaxial growth in the ALE regime.

## 2. Growth rates of CdTe

The experiments were carried out in two molecular beam epitaxy (MBE) machines, one containing only a Cd and a Te source, the other equipped with seven Knudsen cells and an RHEED system. As substrates we used (100)-oriented GaAs or (111)-oriented BaF<sub>2</sub> to investigate growth in the (100), the (111)A and the (111)B directions. The GaAs was chemically etched and preheated to 580 °C (for the growth of (100) CdTe) or 620 °C (for the growth of (111) CdTe). The BaF<sub>2</sub> was cleaved in air before the growth of (111)A CdTe.

Typical standard parameters for the ALE growth of CdTe were a sequence of 2300 alternating Te and Cd pulses of 0.8 s duration with an intermission of 0.2 s, the so-called dead time, between them. The effusion rate of the sources was 1.3 to 1.5 monolayers (ML) of Te and Cd within an evaporation pulse. A substrate temperature of 275 °C was used as a standard value. Experimental details can be found in refs. 2–6.

To investigate the stability range of the ALE process, three of these standard parameters were varied step by step keeping all the other parameters constant. The substrate temperature was varied between 200 and 400 °C, the number of growth cycles between 500 and 4000, and the Te effusion rate between 1.3 and 3 ML per evaporation pulse. In the case of (111) CdTe on GaAs the beam flux intensity ratio between Cd and Te was varied also.

Growth was monitored *in situ* using a 30 kV RHEED system. After growth the thickness was determined



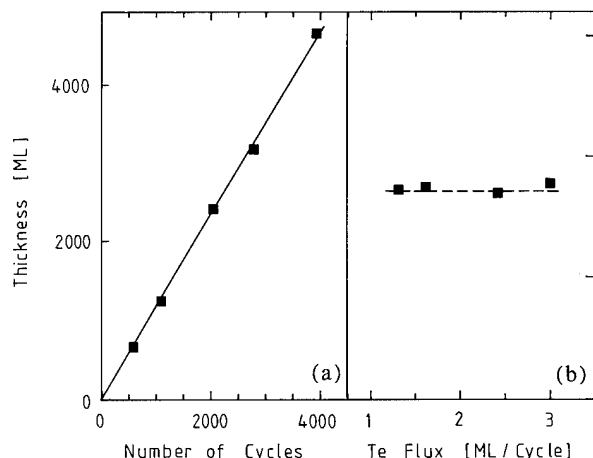


Fig. 1. (a) Film thickness *vs.* the number of completed growth cycles for (111)-oriented CdTe on BaF<sub>2</sub> at a substrate temperature of 275 °C. (b) Film thickness as a function of the Te effusion rate at a substrate temperature of 275 °C. The number of growth cycles was 2300.

from surface profiling scans over a sample edge and Fourier transform IR spectra.

In Fig. 1(a) the thickness of the (111)A CdTe layers grown on BaF<sub>2</sub> using the standard growth parameters is plotted as a function of the number of growth cycles. The one-to-one agreement between the grown monolayers and the number of reaction cycles shows that monolayer-by-monolayer growth is achieved. Moreover, the resulting thickness is independent of the Te flux, as can be seen from Fig. 1(b). This fact proves that the growth process is really self-regulating.

Analogous results are obtained for (100) CdTe on GaAs, whereas for (111)B CdTe on GaAs monolayer growth is only obtained under a high Cd excess. We attribute this to the fact that, in the (111)B direction, Cd on the surface is only loosely bound by one bond, whereas it is triply bound in the (111)A direction.

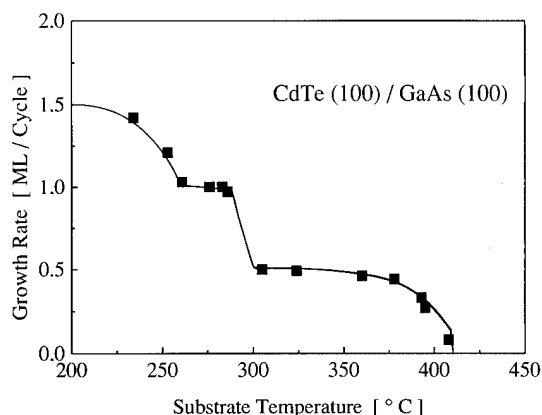


Fig. 2. Growth rate per reaction cycle *vs.* substrate temperature for (100)-oriented CdTe on (100) GaAs. The solid line is the result of our model calculation.

Figure 2 shows the average growth rate per reaction cycle as a function of the substrate temperature for (100) CdTe on GaAs. The occurrence of monolayer growth is limited to a relatively narrow substrate temperature range between 255 and 285 °C. Then an abrupt drop in the growth rate to 0.5 ML per growth cycle takes place. Similar results are obtained for (111)A CdTe on BaF<sub>2</sub>, but in this case two additional plateaux for submonolayer growth with average growth rates of 0.85 and 0.65 ML per growth cycle occur.

### 3. Thermodynamical model of the growth rates

We fitted the experimentally obtained growth rates within the framework of a thermodynamic model, assuming different bound states for surface atoms which correspond to different re-evaporation rates for surface atoms [4]. On raising the substrate temperature, one component becomes unstable and no longer can form a full monolayer coverage. This depends on the growth direction if Cd or Te is the unstable component; in the (111)A direction it is Te, while in the (111)B direction and (100) direction it is Cd.

The results of the fit are shown as solid lines in Fig. 2. With the parameters used for this fit, the growth rate under different growth conditions can be calculated. The model leads essentially to the following conclusions.

(i) The growth rate at low substrate temperatures is exclusively determined by the parameters of the component with the lower vapor pressure—for CdTe this is Te. A low Te deposition rate and a long Te dead time shift the low temperature onset of the monolayer growth plateau towards lower temperatures. This also could be confirmed for ZnSe. Here the material with the lower vapor pressure is Zn. Our calculations, based exclusively on the parameters for the Zn evaporation pulse, predict a low temperature onset for monolayer growth which coincides exactly with the value given by Dosho *et al.* [7].

(ii) The behavior at the high substrate temperature end of a plateau is determined by the parameters for the component which becomes unstable. A long dead time of this material leads to a bending of the plateau, leaving only a very narrow range with full monolayer coverage. It is of essential importance to keep the dead time for the unstable component as short as possible.

In the case of (111)B growth on GaAs the unstable material is Cd, and the low temperature and high temperature sides of the plateau can be affected independently. This has been confirmed experimentally. At a standard Cd deposition rate, monolayer growth is not observed in this growth direction but, for a high Cd deposition rate, a well-developed plateau is observed [5].

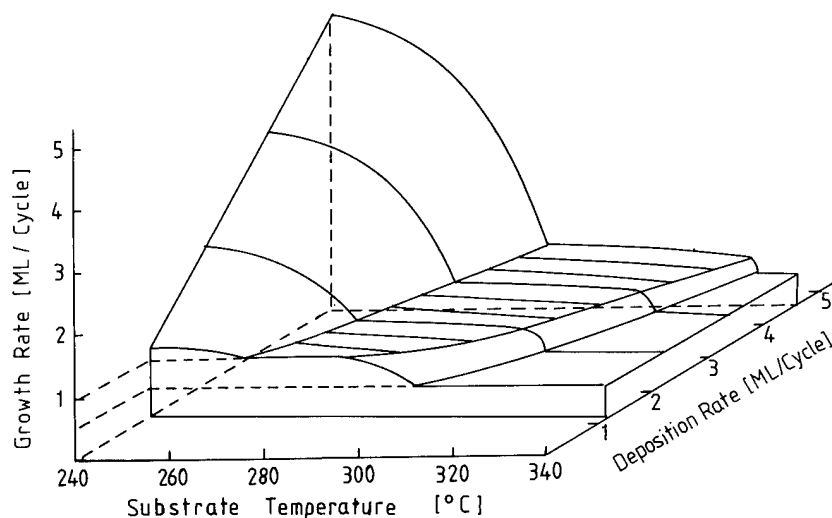


Fig. 3. Results of the model calculation for growth rates as a function of substrate temperature and deposition rate.

For the (100) growth direction, the effect of the deposition rate is demonstrated in Fig. 3 for equal Cd and Te beam intensities. Since in this case the unstable component is assumed to be Cd, a high Cd deposition rate broadens the plateau but simultaneously a high Te rate shifts it to higher substrate temperatures.

#### 4. Observation of RHEED intensity variations

The nucleation stage of CdTe on GaAs was investigated by recording the RHEED streak separation in the (110) azimuth when growth was started in the ALE mode at a substrate temperature of 290 °C. The details concerning the experimental procedure are described elsewhere [8].

Figure 4 shows the surface lattice constant, calculated from the RHEED streak separation, as a function of

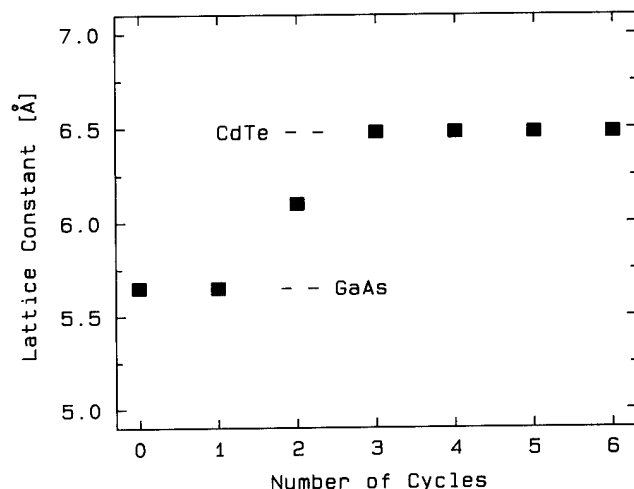


Fig. 4. Surface lattice constant of ALE-grown CdTe on GaAs as a function of growth cycle number.

the growth cycle number. It is clearly visible that after four growth cycles the lattice constant of bulk CdTe is reached.

To investigate the effect of the substrate temperature on the growth rate, RHEED patterns in the (100), (110) and  $(1\bar{1}0)$  azimuth were qualitatively observed. In the temperature range between 260 and 340 °C, the Te-stabilized surface shows a  $(2 \times 1)$  reconstruction, whereas the Cd-stabilized surface reveals a mixture of a  $(2 \times 1)$  and a centered  $(2 \times 2)$  reconstruction. Although the ALE growth rate decreases in that substrate temperature range from 1 to 0.5 ML per reaction cycle, the surface periodicity of both the Cd- and Te-stabilized surface does not change. However, the observed surface periodicity reflects mainly the dimerization of surface atoms, which also occurs at submonolayer coverages.

As a consequence, it was necessary to study not only the periodicity of the RHEED patterns but also the intensity changes. We monitored the intensity of the integral- and half-order streaks in the (110) azimuth under surface resonance conditions. Surface resonance is a secondary scattering event where the primary electrons are scattered into the surface plane and act there as a source beam for the finally observed diffraction.

Since a surface resonance wave propagates directly in the uppermost surface layer, it should be extremely sensitive to coverage changes in this layer. In our case, it was possible to reach simultaneously approximate surface resonance for one integral-order and one half-order streak. In this way, we could adjust conditions where a bright surface resonance spot (spot 1) appeared on the integral-order streak for the Cd-stabilized surface, and another bright spot (spot 2) on the adjacent half-order streak for the Te-stabilized surface.

Figure 5 shows the intensity variation of both spots during a very slow ALE process (pulse time 14.8 s, dead

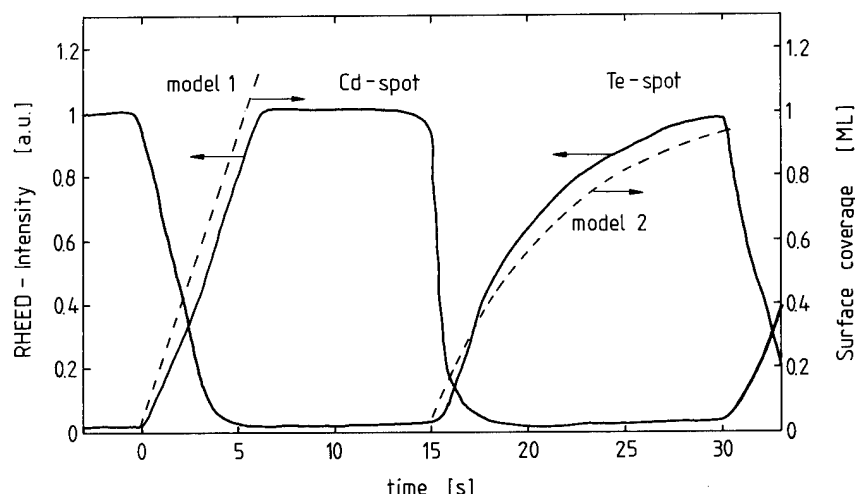


Fig. 5. Intensity of two RHEED spots under surface resonance conditions as a function of time during a slow ALE cycle. The Cd pulse starts at  $t = 0$  and the Te pulse at  $T = 15$  s. The dotted lines represent model calculations described in the text.

time 0.2 s) with a Cd beam intensity of  $9 \times 10^{13}$  atom  $\text{cm}^{-2} \text{s}^{-1}$  and a Te beam intensity of  $8 \times 10^{13}$  atom  $\text{cm}^{-2} \text{s}^{-1}$ . During Cd deposition, the intensity of spot 1 increases linearly with time up to a saturation value. The dotted line marked 'model 1' is the surface coverage calculated from the known Cd beam intensity under the simple assumption that every Cd atom offered sticks. This assumption seems reasonable if one considers that the Cd atoms are relatively small and as single atoms quite mobile at the surface, so that an adsorbed Cd atom can change its site if it is hit by a following Cd atom. Thus we conclude that the increasing intensity of spot 1 is a direct measure of the Cd surface coverage. As soon as a surface coverage of 1 ML is reached, the intensity saturates.

During Te deposition, spot 2 increases in intensity but not proportionally to the Te flux offered. The time until the saturation value of spot 2 is reached is much longer than for spot 1, although the Cd and Te fluxes are approximately equal. We assume that the different behavior reflects a different adsorption behavior of Te compared with that of Cd. This seems reasonable if one considers that Te adsorbs as a large and comparably immobile  $\text{Te}_2$  molecule that cannot easily change its site if it is hit by a second  $\text{Te}_2$  particle. Under the simple assumption that a  $\text{Te}_2$  molecule sticks only if it hits an empty surface site and re-evaporates if it hits an occupied site, one would expect a surface coverage  $C$  as a function of time to be given by

$$C = 1 - \exp(-jt)$$

where  $j$  is the Te beam flux in monolayers per second. With the actual value being  $0.16 \text{ ML s}^{-1}$  for the Te flux, the result of such a calculation is shown as the dotted line marked 'model 2'. Again the correspondence between the intensity of the spot and the simple model is

very good. This confirms that, in analogy to spot 1, the increasing intensity of spot 2 is a direct measure of the Te coverage.

We also measured the intensity of spot 1 under Cd-stabilized and spot 2 under Te-stabilized conditions as a function of the substrate temperature. We observed that the intensity of spot 1 drops to approximately 50% at substrate temperatures higher than  $315^\circ\text{C}$ . The behavior of spot 2 is similar. This result shows that the surface accepts only 0.5 ML of Cd and Te at higher substrate temperatures, with the consequence that the average growth rate drops to 0.5 ML per cycle, as shown by our previous results.

## 5. Monte Carlo simulation of ALE growth

One of the possible methods to simulate crystal growth is to calculate the properties of a system at equilibrium from its distribution function in the phase space. Because this is done by use of random sampling, it is called the 'Monte Carlo method' (MC). In our work, we restricted ourselves to algorithms similar to the so-called 'important sampling method' as described by Metropolis *et al.* [9].

Our simulations were done to study the growth in a two-dimensional cross-section through the substrate and the epilayer. Therefore, we projected the three-dimensional lattice into the (001) surface of a zinc blende structure which is determined by a fourfold symmetry. To describe this situation, we used a directional Lennard-Jones potential, reflecting the fourfold symmetry [10]. The pairwise interaction potential is characterized by the binding energy  $E_0$ , the binding length  $r_{\text{equ}}$  and the parameter  $\beta$  which describes the covalent character of the binding. To simulate the growth of compound

epilayers on compound substrates our model allows us to select  $E_{o,ij}$ ,  $r_{equ,ij}$  and  $\beta_{ij}$  for  $n$  different kinds of atoms. To avoid confusion, we use instead of the indexes  $i$  and  $j$  the symbols  $\circ$ ,  $\times$  and  $*$ . According to the representation in the figures,  $\circ$  indicates a substrate atom, while  $\times$  and  $*$  indicate atoms of the epilayer.

The concept of ALE is based on the fact that in a compound material the bonds between similar kinds of atom are much weaker than the bonds between dissimilar species. Therefore, only 1 ML of a single kind of atom should be found on the surface after each kind of evaporation pulse. To simulate this process, we had to select the growth direction in the (111) orientation, where either two strong or two weak bonds are formed to the next nearest layer. If atoms of a different kind are deposited, then two strong bonds to the underlying monolayer will give a new stable surface. If a monolayer is not complete and an atom of the wrong species is deposited in this monolayer, only two weak bonds would be available for this atom, so that it cannot be incorporated into the wrong layer.

To investigate the effect of the substrate temperature on the ALE growth mode, we simulated a system with a width of 80 atoms, consisting of an elemental substrate and a binary epilayer. The strong bonds between unlike epilayer atoms and the strong bond to the substrate were obtained by setting  $E_{o,\times\times} = 0.2E_{o,\times*}$ ,  $E_{o,**} = 0.2E_{o,\times*}$ ,  $E_{o,\times\circ} = 0.2E_{o,\circ\circ}$  and  $E_{o,*\circ} = E_{o,\circ\circ}$ ,  $E_{o,\times*} = E_{o,\circ\circ}$ . At first, we deposited a number of atoms of one kind, which corresponds to 4 ML. After equilibration of the system, we changed the atom species and repeated the same procedure to finish one digital cycle (1 ALE growth cycle). For each simulation we performed 2 ALE growth cycles. The temperature was chosen in the range from  $T = 0.01$  to  $0.035E_{o,\circ\circ}k_B^{-1}$ .

The lattice pictures of the ALE simulation for different substrate temperatures are shown in Figs. 6(a)–6(f). At the lowest temperature, no layer growth was obtained (see Fig. 6(a)). With increasing temperature, the self-regulatory process became increasingly pronounced (see Figs. 6(b)–6(d)). If the temperature was chosen too high, some parts of the completed monolayers began to evaporate (see Figs. 6(e) and 6(f)).

The macroscopic parameter which can be compared with the experiment is the growth rate given in monolayers per growth cycle. For all the simulations, we calculated this parameter by dividing the number of deposited particles, given in monolayers, by the number of growth cycles. The calculated growth rate as a function of temperature is shown in Fig. 7. It is clear that there exists a temperature range from 0.02 to  $0.03E_{o,\circ\circ}k_B^{-1}$  where a constant growth rate of 1 ML cycle $^{-1}$  can be obtained, reflecting the self-regulatory regime of ALE growth. The lower limit of the plateau is given by the incomplete re-evaporation of weakly

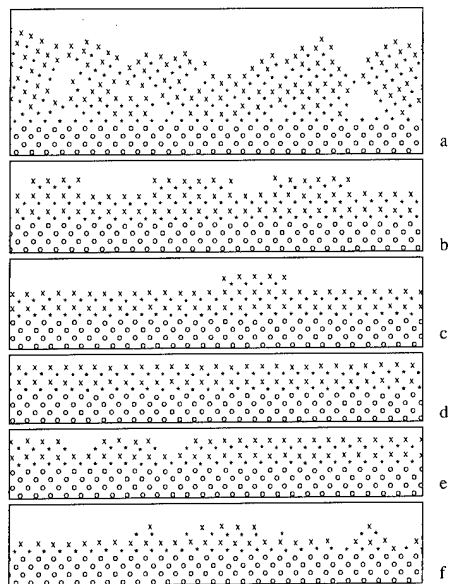


Fig. 6. Typical parts of the resulting lattice from ALE growth simulation for different substrate temperatures given in units of  $E_{o,\times\times}k_B^{-1}$ : (a)  $T = 0.01$ , (b)  $T = 0.017$ , (c)  $T = 0.020$ , (d)  $T = 0.022$ , (e)  $T = 0.027$  and (f)  $T = 0.035$ .

bound atoms. The high temperature limit of the plateau is determined by the evaporation of the compound. The temperature dependence of the growth rate obtained by the MC simulation is in excellent agreement with the experimental results shown in Fig. 2.

## 6. Conclusions

We have shown that monocrystalline (100)-oriented and (111)-oriented CdTe can be grown on (100) GaAs and (111) BaF<sub>2</sub>. In all the investigated cases, we found a temperature range where the growth regulates itself to the rate of 1 ML per reaction cycle. At higher substrate temperatures the growth rate decreases rapidly to sub-monolayer coverages per reaction cycle.

We presented a thermodynamic model to describe these features based on the idea of surface reordering at high substrate temperatures. The model allows the predictions of the effects of changes in several growth parameters and leads to the result that the stability range of the 1 ML growth can be affected mainly by the molecular beam fluxes.

We showed by RHEED experiments that the start of ALE growth on GaAs is not hindered by the formation of misfit dislocations. The surface lattice constant changes swiftly from GaAs to CdTe, and after four reaction cycles the bulk lattice constant of CdTe can be observed. For the observation of the adsorption of the components during growth, it proved to be very useful to observe the intensity variations of different RHEED

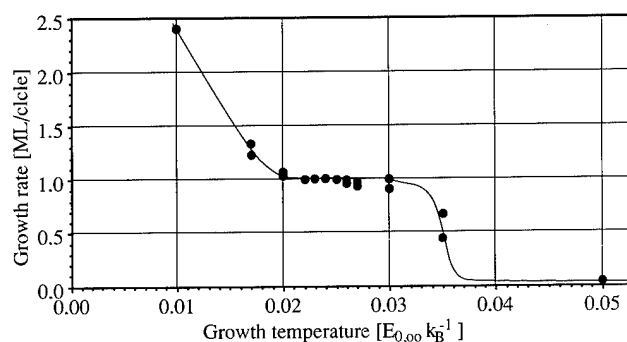


Fig. 7. Calculated growth rate in monolayers per growth cycle in the ALE simulation as a function of temperature.

spots under surface resonance conditions. The intensity of these spots is extremely sensitive and, under proper conditions, proportional to the coverage of the topmost layer, and can be used to study the dynamics of adsorption. This means that the observation of these spots is a simple and fast method to find and control proper growth conditions for the self-regulatory region in ALE.

We have demonstrated the use of a continuous space Monte Carlo method for studies of the epitaxial growth in the self-regulatory regime.

In conclusion, one may consider that UHV-ALE is not automatically a self-regulatory process. This means that timing and dosing in the deposition cycle play crucial roles in this process. Thus, UHV-ALE has to be precisely designed when smooth and flat layers on an atomic scale have to be grown.

## Acknowledgments

The authors would like to thank P. Juza who determined the RHEED intensity data and W. Plotz who did the Monte Carlo simulations. Our sincere appreciation is extended to O. Fuchs for this technical assistance and to E. Hanz for typing the manuscript. This work was partly supported by the 'Fonds zur Förderung der wissenschaftlichen Forschung in Österreich'.

## References

- 1 M. A. Herman and H. Sitter, Molecular Beam Epitaxy, in A. Mooradian and M. B. Panish (eds.), *Springer Ser. Mater. Sci.*, Vol 7, Springer, Berlin, Chaps. 1-3, pp. 1-113.
- 2 W. Faschinger, H. Sitter and P. Juza, *Appl. Phys. Lett.*, 53 (1988) 2519.
- 3 P. Juza, H. Sitter and M. A. Herman, *Appl. Phys. Lett.*, 53 (1988) 1396.
- 4 W. Faschinger and H. Sitter, *J. Cryst. Growth*, 99 (1990) 566.
- 5 H. Sitter and W. Faschinger, *Adv. Solid State Phys.*, 30 (1990) 219.
- 6 M. A. Herman, P. Juza, W. Faschinger and H. Sitter, *Cryst. Res. Technol.*, 23 (1988) 307.
- 7 S. Dosho, Y. Takemura, M. Konagai and K. Takahashi, *J. Appl. Phys.*, 66 (1989) 2597.
- 8 W. Faschinger, P. Juza and H. Sitter, *J. Cryst. Growth*, 115 (1991) 692.
- 9 N. Metropolis, A. W. Rosenblut, N. M. R. Rosenblut, A. H. Teller and E. Teller, *J. Chem. Phys.*, 21 (1953) 1087.
- 10 W. M. Plotz, K. Hingerl and H. Sitter, *J. Cryst. Growth*, 115 (1991) 186.

# Self-limiting growth of zinc chalcogenides and their superlattices

M. Konagai, Y. Takemura, K. Yamasaki and K. Takahashi

Department of Electrical and Electronic Engineering, Tokyo Institute of Technology 2-12-1 Ohokayama, Meguro-ku, Tokyo 152 (Japan)

## Abstract

ZnSe, ZnTe and ZnSe–ZnTe strained-layer superlattices (SLSs) were grown by atomic layer epitaxy (ALE) using molecular beam epitaxy (MBE-ALE). In the ALE growth of ZnTe, a self-limiting mechanism was observed, in which the deposition rate saturated at 0.5 monolayers per cycle. ZnSe films were grown by MBE-ALE with  $N_2$  gas as dopant, and remarkable effects of ALE on the doping efficiency of nitrogen were observed. Furthermore, a new type of short-period SLS which consists of  $(ZnSe)_m-[(ZnTe)_p-(ZnSe)_q]_n$  was grown by MBE-ALE. The  $(ZnSe)_6-[(ZnTe)_1-(ZnSe)_2]_2$  SLS showed very strong photoluminescence at an emission energy of 2.39 eV at 4.2 K.

## 1. Introduction

In a II–VI compound, both the Group II and Group VI elements have extremely high vapor pressures compared with that of the compound, as shown in Fig. 1. Thus, II–VI compounds are potentially more suitable for growth by atomic layer epitaxy (ALE) than III–V compounds. The first report of the ALE of a single-crystal II–VI compound was given by Pessa *et al.* [1]. Our current approach is to use molecular beam epitaxy (MBE) for the ALE growth of wide band gap II–VI compounds. In this paper, the detailed ALE growth conditions for ZnSe and ZnTe are reviewed.

ZnSe is a possible candidate for visible LEDs but is known for its p-type doping problems. Among the

Group V elements, nitrogen is expected to behave as a stable shallow acceptor in ZnSe. However, in general, doping with nitrogen in the MBE process is very difficult, because of the low sticking coefficients of  $N_2$  and  $NH_3$  neutral molecules. Recently, new methods of doping ZnSe with nitrogen were attempted using a radical beam to enhance the sticking coefficient of nitrogen during MBE growth of ZnSe [2–4]. In this paper, ZnSe films were grown by MBE-ALE with  $N_2$  gas as dopant, and remarkable results of using ALE on the doping efficiency of nitrogen were obtained.

The present interest in ALE of II–VI compounds is primarily for epitaxial growth of layered structures such as superlattices. In particular, strained-layer superlattices (SLSs) consisting of ZnS, ZnSe and ZnTe are promising for light-emitting devices with visible wavelengths. The use of ALE for preparing II–VI compound SLSs consisting of very thin layers with large strain is motivated by several benefits, which include a growth temperature lower than those used for conventional MBE, and precise control of the thickness with monolayer accuracy. We have previously reported optical and structural properties of  $(ZnSe)_m-(ZnTe)_n$  SLSs prepared by MBE-ALE [5, 6]. In this paper, the optical properties of more sophisticated SLS structures, which consist of  $(ZnSe)_m-[(ZnTe)_p-(ZnSe)_q]_n$ , are reported.

## 2. ALE of ZnSe and ZnTe by MBE

The conventional MBE system with solid sources of zinc, selenium and tellurium was used for the ALE growth of ZnSe, ZnTe, and ZnSe–ZnTe SLSs. ZnSe and ZnTe layers were grown on (100) GaAs substrates.

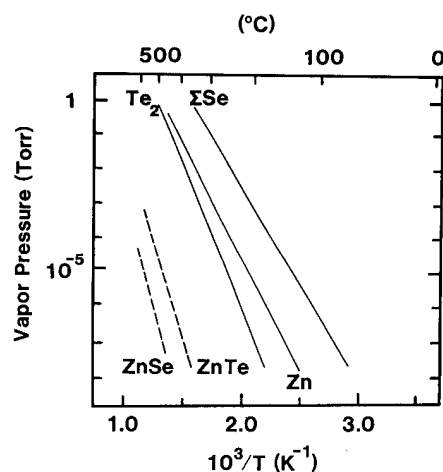


Fig. 1. Vapor pressures of zinc, selenium, tellurium and their compounds.

Nitrogen gas was introduced into the chamber without any plasma (cracking) processes. The shutters of zinc and chalcogens were alternately opened and closed for 7 s with an interval of 1 s. 1000 cycles were used in the entire experiment for ALE of ZnSe and ZnTe.

Figure 2 shows the variation of ZnSe and ZnTe film thicknesses with the growth temperature. It clearly shows that ideal ALE growth was achieved over a range of substrate temperatures between 250 and 350 °C for ZnSe. We also investigated detailed processing windows for ALE of ZnSe. We found that deposition of the ideal number of monolayers per cycle was obtained for the duration of the zinc supply of 4–7 s. It is interesting to note that the growth rate was independent of selenium supply in the range  $83N_s$ – $1380N_s$ , where  $N_s$  is the surface density of zinc or selenium sites, i.e. the processing window for the number of supplied selenium atoms is very wide. We achieved drastic improvements in surface flatness and the optical properties of the ZnSe films, in comparison with ZnSe films prepared by conventional MBE.

Ideal ALE growth of ZnTe was obtained in the range of substrate temperature 240–280 °C with a zinc supply of  $54N_s$  and a tellurium supply of  $8.7N_s$ . The processing window for ALE growth of ZnTe is narrower than that of ZnSe, because the vapor pressure of ZnTe is about two orders of magnitude higher than that of ZnSe, as shown in Fig. 1. Strictly speaking, although ideal ALE growth was achieved for ZnTe, the conditions for obtaining good crystallinity are not the same as the ideal ALE growth conditions. If we adjust the tellurium beam intensity to achieve ALE growth, the surface morphology and crystallinity are degraded by hillocks. The number of hillocks varies with the tellurium beam intensity. The hillocks may be caused by tellurium precipitates.

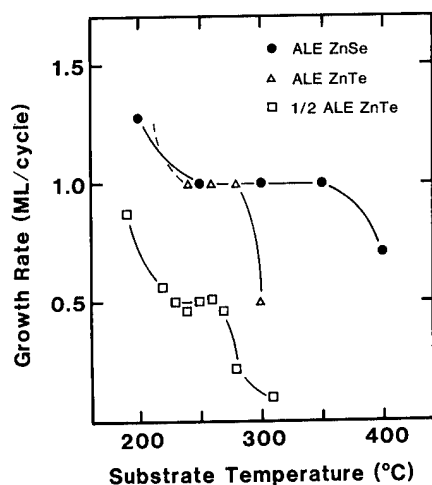


Fig. 2. Growth rates of ZnSe and ZnTe grown at various substrate temperatures by ALE.

In order to remove hillocks, deposition with a low tellurium beam intensity is required. In Fig. 2, the growth rate of ZnTe with a zinc supply of  $6.6N_s$  and a tellurium supply of  $2.0N_s$  is also shown. Under these low-intensity conditions, the growth rate is constant at 0.5 monolayers per cycle in the range of substrate temperature 230–270 °C. We call this type of hot-wall epitaxy “fractional ALE”. The first clear observation of fractional ALE was reported by Faschinger and Sitter for CdTe deposited onto (100)GaAs substrates using hot-wall epitaxy [7]. The surface morphology of ZnTe films prepared by fractional ALE was observed under a Nomarski microscope. Smooth surfaces without any hillocks were obtained for all samples.

The processing windows for fractional ALE were also investigated for ZnTe at the substrate temperature of 250 °C. Figure 3 shows the growth rate per cycle as a function of the zinc supply. The growth rate increases with increasing zinc supply and becomes constant at 0.5 monolayers per cycle for zinc supplies ranging from  $6.6N_s$  to  $44N_s$ . In the figure, the growth rate of ALE ZnSe is also shown as a function of zinc supply. It should be noted that the growth rate for ZnSe is 1 monolayer per cycle for zinc supplies of about  $10N_s$ , while it is 0.5 monolayers per cycle for ZnTe. An excess zinc supply results in a growth rate higher than 0.5 monolayers per cycle, and the growth rate strongly depends on the zinc supply.

We also investigated the growth rate as a function of tellurium supply. In Fig. 4, the growth rate is independent of the tellurium supply for zinc supplies ranging from  $2.2N_s$  to  $17N_s$ . For zinc supplies of  $55N_s$  and  $94N_s$ , a constant growth rate cannot be obtained. Self-limiting growth was obtained over a wide range of tellurium supplies for zinc supplies of  $2.2N_s$ – $17N_s$ , and over a small range of tellurium supply for a zinc supply of  $44N_s$ . The constant growth rate of 0.33 monolayers per cycle may be limited by the shortage of zinc atoms. We did not investigate tellurium supplies larger than  $20N_s$ . However, the range of tellurium

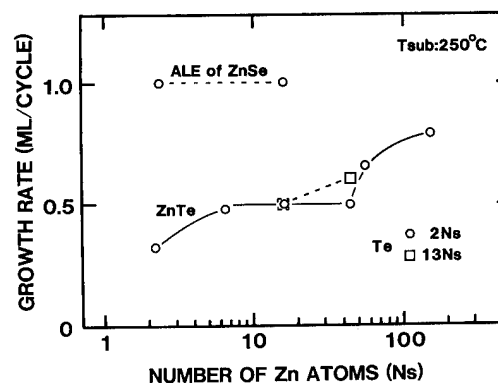


Fig. 3. Growth rate of ZnTe as a function of zinc supply.

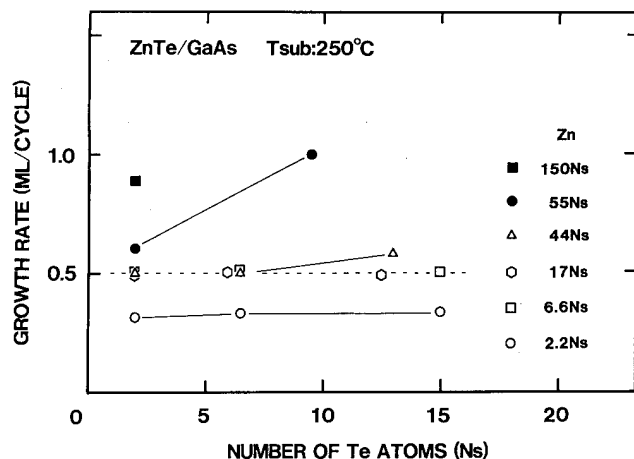


Fig. 4. Growth rate of ZnTe as a function of tellurium supply.

supply for fractional ALE of ZnTe is much narrower than that of selenium supply for ALE ZnSe. This is presumably because the vapor pressure of tellurium is three orders of magnitude lower than that of selenium.

In conventional ALE, the growth rate of compounds is limited by supply of the lower pressure element. For example, in ALE growth of ZnSe, the growth rate is strongly affected by the zinc supply and almost independent of the selenium supply. However, in fractional ALE of ZnTe, although the vapor pressure of zinc is about one order of magnitude higher than that of tellurium at the growth temperature, as shown in Fig. 1, the self-limiting growth rate is limited by the zinc supply. This is presumably because of surface reconstruction and the surface coverage of zinc atoms on the growing surfaces of II–VI compounds.

In ALE of ZnSe and ZnTe,  $c(2 \times 2)$  reflection high-energy electron diffraction patterns were observed after zinc supply [8]. Kobayashi and Horikoshi proposed a missing zinc array structure of the  $c(2 \times 2)$  reconstructed surface [9], which indicates half-coverage of zinc surface sites. The half-coverage of the zinc surface sites explains well the self-limiting growth at 0.5 monolayers per cycle.

### 3. ALE of doped ZnSe

We have previously attempted to grow ALE ZnSe with low resistivity using  $\text{ZnCl}_2$  as an n-type dopant [10]. The shutter of the  $\text{ZnCl}_2$  cell was kept open during the growth. A carrier concentration of  $1.5 \times 10^{18} \text{ cm}^{-3}$  could be obtained with an electron mobility of  $480 \text{ cm}^2 \text{ V}^{-1} \text{ s}^{-1}$  at a  $\text{ZnCl}_2$  cell temperature of  $115^\circ \text{C}$ . Thus, control of n-type conductivity of ZnSe has been successfully achieved by doping with Group VII impurities. However, ZnSe cannot be efficiently doped p-

type. In this work, ZnSe layers doped with nitrogen were grown by ALE, and the optical properties were evaluated.

Nitrogen-doped ZnSe films were grown by ALE with a continuous flow of  $\text{N}_2$  and alternate supplies of zinc and selenium. Figures 5(a) and 5(b) show the photoluminescence (PL) spectra, at 4.2 K, of nitrogen-doped ZnSe grown by ALE. The spectra show neutral acceptor-bound exciton emission ( $I_1$ , 2.792 eV) and donor-acceptor pair emission (DAP, 2.691–2.694 eV for zero-phonon), while the spectrum of undoped layers shows free and donor-bound exciton emission. Although  $\text{N}_2$  gas was introduced into the chamber without any plasma (cracking) processes, the PL spectra suggest incorporation of nitrogen as a shallow acceptor. With an increasing nitrogen flow rate, the intensity of  $I_1$  decreases, whereas the DAP intensity increases. These observations are similar to reported results [11]. The PL spectrum of nitrogen-doped ZnSe grown by conventional MBE shows only donor-bound exciton emission ( $I_2$ ) as shown in Fig. 5(c). Though the growth rate of MBE ZnSe is 16 times higher than that of ALE ZnSe, incorporation of nitrogen as an acceptor into the MBE-grown films was much less than into the ALE-grown films. These results indicate that the ALE processes enhance the sticking coefficient of nitrogen. In ALE growth of ZnSe, zinc and selenium atoms are alternately deposited onto the surface. We speculate that the sticking coefficient of nitrogen on zinc surfaces during the interval might be enhanced.

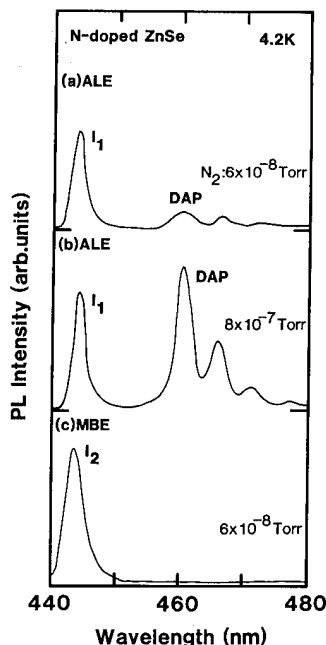


Fig. 5. PL spectra for nitrogen-doped ZnSe: (a) ALE with  $\text{N}_2$ ,  $6 \times 10^{-8}$  Torr; (b) ALE with  $\text{N}_2$ ,  $8 \times 10^{-7}$  Torr; (c) MBE with  $\text{N}_2$ ,  $6 \times 10^{-8}$  Torr.



#### 4. Optical properties of $(\text{ZnSe})_m-[(\text{ZnTe})_p-(\text{ZnSe})_q]_n$ SLSs grown by MBE-ALE

We have previously reported optical and structural properties of  $(\text{ZnSe})_m-(\text{ZnTe})_n$  ( $m, n = 2, 3, 4$ ) SLSs grown on InP substrates, in which the ZnSe layers were prepared by ALE and the ZnTe layers by fractional ALE. Thus, one monolayer of ZnTe is prepared by two cycles of opening and closing the shutters. The substrate temperature was 250 °C, which is 70 °C lower than that used for conventional MBE. Transmission electron microscopy (TEM) was used to investigate the grown SLS structures. The SLSs were deposited directly onto the substrate without a buffer layer. Figure 6 shows a dark-field image of a  $(\text{ZnSe})_3-(\text{ZnTe})_3$  SLS for the 200 diffraction beam. High-contrast stripes, which consist of a dark stripe of ZnSe and a bright stripe for ZnTe, are clearly observed. These stripes are observed from a few periods on the substrate through the whole film. The abruptness and flatness of the interfaces are not as good as those reported for GaAs–AlAs superlattices [12, 13]. In addition to the facts that the  $(\text{ZnSe})_3-(\text{ZnTe})_3$  SLS involves a 7% lattice mismatch and was heteroepitaxially grown on an InP substrate, the TEM image shows a fine short-period superlattice structure which has an abrupt interface with at most one-monolayer steps. The X-ray diffraction satellites also confirm that the actual numbers of ZnSe and ZnTe monolayers are equal to the intended numbers. Raman scattering measurements showed that each layer is strained in free standing with the substrate.

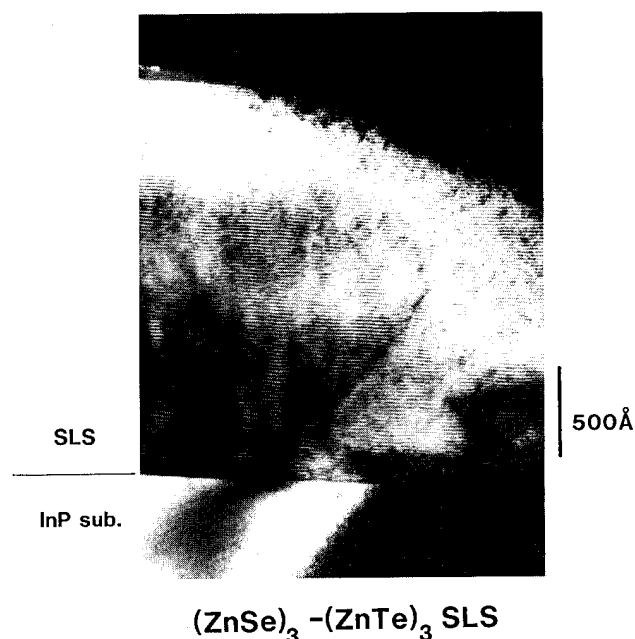


Fig. 6. Dark-field image of  $(\text{ZnSe})_3-(\text{ZnTe})_3$  SLS for the 200 diffraction beam.

We also prepared  $(\text{ZnSe})_1-(\text{ZnTe})_1$  monolayer superlattices. We could not observe X-ray diffraction satellites from this structure, and Raman scattering measurements only showed the shifted LO phonon of ZnSe. These results indicate poor abruptness and flatness of the ZnTe layer, as previously reported [5, 6]. However,  $(\text{ZnSe})_1-(\text{ZnTe})_1$  monolayer superlattices showed very strong green–yellow PL, even at room temperature. Figure 7 shows the 4.2 K PL spectrum of a 750 period  $(\text{ZnSe})_1-(\text{ZnTe})_1$  monolayer superlattice. In order to examine the emission mechanism in this semiconductor system, the temperature dependence of the PL spectrum was studied. We found that the spectrum consists of two peaks. By curve fitting, using the sum of two Gaussians, these peaks were determined to be at 510 nm (2.43 eV) and 538 nm (2.30 eV). These two bands are denoted  $S_1$  and  $S_2$  [14], and are interpreted as the recombination of excitons trapped at tellurium atoms and  $\text{Te}_n$  clusters respectively. It is thought that the strong emission is due to the recombination of excitons tightly bound at tellurium clusters.

New SLS structures, which consist of  $(\text{ZnSe})_m-[(\text{ZnTe})_p-(\text{ZnSe})_q]_n$ , are now proposed to enhance the emission intensity and to control emission wavelength. Usually  $(\text{ZnTe})_p-(\text{ZnSe})_q$  SLSs belong to a type-II system, in which electrons and holes are confined in separate positions in real space. Thus, in general, the emission intensity from type-II SLSs becomes weak. However, short-period  $(\text{ZnTe})_p-(\text{ZnSe})_q$  SLSs have superior light-emitting properties owing to tightly bound excitons at tellurium clusters. In the new SLSs, the  $[(\text{ZnTe})_p-(\text{ZnSe})_q]_n$  layer contributes as a light-emitting region and the  $(\text{ZnSe})_m$  layer as a band gap control region. It is reported that capture is dominated by the hole part of the exciton, and before any substantial exciton recombination across the superlattice sub-band-gap takes place, capture of holes at the tellurium clusters takes place with subsequent strong radiative recombination with electrons.

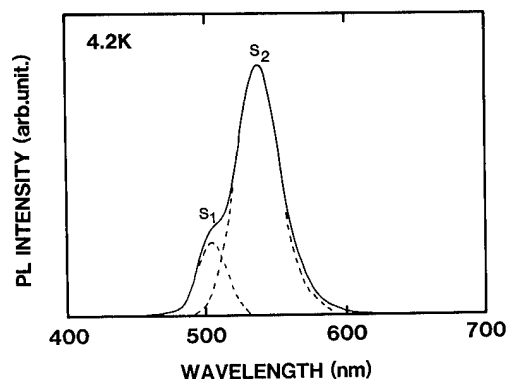


Fig. 7. PL spectrum of  $(\text{ZnSe})_1-(\text{ZnTe})_1$  monolayer superlattice at 4.2 K.

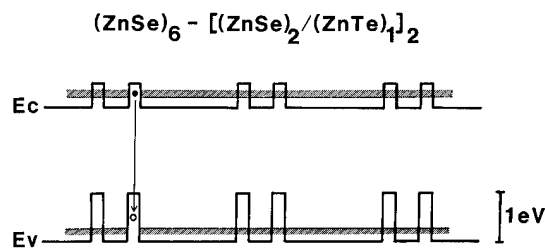


Fig. 8. Energy band structure of  $(\text{ZnSe})_6-[(\text{ZnTe})_1-(\text{ZnSe})_2]_2$  superlattice.

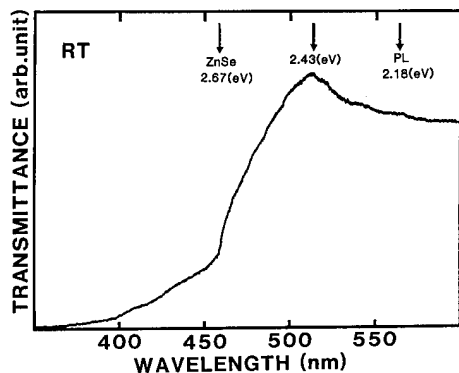


Fig. 9. Transmittance spectrum of  $(\text{ZnSe})_6-[(\text{ZnTe})_1-(\text{ZnSe})_2]_2$  superlattice.

Figure 8 shows the energy band structure of the  $(\text{ZnSe})_6-[(\text{ZnTe})_1-(\text{ZnSe})_2]_2$  SLS. We observed a very strong emission peak at 2.39 eV at 4.2 K and 2.18 eV at room temperature, which corresponds to the  $S_2$  band. The transmittance spectrum of this sample is shown in Fig. 9. The total thickness of the SLS is 515 nm. The GaAs substrate was selectively removed using  $\text{NH}_4\text{OH}-\text{H}_2\text{O}_2$  solution. The PL peak position at room temperature (2.18 eV) is about 0.25 eV smaller than the sub-band-gap energy of the SLS. The difference between the emission peak energy and the sub-band-gap energy corresponds to the binding energy of excitons bound at tellurium isoelectronic traps.

The emission peak energy (2.39 eV) is a little larger than that of the monolayer superlattice (2.30 eV) as shown in Fig. 6. This indicates that the emission peak energy can be controlled by designing the SLS structures.

## 5. Summary

The detailed growth conditions for ALE of ZnSe and ZnTe were discussed. The growth rates of ZnSe and

ZnTe were constant at 1 monolayer per cycle for substrate temperatures of 250–350 and 240–280 °C respectively. A constant growth rate of 0.5 monolayers per cycle was also observed for ALE of ZnTe grown with low beam intensities. We call this type of self-limiting growth “fractional ALE”.

Control of conductivity of ALE-grown ZnSe was investigated. Chlorine-doped films exhibit low resistivity using  $\text{ZnCl}_2$  as an n-type dopant. Nitrogen-doped films were also grown by ALE using  $\text{N}_2$  without any plasma process. The PL spectra of the films showed acceptor-bound excitonic emission and donor–acceptor pair emission, which indicates incorporation of nitrogen as a shallow acceptor in ZnSe. The result indicates that the ALE process enhances the sticking coefficient of nitrogen.

$(\text{ZnSe})_m-(\text{ZnTe})_n$  short-period SLSs grown by ALE exhibit excellent abruptness and flatness at the interfaces with at most one-monolayer steps. Optical properties of more sophisticated superlattice structures, which consist of  $(\text{ZnSe})_m-[(\text{ZnTe})_p-(\text{ZnSe})_q]_n$  were investigated. It was found that the ZnSe–ZnTe SLS is a superior light-emitter in the visible region.

## References

- 1 M. Pessa, P. Huttunen and M. A. Herman, *J. Appl. Phys.*, **54** (1983) 6047.
- 2 K. Ohkawa, T. Karasawa and T. Mitsuyu, *Jpn. J. Appl. Phys.*, **30** (1991) L152.
- 3 R. M. Park, M. B. Troffer, C. M. Rouleau, J. M. DePuydt and M. A. Haase, *Appl. Phys. Lett.*, **57** (1990) 2127.
- 4 H. Jeon, J. Ding, W. Patterson, A. V. Nurmikko, W. Xie, D. C. Grillo, M. Kobayashi and R. L. Gunshor, *Appl. Phys. Lett.*, **59** (1991) 3619.
- 5 Y. Takemura, S. Dosho, M. Konagai and K. Takahashi, *J. Cryst. Growth*, **101** (1990) 81.
- 6 Y. Takemura, H. Nakanishi, M. Konagai and K. Takahashi, *J. Cryst. Growth*, **111** (1991) 802.
- 7 W. Faschinger and H. Sitter, *J. Cryst. Growth*, **99** (1990) 566.
- 8 T. Yao and T. Takeda, *Appl. Phys. Lett.*, **48** (1986) 160.
- 9 N. Kobayashi and Y. Horikoshi, *Jpn. J. Appl. Phys.*, **29** (1990) L236.
- 10 S. Dosho, Y. Takemura, M. Konagai and K. Takahashi, *J. Cryst. Growth*, **95** (1989) 580.
- 11 J. Qiu, J. M. Depuydt, H. Cheng and M. A. Haase, *Appl. Phys. Lett.*, **59** (1991) 2992.
- 12 N. Watanabe and Y. Mori, *Surf. Sci.*, **174** (1986) 10.
- 13 P. M. Petroff, A. C. Gossard, W. Wiegmann and A. Savage, *J. Cryst. Growth*, **44** (1978) 5.
- 14 T. Yao, M. Kato, J. J. Davis and H. Tanino, *J. Cryst. Growth*, **86** (1989) 580.

# Growth and characterization of CdTe, HgTe and HgCdTe by atomic layer epitaxy

N. H. Karam and R. G. Wolfson

*Spire Corporation, One Patriots Park, Bedford, MA 01730 (USA)*

I. B. Bhat, H. Ehsani and S. K. Ghandhi

*Rensselaer Polytechnic Institute, Troy, NY 12180 (USA)*

## Abstract

We present the first demonstration of atomic layer epitaxy (ALE) of HgTe, CdTe and HgCdTe using Hg, Cd and Te alkyl chemistry on GaAs and CdTe substrates. The ALE deposition experiments were done at atmospheric pressure in a horizontal reactor equipped with a fast switching manifold. Methylallyltelluride, dimethylmercury (DMHg) and dimethylcadmium were used for Te, Hg and Cd sources respectively. ALE of HgTe was achieved at 140 °C, and the monolayer per cycle condition extended over a wide range of DMHg flux. ALE growth of CdTe was carried out over a wide temperature range (250–290 °C) and reactant partial pressure. HgCdTe layers were also grown by alternately depositing HgTe and CdTe onto CdTe substrates and then interdiffusing them at higher temperatures.

## 1. Introduction

The deposition of HgTe and its alloy with CdTe onto large-area substrates, with excellent compositional and thickness uniformity, is of great importance to the fabrication of IR focal plane arrays [1]. Atomic layer epitaxy (ALE) is especially suited for the deposition of thin films with monolayer control over film composition and thickness [2–5]. Although ALE of a number of II–VI compounds, including CdTe, ZnTe and ZnSe, has been successfully demonstrated, ALE of Hg-containing compounds (*e.g.* HgTe) has been complicated by the fact that the vapor pressure of Hg over Hg is comparable with that of Hg over HgTe. Moreover, the vapor pressure of Hg over HgTe is very high at typical growth temperatures. Consequently, direct ALE of Hg(Cd)Te using elemental components has not been possible. In this paper we report on the first demonstration of ALE of HgTe, CdTe and HgCdTe using Hg, Cd, and Te alkyl chemistry on GaAs and CdTe substrates.

## 2. Experimental details

The present ALE experiments were conducted in a horizontal metalorganic chemical vapor deposition (MOCVD) reactor operated at atmospheric pressure and equipped with a fast switching manifold. The small-volume quartz reaction chamber (2 inch diameter) was designed to minimize the gas switching time

during the ALE experiments. The samples were mounted on a graphite susceptor r.f. heated to temperatures typically in the range 100–400 °C. Methylallyltelluride (MATE), dimethylmercury (DMHg) and dimethylcadmium (DMCd) were used for Te, Hg and Cd sources respectively. For the case of ALE of HgTe, the walls of the reaction chamber up-stream of the susceptor were heated to 340 °C using a clam shell heater, in order to aid in the partial precracking of DMHg. ALE was achieved by gas switching; a typical ALE cycle was 12 s, consisting of equal periods of exposure of the substrate to the Group II and the Group VI reactants separated by H<sub>2</sub> purging periods of 3 s duration. Films were deposited onto CdTe and GaAs substrates oriented 2° off the (100) towards the  $\langle 110 \rangle$  direction.

The structural, optical and electrical characteristics of the deposited films are reported. Characterization tools include Nomarski optical microscopy, double-crystal X-ray diffraction, cross-sectional transmission electron microscopy (TEM), cross-sectional scanning electron microscopy (SEM), and Fourier transform IR spectroscopy (FTIR).

## 3. Results and discussion

### 3.1. ALE of CdTe

The epitaxial growth of CdTe on CdTe substrates by ALE using elemental Cd and Te sources has been

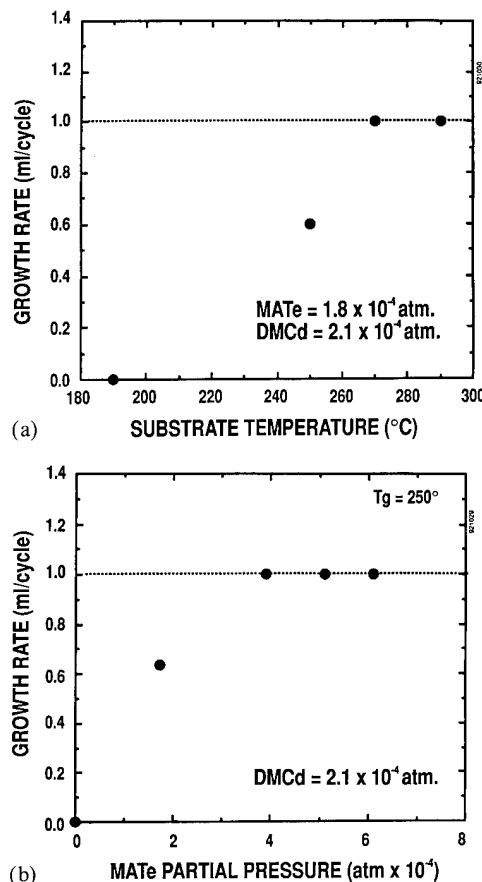


Fig. 1. (a) The change in growth rate as a function of deposition temperature for ALE of CdTe. (b) CdTe growth rate as a function of MATE partial pressure at a constant DMCd pressure of  $2.1 \times 10^{-4}$  atm and temperature ( $T_g = 250^\circ\text{C}$ ).

reported earlier [4, 6], but MOCVD of CdTe by ALE using MATE and DMCd precursors has not been reported. The advantage of MATE is its low decomposition temperature, which has been shown to yield high-quality HgTe and HgCdTe at low deposition temperatures [7]. The initial ALE experiments were devoted to identifying the temperature window for ALE of CdTe using the alkyl precursors. We investigated the temperature range 200–290 °C, using a typical 12 s ALE cycle and keeping the MATE and DMCd partial pressures at  $1 \times 10^{-4}$  and  $2 \times 10^{-4}$  respectively. Figure 1(a) shows the growth rate saturating at the one monolayer per cycle condition in the temperature range 270–290 °C. Increasing the partial pressure of the reactants at a lower temperature (250 °C) resulted in an increase in the growth rate, which saturated at one monolayer per ALE cycle. This condition persisted with increased DMCd and MATE partial pressures. Figure 1(b) shows the self-limiting feature of CdTe ALE at 250 °C with increasing MATE partial pressure. Films deposited onto CdTe and GaAs substrates had excellent surface mor-

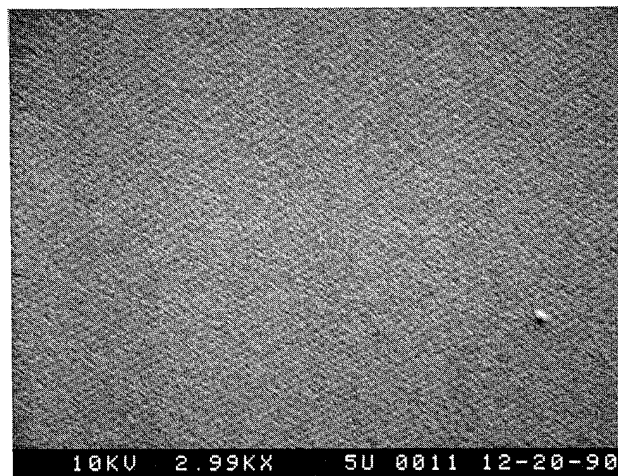


Fig. 2. SEM image of typical surface morphology for ALE CdTe on GaAs.

phologies and thickness uniformities. Figure 2 shows a typical SEM image of the surface morphology of ALE CdTe on GaAs deposited at 250 °C. Previous work on ALE of CdTe by molecular beam epitaxy (MBE) showed monolayer saturation in the temperature range 267–277 °C, which is significantly narrower than that reported in the present experiments (250–290 °C). A lower ALE deposition temperature is desirable to allow isothermal ALE of HgTe and CdTe and to prevent interdiffusion in multilayered structures. This may be possible by using an alternative Cd precursor.

### 3.2. ALE of HgTe

ALE of Hg-containing compounds has eluded researchers in the field owing to the low sticking coefficient of Hg (in the range of  $10^{-4}$ ) at the typical MBE deposition temperatures (180–200 °C), which makes it difficult to saturate a monolayer of Hg during an ALE cycle. In order to address this problem, we decided to lower the ALE deposition temperature to minimize the Hg evaporation rate during the ALE purge cycle; moreover, we believed that an Hg alkyl such as DMHg might be a more stable adsorbent on the HgTe surface. Evaporation experiments were conducted with HgTe films (on CdTe substrates) heated in  $\text{H}_2$  in the absence of Hg over-pressure, simulating the  $\text{H}_2$  purge in an ALE experiment. The weight loss of the wafer was correlated with the evaporation of the film. It was concluded that the substrate temperature must be kept below 200 °C, where the evaporation rate is approximately  $4 \text{ Å s}^{-1}$ ; evaporation at temperatures less than 160 °C is negligible for typical  $\text{H}_2$  purge periods of 4 s. Since precursors decomposing at these low temperatures are not available, partial cracking of the reactants was achieved by holding the front end of the reactor at

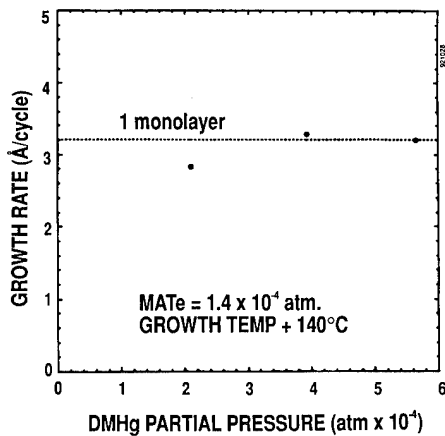


Fig. 3. Deposition rate of ALE HgTe as a function of DMHg partial pressure.

345 °C while the susceptor was maintained at the growth temperature of 120–160 °C.

Using an ALE time sequence of 6/2/4/2 s for DMHg/ $H_2$ /MATE/ $H_2$  respectively, the growth rate was invariant with temperature in the range 120–160 °C. Figure 3 shows the stable one monolayer per cycle condition with increasing DMHg flux at 140 °C and an MATE partial pressure of  $1.4 \times 10^{-4}$  atm. Uniform HgTe films were deposited onto CdTe and GaAs with very smooth morphologies if the growth rate was less than or equal to one monolayer per cycle. However, the growth rate of HgTe does not seem to saturate with increasing MATE partial pressure. This cannot be due to gas phase intermixing, since negligible growth occurs with conventional MOCVD of HgTe at 140 °C for 1 h, while a uniform film obtains with monolayer growth using the ALE sequence at the same temperature. The cause of this behavior is not understood; one possibility may be

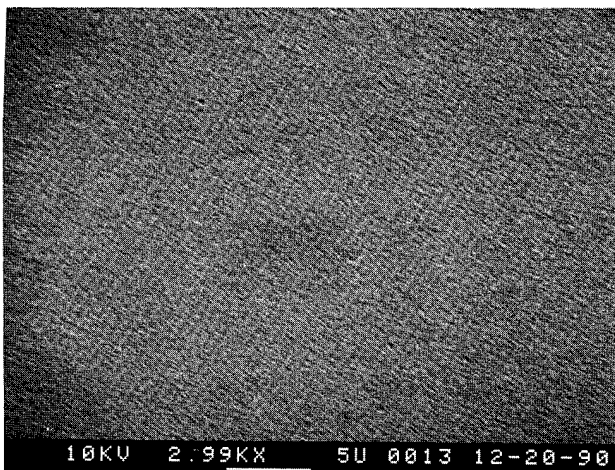


Fig. 4. SEM image of typical surface morphology for ALE HgTe on GaAs.

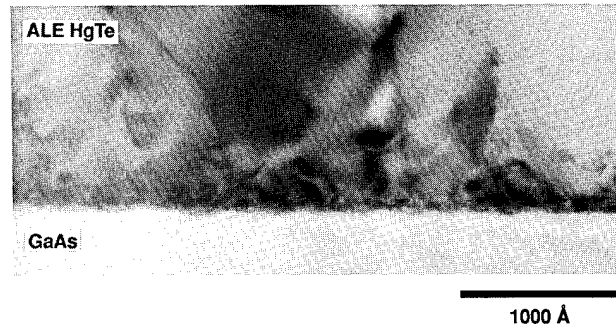


Fig. 5. Cross-sectional TEM bright-field image of ALE HgTe on GaAs, deposited at 140 °C.

Te condensation at these low deposition temperatures. Figure 4 shows a typical surface morphology of ALE HgTe on GaAs deposited at 140 °C. Improved surface morphology is observed when a thin initial ALE CdTe film less than 100 Å thick is deposited onto the GaAs substrate prior to ALE of HgTe. Figure 5 is a cross-sectional TEM image of ALE HgTe on GaAs. An important feature is the absence of planar defects such as microtwins and stacking faults, which illustrates the advantage of ALE in promoting two-dimensional growth. Also of interest is the presence of a uniform array of misfit dislocations at the HgTe–GaAs interface, which efficiently accommodates the lattice mismatch. These features have recently been observed in heteroepitaxy of other lattice-mismatched systems such as GaAs on Si [8]. The electron diffraction pattern of the film shows that it has a similar orientation to that of the substrate [100].

### 3.3. ALE of HgCdTe

Since the temperature windows for ALE of CdTe and HgTe do not overlap, continuous *in situ* growth of the ordered or mixed alloy was not possible. (The requisite isothermal deposition process could, perhaps, be achieved by using an alternate Cd precursor to lower the ALE deposition temperature for CdTe). For the present experiments, HgCdTe was grown by sequentially depositing ALE HgTe and CdTe at their respective ALE growth temperatures. The target HgCdTe composition  $x = 0.33$  was achieved by adjusting the relative thickness ratio of HgTe to CdTe to 2:1; the structure was subsequently homogenized by annealing the wafer at 350 °C for 30 min, typically similar to the interdiffusion-multilayer process (IMP) [9]. The actual structure consisted of 50 nm CdTe at 250 °C followed by 150 nm HgTe at 140 °C, repeated twice, followed by a thin 50 nm CdTe cap. Figure 6 shows the FTIR transmission characteristics. The composition of the film was estimated to be  $x = 0.33$ , in excellent agreement with the target composition.

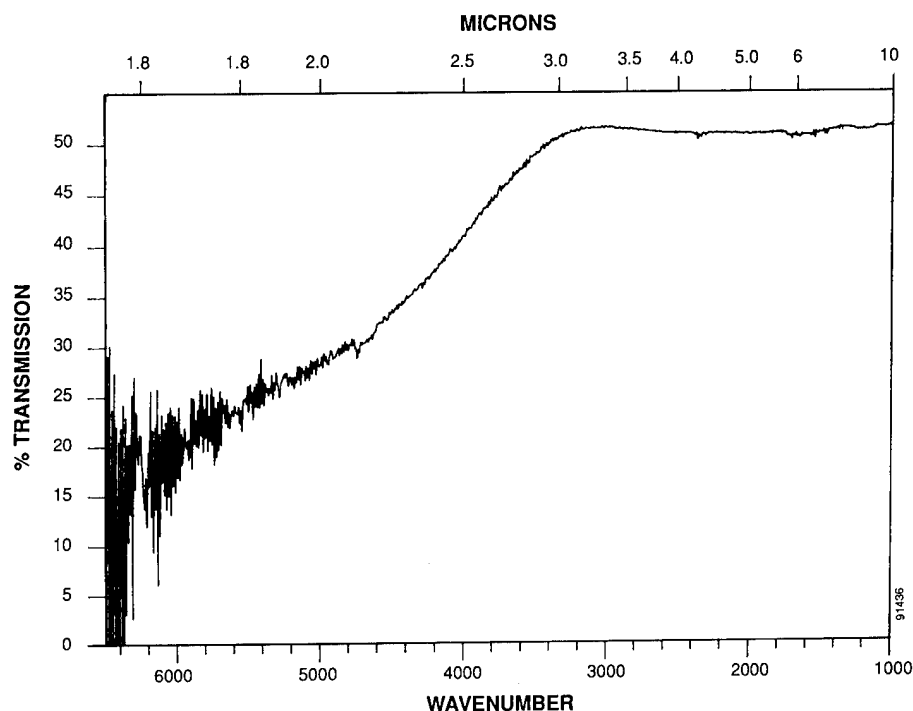


Fig. 6. FTIR transmission curve of 0.42  $\mu\text{m}$  thick HgCdTe film after sequential growth and homogenization of the CdTe–HgTe ALE layers.

#### 4. Conclusions

We have demonstrated for the first time ALE of CdTe on both CdTe and GaAs substrates using MATE and DMCD precursors. High-quality films with excellent surface morphology were deposited at 250 °C. ALE of CdTe is especially suited for passivation of device structures with different topographical features. ALE of HgTe was demonstrated using DMHg and MATE at 140 °C. The one monolayer per cycle condition extended over a wide range of Hg vapor pressure. This is the first demonstration of a self-limiting feature in an Hg-containing compound. HgCdTe films were achieved by interdiffusing sequentially deposited CdTe and HgTe layers. ALE is a powerful deposition tool for high-quality lattice-mismatched heteroepitaxial films.

#### Acknowledgments

This work has been supported by DARPA through a subcontract from Rockwell International Corporation.

The authors wish to thank Dr. M. Al-Jassim for TEM characterization.

#### References

- 1 See for example, *Proc. 1990 US Workshop on the Physics and Chemistry of Mercury Cadmium Telluride and Novel Infrared Detector Materials*, in *J. Vac. Sci. Technol. B*, 9 (3) 1991.
- 2 T. Suntola and J. Antson, *Finnish Patent 52359*, 1974 *US Patent 4058430*, 1977.
- 3 *Proc. 1st Int. Symp. on Atomic Layer Epitaxy, Espoo, June 13–15 1990, Acta Polytech. Scan.*, Chem Tech. Mat. Series, No. 195.
- 4 C. H. L. Goodman and M. V. Pessa, *J. Appl. Phys.*, 60 (1986) R65.
- 5 T. Suntola, *Mater. Sci. Rep.*, 4 (7) (1989) 261.
- 6 M. Pessa, P. Huttunen and M. A. Herman, *J. Appl. Phys.*, 54 (1983) 6047.
- 7 S. K. Ghandhi, I. B. Bhat, H. Ehsani, D. Nucciarone and G. Miller, *Appl. Phys. Lett.*, 55 (1989) 137.
- 8 N. H. Karam, T. Parodos, V. Haven, M. Leonardo and N. A. El-Masry, Presented at *2nd Int. Conf. on Atomic Layer Epitaxy, Raleigh, NC 1992*.
- 9 S. J. C. Irvine, J. B. Mullin and A. Royle, *J. Cryst. Growth*, 57 (1982) 15.

# Growth and characterization of CdTe–ZnTe short-period superlattices

F. Hauzenberger

*Institut für Experimentalphysik, Universität Linz, A-4040 Linz (Austria)*

W. Faschinger

*Institut für Halbleiterphysik, Universität Linz, A-4040 Linz (Austria)*

P. Juza, A. Pesek, K. Lischka and H. Sitter

*Institut für Experimentalphysik, Universität Linz, A-4040 Linz (Austria)*

## Abstract

ZnTe–CdTe superlattices with periods ranging from 13 Å to 38 Å were grown by atomic layer epitaxy on (001) GaAs substrates and monitored *in situ* by reflected high-energy electron diffraction. The substrate temperature was varied from 215 °C to 300 °C. The superlattices were characterized by high-resolution X-ray diffraction and the growth rate per reaction cycle was determined from the separation of satellite peaks. Between 270 and 290 °C, the growth rate maintained itself at exactly 0.5 monolayers per cycle, allowing the growth of precisely tailored structures. As the substrate temperature was reduced below 270 °C, the growth rate increased to approximately 0.8 monolayers per cycle, but it did not reach 1 monolayer per cycle before polycrystalline ZnTe was nucleated at 205 °C.

## 1. Introduction

Atomic layer epitaxy (ALE) of semiconductors has recently attracted considerable interest, because it has the two-fold capability of precisely controlling layer thickness and of growing high quality films at low substrate temperature with minimum interdiffusion. This is a consequence of the fact that, provided the growth parameters are chosen properly, ALE growth occurs in discrete, self-limiting steps.

Multilayers of II–VI wide gap compound semiconductors are of current interest for applications in short-wavelength optoelectronic devices. CdTe and ZnTe are both direct gap semiconductors with band gaps of 1.6 and 2.2 eV respectively. By varying the thicknesses of the CdTe and ZnTe layers the band gap can be tailored. If the thickness of each layer is kept below the critical thickness, these superlattices (SLs) can be grown without introducing additional misfit dislocations. Furthermore, these SL structures may be perfectly suitable as buffer layers for defect reduction [1] in heterostructures such as CdTe on GaAs.

## 2. Experimental procedure

The experiments were performed in a vertical molecular beam epitaxy (MBE) system equipped with a reflection high-energy electron diffraction (RHEED) system (Staib Instruments) and seven effusion cell ports

with fast, magnetically coupled shutters for operation in the ALE mode. For ALE growth of ZnTe and CdTe, elemental zinc, cadmium and tellurium effusion cells were specially constructed. As substrate material, we used semi-insulating GaAs oriented 2° off (100) towards the  $\langle 110 \rangle$  direction. The substrates were chemically cleaned in a standard  $\text{H}_2\text{SO}_4\text{--H}_2\text{O}_2$  etch and preheated at 640 °C before growth in order to desorb the oxide layer. A nude ionization gauge placed near the substrate was calibrated for zinc, cadmium and tellurium beam intensities by depositing polycrystalline zinc, cadmium and tellurium films onto etched and preheated GaAs substrates at a substrate temperature of  $-10$  °C to avoid any re-evaporation.

In all experiments, we grew first a 0.7–1.2 µm thick MBE ZnTe buffer layer at a substrate temperature of 310 °C to overcome the large lattice mismatch between the substrate and the epilayer. In the following ALE growth, the constituents were deposited in alternating pulses of 1–2 s duration with 0.2 s dead time in between. The beam flux intensities were adjusted to deposit 2–5 monolayers (ML) cadmium, 1.6–2.6 ML zinc, and 1.3–2 ML tellurium within one evaporation pulse.

In the first set of experiments, we examined the growth of ZnTe/CdTe superlattices as a function of substrate temperature in the range 215–300 °C. The nominal structure of all superlattices is 12 growth cycles ZnTe and 12 growth cycles CdTe repeated 30 times. Then we grew a series of superlattices with constant

total thickness (560 nm), a nominal composition of 50% and a nominal period ranging from 12 growth cycles ZnTe and 12 growth cycles CdTe to four growth cycles ZnTe and four growth cycles CdTe at a substrate temperature of 280 °C.

After growth, high-resolution X-ray diffraction (HRXD) measurement using Cu K $\alpha$  radiation was carried out around the (004) reflection to determine the SL period from the spacing of satellites. In the case of the superlattice with a period of 20 Å, corresponding to 3MLZnTe/3MLCdTe, we measured four asymmetric ((026), ( $\bar{3}$ 35), (335) and ( $\bar{3}$ 15)) diffractions in order to analyse the layer structure more precisely.

### 3. Results and discussion

A series of superlattices was grown with 12 growth cycles ZnTe and 12 growth cycles CdTe repeated 30 times. The surface of the epilayers was mirror like and showed the same flatness as the GaAs substrate, shown by Nomarski interference contrast micrographs. Figure 1 shows the thickness of the superlattice period *vs.* substrate temperature. Below 205 °C, the ZnTe was polycrystalline, as shown by polycrystalline fringes in the RHEED pattern. The upper solid line is calculated for an ideal ALE process with a growth rate of 1 ML per growth cycle for each compound. It can be seen that ideal ALE growth with 1 ML per growth cycle was not achieved. The lower solid line is calculated for an ALE process with a growth rate of 0.5 ML per growth cycle for each compound. The good agreement with the period thickness of superlattices grown in the tempera-

ture range 270–290 °C suggests that there is a self-regulating region with a growth rate of 0.5 ML per growth cycle. Furthermore, three superlattices with cadmium effusion rates varying from 5 to 2 ML per evaporation pulse, zinc rates varying from 1.6 to 2.6 ML per evaporation pulse, and tellurium rates varying from 1.2 to 2 ML per evaporation pulse were grown at 270 °C. The measured period thickness is the same within experimental error, proving the self-regulating mechanism in this range of substrate temperature. This is in agreement with data reported in the literature. The growth rate of 0.5 ML per growth cycle was reported by Takemura *et al.* [2] for ZnTe and by Faschinger and Sitter [3] for CdTe. Li *et al.* [4] grew ZnTe/CdTe multiquantum wells with a growth rate of about 0.5 ML per growth cycle. Faschinger and Sitter [3] proposed a model for the growth process leading to half-monolayer growth.

For further investigations of the self-regulating region, we grew a series of superlattices with different periods but constant total thickness. Figure 2 shows the experimental superlattice period *vs.* the theoretical superlattice period calculated with a growth rate of 0.5 ML per growth cycle. The solid line denotes the expected result. As one can see, the agreement between calculated and measured period thickness is excellent (discrepancy less than or equal to 5%), proving the high reproducibility due to self-regulating growth. The differences between theoretical and measured period thicknesses are comparable with the results obtained by Lentz *et al.* [5], who grew their ZnTe/Cd<sub>0.9</sub>Zn<sub>0.1</sub>Te superlattices on (001) Cd<sub>0.96</sub>Zn<sub>0.04</sub>Te substrates with phase-locked epitaxy. However, in our case the experi-

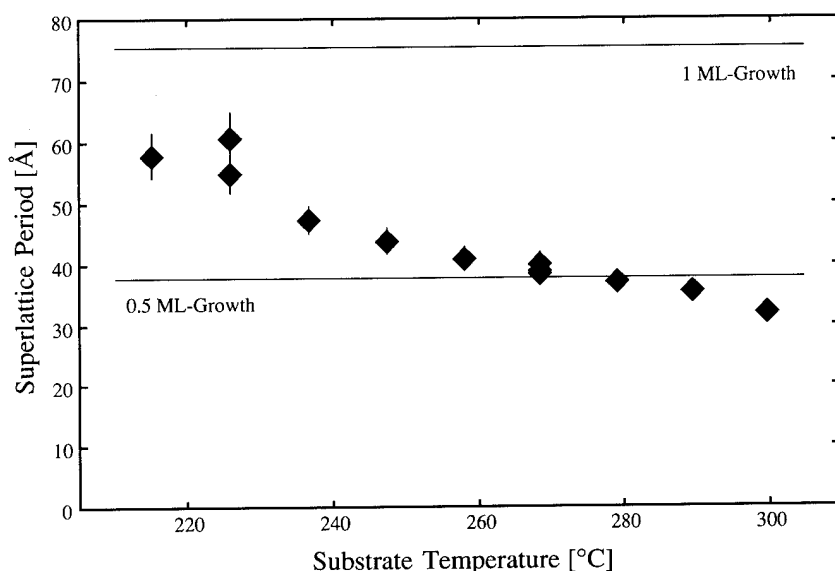


Fig. 1. Superlattice period as a function of substrate temperature. The upper solid line denotes the period for a growth rate of 1 ML per growth cycle, the lower line that for a growth rate of 0.5 ML per growth cycle.



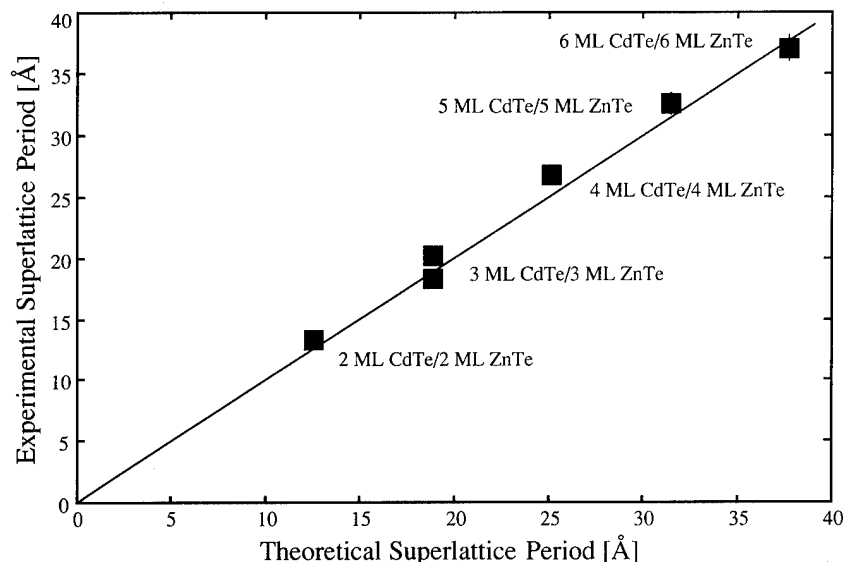


Fig. 2. Superlattice period of the superlattices grown at a substrate temperature of 280 °C vs. theoretical superlattice period for a growth rate of 0.5 ML per growth cycle.

mental requirements are less critical, as the growth regulates itself.

Figures 3(a) and 3(b) show, as an example, the HRXD spectra of superlattices with periodicities 6MLZnTe/6MLCdTe repeated 150 times and 2MLZnTe/2MLCdTe repeated 450 times. The full width at half-maximum (FWHM) of the diffraction peaks is approximately 800 arcsec. This large value reflects the high dislocation density, which is a consequence of the large lattice mismatch (approximately 9%) relative to the GaAs substrate. However, the FWHM of the ZnTe buffer peak

and the SL peaks are comparable, which means that the dislocation density is determined by the quality of the buffer. The spectrum of the superlattice with a period length of 6MLZnTe/6MLCdTe clearly shows satellites up to the order of +2 and −2. The intensity between satellites almost reaches the background intensity level of 1 count per second. This is a sign of highly perfect periodicity, since periodicity fluctuations would result in a rise in background intensity between peaks [6].

The excellent structure of the SLs is demonstrated by Fig. 3(b). The superlattice with a periodicity of

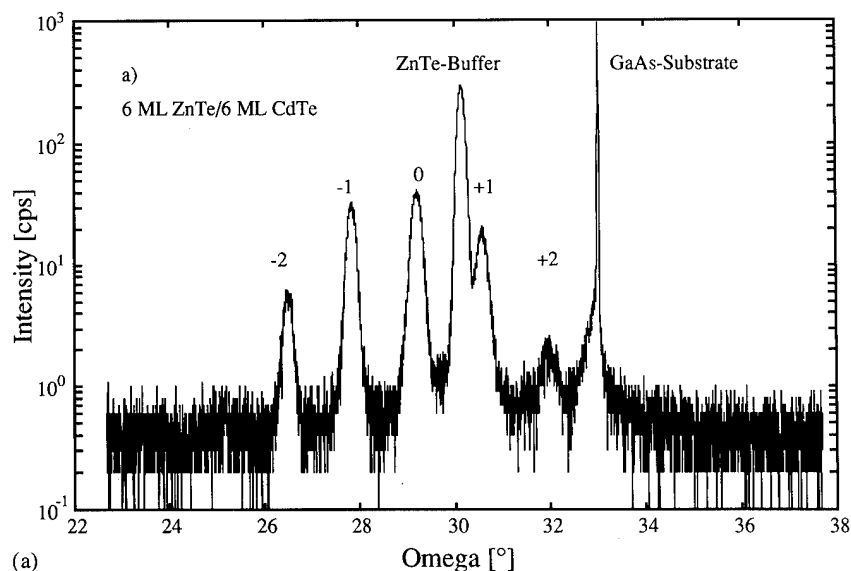


Fig. 3. (a)

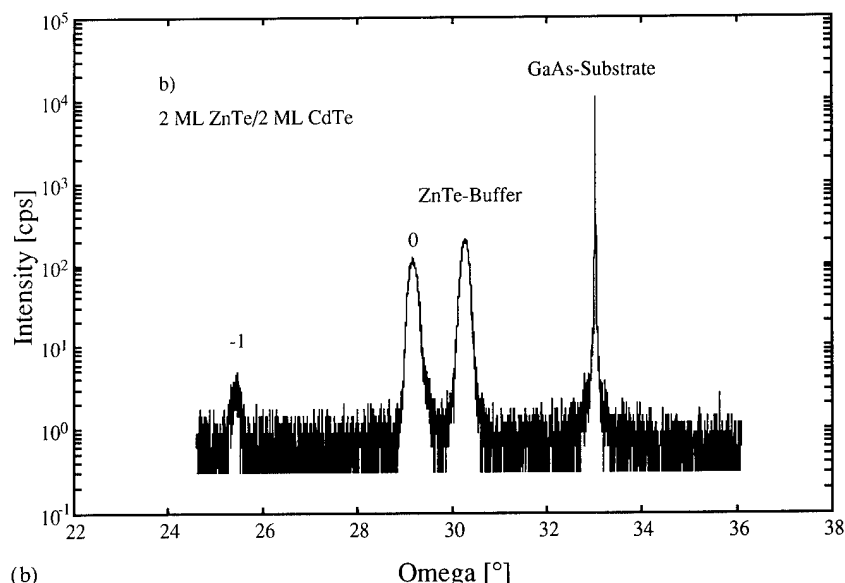


Fig. 3. HRXD spectra of the (004) peak of superlattices with the structures (a) 6MLZnTe/6MLCdTe (150 repetitions), and (b) 2MLZnTe/2MLCdTe (450 repetitions).

2MLZnTe/2MLCdTe is, to our knowledge, the CdTe/ZnTe SL with the smallest periodicity published so far. For a superlattice with such a short period even low interdiffusion or period fluctuations would efficiently reduce satellite peak intensities. Nevertheless, first-order satellites are clearly observed and their relative intensity compared with the zero-order peak corresponds to the value we calculated by dynamic diffraction theory for an ideal 2ML/2ML SL. This is in good agreement with results obtained from far-IR reflectivity measurements of the same series of samples, where the energy shift of phonons confined in the CdTe layers is evaluated [7].

The position of the zero-order peak of asymmetric reflections is determined by the average composition  $x$  of the SL and the strain within the layers. The strain tensor was calculated from the position of measured asymmetric reflections using  $x$  as a parameter. The calculations were done under the following assumptions: (i) the strain tensor is diagonal, (ii) the in-plane components of the strain tensor are equal, and (iii) the vertical component is related to the in-plane components via the elastic constants  $c_{ij}$ .

Figure 4 shows the in-plane lattice constant  $d_{xx}$  calculated for  $x$  values between 0.47 and 0.50 for the sample with periodicity of 3MLCdTe/3MLZnTe. Within these limits, the resulting strain depends strongly on the assumed  $x$  value. It changes from completely relaxed ( $d_{xx} = d_{\text{bulk}}$ ) for  $x = 0.47$  to completely strained ( $d_{xx}[\text{CdTe}] = d_{xx}[\text{ZnTe}]$ ) for  $x = 0.5$ .

Cibert *et al.* [8] reported a critical thickness of 5 ML for CdTe on ZnTe and indicated that a similar value should be valid for ZnTe on CdTe. Sugiyama *et al.* [1] observed a critical thickness for ZnTe/CdTe quantum

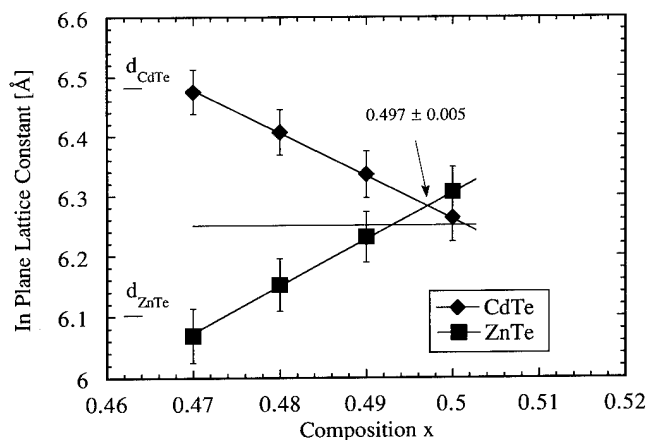


Fig. 4. In-plane lattice constant as a function of composition  $x$  calculated from measurements of asymmetric X-ray reflections. The periodicity of this superlattice is 3MLZnTe/3MLCdTe (300 repetitions). The horizontal solid line denotes the in-plane lattice constant calculated from elastic theory for a free-standing strained-layer superlattice,  $d_{\text{ZnTe}}$  and  $d_{\text{CdTe}}$  denote the corresponding bulk lattice constants.

wells between 17 and 19 Å from photoluminescence measurements. Therefore, we conclude that, for the superlattice with a periodicity of 3MLCdTe/3MLZnTe, the thickness of each individual layer is well below the critical thickness. As a consequence, it is reasonable to assume that this superlattice is of the strained-layer type, which means that the in-plane lattice constants of CdTe and ZnTe are equal. Under this assumption, an  $x$  value of  $0.497 \pm 0.005$  results from Fig. 4. This value, which corresponds exactly with the nominal value, is striking proof for the efficiency of the self-regulating process.

The horizontal solid line in Fig. 4 denotes the in-plane lattice constant calculated by elastic theory for a free-standing strained-layer superlattice [7]. From the agreement with our data for  $x = 0.497$ , we conclude that our superlattice is free standing. The result is an agreement with the data of Miles *et al.* [9], who reported a free-standing configuration for their ZnTe/CdTe superlattices on GaAs substrates from photoluminescence measurements and second-order kp calculations.

#### 4. Conclusion

CdTe–ZnTe short-period superlattices have been grown by ALE on (001) GaAs substrates. We have shown that the ALE method is well suited for the fabrication of precisely tailored structures. In the substrate temperature range between 270 and 290 °C, ALE is maintained at a growth rate of 0.5 ML per growth cycle. HRXD measurements show that superlattices in this substrate temperature range exhibit excellent period constancy and low interdiffusion. The composition is exactly 0.5, which proves the reliability of the self-regulation mechanism.

#### Acknowledgments

This work was supported by the “Fonds zur Förderung der wissenschaftlichen Forschung in Österreich” and the “Gesellschaft für Mikroelektronik”. We thank O. Fuchs for technical assistance.

#### References

- 1 I. Sugiyama, A. Hobbs, O. Ueda, K. Shinohara and H. Takigawa, *Appl. Phys. Lett.*, **5** (8) (1991) 2755.
- 2 Y. Takemura, H. Nakanishi, M. Konagai and K. Takahashi, *Jpn. J. Appl. Phys.*, **30** (1991) L246.
- 3 W. Faschinger and H. Sitter, *J. Cryst. Growth*, **111** (1990) 99.
- 4 J. Li, L. He, W. Shan, X. Cheng and S. Yuan, *J. Cryst. Growth*, **111** (1991) 736.
- 5 G. Lentz, A. Ponchet, N. Magnea and H. Mariette, *Appl. Phys. Lett.*, **55** (1989) 2733.
- 6 V. S. Speriosu and T. Vreeland, Jr., *Appl. Phys. Lett.*, **56** (1984) 2755.
- 7 T. Fromherz, G. Bauer, M. Helm, F. Hauzenberger, W. Faschinger and H. Sitter, *Phys. Rev. B*, in press.
- 8 J. Cibert, Y. Gobil, Le Si Dang, S. Tatarenko, G. Feuillet, P. H. Jouneau and K. Saminadayr, *Appl. Phys. Lett.*, **56** (1990) 292.
- 9 R. H. Miles, G. Y. Wu, M. B. Johnson, T. C. McGill, J. P. Faurie and S. Sivananthan, *Appl. Phys. Lett.*, **48** (1986) 20.

# Self-limiting monolayer epitaxy of wide gap II–VI superlattices

W. Faschinger

*Institut für Halbleiterphysik, Universität Linz, A-4040 Linz (Austria)*

P. Juza, S. Ferreira\*, H. Zajicek, A. Pesek and H. Sitter

*Institut für Experimentalphysik, Universität Linz, A-4040 Linz (Austria)*

K. Lischka

*Forschungsinstitut für Optoelektronik, Universität Linz, A-4040 Linz (Austria)*

## Abstract

We propose a novel growth technique for the preparation of wide gap II–VI compounds and heterostructures, self-limiting monolayer epitaxy (SME). The basic idea of SME is that atoms physisorbed on top of an atomically flat surface are more loosely bound than atoms incorporated into a completed monolayer. Thus one expects eventual re-evaporation of the material which has been deposited in excess to complete monolayers, leading to a two-dimensional and self-limiting growth process. ZnS epitaxial layers and ZnSe/CdSe superlattices were grown on GaAs substrates using the SME technique, giving evidence for the self-limiting behaviour of this growth process. The superlattices grown using this method are of very good quality, as revealed by high-resolution X-ray diffraction and photoluminescence measurements.

## 1. Introduction

Wide gap II–VI heterostructures containing selenium or sulphur compounds have recently attracted considerable interest since blue–green laser diodes have been demonstrated [1, 2]. In order to obtain high quality heterostructures, quantum wells and superlattices (SLs) with well defined thickness and abrupt interfaces, an ultrahigh vacuum (UHV) growth method with precise thickness control on a monolayer (ML) scale is desirable. We have developed a new technique, which we call self-limiting monolayer epitaxy (SME). It combines the advantages of a self-regulating growth process, as achieved by atomic layer epitaxy (ALE) with the feature that both constituents of a compound are present simultaneously at an epilayer surface, as is typical of molecular beam epitaxy (MBE). SME avoids the problems related to ALE and MBE. Monolayer growth in ALE processes is often prohibited by the formation of submonolayer coverages of the more volatile constituents, in our case sulphur and selenium, which re-evaporate easily from the surface [3]. In MBE growth processes, however, a lack of accuracy of flux control leads to interface roughness, which deteriorates the properties of the grown structure.

The main idea of SME is that a particle on top of a flat surface has a smaller number of nearest and next-nearest neighbours and is therefore less strongly bound than a particle incorporated into the flat surface. This difference in bond energy can be used for self regulation. SME is achieved by offering the more volatile constituents sulphur and selenium permanently, while the Group II constituents cadmium or zinc are offered in a pulsed mode. In Fig. 1 we compare typical growth sequences for MBE, ALE and SME. In analogy to ALE we call the time from one Group II evaporation pulse to the next one a growth cycle. An ideal SME growth cycle consists of very short MBE pulses, followed by intermissions during which the material growth in excess of a full monolayer re-evaporates. If one increases the amount of material offered during the pulse times, one would expect that the SME growth rate per cycle would increase in discrete steps of one monolayer.

## 2. Experimental details

### 2.1. ZnS

ZnS was grown in an MBE system from elemental sources. The sulphur source was equipped with a thermal cracker which was kept at 500 °C. The substrate was (100) oriented GaAs. Since it turned out that ZnS did not grow directly on GaAs, a 50–100 Å thick ZnTe

\*Permanent address: Instituto de Pesquisas Espaciais, CP515, 12201–S.J. Campos, SP, Brazil.

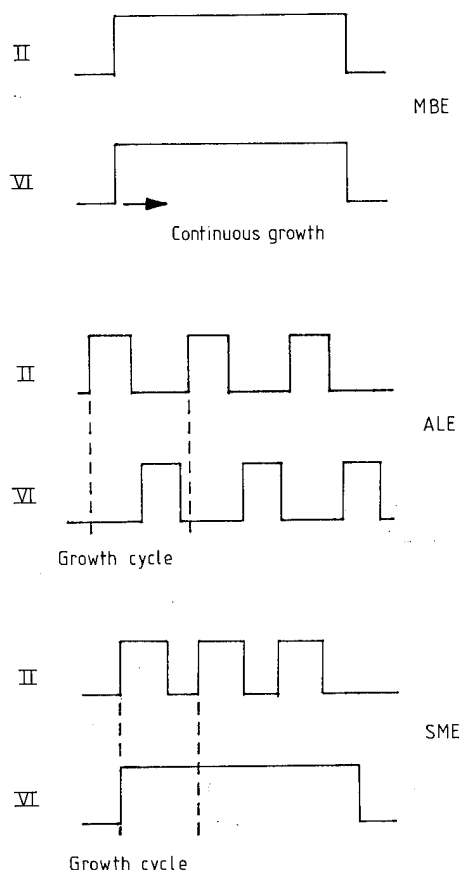


Fig. 1. Shutter sequences for MBE, ALE and SME.

buffer was grown in order to initiate ZnS growth. The substrate temperature was 280 °C except for one sample which was grown at 300 °C. A number of epilayers were prepared in the MBE mode for growth rate determination. For SME grown films the pulse time, in which the zinc source was opened, was varied between 1.5 and 5 s, with an intermission of 1 s. The beam intensities were measured *in situ* using a pressure gauge placed near the substrate. The thickness of the deposited films was determined by scanning over a shadow edge with a calibrated mechanical profilometer.

## 2.2. ZnSe/CdSe superlattices

ZnSe<sub>m</sub>/CdSe<sub>n</sub> superlattices (where *m* and *n* are the numbers of ZnSe and CdSe monolayers respectively) were grown including a series of symmetrical (*m* = *n*) SLs with *m* = *n* ranging from 2 to 6. ZnSe and CdSe epitaxial layers were prepared using the MBE technique to determine the growth rates.

The growth of the selenium compounds and SLs was performed in a vertical UHV growth chamber equipped with seven effusion cells and a reflection high-energy electron diffraction (RHEED) system. A nude ion gauge was situated in the vicinity of the substrate. It was used to measure the beam equivalent pressures

(BEPs) of the atomic and molecular fluxes. Cadmium, zinc and selenium were evaporated from elemental solid source effusion cells, developed in our laboratory, each equipped with two separately controlled heating zones. The selenium source contained a thermal cracker, kept at 470 °C, which efficiently reduces the number of selenium molecules larger than Se<sub>2</sub>.

(100) GaAs substrates misoriented 2° towards the next <110> direction were used for the growth experiments. The SLs were grown on top of ZnSe MBE buffers, the thickness of which ranged from 0.3 to 1 μm. The substrate temperature was 300 °C.

During the superlattice growth process only the shutters of zinc and cadmium were opened and closed while the selenium shutter was permanently open according to the SME scheme described in Fig. 1. The pulse time for cadmium ranged from 1.1 to 1.9 s. In order to demonstrate the stepwise behaviour of the growth rate, three different zinc pulse times, 1 s, 1.5 s and 3.5 s, were chosen which purposely differ by a factor deviating from an integer number. The intermissions were 1 s for both CdSe and ZnSe. The number of ZnSe cycles was varied from 2 to 20, the number of CdSe cycles from 2 to 6.

Post-growth characterization included high-resolution X-ray diffraction (HRXD) analysis and photoluminescence (PL) spectroscopy.

## 3. Results and discussion

### 3.1. ZnS

The ZnS growth rate in the MBE mode was determined to be 0.25 μm h<sup>-1</sup> or 0.25 ZnS ML s<sup>-1</sup>. After opening the zinc shutter, the signal of the beam monitor rose immediately (within less than 0.1 s) to the value used for MBE growth. This means that even for the short SME pulses (1.5–5 s), the amount of material offered within one cycle could be calculated from the MBE calibration. In Fig. 2 the measured SME growth rate per cycle is plotted as a function of the material offered within one cycle (squares). The thickness determination by the calibrated mechanical profilometer is quite precise; nevertheless, to exclude misinterpretations, a maximum error of ±10% is indicated by error bars. The circles denote the according values for ZnSe which will be discussed later. The solid line indicates the behaviour one would expect if SME were simply an interrupted MBE process without any additional re-evaporation. The experimental values deviate considerably from this line. As long as less than 0.5 ML per cycle is offered, no growth occurs at all, indicating that all the offered material re-evaporates. If 0.75 ML per cycle is offered, the growth rate is still a factor of three smaller than expected for MBE growth. However, as

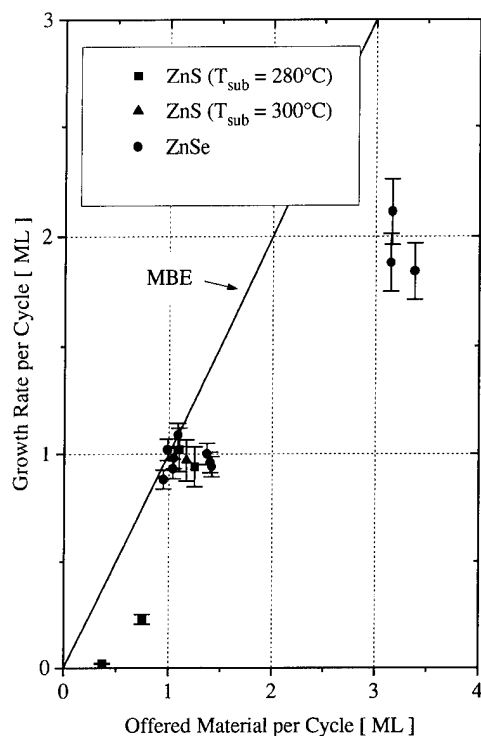


Fig. 2. Growth rate per growth cycle as a function of the material offered within one growth cycle. The solid line represents the expected MBE growth rate.

soon as more than 1 ML per cycle is offered, the growth rate jumps to 1 ML per cycle. Thus the step-like behaviour of the growth rate expected for an ideal SME process is indeed observed, although the step is somewhat smoothened. The sample marked as a triangle was

grown at a substrate temperature of  $300^\circ\text{C}$  instead of  $280^\circ\text{C}$ . The independence of the growth rate on the substrate temperature is an additional indication of a self-regulating regime.

### 3.2. ZnSe/CdSe superlattices

During the growth of the ZnSe and the ZnSe/CdSe SLs, one could always observe a selenium stabilized  $(2 \times 1)$  reconstructed surface in the RHEED patterns. The patterns became diffuse (but not spotty as reported by Samarth *et al.* [4]) immediately after the cadmium shutter was opened for the first time. The quality of the RHEED pattern degraded with each CdSe layer, and improved with each layer of ZnSe, especially during each intermission between zinc evaporation pulses. We attribute this to a smoothing process of the surface which takes place during growth interruptions. It is assumed that additional to surface migration, re-evaporation of particles unable to find appropriate lattice sites takes place.

The superlattice periods were calculated from the angular spacings of the SL satellite peaks in the HRXD spectra. In all the SL X-ray diffraction spectra we could at least observe the first-order SL reflection. Figure 3 shows the HRXD spectrum of a 3MLZnSe/3MLCdSe SL, the period of which was repeated 200 times. In contrast to the X-ray data reported so far for ZnSe/Zn<sub>1-x</sub>Cd<sub>x</sub> SLs ( $0 < x \leq 1$ ) [4, 5], the intensity in our HRXD spectra drops to the noise level between the SL peaks which is a sign of small fluctuations of the SL period [6]. We also rule out strong interdiffusion since this would completely wipe out SL satellite peaks for these very short periods.

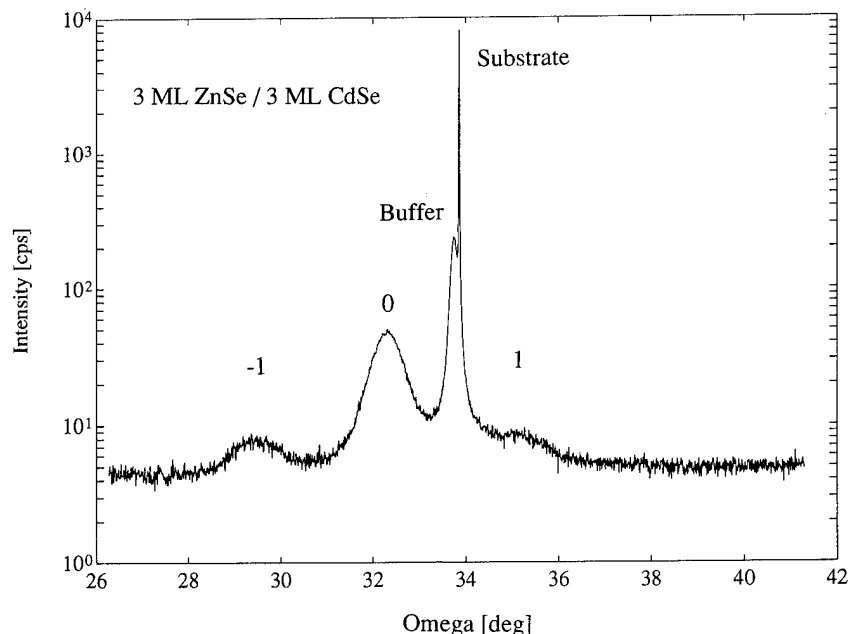


Fig. 3. HRXD spectrum of a 3MLZnSe/3MLCdSe SL. The number of repetitions is 200.

Since the overall thickness of the SL itself ( $0.35\ \mu\text{m}$  in the case of the  $3\text{MLZnSe}/3\text{MLCdSe}$ ) is well beyond the critical thickness of a corresponding  $\text{Zn}_{1-x}\text{Cd}_x\text{Se}$  ( $x = 0.5$ ) ternary compound on ZnSe, one expects a free-standing SL with a relatively high density of dislocations. This is one reason for the large value of the full width at half-maximum (FWHM) of the zeroth order SL peak, which is  $2700\ \text{arcsec}$ . Another reason for the moderate crystalline quality is reported by Samarth *et al.* [4].  $\text{Zn}_{1-x}\text{Cd}_x\text{Se}$  ( $x > 0.5$ ) epilayers show a high density of stacking faults observed by transmission electron microscopy.

For all our SLs the measured SL period thickness is in good agreement with the expected SL period length. The period length was calculated by multiplying the number of ZnSe growth cycles by the thickness of  $i$  ( $i = 1, 2$ ) ZnSe monolayers ( $2.84\ \text{\AA}$ ) and adding the number of CdSe cycles multiplied by  $3.03\ \text{\AA}$ . The underlying assumption of this calculation is obviously that each material grows with growth rates that are integer multiples of 1 ML per growth cycle. Thus one can presume that monolayer growth takes place.

The ZnSe width within one ZnSe/CdSe period was calculated by subtracting the thickness of  $n$  monolayers of CdSe, where  $n$  again is the number of CdSe growth cycles within one SL period from the SL period length. Figure 4 shows the ZnSe layer thickness per SL period determined in this way *vs.* the number of ZnSe growth cycles used to grow one SL period. The line indicate growth rates of 1 ML per growth cycle and 2 ML per growth cycle. All experimental data can be explained by

this assumption, which means that only these two integer growth rates occur, although the zinc evaporation pulse time was varied between 1, 1.5 and 3.5 s.

The ZnSe growth rate per reaction cycle is plotted in Fig. 2 as a function of the offered material alongside the ZnS data. The ZnSe data points are indicated as circles. The error bars correspond to a deviation in the readings of the angular spacings of the SL X-ray reflections of  $0.1^\circ$ . The amount of offered material was determined from the growth rates of ZnSe epilayers prepared by MBE. The experimental error of such growth rate determinations may be of the order of 15%–20%. One can clearly observe a deviation of growth rate from linear dependence on the offered material, which one would expect for MBE growth, indicated by a solid line in Fig. 2. The independence of the ZnSe growth rate per cycle over a range of offered material that extends from 1 ML to about 1.5 ML is strong evidence for a self-limiting growth regime. The data at a growth rate of about 2 ML give rise to the assumption that there might be additional regimes where self-limiting growth with an integer number of monolayers per reaction cycle takes place.

Figure 5 shows the PL spectra obtained from a series of symmetric  $\text{ZnSe}_m/\text{CdSe}_n$  SLs ( $m = n = 2-6$ ) taken at 1.7 K. The excitation wavelength was 488 nm. The spectra for  $n \leq 3$  are dominated by one sharp line which is attributed to near band-edge excitonic emission. The energetic positions of these lines are a measure of the SL band gap. The weak PL emission at lower energies is most probably related to residual

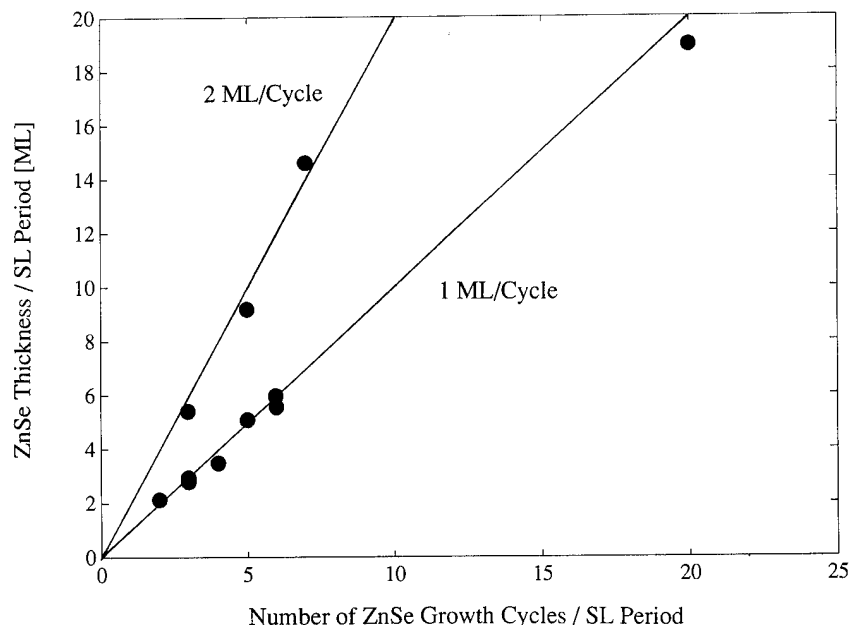


Fig. 4. ZnSe period thickness *vs.* the number of ZnSe growth cycles per SL period.

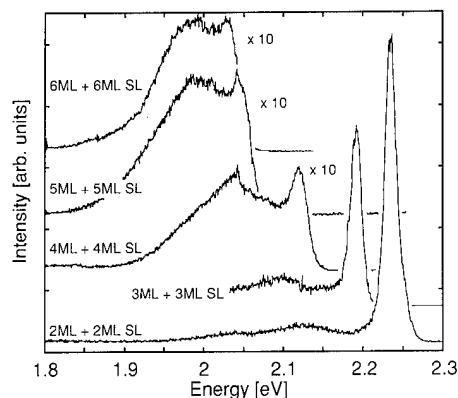


Fig. 5. Photoluminescence spectra of symmetric  $\text{ZnSe}_n/\text{CdSe}_n$  SLs ( $n = 2\text{--}6$ ;  $n$  is the number of monolayers).

impurities. For SLs with  $n > 3$ , a dramatic decrease in the intensity of the near band-edge emission can be observed accompanied by an increase in the defect-related PL. Parbrook *et al.* [5] attributed the similar behaviour of their PL from  $\text{ZnSe}/\text{CdSe}$  SLs to the formation of misfit dislocations, when the  $\text{CdSe}$  wells exceeded the critical thickness  $L_c$  for strained layer growth. They reported a value of  $4 \pm 1$  ML for  $L_c$ , which is in good agreement with the value of 3 ML that we deduce from our data.

One has to note that the FWHM of the near band-edge emission for our symmetric SLs with  $n \leq 3$  is about 17 meV. This value is almost an order of magnitude smaller than that reported for  $\text{ZnSe}/\text{CdSe}$  SLs grown by MOVPE [5, 7] and is close to that of  $\text{ZnSe}/\text{Zn}_{1-x}\text{Cd}_x\text{Se}$  strained layer SLs with a much lower cadmium content ( $x < 0.35$ ) [4]. We assume that this small line width is evidence for the excellent interface quality and the homogeneity of the layer thickness, both within the layers and also between individual layers, which can be achieved by employing SME.

#### 4. Summary

We used SME, a new growth method, to prepare  $\text{ZnS}$  epitaxial layers and  $\text{ZnSe}/\text{CdSe}$  SLs on  $\text{GaAs}$  substrates. The SLs exhibit exceptionally good crystalline and optical quality, as revealed by HRXD and PL measurements. We have given evidence that SME is a self-regulatory growth process which limits itself to an integer number of monolayers during one growth cycle. In contrast to ALE, the self-regulation does not depend on the difference in bond strength, but on the difference in bond numbers. For this reason we are optimistic that SME is not limited to II–VI compounds, as UHV-ALE, but can also be applied to other materials.

#### Acknowledgments

This work was partly supported by the “Fonds zur Förderung der wissenschaftlichen Forschung in Österreich” and the “Jubiläumsfonds der österreichischen Nationalbank”.

#### References

- 1 M. A. Haase, J. Qiu, J. M. DePuydt and H. Cheng, *Appl. Phys. Lett.*, **59** (1991) 1272.
- 2 H. Jeon, J. Ding, W. Patterson, A. V. Nurmikko, W. Xie, D. C. Grillo, M. Kobayashi and R. L. Gunshor, *Appl. Phys. Lett.*, **59** (1991) 3619.
- 3 B. A. Joyce, *J. Cryst. Growth*, **99** (1990) 9.
- 4 N. Samarth, H. Luo, J. K. Furdyna, R. G. Alonso, Y. R. Lee, A. K. Ramdas, B. S. Qadri and N. Otsuka, *Appl. Phys. Lett.*, **56** (1990) 1163.
- 5 P. J. Parbrook, B. Henderson, K. P. O'Donnell, P. J. Wright and B. Cockayne, *Semicond. Sci. Technol.*, **6** (1991) 818.
- 6 V. S. Speriosu and T. Vreeland, Jr., *J. Appl. Phys.*, **56** (1984) 1591.
- 7 F. Yang, P. J. Parbrook, C. Trager, B. Henderson, K. P. O'Donnell, P. J. Wright and B. Cockayne, *Superlattices Microstruct.*, **9** (1991) 461.



# Atomic layer control of the growth of oxide superconductors using laser molecular beam epitaxy

Hitoshi Tabata\* and Tomoji Kawai

The Institute of Scientific and Industrial Research, Osaka University, Mihogaoka, Ibaraki, Osaka 567 (Japan)

## Abstract

The control of atomic layers in high  $T_c$  cuprate compounds has recently become possible using computer-controlled laser molecular beam epitaxy. Taking advantage of this method, a variety of high  $T_c$  superconducting artificial lattices has been constructed by layer-by-layer growth with atomic layer and sub-unit-cell layer accuracy, and the basic structural factors of high  $T_c$  cuprates have been controlled artificially. In  $\text{Bi}_2\text{Sr}_2\text{Ca}_{n-1}\text{Cu}_n\text{O}_{2n+4}$  artificial lattices, the number of  $\text{CuO}_2$  planes in the unit formula was changed from one to as much as eight. Furthermore, site-selective substitution has been carried out by inserting exotic ions into calcium or strontium sites, and the crystal structures and  $T_c$  can be controlled artificially.

## 1. Introduction

The high  $T_c$  superconductivity of cuprate compounds is believed to derive from the two-dimensional  $\text{CuO}_2$  plane doped with a charged carrier. Accordingly, control of the crystal structure based on the  $\text{CuO}_2$  plane is essential for elucidation of high  $T_c$  superconductivity. These structural parameters include the number of  $\text{CuO}_2$  sheets in a unit formula, the spacing between the  $\text{CuO}_2$  sheets [1, 2], the in-plane Cu–O bond length or Cu– $\text{O}_{\text{apex}}$  bond length, as well as the effective concentration of the charged carrier in the  $\text{CuO}_2$  plane [3].

Using layer-by-layer construction of the crystal structure, with atomic layer or unit cell layer accuracy, we are able to control artificially these parameters of the  $\text{CuO}_2$ -based structure which are essential for high temperature superconductivity. This allows the construction of new superconductors which have a new arrangement of atomic layers. Furthermore, we studied the correlation between  $T_c$  and crystal structure (the distance between  $\text{CuO}_2$  layers) by inserting exotic atoms at the strontium or calcium site in  $\text{Bi}_2\text{Sr}_2\text{Ca}_1\text{Cu}_2\text{O}_8$  compounds.

In this article, we describe the control of growth of  $\text{CuO}_2$ -based layers on the atomic layer scale and sub-unit layer scale in the construction of artificial lattices in the  $\text{Bi}_2\text{Sr}_2\text{Ca}_{n-1}\text{Cu}_n\text{O}_{2n+4}$  system. This technique was further employed for site-selective substitution of calcium and/or strontium in  $\text{Bi}_2\text{Sr}_2\text{Ca}_1\text{Cu}_2\text{O}_8$  by exotic ions having different ionic radii and different valences.

## 2. Experiment

Figure 1 is a schematic diagram of the laser molecular beam epitaxy (laser MBE) apparatus used for the construction of superconducting artificial lattices. The ArF excimer laser pulses are focused on the target and ablation is induced on the surface of the target. The emitted atoms and ions accumulate on the substrate surface under  $\text{NO}_2$  atmosphere, and thin layers are grown, layer-by-layer, by changing the target as desired. Growth of the layers is monitored *in situ* by reflection high-energy electron diffraction (RHEED) and Auger electron spectroscopy (AES) and by a thickness monitor [4].

## 3. Results and discussion

### 3.1. Atomic layer and sub-unit-cell layer growth of artificial lattices: $(\text{Ca}, \text{Sr})\text{CuO}_2$ and $\text{Bi}_2\text{Sr}_2\text{Ca}_{n-1}\text{Cu}_n\text{O}_{2n+4}$

The topmost layer of bare  $\text{SrTiO}_3(100)$  was examined first. Monolayers of strontium oxide and titanium oxide were deposited in different sequences onto the substrate, and the RHEED patterns were compared. The deposition of one atomic layer of SrO or TiO could be strictly controlled using the oscillation of RHEED intensity and the thickness monitor using a quartz crystal oscillator [4, 5]. Deposition of the monolayer of strontium oxide onto  $\text{SrTiO}_3$  (Sr/STO) produced a clear oscillation of the RHEED intensity, and a streaky RHEED pattern was maintained throughout the deposition (Fig. 2). This behavior indicates that the SrO layer can be formed on the substrate with two-dimen-

\*On leave from Kawasaki Heavy Ind., Ltd., 1-1 Kawasaki-cho, Akashi 673, Japan.

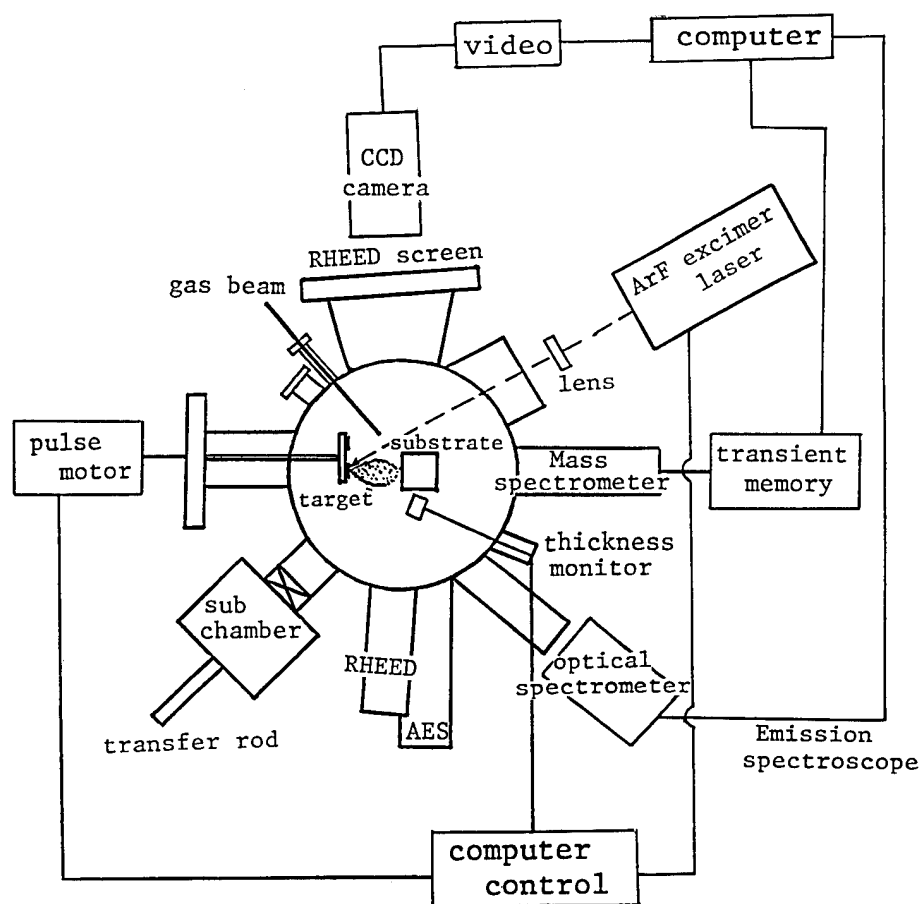


Fig. 1. Apparatus for computer-controlled laser MBE.

sional atomic layer growth. Deposition of the  $\text{TiO}_x$  monolayer onto the  $\text{SrO}_x$  deposited substrate (Ti/Sr/STO) also produced a clear oscillation of the RHEED intensity and the streaky RHEED pattern. However, direct deposition of  $\text{TiO}_x$  onto the substrate (Ti/STO) did not produce a clear intensity oscillation and the RHEED pattern was blurred. This suggests that the  $\text{TiO}_2$  layer is the topmost layer of the bare  $\text{SrTiO}_3$  (100) surface and growth of the SrO layer is suitable as the first layer in the film [6].

The RHEED pattern of SCO on Sr/STO shows that the surface has a  $2 \times 2$  (or twin of a  $2 \times 1$ ) superstructure (see Fig. 2(c)). We think that the superstructure is due to ordered oxygen deficiency in the Sr–O top layer. Because the  $\text{CuO}_2^{2-}$  layer has a negative charge, oxygen deficiency in the SrO layer to form  $\text{Sr}^{2+}$  is needed to maintain charge neutrality.

Finally, the deposition of bismuth oxide onto SCO/Sr/STO produced the  $\text{Bi}_2\text{Sr}_2\text{CuO}_6$  (2201) structure. The  $2 \times 2$  structure of SCO/Sr/STO disappeared after bismuth deposition (Fig. 2(d)). The formation of the 2201 structure was also confirmed by its X-ray diffraction pattern after 10 repetitions of these cycles.

Next, atomic layer control using laser MBE was examined in the (Ca, Sr) $\text{CuO}_2$  system, the parent material of high  $T_c$  cuprate superconductors, and the growth mechanism was investigated by RHEED and AES (Fig. 2) [7]. Analysis of RHEED patterns and intensity oscillations indicates that this material grows by two-dimensional layer growth. When all the metal elements were supplied simultaneously in an  $\text{NO}_2$  atmosphere, layer growth occurred in the unit-cell layer of (Ca, Sr) $\text{CuO}_2$ . The growth unit could be separated into a Ca(Sr) atomic layer and a  $\text{CuO}_2$  atomic layer by monitoring the RHEED intensity oscillation. The successive supply of each metal element in  $\text{NO}_2$  atmosphere resulted in one atomic layer growth of this metal oxide material.

Figure 3 shows the change in X-ray diffraction pattern with the variation in strontium concentration. Figures 3(a)–(c) show the patterns of films formed by codeposition, and those in Figs. 3(d)–(g) were formed by atomic layer stacking. Using codeposition of all the elements,  $\text{Ca}_{1-x}\text{Sr}_x\text{CuO}_2$  thin films can only be formed at strontium concentrations  $x$  below 0.2 (Fig. 3(a)). However, using alternate stacking of atomic layers,  $\text{Ca}_{1-x}\text{Sr}_x\text{CuO}_2$  can be formed for strontium concentra-

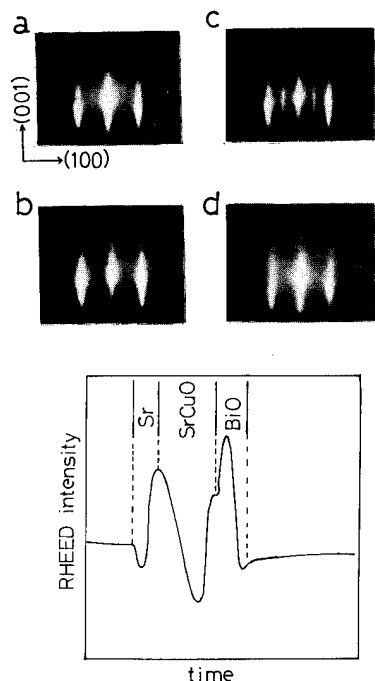


Fig. 2. RHEED pattern and change in intensity during the growth of  $\text{Bi}_2\text{Sr}_2\text{Cu}_1\text{O}_6$  thin film on  $\text{SrTiO}_3(100)$  (a) by the successive deposition of Sr (b) / $\text{SrCuO}$  (c) / $\text{BiO}$  (d).

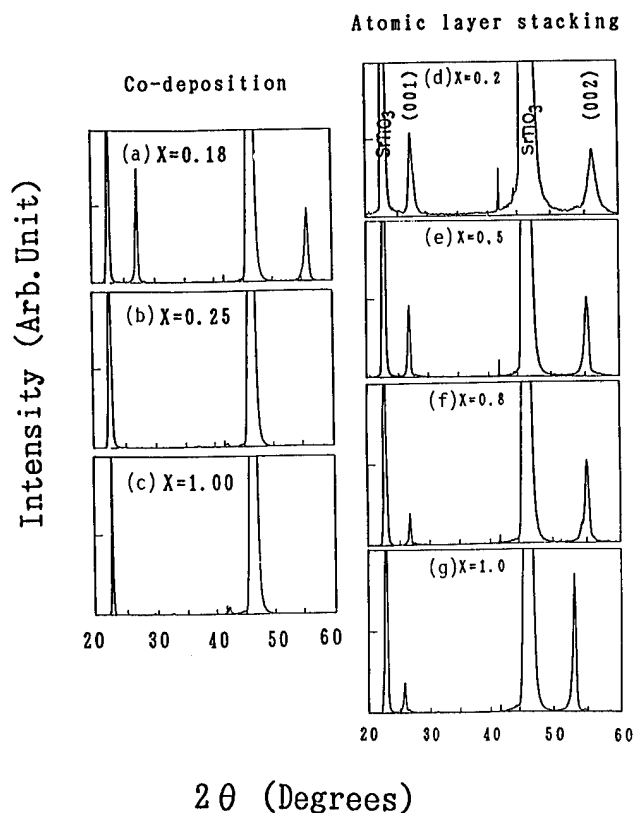


Fig. 3. X-ray diffraction patterns of  $\text{Ca}_{1-x}\text{Sr}_x\text{CuO}_2$  films formed by codeposition (a)–(c), and by atomic layer stacking (d)–(g).

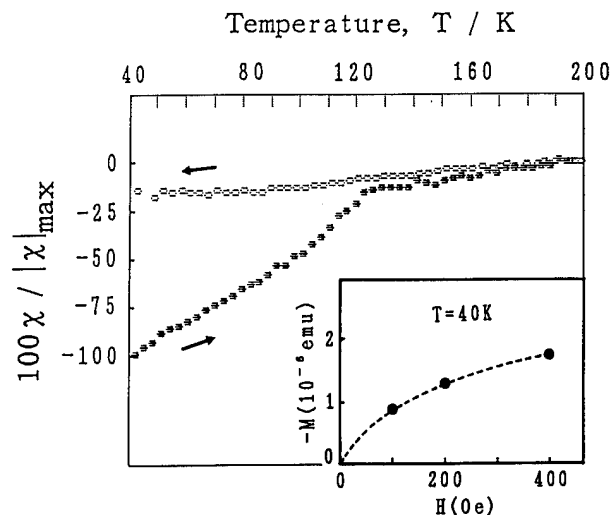


Fig. 4. Temperature dependence of the magnetic susceptibility of  $\text{Ca}_{0.2}\text{Sr}_{0.8}\text{CuO}_2$  thin film.

tions up to  $x = 1.0$  (Fig. 3(g)). This result indicates that the layer-by-layer stacking of atomic layers is effective for the artificial construction of these layered structures. This thin film shows a critical temperature of 120 K (Fig. 4), which is one of the highest values of  $T_c$  for cuprate superconductors.

Using the layer-by-layer method,  $\text{CaCuO}$  and  $\text{SrCuO}$  and bismuth were supplied successively, and  $\text{Bi}_2\text{Sr}_2\text{Ca}_{n-1}\text{Cu}_n\text{O}_{2n+4}$  was formed, with  $n$  in the range from 1 up to 8, by monitoring the surface with RHEED [8].

The RHEED patterns showed streaks throughout the growth process, indicating that these materials can be formed by layer-by-layer growth with flat surfaces. Monitoring the changes in the diffraction intensity and analyzing the total diffraction pattern made it possible to control the growth of the atomic layer or the sub-unit layers in this  $\text{Bi}_2\text{Sr}_2\text{Ca}_{n-1}\text{Cu}_n\text{O}_{2n+4}$  system.

### 3.2. Site-selective substitution

Laser MBE was further applied to site-selective substitution of  $\text{Bi}_2\text{Sr}_2\text{CaCu}_2\text{O}_8$ . The calcium or strontium ion was replaced site selectively by +1, +2, and +3 ions (see Fig. 5) [9].

Figure 6(a) shows the relationship between the lattice constant  $c$  and ionic radii in  $\text{Bi}_2\text{Sr}_2\text{Ca}_1\text{Cu}_2\text{O}_8$  films with ions incorporated at the calcium site. It was found that the lattice parameter  $c$  is dependent on the ionic radius of the incorporated ion. When a small ion, such as magnesium or lithium, was incorporated at the calcium site, the lattice constant  $c$  decreased, and when a large ion, such as barium or potassium, was incorporated it increased. This makes it clear that the distance between  $\text{CuO}_2$  planes increases when large ions are inserted and decreases when small ions are inserted.

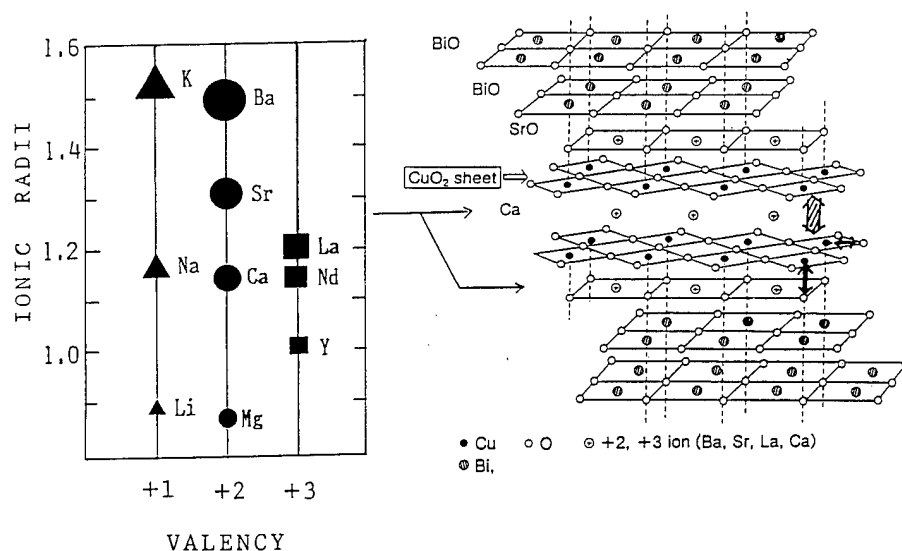


Fig. 5. A schematic diagram of the structure of layered  $\text{Bi}_2\text{Sr}_2\text{Ca}_1\text{Cu}_2\text{O}_8$  superconductor. Important structural factors based on  $\text{CuO}_2$  sheets and the carrier concentration can be changed by incorporation of ions with different radii and valence states.

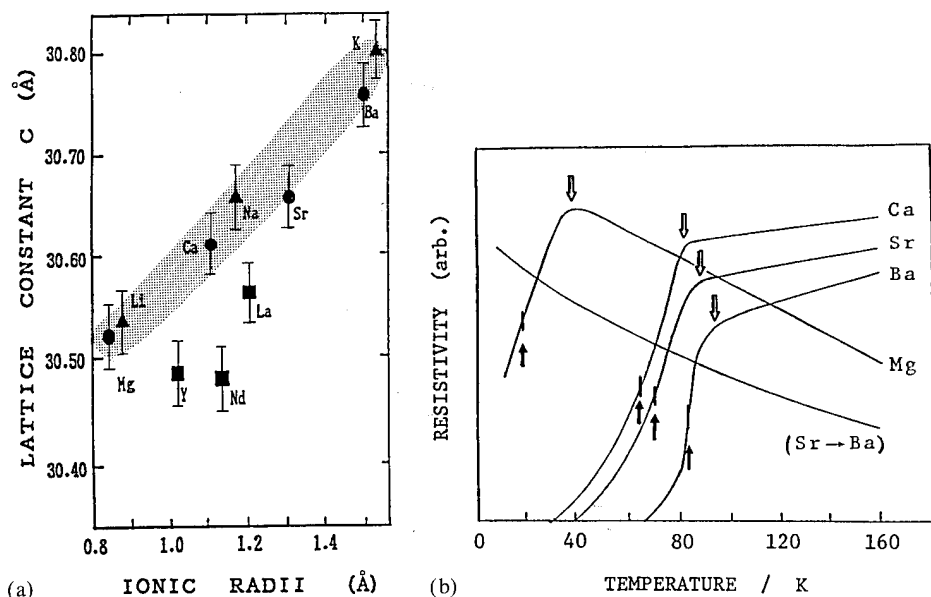


Fig. 6. (a) Lattice constant  $c$  vs. ionic radius of ion incorporated at the calcium site in  $\text{Bi}_2\text{Sr}_2\text{Ca}_1\text{Cu}_2\text{O}_8$  films. (b) Temperature-resistivity curves for  $\text{Bi}_2\text{Sr}_2\text{Ca}_1\text{Cu}_2\text{O}_8$  films containing various +2 ions at the calcium site.

These tailored films in which calcium ions were replaced by +1, +2 or +3 ions showed systematic changes in their resistance-temperature curves. For example, the  $R$ - $T$  curves for +2 ions magnesium, calcium, strontium and barium incorporated at the calcium site are shown in Fig. 6(b). It is clear that the larger the substituted ion, the higher the  $T_c$ . The highest  $T_c$  is that for barium substitution,  $T_{c, \text{onset}}$  was 95 K and  $T_{c, \text{mid}}$  was 83 K. Site-selective substitution of calcium by exotic atoms produced drastic differences in superconductivity depending on the ionic radius and valence state. The insertion of larger ions at the calcium site makes the  $c$  axis longer. Accordingly, the spacing be-

tween double  $\text{CuO}_2$  planes can be changed using this technique, and we found that the spacing of  $\text{CuO}_2$  planes has a strong effect on the value of  $T_c$ . It has been reported that hopping of copper pairs may be important for the  $T_c$  value [10]. The results of our study indicate that the distance between the layers is a very important factor of the  $T_c$  value.

#### 4. Conclusion

In conclusion, we have achieved growth control of  $\text{Bi}_2\text{Sr}_2\text{Ca}_{n-1}\text{Cu}_n\text{O}_{2n+4}$  and  $\text{Ca}_{1-x}\text{Sr}_x\text{CuO}_2$  with

atomic layer or sub-unit-cell accuracy. Furthermore the layer-by-layer laser ablation method has been applied to site-selective substitution of +1, +2, and +3 ions at the calcium and strontium sites of  $\text{Bi}_2\text{Sr}_2\text{Ca}_1\text{Cu}_2\text{O}_8$ , and the correlation between  $T_c$  and lattice parameter  $c$  was explained on the basis of the distance between  $\text{CuO}_2$  layers.

The layer-by-layer growth technique using laser MBE is one of the most promising methods by which to construct a variety of superconducting artificial lattices and to elucidate the mechanism of high  $T_c$  superconductivity.

## References

- 1 T. Siegrist, S. M. Zahurak, D. W. Murphy and R. S. Roth, *Nature*, 334 (1988) 231.
- 2 D. G. Schlom, A. F. Marshall, J. T. Sizemore, Z. J. Chen, J. N. Eckstein, I. Bozovic, K. E. von Dessonneck, J. S. Harris, Jr., and J. C. Bravman, *J. Cryst. Growth*, 102 (1990) 361.
- 3 H. Tabata, T. Kawai and S. Kawai, *Appl. Phys. Lett.*, 58 (1991) 1443.
- 4 M. Kanai, T. Kawai and S. Kawai, *Jpn. J. Appl. Phys.*, 31 (1992) L331.
- 5 M. Kanai, T. Kawai and S. Kawai, *Appl. Phys. Lett.*, 58 (1991) 771.
- 6 T. Sakamoto, N. Kawai, T. Nakagawa, K. Ohta and T. Kojima, *Appl. Phys. Lett.*, 47 (1985) 617.
- 7 X. Li, M. Kanai, T. Kawai and S. Kawai, *Jpn. J. Appl. Phys.*, 31 (1992) L217.
- 8 T. Kawai, Y. Egami, H. Tabata and S. Kawai, *Nature*, 349 (1991) 200.
- 9 H. Tabata, O. Murata, T. Kawai and S. Kawai, *Appl. Phys. Lett.*, 56 (1990) 1576.
- 10 J. M. Wheatley, T. C. Hsu and P. W. Anderson, *Nature*, 333 (1988) 121.

# Analytical and chemical techniques in the study of surface species in atomic layer epitaxy

S. Haukka

*Microchemistry Ltd., P.O. Box 45, 02151 Espoo, and University of Helsinki, Department of Chemistry, Analytical Chemistry Division, Vuorikatu 20, 00100 Helsinki (Finland)*

E.-L. Lakomaa and T. Suntola

*Microchemistry Ltd., P.O. Box 45, 02151 Espoo (Finland)*

## Abstract

An extension of atomic layer epitaxy (ALE) to a porous, high-surface-area substrate commonly used in catalysis is presented. Because of the high surface area, even a sublayer of species bound to the substrate in an ALE sequence can be determined quantitatively. Thus, various analytical and chemical techniques, in addition to the high vacuum techniques, can be applied in the study of surface reactions and surface species in ALE after a single reaction step. Use of Fourier transform IR spectroscopy, nuclear magnetic resonance, X-ray diffraction, chemical analysis and etching experiments in the characterization of different titanium species on porous silica processed using  $\text{TiCl}_4$  and  $\text{H}_2\text{O}$  is presented.

## 1. Introduction

Atomic layer epitaxy (ALE) has been used for the growth of various single-crystal and polycrystalline materials, mainly on small-area substrates. In our previous paper [1] ALE was used to grow  $\text{TiO}_2$  on a porous, high-surface-area silica substrate. The first four reaction cycles of  $\text{TiCl}_4$  and  $\text{H}_2\text{O}$  on silica were studied, but the more thorough study of the reaction mechanisms called for the development and application of different analysis methods [2]. Earlier only reaction temperatures of 175 and 450 °C were used.

The objective of this study was to find out how ALE can be used to bind titanium species to porous  $\text{SiO}_2$  using  $\text{TiCl}_4$  and  $\text{H}_2\text{O}$  vapors as reactants, and to introduce wet-chemical methods together with Fourier transform IR spectroscopy (FTIR), nuclear magnetic resonance (NMR) and X-ray diffraction (XRD) to study the reaction mechanisms involved. The use of these various analysis methods in the study of a single ALE sequence in the temperature range 175–550 °C with silica preheated at 560 °C is dealt with in the following.

## 2. Experimental details

### 2.1. Reagents

$\text{SiO}_2$  (EP 10, Crosfield Ltd.) with a surface area of  $300 \text{ m}^2 \text{ g}^{-1}$ , pore volume of  $1.75 \text{ cm}^3 \text{ g}^{-1}$  and mean particle size of  $100 \mu\text{m}$  was used as the substrate.  $\text{SiO}_2$  was preheated for 16 h at 560 °C in air at atmospheric

pressure and for 3 h in nitrogen flow at 6–10 kPa before the reaction.  $\text{TiCl}_4$  (Merck) without further purification, vaporized at 25 °C, and deionized water vaporized at 25 °C were used as reactants.

### 2.2. Equipment

A modified MC 120 reactor (Microchemistry Ltd.) with a reaction chamber made of quartz was used in the experiments (Fig. 1). The reaction chamber can hold up to 10 g of silica powder. The reactions were carried out at a pressure of 6–10 kPa in nitrogen atmosphere. The sampling was made in an inert glove box in nitrogen atmosphere (MBraun).

### 2.3. ALE procedure

Silica preheated at 560 °C (5–8 g) was stabilized to the reaction temperature. A pulse of  $\text{TiCl}_4$  vapor was fed into the reaction chamber through a solid silica bed supported on a sinter. Pumping of excess reactant and the  $\text{HCl}$  released during the reactions took place from the bottom of the silica bed (Fig. 1). Reaction temperatures of 175, 250, 350, 450 and 550 °C were used. Reaction times were 1–2 h followed by a nitrogen purge of same length at the reaction temperature concerned.

### 2.4. Analysis methods

The total titanium concentration was determined by UV–visible spectrophotometry or neutron activation analysis as described in ref. 3. Etching tests in connection with element determinations were developed for distinguishing titanium species [2, 3]. Amorphous tita-

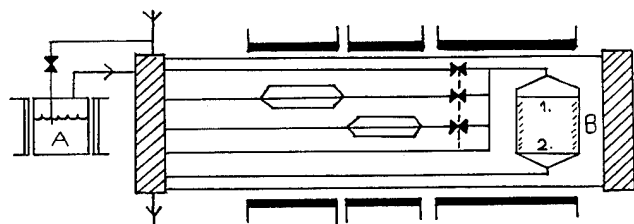


Fig. 1. ALE equipment and sampling for surface saturation studies. Reactants are fed through the silica bed in a flow of nitrogen. Reaction products and excess reactants are pumped from the bottom of the bed. Samples are taken from the surface (1) and the bottom (2): A is the vessel for  $\text{TiCl}_4$  and B is the reaction chamber.

nium species were etched with 3.5 M  $\text{H}_2\text{SO}_4$  and the amount of titanium determined in the solutions by UV-visible spectrophotometry.

Samples for determination of chloride content were weighed immediately in 3 M  $\text{H}_2\text{SO}_4$  after the sample was removed from the reaction chamber so that the air moisture could not release chloride as  $\text{HCl}$ . Potentiometric titration was used to quantify the chloride.

The type of bonding sites and the sites remaining after the ALE reaction on silica were analyzed with an FTIR spectrometer (Galaxy Series 6020) installed in a glove box, into which the samples were transferred inertly. The samples were loaded on the sample holder, and the spectra were recorded using a spectral resolution of  $2\text{ cm}^{-1}$ . The accumulation time was 4.5 min, corresponding to 1000 scans.

XRD spectra were measured with a Siemens 500 diffractometer with  $\text{Cu K}\alpha$  excitation. The  $^1\text{H}$ - and  $^{29}\text{Si}$ -NMR measurement procedure was as described in ref. 2.

### 3. Results and discussion

#### 3.1. Surface species of silica

Porous, high-surface-area silica is a complicated substrate, which consists of different reactive sites: isolated (including single and geminal) and hydrogen-bonded OH groups and siloxane bridges [2, 4]. A simplified picture of these reactive sites is shown in Fig. 2. The groups serving as bonding sites for a reagent depend on the chemical characteristics of the reactant vapor, the chemical state of the substrate and the reaction temperature. Characterization of the support and its bonding sites is vital when studying the reaction mechanisms in ALE. In this work silica preheated at  $560^\circ\text{C}$  was used. This silica contains 1.6 isolated and 0.5 hydrogen-bonded OH groups per square nanometer, measured by  $^1\text{H}$  NMR and reported in ref. 2. The hydrogen-bonded OH groups on  $560^\circ\text{C}$  silica are inaccessible (bulk OH groups) and unreactive towards any reactant.

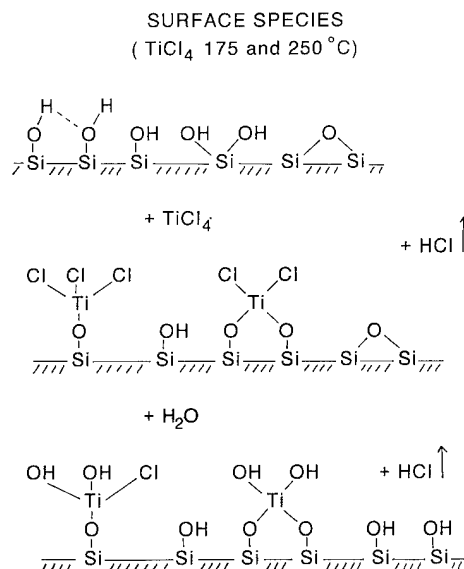


Fig. 2. Bonding sites of silica and titanium surface species at reaction temperatures of 175 and  $250^\circ\text{C}$ , when first  $\text{TiCl}_4$  and then  $\text{H}_2\text{O}$  is brought through the silica bed.

#### 3.2. Surface saturation

Quantitative determination of titanium and chloride bound from the single reaction step of  $\text{TiCl}_4$  is not reliable using instrumental surface analysis techniques, but the amount of titanium can be determined accurately by dissolution of the species concerned and analysis of the solutions with conventional methods such as UV-visible spectrophotometry, or neutron activation analysis as described in ref. 3. A proper sample handling technique assured the quantitation of chloride in the samples. Surface saturation in the silica bed after a single pulse of  $\text{TiCl}_4$  was confirmed by determining titanium and chloride concentrations in samples taken from the surface and the bottom part of the bed. Saturation was achieved when the titanium and chloride concentrations at the surface corresponded to those at the bottom, meaning that the bonding sites inside the pores were also reached by the reactant. The disappearance of bonding sites could be followed by FTIR in both samples. The reproducibility of the ALE process was good as evaluated by titanium saturation levels and the amount of etchable titanium species from parallel runs.

#### 3.3. Surface species after a single pulse of $\text{TiCl}_4$

Two different reaction temperature ranges could be distinguished: a lower reaction temperature range from 175 to  $250^\circ\text{C}$  and a higher range from 350 to  $550^\circ\text{C}$ . Both were studied first by determining titanium, chloride and etchable titanium species from samples prepared at different temperatures. FTIR was used to follow the type of bonding sites used in the reactions.

**Lower reaction temperature.** Figure 2 shows the surface species present at 175 and 250 °C. Earlier [2] it was confirmed by  $^1\text{H}$  NMR measurements that at 175 °C  $\text{TiCl}_4$  reacts directly with OH groups and no siloxane bridges are involved in the reactions. Now this was shown to be true for the reaction temperature of 250 °C as well. The results of the  $[\text{Cl}]/[\text{Ti}]$  ratio indicated that  $\text{TiCl}_4$  reacted both mono- and bifunctionally. The binding took place with the isolated OH groups of silica, but some OH groups remained intact (Fig. 3). Either the activation energy of chemisorption to those OH groups is not yet exceeded at the lower reaction temperatures, or the chlorides bound to titanium species hinder the penetration of  $\text{TiCl}_4$  into these groups. No interaction of the HCl released in the reactions with OH groups of silica was observed at the lower reaction temperatures [2]. Etching with sulfuric acid removed all titanium bound at 175 and 250 °C from the surface. Amorphous titanium was present on the surface as verified by XRD measurements.

Treatment of the  $\text{TiCl}_x\text{-SiO}_2$  surface with water vapor at 175 or 250 °C could not remove all the chloride, but 84%–87% of the chloride present was released. Water vapor did not remove any titanium [2, 3].

**Higher reaction temperature.** The possible surface species present on silica at higher reaction temperatures

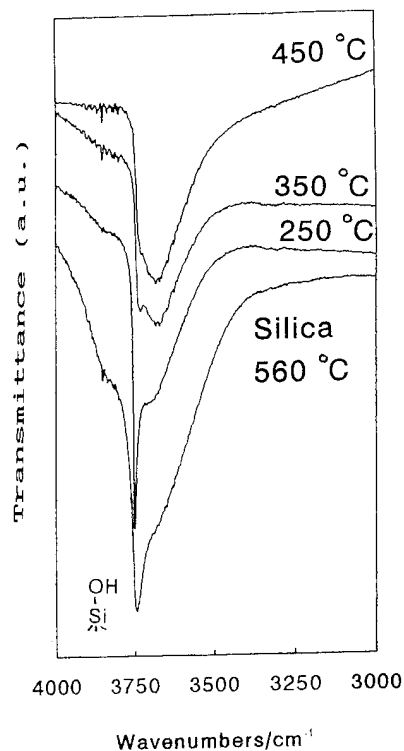


Fig. 3. FTIR spectra of silica preheated at 560 °C and after being treated with  $\text{TiCl}_4$  at 250, 350 and 450 °C. The band of isolated OH groups is shown between 3741 and 3746  $\text{cm}^{-1}$ .

#### SURFACE SPECIES ( $\text{TiCl}_4 > 350^\circ\text{C}$ )

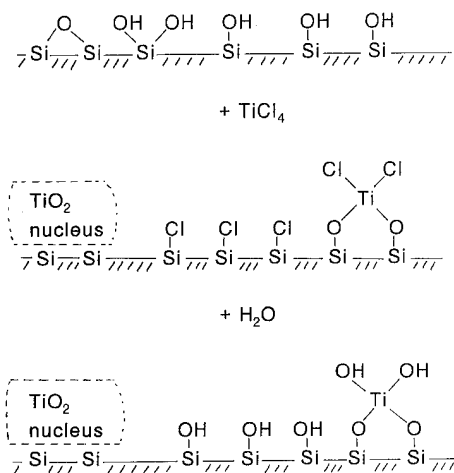


Fig. 4. Bonding sites of silica and titanium surface species at reaction temperatures over 350 °C, when first  $\text{TiCl}_4$  and then  $\text{H}_2\text{O}$  vapor is brought through the silica bed.

are shown in Fig. 4. Earlier we noticed that XRD peaks could be detected after only a single pulse of  $\text{TiCl}_4$  at 450 °C without any high temperature water vapor treatment [2]. Both anatase and rutile forms were found at 450 °C. This phenomenon was studied further using different reaction temperatures. Crystalline  $\text{TiO}_2$  could be measured by XRD first when the reaction temperature was raised to 350 °C and above. In spite of the agglomeration, we found that surface saturation was valid, and isolated OH groups disappeared during the reaction (Fig. 3). Only some of the titanium was etched with sulfuric acid. The amount of these etchable species decreased with increasing reaction temperature from 30% to 18%. The XRD spectra recorded before and after etching were the same, which confirmed that the titanium species released was of amorphous character. It is unclear whether the amorphous species is directly bound to the OH groups of silica. The calculated  $[\text{Cl}]/[\text{Ti}]$  ratio was 2 at 450 °C, which could lead to the conclusion that only bifunctional binding occurred.  $^{29}\text{Si}$ -NMR measurements showed indirectly, however, that most of the OH groups of silica must have been occupied by the chloride, since the water-treated titanium-silica sample gave an identical  $^{29}\text{Si}$ -NMR spectrum to the spectrum recorded from untreated silica [2]. Furthermore, the FTIR spectrum was similar to that of untreated silica. At higher temperatures the interaction of HCl was evident [2]. Therefore, the interaction of HCl evolved during the main reaction could be responsible for the chloride bound to the surface. This interaction of HCl could lead to release of one water molecule per HCl molecule reacted with an OH group, and water



is thus present during the  $\text{TiCl}_4$  pulsing. This could further cause molecular-scale growth of  $\text{TiO}_2$ , which is reproducible on a macroscopic scale and stops when the bonding sites of silica are occupied either by  $\text{TiCl}_x$  or chloride.

The water vapor treatment of  $\text{TiCl}_x\text{-SiO}_2$  at higher reaction temperatures releases chloride below the detection limit of the determination method used in this study, namely less than  $0.006 \text{ atoms nm}^{-2}$ . After the first reaction cycle of  $\text{TiCl}_4 + \text{H}_2\text{O}$ , new OH groups are also formed from Si-Cl and Ti-Cl groups. As verified by  $^1\text{H-NMR}$  measurements [2], only OH groups of titanium bound to amorphous titanium species were present, as illustrated in Fig. 4. These new OH groups of silica and amorphous titanium species serve as bonding sites for the second pulse of  $\text{TiCl}_4$ .

#### 4. Conclusions

ALE was used for binding titanium species on a porous, high-surface-area substrate. The use of saturated surface reactions ensured homogeneous distribution of titanium species of  $\text{SiO}_2$ , as verified by measuring the disappearance of reactive OH groups by FTIR and  $^1\text{H-NMR}$ . XRD measurements and additional measurements on water-treated samples by  $^{29}\text{Si-NMR}$  showed that at reaction temperatures above  $350^\circ\text{C}$  another reaction mechanism leading to Si-Cl groups and release of water takes place. The effect of the side reaction is the formation of agglomerated  $\text{TiO}_2$  on silica. The agglomeration is also controlled by the number of OH groups of silica present at the surface.

The use of several analytical methods is needed in studying the reaction mechanisms on porous, high-surface-area substrates. Analysis of both the support itself and the ALE prepared samples is necessary. Special emphasis must be placed on good accuracy of element

determinations. Proper sample handling before chloride determinations and accurate titanium determinations were essential so that the analytical error of the  $[\text{Cl}]/[\text{Ti}]$  ratio could be decreased. Wet-chemical methods such as the etching test used in this work are of good value for the speciation of different forms present on the surface. The combination of wet-chemical methods and bulk analysis methods such as FTIR and NMR can produce information on the surface species not attainable with ultrahigh vacuum surface analysis techniques.

The study of ALE reaction mechanisms of the first reaction cycles are possible with the analysis methods described here in the case when a high-surface-area substrate is used. Characterization of the bonding sites of the substrate is important, and because of the different character of porous substrates, the reaction mechanisms may differ from those in thin film and single-crystal applications.

#### Acknowledgments

The authors thank M. Rissanen (Microchemistry Ltd.) for the ALE processing, J. Vilhunen and A. Root (Neste Co., Analytical Research) for the XRD and NMR measurements respectively. The University of Joensuu provided us with use of the FTIR equipment. This study was funded in part by the Academy of Finland.

#### References

- 1 E.-L. Lakomaa, S. Haukka and T. Suntola, *Appl. Surf. Sci.*, **60-61** (1992) 742.
- 2 S. Haukka, E.-L. Lakomaa and A. Root, submitted to *J. Phys. Chem.*
- 3 S. Haukka and A. Saastamoinen, *Analyst*, **117** (1992) 1381.
- 4 D. W. Sindorf and G. E. Maciel, *J. Am. Chem. Soc.*, **105** (1983) 1487.

# Self-limiting adsorption and *in situ* optical monitoring for atomic layer epitaxy of oxide superconductors

S. Oda, H. Zama, K. Fujii, K. Sakai and Y. C. Chen

Department of Physical Electronics, Tokyo Institute of Technology, 2-12-1 O-okayama, Meguro-ku, Tokyo 152 (Japan)

## Abstract

Preliminary steps toward atomic layer epitaxy of  $\text{YBa}_2\text{Cu}_3\text{O}_x$  films were studied by chemical vapor deposition (CVD) which may be a suitable method for atomic layer epitaxy since the sticking probability of precursors to the growing substrate surface can be controlled digitally.

The feasibility of self-limiting adsorption of precursors for CVD of  $\text{YBa}_2\text{Cu}_3\text{O}_x$  was investigated using an ultrahigh vacuum CVD apparatus. Experimental observation using a mass analyzer of the amount of adsorbed species for various adsorption times, gas flow rates, and temperatures provides possible, although not conclusive, evidence of self-limiting adsorption.

We applied *in situ* optical diagnostics for the first time to layer-by-layer CVD of  $\text{YBa}_2\text{Cu}_3\text{O}_x$ . Variations in reflectance signals of a 780 nm diode laser from the growing surface were observed, similar to reflectance high-energy electron diffraction oscillation, upon sequential supply of precursors and oxygen. The amplitude of the change in reflectance was surprisingly large. The transient time and steady-state reflectance level depend on the species of the surface. A possible mechanism of reflectance oscillation is discussed.

## 1. Introduction

In order to implement novel high-speed electron devices based on oxide superconductors, with highly anisotropic transport properties and short coherent length, a method for epitaxial growth of thin films with atomic-scale surface smoothness must be developed. Many attempts to prepare thin films of oxide superconductors using layer-by-layer methods have been reported [1, 2]. Some reports are accompanied by reflectance high-energy electron diffraction (RHEED) oscillation data as evidence of atomically controlled growth.

However, for the preparation of atomic-scale smooth surfaces with wafer-scale uniformity, the artificial control system based on counting the number of atoms impinging on the growing surface may not work very well. A crystal growth method with a built-in natural self-limiting mechanism, such as atomic layer epitaxy (ALE) as proposed by Suntola [3], is preferable.

Chemical vapor deposition (CVD) is a suitable method for this purpose because the sticking probability of precursors onto the growing surface can be controlled digitally. In an attempt to evaluate the feasibility of self-limiting growth of  $\text{YBa}_2\text{Cu}_3\text{O}_x$  films, properties of surface-adsorbed species were investigated.

Optical diagnostics are suitable for monitoring atomic layer growth in the CVD environment, where electron-beam methods cannot be applied. Aspnes *et al.* [4] developed reflectance difference spectroscopy based on the symmetry of surface reconstruction to enhance

contributions from the growing surface over that from the bulk. Kobayashi and Horikoshi [5] developed a surface photoabsorption method which used p-polarization light incident at the Brewster angle to minimize the contribution from the bulk. These methods have been used to monitor growth by metal-organic CVD of GaAs and related systems. Information concerning the chemistry of the growing surface has been obtained.

In the course of our investigation of layer-by-layer CVD of oxide superconductors, we found that the reflectance of the growing surface changes significantly when gaseous precursors or oxygen are introduced into the reactor chamber, suggesting that optical measurements may be useful for real-time monitoring of the growth processes.

In this report, we present our recent experimental results on the self-limiting surface adsorption characteristics of precursors and *in situ* optical measurements of CVD of  $\text{YBaCuO}$  films.

## 2. Self-limiting adsorption of precursors

A  $\beta$ -diketonate complex,  $\text{Cu}(\text{DPM})_2$ , one of the precursors for CVD growth of  $\text{YBa}_2\text{Cu}_3\text{O}_x$  films, was vaporized, introduced into a vacuum chamber and then adsorbed onto the surface of a sapphire substrate at a temperature of typically 100 °C. Then, the substrate temperature was raised at a constant rate using a focused IR light so as to heat the substrate only. With

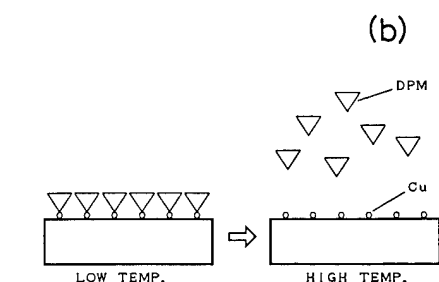
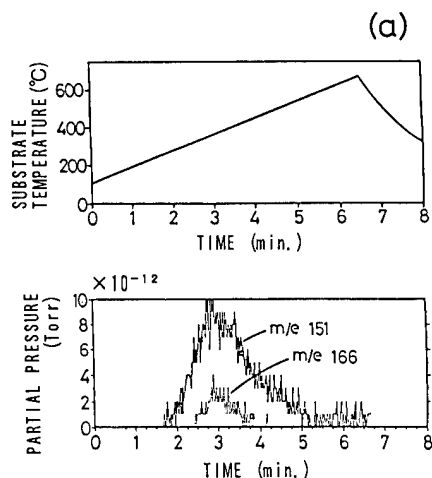


Fig. 1. (a) Variation of the mass-analyzer signal intensity for  $m/e = 151$  and  $m/e = 166$  measured at a constant rise in temperature (top graph). (b) Schematic model for adsorption and desorption of Cu-DPM.

increasing temperature, the adsorbed species acquire enough energy to be released from the surface. A quadrupole mass analyzer was used to monitor the chemical species desorbed from the surface. The sensitivity of the mass analyzer and the background level in the present range of below  $10^{-12}$  Torr, which is enough to characterize the monoatomic layer of the surface.

As shown in Fig. 1(a), when the temperature was increased at a constant rate, a notable change in the mass spectra appeared at mass numbers 151 and 166, fragments of DPM, which started to evolve at 250 °C and 320 °C respectively. As the substrate temperature increased further, the signal of the mass spectra reached a peak and then fell to background levels, where the physically adsorbed species had been removed, leaving the chemically bonded atoms, as depicted in Fig. 1(b). Therefore, by observing the integral amount of thermally desorbed species, we can evaluate the amount of adsorbed species. As shown in Fig. 2, the integral amount of desorbed species with  $m/e = 151$  increases linearly at first with increasing adsorption time, and then saturates at a certain value. When the temperature of the copper vaporizer is raised from 93 °C to 100 °C, *i.e.* the vapor pressure is doubled, the rate of the initial rise in the desorbed species is doubled, the time re-

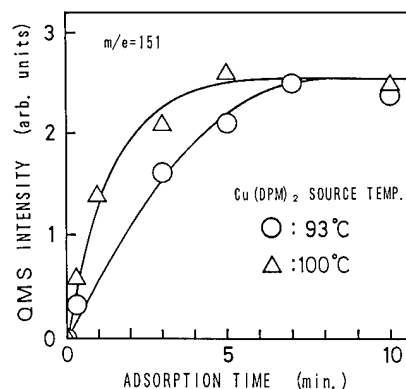


Fig. 2. Integrated mass signal of desorbed species ( $m/e = 151$ ) vs. adsorption time.

quired to reach saturation is half of the original value, but the saturation value is almost the same. This suggests that the saturation is not simply due to the balance between adsorption and desorption, but that self-limiting adsorption takes place [6].

The surface chemistry of the substrate treated by the adsorption of  $\text{Cu}(\text{DPM})_2$  and thermal desorption cycles was analyzed by electron spectroscopy for chemical analysis (ESCA).

The number of copper atoms deduced from ESCA spectra, however, was about 10% of a monoatomic layer. This may be attributed to the steric hindrance of large molecules of DPM, as shown schematically in Fig. 1(b). We have to look for a smaller ligand for self-limiting adsorption with 100% surface coverage by raising the temperature or by using other precursors. The most useful case would be self-limiting adsorption of copper atoms only.

As the present experiment was carried out using an ultrahigh vacuum CVD apparatus, the supply rate of precursors was limited, with the result that it takes an impractically long time to reach saturation of the adsorbed species. This problem is solved by employing a higher supply rate of precursors, as is described in the following section.

### 3. *In situ* optical monitoring of growth

The experimental set-up for optical reflectance measurements with the CVD apparatus has been described elsewhere [7]. The light source was a 780 nm laser diode with continuous wave light power of 5 mW. A silicon photodiode was used to detect the reflected light. The incident angle of the laser beam was 60°. The precursors for CVD were  $\beta$ -diketonate complexes, such as  $\text{Y}(\text{DPM})_3$ ,  $\text{Ba}(\text{DPM})_2$  and  $\text{Cu}(\text{DPM})_2$ . The precursor gases, oxygen as the oxidizing agent and argon for purging, were controlled by a computer program. The



shows X-ray diffraction patterns for films with various oxidation times (E–H). Oxidation proceeds with increasing oxidation time until perfect oxidation (H) where highly (111) oriented CuO crystals are obtained. We can determine the appropriate conditions for oxidation by monitoring the optical reflectance signal from the growing surface.

Because of the preliminary stage of this work, we have not tried to suppress the contribution from the bulk region. Nevertheless, we believe that the change in reflected light intensity is due to surface phenomena since it is not likely that copper precursors or oxygen atoms penetrate into the bulk so quickly at the rather low temperatures used here. If we employ methods to minimize the contribution from the bulk, such as p-polarized light together with the incident Brewster angle, we will obtain more reliable information concerning the surface phenomena. The change in reflected light was not observed at the first stage of deposition, presumably because of the lower refractive index of the MgO substrate compared with CuO<sub>x</sub>. Once a thin layer (less than 10 nm) of CuO<sub>x</sub> is deposited, the change in the reflected light becomes pronounced since the refractive index of CuO<sub>x</sub> is higher than that of the surface layers. After prolonged deposition, the difference in reflectance between the copper-stabilized and oxygen-stabilized surface disappears, accompanied by increased surface roughness. Monitoring the transient reflectance signal may help the search for conditions for self-limiting atomic layer CVD of oxide superconductors.

#### 4. Conclusions

Experimental evidence of self-limiting adsorption of precursors for CVD growth of oxide superconductors was shown for the first time. Although we present results for copper only, this property can be extended to other  $\beta$ -diketonate complexes with a slight change in

temperature range. This fact provides one important step towards atomic layer epitaxy of YBa<sub>2</sub>Cu<sub>3</sub>O<sub>x</sub> films.

We have observed variation of the optical reflection from the growing surface during layer-by-layer CVD of oxide superconductors. This method can be used as a diagnostic tool to monitor crystal growth with atomic scale accuracy, like RHEED oscillation. The dynamic behavior of the structure and the chemistry of the growing surface can be characterized from the transient signal of the reflectance. It is necessary to pursue the work further, for example to clarify the significance of the change in reflectance by separating the contribution from the surface and the bulk, and to characterize the chemical nature of the adsorbed species by measuring the spectral dependence of the change in reflectance.

#### Acknowledgment

This work was supported in part by a Grant-in-Aid for Scientific Research from the Ministry of Education, Science and Culture and by the TEPCO Research Foundation.

#### References

- 1 T. Terashima, Y. Bando, K. Iijima, K. Yamamoto, K. Hirata, K. Hayashi, K. Kamigaki and H. Terauchi, *Phys. Rev. Lett.*, **65** (1990) 2684.
- 2 M. Kanai, T. Kawai and S. Kawai, *Appl. Phys. Lett.*, **58** (1991) 771.
- 3 T. Suntola, *Extended Abstracts, 16th Conf. on Solid State Devices and Materials, Kobe, 1984*, p. 647.
- 4 D. E. Aspnes, R. Bhat, E. Colas, L. T. Florez, J. P. Harbison, M. K. Kelly, V. G. Keramidas, M. A. Koza and A. A. Studna, *Proc. SPIE*, **1037** (1988) 2.
- 5 N. Kobayashi and Y. Horikoshi, *Jpn. J. Appl. Phys.*, **28** (1989) L1880.
- 6 S. Oda, H. Zama, K. Masuda, K. Fujii and Y. C. Chen, *Physica C*, **185–189** (1991) 2001.
- 7 S. Oda, H. Zama, K. Fujii and K. Sakai, *Proc. 5th Topical Meeting on Crystal Growth, Gero, 1992*, p. 227.

# Growth of titanium dioxide thin films by atomic layer epitaxy

Mikko Ritala and Markku Leskelä

*Department of Chemistry, University of Helsinki, SF-00100 Helsinki (Finland)*

Erja Nykänen, Pekka Soininen and Lauri Niinistö

*Laboratory of Inorganic and Analytical Chemistry, Helsinki University of Technology, SF-02150 Espoo (Finland)*

## Abstract

Titanium dioxide thin films were deposited by atomic layer epitaxy using  $\text{TiCl}_4$  and water as reactants. The film growth was performed over the temperature range 150–600 °C in order to study the effects of temperature on the growth rate. The effect of the substrate material on the growth rate and crystal structure was also investigated. Spectrophotometry, X-ray diffraction, Rutherford backscattering spectroscopy and nuclear reaction analysis were used to determine the chemical and physical characteristics of the films. The growth mechanism is discussed on the basis of literature and results obtained.

## 1. Introduction

Owing to its excellent properties, *i.e.* high refractive index, good transmission in the visible and near-IR and chemical stability, titanium dioxide thin films are used in optical and electronic applications.  $\text{TiO}_2$  films have been grown by all the usual deposition techniques, including various physical vapor deposition methods [1], sol-gel processes [2] and chemical vapor deposition (CVD) methods. In addition to  $\text{TiCl}_4$  [3–7], different alkoxides, especially titanium isopropoxide [8–11] but also titanium tert-butoxide [12] and titanium ethoxide [10, 13], are the most typical titanium sources used in CVD. Water and oxygen have been used to provide the oxygen needed for film growth. Because alkoxides contain oxygen as a constituent, an additional oxygen source is not necessarily needed.

The possibility of controlling film thickness simply and precisely by the number of reaction cycles makes atomic layer epitaxy (ALE) an attractive method for depositing  $\text{TiO}_2$  films, especially for optical applications where it is desirable to control film thicknesses as accurately as possible. Films of titanium oxide mixed with aluminum oxide fabricated by ALE are used as dielectric layers in TFEL devices [14]. However, reports of pure  $\text{TiO}_2$  growth by ALE are sparse. Lakomaa *et al.* [15] used ALE to deposit a catalyst-supporting  $\text{TiO}_2$  layer onto silica powder, but the growth was limited to only a few reaction cycles. Although Kawai *et al.* [16] do not use the term ALE in their paper, they used the basic idea of ALE—pulsing of the reactants—when they grew  $\text{TiO}_2$  films on silicon with the assistance of laser irradiation.  $\text{TiCl}_4$  was introduced onto the sub-

strate and after an evacuation sequence the substrate was irradiated with an ArF excimer laser. Subsequently, separate oxygen and hydrogen pulses were introduced. With this procedure rutile films were deposited even at room temperature. The growth rate per cycle was of the order of 1 Å per cycle which is quite typical for ALE deposited oxides [14]. However, owing to the long evacuation periods (10 min after  $\text{TiCl}_4$  and 1 min after oxygen), the growth rate per time unit was below 0.1 Å min<sup>-1</sup>.

In this work we present the results of  $\text{TiO}_2$  growth experiments by ALE using  $\text{TiCl}_4$  and  $\text{H}_2\text{O}$  as reactants. These reactants were chosen in order to achieve the most favorable surface chemistry for ALE growth.

## 2. Experimental details

Titanium oxide films were deposited in a flow type reactor F-120 described in principle earlier [17] and manufactured by Microchemistry Ltd, Espoo. The  $\text{TiCl}_4$  used was an analytically pure commercial reagent.  $\text{TiCl}_4$  and  $\text{H}_2\text{O}$  reservoirs, which were held in water baths outside the reactor at temperatures of 25 and 20 °C, respectively, were connected to the cold end of the reactor through capillaries. Reactant vapors were introduced into the reactor by means of their own pressures, no bubbling systems were used. From the cold end of the reactor, vapors were transported by nitrogen to the heated reaction zone through separated pipes. The total pressure of the reactor was of the order of 10 mbar.  $\text{TiCl}_4$  and  $\text{H}_2\text{O}$  pulses (typically 0.2 s) were separated by a nitrogen pulse (0.5 s). Soda lime glass,

Corning 1733, amorphous  $\text{Al}_2\text{O}_3$  layer on soda lime glass, polycrystalline  $\text{Al}_2\text{O}_3$ , silicon as well as natural phlogopite were used as substrates and the substrate size was  $5 \times 5 \text{ cm}^2$ .

The thicknesses and refractive indices of films on transparent substrates were evaluated by fitting measured transmittance curves according to the matrix method used commonly for calculation of thin film optical device performance [18]. Rutherford backscattering spectroscopy (RBS) was used to measure thicknesses of films on opaque substrates and to analyze chlorine residues. Hydrogen contents of the films were determined by nuclear reaction analysis (NRA) using the  $^1\text{H}(^{15}\text{N}, \alpha\gamma)^{12}\text{C}$  resonant reaction. RBS and NRA measurements were carried out at the Accelerator Laboratory of the University of Helsinki. The crystal structure and crystallite orientation were determined by X-ray diffraction (XRD) measurements with a Philips powder diffractometer MPD 1880 using  $\text{Cu K}\alpha$  radiation. Surface morphology was characterized by a JEOL JSEM-820 scanning electron microscope at the Department of Electron Microscopy, University of Helsinki.

### 3. Results and discussion

#### 3.1. Film growth on glass substrates

The growth temperature was varied between 150 and  $500^\circ\text{C}$  with soda lime glass substrates and between 200 and  $600^\circ\text{C}$  when Corning 1733 was employed as substrate. Film growth took place at all temperatures studied. Figure 1 depicts the growth rate evaluated from films deposited by 2000 reaction cycles. The growth rate varied between  $0.35$  ( $200^\circ\text{C}$ ) and  $0.56$  ( $400^\circ\text{C}$ )  $\text{\AA}$  per cycle. The substrate was observed to have an effect on the growth rate; at  $500^\circ\text{C}$  the growth rate on soda lime was  $0.52$   $\text{\AA}$  per cycle whereas on Corning 1733 it was only  $0.42$   $\text{\AA}$  per cycle.

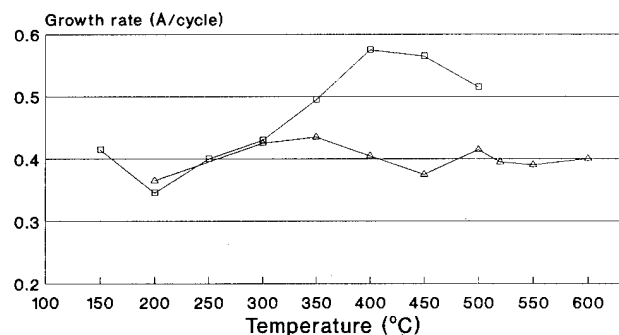
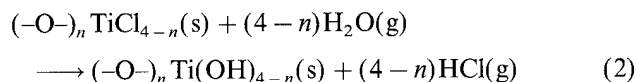
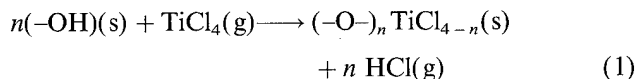


Fig. 1. The growth rates on soda lime (□) and Corning 1733 (Δ) glass substrates as a function of temperature (evaluated from films grown by 2000 cycles).

#### 3.1.1. Ideal growth mechanism

Film growth takes place over a wide temperature range, which is an expected result when the high reactivity of  $\text{TiCl}_4$  towards water and hydroxyl groups is taken into account. On the basis of this high reactivity it is reasonable to expect that the growth mechanism may be largely identical with that proposed for ALE growth of  $\text{Al}_2\text{O}_3$  from  $\text{AlCl}_3$  and water at low temperatures [19]. According to this idealized mechanism,  $\text{TiCl}_4$  and water are anchored onto the growing surface by irreversible exchange reactions:

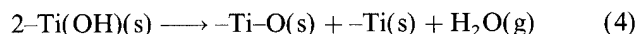
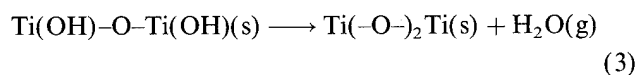


with  $n = 1-3$ . When  $\text{TiCl}_4$  is introduced on the hydroxyl-covered surface it reacts very easily with hydroxyls liberating hydrochloric acid, reaction (1). When all the hydroxyls have reacted, no more  $\text{TiCl}_4$  molecules can be adsorbed on the surface and they are swept out during the purge sequence. As a consequence, the substrate is covered by  $(\text{-O-})_n \text{TiCl}_{4-n}$  species. During the water pulse these intermediates react with water molecules, again releasing HCl and rendering the surface hydroxyl covered, reaction (2). Because both hydroxyls and titanium species are strongly bonded to the growing surface, the activation energy needed for desorption is high and ALE growth is achieved over a wide temperature range.

#### 3.1.2. Complicating processes

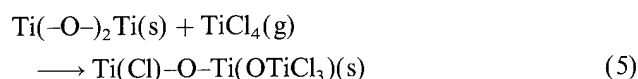
Unfortunately, the real growth mechanism is not as simple as that outlined above. The species involved may exist in different configurations and they may have alternative reaction mechanisms. These variations, which complicate the real process taking place during the film growth, are discussed below.

Hydroxyl groups on the  $\text{TiO}_2$  surface are either terminal or bridging between two cations. Additionally, terminal hydroxyls can be either adjacent with hydrogen bond interaction or isolated [20]. Terminal and bridging hydroxyls are likely to exhibit different chemical behavior, which causes the amphoteric nature of the  $\text{TiO}_2$  surface [21]. Bridging groups are polarized by the cations and are thus acidic whereas terminal hydroxyls are more basic. Instead of reacting with  $\text{TiCl}_4$ , surface hydroxyls can condensate with each other [20]:



If the hydroxyls are adjacent, the remaining oxygen is coordinated to two cations, reaction (3), but if they are

isolated the oxygen is coordinated to only one cation leaving the other one coordinatively unsaturated, reaction (4) [20]. Reaction (3) takes place at lower temperatures than reaction (4) because hydrogen-bonded hydroxyls are more favorable for dehydroxylation than isolated hydroxyls. In the latter case, proton or hydroxyl migration is a prerequisite for reaction (4) to take place. As a consequence, dehydroxylation takes place over a wide temperature range, which extends from 180 to 550 °C in the case of anatase, for example [22]. Consequently, the density and relative amounts of different configurations of surface hydroxyls are temperature dependent, which is expected to change the reactivity of the surface towards  $\text{TiCl}_4$ . It was assumed above that  $\text{TiCl}_4$  reacts only with hydroxyl groups, reaction (1). It can, however, also react with oxygen bridges:

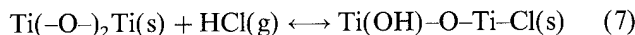
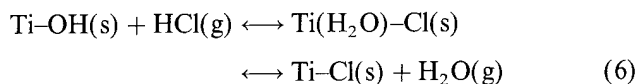


since it has been shown that reactions analogous to (5) take place between silica surfaces and  $\text{TiCl}_4$  [23]. Reaction (5) is probably not as efficient for film growth as reaction (1), since it is entropically less favored because gaseous products are not involved. Furthermore, reaction (5) can be reversible since the products are preserved in close proximity with each other. However, it has been observed that on silica surfaces oxygen bridges are even more reactive towards  $\text{TiCl}_4$  than isolated hydroxyls [23]. It should be noted that owing to the more covalent nature of silica compared with  $\text{TiO}_2$ , oxygen bridges on silica are strained and the strain energy liberated in this reaction may make a noticeable contribution to the total change in free energy. The strain effects on the  $\text{TiO}_2$  surface are less pronounced and as a consequence oxygen bridges on  $\text{TiO}_2$  are likely to be less reactive than on silica. However, the reactivity order of different hydroxyls on silica is more likely to be preserved on the  $\text{TiO}_2$  surface, *i.e.* hydrogen-bonded hydroxyls are more reactive towards  $\text{TiCl}_4$  than isolated hydroxyls [24]. As a result, the dehydroxylation reaction (3) is likely to reduce the growth rate more than reaction (4).

Also the configuration of titanium species, *i.e.*  $n$  in the formula  $(-\text{O}-)_n\text{TiCl}_{4-n}$ , varies with temperature. For example, on a silica surface  $n$  is either 1 or 2 at 175 °C but predominantly 2 at 450 °C [15].

It was assumed above that water is only dissociatively adsorbed. However, at the lowest growth temperatures adsorption of molecular water cannot be neglected. Jones and Hockey [25] have observed that even though the hydrogen-bonded water is outgassed at room temperatures, the removal of coordinatively adsorbed water requires temperatures up to 200 °C. Furthermore, reports of even higher temperatures needed for the complete outgassing of water have been given [21].

A further complication to the growth mechanism is caused by the possibility of the reaction product  $\text{HCl}$  adsorbing on the  $\text{TiO}_2$  surface [26]:



At low temperatures the equilibria have been observed to be on the right, whereas at elevated temperatures they shift to the left. Parfitt *et al.* [26] observed that when a rutile sample saturated with  $\text{HCl}$  at 45 °C was heated under evacuation, desorption of  $\text{HCl}$  took place at two temperatures, 150 and 350 °C, which were related to the reversal of reactions (6) and (7) respectively. The requirement for reaction (6) to take place at such a low temperature is that the species  $\text{Ti}(\text{H}_2\text{O})\text{Cl}$  is preserved on the surface, *i.e.* the water molecule has not desorbed. This condition is fulfilled in the experiment of Parfitt *et al.* since the saturation was carried out at 45 °C. However, the temperature during the film growth is high enough for desorption of water. Since the partial pressure of  $\text{HCl}$  during the  $\text{TiCl}_4$  pulse is higher than the partial pressure of water, the equilibrium (6) can be on the far right, *i.e.* water is desorbed and isolated chlorines are left on the surface and, as a consequence, a higher temperature is needed to desorb chlorine. Chlorine residuals have been observed to increase the amount of molecular water adsorbed on the surface at low temperatures, whereas at higher temperatures they assist dehydroxylation [21]. The probable mechanism for enhanced dehydroxylation is the reverse of reaction (7).

### 3.1.3. The real growth process

As a consequence of the complications discussed above, the real growth process consists of competitive, simultaneous reactions. During a  $\text{TiCl}_4$  pulse, hydroxyl groups can react alternatively with  $\text{TiCl}_4$  (1) or with  $\text{HCl}$  (6) and oxygen bridges with  $\text{TiCl}_4$  (5) or with  $\text{HCl}$  (7). Reactions (1) and (5) lead to film growth whereas (6) and (7) do not. It should be noted that reactions (6) and (7) can also take place during the water pulse. Water liberated in reaction (6) can either be swept out or react with  $\text{TiCl}_4$  in the gas phase or on the surface. Furthermore, the effects of dehydroxylation (reactions (3) and (4)) must be considered.

The results discussed above concerning surface processes were obtained from stable, crystalline  $\text{TiO}_2$  surfaces at equilibrium conditions. In our case amorphous film is growing when an amorphous substrate is used and the gas phase is non-static, which makes the situation even more complicated. Together with kinetic factors, these processes constitute a complex relationship between growth rate and temperature. Furthermore,



owing to the chain-like growth mechanism, where the number of adsorption sites on the uppermost surface layer is determined by the layer on which it has been deposited, the densities of different adsorption sites on substrate surfaces may have an effect on the growth rate. This can be illustrated by making a simplifying assumption that the growth takes place predominantly via surface species  $(-\text{O}-)_2\text{TiX}_2$  ( $\text{X} = \text{Cl}$  or  $\text{OH}$ ). When the first  $\text{TiCl}_4$  pulse is exposed on the substrate, two reactive sites are lost for each  $(-\text{O}-)_2\text{TiCl}_2$  formed. During the subsequent water pulse these species react to form  $(-\text{O}-)_2\text{Ti}(\text{OH})_2$  and as a consequence the number of reactive surface sites remains constant. Naturally, the real situation is more complicated owing to the various species involved. However, the basic idea is that through the chain mechanism the substrate surface may have an effect on the growth rate even when it has been totally covered. This can explain the observed difference between soda lime and Corning 1733 glasses.

Owing to the lack of kinetic data, only suggestions can be made about the dominance of different processes at different temperatures. In the case of soda lime, the decrease in growth rate going from 150 to 200 °C is associated with the desorption of coordinatively adsorbed molecular water. Between 200 and 400 °C the growth process seems to be kinetically limited. This is verified by the observation that when the reactant pulses at 300 °C are elongated from 200 ms to 400 ms, the growth rate is increased by 14% to the same level which is achieved above 400 °C with shorter pulses. The rate-limiting step is related to the adsorption process, since elongation of the purge time from 500 ms to 1000 ms has a reverse effect on growth rate, diminishing it by 9%, which is probably caused by dehydroxylation. The adsorption of  $\text{HCl}$  (reactions (6) and (7)) is diminished when the temperature is elevated, which can also have an effect on the observed increase in the growth rate. Above 400 °C the growth rate achieves a constant value owing to the stabilized surface state. The slight decrease from 400 °C to 500 °C is likely to be caused by dehydroxylation. At 500 °C the purge time has a very small effect on the growth rate: the thicknesses of films grown by 2000 cycles were 104, 103 and 100 nm when the purging times were 200, 500 and 1000 ms respectively. This seems to indicate that owing to fast surface kinetics, a constant surface state is readily achieved at this temperature. Elongation of the reactant pulse above 200 ms has no effect at 500 °C. When Corning 1733 is used as a substrate, a constant growth rate is achieved by 300 °C and is preserved up to 600 °C.

#### 3.1.4. Dependence of the growth rate on film thickness

Figure 2 shows growth rates on soda lime as a function of the number of reaction cycles used at 500 °C. It can be seen that there is a clear decrease in

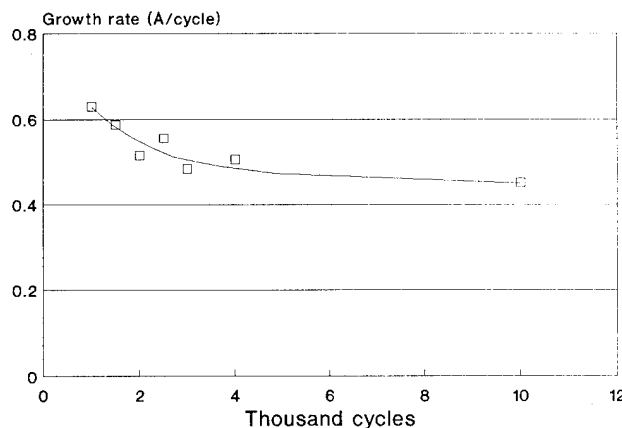


Fig. 2. The dependence of the growth rate at 500 °C on the number of reaction cycles used. The growth rates were evaluated from thicknesses measured 35 mm from the leading edge of the soda lime substrate.

growth rate when the number of cycles is increased. Two alternative explanations can be given for such behavior. As a result of condensation reactions the hydroxyl density of the surface is decreased, which in turn decreases the growth rate, because resulting surface oxides are not as effective adsorption sites for  $\text{TiCl}_4$  as hydroxyls. If a certain fraction of hydroxyls condensate during each reaction cycle, the number of hydroxyls decreases cumulatively with the number of reaction cycles until a constant hydroxyl density is achieved.

However, the decrease in the growth rate can be caused by changes in the morphology of the film during the growth process. If the formation of large three-dimensional nuclei is the first step of film growth, the film is initially coarse with empty space between the nuclei. When the growth proceeds further these holes and pores are filled. As a consequence, the apparent film thickness increases fast in the early stages of film growth whereas the increment is lowered when the holes are filled. This growth mechanism is in conflict with the basic assumption of ALE growth, *i.e.* layer-by-layer growth. It is, however, possible to formulate such a mechanism which leads to three-dimensional nucleation and still preserves the self-limiting growth rate control. This is based on  $\text{HCl}$  adsorption (reaction (6)) which liberates  $\text{H}_2\text{O}$  in the gas phase during the  $\text{TiCl}_4$  pulse. Consequently, gas phase nucleation can take place resulting in small three-dimensional nuclei. The self-limiting control is preserved since the amount of water is dictated by the number of hydroxyl groups. This kind of growth mechanism should have an effect on the film density and consequently on its optical properties. However, refractive indices did not indicate this kind of variation.

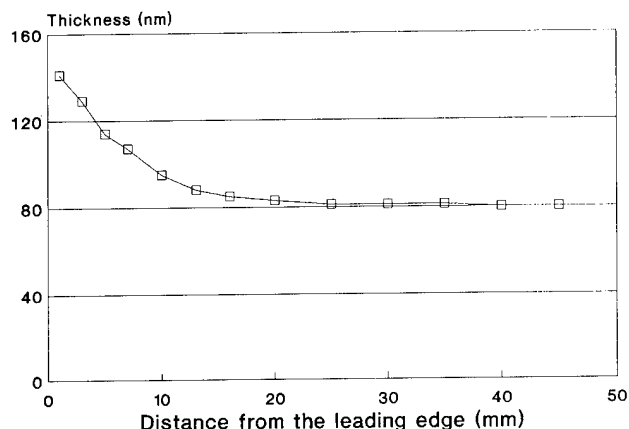


Fig. 3. Film thickness as a function of the distance from the leading edge of the substrate. The film was deposited onto Corning 1733 at 600 °C using 2000 reaction cycles.

### 3.1.5. Uniformity of film thickness

The high reactivity of  $\text{TiCl}_4$  also has drawbacks for the film growth. It was clearly seen from the interference colors that films were thicker at the leading edges of substrates. The thickness had a strong profile and diminished to a constant value after a region which was about 10–20 mm wide (Fig. 3). Outside the profile area, film thicknesses were uniform in the direction perpendicular to the gas flow. The reason for films being thicker at the leading edge is assumed to be caused by reactions of  $\text{TiCl}_4$  molecules with residual gases, especially water and to some extent also oxygen. This was supported by the observation that slow film growth took place at this narrow region even when the water pulses were replaced by nitrogen pulses.

However, the carrier gas and pumping residues seem to be minor sources for profile growth, because it has been shown that the profile problem can be avoided by leading the reactants to the reactor chamber through a common line [27]. According to this observation it seems that the high growth rate at the leading edge is caused mainly by reversible adsorption of the reactants on the walls of pipes. During the pulse sequence molecules are adsorbed before the substrate. Owing to the relatively low desorption rate, molecules of one reactant arrive at the substrate during the pulse sequence of another reactant. As a consequence CVD growth takes place. Because the concentration of the desorbed species is small and the reaction is fast, residues are exhausted from the gas phase almost immediately after the crossing point of the reactant flow routes. In our arrangement this point was only about 1 cm ahead of the leading edge of the substrate, but if the reactants had entered the reactor chamber through a common line, the crossing point would have been well ahead of the substrate and the whole substrate would have been in a pure ALE growth region. When the

reactor temperature was lowered profiles could not be observed visually any more. This is attributed to a lower desorption rate, because a lowered reaction rate would have resulted in a wider profile region.

## 3.2. The effect of substrate on growth rate and crystal structure

### 3.2.1. Growth rate

It is seen above that growth rates on soda lime and Corning 1733 glasses were different, indicating that the substrate has an effect on film growth during the whole process and not just during the first layers. This kind of effect is thought to be caused by the chain-like growth mechanism. In order to study this effect various substrate materials were used at 500 °C. The film thickness on soda lime was determined by both RBS and transmittance methods in order to be able to compare the results. The atomic densities obtained from RBS were converted to geometrical thicknesses using the density of anatase for films having amorphous or anatase structure and the density of rutile for rutile films. This can lead to values which are slightly too low since the density of the amorphous phase is likely to be less than the density of the crystalline phase. Furthermore, in many cases it has been observed that an amorphous buffer layer exists between the substrate and crystalline film, which lowers the average density of the film. The results summarized in Table 1 indicate that there are remarkable variations in growth rates on various substrates. It is interesting to note that in the case of the Corning 1733 substrate there was no remarkable difference between growth temperatures 500 and 600 °C, but when phlogopite was used as a substrate, the growth rate was decreased from 0.40 Å per cycle (500 °C) to 0.33 Å per cycle (600 °C).

The most interesting result on the effects of substrate on the growth rates was obtained when different substrates were used simultaneously. In our reactor two substrates are located face to face. In order to obtain stable flow conditions only a 2 mm wide channel is left

TABLE 1. Comparison of film thicknesses on different substrates grown at 500 °C with 2000 cycles as determined by transmittance measurements  $d(\text{trans})$  and by RBS (atomic density and  $d(\text{RBS})$ )

Substrate	$d(\text{trans})$ (nm)	Atomic density ( $10^{15}$ atoms $\text{cm}^{-2}$ )	$d(\text{RBS})(\text{nm})$
Soda lime glass	103	875	101 <sup>a</sup>
Corning 1733	83	—	—
Amorphous $\text{Al}_2\text{O}_3$	82	—	—
Silicon	—	872	101 <sup>a</sup>
$\text{Al}_2\text{O}_3$	—	924	96 <sup>b</sup>
Phlogopite	—	777	81 <sup>b</sup>

<sup>a</sup>Calculated using density of anatase.

<sup>b</sup>Calculated using density of rutile.

TABLE 2. Observed X-ray diffractions with relative intensities from films grown on different substrates

Substrate	Growth temperature (°C)	Reaction cycles	Crystalline structure
Silicon	500	2000	A(101)/100, A(004)/82
Al <sub>2</sub> O <sub>3</sub>	500	2000	R(110)/100, R(101)/95
Phlogopite	500	1500	R(200)/100
Phlogopite	500	2000	R(200)/100
Phlogopite	500	2000	R(200)/100, A(004)28
Phlogopite	500	4000	A(004)/100, A(112)/11, A(103)/7, R(200)/9, R(111)/1
Phlogopite	600	2000	R(200)/100

A = anatase, R = rutile.

between the substrates. When both substrates were soda lime the growth rate was 0.57 Å per cycle at 450 °C while with Corning 1733 the growth rate was 0.38 Å per cycle. When soda lime and Corning 1733 were used simultaneously the growth rate on Corning 1733 was increased up to 0.51 Å per cycle. On soda lime the growth rate (0.55 Å per cycle) was not changed remarkably. This kind of interplay between substrates is difficult to explain without gas phase migration processes. The adsorption of HCl on hydroxyl sites followed by desorption of water, as discussed above, is a process which could cause such interplay.

### 3.2.2. Crystal structure

All films deposited onto amorphous substrates were amorphous even when prepared at 600 °C. When crystalline substrates, such as silicon, Al<sub>2</sub>O<sub>3</sub> and mica, were used, films were crystalline having either rutile or anatase structure (Table 2). Determination of the preferred orientation in the films was impossible by XRD, because many of the diffraction peaks of rutile and anatase were overlapped with intense peaks of the substrates. However, in every case there was a number of unhidden reflections to be detected but only a few of them were observed. The relative intensities of the reflections found differed markedly from those reported for powders (Table 3) [28].

TABLE 3. X-ray reference diffractions of rutile and anatase powders with relative intensities [28]

Sample	Reflection
Rutile	(110)/100, (211)/60, (101)/50, (111)/25, (220)/20, (301)/20, (112)/12, (210)/10, (002)/10, (310)/10, (200)/8, (221)/2
Anatase	(101)/100, (200)/35, (004)/20, (105)/20, (211)/20, (204)/14, (103)/10, (112)/10, (116)/6, (213)/4

The overlap between the TiO<sub>2</sub> reflections and silicon reflections was not very strong. However, only anatase (101) and (004) reflections could be observed. Their relative intensities were 100 and 80 respectively, compared with 100 and 20 in powder samples (Table 3). On polycrystalline Al<sub>2</sub>O<sub>3</sub> the peak interference was much more severe. The only detectable reflections were rutile (110) and (101) with relative intensities of 100 and 95 compared with 100 and 50 in powders.

Reflections from TiO<sub>2</sub> films on mica were much more intense than reflection from TiO<sub>2</sub> on silicon and Al<sub>2</sub>O<sub>3</sub>, which was attributed to the better crystallinity of the TiO<sub>2</sub> film on mica. The XRD pattern of phlogopite overlaps with the most intense reflection (101) in anatase powder and two of the most intense (110) and (211) reflections in rutile powder. Also, a number of minor peaks were overlapping. The rutile (200) reflection was the only reflection detected in films grown at 500 °C with 1500 cycles and at 600 °C with 2000 cycles. Two samples were made by depositing film for 2000 cycles at 500 °C. Their diffraction patterns were not identical. One showed only the rutile (200) reflection, whereas the other had in addition to rutile (200) the anatase (004) reflection. The thickest film grown with 4000 cycles had the most complex diffraction pattern. In addition to peaks listed in Table 2, the rutile (110) reflection was observed as a small shoulder on the substrate peak. Additionally, a peak having a *d*-value of 2.89 Å was observed. It cannot be assigned to either rutile or anatase but is very close to the brookite (121) reflection which has a tabulated *d*-value of 2.900 Å [28].

Comparison of these results with powder references (Table 3) shows that films are at least partially oriented. For example, (111) and (220) reflections of rutile, which have a higher intensity in powder than the (200) reflection, are not overlapped by mica reflections but only the (200) reflection was detected in most rutile films. Likewise, the (200) reflection of anatase was not observed even though it has a high relative intensity in powders and is not overlapped by mica reflections. To

summarize, films grown for 2000 or 1500 cycles tend to be oriented. However, the crystal structure is not necessarily reproducible from film to film. When the film thickness is increased various orientations are observed.

### 3.3. Film properties

Scanning electron micrographs showed that the films were smooth and crack free. Both the amorphous and crystalline films consisted of grains with a diameter of about 0.1  $\mu\text{m}$ . Densities of films grown on soda lime were estimated by comparing thicknesses obtained by transmittance measurements and RBS. Using the thickness obtained from transmittance measurement as a geometrical thickness, the atomic densities obtained from RBS were converted to mass densities. Films grown at 150 °C had a very low density (3.39 g cm<sup>-3</sup>) which can be related to the porosity of these films. The density of the films grown at 500 °C was higher (3.76 g cm<sup>-3</sup>), approaching the density of bulk anatase (3.84 g cm<sup>-3</sup>) [29]. Refractive indices at a wavelength of 580 nm were observed to increase steadily from 2.4 (150 °C) to 2.6 (450 °C). Film thicknesses had no effect on the refractive index.

The amount of chlorine residue was analyzed by RBS. The film deposited at 150 °C contained about 2 at.% chlorine whereas in the film grown at 500 °C the amount of chlorine was below the detection limit of RBS. NRA showed that the hydrogen profile had a maximum both at the outer surface and at the film-substrate interface related to adsorbed water and hydrocarbon impurities. The hydrogen contents in the bulk of the film were low even in the film grown at 150 °C (0.3 at.%). As expected, the hydrogen content was still lower in the film grown at 500 °C, only 0.1 at.%.

Films were etched by 70% H<sub>2</sub>SO<sub>4</sub> at 120 °C. The growth temperature was observed to have a remarkable effect on the etchability. Films grown at 150–200 °C were easily etched at a rate of 12 nm min<sup>-1</sup> whereas films grown at higher temperatures (300–500 °C) were etched very slowly, *i.e.* 5 nm h<sup>-1</sup>. Film deposited at 250 °C was etched at a rate of 14 nm h<sup>-1</sup>. Similar behavior has been observed for ALE grown Al<sub>2</sub>O<sub>3</sub> films [30]. In that case the high etchability of films deposited at low temperatures was related to hydrogen and chloride residues. Also in this case the etchability seems to indicate that the growth reaction is not complete at low temperatures, which was verified by the observed residues. Since the chlorine content in the film grown at 150 °C was an order of magnitude higher than the hydrogen content, the oxochloride species rather than the hydroxide species are likely to be the main result of the incomplete reaction and thus the origin of the etchability. Our results can be compared with those of Balog *et al.* [8], who reported that TiO<sub>2</sub> films grown by

CVD from titanium isopropoxide were easily—the temperature was not specified—etched by 70% H<sub>2</sub>SO<sub>4</sub>.

### 3.4. CVD growth

Film deposition was also performed in CVD mode, *i.e.* the reactants were led simultaneously onto the soda lime substrate at 500 °C. The thickness of the resulting film decreased significantly in the direction of the gas flow which was an expected result on the basis of the reactor geometry. The CVD growth rate in the middle of the substrate was of the order of 1800 Å min<sup>-1</sup>. If the ALE growth rate is converted to similar units taking into account the total time needed for deposition (1.4 s per cycle) the result is 22 Å min<sup>-1</sup>. If the growth rate is calculated per pulsing time of only one of the reactants (0.2 s per cycle), the growth rate is still only 150 Å min<sup>-1</sup>. CVD films of comparable thicknesses with ALE films were also amorphous, but thicker CVD films had rutile structure with (110) and (200) as the most intense reflections.

## 4. Conclusion

The ALE process was used to deposit TiO<sub>2</sub> films with reproducible and uniform film thicknesses onto the substrate area which was at least 3 cm downstream from the crossing points of the reactant flow routes. The growth temperature had a marked effect on the growth rate which was attributed to temperature-dependent surface processes. The substrate material had an effect on the growth rate and on the crystal structure of the films. On amorphous substrates films were amorphous, but on crystalline substrates they were crystalline and partially oriented.

## Acknowledgments

The authors wish to thank Mr. Eero Rauhala and Mr. Pekka Haussalo for carrying out the RBS and NRA measurements. This work was supported in part by the Academy of Finland and Technology Development Centre (TEKES), Helsinki, Finland.

## References

- 1 J. M. Bennett, E. Pelletier, G. Albrand, J. P. Borgogno, B. Lazarides, C. K. Carniglia, R. A. Schmell, T. H. Allen, T. Tuttle-Hart, K. H. Guenther and A. Saxer, *Appl. Opt.*, 28 (1989) 3303.
- 2 Y. Takahashi and Y. Matsuoka, *J. Mater. Sci.*, 23 (1988) 2259.
- 3 G. Hass, *Vacuum*, 2 (1952) 331.
- 4 R. N. Ghostagore, *J. Electrochem. Soc.*, 117 (1970) 529.
- 5 R. N. Ghostagore and A. J. Noreika, *J. Electrochem. Soc.*, 117 (1970) 1310.

- 6 S. Hayashi and T. Hirai, *J. Cryst. Growth*, **36** (1976) 157.
- 7 K. S. Yeung and Y. W. Lam, *Thin Solid Films*, **109** (1983) 169.
- 8 M. Balog, M. Schieber, S. Patai and M. Michman, *J. Cryst. Growth*, **17** (1972) 298.
- 9 E. T. Fitzgibbons, K. J. Sladek and W. H. Hartwig, *J. Electrochem. Soc.*, **119** (1972) 735.
- 10 S. R. Kurtz and R. G. Gordon, *Thin Solid Films*, **147** (1987) 167.
- 11 Y. Gao, K. L. Merkle, H. L. M. Chang, T. J. Zhang and D. J. Lam, *J. Mater. Res.*, **6** (1991) 2417.
- 12 W. Luo and Z. Tan, *Proc. 7th European Conf. on Chemical Vapour Deposition*, in *J. Phys. Colloq.*, **C5** (1989) 773.
- 13 Y. Takahashi, K. Tsuda, K. Sugiyama, H. Midoura, D. Makino and M. Tsuiki, *J. Chem. Soc., Faraday Trans. I*, **77** (1981) 1051.
- 14 M. Leskelä and L. Niinistö, in T. Suntola and M. Simpson (eds.), *Atomic Layer Epitaxy*, Blackie, Glasgow, 1990, p. 1.
- 15 E.-L. Lakomaa, S. Haukka and T. Suntola, *Appl. Surf. Sci.*, **60/61** (1992) 742.
- 16 T. Kawai, T. Choda and S. Kawai, *Mater. Res. Soc. Symp. Proc.*, **75** (1987) 289.
- 17 T. Suntola, A. Pakkala and S. Lindfors, *US Patent*, **4 389 973**, 1983.
- 18 H. A. M. Macleod, in T. J. Coutts (ed.), *Active and Passive Thin Film Devices*, Academic Press, London, 1978, p. 321.
- 19 J. Aarik, A. Aidla, A. Jaek, A.-A. Kiisler and A.-A. Tammik, *Acta Polytech. Scand., Ser. Chem. Techn. Ch.*, **195** (1990) 201.
- 20 M. Primet, P. Pichat and M.-V. Mathieu, *J. Phys. Chem.*, **75** (1971) 1216.
- 21 G. D. Parfitt, *Progr. Surf. Membrane Sci.*, **11** (1976) 181.
- 22 C. Morterra, *J. Chem. Soc., Faraday Trans. I*, **84** (1988) 1617.
- 23 J. B. Kimney and R. H. Staley, *J. Phys. Chem.*, **87** (1983) 3735.
- 24 J. Kunawicz, P. Jones and J. A. Hockey, *Trans. Faraday Soc.*, **67** (1971) 848.
- 25 P. Jones and J. A. Hockey, *J. Chem. Soc., Faraday Trans. I*, **68** (1972) 907.
- 26 G. D. Parfitt, J. Ramsbotham and C. H. Rochester, *Trans. Faraday Soc.*, **67** (1971) 3100.
- 27 S. Lindfors and T. Suntola, private communication, 1992.
- 28 M. E. Mrose, B. Post, S. Weissmann, H. F. McMurdie, M. C. Morris and W. F. McClune (eds.), *Powder Diffraction Data*, Joint Committee on Powder Diffraction Data Standards, Swarthmore, PA, 1976, cards 16-617, 21-1272 and 21-1276.
- 29 *CRC Handbook of Chemistry and Physics*, CRC Press, Boca Raton, FL p. B-140, 69th edn., 1988.
- 30 L. Hiltunen, H. Kattelus, M. Leskelä, M. Mäkelä, L. Niinistö, E. Nykänen, P. Soininen and M. Tiitta, *Mater. Chem. Phys.*, **28** (1991) 379.

# Layered tantalum–aluminum oxide films deposited by atomic layer epitaxy

H. Kattelus, M. Ylilammi and J. Saarilahti

VTT Semiconductor Laboratory, Otakaari 7 B, SF-02150 Espoo (Finland)

J. Antson and S. Lindfors

Microchemistry Ltd., Keilaranta 6, SF-02150 Espoo (Finland)

## Abstract

Insulating films consisting of thin layers of tantalum oxide and aluminum oxide were deposited using the atomic layer epitaxy technique at a temperature of 300 °C from metallic chlorides and H<sub>2</sub>O. The average film composition can be modified between pure aluminum oxide and pure tantalum oxide by varying the pulsing ratio. The effective refractive index is adjustable between 1.67 and 2.23 and the relative permittivity between 8.4 and 24. The leakage current of tantalum oxide is significantly reduced by thin interposed layers of aluminum oxide. These multilayers will potentially be useful, for example for applications in future memory integrated circuit and large-area display technologies.

## 1. Introduction

High permittivity insulators exhibiting good dielectric strength have a wide range of applications. They will be needed in the high density memory integrated circuits of the future for which the dielectric constant of silicon oxide–nitride is insufficient [1–4]. In thin film electroluminescent displays a large proportion of the applied electric field remains across the active layer when high permittivity insulators are used [5]. A highly reliable process to deposit insulating thin films of high quality onto large-area substrates is needed in the fabrication of active matrix liquid crystal displays [6]. When the dielectric constant is large the leakage current, however, tends to be large as well [7].

Atomic layer epitaxy (ALE) is a deposition method that has potential to produce tailored materials for specific applications. We deposited layered tantalum–aluminum oxide films by ALE to study the properties of the intermediate average compositions between pure tantalum oxide and aluminum oxide. Optical, electrical and material properties were measured.

## 2. Experimental details

The Ta<sub>x</sub>Al<sub>y</sub>O films were deposited onto soda lime glass substrates at 300 °C using the MC-120 ALE reactor manufactured by Microchemistry Ltd. The solid source materials AlCl<sub>3</sub> and TaCl<sub>5</sub> were evaporated from open boats at 90 °C and H<sub>2</sub>O vapor was delivered through a needle valve. The switching was performed with solenoid valves. Pure nitrogen was used as a carrier gas at a pressure of approximately 1 kPa. The pulse durations for the source materials were 0.2 s and the subsequent purging times 0.4–0.5 s. The pulsing sequences for the different Ta<sub>x</sub>Al<sub>y</sub>O samples (A to D) are given in Table 1. Some substrate glasses were covered prior to the ALE deposition with an indium–tin–oxide layer 400 nm thick and delineated to form capacitor electrodes. The capacitors were completed after growing the insulator with sputter-deposited aluminum metallization 200 nm thick patterned for the top electrodes. The area of the capacitors was about 0.2 mm<sup>2</sup>. The thicknesses and the effective refractive indices of the films were determined by fitting calcu-

TABLE 1. Pulsing sequences used for the deposition of Ta<sub>x</sub>Al<sub>y</sub>O films of four different compositions;  $N(\text{Ta})/(N(\text{Ta}) + N(\text{Al}))$  denotes the fraction of supplied tantalum oxide pulses in the oxide mixture

Sample	Pulsing sequence	$N(\text{Ta})/(N(\text{Ta}) + N(\text{Al}))$
A	15 × (100 cycles of Al–O + 100 cycles of Ta–O)	0.500
B	30 × (20 cycles of Al–O + 40 cycles of Ta–O)	0.667
C	30 × (20 cycles of Al–O + 60 cycles of Ta–O)	0.750
D	40 × (10 cycles of Al–O + 60 cycles of Ta–O)	0.857

lated optical transmission spectra to the measured spectra, taking film dispersion into account with a single-term Sellmeier model [8]. Capacitances and loss factors were measured at a frequency of 100 kHz using an HP 4192A impedance analyzer, and the  $I$ – $V$  curves with an HP 4142B modular d.c. source at a ramp rate of  $1$ – $3$  V s $^{-1}$ . The elemental composition of the films was analyzed using backscattering spectrometry.

### 3. Results and discussion

#### 3.1. Backscattering analysis and thickness determination

The compositions of the deposited films were determined using backscattering spectrometry. The atomic ratio  $[Ta]/[Ta + Al]$  is shown in Fig. 1 as a function of the cycle ratio  $N(Ta)/(N(Ta) + N(Al))$  used for film deposition (see Table 1). The tantalum concentration in the films is clearly smaller than the relative amount of supplied tantalum, showing that the deposition rate of tantalum oxide onto aluminum oxide is smaller than the deposition rate of aluminum oxide onto tantalum oxide. Additionally, in all the films about 1–2 at.% chlorine impurity is observed.

The film thicknesses as measured using optical transmission analysis vary between 70 and 100 nm with the exception of sample A which is 170 nm thick. Combining the thickness data with the backscattering results indicates that the deposition rate is not a constant figure for the very thin constituent layers used here (each layer of aluminum oxide or tantalum oxide is only 0.5–10 nm thick) but is a function of the number of cycles supplied. In particular, there seems to be a period of remarkably slow deposition rate during the very first few cycles. In steady state condition the deposition rate for tantalum oxide is of the order of 0.03 nm per cycle and for aluminum oxide approximately 0.09 nm per cycle at 300 °C.

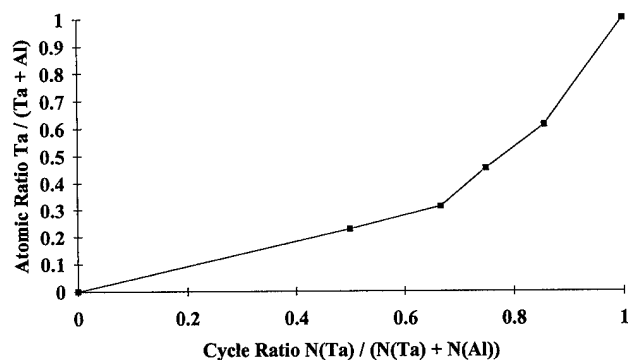


Fig. 1. The atomic ratio  $x/(x + y)$  of  $Ta_xAl_yO$  composite films as a function of the relative amount of supplied tantalum.

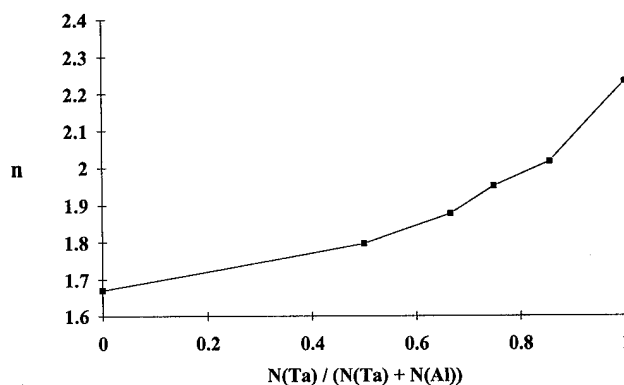


Fig. 2. The refractive index of  $Ta_xAl_yO$  composite films as a function of the relative amount of supplied tantalum.

#### 3.2. Refractive index

The measured effective refractive indices of the deposited films at the wavelength  $\lambda = 580$  nm are shown in Fig. 2 as a function of  $N(Ta)/(N(Ta) + N(Al))$ . Pure aluminum oxide and tantalum oxide deposited by ALE have refractive indices of  $n = 1.67$  and  $n = 2.23$  respectively. The  $Ta_xAl_yO$  composite films A to D show an increasing refractive index with an increasing amount of supplied tantalum.

#### 3.3. Permittivity

The dielectric constant of aluminum oxide deposited by ALE is  $\epsilon_r = 8.4$  and that of tantalum oxide is  $\epsilon_r = 23$ – $24$ . Intermediate values are obtained by intermixing the oxides as can be seen in the curve of Fig. 3. As can be expected from the facts that the overall effective dielectric constant of a multilayer is dominated by the low permittivity material and that the deposition rate of tantalum oxide is smaller than that of aluminum oxide in the ALE deposition conditions used here, a large amount of tantalum is needed to be able to operate in the high permittivity end of the available range.

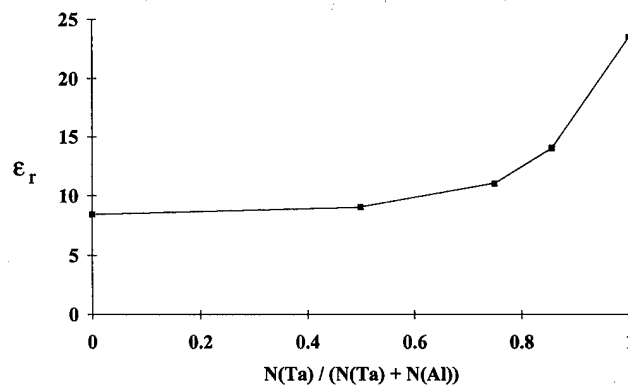


Fig. 3. The dielectric constant of  $Ta_xAl_yO$  composite films as a function of the relative amount of supplied tantalum.

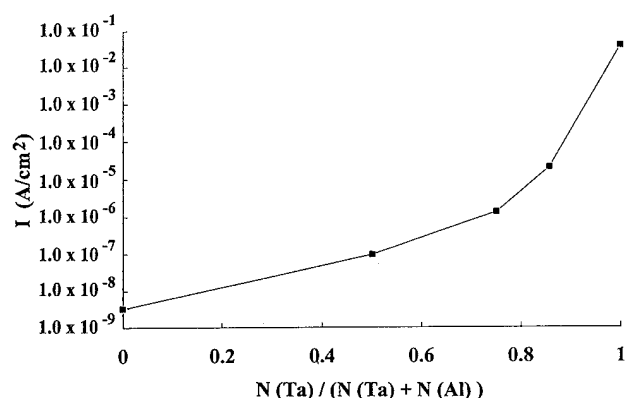


Fig. 4. Leakage current of  $\text{Ta}_x\text{Al}_{1-x}\text{O}_3$  composite films at an electric field of  $1 \text{ MV cm}^{-1}$  as a function of the relative amount of supplied tantalum.

### 3.4. Leakage current

The leakage current was measured by applying an electric field of  $1 \text{ MV cm}^{-1}$  across the oxide layer. When looking at the results shown in Fig. 4, one can see that the considerable leakage of tantalum oxide is reduced by several orders of magnitude when thin layers of aluminum oxide are introduced. The leakage currents for the composite films are sufficiently low for several applications but do not fulfil the the most stringent requirements posed, e.g. for a 64 Mbit DRAM. Tantalum oxide films previously deposited for that purpose have been annealed at high temperature in an ambient where radical oxygen species are present [1, 2]. Our films were deposited at a low temperature of  $300^\circ\text{C}$ , and they have not experienced any post-deposition treatments. Annealing in active oxygen would be interesting to obtain information on the ultimate performance obtainable with layered tantalum–aluminum oxide films. Other means of improving the leakage properties would be to study chlorine-free source materials [2, 4], plasma or UV activated deposition [1], or the effects of the deposition temperature.

The films do not typically show electrical breakdown upon ramping the current up to 1 mA corresponding to

a current density of  $0.5 \text{ A cm}^{-2}$ . This condition is reached between electric field values of  $2.0 \text{ MV cm}^{-1}$  (for pure tantalum oxide) and  $6.6 \text{ MV cm}^{-1}$  (for sample A).

## 4. Conclusion

Tantalum–aluminum oxide composite films were deposited in the form of layered structures using atomic layer epitaxy. The composition can be varied in a controllable fashion by altering the pulse sequence of the deposition process. Film properties such as the refractive index, permittivity, and leakage current are modified respectively. Even a small amount of aluminum oxide introduced as thin layers in the tantalum oxide results in a significant improvement in the dielectric properties.

## Acknowledgments

The authors wish to thank T. Ranta-aho (VTT) for his help in ALE depositions and L. Kassinen and L. Valkonen (VTT) for technical assistance.

## References

- 1 S. Tanimoto, M. Matsui, K. Kamisako, K. Kuroiwa and Y. Tarui, *J. Electrochem. Soc.*, **139** (1992) 320.
- 2 T. Tabuchi, Y. Sawado, K. Uematsu and S. Koshiha, *Jpn. J. Appl. Phys.*, **30** (1991) L1974.
- 3 K. Nomura and H. Ogawa, *J. Electrochem. Soc.*, **138** (1991) 3701.
- 4 S.-O. Kim, J. S. Byun and H. J. Kim, *Thin Solid Films*, **206** (1991) 102.
- 5 S. K. Tiku and S. H. Rustomji, *IEEE Trans. Electron Devices*, **36** (1989) 1947.
- 6 Z. Yaniv and W. den Boer, *Eurodisplay '90, Tenth Int. Display Research Conf., Amsterdam, September 25–27, 1990*, Vde-Verlag, Berlin, 1990, p. 164.
- 7 Q. X. Jia, Z. Q. Shi and W. A. Anderson, *Thin Solid Films*, **209** (1992) 230.
- 8 X. Ying, A. Feldman and E. N. Farabaugh, *J. Appl. Phys.*, **67** (1990) 2056.



## Author Index of Volume 225

- Ailey-Trent, K. S., 244  
 Antson, J., 296  
 Aoyagi, Y., 40, 120, 136, 240  
 Aspnes, D. E., 26  
 Banerjee, S., 177  
 Bansenauer, B. A., 17  
 Beach, D. B., 173  
 Bedair, S. M., 59, 99, 109, 183  
 Bhat, I. B., 261  
 Bhat, R., 26  
 Bramblett, T. R., 191  
 Brasil, M. J. S., 26  
 Brierley, S., 64  
 Carter, J., 64  
 Chen, P. J., 140, 196  
 Chen, Q., 115  
 Chen, Y. C., 284  
 Cheng, C. C., 140, 150, 196  
 Choi, S.-D., 235  
 Choyke, W. J., 140, 150, 196  
 Clemen, L., 196  
 Cohen, S. M., 155  
 Colaianni, M. L., 150, 196  
 Colter, P. C., 99, 109, 183  
 Creighton, J. R., 17  
 Dapkus, P. D., 12, 115  
 Davis, R. F., 219, 244  
 Dip, A., 99, 109  
 D'Evelyn, M. P., 155, 203, 212  
 Eberl, K., 163  
 Ehsani, H., 261  
 Ek, B. A., 163  
 El-Masry, N. A., 59  
 Eldallal, G. M., 99, 109  
 Faschinger, W., 250, 265, 270  
 Ferreira, S., 270  
 Florez, L. T., 26  
 Fujii, K., 284  
 Fujita, H., 82  
 Fuyuki, T., 225  
 Gamo, K., 120  
 Gao, Q., 140, 150  
 Gates, S. M., 160, 173  
 Ghandhi, S. K., 261  
 Goldman, L., 64  
 Greene, J. E., 191  
 Gregory, S., 26  
 Grützmacher, D. A., 163  
 Gutleben, H., 196  
 Hara, S., 240  
 Harbison, J. P., 26  
 Hauka, S., 280  
 Hauzenberger, F., 265  
 Hein, S., 64  
 Horiike, Y., 124  
 Howe, D., 64  
 Hsieh, K. C., 64  
 Hukka, T. I., 155, 212  
 Iguchi, A., 78  
 Iizuka, T., 168  
 Ikeda, H., 82  
 Imai, S., 168  
 Irby, J., 177  
 Ishii, M., 136  
 Ishizaki, M., 74  
 Iwai, S., 40  
 Iyer, S. S., 163  
 Juza, P., 265, 270  
 Kajimoto, A., 70  
 Kamiya, I., 26  
 Kano, N., 74  
 Karam, N. H., 261  
 Kattelus, H., 296  
 Kawai, M., 240  
 Kawai, T., 275  
 Kawanishi, H., 82  
 Kawasaki, K., 120  
 Kawasaki, T., 124  
 Kern, R. S., 219  
 Kim, K., 235  
 Kinosky, D., 177  
 Kobayashi, N., 32  
 Kobayashi, Y., 32  
 Kodama, K., 136  
 Koleske, D. D., 160, 173  
 Konagai, M., 256  
 Kreinin, O., 91  
 Kukimoto, H., 74  
 Kupferberg, L., 64  
 Lakomaa, E.-L., 280  
 Lapiano-Smith, D. A., 187  
 Leskelä, M., 130, 288  
 Lindfors, S., 296  
 Lischka, K., 265, 270  
 Liu, H., 105  
 Lubben, D., 191  
 Luscombe, J. H., 99  
 Maa, B. Y., 12  
 Maayan, E., 91  
 Mahajan, A., 177  
 Matsumura, M., 168  
 Matsunami, H., 70, 225  
 McFeely, F. R., 187  
 McIntosh, F. G., 183  
 Meguro, T., 40, 136, 240  
 Misawa, S., 240  
 More, K. L., 244  
 Myers, A. F., 59  
 Nagasawa, H., 230  
 Nahory, R. E., 26  
 Nakamoto, I., 120  
 Namba, S., 120  
 Niinistö, L., 130, 288  
 Nishi, K., 47  
 Nishizawa, J.-I., 1  
 Norris, P. E., 105  
 Nykänen, E., 288  
 Obitsu, T., 82  
 Oda, S., 284  
 Ohsawa, F., 82  
 Oyama, Y., 1  
 Ozasa, K., 40  
 Pan, N., 64  
 Pesek, A., 265, 270  
 Picraux, T., 177  
 Powell, A. R., 163  
 Pudensi, M. A. A., 26  
 Qian, R., 177  
 Quinn, W. E., 26  
 Randall, J. N., 99  
 Rawles, R. E., 212  
 Reid, K. G., 59  
 Ritala, M., 288  
 Rowland, L. B., 219  
 Saarihahti, J., 296  
 Sakai, K., 284  
 Sakaki, H., 47  
 Sakaue, H., 124  
 Sakuma, E., 240  
 Sakuraba, H., 1  
 Salzman, J., 91  
 Schwarz, S. A., 26  
 Seabaugh, A. C., 99  
 Sedgwick, T. O., 163  
 Shingubara, S., 124  
 Shinmura, K., 120  
 Simko, J. P., 40  
 Sitar, Z., 244  
 Sitter, H., 250, 265, 270  
 Soininen, P., 288  
 Struck, L. M., 203  
 Sugano, T., 40  
 Sugiura, O., 168  
 Sumakeris, J. J., 219, 244  
 Suntola, T., 96, 280  
 Sutcu, L. F., 203  
 Tabata, H., 275  
 Takahashi, K., 256  
 Takemura, Y., 256  
 Tamargo, M., 26  
 Tanaka, H., 26  
 Tanaka, S., 219  
 Tasch, A., 177  
 Taylor, P. A., 196  
 Tempelhoff, K., 86

Thomas, S., 177  
Tsu, R., 191

Usui, A., 47, 53

Wallace, R. M., 196  
Wang, K. L., 235  
Weinberg, W. H., 196  
Wolfson, R. G., 261

Yamaga, S., 78  
Yamaguchi, Y., 230  
Yamamoto, J., 124  
Yamamoto, Y., 136  
Yamasaki, K., 256  
Yang, Y. L., 155, 203  
Yates, Jr, J. T., 140, 150, 196  
Ylilammi, M., 296  
Yoder, M. N., 145  
Yoshida, S., 240

Yoshikawa, A., 78  
Yoshimoto, M., 70  
Yoshino, J., 74  
Yoshinobi, T., 225  
Yu, M. L., 7

Zajicek, H., 270  
Zama, H., 284  
Zawadzki, P. A., 105

## Subject Index of Volume 225

- Aluminium arsenide
  - atomic layer epitaxy of AlAs and  $\text{Al}_x\text{Ga}_{1-x}\text{As}$  for device application, 109
  - atomic layer epitaxy of AlAs and  $(\text{AlAs})_n(\text{GaAs})_n$ , 74
- Aluminium oxide
  - layered tantalum–aluminum oxide films deposited by atomic layer epitaxy, 296
- Arsenic
  - atomic layer doping for Si, 163
- Atomic beam studies
  - atomic H: a reagent for the extraction of chemical species from Si surfaces, 150
  - atomic layer epitaxy of Si using atomic H, 168
  - group IV atomic layer epitaxy, 145
- Auger electron spectroscopy
  - comparison of  $\text{Cl}_2$  and  $\text{HCl}$  adsorption on  $\text{Si}(100) - (2 \times 1)$ , 140
  - microscopic mechanisms of accurate layer-by-layer growth of  $\beta\text{-SiC}$ , 240
- Cadmium selenide
  - self-limiting monolayer epitaxy of wide gap II–VI superlattices, 270
- Cadmium sulphide
  - cost-effective processing by atomic layer epitaxy, 96
- Cadmium telluride
  - growth and characterization of CdTe, HgTe and HgCdTe by atomic layer epitaxy, 261
  - growth and characterization of CdTe–ZnTe short-period superlattices, 265
  - ultra high vacuum atomic layer epitaxy of CdTe, 250
- Carbon
  - atomic layer epitaxy of AlAs and  $(\text{AlAs})_n(\text{GaAs})_n$ , 74
  - group IV atomic layer epitaxy, 145
- Catalysis
  - analytical and chemical techniques in the study of surface species in atomic layer epitaxy, 280
- Chemical beam epitaxy
  - laser-assisted atomic layer epitaxy of GaP in chemical beam epitaxy, 70
- Chemical vapour deposition
  - atomic layer doping for Si, 163
  - atomic layer epitaxy for resonant tunneling devices, 99
  - atomic layer epitaxy of 3C–SiC by low pressure vapour deposition with alternating gas supply, 230
  - atomic layer epitaxy of AlAs and  $\text{Al}_x\text{Ga}_{1-x}\text{As}$  for device application, 109
- GaAs/AlGaAs atomic layer epitaxy in a commercial MOCVD reactor, 105
  - growth and characterization of CdTe, HgTe and HgCdTe by atomic layer epitaxy, 261
  - silicon monolayer growth using dichlorosilane and hydrogen in a near atmospheric pressure chemical vapor deposition reactor, 183
  - wavelength dependence of photoenhanced organometallic chemical vapor deposition, 91
- Chemisorption
  - novel method for chemical vapor deposition and atomic layer epitaxy using radical chemistry, 212
- Diamond
  - chemistry of hydrogen on diamond (100), 203
  - novel method for chemical vapor deposition and atomic layer epitaxy using radical chemistry, 212
- Diffusion
  - conditions for light-induced short-time growth of GaAs and InP by chloride epitaxy, 86
- Electron energy loss spectroscopy
  - comparison of  $\text{Cl}_2$  and  $\text{HCl}$  adsorption on  $\text{Si}(100) - (2 \times 1)$ , 140
  - $\text{Si}_2\text{H}_6$  adsorption and dissociation pathways on  $\text{Ge}(001)2 \times 1$ : mechanisms for heterogeneous atomic layer epitaxy, 191
- Electronic devices
  - Si heterojunction diodes with a thin  $\beta\text{-SiC}$  layer prepared with gas layer source molecular beam epitaxy, 235
- Epitaxy
  - self-limiting growth on zinc chalcogenides and their superlattices, 256
- Etching
  - atomic layer manipulation of III–V compounds, 120
  - digital etching study and fabrication of fine Si lines and dots, 124
  - dopants on  $\text{Si}(100)$  surfaces: useful probes of silicon atomic layer epitaxy?, 160
  - surface processes in digital etching of GaAs, 136
- Fourier transform infrared spectroscopy
  - analytical and chemical techniques in the study of surface species in atomic layer epitaxy, 280
- Gallium arsenide
  - atomic layer epitaxy for resonant tunneling devices, 99
  - atomic layer manipulation of III–V compounds, 120
  - conditions for light-induced short-time growth of GaAs and InP by chloride epitaxy, 86
  - GaAs/AlGaAs atomic layer epitaxy in a commercial MOCVD reactor, 105
  - growth and characterization of device quality GaAs produced by laser-assisted atomic layer epitaxy using triethylgallium, 115
  - in situ* monitoring and control of atomic layer epitaxy by surface photo-absorption, 32
  - in situ* optical characterization of GaAs and InP surfaces during chloride atomic layer epitaxy, 47
  - molecular layer epitaxy of GaAs, 1
  - real-time optical diagnostics for measuring and controlling epitaxial growth, 26
  - study of photocatalytic growth-rate enhancement in MOMBE of GaAs on ZnSe by surface photoabsorption, 78
  - study of self-limiting growth mechanism in chloride ALE, 53
  - study of surface reactions in atomic layer epitaxy of GaAs using trimethylgallium by reflectance difference spectroscopy and mass spectroscopy, 12
  - surface chemistry and kinetics of GaAs atomic layer epitaxy, 17
  - surface photo-absorption study of the laser-assisted atomic layer epitaxial growth process of GaAs, 40
  - surface processes in digital etching of GaAs, 136
  - wavelength dependence of photoenhanced organometallic chemical vapor deposition, 91

- Gallium nitride
  - layer-by-layer epitaxial growth of GaN at low temperatures, 244
- Gallium phosphide
  - laser-assisted atomic layer epitaxy of GaP in chemical beam epitaxy, 70
- Gallium selenide
  - impact of short exposure times on the ALE self-limiting process: potential mechanisms, 59
- Germanium
  - chemisorption and reaction of  $\text{GeCl}_4$  with Si(100), 187
- High energy electron diffraction
  - atomic layer control of the growth of oxide superconductors using laser molecular beam epitaxy, 275
  - atomic layer epitaxy controlled by surface superstructures in SiC, 225
  - self-limiting adsorption and in situ optical monitoring for atomic layer epitaxy of oxide superconductors, 284
  - Si atomic layer epitaxy based on  $\text{Si}_2\text{H}_6$  and remote He plasma bombardment, 177
  - $\text{Si}_2\text{H}_6$  adsorption and dissociation pathways on  $\text{Ge}(001)2 \times 1$ : mechanisms for heterogeneous atomic layer epitaxy, 191
  - ultra high vacuum atomic layer epitaxy of CdTe, 250
- Hydrocarbons
  - hydrocarbon surface chemistry on Si(100), 196
- Impurities
  - potential Si atomic layer epitaxy processes using halogenated Si precursors, 173
- Indium arsenide
  - in situ* monitoring and control of atomic layer epitaxy by surface photo-absorption, 32
- Indium phosphide
  - atomic layer epitaxy of InP using trimethylindium and tertiarybutylphosphine, 64
  - conditions for light-induced short-time growth of GaAs and InP by chloride epitaxy, 86
  - determining lattice mismatch or the composition of a single ultra thin GaInAs layer grown in InP, 82
  - in situ* monitoring and control of atomic layer epitaxy by surface photo-absorption, 32
  - in situ* optical characterization of GaAs and InP surfaces during chloride atomic layer epitaxy, 47
- Infrared spectroscopy
  - chemistry of hydrogen on diamond (100), 203
- Ion bombardment
  - atomic layer manipulation of III-V compounds, 120
  - digital etching study and fabrication of fine Si lines and dots, 124
- Laser ablation
  - atomic layer control of the growth of oxide superconductors using laser molecular beam epitaxy, 275
- Laser irradiation
  - growth and characterization of device quality GaAs produced by laser-assisted atomic layer epitaxy using triethylgallium, 115
  - study of photocatalytic growth-rate enhancement in MOMBE of GaAs on ZnSe by surface photoabsorption, 78
  - surface photo-absorption study of the laser-assisted atomic layer epitaxial growth process of GaAs, 40
  - wavelength dependence of photoenhanced organometallic chemical vapor deposition, 91
- Low energy electron diffraction
  - hydrocarbon surface chemistry on Si(100), 196
  - microscopic mechanisms of accurate layer-by-layer growth of  $\beta$ -SiC, 240
- Luminescence
  - determining lattice mismatch or the composition of a single ultra thin GaInAs layer grown in InP, 82
- Mercury telluride
  - growth and characterization of CdTe, HgTe and HgCdTe by atomic layer epitaxy, 261
- Metal-organics
  - laser-assisted atomic layer epitaxy of GaP in chemical beam epitaxy, 70
- Molecular beam epitaxy
  - atomic layer control of the growth of oxide superconductors using laser molecular beam epitaxy, 275
  - atomic layer epitaxy controlled by surface superstructures in SiC, 225
  - atomic layer epitaxy of Si using atomic H, 168
  - self-limiting growth on zinc chalcogenides and their superlattices, 256
  - Si heterojunction diodes with a thin  $\beta$ -SiC layer prepared with gas layer source molecular beam epitaxy, 235
- Molecular beam studies
  - atomic H: a reagent for the extraction of chemical species from Si surfaces, 150
  - group IV atomic layer epitaxy, 145
- Molybdenum
  - group IV atomic layer epitaxy, 145
- Monolayers
  - atomic layer epitaxy for resonant tunneling devices, 99
  - atomic layer epitaxy of 3C-SiC by low pressure vapour deposition with alternating gas supply, 230
  - atomic layer epitaxy of AlAs and  $\text{Al}_x\text{Ga}_{1-x}\text{As}$  for device application, 109
  - atomic layer epitaxy of AlAs and  $(\text{AlAs})_n(\text{GaAs})_n$ , 74
  - atomic layer epitaxy of InP using trimethylindium and tertiarybutylphosphine, 64
  - atomic layer epitaxy of Si using atomic H, 168
  - atomic layer epitaxy: chemical opportunities and challenges, 130
  - atomic layer manipulation of III-V compounds, 120
  - chemisorption and reaction of  $\text{GeCl}_4$  with Si(100), 187
  - cost-effective processing by atomic layer epitaxy, 96
  - dopants on Si(100) surfaces: useful probes of silicon atomic layer epitaxy?, 160
  - GaAs/AlGaAs atomic layer epitaxy in a commercial MOCVD reactor, 105
  - group IV atomic layer epitaxy, 145
  - growth and characterization of CdTe, HgTe and HgCdTe by atomic layer epitaxy, 261
  - growth and characterization of device quality GaAs produced by laser-assisted atomic layer epitaxy using triethylgallium, 115
  - impact of short exposure time on the ALE self-limiting process: potential mechanisms, 59
  - layer-by-layer epitaxial growth of GaN at low temperatures, 244
  - model for the atomic layer epitaxy of GaAs, 7
  - molecular layer epitaxy of GaAs, 1
  - potential Si atomic layer epitaxy processes using halogenated Si precursors, 173
  - real-time optical diagnostics for measuring and controlling epitaxial growth, 26

- self-limiting monolayer epitaxy of wide gap II–VI superlattice, 270
- Si atomic layer epitaxy based on  $\text{Si}_2\text{H}_6$  and remote He plasma bombardment, 177
- silicon monolayer growth using dichlorosilane and hydrogen in a near atmospheric pressure chemical vapor deposition reactor, 183
- study of photocatalytic growth-rate enhancement in MOMBE of GaAs on ZnSe by surface photoabsorption, 78
- study of self-limiting growth mechanism in chloride ALE, 53
- study of surface reactions in atomic layer epitaxy of GaAs using trimethylgallium by reflectance difference spectroscopy and mass spectroscopy, 12
- surface processes in digital etching of GaAs, 136
- surface chemistry and kinetics of GaAs atomic layer epitaxy, 17
- ultra high vacuum atomic layer epitaxy of CdTe, 250
- Multilayers
  - atomic layer epitaxy: chemical opportunities and challenges, 130
  - layered tantalum–aluminum oxide films deposited by atomic layer epitaxy, 296
- Nuclear magnetic resonance
  - analytical and chemical techniques in the study of surface species in atomic layer epitaxy, 280
- Oxides
  - atomic layer control of the growth of oxide superconductors using laser molecular beam epitaxy, 275
  - atomic layer epitaxy: chemical opportunities and challenges, 130
  - self-limiting adsorption and *in situ* optical monitoring for atomic layer epitaxy of oxide superconductors, 284
- Photo-processes
  - laser-assisted atomic layer epitaxy of GaP in chemical beam epitaxy, 70
- Plasma processing and deposition
  - Si atomic layer epitaxy based on  $\text{Si}_2\text{H}_6$  and remote He plasma bombardment, 177
- Quantum effects
  - atomic layer epitaxy for resonant tunneling devices, 99
  - atomic layer epitaxy of AlAs and  $\text{Al}_x\text{Ga}_{1-x}\text{As}$  for device application, 109
  - determining lattice mismatch or the composition of a single ultra thin GaInAs layer grown in InP, 82
- Raman scattering
  - novel method for chemical vapor deposition and atomic layer epitaxy using radical chemistry, 212
- Reflection spectroscopy
  - in situ* monitoring and control of atomic layer epitaxy by surface photo-absorption, 32
  - in situ* optical characterization of GaAs and InP surfaces during chloride atomic layer epitaxy, 47
  - real-time optical diagnostics for measuring and controlling epitaxial growth, 26
  - study of surface reactions in atomic layer epitaxy of GaAs using trimethylgallium by reflectance difference spectroscopy and mass spectroscopy, 12
  - surface photo-absorption study of the laser-assisted atomic layer epitaxial growth process of GaAs, 40
- Rutherford backscattering spectroscopy
  - growth of titanium dioxide thin films by atomic layer epitaxy, 288
- Secondary ion mass spectrometry
  - growth and characterization of device quality GaAs produced by laser-assisted atomic layer epitaxy using triethylgallium, 115
- Segregation
  - atomic layer doping for Si, 163
- Semiconductors
  - layer-by-layer growth of SiC at low temperatures, 219
- Silicon
  - atomic H: a reagent for the extraction of chemical species from Si surfaces, 150
  - atomic layer doping for Si, 163
  - atomic layer epitaxy of Si using atomic H, 168
  - comparison of  $\text{Cl}_2$  and HCl adsorption on  $\text{Si}(100) - (2 \times 1)$ , 140
  - digital etching study and fabrication of fine Si lines and dots, 124
  - dopants on  $\text{Si}(100)$  surfaces: useful probes of silicon atomic layer epitaxy?, 160
  - hydrocarbon surface chemistry on  $\text{Si}(100)$ , 196
  - Hydrogen–halogen chemistry on semiconductor surfaces, 155
  - potential Si atomic layer epitaxy processes using halogenated Si precursors, 173
  - Si atomic layer epitaxy based on  $\text{Si}_2\text{H}_6$  and remote He plasma bombardment, 177
  - $\text{Si}_2\text{H}_6$  adsorption and dissociation pathways on  $\text{Ge}(001)2 \times 1$ : mechanisms for heterogeneous atomic layer epitaxy, 191
  - silicon monolayer growth using dichlorosilane and hydrogen in a near atmospheric pressure chemical vapor deposition reactor, 183
- Silicon carbide
  - atomic layer epitaxy controlled by surface superstructures in SiC, 225
  - atomic layer epitaxy of 3C–SiC by low pressure vapour deposition with alternating gas supply, 230
  - layer-by-layer growth of SiC at low temperatures, 219
  - microscopic mechanisms of accurate layer-by-layer growth of  $\beta$ -SiC, 240
  - Si heterojunction diodes with a thin  $\beta$ -SiC layer prepared with gas layer source molecular beam epitaxy, 235
- Superconductivity
  - self-limiting adsorption and *in situ* optical monitoring for atomic layer epitaxy of oxide superconductors, 284
- Superlattices
  - atomic layer epitaxy of AlAs and  $(\text{AlAs})_n(\text{GaAs})_n$ , 74
  - growth and characterization of CdTe–ZnTe short-period superlattices, 265
  - self-limiting growth on zinc chalcogenides and their superlattices, 256
  - self-limiting monolayer epitaxy of wide gap II–VI superlattices, 270
- Surface composition
  - model for the atomic layer epitaxy of GaAs, 7
  - molecular layer epitaxy of GaAs, 1
  - silicon monolayer growth using dichlorosilane and hydrogen in a near atmospheric pressure chemical vapor deposition reactor, 183
  - surface chemistry and kinetics of GaAs atomic layer epitaxy, 17
- Surface energy
  - hydrogen–halogen chemistry on semiconductor surfaces, 155

## Surface processes

- laser-assisted atomic layer epitaxy of GaP in chemical beam epitaxy, 70

## Tantalum

- layered tantalum–aluminum oxide films deposited by atomic layer epitaxy, 296

## Thermal desorption

- atomic H: a reagent for the extraction of chemical species from Si surfaces, 150
- chemistry of hydrogen on diamond (100), 203
- comparison of  $\text{Cl}_2$  and HCl adsorption on  $\text{Si}(100) - (2 \times 1)$ , 140
- hydrocarbon surface chemistry on  $\text{Si}(100)$ , 196
- hydrogen–halogen chemistry on semiconductor surfaces, 155
- impact of short exposure time on the ALE self-limiting process: potential mechanisms, 59
- model for the atomic layer epitaxy of GaAs, 7
- study of self-limiting growth mechanism in chloride ALE, 53
- surface chemistry and kinetics of GaAs atomic layer epitaxy, 17

## Titanium oxide

- cost-effective processing by atomic layer epitaxy, 96

- growth of titanium dioxide thin films by atomic layer epitaxy, 288

## Transmission electron microscopy

- layer-by-layer epitaxial growth of GaN at low temperatures, 244

## X-Ray diffraction

- determining lattice mismatch or the composition of a single ultra thin GaInAs layer grown in InP, 82
- growth and characterization of CdTe–ZnTe short-period superlattices, 265
- growth of titanium dioxide thin films by atomic layer epitaxy, 288
- self-limiting monolayer epitaxy of wide gap II–VI superlattice, 270

## X-Ray photoelectron spectroscopy

- atomic layer epitaxy of InP using trimethylindium and tertiarybutylphosphine, 64
- chemisorption and reaction of  $\text{GeCl}_4$  with  $\text{Si}(100)$ , 187

## Zinc selenides

- study of photocatalytic growth-rate enhancement in MOMBE of GaAs on ZnSe by surface photoabsorption, 78

---

SEND FOR A FREE SAMPLE COPY...

---

# PROGRESS IN CRYSTAL GROWTH AND CHARACTERIZATION OF MATERIALS

Editor-in-Chief: **J. BRIAN MULLIN**, *"The Hoo", Brockhill Road, West Malvern, Worcs WR14 4DL, UK*

Associate Editors: **CLAUDE SCHWAB**, *Centre de Recherches Nucleaires, Université Louis Pasteur, G.R.P.M., 23 Rue du Loess, 67037 Strasbourg Cedex, France*, **P KRISHNA**, *Department of Physics, Banaras Hindu University, Varanasi 221 005, India* and **N B SINGH**, *Westinghouse Electric Corporation, 1310 Beulah Road, Pittsburgh, PA 15235, USA*

Advances in the techniques of growing and assessing ever more perfect crystals of a wide range of materials lie at the roots of much of today's advanced technology. The literature of crystal growth is expanding faster than almost any comparable field of science.

Crystal growth and characterization (or assessment) is of vital interest to many scientists in industry and in universities. The journal covers all aspects of crystal growth and characterization including crystals of semiconductors and electronic materials, oxides, synthetic minerals, magnetic and optical crystals, organic crystals and metals. Topics in eutectics, thin film and theory of crystal growth are included and also methods of assessing crystal perfection and purity.

This journal carries full review articles, state-of-the-art reports, reviews of important new publications and lists of forthcoming meetings in the field of crystal growth and characterization.

## A Selection of Papers

**J. A. NEFF** (USA), The need for nonlinear optical materials.

**L. K. CHENG, W. R. BOSENBERG & C. L. TANG** (USA), Growth and characterization of nonlinear optical crystals suitable for frequency conversion.

**D. EIMERL, S. VELSKO, L. DAVIS, & F. WANG** (USA), Progress in nonlinear optical materials for high power lasers.

**R. S. FEIGELSON, R. J. RAYMAKERS & R. K ROUTE** (USA), Growth of nonlinear crystals for frequency conversion.

**N. B. SINGH, T. HENNINGSEN, Z. K. KUN, K. C. YOO, R. H. HOPKINS & R. MAZELSKY** (USA), Growth and characterization of thallium arsenic selenide crystals for nonlinear optical applications.

**Indexed/Abstracted in:** *Current Contents, Chemical Abstracts, INSPEC, Cam Sci Abstr, Materials Science Citation Index*

(00492)

## Subscription Information

1993: Volumes 26 & 27 (8 issues)

Annual subscription (1993)

£550.00

US\$1045.00\*

ISSN: 0146-3535



## PERGAMON PRESS

Pergamon Press Ltd, Headington Hill Hall, Oxford OX3 0BW, UK

Pergamon Press Inc., 660 White Plains Road, Tarrytown, NY 10591-5153, USA

*A member of the Elsevier Science Publishing Group*

First price quoted is definitive. Prices include postage and insurance. \* Asterisked price is quoted for convenience only and is subject to exchange rate fluctuation.

---

---

SEND FOR A FREE SAMPLE COPY OF...

---

# PROGRESS IN QUANTUM ELECTRONICS

AN INTERNATIONAL REVIEW JOURNAL

Executive Editor: **P. T. LANDSBERG**, *Faculty of Mathematical Studies, University of Southampton, Highfield, Southampton, SO9 5NH, UK*

North American Editor: **M. OSINSKI**, *Center for High Technology Materials, University of New Mexico, Albuquerque, NM 87131-6081, USA*

*Progress in Quantum Electronics* covers a diverse collection of topics, many of which now have well established technological applications but all of which contain a wide variety of problems and techniques in the realm of pure science. It is mainly concerned with the broad field of interaction of radiation and matter, e.g. in lasers or photodetectors, but also includes solid state topics such as superconductivity and quantum effects in semiconductors.

## A Selection of Recent Reviews

**E. O. GÖBEL & K. PLOOG** (Germany), Fabrication and optical properties of semiconductor quantum wells and superlattices.

**T. IMASAKA & N. ISHIBASHI** (Japan), Analytical techniques using lasers.

**A. ROGALSKI** (Poland),  $\text{InAs}_{1-x}\text{Sb}_x$  infrared detectors.

**K. A. SHORE & M. W. MCCALL** (UK), Nonlinear and quantum optics in semiconductor lasers.

**Indexed/Abstracted in:** *Curr Cont ASCA, Cam Sci Abstr, Chem Abstr Serv, Curr Cont Ind Sci Rev, Curr Cont Sci Cit Ind, Curr Cont SCISEARCH Data*

(00410)

## Subscription Information

1993: Volume 17 (4 issues)

Annual subscription (1993)

£195.00

US\$371.00\*

ISSN: 0079-6727



## PERGAMON PRESS

Pergamon Press Ltd, Headington Hill Hall, Oxford OX3 0BW, UK

Pergamon Press Inc., 660 White Plains Road, Tarrytown, NY 10591-5153, USA

*A member of the Elsevier Science Publishing Group*

---

First price quoted is definitive. Prices include postage and insurance. \* Asterisked price is quoted for convenience only and is subject to exchange rate fluctuation.

---



# Instructions to Authors

## MANUSCRIPT PREPARATION

Three copies of the manuscript should be submitted, in double-spaced typing on pages of uniform size with a wide margin on the left. Some flexibility of presentation will be allowed but authors are urged to arrange the subject matter clearly under such headings as Introduction, Experimental details, Results, Discussion, etc. Each paper should have an abstract of 100–200 words.

References should be numbered consecutively (numerals in square brackets) throughout the text and collected together in a reference list at the end of the paper. Journal titles should be abbreviated according to the Chemical Abstracts Service Source Index, 1970 edition, and supplements. The abbreviated title should be followed by volume number, year (in parentheses) and page number.

## Submission of Electronic Text

The final text may be submitted on a 3.5 in or 5.25 in diskette (in addition to a hard copy with original figures). Double density (DD) or high density (HD) diskettes formatted for MS-DOS or Apple Macintosh compatibility are acceptable, but must be formatted to their capacity before the files are copied on to them. The files should be saved in the native format of the wordprocessing program used. Most popular wordprocessor file formats are acceptable. It is essential that the name and version of the wordprocessing program, type of computer on which the text was prepared, and format of the text files are clearly indicated.

## Illustrations

Line drawings should be in a form suitable for reproduction, drawn in black ink on drawing paper (letter height, 3–5 mm). They should preferably all require the same

degree of reduction, and should be submitted on paper of the same size as, or smaller than, the main text to prevent damage in transit. Photographs should be submitted as clear black-and-white prints on glossy paper. Each illustration must be clearly numbered.

Legends to the illustrations must be submitted in a separate list.

All tables and illustrations should be numbered consecutively and separately throughout the paper.

## Languages

Papers will be published in English only.

## Proofs

Authors will receive proofs, which they are requested to correct and return as soon as possible. Authors should answer clearly any question in the proofs. No new material may be inserted in the text at the time of proofreading.

## Reprints

Twenty-five reprints will be supplied free of charge to the author(s). Additional reprints can be ordered at prices shown on the reprint order form which accompanies the proofs.

## Abstracting–Indexing Services

This journal is cited by the following Abstracting and/or Indexing Services.

Metal Abstracts, Chemical Abstracts, Physics Abstracts, Current Contents – Physical and Chemical Sciences, Current Contents – Engineering, Technology and Applied Sciences, Engineering Index, Cambridge Scientific Abstracts, Physikalische Berichte, Science Citation Index, Research Alert™, PASCAL (Centre National de la Recherche Scientifique), Fiz Karlsruhe.

© 1993–Elsevier Sequoia. All rights reserved

0040-6090/93/\$6.00

No part of this publication may be reproduced, stored in a retrieval system or transmitted in any form or by any means, electronic, mechanical, photocopying, recording or otherwise, without the prior written permission of the publisher, Elsevier Sequoia, S.A., P.O. Box 564, 1001 Lausanne 1, Switzerland.

Submission of an article for publication implies the transfer of the copyright from the author(s) to the publisher and entails the author(s) irrevocable and exclusive authorization of the publisher to collect any sums or considerations for copying or reproduction payable by third parties. Upon acceptance of an article by the journal, the author(s) will be asked to transfer copyright of the article to the publisher. This transfer will ensure the widest possible dissemination of information.

### For Material Subject to US Copyright Law

#### *Special regulations for readers in the USA*

This journal has been registered with the Copyright Clearance Center, Inc., 21 Congress Street, Salem, MA 01970, USA. Consent is given for copying of articles for personal use, or for the personal use of specific clients. This consent is given on the condition that the copier pays through the Center the per-copy fee stated in the code on the first page of each article for copying beyond that permitted by Sections 107 or 108 of the US Copyright Law. If no code appears in an article, the author has not given broad consent to copy and permission to copy must be obtained directly from the author. All articles published prior to 1982 may be copied for a per-copy fee of US\$2.50, also payable through the Center. This consent does not extend to other kinds of copying, such as for general distribution, resale, advertising and promotion purposes or for creating new collective works. Special written permission must be obtained from the publisher for such copying.

No responsibility is assumed by the Publisher for any injury and/or damage to persons or property as a matter of products liability, negligence or otherwise, or from any use or operation of any methods, products, instructions or ideas contained in the material herein.

---

SEND FOR A FREE SAMPLE COPY OF...

---

# PROGRESS IN SURFACE SCIENCE

AN INTERNATIONAL REVIEW JOURNAL

Editor: **SYDNEY G. DAVISON**, *Applied Mathematics Department, University of Waterloo, Ontario, Canada N2L 3G1*

Managing Editor: **W. K. LIU**, *Physics Department, University of Waterloo, Ontario, Canada N2L 3G1*

By separating matter into its three phases, surfaces (or interfaces) play a leading role in nature. As a result of this, surface science has evolved as an interdisciplinary subject, so that phenomena associated with surfaces are of fundamental interest to a wide variety of scientists. With this in mind, the *Progress in Surface Science* series publishes review articles on as wide a range of surface phenomena topics as possible.

## A Selection of Papers

**M. E. EBERHART, M. M. DONOVAN, J. M. MACLAREN & D. P. CLOUGHERTY (USA)**, Towards a chemistry of cohesion and adhesion.

**S. HOFMANN (Germany)**, Compositional depth profiling by sputtering.

**A. A. MARADUDIN, R. F. WALLIS & G. I. STEGEMAN (USA)**, The optics of surface and guided wave polaritons.

**L. K. DORAISWAMY (USA)**, Catalytic reactions and reactors: a surface science approach.

**G. S. WAS (USA)**, Ion beam modification of metals: compositional and microstructural changes.

**T. SAKURAI, T. HASHIZUME, I. KAMIYA, Y. HASEGAWA, N. SANO, H. W. PICKERING & A. SAKI (Japan)**, Field ion-scanning tunneling microscopy.

**I. P. BATRA (USA), E. TEKMAN & S. CIRACI (Turkey)**, Theory of Schottky Barrier and metallization.

**G. H. VURENS, M. SALMERON & G. A. SOMORJAI (USA)**, The preparation of thin ordered transition metal oxide films on metal single crystals for surface science studies.

**V. A. GRAZHULIS (Russia)**, Low temperature studies of semiconductor surfaces.

**A. M. BRODSKY (USA) & M. I. URBACH (Israel)**, Optical properties of microrough metal surfaces.

**Indexed/Abstracted in:** *Current Contents/Phys, Chem & Earthsci, Chemical Abstracts, Science Citation Index, Index to Scientific Rev, Engng Ind Monthly & Author Index, PASCAL/CNRS Database, INSPEC, Materials Science Citation Index*

(00411)

## Subscription Information

1993: Volumes 42 - 44 (12 issues)

Annual subscription (1993)

£360.00

US\$684.00\*

ISSN: 0079-6816



## PERGAMON PRESS

Pergamon Press Ltd, Headington Hill Hall, Oxford OX3 0BW, UK

Pergamon Press Inc., 660 White Plains Road, Tarrytown, NY 10591-5153, USA

*A member of the Elsevier Science Publishing Group*

First price quoted is definitive. Prices include postage and insurance. \* Asterisked price is quoted for convenience only and is subject to exchange rate fluctuation.